Syntheses of ternary oxyhydrates and oxides in the calcium-uranium system:

Stoichiometric influences on their structural affinity, precipitation mechanisms, and solid-state transformations

Weixuan Ding

Submitted in accordance with the requirements for the degree of
Doctor of Philosophy

The University of Leeds
School of Chemical and Process Engineering

July, 2017

The candidate confirms that the work submitted is his/her own, except where work which has formed part of jointly-authored publications has been included. The contribution of the candidate and the other authors to this work has been explicitly indicated below. The candidate confirms that appropriate credit has been given within the thesis where reference has been made to the work of others.

Acknowledgements

Firstly, I must extend my profound thanks towards Ian T. Burke (never without the T.), who has stuck with me in spite of my quirks, field-trip misfortunes, and recurrent changes of mind. Perhaps his never-ending and commendable patience is a part of Irish upbringing, or hard-earned from his years in academia. Nevertheless, his role as mentor and sincere and hearty approach to supervision has been invaluable to my continuing development as a scientist. Gratitude is also due to Bruce Hanson, for providing me with the absolute freedom to pursue and develop my own research and ideas; and in doing so, gain independence as a researcher.

I am indebted to Sven Schroeder, whose open mind and expansive knowledge of all things synchrotron helped me immeasurably in applying for beam-time and as well as designing experiments. Your views on science, research and our place in the international community has opened my mind to several future pathways.

Sin-Yuen Chang, I am forever grateful for lending me your time and deep knowledge of EXAFS and XANES modelling throughout the last two years. I have also thoroughly enjoyed our conversations on subjects ranging from the carnivorous plants (Nepenthes) native to Mount Kinabalu, to the delicious cuisines of Malaysia.

Many, many thanks are due to the technicians and staff within the department who have trained me in several analytical techniques, as well as designing experiments, or even being the saviour to my administration and bureaucracy woes. Andy Connelly, Stephen Reid, Lesley Neve, John Harrington, Mike Ward, Stuart Micklethwaite, Susanne Patel, Tim Comyn, Janet Bell, Abby Ward, Jim Young, you guys are truly the unsung heroes of this University.

With me throughout my journey, my father Yulong and mother Huixia have contributed greatly in loving support for my decisions, and to always move forwards. As sources of wisdom endless, they have enabled me to open my eyes several times from non-academic viewpoints. The inception of ideas is always difficult, and rarely does anyone remember the source. My father, the earliest source to my academic ambitions, has supported me academically throughout my life, and has given me morale at the most desperate of times. With any luck, perhaps even a speck of your immense work ethic has rubbed off on me.

To Henrieta, your outwardly calm and reserved nature has kept me calm on numerous occasions in recent years, whilst also allowing your inner bull to rant with me when in need. Thank you for your patience.

Where supervisors, academics, and family have been the source of reason and compassion, my colleague and friend Andre (never Johannes) Botha has been the

source of comedy, discussion, and truthfully, a touch of madness. Your unique quirkiness and batty nature has ensured that I keep my sanity, by learning to laugh at or shrug-off even the worst scenarios. We have failed and succeeded, laughed and ranted, and we have travelled the world. There is much yet to explore, comrade, and many sights to see.

My friends, colleagues, and office mates, thank you for sharing your knowledge, expertise, and anecdotes with me. Amongst many others, Rebecca, Mathieu, EJ, Josh, John, Nathaniel, Thoko, Ben, Rob, and Alex; your academic and moral support over the years have been priceless.

Much thanks are due to the doctors and nurses, and medical staff at the Leeds General Infirmary orthopaedic trauma, and obstetrics units, for allowing me the honour to volunteer and shadow with you all. The experiences gained there are precious, and have helped considerably in my development.

I would like to acknowledge the EPSRC, the Nuclear Decommissioning Authority, Sellafield Ltd., for their financial support; The University of Leeds, and The Diamond Light Source for allowing me to use their equipment. Without the assistance of these organisations, none of this would have been possible.

My time at the University of Leeds has brought sweat, anguish, and most of all, great happiness. The building anticipation from gathering and analysing data, contemplating trends over tar-like coffee, then either admitting defeat and returning to the laboratory, or once every so often, celebrating in ecstasy. This essence of academic research, is obsessive, unforgiving, and demanding. I would not relinquish my experiences for the world.

Abstract

Calcium uranyl(VI) oxyhydrates and uranates are structurally related U(VI)-phases featuring uranium oxo-polyhedral sheets, with calcium ions occupying the interlayer. Both coordination environments appear throughout the nuclear fuel-cycle as alteration products, colloids, and sorption complexes. However, concerted studies spanning the aqueous precipitation mechanisms of uranyl(VI) oxyhydrates, their solid-state transformations, and structural relationships with uranates, have hitherto remained largely unexplored.

A series of calcium-based uranyl(VI) oxyhydrates were precipitated via alkalisation of aqueous precursor solutions in titration and batch reactions. The bulk stoichiometric ratio of calcium to uranium (Ca/U) of precipitates was varied by modifying precursor stoichiometry, reaction temperature, or extraction pH. The rate of precipitation and its dependency on temperature was quantified in-situ using a quartz crystal microbalance. Novel insight was revealed on the mechanisms influencing nucleation and growth, by determining associated kinetic barriers as a function of precursor-Ca/U.

Remarkably, as the bulk precipitate Ca/U increased from ~⅛ to unity, there was a transition from crystalline Becquerelite to primary or secondary amorphous phases, with uranate-like coordination environments. Formation of the latter was driven by solution alkalinity, and comprises a poorly-ordered matrix with occlusions of Ca^{2+}-rich nano-clusters. A congruency limit lies Ca/U of ~1.5 Ca/U, whereupon discrete Portlandite crystallises.

Solid-state transformation of all Ca^{2+}-U(VI)-phases studied involved dehydration, dehydroxylation-decarbonation, and desorption processes. Associated kinetic barriers were catalysed by higher Ca^{2+}-contents, and was reflected by reaction enthalpies for dehydration and desorption. Crystalline Becquerelite (~⅛ Ca/U) underwent amorphisation-crystallisation via partial egress of interlayer calcium, followed by reduction of β-UO_3 to form a novel intercalation compound $Ca_{0.18}$.α-U_3O_8. The endmember uranates $Ca_3U_{11}O_{36}$, CaU_2O_7, $Ca_2U_3O_{11}$, and $CaUO_4$ crystallised from amorphous precursors with higher bulk Ca/U (~⅓, ~½, ~⅔, ~1), where $Ca_3U_{11}O_{36}$ is a novel compound that is isostructural to $(Pb/Sr)_3U_{11}O_{36}$. Nucleation and growth became predominant in the presence of Ca^{2+}-rich occlusions. A higher Ca^{2+}-loading facilitated the progressive ingress of interlayer-Ca^{2+}, inducing a concerted axial compression in uranyl(VI) oxo-polyhedra towards the uranate-like coordination environment.

Table of Contents

List of Tables

List of Figures

List of schemes and equations

Schemes

Equations

Supplementary equations

1. Introduction

2017 marks the 150th anniversary of Maria Skłodowska Curie's birth, the first female Nobel Laureate, and sole-winner in two categories. Her pioneering work in radiochemistry resulted in the discovery of polonium and radium, just 7 years after discovery of radioactivity by Henri Becquerel. Since then, several new radionuclides have been discovered, and their applications have ranged from academic curiosity, to warfare, and civil power generation. Several actinides are sourced from the nuclear fuel cycle (Figure 1.1), which begins at extraction of natural uranium from the geosphere.

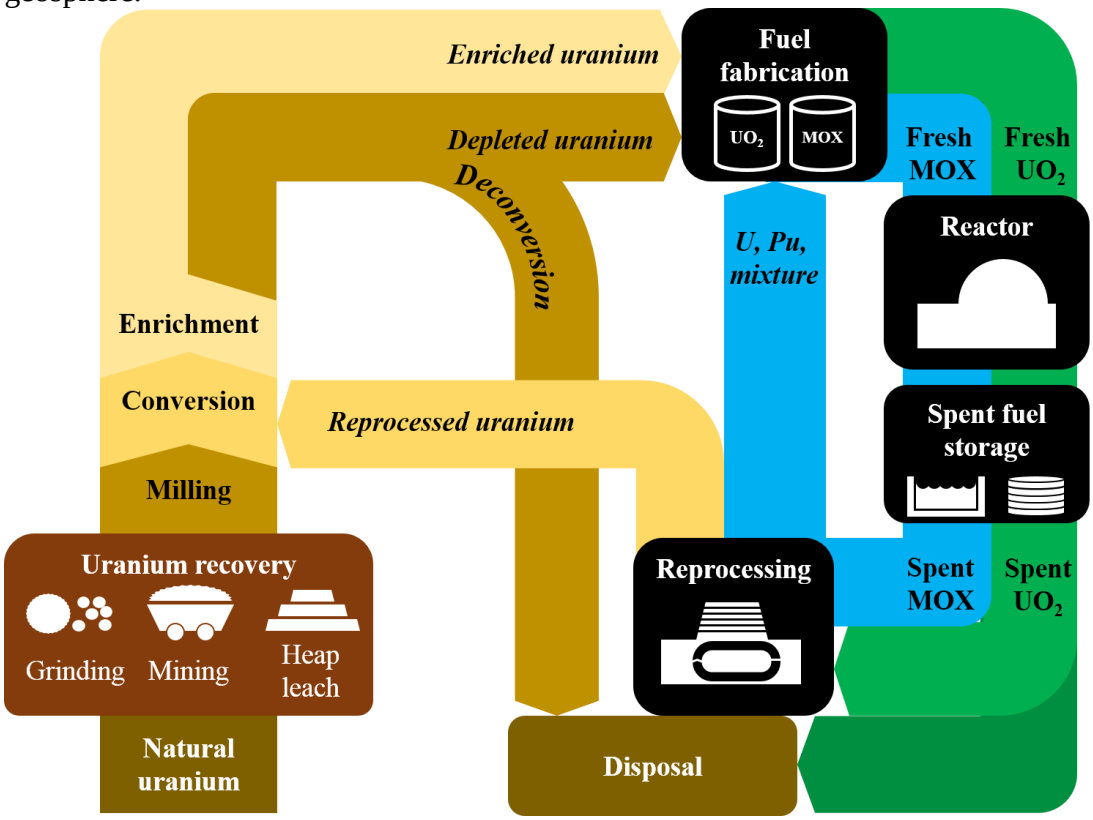

Figure 1.1 A typical nuclear fuel cycle. ***Adapted from [1].***

Uranium is mined principally from Uraninite, Coffinite or Brannerite, which consist of uranium dioxide, silicate and titanate phases. Due to numerous impurities, ores are ground, then taken through physical means of concentrating the uranium. This can included gravitational, electrostatic, or flotation methods, which rely mostly on the high density of uranium. Pre-concentration is followed by roasting or calcination to remove carbon, sulphur, and reductant impurities, where various fluxes or salts are utilised in easing subsequent extraction steps. As oxidising the uranium into the soluble +6 oxidation state is key, this porous intermediate is acid-leached to extract the uranium into an aqueous phase, drawing parallels with extraction practices for

other transition metals [2, 3]. In most cases, the uranium is recovered from aqueous phase through ion exchange, solvent extraction or direct precipitation, where practices vary by territory, and history. All three variants feature forming a high grade uranium concentration, formed through precipitation via the use of alkalising agents such as ammonia. This forms a concentrate in the form of ammonium diuranate (ADU), which may be further purified, then calcined to form the anhydrous oxides UO_3, U_3O_8. Despite the chemical differences between these intermediates, they are collectively named *Yellowcake*.

These oxide phases are subsequently calcined under NH_3 or H_2 to regenerate UO_2, which may be purified via solvent extraction, or fluoride volatility processes. The latter involves hydro-fluorinated (HF-gas) at 600 °C to form UF_4, which is followed by fluorination (F_2-gas) to form UF_6. As UF_6 sublimes at low temperature (~65 °C), this allows removal of non-volatile fluoride impurities such as silica-fluorides during distillation. However as natural uranium only contains ~0.71 % U-235, the thermally fissile isotope, enrichment of UF_6 is required via gas centrifugation, which relies upon the higher density of U-238, to separate the isotopes. The enriched faction (~3.5 % U-235) is then converted back to UO_2 via H_2/steam reformation. This low enriched UO_2 is formed into fuel pellets, and packed into fuel rods, before usage in thermal nuclear reactors. Spent fuel requires cooling in ponds due to heat stemming from radioactive decay of unstable fission products and radionuclides, which are subsequently removed during reprocessing, where some fuel is recycled whilst excess dU is dry stored in casks.

Widespread usage of thermal nuclear power, coupled with low uranium market and enrichment cost, and a lack in fast-reactor technology until at least 2030 [4] diminishes the economic case for using depleted uranium (dU, ~0.3% U-235) in power generation. This has resulted in global stockpiles of dU arising to ~1.2 million tonnes [5]. In most countries, 80% of legacy dU is stored as condensed uranium hexafluoride (UF_6) with some as UO_3, U_3O_8 and UO_2 [5]. The uranium oxides are relatively stable, whilst UF_6 is hygroscopic and reacts violently with water to form a uranyl(VI) fluoride and hydrofluoric acid (HF) aerosol [6], both of which hold considerable radio- or chemo-toxic properties. In spite of this, steel canisters of UF_6 are stored in open-air yards [7]. Furthermore, a present lack in demand for dU has resulted in its categorisation as assets of zero value [8], where interim storage or permanent disposal requires deconversion [9] into UO_2. Moving forwards, the majority of nuclear waste is expected to be entombed in engineered materials such as cement [10], clay [11] and copper within deep geological disposal facilities [12, 13]. Legacy practices stemming from a lack of understanding in the environmental implications has ensured both surface and sub-surface contamination by uranium. Whether incidental via inadequate policy-making, or accidental, this spans several

parts of the fuel cycle, namely, mining and refinement [14, 15], reprocessing [16-19], and disposal [20]. Civil power generation accidents (Chernobyl [21], Fukushima [22]) and warfare applications (exotic munitions [5, 19, 23], nuclear weapons [24]) have further confounded the issue.

The complexity of uranium chemistry and its radioactivity [25-27], is complimented by a relative dearth in past research compared to transition metals, though the search for U(VI) materials with novel chemical or structural properties [28-34] has revealed numerous compounds [26], whilst naturally occurring [35-38] and synthetic [26, 31, 32, 34, 39, 40] U(VI)-phases are still being discovered. With the exception of a few environmental [41], spectroscopic [42], or adsorption studies [43, 44] studies, two particular U(VI) sub-families uranyl(VI) oxyhydrates and uranates are segregated in the literature. The former deals almost exclusively with the oxic paragenesis of natural uraninite [45-52], or during alteration of UO_{2+x} present in contaminated industrial sites [53, 54] and battlefields [5, 19, 23, 55]. Whereas the latter is confined to post-WWII publications stemming from the Manhattan project [27, 56-59], or in more contemporary works on molten salt actinide-precipitation [60-67]. Whilst both anhydrous uranates [36, 68-70] and uranyl(VI) oxyhydrates occur naturally in addition to that expected from anthropological [41] activities, relatively little work has spanned the interface and is exacerbated by the difficulty in tailoring stoichiometry of uranates containing dipositive cations such as calcium, whereas uranyl(VI) oxyhydrates are commonly associated with Sr^{2+}/Ca^{2+} [71], Ba^{2+} [72-75], and Pb^{2+} [76, 77].

Whilst knowledge of the behaviour of uranium in the environment [52, 78-83], geosphere, and under conditions relevant to nuclear waste disposal [41, 51, 52, 84], has been improved by some understanding of general trends in the chemistry of several classes of uranyl(VI) compounds, further exploration of uranyl(VI) chemistry across the interface between solution and solid-state is crucial in improving predictive ability for future academic and industrial applications. This project marks the first integrated effort to explore U(VI)-chemistry across the solution-solid interface, with particular focus on the ternary Ca-U(VI)-O system.

1.1 Aims, objectives, and thesis layout

The principal aim, is to provide a solution-based pathway for the synthesis of uranate phases with discrete stoichiometry between calcium and uranium for further academic study and industrial applications. To realise this goal, a deeper understanding of the relationship between uranium solution and solid-state chemistry is required by addressing three key interrelated aspects; **(1)** if calcium-uranium oxides can be synthesised from simple aqueous precursors, **(2)** can precipitation be influenced by

precursor stoichiometry and temperature, and if so, **(3)** how is the structural and solid-state chemistry affected?

To this end, the thesis begins by introducing the global context and significance (Chapter 1). This is followed by a 2nd chapter (Chapter 2), which will provide a review and summary of relevant science and knowledge from the literature.

Chapter 3 introduces the experimental techniques and concepts used. Within the following three data chapters, more specific literature studies and experimental layouts such as rig-design or sampling methodology will be introduced. The experimental data, in-depth discussions, and key-conclusions are then presented in discrete sections.

The first data chapter (Chapter 4) has been adapted from a publication [85] and details a preliminary solution-based methodology for the synthesis of ternary calcium uranium oxides via a poorly-ordered precipitate. The mechanisms by which U(VI)-precipitation occurs and its solid-state processes are discussed for a single stoichiometric ratio (0.67 Ca/U).

Chapter 5 builds upon this by exploring how kinetics and mechanisms influence the formation of Ca^{2+}-U(VI)-oxyhydrate colloids; whilst also introducing the use of a novel in-situ technique for characterising the formation or aggregation of solids in solution. In particular, the influence of calcium and organic frame-working agent stoichiometry in solution on precipitation is explored.

Chapter 6 expands on the narrative of Ca/U-stoichiometry, by providing an in-depth study of solid-state amorphisation and crystallisation processes for calcium uranyl(VI) oxyhydrates. The effects of frame-working agent degradation and dehydration on local coordination chemistry, and localised structural relationships of crystalline endmembers are revealed.

1.2 References

1. Evans, G.J., *Eliminating Nuclear Threats: A Practical Agenda for Global Policymakers.* Survival, 2010. **52**(2): p. 209-216.
2. Bruen, C.P., Low, W.W., and Smalley, E.W., *Process for the Production of Sodium Chromate from Chromite Ore*, U.S. Patent, Editor. 1974, Allied Chemical Corporation: USA.
3. Burke, T., Fagliano, J., Goldoft, M., Hazen, R.E., Iglewicz, R., and McKee, T., *Chromite Ore Processing Residue in Hudson County, New Jersey.* Environmental Health Perspectives, 1991. **92**: p. 131-137.
4. OECD, *Technology Roadmap Update for Generation Iv Nuclear Energy Systems*. 2014, OECD.
5. OECD, *Management of Depleted Uranium: A Joint Report by the Oecd Nuclear Energy Agency and the International Atomic Energy Agency*. 2001, Organisation for Economic Co-operation and Development: France.
6. Sullivan, R. *Have There Been Accidents Involving Uranium Hexafluoride?* ; Available from: http://web.ead.anl.gov/uranium/faq/health/faq30.cfm.
7. Office for Nuclear Regulation, *Urenco Uk Ltd.* 2009.
8. NDA, *Strategy: Effective from April 2011*. 2011: UK.

9. Roach, A.M., *Consideration of Safeguards Requirements During the Design of the Urenco Tails Management Facility*. 2010, International Atomic Energy Agency.
10. Bamforth, P., Baston, G., Berry, J., Glasser, F., Heath, T., Jackson, C., Savage, D., and Swanton, S., *Cement Materials for Use as Backfill, Sealing and Structural Materials in Geological Disposal Concepts, a Review of Current Status*. 2012, Serco Report SERCO/005125/001 Issue 3.
11. Alexander, W.R., Milodowski, A.E., Pitty, A.F., Hardie, S.M.L., Kemp, S.J., Korkeakoski, P., Rigas, M., Rushton, J.C., Sellin, P., and Tweed, C.J., *Reaction of Bentonite in Low-Alkali Cement Leachates: An Overview of the Cyprus Natural Analogue Project (Cnap).* Mineralogical Magazine, 2012. **76**(8): p. 3019-3022.
12. Hicks, T.W., Watson, S., Norris, S., Towler, G., Reedha, D., Paulley, A., Baldwin, T., and Bond, A.E., *Interactions between the Co-Located Intermediate-Level Waste/Low-Level Waste and High-Level Waste/Spent Fuel Compunents of a Geological Disposal Facility*. 2012, Mineralogical Magazine. p. 3475-3482.
13. Environment, G.B.D.f., Affairs, R., Environment, D.f., Food, Staff, R.A., Business, G.B.D.f., Enterprise, and Reform, R., *Managing Radioactive Waste Safely: A Framework for Implementing Geological Disposal*. Vol. 7386. 2008: The Stationery Office.
14. Landa, E.R. and Gray, J.R., *Us Geological Survey Research on the Environmental Fate of Uranium Mining and Milling Wastes.* Environmental Geology, 1995. **26**(1): p. 19-31.
15. Au, W.W., McConnell, M.A., Wilkinson, G.S., Ramanujam, V.M.S., and Alcock, N., *Population Monitoring: Experience with Residents Exposed to Uranium Mining/Milling Waste.* Mutation Research/Fundamental and Molecular Mechanisms of Mutagenesis, 1998. **405**(2): p. 237-245.
16. Chamberlain, A.C., *Emissions from Sellafield and Activities in Soil.* Science of The Total Environment, 1996. **177**(1): p. 259-280.
17. Baker, R.J., *Uranium Minerals and Their Relevance to Long Term Storage of Nuclear Fuels.* Coordination Chemistry Reviews, 2014. **266–267**(0): p. 123-136.
18. Jones, S.R., Willans, S.M., Smith, A.D., Cawse, P.A., and Baker, S.J., *Deposition of Actinides in the Vicinity of Sellafield, Cumbria: Accounting for Historical Discharges to Atmosphere from the Plant.* Science of The Total Environment, 1996. **183**(3): p. 213-229.
19. Hamilton, E.I., *Depleted Uranium (Du): A Holistic Consideration of Du and Related Matters.* Science of The Total Environment, 2001. **281**(1–3): p. 5-21.
20. Small, J., Lennon, C., Kwong, S., and Scott, R. *Development and Validation of a Model of Uranium Release to Groundwater from Legacy Disposals at the Uk Low Level Waste Repository*. in *MRS Proceedings*. 2008. Cambridge Univ Press.
21. Abagyan, A., Asmolov, V., and Gusikova, A., *The Information on the Chernobyl Accident and Its Consequences, Prepared for Iaea.* At Energ, 1986. **3**(5).
22. Shinonaga, T., Steier, P., Lagos, M., and Ohkura, T., *Airborne Plutonium and Non-Natural Uranium from the Fukushima Dnpp Found at 120 Km Distance a Few Days after Reactor Hydrogen Explosions.* Environmental science & technology, 2014. **48**(7): p. 3808-3814.
23. Salbu, B., Janssens, K., Lind, O., Proost, K., Gijsels, L., and Danesi, P., *Oxidation States of Uranium in Depleted Uranium Particles from Kuwait.* Journal of Environmental Radioactivity, 2004. **78**(2): p. 125-135.
24. Duff, M.C., Mason, C.F., and Hunter, D.B., *Comparison of Acid and Base Leach for the Removal of Uranium from Contaminated Soil and Catch-Box Media.* Canadian journal of soil science, 1998. **78**(4): p. 675-683.
25. Gorman-Lewis, D., Burns, P.C., and Fein, J.B., *Review of Uranyl Mineral Solubility Measurements.* The Journal of Chemical Thermodynamics, 2008. **40**(3): p. 335-352.
26. Krivovichev, S., Burns, P., and Tananaev, I., *Structural Chemistry of Inorganic Actinide Compounds*. 2006: Elsevier.
27. Morss, L.R., Edelstein, N.M., Fuger, J., and Katz, J.J., *The Chemistry of the Actinide and Transactinide Elements (Volumes 1-5): Vol. 1*. Vol. 1. 2007: Springer.
28. Locock, A.J. and Burns, P.C., *The Crystal Structure of Triuranyl Diphosphate Tetrahydrate.* Journal of Solid State Chemistry, 2002. **163**(1): p. 275-280.
29. Krivovichev, S., Cahill, C., and Burns, P., *Syntheses and Crystal Structures of Two Topologically Related Modifications of* $Cs_2[(Uo_2)_2(Moo_4)_3]$. Inorganic chemistry, 2002. **41**(1): p. 34-39.
30. Krivovichev, S.V. and Burns, P.C., *Crystal Chemistry of Rubidium Uranyl Molybdates: Crystal Structures of* $Rb_6[(Uo_2)(Moo_4)_4]$, $Rb_6[(Uo_2)_2o(Moo_4)_4]$, $Rb_2[(Uo_2)(Moo_4)_2]$, $Rb_2[(Uo_2)_2(Moo_4)_3]$ *and* $Rb_2[(Uo_2)_6(Moo_4)_7(H_2o)_2]$. Journal of Solid State Chemistry, 2002. **168**(1): p. 245-258.

31. Krivovichev, S.V., Kahlenberg, V., Kaindl, R., Mersdorf, E., Tananaev, I.G., and Myasoedov, B.F., *Nanoscale Tubules in Uranyl Selenates.* Angewandte Chemie, 2005. **117**(7): p. 1158-1160.
32. Krivovichev, S.V., Kahlenberg, V., Tananaev, I.G., Kaindl, R., Mersdorf, E., and Myasoedov, B.F., *Highly Porous Uranyl Selenate Nanotubules.* Journal of the American Chemical Society, 2005. **127**(4): p. 1072-1073.
33. Almond, P.M., McKee, M.L., and Albrecht‐Schmitt, T.E., *Unusual Uranyl Tellurites Containing $[Te_2O_6]^{4-}$ Ions and Three‐Dimensional Networks.* Angewandte Chemie International Edition, 2002. **41**(18): p. 3426-3429.
34. Burns, P.C., Kubatko, K.A., Sigmon, G., Fryer, B.J., Gagnon, J.E., Antonio, M.R., and Soderholm, L., *Actinyl Peroxide Nanospheres.* Angewandte Chemie International Edition, 2005. **44**(14): p. 2135-2139.
35. Ondrus, P., Skála, R., Veselovsky, F., Sejkora, J., and Vitti, C., *Cejkaite, the Triclinic Polymorph of $Na_4(UO_2)(CO_3)_3$—a New Mineral from Jáchymov, Czech Republic.* American Mineralogist, 2003. **88**(4): p. 686-693.
36. Finch, R.J. and Ewing, R.C., *Clarkeite: New Chemical and Structural Data.* American Mineralogist, 1997. **82**(5-6): p. 607-619.
37. Galuskin, E.V., Armbruster, T., Galuskina, I.O., Lazic, B., Winiarski, A., Gazeev, V.M., Dzierżanowski, P., Zadov, A.E., Pertsev, N.N., and Wrzalik, R., *Vorlanite (Cau^{6+})O_4—a New Mineral from the Upper Chegem Caldera, Kabardino-Balkaria, Northern Caucasus, Russia.* American Mineralogist, 2011. **96**(1): p. 188-196.
38. Galuskin, E.V., Galuskina, I.O., Dubrovinsky, L.S., and Janeczek, J., *Thermally Induced Transformation of Vorlanite to "Protovorlanite": Restoration of Cation Ordering in Self-Irradiated $Cauo_4$.* American Mineralogist, 2012. **97**(5-6): p. 1002-1004.
39. Miller, M.L., Finch, R.J., Burns, P.C., and Ewing, R.C., *Description and Classification of Uranium Oxide Hydrate Sheet Anion Topologies.* Journal of Materials Research, 1996. **11**(12): p. 3048-3056.
40. Glatz, R.E., Li, Y., Hughes, K.-A., Cahill, C.L., and Burns, P.C., *Synthesis and Structure of a New Ca Uranyl Oxide Hydrate, $Ca[(UO_2)_4O_3(OH)_4](H_2O)_2$, and Its Relationship to Becquerelite.* The Canadian Mineralogist, 2002. **40**(1): p. 217-224.
41. Bots, P., Morris, K., Hibberd, R., Law, G.T.W., Mosselmans, J.F.W., Brown, A.P., Doutch, J., Smith, A.J., and Shaw, S., *Formation of Stable Uranium(Vi) Colloidal Nanoparticles in Conditions Relevant to Radioactive Waste Disposal.* Langmuir, 2014. **30**(48): p. 14396-14405.
42. !!! INVALID CITATION !!!
43. Mace, N., Wieland, E., Dahn, R., Tits, J., and Scheinost, A.C., *Exafs Investigation on U(Vi) Immobilization in Hardened Cement Paste: Influence of Experimental Conditions on Speciation.* Radiochimica Acta, 2013. **101**(6): p. 379-389.
44. Tits, J., Walther, C., Stumpf, T., Mace, N., and Wieland, E., *A Luminescence Line-Narrowing Spectroscopic Study of the Uranium(Vi) Interaction with Cementitious Materials and Titanium Dioxide.* Dalton Transactions, 2015. **44**(3): p. 966-976.
45. Burns, P.C., Miller, M.L., and Ewing, R.C., *U6+ Minerals and Inorganic Phases: A Comparison and Hierarchy of Crystal Structures.* Canadian Mineralogist, 1996. **34**: p. 845-880.
46. Casas, I., Bruno, J., Cera, E., Finch, R.J., and Ewing, R.C., *Characterization and Dissolution Behavior of a Becquerelite from Shinkolobwe, Zaire.* Geochimica Et Cosmochimica Acta, 1997. **61**(18): p. 3879-3884.
47. Casas, I., de Pablo, J., Giménez, J., Torrero, M.E., Bruno, J., Cera, E., Finch, R.J., and Ewing, R.C., *The Role of Pe, Ph, and Carbonate on the Solubility of Uo2 and Uraninite under Nominally Reducing Conditions.* Geochimica Et Cosmochimica Acta, 1998. **62**(13): p. 2223-2231.
48. Finch, R. and Murakami, T., *Systematics and Paragenesis of Uranium Minerals.* Reviews in Mineralogy, 1999. **38**: p. 91-180.
49. Finch, R.J., Cooper, M.A., Hawthorne, F.C., and Ewing, R.C., *The Crystal Structure of Schoepite,$[(UO_2)_8O_2(OH)_{12}](H_2O)_{12}$.* Canadian Mineralogist, 1996. **34**: p. 1071-1088.
50. Finch, R.J., Hawthorne, F.C., and Ewing, R.C., *Structural Relations among Schoepite, Metaschoepite and" Dehydrated Schoepite".* Canadian Mineralogist, 1998. **36**: p. 831-846.
51. Finch, R.J., Miller, M.L., and Ewing, R.C., *Weathering of Natural Uranyl Oxide Hydrates: Schoepite Polytypes and Dehydration Effects.* Radiochimica Acta, 1992. **58**(2): p. 433-444.
52. Giammar, D.E. and Hering, J.G., *Influence of Dissolved Sodium and Cesium on Uranyl Oxide Hydrate Solubility.* Environmental Science & Technology, 2004. **38**(1): p. 171-179.

53. Liu, C., Zachara, J.M., Qafoku, O., McKinley, J.P., Heald, S.M., and Wang, Z., *Dissolution of Uranyl Microprecipitates in Subsurface Sediments at Hanford Site, USA.* Geochimica Et Cosmochimica Acta, 2004. **68**(22): p. 4519-4537.
54. Wang, Z., Zachara, J.M., Gassman, P.L., Liu, C., Qafoku, O., Yantasee, W., and Catalano, J.G., *Fluorescence Spectroscopy of U(Vi)-Silicates and U(Vi)-Contaminated Hanford Sediment.* Geochimica Et Cosmochimica Acta, 2005. **69**(6): p. 1391-1403.
55. Salbu, B., Janssens, K., Lind, O., Proost, K., and Danesi, P., *Oxidation States of Uranium in Du Particles from Kosovo.* Journal of Environmental Radioactivity, 2003. **64**(2): p. 167-173.
56. Zachariasen, W.H., *Crystal Chemical Studies of the 5f- Series of Elements. 4. The Crystal Structure of $Ca(Uo_2)O_2$ and $Sr(Uo_2)O_2$.* Acta Crystallographica, 1948. **1**(1-6): p. 281-285.
57. Zachariasen, W.H., *Manhattan Project Report,* . 1945.
58. Zachariasen, W., *Crystal Chemical Studies of the 5f-Series of Elements. Xxiii. On the Crystal Chemistry of Uranyl Compounds and of Related Compounds of Transuranic Elements.* Acta Crystallographica, 1954. **7**(12): p. 795-799.
59. Zachariasen, W.H., *Crystal Chemical Studies of the 5f-Series of Elements .21. The Crystal Structure of Magnesium Orthouranate.* Acta Crystallographica, 1954. **7**(12): p. 788-791.
60. A. Volkovich, V., R. Griffiths, T., J. Fray, D., and C. Thied, R., *Solubilities and Solubilisation Enthalpies of Alkali Metal Uranates(Vi) in Carbonate Melts.* Physical Chemistry Chemical Physics, 1999. **1**(14): p. 3297-3302.
61. Griffiths, T.R. and Volkovich, V.A., *A Review of the High Temperature Oxidation of Uranium Oxides in Molten Salts and in the Solid State to Form Alkali Metal Uranates, and Their Composition and Properties.* Journal of Nuclear Materials, 1999. **274**(3): p. 229-251.
62. Volkovich, V., Griffiths, T.R., Fray, D.J., Fields, M., and Wilson, P.D., *Oxidation of Uo2 in Molten Alkali-Metal Carbonate Mixtures: Formation of Uranates and Diuranates.* Journal of the Chemical Society-Faraday Transactions, 1996. **92**(24): p. 5059-5065.
63. Volkovich, V.A., Griffiths, T.R., Fray, D.J., and Fields, M., *Vibrational Spectra of Alkali Metal (Li, Na and K) Uranates and Consequent Assignment of Uranate Ion Site Symmetry.* Vibrational Spectroscopy, 1998. **17**(1): p. 83-91.
64. Volkovich, V.A., Griffiths, T.R., Fray, D.J., and Fields, M., *Increased Oxidation of Uo_2 in Molten Alkali-Metal Carbonate Based Mixtures by Increasing Oxygen Solubility and by Controlled Generation of Superoxide Ions, and Evidence for a New Sodium Uranate.* Journal of the Chemical Society-Faraday Transactions, 1997. **93**(21): p. 3819-3826.
65. Volkovich, V.A., Griffiths, T.R., Fray, D.J., and Thied, R.C., *The Electronic Spectra of Alkali Metal Uranates and Band Assignments: An Analysis of Their Diffuse Reflectance Spectra*. Physical Chemistry Chemical Physics, 2001. **3**(23): p. 5182-5191.
66. Volkovich, V.A., Griffiths, T.R., Fray, D.J., and Thied, R.C., *Chemical Solubility of Alkali Metal Uranate(Vi) Species in Molten Carbonates under Basic and Acidic Conditions.* Physical Chemistry Chemical Physics, 2000. **2**(13): p. 3029-3035.
67. Volkovich, V.A., Lain, M.B., Griffiths, T.R., John, M.C.D., and Lewin, B., *Four Thallium(I) Uranates(Vi), Their Preparation, Structure and Properties.* Journal of Nuclear Materials, 2005. **344**(1-3): p. 73-78.
68. Gruner, J., *The Chemical Formula of Clarkeite.* American Mineralogist, 1954. **39**(9-10): p. 836-838.
69. Rogova, V., Belova, L., Kiziyarov, G., and Kuznetsova, N., *Calciouranoite, a New Hydroxide of Uranium.* International Geology Review, 1974. **16**(11): p. 1255-1256.
70. Rogova, V., Belova, L., Kiziyarov, G., and Kuznetsova, N., *Bauranoite and Metacalciouranoite, New Minerals of the Hydrous Uranium Oxides Group.* International Geology Review, 1974. **16**(2): p. 214-219.
71. Burns, P.C. and Li, Y., *The Structures of Becquerelite and Sr-Exchanged Becquerelite.* American Mineralogist, 2002. **87**(4): p. 550-557.
72. Cejka, J., Sejkora, J., Skala, R., Cejka, J., Novotna, M., and Ederova, J., *Contribution to the Crystal Chemistry of Synthetic Becquerelite, Billietite and Protasite.* Neues Jahrbuch Fur Mineralogie Abhandlungen, 1998. **174**: p. 159-180.
73. Schindler, M., Hawthorne, F.C., Halden, N.M., Burns, P.C., and Maurice, P.A., *Dissolution of Uranyl-Oxide-Hydroxy-Hydrate Minerals. Iii. Billietite.* The Canadian Mineralogist, 2007. **45**(4): p. 945-962.
74. Srnwlnr, J.L.M., *Crystal Structures and Crystal Chemistry of the Uranyl Oxide Hydrates Becquerelite, Billietite, and Protasite.* American Mineralogist, 1987. **72**: p. 1230-1238.
75. Schindler, M., Mandaliev, P., Hawthorne, F.C., and Putnis, A., *Dissolution of Uranyl-Oxide-Hydroxy-Hydrate Minerals. I. Curite.* The Canadian Mineralogist, 2006. **44**(2): p. 415-431.

76. Vochten, R. and Vanhaverbeke, L., *Transformation of Schoepite into the Uranyl Oxide Hydrates - Becquerelite, Billietite and Wolsendorfite.* Mineralogy and Petrology, 1990. **43**(1): p. 65-72.
77. Burns, P.C., *A New Complex Sheet of Uranyl Polyhedra in the Structure of Wölsendorfite.* American Mineralogist, 1999. **84**(10): p. 1661-1673.
78. Buck, E.C., Brown, N.R., and Dietz, N.L., *Contaminant Uranium Phases and Leaching at the Fernald Site in Ohio.* Environmental science & technology, 1995. **30**(1): p. 81-88.
79. Roh, Y., Lee, S., Choi, S., Elless, M., and Lee, S., *Physicochemical and Mineralogical Characterization of Uranium-Contaminated Soils.* Soil and Sediment Contamination, 2000. **9**(5): p. 463-486.
80. Li, Y. and Burns, P.C., *The Structures of Two Sodium Uranyl Compounds Relevant to Nuclear Waste Disposal.* Journal of Nuclear Materials, 2001. **299**(3): p. 219-226.
81. Burns, P.C., Olson, R.A., Finch, R.J., Hanchar, J.M., and Thibault, Y., *$Kna_3(Uo_2)_2(Si_4o_{10})_2(H_2o)_4$, a New Compound Formed During Vapor Hydration of an Actinide-Bearing Borosilicate Waste Glass.* Journal of Nuclear Materials, 2000. **278**(2): p. 290-300.
82. Kubatko, K.-A.H., Helean, K.B., Navrotsky, A., and Burns, P.C., *Stability of Peroxide-Containing Uranyl Minerals.* Science, 2003. **302**(5648): p. 1191-1193.
83. Burns, P.C., Deely, K.M., and Skanthakumar, S., *Neptunium Incorporation into Uranyl Compounds That Form as Alteration Products of Spent Nuclear Fuel: Implications for Geologic Repository Performance.* Radiochimica Acta/International journal for chemical aspects of nuclear science and technology, 2004. **92**(3/2004): p. 151-160.
84. Burns, P.C., Ewing, R.C., and Navrotsky, A., *Nuclear Fuel in a Reactor Accident.* Science(Washington), 2012. **335**(6073): p. 1184-1188.
85. Ding, W., Botha, J.A., Hanson, B.C., and Burke, I.T., *Aqueous Hydroxylation Mediated Synthesis of Crystalline Calcium Uranate Particles.* Journal of Alloys and Compounds, 2016. **688, Part B**: p. 260-269.

2. Literature review

This chapter begins with a general overview of some unique chemical properties of the actinide elements, before focusing on the electronic properties unique to the uranyl(VI) ion. This is followed by a description of potential mechanisms by which uranyl(VI) ions may undergo hydrolysis in solution, much of which stems from understanding of transition metal chemistry. Finally, structural relationships surrounding the uranyl(VI) oxyhydrates, and related binary or ternary (uranate) uranium oxides are reviewed.

2.1 The f-block actinides

The large number of 5f-orbitals gives some indication as to the complexity of actinide elements their chemical complexity. Due to this, lanthanide compound chemistry exhibits markedly better predictability compared to the latter. Much like in the transition metals, the maximum oxidation states of actinides from actinium (Ac) to neptunium (Np) reflects the total number of electrons that may be removed from the 6d and 5f valence orbitals (Table 2.1), though not necessarily the most stable.

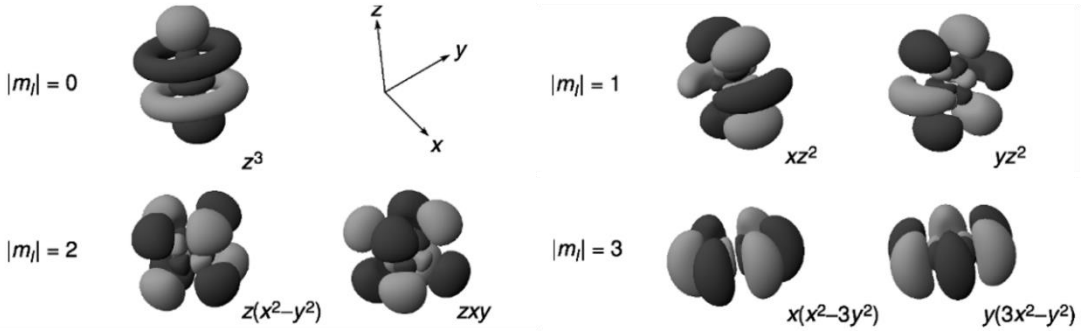

Figure 2.1 Representation of the 5f-orbital angular functions. ***Adapted from [1].***

The number of ground-state degenerate atomic orbitals is considerable, and makes precise prediction of energy levels difficult. However, the valence orbitals of the early actinides (including uranium) are generally stabilised to the extent that they are similar in energy to 5f electrons. As the effective binding energy of the 5f electrons is reduced, a larger range of oxidation states becomes available via ionisation of the 6s, 6d, and 5f-orbitals. In addition, bond formation tends towards higher relative covalency [2-4]. For example, a uranium atom may ionise from $[Rn]5f^3 6d^1 7s^2$ to $[Rn]5f^3$ to give U^{3+}, $[Rn]5f^2$ for the U^{4+} (Table 2.1), or if forming U^{6+} only [Rn] electron configuration remains. The latter VI-oxidation state is the most stable in aqueous solution, whilst the former IV-oxidation state is stabilised by removing oxidants from solution.

Table 2.1 Summary of known (red, green) and common (blue) oxidation states of actinide elements from actinium to lawrencium [3].

Name	Symbol	Electronic configuration	Oxidation state					
			2+	3+	4+	5+	6+	7+
Actinium	Ac	$[Rn]6d^1 7s^2$						
Thorium	Th	$[Rn]6d^2 7s^2$						
Proctinium	Pa	$[Rn]5f^2 6d^1 7s^2$						
Uranium	U	$[Rn]5f^3 6d^1 7s^2$						
Neptunium	Np	$[Rn]5f^4 6d^1 7s^2$						
Plutonium	Pu	$[Rn]5f^6 7s^2$						
Americium	Am	$[Rn]5f^7 7s^2$						
Curium	Cm	$[Rn]5f^7 6d^1 7s^2$						
Berkelium	Bk	$[Rn]5f^9 7s^2$						
Californium	Cf	$[Rn]5f^{10} 7s^2$						
Einsteinium	Es	$[Rn]5f^{11} 7s^2$						
Fermium	Fm	$[Rn]5f^{12} 7s^2$						
Mendelevium	Md	$[Rn]5f^{13} 7s^2$*						
Nobelium	No	$[Rn]5f^{14} 7s^2$*						
Lawrencium	Lr	$[Rn]5f^{14} 6d^1 7s^2$*						

2.2 The uranyl(VI) ion

Due to considerable nuclear and cationic charge, the U^{6+} ion is an exceptional Lewis acid, resulting in formation of the uranyl(VI) (UO_2^{2+}) ion via deoxygenation of water. This property is common to other actinides such as neptunium or plutonium, as well as transition metallions of similar charge or acidity such as molybdenum [5] or vanadium [6], though the latter typically features bent O=M=O bonds. The uranyl(VI) ion comprises 2 short bonds of ~1.8 Å and is reflected by other actinyl ions (Pu, Np, etc.), which range 1.7 – 2.0 Å [1]. In spite of the considerably larger ionic radii of uranium (~0.73 Å), the U-O_{yl} bond length is similar to that of the isostructural osmyl OsO_2^{2+} ion (I.R ~0.55 Å) [7], indicating an effective bond order greater than 2. This occurs via overlap between uranium 6d5f and the O 2p orbitals (Figure 2.2), to form one σ [U-6d(z^2)5f(z^3)↔O-sp(z)] and two π-bonds [U-d^2(xy, yz), f^2(xy^2, yz^2)↔O-p(x, y)], where 12 valence electrons from U(VI) are accommodated by σ_g, σ_u, π_g, and π_u molecular bonding orbitals (MO). The unfilled ungerade ϕ_u and δ_u MOs should be close to degenerate (same energy) in-vacuo, whereas ligand to metal charge transfer from ligands in the equatorial plane is expected to stabilise the ϕ_u orbital (lower energy) to varying levels dependant on the extent of charge donation [8]. The linearity of U=O must arise from π-overlap with unfiled 5f-orbitals, contrasting with the isoelectronic ThO_2 species, wherein its empty 6d is higher in energy and overlap with O 2p should produce non-linear bonds (note the destabilised δ_g orbitals in UO_2^{2+}).

Indeed, O=Th=O bond angles are ~122 ° [9, 10]. The U=O_{yl} bonds are essentially permanent, given the exceedingly long kinetic half-life for oxygen-exchange with water [11]. Though is expected to undergo relatively facile exchange with equatorial hydroxo-ligands at room temperature [12]. Ligand exchange, polymerisation, or substitution reactions at the equatorial plane dominates over uranyl(VI) chemistry in solution and often in the solid-state.

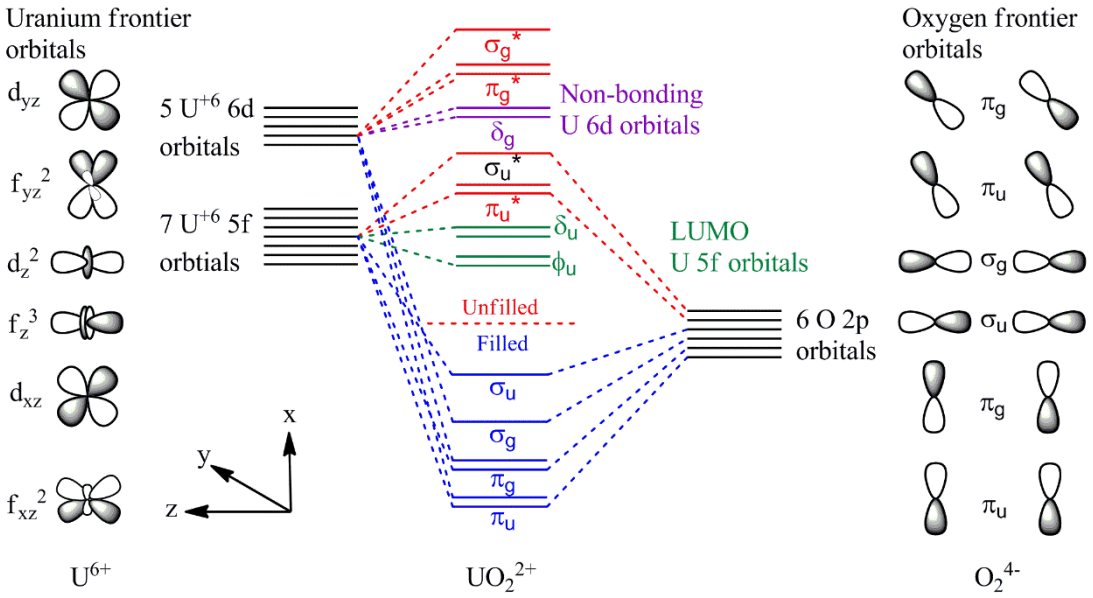

Figure 2.2 Simplified frontier orbital bonding interaction between uranium (5f, 6d) and two oxygen (2p) atoms in uranyl(VI) ions along the z axis forming filled σ_u, σ_g, π_u and π_g molecular orbitals (valence band) with the unfilled conductance band above. Whilst the U6s and U6p orbitals are excluded here for clarity, the former 6s shell is close in radial extension to 5f, whilst extension of the latter is inversely proportional to bond length [13], indicating both contribute to bonding interaction. O2s shell is also excluded, which would otherwise exhibit overlap with the U6p [14], whilst the U7s$_\sigma$ is highly diffuse and overlaps extensively with the O2p$_\sigma$ (max. amplitude at r_{Bohr} ~3.2 Å) [14]. Note the 6d δ_g molecular orbitals are destabilised to above π_u stemming from antibonding overlap with O 2p [3, 14-16]. *Adapted from [1, 17].*

2.3 Uranium in solution

The aqueous solution chemistry of uranium is often controlled by complexation reactions involving solvent molecules, background electrolytes, or other electron donating ligand species [18]. These properties have been utilised in various aspects of uranium chemistry, and apply somewhat to other elements in the actinide series. Whilst both U(IV) and U(VI) oxidation states feature in both environmental and industrial applications, the latter will be focused on here, given its direct relevance in subsequent chapters. As complexation reactions are critical in the transition of

dissolved precursor molecules into the solid phase [19, 20], an overview of the mechanisms that could affect aqueous uranium precipitation is provided.

2.3.1 Uranyl(VI) hydrolysis

In aqueous solutions of hexavalent uranium (U(VI)), the simplest U(VI)-monomer exists as the solvated uranyl(VI)-complex $[(UO_2)(H_2O)_{4\text{-}6}]^{2+}$ (Figure 2.3), whereby equatorial H_2O (aqua) ligands bind via ligand-to-metal electron σ-donation to the acidic U(VI)-centre [18]. Electron acceptor orbitals on the uranium with the correct geometry are the 6d(x^2-y^2), 6d(xy), 5f(x^3-3xy^2), 5f(y^3-3x^2y), as well as the 7s and 7p. This stabilises the cationic metal centre, whilst the aqua-ligand OH-bonds are destabilised (lengthened), facilitating deprotonation (Figure 2.3). π-donation from hydroxo-ligand lone pairs compete with the U-O_{yl} π_u, π_g overlap [21], presumably stabilising the surprisingly facile exchange mechanism with U-O_{yl} oxygen [12, 22, 23].

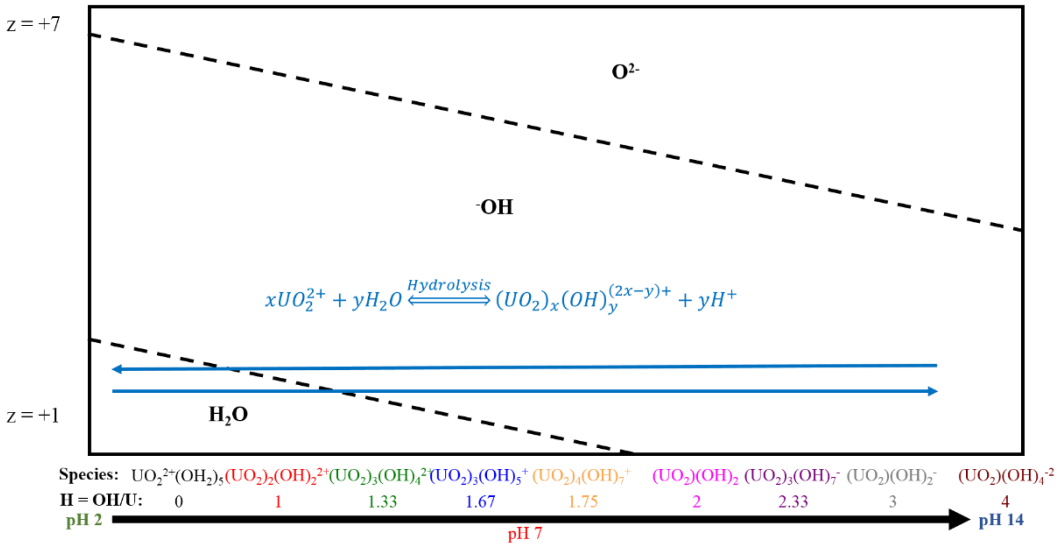

Figure 2.3 Conceptual diagram of regions of stability for aqua, hydroxo, and oxo ligands. ***Adapted from [20]***

This dynamic equilibrium is dependent on solution pH, in addition to the cation charge, size, or electronic properties [24]. For the uranyl(VI) cation, with increasing pH, aqua-ligands progressively exchange with uranyl(VI)-OH^- ligands (hydroxo) in accordance with the Chernyaev-Schelokov row [25], an analogue to the spectrochemical series used in transition metal coordination chemistry representing the favourability of ligand exchange reactions. Or alternatively, the deprotonation of aqua-ligands are favoured by association with increasing hydroxyl species in the outer-coordination sphere. With high enough pH, more aqua ligands become deprotonated, increasing the cation hydrolysis ratio. As alluded to earlier, the complexity of actinide chemistry applies to the solution chemistry of U(VI), where a mixture of olation and oxolation takes place to form mono, di, tri, and tetra-nuclear

uranyl(VI) aqua-oxo-hydroxo-complexes. Formal cationic or anionic charges depend on the extent of uranyl(VI) hydrolysis (Figure 2.3), where the stability of each complex is characterised by acid-base equilibrium constants [26-28] (see chapters 4, and 5, for relevant U(VI) speciation diagrams).

2.3.2 Mechanisms of oligomerisation

The likelihood of ligand substitution may be understood via an adapted 18-electron rule, generated from ligand electron-donor data from crystallographically defined U(VI)-phases [29], and relates to the theory of partial charges that apply to many aqueous metal hydroxide mechanisms [18, 20]. The O^{2-} ligand in UO_2^{2+} monomers has an electron donor ability of 3.9 ± 1, or a total number of electrons donated of ~7.8 (N_e = 7.8e^-) to the central U(VI). UO_2^{2+} therefore requires another 10.2 electrons to become stable (18 – 7.8e^-), whereby complexes with N_e < 18 are electron deficient and N_e > 18 excessive. Under both conditions, ligands are associated, dissociated or substituted [30] to reach 18 e^-; where ΔN_e^2 must be smaller than ΔN_e^1 for the process to be favoured. Utilising these rules, monomeric U(VI) must therefore exist as $[(UO_2)(H_2O)_5]^{2+}$, where N_e of $[(UO_2)(H_2O)_6]^{2+}$ and $[(UO_2)(H_2O)_4]^{2+}$ are 19.2 (1.2) and 15.4 (2.6) respectively have ΔN_e values larger than 17.3 (0.7). This is strongly supported by empirical evidence from various spectroscopic, chemometric, and modelling studies [22, 23, 31-46] that place the aqua-complex somewhere between 4 and 6 equatorial ligands.

The electron deficiency in the penta-aqua mono-U(VI) complex is larger than the uncertainty (0.3 e^-), revealing a susceptibility to dynamic substitution by ligands that reduce ΔN_e. As UO_2^{2+} is a poor electron-donor compared to H_2O, substitution must occur from other ligands or via inner complexation through a shared ligand. Given the initial di-positive charge of the cation (uranyl(VI)), its electrophilic properties (strong Lewis acid) are strong and is highly susceptible to nucleophilic attack by hydroxide or hydroxo-ligands (Lewis bases). This suggests a stepwise condensation process [47] that progressively saturates the electrophilicity of cationic U(VI)-species, prior to formation of oligomers via the same mechanism (Scheme 2.1).

$$(1)\ [\boldsymbol{UO_2(H_2O)_5}]^{2+}(\boldsymbol{N_e = 17.3})$$
$$\rightarrow(2)\ [\boldsymbol{(UO_2)_2(OH)_2(H_2O)_4}]^{2+}\ (\boldsymbol{N_e = 17.95})$$
$$\rightarrow(3)[\boldsymbol{(UO_2)_3(OH)_5(H_2O)_5}]^{+}\ (\boldsymbol{N_e = 17.72}),$$
$$[\boldsymbol{(UO_2)_4(OH)_7(H_2O)_4}]^{+}\ (\boldsymbol{N_e = 17.68})$$

Scheme 2.1

The electron counting rules [29] reveal that neither of the two neutral-pH condensation products ((3) tri-, (4) tetra-nuclear) are ideal (≠ 18e^-); and much like the mononuclear aqua-complex, probably remains in dynamic equilibrium between 17.72 – 18.35e^- and 17.68 – 18.15e^- respectively via exchange of one aqua-ligand, both

ranges are within margin of error and appear almost equally favourable [22, 23, 40, 42, 44, 48]. These oligomerisation reactions involving aqua ligands, olation, are driven by an increase in entropy and kinetically controlled by ligand dissociation (Scheme 2.2).

$$\boldsymbol{MOH + MOH_2 \xrightarrow{olation} [M - OH - M] + H_2O} \qquad \textbf{Scheme 2.2}$$

Under alkaline pH (7 < pH < 11), anionic U(VI)-hydroxo-species dominate [44] due to continuous aqua-hydroxo ligand substitution, where the more complex oxolation reaction takes place (Scheme 2.3a, b). Oxolation proceeds by an initial nucleophilic addition ($^{\delta-}$OH-group is nucleophile) between two metal hydroxo-complexes (Scheme 2.3a) to create an intermediate adduct. This is followed by proton transfer (Scheme 2.3, H^+ transfer) from the bridging μ_2OH-bridge to a terminal OH-ligand to form the aqua (H_2O) leaving group, resulting in the formation of an M-O-M oxo-bridge. With increasing acidity, association of acidic species with the transition state stabilises the leaving group, favouring H_2O-dissociation, and the forward reaction. Though if acidity is too high, the nucleophilicity of the attacking hydroxo-group is reduced, and the reaction becomes hindered. Alternatively, under basic conditions, hydroxyl association with the metal centre or the M-OH proton increases the nucleophilicity of the OH-ligand to favour formation of the transition state (Scheme 2.3e). However available hydroxyl leaving groups are reduced [20], which progressively disfavours continuing substitutions. As such, oxolation may be catalysed by acid (Scheme 2.3c) or base (Scheme 2.3e) species present in solution.

Nucleophilic substitution is generally favoured due to saturation of the equatorial uranyl(VI) coordination sphere (Scheme 2.1) by aqua or hydroxo-ligands [2], where three reaction pathways are available in analogue to those occurring for organic chemistry, and compatible with uranyl(VI) ligand exchange mechanisms from the literature [30]. ***Dissociative*** substitution is a two-step mechanism involving removal of the leaving group prior to nucleophilic attack. The former step is rate limiting, rending the reaction an SN_1 (unimolecular) substitution. The ***associative*** path is inverse, and can require oversaturation of the coordination sphere in the transition state before leaving group dissociation. Alternatively, a ***concerted*** (interchange) substitution can occur, in which both nucleophile and leaving group are present in the transition complex. Both associative and concerted substitutions are rate-limited by coalescence of two molecular species, and are hence SN_2 (bimolecular) substitution reactions.

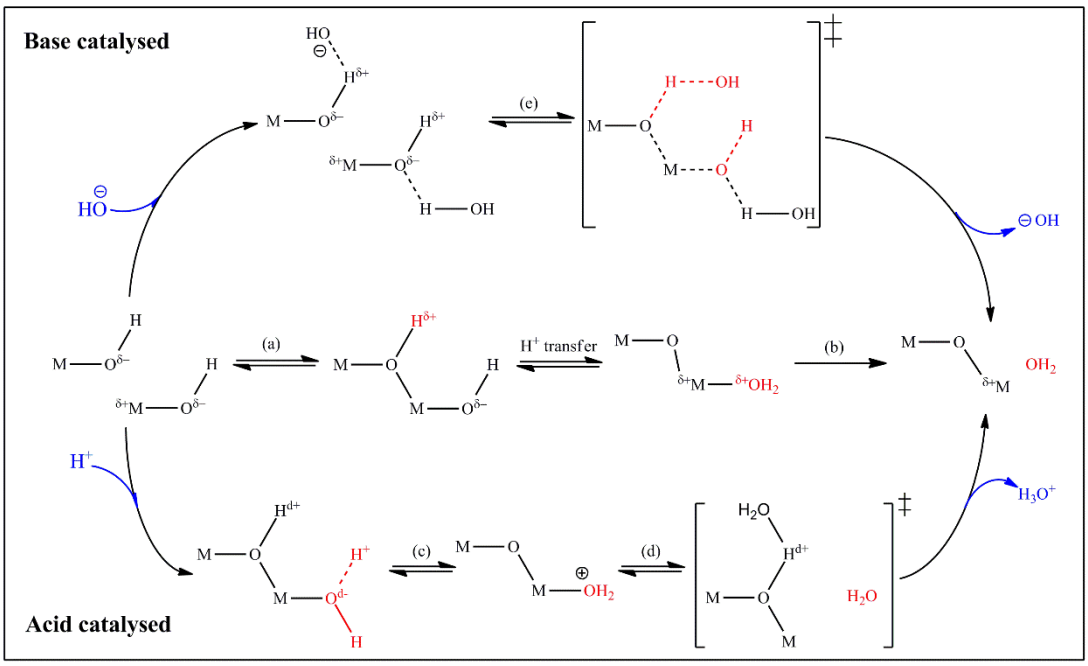

Scheme 2.3 A typical oxolation reaction (middle) between two metal (M) centres with hydroxo ligands. Base and acid catalysed reactions are top and bottom respectively.

The need for charge donation precludes aqua ligands from acting as nucleophile, whereas many mild-acidity U(VI)-complexes are aqua-hydroxo hybrids. Where due to the excellent leaving group properties of aqua ions, dissociative condensation in U(VI)-hydroxides may be facilitated. The dissociated aqua ligand would be stabilised further by hydrogen bonding with the U-O_{yl} oxygen in a second hydration shell [49, 50]. However, early modelling [31, 51] and experimental [52] studies have highlighted the energetic favourability of both associative (6-coordinate transition state) and concerted (5-coordinate transition state) relative to dissociative (4-coordinate transition state) mechanisms in penta-aqua uranyl(VI) complexes. Whilst the former two were almost indistinguishable [31], other modelling studies have narrowed this somewhat towards an associative-interchange mechanism [53, 54].

High-pH solutions (pH 14) are dominated by U(VI)-hydroxo monomers ($UO_2(OH)_4^{2-}$) [55] (Scheme 2.1), which undergo oxolation at significantly slower rates if the equatorial coordination sphere consists exclusively of hydroxo ligands [44]. This is supported by general experimental trends for various high charge metals [19, 20] as well as in-house observations (unreported), where high ionic strength (~3 mol kg^{-1}) tetramethylammonium hydroxide solutions caused initial precipitation of U(VI) followed by a slow dissolution and re-precipitation. Anionic hydroxo-complexes are of significantly lower lability compared to aqua-ligands (olation), and the electrophilicity (Lewis acidity) of the U(VI)-centre is strongly inhibited.

2.3.3 Nucleation

The transition of a dissolved metal ion from solution to solid phase (colloids, surface precipitate) involves four kinetic steps [20, 56-59] that may be more or less coincident depending on the favourability of each mechanism. These include ***(1)*** formation of a neutral complex from charged species (neutralisation), ***(2)*** condensation of zero-charge precursors (coalescence), ***(3)*** surface mass-addition (growth), ***(4)*** aging of particles (Ostwald ripening) [20]. This section provides a brief theoretical treatment of the kinetics and thermodynamics, that may be used in understanding the various influences (ionic strength, pH, temperature, etc.) on precipitation of uranyl(VI) oxy-phases. Whilst kinetic and nucleation studies in uranyl(VI) oxyhydrate phases are almost non-existent, findings and knowledge from several other systems studied in the literature are reviewed.

2.3.3.1 Classical

Nucleation refers to the coalescence of neutral precursor complexes in stage (2), that occur to a large enough extent, forming solid nuclei. From a thermodynamic viewpoint, the formation of a solid nuclei P_n from a number (n) of precursor complexes (P) in the solution phase, incurs an energetic cost. This may be represented by a relationship (Equation 2.1a) between the Gibbs energy of nucleation (ΔG_N) and the difference in chemical potential of precursor P in solution (μ_s) versus solid-state (μ_N). However, with reducing nuclei size, the number of unresolved bonds at the particle surface relative to the bulk increases (i.e. Larger surface area to volume ratio). This excess cost manifests as an incremental increase ($\delta G/\delta A$) in interfacial energy (γ) and the surface area term (A) (Equation 2.1b). The change in chemical potential ($\Delta\mu_R$) may be presented as a function of precursor concentration (c_s) (activity) and the solubility (c_N) of the nuclei phase (Equation 2.1c). The inverse ratio of which, is the extent of supersaturation S (Equation 2.1d). If nuclei are spherical, then the surface area of nuclei with radii $r = (2nv/4\pi)^{1/3}$, coalesced from n precursors with molar volume v, replaces A (Equation 2.1d, red).

$$\text{(a) } \Delta G_N = n(\mu_N - \mu_S)$$

$$\text{(b) } \Delta G_N = n(\mu_N - \mu_S) + A_s\gamma, \qquad where\ (\gamma = \frac{\delta G}{\delta A})$$

$$\text{(c) } \Delta G_N = nk_BT\ln(\frac{C_N}{C_s}) + A_s\gamma$$

$$\text{(d) } \Delta G_N = -nk_BT\ln(s) + n^{\frac{2}{3}}(36\pi v^2)^{\frac{1}{3}}\gamma$$

Equation 2.1

This classical thermodynamic treatment (Equation 2.1d) separates the bulk energetics (Equation 2.1d, green) of homogeneous nucleation (solid formation) into its two contributions, the volume energy (Equation 2.1d, blue), and the interfacial energy between solution and solid (Equation 2.1d, red). When the surface energy is positive

(γ >0), and the solution is supersaturated (S >1) with respect to the nucleating phase, then precipitation is spontaneous. Under these conditions, a graphical representation (Figure 2.4a) reveals that with increasing nuclei number or radius, the hybridised Gibbs energy of nucleation, ΔG_N, goes through a maximum, where $\delta\Delta G/\delta(r, n) = 0$. This corresponds to the transition state of a chemical reaction, and any lateral movement in reaction coordinate results in either dissolution of nuclei, or growth. The Gibbs energy with the coalescence of precursor nuclei, is therefore $\Delta G_{max} = \Delta G^*$ (Figure 2.4a, green), where a larger supersaturation S reduces the energy barrier ($\Delta G^*_1 \rightarrow \Delta G^*_2$), so that $S_2 > S_1 > 1$. However, if S<1, then $\Delta G_N \rightarrow$ infinity. The number of precursor molecules consumed from solution is n* and is proportional to the radius of critical nuclei (r*) via the molar volume v. Nuclei with radii greater than r*, crystal growth becomes favoured (Figure 2.4b), otherwise, re-dissolution becomes likely [60].

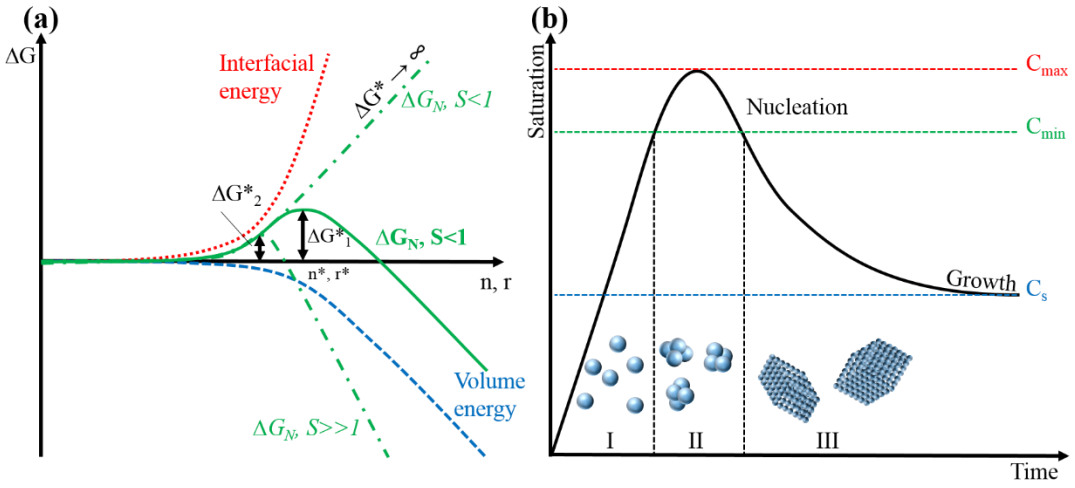

Figure 2.4 (a) Graphical representation of classical homogeneous nucleation thermodynamics. (b) classical nucleation (II) from monomers (I), and nuclei growth (II) as functions of monomer saturation and time. ***Adapted from [60, 61].***

The former n* may be attained via $\delta\Delta G/\delta(r, n) = 0$ (Equation 2.2a), which leads to an expression for the Gibbs energy change ΔG* of nucleation (Equation 2.2b). This allows description of critical nuclei radius r* via the Gibbs-Kelvin equation (Equation 2.2c).

$$(a)\ n^* = \frac{32\pi\gamma^3 v^2}{3(k_B T \ln(S))^3}$$

$$(b)\ \Delta G^* = \frac{n^*}{2} k_B T ln(S) = \frac{16\pi\gamma^3 v^2}{3(k_B T ln(S))^2} \qquad \text{Equation 2.2}$$

$$(c)\ r^* = \left(\frac{3n^* v}{4\pi}\right)^{\frac{1}{3}} = \frac{2\gamma v}{kT ln\, S}$$

As the critical nuclei radius r* is proportional to the interfacial energy (surface tension) of the solid-phase, a reduction in the latter, leads to a reduction in the former. The interfacial energy is intimately related to the local solution composition via the Gibbs adsorption equation (Equation 2.3a), where Σn_i^S is the difference between total moles of the ith component in the system, and moles of surface-adsorbed ith component.

$$(a)\ \delta\gamma = -\frac{\Sigma n_i^S}{A}\delta\mu_i = -\Sigma\Gamma_i\delta\mu_i$$
$$(b)\ \delta\gamma = -(\Gamma_H - \Gamma_{OH})\delta\mu_{OH} - (\Gamma_X - \Gamma_Y)\delta\mu_{XY} \qquad \text{Equation 2.3}$$

This is represented by the surface excess, or adsorption density of the ith component, Γ_i. However, taking into account surface charge of metal oxides, the incremental change in surface energy, $\delta\gamma$, occurs as a function of ion adsorption (Equation 2.3b). The adsorption of protons (Γ_H) and hydroxides (Γ_{OH}), or specific sorption of ionic species (Γ_X, Γ_Y), is dependent on solution pH, and ionic strength of electrolyte XY respectively (Equation 2.3b) [20, 62], where Γ_i is in terms of moles per unit area. Thusly, an increase in pH or ionic strength, increases the surface adsorption density, which enhances the reduction in interfacial or surface energy (Equation 2.3b, larger -$\delta\gamma$) via disruption of solvent-solvent and solvent-surface interactions (H-bonding). This ultimately leads to a reduction in the critical nuclei radius r*, as well as ΔG^* [20, 61], and was demonstrated in various precipitation systems [63-66]. In terms of ion-solvent interactions, an increase in charge density of electrolyte species (i.e. high charge, small ionic radii, see Born solvation radii [67]) increases disruption of solvent-solvent interactions (H-bonding in water), which consequently reduces interfacial energy and indeed critical nuclei radius r*. This is related to the Hofmeister, salting-in/out effect [68, 69], or more broadly, the kosmotropic or chaotropic properties of dissolved components (see section 2.3.5).

The kinetics of homogeneous nucleation may be represented as an Arrhenian relationship (Equation 2.4). Where J is the rate at which nuclei increase in number, per unit volume; J_0 is the precursor collisional frequency; ΔG^* and ΔG^R account for the energy barriers to solid formation (Equation 2.2b, Figure 2.4) and the condensation mechanism (olation or oxolation). The latter is on the order of 35 kJ mol^{-1} and may be reduced via acid or base catalysis [20, 70-73].

$$J = J_0 \exp\left(\frac{-\Delta G^* + \Delta G^R}{k_B T}\right) = J_0 \exp\left(\frac{\Delta G^R}{k_B T}\right).\exp\left(\frac{16\pi\gamma^3 v^2}{3(k_B T ln(S))}\right) \qquad \text{Equation 2.4}$$

The activation energy of solid formation may be reduced by the introduction of seed crystals into solution [74, 75], which catalyses nucleation by reducing the solid-solid interfacial energy below that of solid-solution. This is due to compatibility between seed and nucleating-phase in terms of crystallinity/phase, chemistry, or morphology,

allowing catalysis by dissimilar phases [56], and facilitating epitaxial nucleation on seed crystals.

2.3.3.2 Non-classical

Since development of classical nucleation theories, several experimental and modelling studies on various systems have revealed the occurrence of complex nucleation mechanisms involving the formation of intermediates in colloid analogues [76], proteins [77-79], glasses [80, 81], ionic salts [82-84], and biomimetic or mineral phases [85-88]. Thermodynamically, this is epitomised by the Ostwald rule of stages, or Ostwald step rule [89, 90], which imparts the notion that transition of a system from a disordered to an ordered state prioritises the formation of intermediates closest in Gibbs energy to the initial state. In addition, the first distinct intermediate should separate from the initial state by the smallest Gibbs energy barrier [91, 92]. These assertions were applied in the first instance to protein crystallisation [77-79], where precursor macromolecules were treated as hard spheres with short ranges of interaction [78, 93]. This may be described by a binodal interface in the temperature-volume fraction phase-diagram, which represents the coexistence of both colloid and crystal-phase [61] and describes the solubility of the crystal phase (equivalent chemical potential for all phases). The limits of stability for the binodal interface is represented by the intersecting spinodal curve, which contains the fluid-fluid phase region.

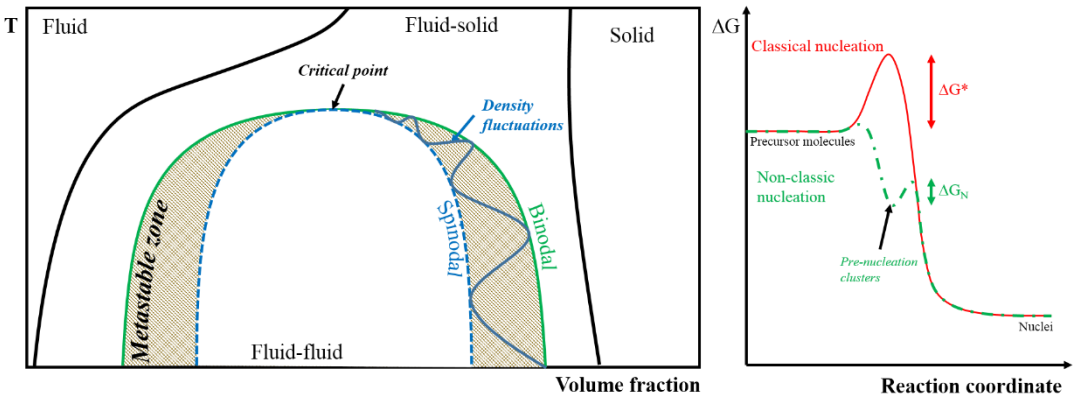

Figure 2.5 Left: Temperature-volume fraction phase diagram showing the fluid, fluid-solid, solid, and fluid-fluid phases, with metastable regions between binodal (green line) and spinodal (dashed blue) interfaces. Density fluctuations are drawn in blue. Right: conceptual comparison between classical and non-classical (2-step) nucleation mechanisms. *Adapted from [61, 86].*

The binodal and spinodal curves intersect at the critical point, and the area between the two interfaces, represents a region of metastasis with varying degrees of flexibility in terms of allowable density fluctuations. Density fluctuations become more constrained towards the critical point (increasing temperature) [79, 94], and as such results in localised regions of supersaturation in the system, favouring the nucleation

rate of a solid phase (Equation 2.4). This two-step mechanism [61, 77] becomes favoured when the Gibbs energy change of both steps are lower than that of classical nucleation. It asserts that nucleation proceeds via initial formation of dense clusters of precursor constituents, these fluctuating metastable clusters then undergo structural ordering to form nascent nuclei. As the pre-nucleation clusters are stable with respect to the solution-phase, the energetic cost of formation may be lower than the thermal energy of the system (i.e. ~no kinetic barrier). The latter crystallisation is therefore rate limiting (Figure 2.5, right) [86].

Some naturally occurring examples of two-stage nucleation is during biomineralisation of calcium carbonate (shells, exoskeletal structures), which initially forms amorphous calcium carbonate (ACC) from pre-nucleation clusters [85-87, 95], before direct nucleation into Calcite, or via a crystalline Vaterite intermediate [96]. The pre-nucleation clusters are stabilised by bicarbonate, or kinetically by aspartate-based surfactants or macromolecular frameworks to allow for directed morphological control during crystallisation [61]. This is similar to the crystallisation of amorphous calcium phosphate (teeth, bone), which may also undergo heterogeneous nucleation on existing crystals [97].

The transition from solvated pre-nucleation clusters, to amorphous pre-nucleation species, and crystallisation into endmember phases, could be metanarrative in several systems [61, 77, 98, 99]. In particular, during crystallisation of hydrous metal alumina-silicates or zeolites, which form amorphous pre-nucleation species via condensation of oligomeric/polymeric or poly-tetrahedral precursors [61, 98, 100, 101]. This behaviour could underpin studies on uranyl(VI) oxyhydrates nucleation, given the similar condensation mechanisms. Indeed the phase separation of oligomeric pre-nucleation species as a primary amorphous phase is observed in both systems [61, 98, 102-104], and could form as gels [102] or colloids [103]. The primary amorphous zeolite is a heterogeneous non-equilibrium product (Ostwald step rule), consisting a coagulated mixture of hydroxylated precursor polymers [98].

This primary amorphous phase undergoes solution-mediated equilibration into a secondary pseudo-steady-state intermediate [105-107], which is characterised by broad reflections in X-ray diffractograms. Experimental studies revolved around pH-change [108, 109] suggests a base-catalysed mechanism that occurs via partial dissolution and mass-transport [110] or re-precipitation [98, 111] of constituent silicate and aluminate species. The presence of organic frame-working agents (tetramethylammonium) and electrolyte cations (Na^+) [112] during equilibration may facilitate or hinder the transport of dissolved species via electrostatic or hydrophobic association [113-119]. Furthermore, the incorporation of either frame-working and cation species into the secondary intermediate coincided with localised structure [110,

120] in neighbouring Si and Al coordination environments [98, 121]. This discrepancy between *XRD-amorphous* [122] and *spectroscopic-crystalline* (FTIR [123], NMR [124, 125]) has been rationalised in terms of crystallite size, or bulk analyte concentration. i.e. The secondary zeolite crystallites approach a mere ~4^3 unit cells, compared to ~10^3 in the crystalline state [126]. However, it has been noted that the secondary intermediate comprises a majority amorphous phase, whilst some nanoscales domains are zeolite-like in structure, though distinct from the endmember zeolite [98].

A key factor that appears common to primary amorphous precipitates is extent of hydration, where primary amorphous phases transition towards progressively crystalline states via the removal of water. Modelling of 2-step nucleation using simple electrolyte solutions (NaCl) reveal that this dehydration process could begin as early as the pre-nucleation stage, where the de-solvation of Na-cations is coincident with coordination of Cl-anions to form the Na^+Cl^- clusters. These clusters undergo progressive densification (fluctuating) towards nucleation, and further dehydration towards NaCl crystallites [82-84]. Whilst dehydration broadly features in the amorphous → crystalline direction, nucleation in the solid-state is expected to occur via liquid intermediates [127, 128], or via partial dissolution and re-precipitation [129]. However, both processes emphasise the separation of amorphous and crystalline domains by a fluid-like interfacial layer, which occurs due to a lower activation barrier compared to the lattice enthalpy of nascent nuclei with small critical radii (Equation 2.2) [61].

2.3.4 Growth

2.3.4.1 Classical

Regardless of nucleation from classical and non-classical considerations, the relatively thermodynamic instability of nascent nuclei favours continuing growth of the solid phase to reduce surface-area to volume ratios [20, 60]. Kinetically, surface mass-addition may be rate-limited by diffusion of precursor molecules between bulk solution and solid surface, or alternatively, by a chemical reaction occurring at the solid-solution interface [20, 56]. Diffusion-limited or diffusion-influenced growth takes place when the reaction rate of solution → solid transition by precursor molecules is rapid relative to the rate at which they diffuse to the surface. The growth rate may be described as a function of the diffusion coefficient (D), molar volume (V_m), solution concentration (C), and solid phase solubility (C_s) (Equation 2.5a). Crystal growth within this regime are poorly monodisperse at high supersaturation, due to an overlap of nucleation and growth during precipitation. This may be described as a relationship between the relative particle size distribution ($\Delta r/r$) and the

nuclei size (r_0) and distribution (Δr_0), which indicates that monodispersity increases as growth dominates (Equation 2.5b) [20, 66].

$$(a)\ \frac{dr}{r} = \frac{DV_m(C - C_s)}{r}$$
$$(b)\ \frac{\Delta r}{r} = \left(\frac{r_0}{r}\right)^2 \frac{\Delta r_0}{r_0}$$

Equation 2.5

Conversely, if precursor diffusion to the surface is rapid relative to the interfacial chemical reaction, then a secondary two-dimensional nucleation and growth occurs on the solid surface, which could propagate laterally. Notably, whilst 2D-surface nucleation is analogous to primary (3D) homogeneous nucleation (see section 2.3.3), the activation energy of the former should be lower, given the lower geometric contributions. Surface growth may be further categorised into mono- and polynuclear mechanisms, where growth rate limits the former, and exhibits surface area dependency. Whereas if growth and surface nucleation rates are similar, then surface mass-addition becomes chaotic, with simultaneous formation of multiple surface nuclei and layer growth.

2.3.4.2 Non-classical

To complement classical growth theories (surface mass-addition), particle mediated growth could follow formation of primary crystallites (Figure 2.4b, stage III) during nucleation. This may occur via a chaotic non-directional coalescence to produce fractal precipitates, which consist of permanently aggregated particles (Figure 2.6, IV) [130, 131], or alternatively, or via a more ordered mechanism (Figure 2.6, V→VI). The latter is mediated by oriented aggregation, which occurs via rearrangement of primary crystallites, allowing crystallographic alignment prior to permanent attachment (Figure 2.6, IV→VI) [60, 132, 133]. However, initial non-directional coalescence is inherent in oriented attachment mechanisms [131, 133], and could therefore be considered as a stepwise process with overlap between nucleation and growth, coalescence, and oriented attachment. With progression towards stage VI, sample crystallinity is expected to increase as the contiguous crystallite domain becomes larger. This manifests as a reduction in XRD peak FWHM for specific HKL-planes in accordance with the Scherrer relationship, and has been observed for several mineral systems [132, 134-138].

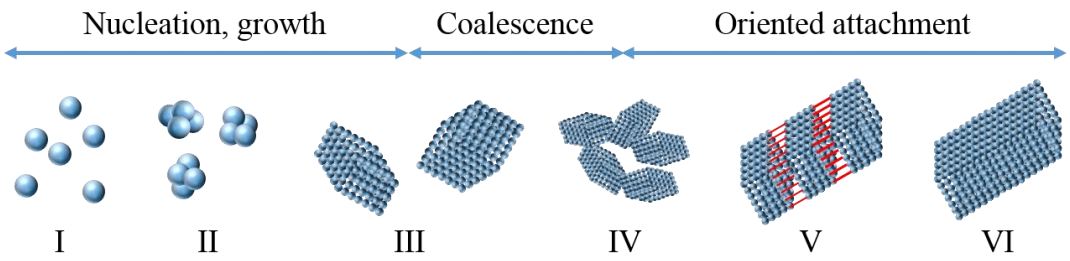

Figure 2.6 Schematic illustrating the progression from (I→II) nucleation and (II→III) growth, to (III→IV) coalescence of primary crystals into mesoscopic aggregates resembling outer-sphere complexation, (V) orientation via Brownian motion to align crystallographic planes, and finally (VI) irreversible attachment to form a contiguous crystal. *Adapted from [132].*

Colloidal stability is affected by various energetic interactions at the solid-solution interface, which may influence the coalescence-mediated crystal growth. As primary crystallites (Figure 2.6, II, III) reduce in size or mass, Brownian motion predominates, favouring spontaneous dispersion of particles. This sol is homogenous and stable. However, with increasing size or mass, aggregation becomes more favoured due to an increase in attractive forces. The balance between dispersive (repulsive) and attractive forces relates directly to the interfacial tension of particles (see section 2.3.3.1, thermodynamic stabilisation), and is therefore affected by solution pH, and ionic strength. The kinetic barrier of aggregation for a given colloidal suspension may be rationalised using the Dejarguin, Landau, Verwey, Overbeek (DLVO) theory. DLVO theory considers kinetic stability in terms of inter-particle (i) London-Van der Waals (VDW) attraction (Equation 2.6a, $W_a(D)$); and (ii) repulsive electrostatic interactions (Equation 2.6a, $W_r(D)$) between particle electrical double layers.

$$(a)\ W_{total}(D) = W_a(D) + W_r(D)$$

$$(b)\ W_{total}(D) = -\frac{AR}{12D} + 2\pi\varepsilon\varepsilon_0 R\psi^2 \exp(-\kappa D) \qquad \text{Equation 2.6}$$

$$(c)\ {\lambda_D}^{-1} = \kappa = \left[\sum \frac{z^2 e^2 c^2}{k_B T}\right]^2$$

Attractive VDW contributions (Equation 2.6b, $W_a(D)$) between two identical bodies is proportional to their common radii (R) and Hamaker constant (A), and inversely proportional to surface-surface separation distance (D). Repulsive electrostatic contributions (Equation 2.6b, $W_r(D)$) are proportional to the integral of the electrical double layer (EDL) force (see Figure 3.3, upper), where ε is the vacuum permittivity, ε_0 is the dielectric constant, and ψ^2 is the electrical surface potential. The Debye constant κ, is related to the ionic charge z, and ion concentration c (e is the elementary charge). Visualisation of the hybrid function $W_{total}(D)$ (Figure 2.7a) reveals an increase in the kinetic aggregation barrier as a function of decreasing ion

concentration at constant particle size, or increasing particle size at constant ion concentration (Figure 2.7b) [60, 62]. The former may be rationalised via an expansion in the Debye length or thickness of the EDL (Equation 2.6c, $\lambda_D \propto c$) to enhance electrostatic repulsion, whilst the latter arises due to direct proportionality to particle radii R.

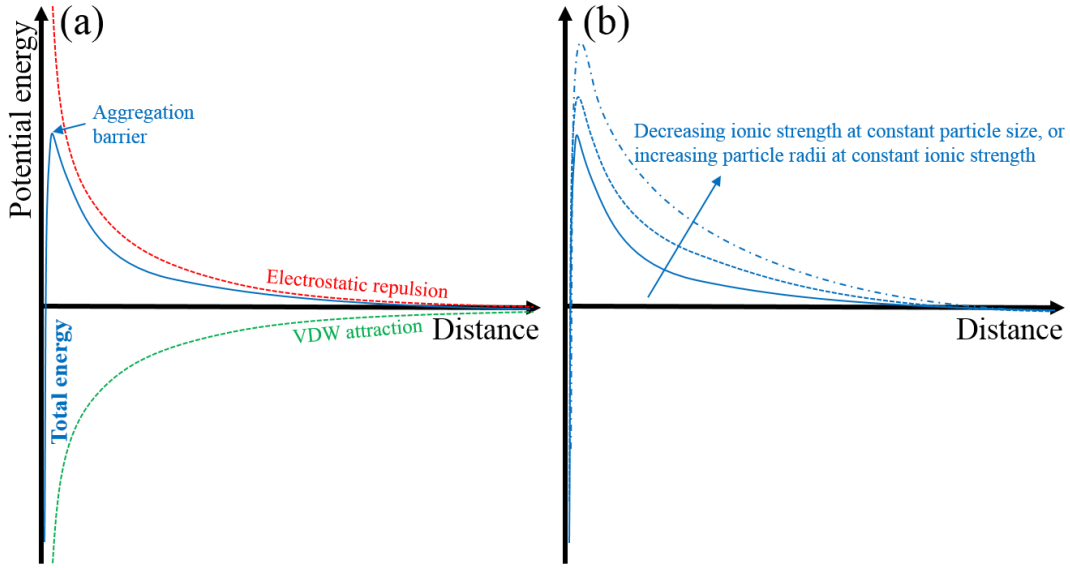

Figure 2.7 (a) Visualisation of hybridised total interaction energy in terms of Van der Waals attraction (green), and surface electrostatic repulsion (red). (b) Change in aggregation barrier as a function of increasing ion concentration c, or particle radii, R.

2.3.5 Solvent-electrolyte interactions

Ion-desolvation has been identified as the rate-limiting step during the transitory dehydration series [molecular precursors] → [prenucleation intermediates] → [primary nuclei] → [crystallites] for barium sulphate precipitation [63, 64, 139]. In aqueous systems, this relates to the extent of ion-hydration, which is influenced by the balance between electrostatic attraction and hydrogen bonding. The former is favoured by dissolved anionic (F^- [140], OH^- [141, 142]) or cationic (Ca^{2+}, Na^+ [143], UO_2^{2+} [144]) species with high charge density that rearrange water dipoles within their immediate solvation-shells accordingly, and are categorised as kosmotropes (structure-makers). Conversely, neutral or low charge-density chaotropes (structure-breakers) favour bulk solvent interactions or hydrogen bonding [63, 140, 145]. This may be graphically represented by comparing the relative hydration entropies of charged ions (from [146]) as a function of their ionic radii (Figure 2.8). The threshold between chaos and kosmos lies at 0 J K^{-1} mol^{-1}, though some contemporary literature indicates a slightly lower boundary (Figure 2.8, dashed-line) coinciding with Na^+. Irrespective of absolute values, the combination of kosmotropic cations with chaotropic counterions (TMA^+, NO_3^-, Cl^-) results in oppositely-hydrated ion-pairs

(kosmotrope-chaotrope), which increases kosmotrope-chaotrope ion separation distance to further enhance kosmotrope-hydration [140]. This reduces the mobility of bound water relative to bulk water [147] to promote competitive ion-solvent interactions in multi-electrolyte systems. This alleviates relative kinetic desolvation barriers (lower residence water times [63, 64, 148]), which in turn reduces interfacial tension [139] and critical nuclei radii according to classical nucleation theory [99, 149]. This theory applies to 2D nucleation and crystal growth, and is also pertinent to mineral dissolution mechanisms [142, 148].

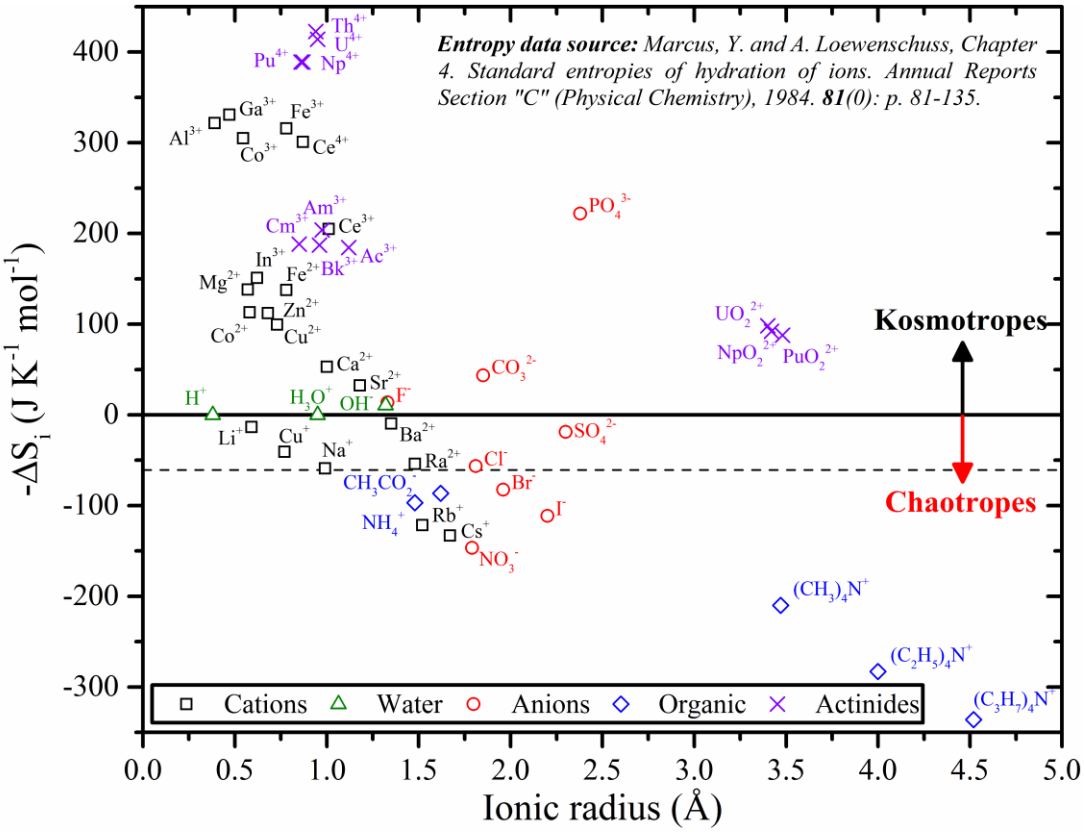

Figure 2.8 Standard partial molar hydration entropies ($-\Delta S_i$) of selected charged species as functions of their ionic radii.

2.4 Uranium in the solid-state

Uranium forms solid compounds with various non-metallic elements, to form rigid coordination polyhedra. Perhaps due to the abundance of oxygen in the geosphere, uranium oxides are most commonly studied [1]. In addition, the stability of U(IV) and U(VI) oxidation states manifests itself as various binary, ternary and quaternary compounds. Depending on the origin of formation, U(VI) may be present as oxide hydrates (oxyhydroxides) or oxides.

2.4.1 Uranyl(VI) oxyhydrates

Uranyl(VI) oxyhydrate phases lie closest to their corresponding solvated U-oligomers in terms of structure and chemistry [150-153]. Most phases in this family compound can be represented by the generic formula $M_n[(UO_2)_xO_y(OH)_z](H_2O)_m]$, where M is a dipositive counter ion and x, y, z, m and n are stoichiometry coefficients accounting for charge balance within the structural unit in square brackets. Due to the permanent uranyl(VI) unit, uranyl(VI) oxyhydrates are characterised by repeating polyhedra linked via the equatorial ligands. Various known uranyl(VI) oxyhydrates may be described by changing the counterion M (Table 2.2). Coordination numbers of equatorial O^{2-}or OH^- ligands, can therefore vary between 4, 5, or 6, to form square, pentagonal, or hexagonal bipyramidal polyhedra (Figure 2.9). Equatorial U-O ($U\text{-}O_{eq}$) bond lengths are almost exclusively longer than the uranyl(VI) $U\text{-}O_{yl}$ bond (~1.79 Å) [25], and extend further as a function of coordination number, increasing from ~2.26, 2.37, 2.46 Å for 4, 5, and 6 oxygens respectively [1].

The $U\text{-}O_{yl}$ bond length is comparatively unaffected in the same way as equatorial coordination number [25]. Notably, the latter hexagonal coordination is relatively rare, and most oxyhydrates contain a mixture of square and pentagonal bipyramids. O^{2-} or OH^- ligands are shared between adjacent UO-polyhedra via edge or corner-linkages to form infinitely repeating sheets or chains, thereby equalising anion charge over several U(VI)-centres. O^{2-} is generally shared between 3 U(VI)-centres, whereas OH^- either 2, or 3, where the bond length is extended in the latter due to charge donation to H^+ from O^{2-}. UO-polyhedra layers stack vertically, parallel to the basal plane.

The interlayer spaces are occupied by water only for phases that contain no additional ions (Schoepite [154, 155], Metaschoepite [156]), binding the layers via hydrogen bonding. In phases such as Becquerelite [157, 158] or Compreignacite [159, 160] etc., cations (Sr, Ca, Pb) [161, 162] coordinate with water in the interlayer, providing additional electrostatic stabilisation.

Table 2.2 Some uranyl(VI) containing minerals with layered structures bound by interlayer cationic species or waters of hydration.

Mineral	Composition	Uranyl(VI) equatorial plane coordination
Schoepite	$(UO_2)_8O_8(OH)_{12}\cdot 12H_2O$	Pentagonal
Meta-Schoepite	$(UO_2)_8O_8(OH)_{12}\cdot 10H_2O$	Pentagonal
Dehydrated-Schoepite	$UO_3\cdot(2\text{-}x)H_2O$	Pentagonal
Becquerelite	$Ca(UO_2)_6O_4(OH)_6\cdot 8H_2O$	Pentagonal
Clarkeite	$Na[(UO_2)O(OH)]\cdot H_2O$	Pentagonal/hexagonal
Compreignacite	$K_2U_6O_{19}\cdot 11H_2O$	Pentagonal

The structure and stability of polyhedra sheets may be described or predicted using a semi-empirical anion-topology approach [1, 25, 150, 151, 163], via parameters summarised from 368 mineral and synthetic uranyl(VI) phases. To begin, bonds between U(VI) and low valence cations or hydrogen bonds are ignored. From a top-down view of a uranyl(VI) polyhedra sheet, Anions (O^{2-}, OH^{-}) with more than 2 bonded cations are considered (Figure 2.9, left), and lines are drawn to represent anion-anion distances ≤3.5 Å.

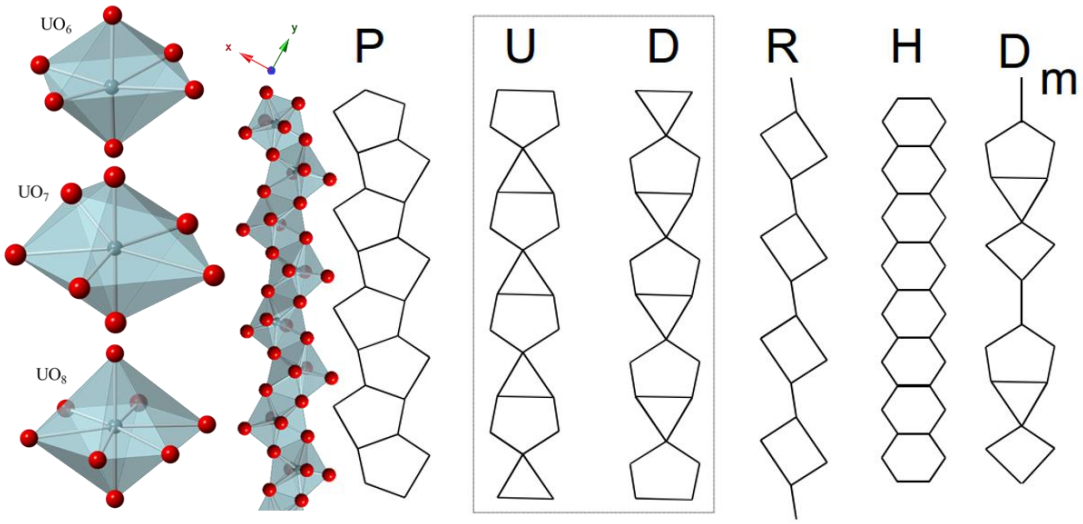

Figure 2.9 Left: 3D representations of uranyl(VI) UO_{4-6} polyhedra. Example uranyl(VI) oxyhydrate chain isolated from the sheet structure of Becquerelite, with a comparison of anion hierarchy types P, U, D, R, H, and D_m. ***Adapted from [25].***

This reduces complex uranyl(VI) sheet structures into a simplified 2D representation comprising series of repeating chain types. Each chain type is unique in terms of edge or corner sharing to give the designated letters P, U, D, R, H, and D_m. For example, the 3D projection shown (Figure 2.9, left) is a single P-chain, which when combined consecutively with the D chain (PDPDPD…) becomes the α-U_3O_8 sheet structure, and extends towards several other phases, namely Becquerelite [157], Protasite [164, 165], Billietite [165], Compreignacite [159], etc.

2.4.2 Anhydrous uranium oxides

The uranium oxide system is complex, with several phases exhibiting extensive isomerisation depending on synthesis conditions, temperature, and pressure. The complexity of uranium chemistry continues to be reflected by the number of available oxidation states and zones of solid solution (Figure 2.11). Thusly a brief overview of synthesis, and structural properties of anhydrous binary and ternary U-oxides is provided below.

2.4.2.1 Binary oxides

One of the most studied uranium oxide is UO_3, which probably stems from the large polymorphic variety. There are seven known structural isomers that have been synthesised with varying levels of success, amorphous (A), α, β, γ, δ, ε, and ζ. The synthesis routes are varied (Figure 2.10), though are achieved mostly via calcination of hydrated uranyl(VI) salts of nitrate or ammonia. The phase selectivity appears both temperature and seldom atmosphere dependent.

Washed uranium peroxide ($UO_4.2H_2O$) undergoes amorphisation during calcination up to 200 °C [166] to form a U_2O_7 intermediate[167]. Calcination of amorphous-U_2O_7 ($UO_4.2H_2O$), Schoepite ($UO_3.2H_2O$), uranyl(VI) oxalate ($UO_2C_2O_4.3H_2O$), and ammonium uranyl(VI) carbonate ($(NH_4)_4UO_2(CO_3)_3$) at 400 °C forms amorphous-UO_3 (Figure 2.10, UO_3(A)).

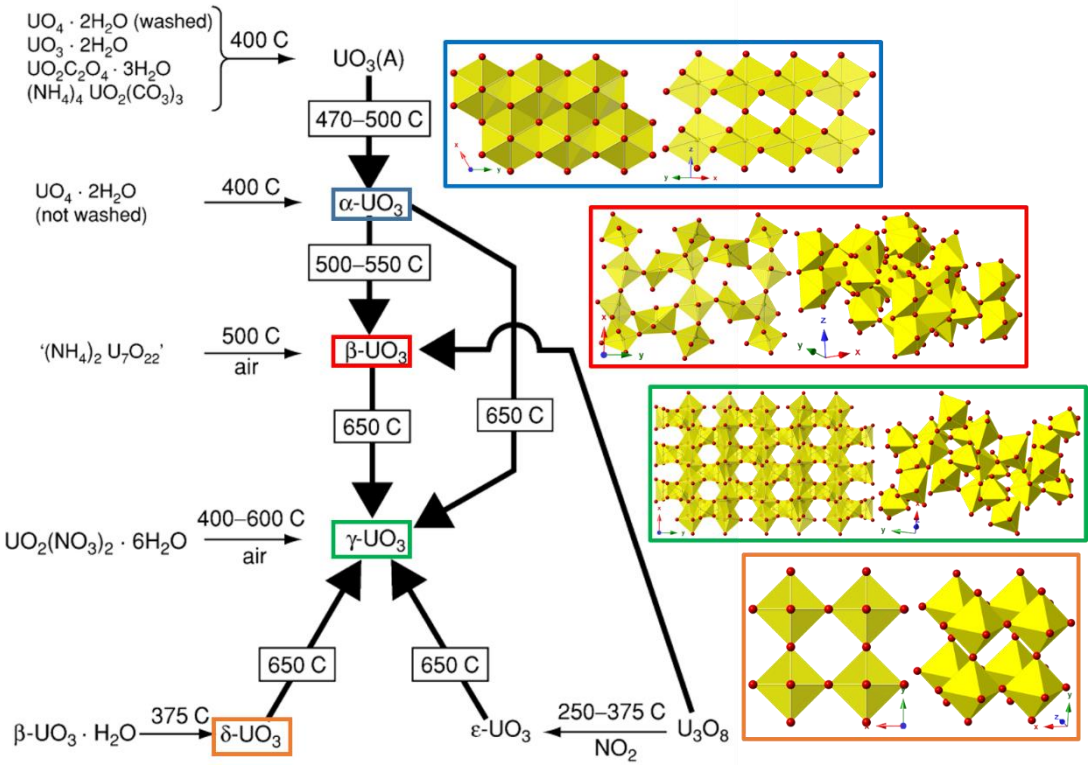

Figure 2.10 Summary of calcination-mediated synthesis routes of the structural isomers of UO_3, showing temperature, atmosphere, and starting products. ***Adapted from [1], 3D structural representations generated from crystallographic information files from the ICSD.***

Upon further calcination at 470 – 500 °C, anhydrous α-UO_3 crystallises. This may be achieved directly using unwashed uranium peroxide. The α-UO_3 structure comprises infinite layers of buckled-UO_8 polyhedra (Figure 2.10, blue), that are linked through the c-axis [168-170]. Heating of α-UO_3 at 500 – 550 °C or (rapidly heating) ammonium polyuranate ($(NH_4)_2U_7O_{22}$) to 500 °C in air, results in formation of β-UO_3 (Figure 2.10, red), comprising irregular chains of distorted UO_6 octahedra linked

along equatorial vertices. Along the c-axis, chains of UO-polyhedra run alternately parallel and perpendicular, leaving large interstitial voids [171, 172].

The most thermodynamically most stable γ-UO_3 phase forms during heating of α-, β-, δ-, or ε-UO_3 at 650 °C, or during thermal degradation of uranyl(VI) nitrate hydrate ($UO_2(NO_3)_2.6H_2O$) between 400 – 600 °C [173, 174]. The complex γ-UO_3 structure (Figure 2.10, orange) comprises infinite edge-linked UO_8 polyhedra arranged parallel in alternating layers, interspersed by perpendicular chains and isolated polyhedra. One striking feature are the tunnel-like interstices running parallel to the c-axis with a flattened 6-side projected geometry, measuring ~4.8 – 5.5 Å across.

Within the formal U(IV)-oxidation state, lies uranium dioxide (UO_2), a synthetic analogue of naturally occurring Uraninite (Figure 2.11). UO_2 may be synthesised via hydrogen reduction from UO_3, or U_3O_8 at 800 – 1100 °C, and crystallises in the Fluorite face-centred-cubic (FCC) structure ($a = b = c$, $\alpha = \beta = \gamma = 90°$). Uranium atoms occupy the positions (0, 0, 0), (½, ½, 0), (½, 0, ½), (0, ½, ½), whilst oxygens occupy all equivalent (¼, ¼, ¼) positions, resulting in a series of alternating cubic UO_8-polyhedra, that are edge-linked, with each layer stacked via the sequence ABCABC. Increasing calcination temperature towards 1700 °C improves density towards crystallographic predictions, and is often utilised in nuclear fuel fabrication processes. Industrial applications usually begin from ammonium diuranate [175], peroxides, or fluorides (see section 1), involving several cold-press and sinter steps [1]. Some novel recent studies have successfully synthesised colloidal UO_2 and U_3O_8 nanoparticles via thermal degradation in non-aqueous solvents [176-178]. UO_{2+x} tends to form via oxygen diffusion during cooling below 300 °C, or if O_2 impurities are present in the H_2-gas flow [179-183], where hyper-stoichiometric oxygen atoms occupy positions displaced ~1 Å from [110] and [111] planes [184].

Between $U^{VI}O_3$ and $U^{IV}O_2$ oxidation states or O/U-stoichiometry between 3 and 2, lie several UO-phases (Figure 2.11), each with their own structural isomers [1, 7, 185]. U_3O_8 or triuranium octoxide [186, 187], is sometimes given the misnomer uranyl(VI) uranate. However, with an oxidation state lying between U(VI) and U(V) [188, 189] the uranyl(VI) ion is absent, whilst the UO-sheet structure deviates far from traditional $M^{II}UO4$ uranates. Between UO_3 and U_3O_8, is $UO_{2.9}$ ($U_{12}O_{35}$) [186], a suspected distinct phase with structural properties lying somewhere between U_3O_8 and UO_3 in terms of oxygen vacancies.

Several phase transformation routes are apparent between UO_3 and U_3O_8 phases. For example, U_3O_8 forms via heating of δ/ε-UO_3 at 450 °C in air with moderate heating rates, otherwise heating to 620 – 700 °C is required due to re-oxidation to γ-UO_3. Alternatively, oxidation of UO_2 using air at 800 °C with slow cooling, results in α-U_3O_8 [190, 191]. A-U_3O_8 is closely related to the αProtasite or Becquerelite sheet

structure (see section 2.4.1), though the layers of P, D-type chains are linked vertically via U-O-U bonds.

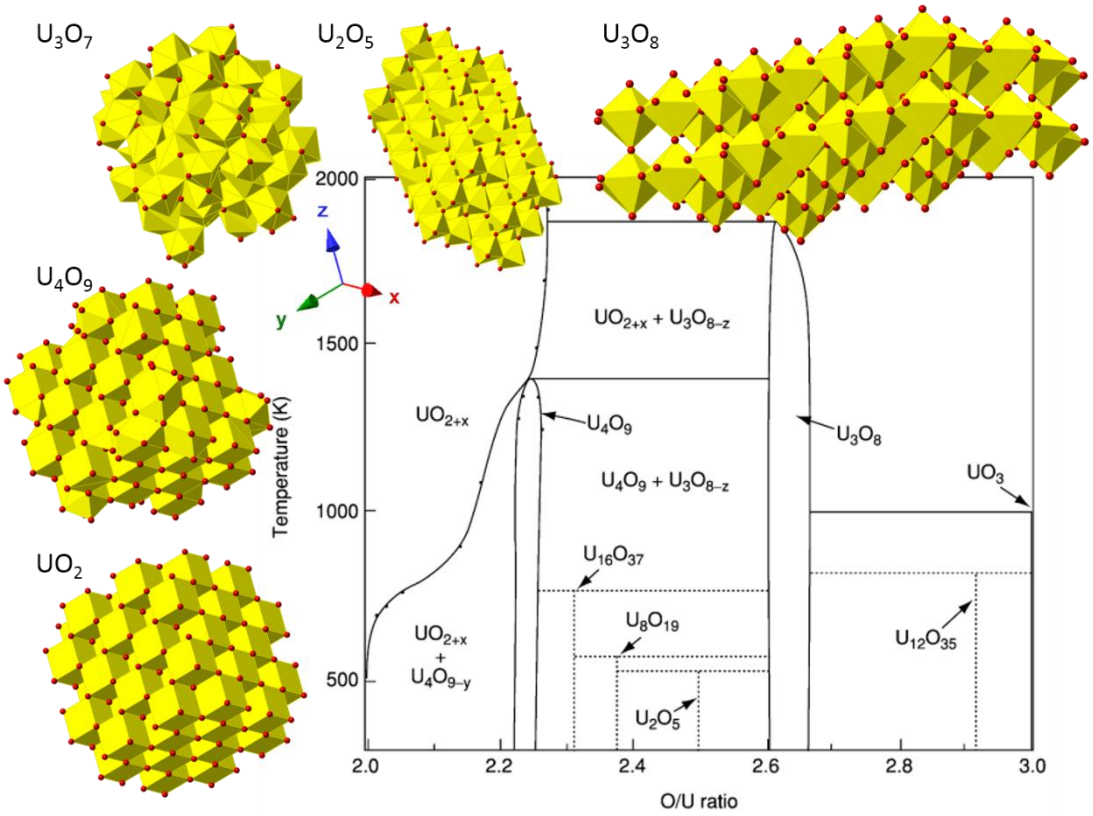

Figure 2.11 Temperature – O/U phase diagram for the binary UO-system. Note the transition from cubic Fluorite-like crystal structure towards U^{IV}, and the layered structures towards U(VI). ***Phase diagram Adapted from [1]. 3D structural representations generated from crystallographic information files from the ICSD.***

Due to the similarity between the α-U_3O_8 [001] and UO_2 [111] planes, and almost no change in UU-distances nor angles during oxidation, it was proposed that lattice infusion of oxygen causes stepwise distortion of the fluorite structure (UO_2) towards tetragonal (U_3O_7), monoclinic-distorted fluorite (U_2O_5). U_2O_5 undergoes phase transitions via layered-β and α forms before further oxidation to α-U_3O_8 [191, 192]. β-U_3O_8 is synthesised via heating of α-U_3O_8 at 1350 °C in air/O_2 followed by cooling at 100° day^{-1} to room temperature [193].

U_2O_5 (2.5 O/U), U_3O_7 (2.33 O/U) and U_4O_9 (2.25 O/U) all have α, β, and γ polymorphs. U_2O_5 and U_4O_9 are both synthesised from stoichiometric mixtures of UO_2 and U_3O_8 precursors, whereas α/β-U_3O_7 is synthesised from UO_2, and γ-U_3O_7 from U_4O_9.

α-U_2O_5 is synthesised via solid-state reaction between UO_2 and U_3O_8 at 400 °C and 3 mPa pressure for 8 hours, or at half the pressure (1.5 mPa) when temperature was elevated 500 °C. At 40 – 50 mPa and temperature (> 800 °C), hexagonal-β-U_2O_5

forms. At higher pressure (60 mPa) monoclinic γ-U_2O_5 [194]. Remarkably, the sheet-structure for U_2O_5 exhibits similar features to $(Sr/Pb)_3U_{11}O_{36}$ [195, 196], where equatorially aligned sheets of UO_7 and UO_6 polyhedra are interspersed by trimeric UO-defects, which would otherwise be occupied by (Sr/Pb)O polyhedra.

α-U_3O_7 forms during oxidation of UO_2 at <160 °C [197-201], whereas the β-polymorph forms above 200 °C [202]. The γ-polymorph forms via oxidation of U_4O_9 at 160 °C [186]. All three polymorphs of U_3O_7 are tetragonal, with some minor alterations in unit cell dimensions (c/a ~1.01 ±0.02) and O/U-stoichiometry (2.3 – 2.33).

Ceramic synthesis of α-U_4O_9 involves calcination of UO_2 with half molar equivalent of U_3O_8 at 1000 °C for up to 2 weeks [203, 204], followed by a 2 week cooling period. Reversible phase transformations occur at ~77 (β-U_4O_9) and ~577 °C (γ-U_4O_9) , indicating that only the α-form is stable at room temperature. The β-forms of U_4O_9 and U_3O_7 (Figure 2.11) exhibit increasingly distorted cubic structures with furthering deviation of O/U-stoichiometry from UO_2 [1, 185], and appear far more distinct from the layered polymorphs typical of U_2O_5 or U_3O_8. Excess oxygens for both phases are expected to be accommodated in cuboctahedral clusters [202].

2.4.2.2 Ternary oxides (uranates)

Anhydrous uranates are inorganic compounds with the general formula $M_n^c(U_xO_y^{z-})$, in which the uranium atoms (U) are stoichiometrically associated with oxygen atoms (O) to form anion polyhedra. Anion units ($U_xO_y^{z-}$) are balanced electrostatically by cations (M_n^c) of charge c, that span alkali [205-214], alkaline-earth [208, 215-227], and transition metals [228-231], though lanthanide [232-236] and metalloid [237] uranates with interesting catalytic properties are known [238-240]. Perhaps most common are the alkali and alkaline-earth uranates, which are defined by the generic formulae $M^+_2U_nO_{3n+1}$ and $M^{2+}U_nO_{3n+1}$ for mono- and di-uranates, and are accompanied by various polyuranate forms; $M^+_4UO_5$; $M^{2+}_2UO_5$; $M^{2+}_3UO_6$; $M^{2+}_2U_3O_{11}$ [1]. In relation to the binary oxides, the uranium cation can vary between (VI), (V) and (IV) oxidation states. Naturally occurring crystalline phases are exceedingly rare [241-244] or tend to be amorphous [245, 246], rendering the literature studies towards synthetic uranates by majority [1].

Synthetic alkali/alkali-earth metal uranates are characterised by three common lattice arrangements (Figure 2.12). Similar to oxyhydrates, the uranyl(VI) unit features in many uranates, where two oxygen atoms are arranged collinearly to a central U(VI)-cation (see section). Lattice distortion results in a minor reduction of bond order from 3 depending on immediate electronic interactions. Differences in bond-strength is reflected by shifts in the anti-symmetric stretch of UO_2^{2+} in the infra-red 600 – 900

cm^{-1} region [247, 248]. Varying numbers of equatorial oxygens are coordinated perpendicular to the uranyl(VI) oxygens resulting in flattened polyhedra. The monouranate unit UO_4^{2-} is therefore better represented by the stoichiometric formula of $[(UO_2)O_2]^{2-}$; and the diuranate $U_2O_7^{2-}$ by $[(UO_2)O_{1.5}]_2^{2-}$.

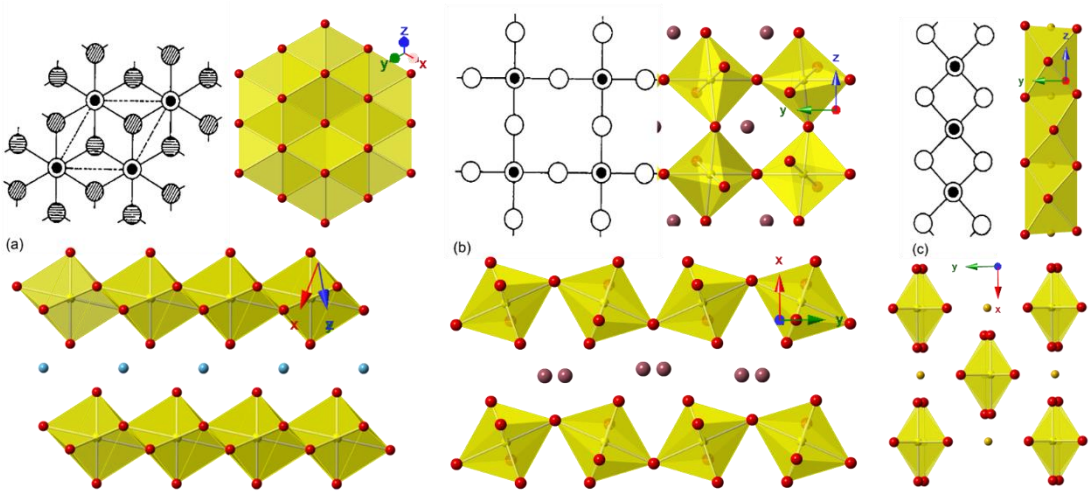

Figure 2.12 Topographical view of three common uranate UO-lattice arrangements. Open circles (○) represent primary uranyl(VI) oxygen atoms on the plane of the page; (●) represent the central uranium atom on the plane of the page; (◍) represent secondary oxygen atoms slightly above plane of uranium/page; (◍) represent secondary oxygen atoms slight below the plane of the uranium/page; (◉) represents the top-down view (c-axis) of the uranyl(VI) ion with primary oxygen atoms above and below plane of uranium/page. ***Adapted from [1], and 3D representations generated from crystallographic information files for (a) $CaUO_4$, (b) $BaUO_4$, and (c) $MgUO_4$.***

These units may be linked at corners (Figure 2.12b) giving an infinite plane of uranyl(VI) units separated by equatorial oxygen ions. Alternatively, the truncated octahedral units are edge linked to give contiguous infinite chains of UO_6^{6-} polyhedral (Figure 2.12c). However the X-ray diffraction data for the alkali-metal diuranates are under contention; for example both sodium and potassium diuranates have crystal systems ranging between rhombohedral [249], orthorhombic [211] and monoclinic [250]; with space groups ranging between R3m, $P2_I/m$ and $P2_I$ depending on the work referenced.

Similar to the topological anion-chain classification of uranyl(VI) oxyhydrates, some structural relationships may be drawn between binary and ternary uranium oxides, with the advantage of describing exclusively synthetic phases with significantly greater cation/uranium stoichiometry [16]. These relationships stem from a symmetry-based treatment of valence U 6d5f and diffuse U 7s orbitals, resulting in a 13-orbital (12+1) manifold to take into consideration the covalency of U-O bonds [14-16, 251]. Therefore, from group theory perspectives, 12 ($7s6d^55f^6$) and 10 ($7s6d^45f^5$)

orbitals are centrosymmetric [1] and contribute towards tetragonal and hexagonal bipyramidal polyhedra, whilst a non-centrosymmetric 11 ($7s6d^5 5f^5$) orbital contribution results in pentagonal bipyramid polyhedra. This provides five symmetry-allowed motifs based on available U-O σ and π-orbital interactions (Table 2.3), of which, three are octahedral, one is pentagonal and one hexagonal bipyramid. The first two octahedral motifs are characterised by 12-orbital overlap between U and O atoms.

Regular-O_h polyhedra is formed via equidistributional overlap of U-O σ and π orbitals, resulting in a six-fold coordination comprising an effective bond order of 2 (6 O-ligands = 12 orbitals). The uranyl(VI) unit is not present here. Representative phases include $M^{II}_3UO_6$ (M^{II} = Ca, Ba, Sr, etc), or $M^{I}_6UO_6$ (M^{I} = Li) [1, 223, 229, 252-254].

Elongated-D_{4h} exhibits an anti-uranyl(VI) arrangement, where axial U-O_{yl} bonds are longer (weaker) than equatorial U-$O_{eq,}$ which is reflective of higher electron-density in the equatorial axes, resulting in an equatorial bond order of 2.5. Uranates that fall into this category include $(Li/Na)_4UO_5$, where UO_6^{2-}-chains link along the c-axis, and the discrete uranyl(VI) unit is lost [255].

Flattened-D_{4h} deviates from the previous two octahedral geometries via a 10-orbital overlap, caused by 3-fold U-O_{yl} bond order, which renders the axial bonds shorter than equatorial. This geometry describes the monouranates $M^{I}_2UO_4$ (where M^{I}=Na^+, K^+) and $M^{II}UO_4$ (where M^{II} = Mg^{2+}, Ba^{2+}). The latter is visualised in Figure 2.12b, and c, manifesting in $BaUO_4$ and $MgUO_4$ to give infinite layers and chains of UO_6 truncated octahedra, respectively. Alkali/alkali earth metals occupy the positions between the uranyl(VI) polyhedra (Figure 2.12) to stabilise the structure through electrostatic forces [170] in a similar way to the uranyl(VI) oxyhydrates, though without water.

Pentagonal-D_{5h} geometry is equivalent to the P-type anion-chain in oxyhydrate classifications. It has similar axial orbital overlap as D_{4h}, though singular π-bonding in the equatorial plane results in bond order of unity for U-O_{eq} bonds. As the most common geometry, it may be used to describe α-U_3O_8-like sheet structures.

Hexagonal-D_{6h}, visualised in Figure 2.12a, is prevalent in β$LiUO_4$ [256], $CaUO_4$ and β$SrUO_4$ [257], as well as pure α-UO_3 [169], which resemble the H-type anion-chain in oxyhydrates. Due to the 8-coordinate UO-polyhedra, a 10-orbital overlap reduces U-O_{yl} to a double-bond, which is reflected by longer (weaker) axial bonds (~1.9 Å). This arises from electron-donation from O 2p towards coordinated interlayer cations.

---

[1] An equal number of overlapping atomic orbitals that are gerade (in-phase σ_g, π_g) and ungerade (out-of-phase σ_u, π_u).

The U-O_{eq} are characterised by alternating equatorial oxygens located 0.5 Å below and 0.5 Å above the uranium plane, resulting in a 'buckled' arrangement. Notably, the α-UO_3 ↔ α-U_3O_8 transformation involves the exchange of one 6th of lattice O-anion positions, represented by a transition between the H and U-type chains.

Finally, the uranate-unique feature of high cation loading, or lack of, in uranium oxides, may also be related to known phases. To this end, the uranates and uranium oxides have been classified into three categories, cation-rich, cation-neutral, and cation-poor [16]. This requires consideration of the formal charge imparted upon uranium within anion-units. Using the anion-unit formula $U_xO_y^{z-}$, where Z- is unit charge and X is U-stoichiometry, the Z/X-ratio may be calculated for various binary and ternary phases. Accordingly, the region Z/X < 2 contains example phases such as α/β-UO_3 and α/β-U_3O_8 (Z/X = 0). With no formal occupancy of the interlayer, axial oxygens are shared vertically between U(VI)-centres to form infinite repeating layers UO-polyhedra. Uranates in this region are therefore related in terms of UO-sheet structure, or appear as defect structures of α-U_3O_8. Excellent examples of this trend manifest in the Sr/Pb-polyuranates with general formula $M_3U_{11}O_{36}$ (Z/X ~0.55), where the structure is almost identical to that α-U_3O_8 except for edge-sharing trimeric chains of defects in the UO-sheet, that are instead occupied by (Sr/Pb)O_7 polyhedra [195, 196]. Although keeping with sheet-structure along the equatorial plane, the Cs-polyuranates $Cs_2U_{15}O_{46}$ (Z/X ~0.13), and $Cs_2U_7O_{22}$, (Z/X ~0.29) [258], instead exhibit axial separation of UO-sheets, resulting in alternating layers of CsO and UO-polyhedra. This is likely a consequence of the significant increase in ionic radii from Pb^{2+} (~1.33 Å) and Ca^{2+} (~1.14 Å), to that of Cs^+ (~1.81 Å). The alkaline-metal diuranates $M^I_2U_2O_7$ (where M = Na^+, K^+) exhibit similar alternating layers. However, the UO-sheet structure now resembles that of β-U_3O_8 , consisting chains of UO_6 and UO_7 polyhedra. This is equivalent to alternating chains of P and R-type chains from uranyl(VI) oxyhydrate classifications. Again, via expansion of cation radii, Cs (R_{Cs} = 1.81 Å) and Rb (R_{Cs} = 1.66 Å) are accommodated in diuranate sheet-structures comprising staggered UO_6-chains.

Table 2.3 Summary of bonding interactions using the 12+1 U $7s^1 6d^5 5f^7$ orbitals, (see Table 2.4 for summary of point group numbers). ***Adapted from [15, 16]***

	Octahedral derivatives				
	Regular O_hUO_6	**Elongated $D_{4h}UO_4^eO_{2/2}^a$**	**Flattened $D_{4h}UO_2^aO_{4/2}^e$**	**D_{5h} pentagonal bipyramidal $UO_2^aO_5^e$**	**D_{6h} hexagonal bypyramidal $UO_2^aO_6^e$**
Orbitals involved in σ-bonding (Γ_σ)	$A_{1g}(s)$ $E_g(x^2\text{-}y^2, z^2)$ $T_{1u}(\phi_\delta)$	$2A_{1g}(s, z^2)$ $B_{1g}(x^2\text{-}y^2)$ $A_{2u}(z^3)$ $E_u[x(x^2\text{-}3y^2, y(3x^2\text{-}y^2)]$	$2A_{1g}(s, z^2)$ $B_{1g}(x^2\text{-}y^2)$ $A_{2u}(z^3)$ $E_u[x(x^2\text{-}3y^2, y(3x^2\text{-}y^2)]$	$2A_{1g}(s, z^2)$ $E_1'[x(x^2\text{-}3y^2, y(3x^2\text{-}y^2)]$ $E_2'[x(x^2\text{-}3y^2, y(3x^2\text{-}y^2)]$	$2A_{1g}(s, z^2)$ $E_{2g}(x^2\text{-}y^2, xy)$ $A_{2u}(z^3)$ $B_{1u}([x(x^2\text{-}3y^2)]$ $E_{1u}(xz^2, yz^2)$
Orbitals involved in π-bonding (Γ_π)	T_{1g} $T_{2g}(xy, xz, yz)$ T_{1u} (used for σ) $T_{2u}(\phi_\varepsilon)$	A_{2g} $B_{2g}(xy)$ $E_g(xz, yz)$ A_{2u}(used for σ) $B_{2u}(z^2(x^2\text{-}y^2)$ $E_u(xz^2, yz^2)$	$E_g(xz, yz)$ $E_u(xz^2, yz^2)$	$E_1'(xz^2, yz^2)$ $E_1''(xz, yz)$	$E_{1g}(xz, yz)$ E_{1u}(used for σ)
Oxygen atoms involved in π-bonding	6(all)	4(equatorial)	2(axial)	2(axial)	2(axial)
Average π-bond order per oxygen atom	6/6=1	¾ π (∥) ¾ π (⊥) $^6/_4 = {}^3/_2$ π (total)	$^4/_2$=2	$^4/_2$=2	$^2/_2$=1
Total bond order for π-bonded oxygen atoms	2	2½	3	3	2

Only the monouranates ($M^{II}UO_4$) reside in the cation neutral region where Z/X = 2, and vary somewhat in UO-lattice structure. Ranging from the buckled UO_8 polyhedra present $CaUO_4$ and $\beta SrUO_4$ (Figure 2.12a), to the infinitely repeating chains in $(\alpha Sr/Ba/Pb)UO_4$ (Figure 2.12b). The differences in UO-polyhedra across $M^{II}UO_4$ monouranates stem from the coordination trends in counterion radii or mass [16], where monouranate MO_x-coordination environments consist of $(Cu^{2+}/Mg^{2+})O_6$, $(Ba^{2+}/\alpha Sr^{2+}/Pb^{2+})O_7$ [259], or $(\beta Sr^{2+}/Ca^{2+})O_8$ polyhedra [220, 253, 259]. Indeed the K_2UO_4 [260](R_K = 1.51 Å), and Rb_2UO_4 (R_{Rb} = 1.66 Å) sheet-structure is similar to that in $BaUO_4$ (R_{Ba} = 1.52) (Figure 2.12c) [259, 261].

Towards the cation-excessive Z/X > 2 region, uranates are mostly characterised by anti-uranyl(VI) and perovskite like UO-polyhedra. The former may be represented by $M_2^{II}UO_5$ ($M = Ca^{2+}$, Sr^{2+}) or $M_4^{I}UO_5$ ($M = Li^+$, Na^+) [255, 262], where elongated NaO_6 and UO_6 polyhedra alternate in position in the equatorial plane, and are linked through oxygen bonds running along the c-axis (Figure 2.12a, b).

The O_h-symmetry UO-polyhedra in $M^{II}{}_3UO_6$ (where $M^{II} = Ca^{2+}$, Ba^{2+}, Sr^{2+}, etc.), or $M^{I}{}_6UO_6$ (where $M^{I} = Li^+$), are further detached compared to Na_4UO_5 (Figure 2.13a, b), and consist of alternating M- and U-oxide polyhedra arranged in a distorted perovskite structure with no common U-O-U linkages [1, 223, 229, 252-254].

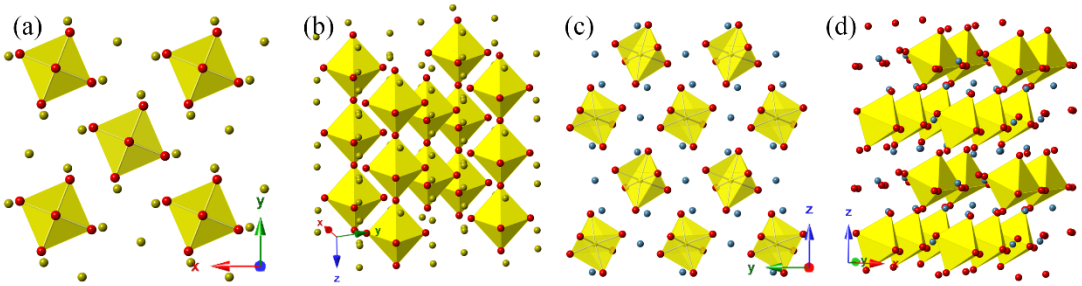

Figure 2.13 Structures of $M_2^{II}UO_5$ (M = Ca, Sr) or $M_4^{I}UO_5$ (M = Li, Na) in (a), (c) top down and (b), (d) isometric view; respectively.

2.4.2.2.1 Solid-state synthesis

The most common method for synthesis of the uranates involve high temperature solid state reactions between an intimate mixture metal salt and U-oxide with the correct stoichiometry. Much of the literature is based on alkali uranates, formed as generally yellow-orange solids during solid-state reactions with a range of oxidising agents (oxides, nitrates, chlorates, peroxides), though the uranium donor is usually UO_2, U_3O_8 or UO_3. However, the final product may be oxygen deficient due to localised non-stoichiometry as observed in the high temperature reaction between U_3O_8 with sodium/lithium carbonate [217].

High temperature reaction between sodium oxide/peroxide (Na_2O, Na_2O_2 respectively) and UO_2; U_3O_8; UO_3 have all been used during the formation of sodium uranates. It is apparent that the formation of uranates from UO_2 (U(IV)) result in a mixture of sodium uranates at 360-800 ºC (Equation 2.7) [263]. Prior dissolution of the oxide/peroxide in (Li^+-Na^+-K^+)-carbonate melts provide selectivity to the mono-uranate (Na_2UO_4) at 400-600 ºC [210].

$$UO_2 + 2Na_2O_2 \rightarrow Na_4UO_5 + \frac{1}{2}O_2 \text{ (360 °C)}$$
$$2UO_2 + Na_2O_2 + \frac{1}{2}O_2 \rightarrow Na_2U_2O_7$$
$$Na_2U_2O_7 + 3Na_2O_2 \rightarrow Na_4UO_5 + \frac{3}{2}O_2$$
$$Na_4UO_5 + Na_2U_2O_7 \rightarrow Na_2UO_4$$

Equation 2.7

A similar result is attained in the solid-state via reaction between U_3O_8 and the peroxide salt at 700-900 ºC [250]. Upon replacement with UO_3, the product tends towards di- and poly-uranates.

$$U_3O_8 + 3Na_2O_2 \rightarrow 3Na_2UO_4 + O_2$$
$$UO_3 + 3Na_2O_2 \rightarrow 3Na_2UO_4 + O_2$$

Equation 2.8

Generalised reactions between carbonates and uranium oxides are given below, where M stands for any normal alkali metal such as Li^+, Na^+, and K^+ [260, 264, 265].

$$\frac{y}{3}U_3O_8 + xM_2CO_3 + \frac{y}{6}O_2 \rightarrow (M_2O)_x(UO_3)_y + xCO_2 \quad \text{Equation 2.9}$$

For sodium or potassium carbonate and U_3O_8, reaction begins at 400 ºC with the endothermic reaction rate increasing with temperature. The conversion is initially reaction controlled, before transitioning to mass-transfer control that is rate-limited by diffusion of sodium carbonate through the sodium uranate product layer [207]. Sodium diuranate ($Na_2U_2O_7$) is the first product formed regardless of sodium-uranium reactant ratio [207], though excess carbonate will result in higher oxidised products such as $NaUO_4$ and Na_4UO_5 [250, 255]. The rate-limiting step forms oxygen deficient uranates, which is followed by oxidation towards U(VI) [266]. If U_3O_8 is replaced by UO_3, sodium diuranate forms at 546 ºC, followed by conversion to sodium monouranate ($NaUO_4$) from 680 ºC upwards [207], though for UO_3, only Na_2UO_4 and $Na_2U_2O_7$ forms between 200 and 1000 ºC [267], compared to the additional polyuranates for U_3O_8. The generic reaction for many alkali-compounds is shown below for UO_3 (Equation 2.10) [208, 264, 268].

$$yUO_3 + xM_2CO_3 \rightarrow (M_2O)_x(UO_3)_y + xCO_2 \quad \text{Equation 2.10}$$

When calcium, strontium, or barium carbonate precursors are used, decomposition processes begin at 580 ºC, exhibiting steep mass-loss above 700 ºC. This behaviour is assumed to be due to a two-step reaction occurring via preliminary decomposition of

calcium carbonate to calcium oxide and carbon dioxide (Equation 2.11, I), which precedes the reaction of calcium oxide with U_3O_8 at 850 ºC (Equation 2.11, III) [227]. Indeed, reactions between calcium, strontium, or barium oxides, with U_3O_8 (Equation 2.11, III) appear favoured at temperatures as low as 400 ºC compared to the carbonate reactions (Equation 2.11, I).

$$I.\ \tfrac{1}{3}U_3O_8 + MCO_3 + \tfrac{1}{6}O_2 \rightarrow CaUO_4 + CO_2$$

$$II.\ CaCO_3 + O_2 \rightarrow CaO + CO_2\ (580^oC - 700^oC) \qquad \text{Equation 2.11}$$

$$III.\ \tfrac{1}{3}U_3O_8 + CaO + \tfrac{1}{6}O_2 \rightarrow CaUO_4\ (> 850^oC)$$

The Ca^{2+}-U(VI)-O system is complex, containing numerous high temperature phases with Ca/U-stoichiometry of 0.25, 0.5, 0.667, 1, 2, 3 [269], which correspond to the compounds CaU_4O_{13}, CaU_2O_7 [219], $Ca_2U_3O_{11}$ [102, 269], $CaUO_4$ [257], Ca_2UO_5 [226] and Ca_3UO_6 [223]. However, studies are incomplete due to the difficulties in obtaining pure products for XRD-characterisation.

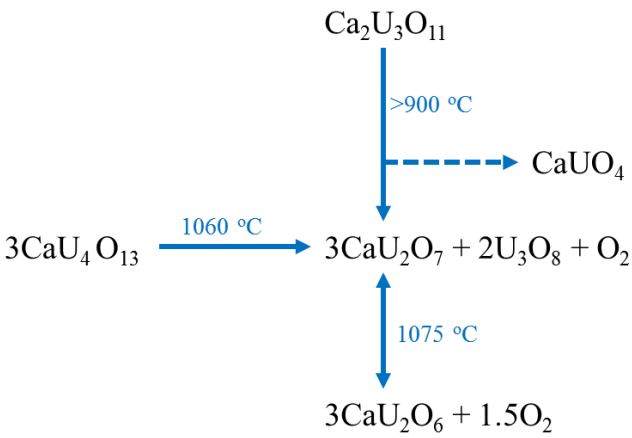

Equation 2.12

Usually the $CaUO_4$ (Ca/U = 1) is formed after 3 hours under heating to 950 ºC, independent of the reactant ratios, before converting to CaU_2O_7 after 4 days of heating with impurities of CaU_4O_{13} or $Ca_2U_3O_{11}$. Further heating at 1060 ºC and 1075 ºC results in a reversible degradation mechanism (Equation 2.12 [269]). Similar behaviour is observed for high temperature degradation of barium polyuranates [270].

2.5 Summary

Significant advances in the chemistry and syntheses of compounds within the ternary metal-U(VI)-oxygen system have enabled the structural characterisation of several crystalline oxyhydrates, oxides, and uranates. However, considerable shortfalls in understanding exist regarding the precipitation, dehydration, and crystallisation mechanisms that span the interface between solution and solid-state chemistry.

Some analogy exists between crystallisation from solution and via solid-state dehydration, with overlapping phenomena relating to desolvation/hydrate-content,

structural transformations, and stoichiometry. Crystalline uranates are formed from low-water content phases and high metal ion/uranium stoichiometric ratio, whereas crystalline uranyl oxyhydrates tend to arise under conditions of high water content and low metal ion/uranium stoichiometric ratio. Under intermediate conditions, i.e., with increasing metal-uranium stoichiometric ratios, amorphous phase formation or cryptocrystallinity ensues.

These relationships between dehydration, crystallinity and structure have been studied for many non-actinide phases, though tertiary stoichiometric influences on these critical processes has been hindered by difficulties in characterising amorphous structure, whilst remaining almost entirely unexplored for the actinides.

Clearly, a deeper understanding of the complex relationships between these phases could have profound enabling influences on rationalising the solid-state chemistry of natural uranium(VI) phases and of anthropogenic phases in the nuclear fuel cycle. Moreover, better knowledge of one complex actinide system could provide a reference point for other actinide or non-actinide materials.

2.6 Symmetry and point group codes

Table 2.4 Symmetry and point group codes. ***Adapted from [2]***

Atomic orbital	Symmetry groups				
	C_{2v}	D_{3h}	D_{4h}	T_d	O_h
s	a_1	a_1'	a_{1g}	a_1	a_{1g}
p_x	b_1	e'	e_u	t_2	t_{1u}
p_y	b_2	e'	e_u	t_2	t_{1u}
p_z	a_1	a_2"	a_{2u}	t_2	t_{1u}
d_z^2	a_1	a_1'	a_{1g}	e	e_g
$d_{x^2-y^2}$	a_1	e'	b_{1g}	e	e_g
d_{xy}	a_2	e'	b_{2g}	t_2	t_{2g}
d_{xz}	b_1	e"	e_g	t_2	t_{2g}
d_{yz}	b_2	e"	e_g	t_2	t_{2g}

C_{2v}			D_{3h}			O_h		
A_1	z	x^2, y^2, z^2	A_1'		x^2+y^2, z^2	A_{1g}		x^2+y^2, z^2
A_2	R_z	xy	A_2'	R_z		E_g		$(2z^2-x^2-y^2$, $x^2-y^2)$
B_1	x, R_y	xz	E'	(z,y)	x^2-y^2, xy	T_{1g}	(R_x,R_y,R_z)	
B_2	y, R_x	yz	A_1"			T_{2g}		(xz, yz, xy)
			A_2"	z		T_{1u}	(xyz)	
			E"	(R_x,R_y)	(xz, yz)	…		

D_{4h}			T_d		
A_{1g}		x^2+y^2, z^2	A_1		$x^2+y^2+z^2$
B_{1g}		x^2-y^2	A_2		
B_{2g}		xy	E		$(2z^2-x^2-y^2$, $x^2-y^2)$
E_g	(R_x, R_y)	(xz, yz)	T_1	(R_x,R_y,R_z)	
A_{2u}	z		T_2	(x, y, z)	(xz, yz, xy)
E_u	(x, y)				

2.7 References

1. Morss, L.R., Edelstein, N.M., Fuger, J., and Katz, J.J., *The Chemistry of the Actinide and Transactinide Elements (Volumes 1-5): Vol. 1*. Vol. 1. 2007: Springer.
2. Atkins, P., Overton, T., Rourke, J., Weller, M., and Armstrong, F., *Shriver & Atkin's Inorganic Chemistry*. 5 ed. 2010, UK: Oxford University Press.
3. Cotton, S., *Lanthanide and Actinide Chemistry*. 2013: John Wiley & Sons.
4. King, R.B., *Chemical Applications of Topology and Group Theory. 27. Covalent Bonding in Actinide Derivatives.* Inorganic Chemistry, 1992. **31**(10): p. 1978-1980.
5. Bendix, J. and Bøgevig, A., *Synthesis and Characterization of a Stable Trans-Dioxo Tungsten (Iv) Complex and Series of Mono-Oxo Molybdenum (Iv) and Tungsten (Iv) Complexes. Structural and Electronic Effects of Π-Bonding in Trans-$[M(O)(X)(Dppe)_2]^+$ Systems.* Inorganic chemistry, 1998. **37**(23): p. 5992-6001.
6. Ballhausen, C.J. and Gray, H.B., *The Electronic Structure of the Vanadyl Ion.* Inorganic Chemistry, 1962. **1**(1): p. 111-122.
7. Greenwood, N.N. and Earnshaw, A., *Chemistry of the Elements*. 2012: Elsevier.
8. Nockemann, P., Servaes, K., Van Deun, R., Van Hecke, K., Van Meervelt, L., Binnemans, K., and Görller-Walrand, C., *Speciation of Uranyl Complexes in Ionic Liquids by Optical Spectroscopy.* Inorganic Chemistry, 2007. **46**(26): p. 11335-11344.

9. Pyykko, P., Laakkonen, L.J., and Tatsumi, K., *Rex Calculations. 12. Iteration Parameters for the 5f-Element Organometallics of Thorium-Neptunium. Geometries of Thorium Dioxide and Uranyl Ion Revisited.* Inorganic Chemistry, 1989. **28**(10): p. 1801-1805.
10. van Besien, E., Pierloot, K., and Gorller-Walrand, C., *Electronic Spectra of Uranyl Chloride Complexes in Acetone: A Casscf/Caspt2 Investigation.* Physical Chemistry Chemical Physics, 2006. **8**(37): p. 4311-4319.
11. Gordon, G. and Taube, H., *The Exchange Reaction between Uranyl Ion and Water in Perchloric Acid Solution.* Journal of Inorganic and Nuclear Chemistry, 1961. **19**(1-2): p. 189-191.
12. Shamov, G.A. and Schreckenbach, G., *Theoretical Study of the Oxygen Exchange in Uranyl Hydroxide. An Old Riddle Solved?* Journal of the American Chemical Society, 2008. **130**(41): p. 13735-13744.
13. Veal, B., Lam, D., Carnall, W., and Hoekstra, H., *X-Ray Photoemission Spectroscopy Study of Hexavalent Uranium Compounds.* Physical Review B, 1975. **12**(12): p. 5651.
14. Denning, R.G., *Electronic Structure and Bonding in Actinyl Ions and Their Analogs.* The Journal of Physical Chemistry A, 2007. **111**(20): p. 4125-4143.
15. King, R., *Chemical Applications of Topology and Group Theory. 27. Covalent Bonding in Actinide Derivatives.* Inorganic Chemistry, 1992. **31**(10): p. 1978-1980.
16. King, R.B., *Some Aspects of Structure and Bonding in Binary and Ternary Uranium(Vi) Oxides.* Chemistry of Materials, 2002. **14**(9): p. 3628-3635.
17. Baker, R.J., *New Reactivity of the Uranyl(Vi) Ion.* Chemistry–A European Journal, 2012. **18**(51): p. 16258-16271.
18. Knope, K.E. and Soderholm, L., *Solution and Solid-State Structural Chemistry of Actinide Hydrates and Their Hydrolysis and Condensation Products.* Chemical Reviews, 2013. **113**(2): p. 944-994.
19. Henry, M., Jolivet, J., and Livage, J., *Aqueous Chemistry of Metal Cations: Hydrolysis, Condensation and Complexation.* Chemistry, Spectroscopy and Applications of Sol-Gel Glasses, 1992: p. 153-206.
20. Jolivet, J.-P., Henry, M., and Livage, J., *Metal Oxide Chemistry and Synthesis: From Solution to Solid State*. 2000: Wiley-Blackwell.
21. Schreckenbach, G., Hay, P.J., and Martin, R.L., *Theoretical Study of Stable Trans and Cis Isomers in $[Uo_2(Oh)_4]^{2-}$ Using Relativistic Density Functional Theory.* Inorganic chemistry, 1998. **37**(17): p. 4442-4451.
22. Clark, D.L., Conradson, S.D., Donohoe, R.J., Keogh, D.W., Morris, D.E., Palmer, P.D., Rogers, R.D., and Tait, C.D., *Chemical Speciation of the Uranyl Ion under Highly Alkaline Conditions. Synthesis, Structures, and Oxo Ligand Exchange Dynamics.* Inorganic Chemistry, 1999. **38**(7): p. 1456-1466.
23. Fortier, S. and Hayton, T.W., *Oxo Ligand Functionalization in the Uranyl Ion (Uo_2^{2+}).* Coordination Chemistry Reviews, 2010. **254**(3–4): p. 197-214.
24. CF Jr, B. and Mesmer, R., *The Hydrolysis of Cations*. 1976: John Wiley and Sons, New York.
25. Krivovichev, S., Burns, P., and Tananaev, I., *Structural Chemistry of Inorganic Actinide Compounds*. 2006: Elsevier.
26. Grenthe, I., Fuger, J., Konings, R.J., Lemire, R.J., Muller, A.B., Nguyen-Trung, C., and Wanner, H., *Chemical Thermodynamics of Uranium*. 1992, Amsterdam, Netherlands: Elsevier.
27. Guillaumont, R., Fanghänel, T., Neck, V., Fuger, J., Palmer, D.A., Grenthe, I., and Rand, M.H., *Update on the Chemical Thermodynamics of Uranium, Neptunium, Plutonium, Americium and Technetium*. 2003, Amsterdam, the Netherlands: Elsevier.
28. Altmaier, M., Gaona, X., and Fanghanel, T., *Recent Advances in Aqueous Actinide Chemistry and Thermodynamics.* Chemical Reviews, 2013. **113**(2): p. 901-943.
29. Serezhkin, V.N., *Chapter 2 - Some Features of Stereochemistry of U(Vi) A2 - Tananaev, Sergey V. Krivovichevpeter C. Burnsivan G*, in *Structural Chemistry of Inorganic Actinide Compounds*. 2007, Elsevier: Amsterdam. p. 31-65.
30. Langford, C.H. and Gray, H.B., *Ligand Substitution Processes*. 1966: WA Benjamin, Inc.
31. Vallet, V., Wahlgren, U., and Grenthe, I., *Probing the Nature of Chemical Bonding in Uranyl(Vi) Complexes with Quantum Chemical Methods.* The Journal of Physical Chemistry A, 2012. **116**(50): p. 12373-12380.
32. Wahlgren, U., Moll, H., Grenthe, I., Schimmelpfennig, B., Maron, L., Vallet, V., and Gropen, O., *Structure of Uranium (Vi) in Strong Alkaline Solutions. A Combined Theoretical and Experimental Investigation.* The Journal of Physical Chemistry A, 1999. **103**(41): p. 8257-8264.

33. Brooker, M.H., Huang, C.B., and Sylwestrowicz, J., *Raman Spectroscopic Studies of Aqueous Uranyl Nitrate and Perchlorate Systems.* Journal of Inorganic and Nuclear Chemistry, 1980. **42**(10): p. 1431-1440.
34. Denecke, M.A., *Actinide Speciation Using X-Ray Absorption Fine Structure Spectroscopy.* Coordination Chemistry Reviews, 2006. **250**(7-8): p. 730-754.
35. Fujii, T., Fujiwara, K., Yamana, H., and Moriyama, H., *Raman Spectroscopic Determination of Formation Constant of Uranyl Hydrolysis Species $(Uo_2)_2(Oh)_2^{2+}$.* Journal of Alloys and Compounds, 2001. **323–324**(0): p. 859-863.
36. Hemmingsen, L., Amara, P., Ansoborlo, E., and Field, M.J., *Importance of Charge Transfer and Polarization Effects for the Modeling of Uranyl−Cation Complexes.* The Journal of Physical Chemistry A, 2000. **104**(17): p. 4095-4101.
37. Kirishima, A., Kimura, T., Tochiyama, O., and Yoshida, Z., *Speciation Study on Uranium(Vi) Hydrolysis at High Temperatures and Pressures.* Journal of Alloys and Compounds, 2004. **374**(1–2): p. 277-282.
38. Kramer-Schnabel, U., Bischoff, H., Xi, R., and Marx, G., *Solubility Products and Complex Formation Equilibria in the Systems Uranyl Hydroxide and Uranyl Carbonate at 25 C and I= 0.1 M.* Radiochimca Acta, 1992. **56**(4): p. 183-188.
39. Meinrath, G., Kato, Y., and Yoshida, Z., *Spectroscopic Study of the Uranyl Hydrolysis Species $(Uo_2)_2(Oh)_2^{2+}$.* Journal of Radioanalytical and Nuclear Chemistry-Articles, 1993. **174**(2): p. 299-314.
40. Meinrath, G. and Schweinberger, M., *Hydrolysis of the Uranyl(Vi) Ion - a Chemometric Approach.* Radiochimica Acta, 1996. **75**(4): p. 205-210.
41. Ostanin, S. and Zeller, P., *Ab Initio Study of the Uranyl Oxide Hydrates: A Proton Transfer Mediated by Water.* Journal of Physics-Condensed Matter, 2007. **19**(24).
42. Palmer, D. and Nguyen-Trung, C., *Aqueous Uranyl Complexes. 3. Potentiometric Measurements of the Hydrolysis of Uranyl(Vi) Ion at 25°C.* Journal of Solution Chemistry, 1995. **24**(12): p. 1281-1291.
43. Quilès, F. and Burneau, A., *Infrared and Raman Spectra of Uranyl(Vi) Oxo-Hydroxo Complexes in Acid Aqueous Solutions: A Chemometric Study.* Vibrational Spectroscopy, 2000. **23**(2): p. 231-241.
44. Quilès, F., Nguyen-Trung, C., Carteret, C., and Humbert, B., *Hydrolysis of Uranyl(Vi) in Acidic and Basic Aqueous Solutions Using a Noncomplexing Organic Base: A Multivariate Spectroscopic and Statistical Study.* Inorganic Chemistry, 2011. **50**(7): p. 2811-2823.
45. Sémon, L., Boehme, C., Billard, I., Hennig, C., Lützenkirchen, K., Reich, T., Roßberg, A., Rossini, I., and Wipff, G., *Do Perchlorate and Triflate Anions Bind to the Uranyl Cation in an Acidic Aqueous Medium? A Combined Exafs and Quantum Mechanical Investigation.* ChemPhysChem, 2001. **2**(10): p. 591-598.
46. Spencer, S., Gagliardi, L., Handy, N.C., Ioannou, A.G., Skylaris, C.-K., Willetts, A., and Simper, A.M., *Hydration of Uo_2^{2+} and Puo_2^{2+}.* The Journal of Physical Chemistry A, 1999. **103**(12): p. 1831-1837.
47. Steppert, M., Walther, C., Fuss, M., and Büchner, S., *On the Polymerization of Hexavalent Uranium. An Electrospray Mass Spectrometry Study.* Rapid Communications in Mass Spectrometry, 2012. **26**(6): p. 583-591.
48. Meinrath, G., Kato, Y., Kimura, T., and Yoshida, Z., *Solid-Aqueous Phase Equilibria of Uranium(Vi) under Ambient Conditions.* Radiochimica Acta, 1996. **75**(3): p. 159-167.
49. Tsushima, S. and Suzuki, A., *Ab Initio Effective Core Potential Study of Equatorially Coordinated Uranyl Species: Effect of Hydration to the Calculated Properties.* Journal of Molecular Structure: THEOCHEM, 1999. **487**(1): p. 33-38.
50. Hay, P.J., Martin, R.L., and Schreckenbach, G., *Theoretical Studies of the Properties and Solution Chemistry of Ano_2^{2+} and Ano^{2+} Aquo Complexes for an= U, Np, and Pu.* The Journal of Physical Chemistry A, 2000. **104**(26): p. 6259-6270.
51. Tsushima, S., *Hydration and Water-Exchange Mechanism of the Uo_2^{2+} Ion Revisited: The Validity of the "N + 1" Model.* The Journal of Physical Chemistry A, 2007. **111**(18): p. 3613-3617.
52. Farkas, I., Bányai, I., Szabó, Z., Wahlgren, U., and Grenthe, I., *Rates and Mechanisms of Water Exchange of $Uo_2^{2+(Aq)}$ and $Uo_2(Oxalate)F(H_2o)_2^-$: A Variable-Temperature ^{17}o and ^{19}f Nmr Study.* Inorganic chemistry, 2000. **39**(4): p. 799-805.
53. Bühl, M. and Kabrede, H., *Mechanism of Water Exchange in Aqueous Uranyl(Vi) Ion. A Density Functional Molecular Dynamics Study.* Inorganic Chemistry, 2006. **45**(10): p. 3834-3836.

54. Kerisit, S. and Liu, C., *Structure, Kinetics, and Thermodynamics of the Aqueous Uranyl (Vi) Cation.* The Journal of Physical Chemistry A, 2013. **117**(30): p. 6421-6432.
55. Whalen, J.M. and Clair, T.S., *Fluorinated Silica, Part Ii: Incorporation of Fluorine into Silica Glass Via High Temperature Gas-Solid Reactions.* Abstracts of Papers of the American Chemical Society, 2002. **224**: p. U552-U552.
56. Nielsen, A.E., *Kinetics of Precipitation*. Vol. 350. 1964: Pergamon Press Oxford.
57. LaMer, V.K. and Dinegar, R.H., *Theory, Production and Mechanism of Formation of Monodispersed Hydrosols.* Journal of the American Chemical Society, 1950. **72**(11): p. 4847-4854.
58. Sugimoto, T., *Preparation of Monodispersed Colloidal Particles.* Advances in Colloid and Interface Science, 1987. **28**: p. 65-108.
59. Haruta, M. and Delmon, B., *Preparation of Homodisperse Solids.* Journal de chimie physique, 1986. **83**(11-12): p. 859-868.
60. Polte, J., *Fundamental Growth Principles of Colloidal Metal Nanoparticles–a New Perspective.* CrystEngComm, 2015. **17**(36): p. 6809-6830.
61. Karthika, S., Radhakrishnan, T., and Kalaichelvi, P., *A Review of Classical and Nonclassical Nucleation Theories.* Crystal Growth & Design, 2016. **16**(11): p. 6663-6681.
62. Hunter, R.J., *Foundations of Colloid Science*. 2001: Oxford University Press.
63. Kowacz, M., Prieto, M., and Putnis, A., *Kinetics of Crystal Nucleation in Ionic Solutions: Electrostatics and Hydration Forces.* Geochimica et Cosmochimica Acta, 2010. **74**(2): p. 469-481.
64. Kowacz, M. and Putnis, A., *The Effect of Specific Background Electrolytes on Water Structure and Solute Hydration: Consequences for Crystal Dissolution and Growth.* Geochimica et Cosmochimica Acta, 2008. **72**(18): p. 4476-4487.
65. Vayssières, L., Chanéac, C., Tronc, E., and Jolivet, J.P., *Size Tailoring of Magnetite Particles Formed by Aqueous Precipitation: An Example of Thermodynamic Stability of Nanometric Oxide Particles.* Journal of colloid and interface science, 1998. **205**(2): p. 205-212.
66. Jolivet, J.-P., Tronc, É., and Chanéac, C., *Synthesis of Iron Oxide-Based Magnetic Nanomaterials and Composites.* Comptes Rendus Chimie, 2002. **5**(10): p. 659-664.
67. Bashford, D. and Case, D.A., *Generalized Born Models of Macromolecular Solvation Effects.* Annual review of physical chemistry, 2000. **51**(1): p. 129-152.
68. Horinek, D., *Specific Ion Effects, Theory*, in *Encyclopedia of Applied Electrochemistry*, G. Kreysa, K.-i. Ota, and R.F. Savinell, Editors. 2014, Springer New York: New York, NY. p. 2050-2053.
69. Lima, E., De Melo, B., Baptista, L., and Paredes, M., *Specific Ion Effects on the Interfacial Tension of Water/Hydrocarbon Systems.* Brazilian Journal of Chemical Engineering, 2013. **30**(1): p. 55-62.
70. Kruger, H., *Techniques for the Kinetic Study of Fast Reactions in Solution.* Chemical Society Reviews, 1982. **11**(3): p. 227-255.
71. Schubert, U. and Nicola, H., *Synthesis of Inorganic Materials*. 2012: John Wiley & Sons.
72. Livage, J., *Sol–Gel Synthesis of Heterogeneous Catalysts from Aqueous Solutions.* Catalysis Today, 1998. **41**(1–3): p. 3-19.
73. Livage, J., Henry, M., and Sanchez, C., *Sol-Gel Chemistry of Transition Metal Oxides.* Progress in solid state chemistry, 1988. **18**(4): p. 259-341.
74. Furedi-Milhofer, H., *Spontaneous Precipitation from Electrolytic Solutions.* Pure and Applied Chemistry, 1981. **53**(11): p. 2041-2055.
75. Penners, N. and Koopal, L., *Preparation and Optical Properties of Homodisperse Haematite Hydrosols.* Colloids and Surfaces, 1986. **19**(4): p. 337-349.
76. Anderson, V.J. and Lekkerkerker, H.N., *Insights into Phase Transition Kinetics from Colloid Science.* Nature, 2002. **416**(6883): p. 811-815.
77. Vekilov, P.G., *Dense Liquid Precursor for the Nucleation of Ordered Solid Phases from Solution.* Crystal growth & design, 2004. **4**(4): p. 671-685.
78. ten Wolde, P.R. and Frenkel, D., *Enhancement of Protein Crystal Nucleation by Critical Density Fluctuations.* Science, 1997. **277**(5334): p. 1975-1978.
79. Haas, C. and Drenth, J., *Understanding Protein Crystallization on the Basis of the Phase Diagram.* Journal of crystal growth, 1999. **196**(2): p. 388-394.
80. Burgner, L.L., Lucas, P., Weinberg, M.C., Soares, P.C., and Zanotto, E.D., *On the Persistence of Metastable Crystal Phases in Lithium Disilicate Glass.* Journal of non-crystalline solids, 2000. **274**(1): p. 188-194.
81. Kinser, D. and Hench, L., *Hot Stage Transmission Electron Microscopy of Crystallisation in a Lithia-Silica Glass.* Journal of Materials Science, 1970. **5**(5): p. 369-373.

82. Alejandre, J. and Hansen, J.-P., *Ions in Water: From Ion Clustering to Crystal Nucleation.* Physical Review E, 2007. **76**(6): p. 061505.
83. Zahn, D., *Atomistic Mechanism of Nacl Nucleation from an Aqueous Solution.* Physical review letters, 2004. **92**(4): p. 040801.
84. Chakraborty, D. and Patey, G., *How Crystals Nucleate and Grow in Aqueous Nacl Solution.* The journal of physical chemistry letters, 2013. **4**(4): p. 573-578.
85. Demichelis, R., Raiteri, P., Gale, J.D., Quigley, D., and Gebauer, D., *Stable Prenucleation Mineral Clusters Are Liquid-Like Ionic Polymers.* Nat Commun, 2011. **2**: p. 590.
86. Gebauer, D., Völkel, A., and Cölfen, H., *Stable Prenucleation Calcium Carbonate Clusters.* Science, 2008. **322**(5909): p. 1819-1822.
87. Gebauer, D., Kellermeier, M., Gale, J.D., Bergström, L., and Cölfen, H., *Pre-Nucleation Clusters as Solute Precursors in Crystallisation.* Chemical Society Reviews, 2014. **43**(7): p. 2348-2371.
88. De Yoreo, J.J., Gilbert, P.U., Sommerdijk, N.A., Penn, R.L., Whitelam, S., Joester, D., Zhang, H., Rimer, J.D., Navrotsky, A., and Banfield, J.F., *Crystallization by Particle Attachment in Synthetic, Biogenic, and Geologic Environments.* Science, 2015. **349**(6247): p. aaa6760.
89. Van Santen, R., *The Ostwald Step Rule.* The Journal of Physical Chemistry, 1984. **88**(24): p. 5768-5769.
90. Wagner, C., *Theorie Der Alterung Von Niederschlägen Durch Umlösen (Ostwald ‐ Reifung).* Berichte der Bunsengesellschaft für physikalische Chemie, 1961. **65**(7 ‐ 8): p. 581-591.
91. Stranski, I. and Totomanow, D., *Keimbildungsgeschwindigkeit Und Ostwaldsche Stufenregel.* Zeitschrift für Physikalische Chemie, 1933. **163**(1): p. 399-408.
92. Stranski, I. and Totomanow, D., *Rate of Formation of (Crystal) Nuclei and the Ostwald Step Rule.* Z. Phys. Chem, 1933. **163**: p. 399-408.
93. Gliko, O., Neumaier, N., Pan, W., Haase, I., Fischer, M., Bacher, A., Weinkauf, S., and Vekilov, P.G., *A Metastable Prerequisite for the Growth of Lumazine Synthase Crystals.* Journal of the American Chemical Society, 2005. **127**(10): p. 3433-3438.
94. Talanquer, V. and Oxtoby, D.W., *Crystal Nucleation in the Presence of a Metastable Critical Point.* The Journal of chemical physics, 1998. **109**(1): p. 223-227.
95. Pouget, E.M., Bomans, P.H., Goos, J.A., Frederik, P.M., and Sommerdijk, N.A., *The Initial Stages of Template-Controlled $Caco_3$ Formation Revealed by Cryo-Tem.* Science, 2009. **323**(5920): p. 1455-1458.
96. Rodriguez-Blanco, J.D., Shaw, S., and Benning, L.G., *The Kinetics and Mechanisms of Amorphous Calcium Carbonate (Acc) Crystallization to Calcite, Via Vaterite.* Nanoscale, 2011. **3**(1): p. 265-271.
97. Dey, A., Bomans, P.H., Müller, F.A., Will, J., Frederik, P.M., de With, G., and Sommerdijk, N.A., *The Role of Prenucleation Clusters in Surface-Induced Calcium Phosphate Crystallization.* Nature materials, 2010. **9**(12): p. 1010-1014.
98. Cundy, C.S. and Cox, P.A., *The Hydrothermal Synthesis of Zeolites: Precursors, Intermediates and Reaction Mechanism.* Microporous and Mesoporous Materials, 2005. **82**(1–2): p. 1-78.
99. De Yoreo, J.J. and Vekilov, P.G., *Principles of Crystal Nucleation and Growth.* Reviews in mineralogy and geochemistry, 2003. **54**(1): p. 57-93.
100. Barrer, R.M., *Mineral Synthesis by Hydrothermal Technique.* Chemistry in Britain, 1966. **2**(9): p. 380-+.
101. Barrer, R.M., Baynham, J.W., Bultitude, F.W., and Meier, W.M., *36. Hydrothermal Chemistry of the Silicates. Part Viii. Low-Temperature Crystal Growth of Aluminosilicates, and of Some Gallium and Germanium Analogues.* Journal of the Chemical Society (Resumed), 1959(0): p. 195-208.
102. Ding, W., Botha, J.A., Hanson, B.C., and Burke, I.T., *Aqueous Hydroxylation Mediated Synthesis of Crystalline Calcium Uranate Particles.* Journal of Alloys and Compounds, 2016. **688, Part B**: p. 260-269.
103. Bots, P., Morris, K., Hibberd, R., Law, G.T.W., Mosselmans, J.F.W., Brown, A.P., Doutch, J., Smith, A.J., and Shaw, S., *Formation of Stable Uranium(Vi) Colloidal Nanoparticles in Conditions Relevant to Radioactive Waste Disposal.* Langmuir, 2014. **30**(48): p. 14396-14405.
104. Li, M. and Dincă, M., *On the Mechanism of Mof-5 Formation under Cathodic Bias.* Chemistry of Materials, 2015. **27**(9): p. 3203-3206.
105. Zhdanov, S., *Some Problems of Zeolite Crystallization*. 1971, ACS Publications.
106. Zhdanov, S., *Molecular Sieves.* Society of Chemical Industry, London, 1968: p. 62.

107. Derouane, E.G., Determmerie, S., Gabelica, Z., and Blom, N., *Synthesis and Characterization of Zsm-5 Type Zeolites I. Physico-Chemical Properties of Precursors and Intermediates.* Applied catalysis, 1981. **1**(3-4): p. 201-224.
108. Lowe, B.M., *An Equilibrium Model for the Crystallization of High Silica Zeolites.* Zeolites, 1983. **3**(4): p. 300-305.
109. Casci, J. and Lowe, B., *Use of Ph-Measurements to Monitor Zeolite Crystallization.* Zeolites, 1983. **3**(3): p. 186-187.
110. Angell, C. and Flank, W., *Mechanism of Zeolite a Synthesis*. 1977, ACS Publications.
111. Nicolle, M.A., Di Renzo, F., Fajula, F., Espiau, P., and Courieres, T.D., *A Microporous Tetraethylammonium Permutite as Synthesis Intermediate of the Zeolite Beta*, in *Proceedings from the Ninth International Zeolite Conference*. 1993, Butterworth-Heinemann. p. 313-320.
112. Hasegawa, I. and Sakka, S., *Silicate Species with Cagelike Structure in Solutions and Rapid Solidification with Organic Quaternary Ammonium Ions*. 1989, ACS Publications.
113. Andrade, Â.L., Fabris, J.D., Ardisson, J.D., Valente, M.A., and Ferreira, J.M., *Effect of Tetramethylammonium Hydroxide on Nucleation, Surface Modification and Growth of Magnetic Nanoparticles.* Journal of Nanomaterials, 2012. **2012**: p. 15.
114. Bourgeat-Lami, E., Di Renzo, F., Fajula, F., Mutin, P.H., and Des Courieres, T., *Mechanism of the Thermal Decomposition of Tetraethylammonium in Zeolite. Beta.* The Journal of Physical Chemistry, 1992. **96**(9): p. 3807-3811.
115. Fokema, M.D., Chiu, E., and Ying, J.Y., *Synthesis and Characterization of Nanocrystalline Yttrium Oxide Prepared with Tetraalkylammonium Hydroxides.* Langmuir, 2000. **16**(7): p. 3154-3159.
116. Marcus, Y., *Tetraalkylammonium Ions in Aqueous and Non-Aqueous Solutions.* Journal of Solution Chemistry, 2008. **37**(8): p. 1071-1098.
117. Van der Donck, J., Vaessen, G., and Stein, H., *Adsorption of Short-Chain Tetraalkylammonium Bromide on Silica.* Langmuir, 1993. **9**(12): p. 3553-3557.
118. de Keizer, A., van der Ent, E.M., and Koopal, L.K., *Surface and Volume Charge Densities of Monodisperse Porous Silicas.* Colloids and Surfaces A: Physicochemical and Engineering Aspects, 1998. **142**(2–3): p. 303-313.
119. Perez-Pariente, J., Martens, J.A., and Jacobs, P.A., *Factors Affecting the Synthesis Efficiency of Zeolite Beta from Aluminosilicate Gels Containing Alkali and Tetraethylammonium Ions.* Zeolites, 1988. **8**(1): p. 46-53.
120. Fahlke, B., Starke, P., Seefeld, V., Wieker, W., and Wendlandt, K.-P., *On the Intermediates in Zeolite Y Synthesis.* Zeolites, 1987. **7**(3): p. 209-213.
121. Murakami, Y., Iijima, A., and Ward, J.W., *New Developments in Zeolite Science and Technology*. Vol. 28. 1986: Elsevier.
122. Jacobs, P.A., Derouane, E.G., and Weitkamp, J., *Evidence for X-Ray-Amorphous Zeolites.* Journal of the Chemical Society, Chemical Communications, 1981(12): p. 591-593.
123. Schoeman, B.J., *A Spectroscopic Study of the Initial Stage in the Crystallization of Tpa-Silicalite-1 from Clear Solutions.* Studies in Surface Science and Catalysis, 1997. **105**: p. 647-654.
124. Gabelica, Z., Nagy, J., Debras, G., and Derouane, E., *Characterization of X-Ray Amorphous Zsm-5 Zeolites by Thermal Analysis and High Resolution Solid State Multinuclear Nmr Spectroscopy.* Acta Chimica Hungarica, 1985. **119**(2-3): p. 275-284.
125. Gabelica, Z., Nagy, J.B., and Debras, G., *Characterization of X-Ray Amorphous Zsm-5 Zeolites by High Resolution Solid State ^{13}c-Nmr Spectroscopy.* Journal of Catalysis, 1983. **84**(1): p. 256-260.
126. Schlenker, J.L. and Peterson, B.K., *Computed X-Ray Powder Diffraction Patterns for Ultrasmall Zeolite Crystals.* Journal of Applied Crystallography, 1996. **29**(2): p. 178-185.
127. Peng, Y., Wang, F., Wang, Z., Alsayed, A.M., Zhang, Z., Yodh, A.G., and Han, Y., *Two-Step Nucleation Mechanism in Solid-Solid Phase Transitions.* Nature materials, 2015. **14**(1): p. 101.
128. Qi, W., Peng, Y., Han, Y., Bowles, R.K., and Dijkstra, M., *Nonclassical Nucleation in a Solid-Solid Transition of Confined Hard Spheres.* Physical review letters, 2015. **115**(18): p. 185701.
129. Ihli, J., Wong, W.C., Noel, E.H., Kim, Y.-Y., Kulak, A.N., Christenson, H.K., Duer, M.J., and Meldrum, F.C., *Dehydration and Crystallization of Amorphous Calcium Carbonate in Solution and in Air.* Nature communications, 2014. **5**.
130. Zheng, H., Smith, R.K., Jun, Y.-w., Kisielowski, C., Dahmen, U., and Alivisatos, A.P., *Observation of Single Colloidal Platinum Nanocrystal Growth Trajectories.* Science, 2009. **324**(5932): p. 1309-1312.

131. Thanh, N.T.K., Maclean, N., and Mahiddine, S., *Mechanisms of Nucleation and Growth of Nanoparticles in Solution.* Chemical Reviews, 2014. **114**(15): p. 7610-7630.
132. Penn, R.L. and Soltis, J.A., *Characterizing Crystal Growth by Oriented Aggregation.* CrystEngComm, 2014. **16**(8): p. 1409-1418.
133. Yuwono, V.M., Burrows, N.D., Soltis, J.A., and Penn, R.L., *Oriented Aggregation: Formation and Transformation of Mesocrystal Intermediates Revealed.* Journal of the American Chemical Society, 2010. **132**(7): p. 2163-2165.
134. Zacher, D., Baunemann, A., Hermes, S., and Fischer, R.A., *Deposition of Microcrystalline [$Cu_3(Btc)_2$] and [$Zn_2(Bdc)_2(Dabco)$] at Alumina and Silica Surfaces Modified with Patterned Self Assembled Organic Monolayers: Evidence of Surface Selective and Oriented Growth.* Journal of Materials Chemistry, 2007. **17**(27): p. 2785-2792.
135. Park, W.I., Kim, D.H., Jung, S.-W., and Yi, G.-C., *Metalorganic Vapor-Phase Epitaxial Growth of Vertically Well-Aligned Zno Nanorods.* Applied Physics Letters, 2002. **80**(22): p. 4232-4234.
136. Yin, S., Huang, F., Zhang, J., Zheng, J., and Lin, Z., *The Effects of Particle Concentration and Surface Charge on the Oriented Attachment Growth Kinetics of Cdte Nanocrystals in H_2o.* The Journal of Physical Chemistry C, 2011. **115**(21): p. 10357-10364.
137. Niederberger, M. and Cölfen, H., *Oriented Attachment and Mesocrystals: Non-Classical Crystallization Mechanisms Based on Nanoparticle Assembly.* Physical chemistry chemical physics, 2006. **8**(28): p. 3271-3287.
138. Li, D., Nielsen, M.H., Lee, J.R., Frandsen, C., Banfield, J.F., and De Yoreo, J.J., *Direction-Specific Interactions Control Crystal Growth by Oriented Attachment.* Science, 2012. **336**(6084): p. 1014-1018.
139. Kowacz, M., Putnis, C., and Putnis, A., *The Effect of Cation: Anion Ratio in Solution on the Mechanism of Barite Growth at Constant Supersaturation: Role of the Desolvation Process on the Growth Kinetics.* Geochimica et Cosmochimica Acta, 2007. **71**(21): p. 5168-5179.
140. Hribar, B., Southall, N.T., Vlachy, V., and Dill, K.A., *How Ions Affect the Structure of Water.* Journal of the American Chemical Society, 2002. **124**(41): p. 12302-12311.
141. Tuckerman, M., Laasonen, K., Sprik, M., and Parrinello, M., *Ab Initio Molecular Dynamics Simulation of the Solvation and Transport of Hydronium and Hydroxyl Ions in Water.* The Journal of Chemical Physics, 1995. **103**(1): p. 150-161.
142. Ruiz-Agudo, C., Putnis, C.V., Ruiz-Agudo, E., and Putnis, A., *The Influence of Ph on Barite Nucleation and Growth.* Chemical Geology, 2015. **391**: p. 7-18.
143. Peschke, M., Blades, A.T., and Kebarle, P., *Hydration Energies and Entropies for Mg^{2+}, Ca^{2+}, Sr^{2+}, and Ba^{2+} from Gas-Phase Ion−Water Molecule Equilibria Determinations.* The Journal of Physical Chemistry A, 1998. **102**(48): p. 9978-9985.
144. Chopra, M. and Choudhury, N., *Effect of Uranyl Ion Concentration on Structure and Dynamics of Aqueous Uranyl Solution: A Molecular Dynamics Simulation Study.* The Journal of Physical Chemistry B, 2014. **118**(49): p. 14373-14381.
145. Tomson, M.B., Kan, A.T., and Fu, G. *Inhibition of Barite Scale in the Presence of Hydrate Inhibitors*. in *SPE International Symposium on Oilfield Scale*. 2004. Society of Petroleum Engineers.
146. Marcus, Y. and Loewenschuss, A., *Chapter 4. Standard Entropies of Hydration of Ions.* Annual Reports Section "C" (Physical Chemistry), 1984. **81**(0): p. 81-135.
147. Samoĭlov, O.I.A.k., *Structure of Aqueous Electrolyte Solutions and the Hydration of Ions*. 1965: Consultants Bureau.
148. Ruiz-Agudo, E., Kowacz, M., Putnis, C., and Putnis, A., *The Role of Background Electrolytes on the Kinetics and Mechanism of Calcite Dissolution.* Geochimica et cosmochimica acta, 2010. **74**(4): p. 1256-1267.
149. Thomson, W., *Ix. On the Equilibrium of Vapour at a Curved Surface of Liquid.* Philosophical Magazine, 1871. **42**(282): p. 448-452.
150. Burns, P.C., Miller, M.L., and Ewing, R.C., *U6+ Minerals and Inorganic Phases: A Comparison and Hierarchy of Crystal Structures.* Canadian Mineralogist, 1996. **34**: p. 845-880.
151. Miller, M.L., Finch, R.J., Burns, P.C., and Ewing, R.C., *Description and Classification of Uranium Oxide Hydrate Sheet Anion Topologies.* Journal of Materials Research, 1996. **11**(12): p. 3048-3056.
152. Schindler, M., Hawthorne, F.C., Burns, P.C., and Maurice, P.A., *Dissolution of Uranyl-Oxide-Hydroxy-Hydrate Minerals. Ii. Becquerelite.* The Canadian Mineralogist, 2006. **44**(5): p. 1207-1225.

153. Schindler, M., Hawthorne, F.C., Mandaliev, P., Burns, P.C., and Maurice, P., *An Integrated Study of Uranyl Mineral Dissolution Processes: Etch Pit Formation, Effects of Cations in Solution, and Secondary Precipitation.* Radiochimica Acta International journal for chemical aspects of nuclear science and technology, 2011. **99**(2): p. 79-94.
154. Allen, P., Shuh, D., Bucher, J., Edelstein, N., Palmer, C., Silva, R., Nguyen, S., Marquez, L., and Hudson, E., *Determinations of Uranium Structures by Exafs: Schoepite and Other U(Vi) Oxide Precipitates.* Radiochimca Acta, 1996. **75**(1): p. 47-54.
155. Finch, R.J., Cooper, M.A., Hawthorne, F.C., and Ewing, R.C., *The Crystal Structure of Schoepite,[(Uo2)8o2(Oh)12](H2o)12.* Canadian Mineralogist, 1996. **34**: p. 1071-1088.
156. Weller, M.T., Light, M.E., and Gelbrich, T., *Structure of Uranium(Vi) Oxide Dihydrate, Uo3.2h2o; Synthetic Meta-Schoepite (Uo2)4o(Oh)6.5h2o.* Acta Crystallographica Section B, 2000. **56**(4): p. 577-583.
157. Burns, P.C. and Li, Y., *The Structures of Becquerelite and Sr-Exchanged Becquerelite.* American Mineralogist, 2002. **87**(4): p. 550-557.
158. Glatz, R.E., Li, Y., Hughes, K.-A., Cahill, C.L., and Burns, P.C., *Synthesis and Structure of a New Ca Uranyl Oxide Hydrate, Ca[(Uo2)4o3(Oh)4](H2o)2, and Its Relationship to Becquerelite.* The Canadian Mineralogist, 2002. **40**(1): p. 217-224.
159. Burns, P.C., *The Structure of Compreignacite, K2[(Uo2)3o2(Oh)3]2(H2o)7.* The Canadian Mineralogist, 1998. **36**(4): p. 1061-1067.
160. Burns, P.C., Ewing, R.C., and Miller, M.L., *Incorporation Mechanisms of Actinide Elements into the Structures of U6+ Phases Formed During the Oxidation of Spent Nuclear Fuel.* Journal of Nuclear Materials, 1997. **245**(1): p. 1-9.
161. Burns, P.C., *A New Complex Sheet of Uranyl Polyhedra in the Structure of Wölsendorfite.* American Mineralogist, 1999. **84**(10): p. 1661-1673.
162. Vochten, R. and Vanhaverbeke, L., *Transformation of Schoepite into the Uranyl Oxide Hydrates - Becquerelite, Billietite and Wolsendorfite.* Mineralogy and Petrology, 1990. **43**(1): p. 65-72.
163. Burns, P.C., Ewing, R.C., and Hawthorne, F.C., *The Crystal Chemistry of Hexavalent Uranium: Polyhedron Geometries, Bond-Valence Parameters, and Polymerization of Polyhedra.* Canadian Mineralogist, 1997. **35**: p. 1551-1570.
164. Cejka, J., Sejkora, J., Skala, R., Cejka, J., Novotna, M., and Ederova, J., *Contribution to the Crystal Chemistry of Synthetic Becquerelite, Billietite and Protasite.* Neues Jahrbuch Fur Mineralogie Abhandlungen, 1998. **174**: p. 159-180.
165. Srnwlnr, J.L.M., *Crystal Structures and Crystal Chemistry of the Uranyl Oxide Hydrates Becquerelite, Billietite, and Protasite.* American Mineralogist, 1987. **72**: p. 1230-1238.
166. Sato, T., *Thermal Decomposition of Uranium Peroxide Hydrates.* Journal of Applied Chemistry and Biotechnology, 1976. **26**(1): p. 207-213.
167. Boggs, J.E. and El-Chehabi, M., *The Thermal Decomposition of Uranium Peroxide, Uo4.2h2o.* Journal of the American Chemical Society, 1957. **79**(16): p. 4258-4260.
168. Greaves, C.t. and Fender, B., *The Structure of A-Uo3 by Neutron and Electron Diffraction.* Acta Crystallographica Section B: Structural Crystallography and Crystal Chemistry, 1972. **28**(12): p. 3609-3614.
169. Loopstra, B.O. and Cordfunke, E.H.P., *On the Structure of A - Uo3.* Recueil des Travaux Chimiques des Pays-Bas, 1966. **85**(2): p. 135-142.
170. Zachariasen, W., *Crystal Chemical Studies of the 5f-Series of Elements. Xxiii. On the Crystal Chemistry of Uranyl Compounds and of Related Compounds of Transuranic Elements.* Acta Crystallographica, 1954. **7**(12): p. 795-799.
171. Debets, P., *The Structure of B-Uo3.* Acta Crystallographica, 1966. **21**(4): p. 589-593.
172. Debets, P. and Loopstra, B.O., *On the Uranates of Ammonium—Ii: X-Ray Investigation of the Compounds in the System Nh3 · Uo3 · H2o.* Journal of Inorganic and Nuclear Chemistry, 1963. **25**(8): p. 945-953.
173. Hoekstra, H. and Siegel, S. *Chemistry and Crystallography of Uranium Oxide Systems*. in *Journal of Inorganic & Nuclear Chemistry*. 1958. PERGAMON-ELSEVIER SCIENCE LTD THE BOULEVARD, LANGFORD LANE, KIDLINGTON, OXFORD OX5 1GB, ENGLAND.
174. Engmann, R.d. and De Wolff, P., *The Crystal Structure of Γ-Uo3.* Acta Crystallographica, 1963. **16**(10): p. 993-996.
175. Janov, J., Alfredson, P.G., and Vilkaitis, V.K., *The Influence of Precipitation Conditions on the Properties of Ammonium Diuranate and Uranium Dioxide Powders.* Journal of Nuclear Materials, 1972. **44**(2): p. 161-174.

176. Hudry, D., Apostolidis, C., Walter, O., Gouder, T., Courtois, E., Kubel, C., and Meyer, D., *Controlled Synthesis of Thorium and Uranium Oxide Nanocrystals.* Chemistry-a European Journal, 2013. **19**(17): p. 5297-5305.
177. Hudry, D., Apostolidis, C., Walter, O., Gouder, T., Courtois, E., Kübel, C., and Meyer, D., *Non-Aqueous Synthesis of Isotropic and Anisotropic Actinide Oxide Nanocrystals.* Chemistry – A European Journal, 2012. **18**(27): p. 8283-8287.
178. Wu, H., Yang, Y., and Cao, Y.C., *Synthesis of Colloidal Uranium− Dioxide Nanocrystals.* Journal of the American Chemical Society, 2006. **128**(51): p. 16522-16523.
179. Berggren, G. and Brown, A., *Influence of Oxide Additions on the Reduction of UO_3 and U_3O_8 as Measured by Dta and Tg*, in *Thermal Analysis*. 1969.
180. Brun, C., Valdivieso, F., Pijolat, M., and Soustelle, M., *Reduction by Hydrogen of U_3O_8 into UO_2: Nucleation and Growth, Influence of Hydration.* Physical Chemistry Chemical Physics, 1999. **1**(3): p. 471-477.
181. Pijolat, M., Brun, C., Valdivieso, F., and Soustelle, M., *Reduction of Uranium Oxide U_3O_8 to UO_2 by Hydrogen.* Solid State Ionics, 1997. **101**: p. 931-935.
182. Notz, K., Huntington, C., and Burkhardt, W., *Hydrogen Reduction of Uranium Oxides. A Phase Study by Means of a Controlled-Atmosphere Diffractometer Hot Stage.* Industrial & Engineering Chemistry Process Design and Development, 1962. **1**(3): p. 213-217.
183. Notz, K. and Mendel, M., *X-Ray and Kinetic Study of the Hydrogen Reduction of Γ-UO_3.* Journal of Inorganic and Nuclear Chemistry, 1960. **14**(1-2): p. 55-64.
184. Willis, B., *Structures of UO_2, UO_{2+X} and U_4O_9 by Neutron Diffraction.* Journal de Physique, 1964. **25**(5): p. 431-439.
185. Seaborg, G.T., Katz, J.J., and Morss, L.R., *The Chemistry of the Actinide Elements*. Vol. 2. 2012: Springer Science & Business Media.
186. Hoekstra, H.R. and Siegel, S., *The Uranium-Oxygen System: $U_3O_8 \cdot UO_3$.* Journal of Inorganic and Nuclear Chemistry, 1961. **18**(0): p. 154-165.
187. Herak, R., *The Crystal Structure of the High Temperature Modification of U_3O_8.* Acta Crystallographica Section B: Structural Crystallography and Crystal Chemistry, 1969. **25**(12): p. 2505-2508.
188. Sanyal, K., Khooha, A., Das, G., Tiwari, M.K., and Misra, N.L., *Direct Determination of Oxidation States of Uranium in Mixed-Valent Uranium Oxides Using Total Reflection X-Ray Fluorescence X-Ray Absorption near-Edge Spectroscopy.* Analytical Chemistry, 2016. **89**(1): p. 871-876.
189. Kvashnina, K., Butorin, S.M., Martin, P., and Glatzel, P., *Chemical State of Complex Uranium Oxides.* Physical review letters, 2013. **111**(25): p. 253002.
190. Loopstra, B., *The Phase Transition in A-U_3O_8 at 210 C.* Journal of Applied Crystallography, 1970. **3**(2): p. 94-96.
191. Allen, G. and Holmes, N., *A Mechanism for the UO_2 to A-U_3O_8 Phase Transformation.* Journal of nuclear materials, 1995. **223**(3): p. 231-237.
192. Allen, G., Tempest, P., and Tyler, J., *The Formation of U_3O_8 on Crystalline UO_2.* Philosophical Magazine B, 1986. **54**(2): p. L67-L71.
193. Loopstra, B., *The Structure of B-U_3O_8.* Acta Crystallographica Section B: Structural Crystallography and Crystal Chemistry, 1970. **26**(5): p. 656-657.
194. Hoekstra, H.R., Siegel, S., and Gallagher, F.X., *The Uranium-Oxygen System at High Pressure.* Journal of Inorganic and Nuclear Chemistry, 1970. **32**(10): p. 3237-3248.
195. Cordfunke, E.H.P., Van Vlaanderen, P., Onink, M., and Ijdo, D.J.W., *$Sr_3U_{11}O_{36}$: Crystal Structure and Thermal Stability.* Journal of Solid State Chemistry, 1991. **94**(1): p. 12-18.
196. Ijdo, D., *$Pb_3U_{11}O_{36}$, a Rietveld Refinement of Neutron Powder Diffraction Data.* Acta Crystallographica Section C: Crystal Structure Communications, 1993. **49**(4): p. 654-656.
197. Hoekstra, H., Santoro, A., and Siegel, S., *The Low Temperature Oxidation of UO_2 and U_4O_9.* Journal of Inorganic and Nuclear Chemistry, 1961. **18**: p. 166-178.
198. Westrum, E. and Grønvold, F., *Triuranium Heptaoxides: Heat Capacities and Thermodynamic Properties of A-and B-U_3O_7 from 5 to 350 K.* Journal of Physics and Chemistry of Solids, 1962. **23**(1-2): p. 39-53.
199. Rousseau, G., Desgranges, L., Nièpce, J.-C., Bérar, J.-F., and Baldinozzi, G. *Synchrotron Diffraction Study of the Isothermal Oxidation of Uranium Dioxide at 250° C*. in *MRS Proceedings*. 2003. Cambridge Univ Press.
200. Janeczek, J., Ewing, R.C., and Thomas, L.E., *Oxidation of Uraninite: Does Tetragonal U_3O_7 Occur in Nature?* Journal of nuclear materials, 1993. **207**: p. 177-191.
201. McEachern, R.J. and Taylor, P., *A Review of the Oxidation of Uranium Dioxide at Temperatures Below 400°C.* Journal of Nuclear Materials, 1998. **254**(2–3): p. 87-121.

202. Garrido, F., Ibberson, R., Nowicki, L., and Willis, B., *Cuboctahedral Oxygen Clusters in U_3O_7.* Journal of nuclear materials, 2003. **322**(1): p. 87-89.
203. Westrum Jr, E.F., Takahashi, Y., and Grønvold, F., *Λ-Type Thermal Anomaly in Tetrauranium Enneaoxide at 348° K.* The Journal of Physical Chemistry, 1965. **69**(9): p. 3192-3193.
204. Gotoo, K. and Naito, K., *Study on U_4O_9—Part I. An Anomaly of the Heat Capacity near the Room Temperature.* Journal of Physics and Chemistry of Solids, 1965. **26**(11): p. 1673-1677.
205. A. Volkovich, V., R. Griffiths, T., J. Fray, D., and C. Thied, R., *Solubilities and Solubilisation Enthalpies of Alkali Metal Uranates(Vi) in Carbonate Melts.* Physical Chemistry Chemical Physics, 1999. **1**(14): p. 3297-3302.
206. Bera, S., Sali, S.K., Sampath, S., Narasimhan, S.V., and Venugopal, V., *Oxidation State of Uranium: An Xps Study of Alkali and Alkaline Earth Uranates.* Journal of Nuclear Materials, 1998. **255**(1): p. 26-33.
207. Griffiths, T.R. and Volkovich, V.A., *A Review of the High Temperature Oxidation of Uranium Oxides in Molten Salts and in the Solid State to Form Alkali Metal Uranates, and Their Composition and Properties.* Journal of Nuclear Materials, 1999. **274**(3): p. 229-251.
208. Prigent, J. and Lucas, J., *Alkaline, Thallous, and Alkaline Earth Uranates and Hypo-Uranates*. 1965, Faculte des Sciences, Rennes, France.
209. Toussaint, C.J. and Avogadro, A., *Concerning Uranate Formation in Alkali Nitrate Melts.* Journal of Inorganic and Nuclear Chemistry, 1974. **36**(4): p. 781-784.
210. Volkovich, V., Griffiths, T.R., Fray, D.J., Fields, M., and Wilson, P.D., *Oxidation of Uo2 in Molten Alkali-Metal Carbonate Mixtures: Formation of Uranates and Diuranates.* Journal of the Chemical Society-Faraday Transactions, 1996. **92**(24): p. 5059-5065.
211. Volkovich, V.A., Griffiths, T.R., Fray, D.J., and Fields, M., *Vibrational Spectra of Alkali Metal (Li, Na and K) Uranates and Consequent Assignment of Uranate Ion Site Symmetry.* Vibrational Spectroscopy, 1998. **17**(1): p. 83-91.
212. Volkovich, V.A., Griffiths, T.R., Fray, D.J., and Fields, M., *Increased Oxidation of Uo_2 in Molten Alkali-Metal Carbonate Based Mixtures by Increasing Oxygen Solubility and by Controlled Generation of Superoxide Ions, and Evidence for a New Sodium Uranate.* Journal of the Chemical Society-Faraday Transactions, 1997. **93**(21): p. 3819-3826.
213. Volkovich, V.A., Griffiths, T.R., Fray, D.J., and Thied, R.C., *The Electronic Spectra of Alkali Metal Uranates and Band Assignments: An Analysis of Their Diffuse Reflectance Spectra.* Physical Chemistry Chemical Physics, 2001. **3**(23): p. 5182-5191.
214. Volkovich, V.A., Griffiths, T.R., Fray, D.J., and Thied, R.C., *Chemical Solubility of Alkali Metal Uranate(Vi) Species in Molten Carbonates under Basic and Acidic Conditions.* Physical Chemistry Chemical Physics, 2000. **2**(13): p. 3029-3035.
215. Allen, G., Griffiths, A., and Lee, B., *X-Ray Photoelectron Spectroscopy of Alkaline Earth Metal Uranate Complexes.* Transition Metal Chemistry, 1978. **3**(1): p. 229-233.
216. Allen, G.C. and Griffiths, A.J., *Vibrational Spectroscopy of Alkaline-Earth Metal Uranate Compounds.* Journal of the Chemical Society, Dalton Transactions, 1979(2): p. 315-319.
217. Allen, G.C., Griffiths, A.J., and Vanderheijden, A.N., *Electronic Absorption-Spectroscopy of Alkaline-Earth Metal Uranate Compounds.* Transition Metal Chemistry, 1981. **6**(6): p. 355-360.
218. Hoekstra, H. and Katz, J.J., *Alkaline Earth Polyuranates*. 1949, Argonne National Laboratory: USA.
219. Hoekstra, H.R. and Katz, J.J., *Studies on the Alkaline Earth Diuranates.* Journal of the American Chemical Society, 1952. **74**(7): p. 1683-1690.
220. Loopstra, B.O. and Rietveld, H.M., *The Structure of Some Alkaline-Earth Metal Uranates.* Acta Crystallographica Section B, 1969. **25**(4): p. 787-791.
221. Morss, L.R., *Ternary Oxides of the Actinides with Alkali and Alkaline Earth Elements: Stability and Acid-Base Relationships.* Journal of Chemical Thermodynamics, 2002. **34**(2): p. 229-237.
222. Rao, C.N.R., Randhawa, H.S., Reddy, N.V.R., and Chakravorty, D., *Vibrational-Spectra of Alkali and Alkaline-Earth Metal-Complexes, Oxide Glasses and Oxyanion Salts.* Spectrochimica Acta Part a-Molecular and Biomolecular Spectroscopy, 1975. **31**(9-10): p. 1283-1291.
223. Rietveld, H., *The Crystal Structure of Some Alkaline Earth Metal Uranates of the Type M_3uo_6.* Acta Crystallographica, 1966. **20**(4): p. 508-513.
224. Rojas, R.M., Gonzalez, V., Bermúdez, J., and De Paz, M.L., *Alkaline-Earth Uranates from Thermal Decomposition of Uranyl Carboxylates.* Thermochimica Acta, 1979. **32**(1–2): p. 257-264.

225. Sali, S.K., Sampath, S., and Venugopal, V., *Thermal Studies on Alkaline Earth Uranates.* Journal of Nuclear Materials, 2000. **277**(1): p. 106-112.
226. Sawyer, J.O., *The Polyalkaline Earth Uranates Sr_2uo_5 and Ca_2uo_5.* Journal of Inorganic and Nuclear Chemistry, 1963. **25**(7): p. 899-902.
227. Tagawa, H., Fujino, T., and Yamashita, T., *Formation and Some Chemical Properties of of Alkaline-Earth Metal Monouranates.* Journal of Inorganic and Nuclear Chemistry, 1979. **41**(12): p. 1729-1735.
228. Nipruk, O., Chernorukov, N., Chaplieva, K., and Chernorukov, G., *Synthesis and Characterization of the $Miiu_3o_{10}\cdot 6h_2o$ (Mii= Ni, Zn) Triuranates.* Inorganic Materials, 2016. **52**(5): p. 504-509.
229. Roof, I.P., Smith, M.D., and Zur Loye, H.-C., *High Temperature Flux Crystal Growth of Uranium-Containing Perovskites: Sr_3uo_6 and Ba_2muo_6 (M= Cu, Ni, Zn).* Journal of Chemical Crystallography, 2010. **40**(6): p. 491-495.
230. Read, C.M., Smith, M.D., and zur Loye, H.-C., *Single Crystal Growth and Structural Characterization of Ternary Transition-Metal Uranium Oxides: Mnuo4, Feuo4, and Niu2o6.* Solid State Sciences, 2014. **37**: p. 136-143.
231. Guo, X., Tiferet, E., Qi, L., Solomon, J.M., Lanzirotti, A., Newville, M., Engelhard, M.H., Kukkadapu, R.K., Wu, D., and Ilton, E.S., *U(V) in Metal Uranates: A Combined Experimental and Theoretical Study of $Mguo_4$, $Cruo_4$, and $Feuo_4$.* Dalton Transactions, 2016. **45**(11): p. 4622-4632.
232. Fonteneau, G., L'Helgoualch, H., and Lucas, J., *Sodium and Lanthanide Uranates.* Revue de Chimie Minerale, 1975. **12**(4): p. 382-390.
233. Lazarraga, M., Pico, F., Amarilla, J., Rojas, R., and Rojo, J., *The Cubic $Bi_{1.76}u_{0.12}la_{0.12}o_{3.18}$ Mixed Oxide: Synthesis, Structural Characterization, Thermal Stability and Electrical Properties.* Solid State Ionics, 2005. **176**(29): p. 2313-2318.
234. Amarilla, J.M., Alonso, J.A., and Rojas, R.M., *Structural Study of the Trigonal $Bi_{2.34}u_{0.33}la_{0.33}o_5$ Oxide Ion Conductor: Rietveld Refinement of X-Ray and Neutron Powder Diffraction Data.* Journal of the Chemical Society, Dalton Transactions, 1999(7): p. 1137-1142.
235. Kalekar, B., Raje, N., and Reddy, A., *Solid State Interaction Studies on Binary Nitrate Mixtures of Uranyl Nitrate Hexahydrate and Lanthanum Nitrate Hexahydrate at Elevated Temperatures.* Journal of Nuclear Materials, 2017. **484**: p. 16-23.
236. Zubova, N., Makarov, V., Nikol'skii, V., Petrov, P., Teterin, E., and Chebotarev, N., *Infrared Spectra and Molecular Structure of the Uranates of Some Rare Earth Elements.* Zh. Neorg. Khim., 13: 940-7 (Apr. 1968). 1968.
237. Koster, A., Renaud, J., and Rieck, G., *The Crystal Structures at 20 and 1000° C of Bismuth Uranate, Bi_2uo_6.* Acta Crystallographica Section B: Structural Crystallography and Crystal Chemistry, 1975. **31**(1): p. 127-131.
238. Bonanos, N., *High Oxide Ion Conductivity in Bismuth Uranate, Bi_2uo_6.* Materials research bulletin, 1989. **24**(12): p. 1531-1540.
239. De Jong, J.S., Guffens, C., and Van Der Baan, H., *The Oxidative Demethylation of Toluene, Using Bismuth Uranate as Oxidant.* Journal of Catalysis, 1972. **26**(3): p. 401-415.
240. De Jong, J.S., Guffens, C., and Van Der Baan, H., *The Oxidative Demethylation of Toluene: Ii. Kinetics of the Reduction of Bismuth Uranate by Toluene.* Journal of Catalysis, 1973. **31**(2): p. 149-166.
241. Finch, R.J. and Ewing, R.C., *Clarkeite: New Chemical and Structural Data.* American Mineralogist, 1997. **82**(5-6): p. 607-619.
242. Gruner, J., *The Chemical Formula of Clarkeite.* American Mineralogist, 1954. **39**(9-10): p. 836-838.
243. Galuskin, E.V., Armbruster, T., Galuskina, I.O., Lazic, B., Winiarski, A., Gazeev, V.M., Dzierżanowski, P., Zadov, A.E., Pertsev, N.N., and Wrzalik, R., *Vorlanite (Cau^{6+})O_4—a New Mineral from the Upper Chegem Caldera, Kabardino-Balkaria, Northern Caucasus, Russia.* American Mineralogist, 2011. **96**(1): p. 188-196.
244. Galuskin, E.V., Galuskina, I.O., Dubrovinsky, L.S., and Janeczek, J., *Thermally Induced Transformation of Vorlanite to "Protovorlanite": Restoration of Cation Ordering in Self-Irradiated $Cauo_4$.* American Mineralogist, 2012. **97**(5-6): p. 1002-1004.
245. Rogova, V., Belova, L., Kiziyarov, G., and Kuznetsova, N., *Calciouranoite, a New Hydroxide of Uranium.* International Geology Review, 1974. **16**(11): p. 1255-1256.
246. Rogova, V., Belova, L., Kiziyarov, G., and Kuznetsova, N., *Bauranoite and Metacalciouranoite, New Minerals of the Hydrous Uranium Oxides Group.* International Geology Review, 1974. **16**(2): p. 214-219.

247. Allpress, J.G., *The Crystal Structure of Barium Diuranate, Bau_2o_7.* Journal of Inorganic and Nuclear Chemistry, 1965. **27**(7): p. 1521-1527.
248. Carnall, W.T., Neufeldt, S.J., and Walker, A., *Reactions in Molten Salt Solutions .I. Uranate and Neptunate Formation in Molten Lithium Nitrate-Sodium Nitrate.* Inorganic Chemistry, 1965. **4**(12): p. 1808-&.
249. Hoekstra, H.R., *Infra-Red Spectra of Some Alkali Metal Uranates.* Journal of Inorganic and Nuclear Chemistry, 1965. **27**(4): p. 801-808.
250. Cordfunke, E.H.P. and Loopstra, B.O., *Sodium Uranates: Preparation and Thermochemical Properties.* Journal of Inorganic and Nuclear Chemistry, 1971. **33**(8): p. 2427-2436.
251. Denning, R., *Electronic Structure and Bonding in Actinyl Ions.* Complexes, clusters and crystal chemistry, 1992: p. 215-276.
252. De Blieck, R., Van Cappellen, E., Van Tendeloo, G., Amelinckx, S., Gens, R., and Fuger, J., *On the Lattice of Ba_3uo_6.* Journal of Solid State Chemistry, 1987. **68**(2): p. 375-378.
253. Read, C.M., Bugaris, D.E., and zur Loye, H.-C., *Single Crystal Growth and Structural Characterization of Four Complex Uranium Oxides: Cauo4, B-Ca_3uo_6, $K_4cau_3o_{12}$, and $K_4sru_3o_{12}$.* Solid State Sciences, 2013. **17**: p. 40-45.
254. Holc, J. and Golič, L., *The Synthesis and Crystal Structure of A-Ca_3uo_6.* Journal of Solid State Chemistry, 1983. **48**(3): p. 396-400.
255. Hoekstra, H. and Siegel, S., *Structural Studies on Li_4uo_5 and Na_4uo_5.* Journal of Inorganic and Nuclear Chemistry, 1964. **26**(5): p. 693-700.
256. Zachariasen, W.H., *Manhattan Project Report,* . 1945.
257. Zachariasen, W.H., *Crystal Chemical Studies of the 5f- Series of Elements. 4. The Crystal Structure of $Ca(Uo_2)O_2$ and $Sr(Uo_2)O_2$.* Acta Crystallographica, 1948. **1**(1-6): p. 281-285.
258. Van Egmond, A.B., *Investigations on Cesium Uranates—V: The Crystal Structures of Cs_2uo_4, $Cs_4u_5o_{17}$, $Cs_2u_7o_{22}$ and $Cs_2u_{15}o_{46}$.* Journal of Inorganic and Nuclear Chemistry, 1976. **38**(9): p. 1649-1651.
259. Murphy, G., Kennedy, B.J., Johannessen, B., Kimpton, J.A., Avdeev, M., Griffith, C.S., Thorogood, G.J., and Zhang, Z., *Structural Studies of the Rhombohedral and Orthorhombic Monouranates: Cauo4, A-$Sruo_4$, B-$Sruo_4$ and $Bauo_4$.* Journal of Solid State Chemistry, 2016. **237**: p. 86-92.
260. Kovba, L., *Crystal Structures of Potassium and Sodium Monouranates.* Sov. Radiochem.(Engl. Transl.) 13: No. 2, 319-20 (Mar-Apr 1971). 1971.
261. Reis, A.H., Hoekstra, H.R., Gebert, E., and Peterson, S.W., *Redetermination of Crystal-Structure of Barium Uranate.* Journal of Inorganic & Nuclear Chemistry, 1976. **38**(8): p. 1481-1485.
262. Bickel, M., Kanellakopulos, B., and Powietzka, B., *The Structural and Electronic Properties of Na_4uo_5 and Na_4npo_5.* Journal of the Less Common Metals, 1991. **170**(1): p. 161-169.
263. Tso, T.C., Brown, D., Judge, A.I., Holloway, J.H., and Fuger, J., *Thermodynamics of the Actinoid Elements .6. The Preparation and Heats of Formation of Some Sodium Uranates(Vi).* Journal of the Chemical Society-Dalton Transactions, 1985(9): p. 1853-1858.
264. Efremova, K., Ippolitova, E., Simanov, Y.P., and Spitsyn, V., *Investigations in the Field of Uranium Chemistry.* Moscow University Press, Moscow, 1961: p. 59.
265. Hinatsu, Y., Fujino, T., and Edelstein, N., *Studies on Magnetic Susceptibility, Electron Paramagnetic Resonance, and Absorption Spectrum of Li_3uo_4, an Octahedral U^{5+} Compound with a Small Tetragonal Distortion.* Journal of Solid State Chemistry, 1992. **99**(1): p. 95-102.
266. Fujino, T., Ouchi, K., Yamashita, T., and Natsume, H., *Reaction of Lithium and Sodium Nitrates and Carbonates with Uranium Oxides.* Journal of Nuclear Materials, 1983. **116**(2–3): p. 157-165.
267. KRYUKOVA, A., KLAPSHIN, Y., SKIBA, O., and KHAZOV, S., *Reaction of Uranium-Oxides with Melts of Alkali-Metal Carbonates. 1. Reaction of U (Vi) Oxide with Sodium-Carbonate Studied by Dta.* Soviet Radiochemistry, 1990. **32**(5): p. 525-528.
268. Kovba, L., Simanov, Y.P., Ippolitova, E., and Spitsyn, V., *Investigations in the Field of Uranium Chemistry.* ANL-Trans-33, 1961: p. 17.
269. Cordfunke, E.H.P. and Loopstra, B.O., *Preparation and Properties of the Uranates of Calcium and Strontium.* Journal of Inorganic and Nuclear Chemistry, 1967. **29**(1): p. 51-57.
270. Allpress, J.G., *Barium Polyuranates.* Journal of Inorganic and Nuclear Chemistry, 1964. **26**(11): p. 1847-1851.

3. Methodology

3.1 Quartz Crystal Microbalance (QCM)

The Quartz Crystal Microbalance (QCM) is a high sensitivity mass balance that employs a resonating crystal to derive quantitative (mass, concentration, number) or qualitative (mechanistic information) on chemical processes occurring within the analyte substance. QCM is composed of a closed circuit that applies an alternating current through a piezoelectric crystal via conductive electrodes at its edge (Figure 3.1). Commonly, an AT-cut quartz plate (35° tilt from the Z-axis) is used. This alternating voltage induces repetitive lateral mechanical shear deformations on the order of ~3 pm V^{-1}, with crystal oscillations at constant resonant frequencies (f_0) that range between 1 and 30 MHz. The displacement caused by this shear mode resonance through the crystal is sinusoidal in shape, with the number of antinodes equal to the overtone order. As the direction of the mechanical strain is related to the relative orientation of applied electrical field and crystal axis, the anterior and posterior electrodes are shaped to allow energy trapping to take place. This shifts mechanical displacement towards the centre of the crystal, reducing dampening effects resulting from edge contacts (electrodes, frame).

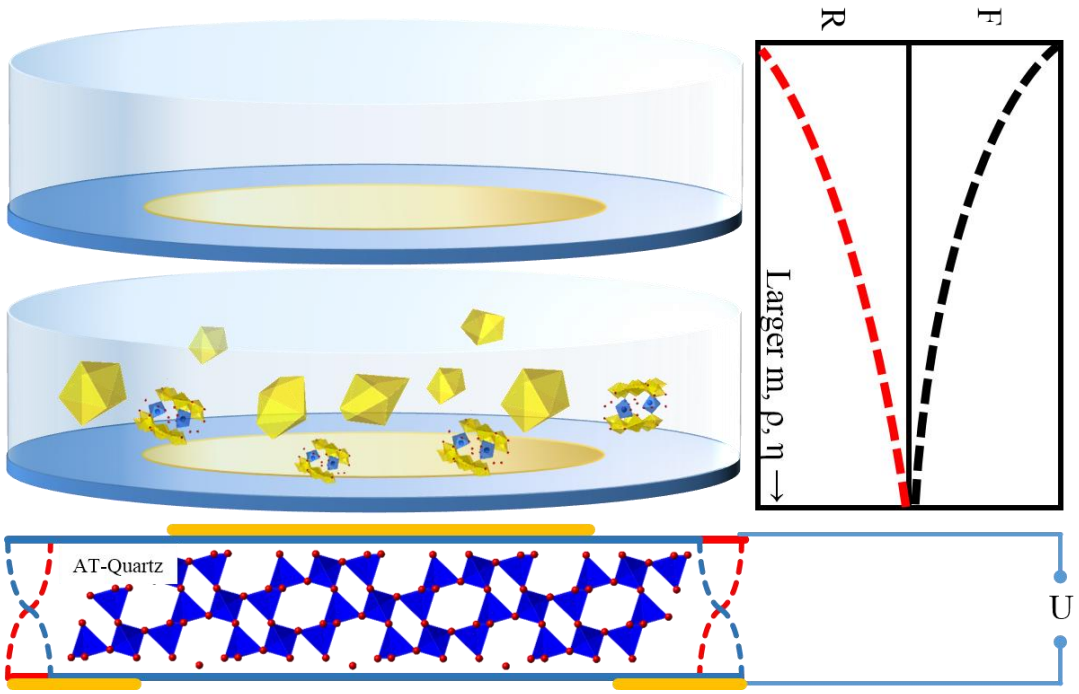

Figure 3.1 Conceptual graphical representation of an operating QCM crystal under the influence of mass addition, or increasing solution viscosity.

When contacted with a solid of mass m, the crystal loses energy to the sorbed material, dampening its vibration frequency. From Sauerbrey (Equation 3.1) [1, 2], the frequency shift (ΔF) value is directly proportional to a negative change in mass deposited. However, this mathematical relationship may only be valid for strongly sorbed spherical particles that are rigid, non-slip and are distributed homogeneously in a thin layer [3].

$$\Delta \boldsymbol{f} = \frac{-\boldsymbol{2f_0^2}}{\boldsymbol{A\sqrt{\mu_q \rho_q}}} \Delta \boldsymbol{m} \qquad \text{Equation 3.1}$$

Where ΔF is the relative frequency change (Hz); f_0, the crystal resonant frequency (Hz); Δm, the mass change (g); A, piezoelectro-active crystal area (cm^2); ρ_q, density of quartz (2.678 g cm^{-3}); μ_q, shear modulus of AT-cut quartz ($2.947*10^{11}$ g cm^{-1} s^{-2}).

A negative frequency shift as a function of increasing mass deposition, implies a crystal-to-substrate energy transfer taking place. This dissipates the sinusoidal waves propagating into the bulk substrate exponentially as a function of time when the voltage is disengaged (Equation 3.2) [4, 5].

$$q(t) = A_0 \exp\left(\frac{-\mathrm{t}}{\tau}\right) \sin(\omega t + \phi), t \geq 0 \qquad \text{Equation 3.2}$$

Where A_0 is amplitude at t_0, τ is the decay constant, t is time, ω is angular frequency, ϕ is phase and q(t) is substrate displacement. A dissipation constant D is therefore inversely proportional to the decay constant (Equation 3.3) [4] and directly proportional to the resistance to motion of the resonating body. Where L_u, inductance; and R is the corresponding electrical resistance in series due to the resonating body (Ohm).

$$D = \frac{2}{\omega\tau} = \frac{R}{\omega \mathrm{L}_u} \qquad \text{Equation 3.3}$$

The frequency shift is therefore a crystal orientated property, whereas the resistance shift is a secondary property of the system. i.e. The electrical resistance within the resonator circuit is affected by the impedance to oscillation and is therefore, a measure of the work done by the circuit in oscillating the crystal as a result of the additional mass deposited (R ∝ W). For this reason, during Sauerbrey-like mass deposition processes, as frequency reduces from equilibria (negative δF) the corresponding resistance must increase (positive δR).

In non-Sauerbrey Newtonian liquid environments, the limitations of the Sauerbrey equation (non-rigid sorbed, thick layers) may be adjusted via the Kanazawa and Gordon derivation (Equation 3.4) [6].

$$\Delta F = -f_0^{3/2} \left(\frac{\eta_s \rho_s}{\pi \mu_q \rho_q}\right)^{1/2} \qquad \text{Equation 3.4}$$

Where ΔF is frequency shift relative to air ($F_{air} - F_{current}$); f_0, resonance frequency of crystal; μ_q and ρ_q, shear modulus and density of quartz respectively; η_s and ρ_s the dynamic (absolute) viscosity and density of the sorbed fluid layer respectively.

The energy transfer at the crystal – fluid interface induces propagation of shear waves (transverse waves) into the bulk fluid. However, due to the viscoelastic nature of the substrate, frictional losses are greater, decaying the shear wave oscillation exponentially as a function of distance. With maximum penetration depth into water (5 MHz oscillator) of approximately 250 nm [7], the QCM is indeed a surface oriented technique in submersed liquid conditions when compared to related acoustic techniques.

Nanofluids are defined as colloidal suspensions of nano- to micron-sized particle of metals, alloys or their compounds (chalcogenides, oxides etc) within a fluid matrix. Often studied for their enhanced chemophysical properties such as heat transfer [8], rheology [9] or mechanical resistance [10] when compared to the base fluid, they have been applied widely within industry and research. By increasing the volume fraction of particles or reducing particle size, collisional particle-particle interactions or available surface area is increased. Leading to increased thermal conductivity, heat capacity and turbulent mixing of the carrier fluid [11].

Particle-particle and particle-fluid interactions within the suspension cause energy losses due to frictional or motional resistance. An increase in particle concentration [12], particle size [13] or a change in particle shape (surface area) [14] could therefore affect the viscosity and density of the suspension relative to the base fluid.

3.1.1 Particle volume fraction ϕ

If nanofluids may be approximated as a single or homogenous dual phase, then the Kanazawa-Gordon relationship (Equation 3.4) may be extended using Brinkman's development (Equation 3.5) [15] of Einstein's equation [12] predicting fluid viscosity as a function of particle concentration.

$$\eta_{nf} = \frac{\eta_f}{(1-\phi)^{5/2}} \qquad \text{Equation 3.5}$$

Where η_{nf} is the dynamic viscosity of the particle-fluid suspension; η_f, viscosity of the base fluid or fluid at t = 0 s; and ϕ, the particle-fluid volume fraction.

Given that bulk density of the reactant solution in both titration and batch reactions ($V_{TMAH\ titrant} << V_{Ca/U\ bulk}$; $V_{Ca/U\ spike} << V_{TMAH\ bulk.}$ respectively) changes little with reaction progression, the overall solution density detected by the QCM may be assumed constant throughout the reaction. This allows rearrangement of Equation 3.4 to isolate apparent nanofluid viscosity η_{nf} (Equation 3.6, where $\rho_f \equiv \rho_s$).

$$\left(\frac{\Delta F}{-f_0{}^{3}/_{2}}\right)^2 . \frac{\pi \mu_q \rho_q}{\rho_f} = \eta_{nf} \qquad \text{Equation 3.6}$$

As a precipitation reaction proceeds, crystallites will nucleate randomly throughout the bulk solution when suitable conditions are reached. If homogeneous nucleation occurs, the number of nuclei forming within the first 250 nm of fluid sorbed to the vibrating QCM crystal will be equal to that of the bulk fluid. Assuming that boundary layer thickness → 0 at reaction time t >> 0 s, the apparent QCM η will therefore become η_{nf} (Equation 3.7).

$$\left(\frac{\Delta F}{-f_0{}^{3}/_{2}}\right)^2 . \frac{\pi \mu_q \rho_q}{\rho_f} = \eta_{nf} = \frac{\eta_f}{(1-\phi)^{5}/_{2}} \qquad \text{Equation 3.7}$$

Rearranging Equation 3.7, the relative apparent particle fraction ϕ, may be isolated (Equation 3.8). This allows analysis of measured trends in terms of both frequency shift and as the extent of reaction progression.

$$\phi = 1 - \left[\frac{\eta_f}{\left(\frac{\Delta F}{-f_0{}^{3}/_{2}}\right)^2 . \frac{\pi \mu_q \rho_q}{\rho_f}}\right]^{\frac{2}{5}} \qquad \text{Equation 3.8}$$

3.1.1.1 TMACl concentration effects

From the Vand [16] and Angell [17] approach, the viscosity of TMACl [18] electrolyte solutions is shown to decrease greatly with increasing temperature. Values increase logarithmically with each 10 ºC increase in temperature; and are ~1 – 2.5 orders of magnitude greater in effect when compared to the effects of increasing concentration at isothermal conditions (Figure 3.2).

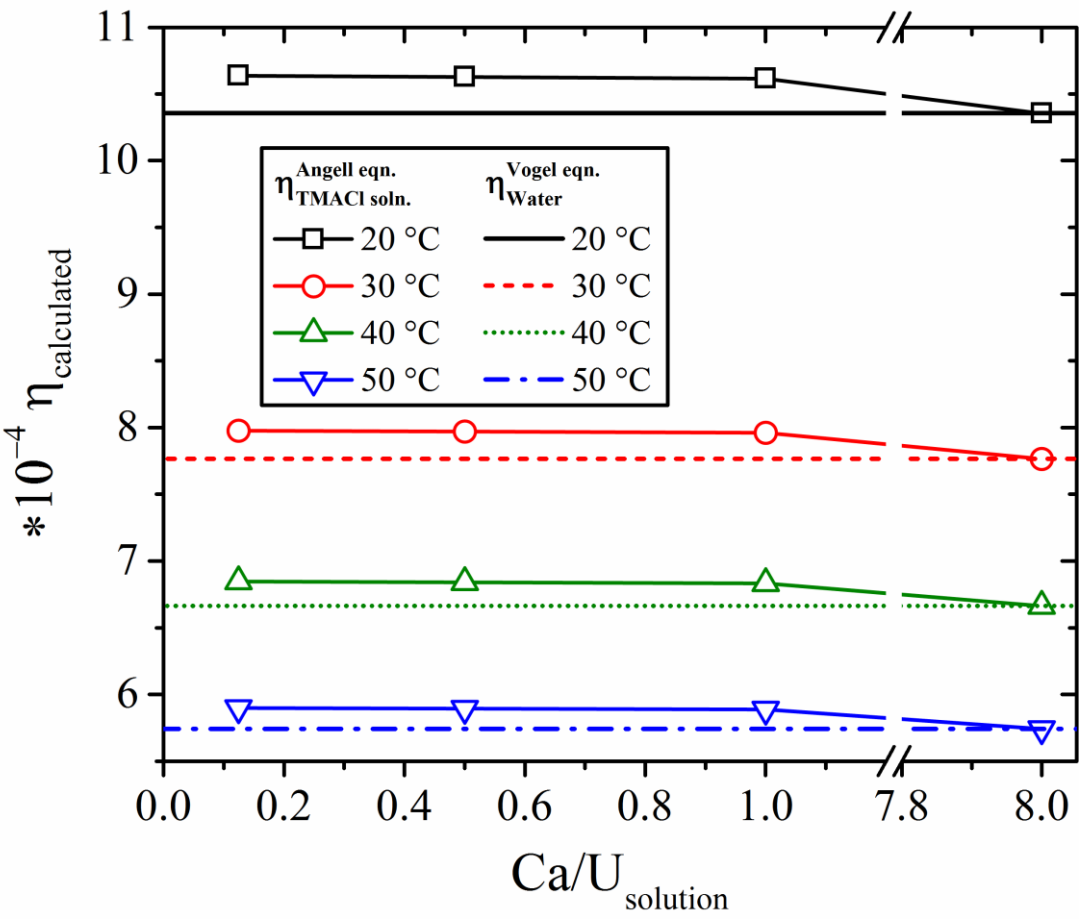

Figure 3.2 Predicted change in viscosity of solution due to increasing concentration of tetramethylammonium chloride (TMACl) concentration compared to pure water.

3.1.1.2 Baseline measurements

Baseline QCM measurements were made to characterise drift range for frequency and resistance trends under the conditions (time, pH, TMA^+ concentration) used in subsequent experiments. Where instead of uranium and calcium salts, tetramethylammonium chloride (TMACl) and HNO_3 was used to mimic the expected ionic strengths and pH values for Ca and U(VI) containing solutions. These titration reactions were carried out at 20 and 50 °C in 0.0005, 0.05 and 0.2 mol kg^{-1} ionic strengths at pH 3. Other reaction conditions used such as base inlet and stir rate were the same as latter Ca and U(VI) containing reactions.

The ΔF trends exhibited some variation across the temperatures and ionic strengths tested, with maximum ΔF values lying at $-7 < \Delta F_{20\,°C} < 22$ and $-50 < \Delta F_{50\,°C} < 2$ (Figure 3.3). Although these ranges are < ~5% of ΔF for typical U(VI) containing reactions, they are significantly larger than would otherwise be expected for baseline noise (< ~1 Hz) or simple dilution over the same time period.

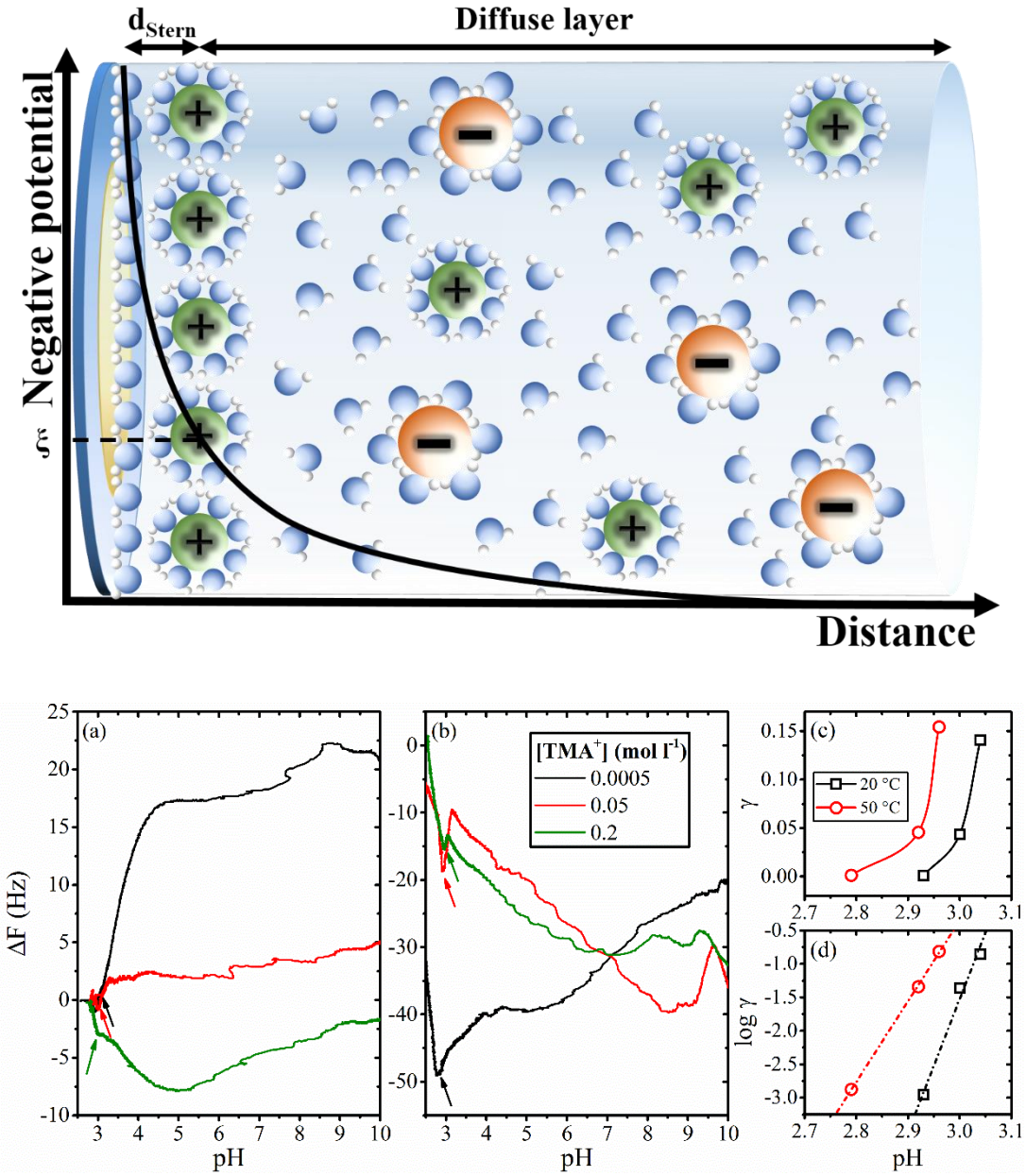

Figure 3.3 Upper: Graphical representation of the Gouy-Chapman-Stern model of the electrical double layer (EDL) at the QCM-crystal – solution interface. The charged surface is solvated and complexed by cations (protons, TMA^+, Ca^{2+}) in the Stern layer, whilst the zeta-potential (electrokinetic) is the charge potential where the diffuse layer begins. Lower: Baseline ΔF versus pH data for TMA^+ concentrations 0.0005, 0.05 and 0.2 mol l^{-1} at (a) 20 °C and (b) 50 °C. Linear (c) and log scale (d) calculated ionic strength is plotted as a function of peak minima positions (arrows).

ΔF trends over the whole pH range show a series of broad peaks and troughs at the temperature extremes and all three ionic strengths tested. In addition to the broad trends, some prominent peaks are present at ~pH 3 in all baseline tests (Figure 3.3 (a), (b), arrows). The position of these peaks (minima position) appear dependent on TMA^+ concentration and temperature, whilst at 50 °C peaks become more prominent.

Peaks (Figure 3.3 (c), (d)) move towards higher pH with increasing ionic strength and is enhanced by higher temperatures.

3.1.1.2.1 Effects of TMA^+-sorption on solution-surface interactions

At pH values below 3, the otherwise negative surface of the crystal (quartz, gold and thin Au-oxide, Au-hydroxides layer) becomes neutralised via specific sorption of positive ions such as protons or dissolved metallions (i.e. chemisorption) [19] (or positive zeta potential). Although TMA^+ ions are normally considered to be non-complexing due to its low charge density [20], this appears contradictory to other studies that demonstrate specific sorption of TMA^+ to silica surfaces in a similar mechanism to Na^+ [21]; with higher TMA^+ promoting a higher sorption density [22]. Given this, the ΔF dips occurring at both temperature extremes (Figure 3.3, (a), (b) coloured arrows) are likely related to the natural PZC of Au-hydroxide and specific sorption (or attraction due to reduction in exposed hydrophobic surface area of molecular alkyl-chains) effects of TMA^+ cations. Both the surface and the diffuse layer become more saturated with TMA^+ ions as a function of concentration. As the solution is alkalised, hydroxide ions penetrate the diffuse layer and stern layer (Figure 3.3), Au-O-H functional groups are deprotonated, decreasing net surface charge until neutrality is reached at a given pH. This compresses the electrical double layer (EDL), increasing the apparent viscosity detected by the QCM, thereby decreasing the frequency (increase in energy loss) and manifesting as a depression in the ΔF trend (Figure 3.3 arrows). As more OH- is added, charge balance is lost and the EDL expands once again to reduce the detected viscosity, allowing the trend to trend recover. A higher TMA^+ sorption density driven by higher solution concentration, would require a further extent of alkalisation (higher hydroxide concentration) before the surface charge shielding is compromised [23] and apparent point of zero charge is reached, as is reflected by an upshift in pH of ΔF minima (Figure 3.3c, d). Whilst material dependent, this PZC altering effect appears common for TMA^+ type salts in other systems [22, 24, 25]. Although an interesting extension to the abilities of the QCM, its effects on the following experimental data are not expected to be significant.

3.2 TGA-DSC-MS

Thermo-Gravimetric Analysis and Differential-Scanning-Calorimetry, or TGA-DSC in short, is a high sensitivity mass-balance that allows in-situ quantification of chemical reactions, or physical transformations in terms of mass-change. The instrument consists of a semi-sealed tube furnace (Figure 3.4) allowing passage of the sample arm. The sample arm connects to an ultra-balance in a separate chamber that is usually protected by inert gas-flow such as N_2. The arm may be composed of alumina, and usually has a series of Pt-thermocouples running through it, allowing for

simultaneous calorimetry measurements. Measurement sensitivity is limited by environmental stability (vibration etc.) and innate sensitivity of the ultra-balance. Samples are loaded in crucibles (Pt, 40 μL), then placed onto the balance arm with a blank reference crucible of the same material. A heating profile is programmed at given heating rate or plateau temperature, whilst mass (TGA) and heat flow (DSC) data are continuously streamed to the PC. All data analysis was accomplished using the Mettler-Toledo StarE Evaluation software, and Microsoft Excel.

The TGA-DSC was used to quantify mass-loss during dehydration or degradation reactions for uranyl(VI) oxyhydrate particles in chapters 4, and 6. In the latter, a mass-spectrometer (MKS Cirrus^{TM} 2) was attached to the gas-output port (Figure 3.4, 3) to analyse the output gas products in terms of fragment-mass. The mass spectrometer was used qualitatively here, whilst corroboration with TGA mass-loss values allowed more in-depth analysis of the chemical mechanisms occurring.

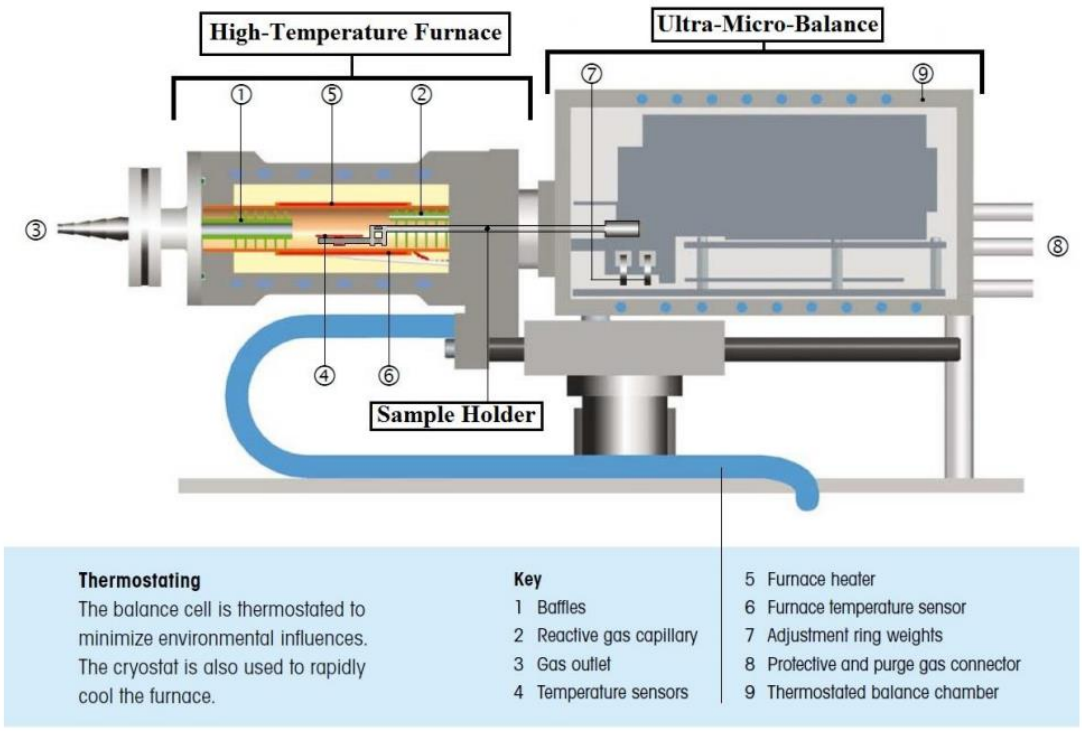

Figure 3.4 Schematic view of a Mettler-Toledo TGA-DSC.

The mass spectrometer begins by ionising the gas-flow using an ion source, usually composed broadly of a cathodic electron source, and an anode sink. The analyte gas-flow passes through the electron beam, causing ionisation (tungsten filament in this case). Positive ions are then pass through a quadrupole analyser, which consists of two pairs of parallel electromagnets. Depending on the voltage applied to the magnets, only ions of a certain mass may pass through, whilst the trajectory of lower or higher M/Z ions are destabilised, resulting in collision with the magnets. The magnets therefore act as a highly selected ion filter. This allows almost simultaneous analysis of many different sized analyte-fragments, though focus was given to mass 44, 18 and 32, which could represent CO_2, H_2O, and O_2.

The macroscopic activation energy associated with a mass-loss or degradation reaction may be derived using various methods. One of the most prevalently and convenient are the Flynn-Wall-Ozawa (FWO) [26, 27], Kissinger-Akahira-Sunose (KAS) [28-30] and Starink [31, 32] isoconversional methods. Briefly, mass-loss steps are separated and normalised to give change in reaction extent (Figure 3.5a), before using the Flynn-Wall-Ozawa (FWO) [26, 27], Kissinger-Akahira-Sunose (KAS) [28-30] and Starink [31, 32] integral methods (Table 3.1) to calculate the apparent activation energies (E_a) associated with each step.

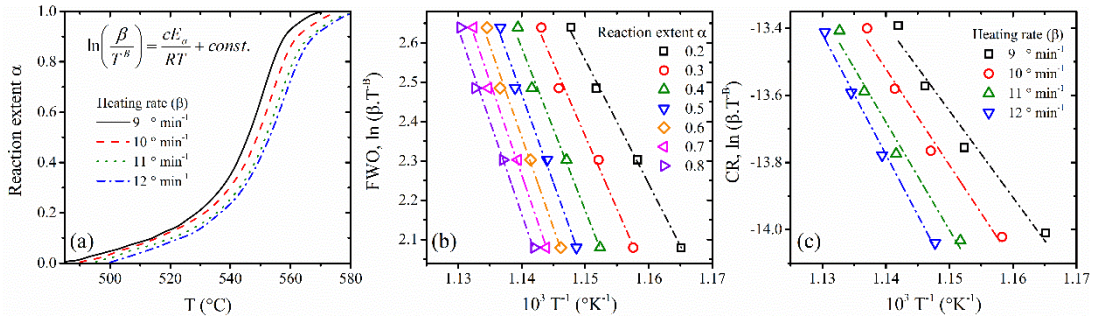

Figure 3.5 Typical plots (Ca/U = 0.124, step 4) representing (a) change in reaction extent (α) with increasing temperature; (b), (c) Linear plots of ln(β.T^{-B}) versus T^{-1} for FWO and CR methods (Table 3.1); where β, is the heating rate; T, absolute temperature at conversion extent α; Ea, activation energy; R, molar gas constant.

These isoconversional methods reveal the change in E_a at varying extents of conversion (α), and provide information on E_a-variation throughout each reaction. An alternate method (Table 3.1, Coats-Redfern (CR)) [33, 34] relies on model fitting of data at various conversion extents and constant heating rate using potential reaction models (Table 3.2, g(α)), providing a single representative E_a and reaction mechanism. All four methods are based on an altered Arrhenius equation (Figure 3.5a, equation) to derive E_a via linear regression analysis. Analysis methodologies are summarised in Table 3.1.

Table 3.1 Kinetic methods used in evaluation of activation energies.

Method	β	B	c	Notes
Flynn-Wall-Ozawa (FWO)	9, 10, 11, 12 °min^{-1}	0	1.052	Linear plot of ln (β/T^B) versus T^{-1}, $-cE_a/R$ is given by line gradient.
Kissinger-Akahira-Sunose (KAS)		2	0.4567	
Starink		1.8	1.008	
Coats-Redfern (CR)	g(α)	2	1	Linear plot of ln ($g(\alpha)/T^B$) versus T^{-1}, where g(α) represents the reaction model (see appendix). The function with the highest R^2 value (higher is better) with activation energy coinciding with that from FWO method is then taken as the most suitable model.

Table 3.2 g(α) reaction models used in data-fitting via Coats-Redfern method.

Mechanism	g(α)
Nucleation models	
Power law 1	$\alpha^{1/4}$
Power law 2	$\alpha^{1/3}$
Power law 3	$\alpha^{1/2}$
Avrami-Erofeev	$[-\ln(1-\alpha)]^{1/4}$
Avrami-Erofeev	$[-\ln(1-\alpha)]^{1/3}$
Avrami-Erofeev	$[-\ln(1-\alpha)]^{1/2}$
Diffusion models	
1D Diffusion	α^2
2D Diffusion (Janders)	$[1-(1-\alpha)^{1/3}]^2$
3D Diffusion (Crank)	$1-(2/3)\alpha-(1-\alpha)^{2/3}$
Reaction order	
1st order reaction (Mampel)	$-\ln(1-\alpha)$
2nd order reaction	$[(1-\alpha)^{-1}]-1$
Geometric contraction models	
Contracting cylinder	$1-(1-\alpha)^{1/2}$
Contracting sphere	$1-(1-\alpha)^{1/3}$

3.3 Electron microscopy

The smaller wavelengths of electrons (10^{-2} – 10^{-3} nm) allows resolution of significantly smaller features compared to visible light-based (400 – 700 nm) imaging. Much like the mass spectrometer, electrons are generated from tungsten filaments [35] inside a thermionic emission or field emission electron (FEG) gun [36]. The electrons are focused by passing through a series of electromagnetic lenses prior to interaction with the sample. Most electron microscopes conduct imaging under vacuum to reduce losses due to collisions with gases. Upon impingement of the electron beam with a sample surface, reflected electrons of varied energy in the form of backscattered (elastic scattering), secondary or auger electrons (inelastic scattering), and X-rays are

emitted [37]. In scanning electron microscopy, the electron beam rasters across the sample surface, to regenerate an image based on detection of reflected electrons by surrounding detectors [38]. Secondary electrons are most abundant due to excitation of several atoms per incident electron, though due to their low kinetic energy, are mostly surface sensitive. The more energetic backscattered electrons allow some characterisation at a deeper level, as well as some distinction between elements with high mass numbers due to higher scattering efficiency. Transmission electron microscopy (TEM) instead relies on direct transmission of a parallel electron beam through a sample with ideal thickness ~ 100 nm. Transmitted electrons are detected on the opposite side of the sample and are mostly unchanged from incident state [39], where image contrast is caused by electrons that are scattered in areas containing sample, versus areas that do not. Higher density or thickness reduces transmission efficiency, resulting in a grayscale contrast through regions within the sample or particle. Measurement of the scattering electrons during selected area electron diffraction (SAED) also provides diffraction patterns that may be indexed in much the similar way as in XRD. Energy dispersive X-ray spectroscopy is available to both SEM and TEM, where atomic excitation by incident electrons followed by relaxation events releases photoelectrons (X-rays) of wavelengths that are element specific. This allow elemental mapping of particles or images with approximate spatial resolution, which may be used together with SAED to characterise phase segregation. A suspension of particles in propan-2-ol was deposited onto carbon holey film copper-grids, before analysis in both TEM, then SEM.

3.4 Spectroscopic techniques

Several spectroscopic techniques have been utilised throughout this project, each with specific applications unique to the wavelength of radiation used as the energy source. Spectroscopy broadly relies upon the interaction of electromagnetic radiation with a sample, where the measured data is affected directly or indirectly by material-specific electronic properties at the atomic or molecular level.

3.4.1 ICP-OES

Inductively coupled plasma (ICP) optical or atomic emission spectrometry (OES, AES) are techniques used for elemental quantification of aqueous samples. Measurement sensitivity is typically as low as parts per trillion (PPT) for MS, and approximately 10^3 larger values for OES. For solids samples, digestion in a strong

acid and/or complexing agent is required before analysis. For all analyses, samples are typically digested with a small aliquot of 70% Aristar® HNO_3, before dilution to 10% using 18.2 MΩ deionised water (see experiment sections for further details). During analysis, the sample is peristaltically pumped into a nebuliser and aerosolised. The aerosol is passed through an argon plasma running at temperatures of the order ~10^4 K [40], resulting in atomisation and ionisation of the analyte. Relaxation of exited analyte ions release radiation at wavelengths that are characteristic of specific elements, which is subsequently detected by the spectrometer. Generally, elements have several characteristic bands at differing wavelengths and FWHM, and the detected intensity is proportional to the concentration [41]. If several elements are being analysed simultaneously, then a polychromator may be used to select specific wavelengths, though some peak overlap is inevitable with complex samples with many analytes. This is accounted for via prior calibration using known external and internal standards to account for inter-analyte masking effects [41]. The external standards contain known concentrations of the analyte of interest, that may be used to calibrate against output intensity in a linear plot. Whilst similar, the internal standard must contain an element that is not present in the sample, to account for instrumental masking or drift. Usually yttrium or cobalt solutions were used here.

3.4.2 FTIR spectroscopy

Fourier Transform Infra-Red (FTIR) spectroscopy allows the analysis of specific chemical groups in a bulk analyte [42]. The technique relies on excitation of chemical bonds present in the sample using IR-radiation generated from a silicon carbide source (5000 – 400 cm^{-1}) with a broad range of frequencies. Depending on bond length/strength, or atomic donor-acceptor properties, incident IR-radiation is absorbed at characteristic frequencies, which appear on spectra as a series of adsorption maxima. Usually the absorption frequency (υ) is usually quoted in wavenumbers ($\tilde{\nu}$, cm^{-1}), which may be converted via $\upsilon = c.\tilde{\nu}$, where c is the speed of light. Often used for qualitative analyses, shifts in positions of IR-absorption maxima signify variation of bond length or strength, that may be used to infer structural or chemical changes occurring within a sample.

3.4.3 UV-vis spectroscopy

Ultraviolet-Visible spectroscopy features commonly in quantitative analysis, relying on excitation from bonding (HOMO) or non-bonding lone-pairs (NB), to antibonding (LUMO) electronic orbitals within a material ($\pi \rightarrow \pi^*$, $\sigma \rightarrow \sigma^*$, $n \rightarrow \sigma^*$, etc.). Only transmission solution UV-vis is utilised here, though solid and gaseous samples may also be analysed in general. The Beer-Lambert law (Equation 3.9) states that the transmission efficiency (loss through absorption) of electromagnetic radiation through a sample is proportional to sample thickness, or the transmission path-length through

the sample. Generally UV-vis and FTIR-spectrometers operate similarly, though the former consists of a deuterium and tungsten lamp source, which emit radiation in the 190 – 400, and 300 – 2500 nm ranges respectively. The emitted light is passed through a wavelength filter and monochromator, before being split in some spectrometers, to allow simultaneous analysis of a blank reference solution with the analyte solution. This HOMO→LUMO transition may be extended to analysis of inorganic uranyl(VI) ions, wherein f→f transitions within U(VI) metal centres [43] are weak due to symmetry forbidden (u→u) transitions from HOMO σ_u orbitals with O2p and U5f character to LUMO ϕ_u, δ_u orbitals (U5f) [44, 45], though are intensified by vibronic coupling to the uranyl(VI) symmetric (v_1), asymmetric stretching (v_2) and bending (v_3) modes, giving rise to characteristic electronic fine structure observable in empirical data (see **Figure 4.4**b) [46]. Indeed, an increase in temperature increases vibronic coupling to improve absorption intensity [47].

3.4.4 XAS

Used since the 1970s [48] in synchrotron radiation facilities, X-ray absorption spectroscopy (XAS) is an element specific technique that can characterise local the chemical and structural states within gaseous, liquid and solid samples [49]. According to the Bohr model, the atom consists of a positively charged nucleus of densely packed proton(s) (and neutrons), that is stabilised electrostatically by spherical layer(s) of electrons with varying energy. The Z number of a given element corresponds to the number of protons and therefore the number of electrons present in the atom, where electrons populate levels in order of increasing energy as described by the Aufbau principle. This gives rise to s, p, d, and f[1], atomic orbitals, which contain up to 2, 6, 10, and 14 electrons respectively. The outermost electrons (valence) being highest in energy, determine its chemical properties and require the least additional energy to excite into the continuum, thereby forming a charged ion. With decreasing radius of the electron cloud, the required ionisation energy (binding energy) increases towards the innermost electrons (core). These energy states may be expanded using principle quantum numbers n = 1, 2, 3,…; the azimuthal (l = 0, 1, 2,…, n-1; ≡ s, p, d, f respectively); and total angular momentum (j = l + s, where s is the electron spin +½ and -½). The principle quantum numbers 1 – 4 are often replaced by the letters K, L, M, N-shells, which may in turn be filled by electrons in the order (1s), (2s, 2p), (3s, 3p, 3d), etc. Electrons filling of orbitals occurs via two potential spin-states (up, down), where the Fermi correlation prioritises filling of each orbital by like-spin electrons as this minimises interaction. As a consequence of this (Pauli exclusion

[1] The d and f-orbitals are separated further into 5 and 7 pairs of electrons, each of a different orientation as to minimise inter-orbital interaction energy.

principle), a charged state (ion) is most stable in fully-occupied, half-filled, or empty states, where each orbital pair is filled with electrons of unique spin (i.e. up, or up and down).

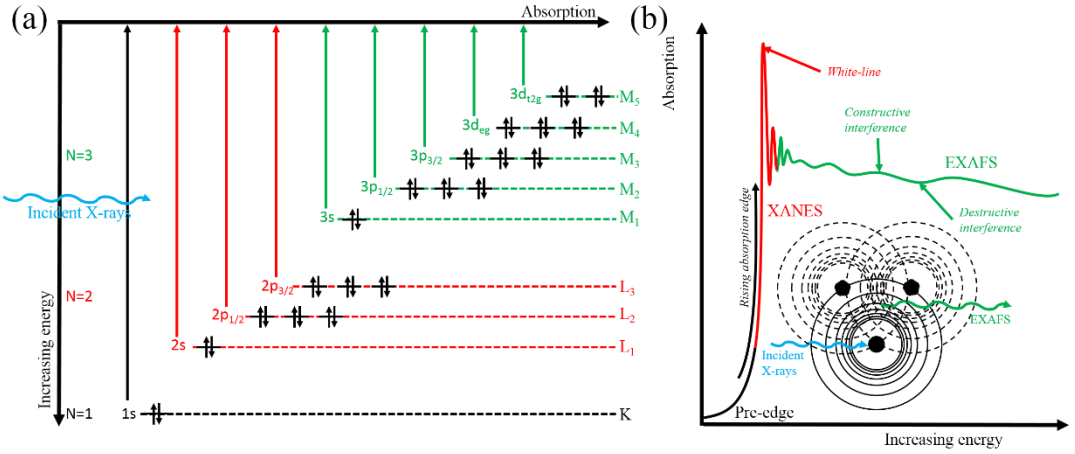

Figure 3.6 (a) conceptual representation of electronic energy levels at various edges. (b) Typical X-ray absorption spectra showing the pre-edge, XANES and EXAFS regions, as a function of incident X-ray energy.

X-rays are a form of electromagnetic radiation, which amongst many others of varying energy (UV, gamma or micro) may be treated using both wave-like and particle-like characteristics. An incident X-ray may therefore excite an atom to higher energy levels via the complete absorption of a quanta (package) of energy (photon) to form a photoelectron. The total number of electron transmitted by a sample is described by the Beer-Lambert law (Equation 3.9), where I_t and I_0 are transmitted and incident X-ray intensities; μ, is the absorption coefficient of the sample; x, the thickness. It follows that the total X-ray intensity transmitted through sample (I_t/I_0) increases exponentially with sample thickness or absorption coefficient.

$$\mathbf{I_t = I_0 e^{-\mu x}} \qquad \text{Equation 3.9}$$

Depending on the total energy absorbed and atomic orbital occupancy, electrons are excited to higher unoccupied states, or ejected into the continuum. This leaves an electron hole, or corehole if excitation occurred from a core-orbital, which is followed by a cascade of electron-hole filling by higher orbital electrons. Each relaxation releases photons of energy equal to the difference in energy between the two levels. The dipole selection rule ensures that electronic transitions may only occur between states with azimuth values (l) that differ by ±1. e.g. 1s → 2s is 'forbidden', whilst 1s → 2p is allowed. With tuning of the incident X-ray energy, energy thresholds may therefore be targeted towards specific elements and the total adsorbed intensity (spectra) may be analysed further. A typical X-ray absorption spectrum (Figure 3.6b) consists of the pre-edge region and the rapidly rising absorption edge, which is followed by a step-like feature caused by excitation of the photoelectron into the

continuum. There are usually oscillations after this edge, which in the case of uranium, includes a strong peak at the top called the white-line, as well as other peaks or shoulders that extend up to ~50 eV above the absorption edge. As these features are affected by the density of unoccupied orbitals, the core electrons of an element with a higher oxidation state become stabilised (less shielding from the nucleus) and require a higher energy to excite or ionise; upshifting the edge-feature by a few electronvolts. This is sometimes accompanied by the presence of a 'pre-edge' feature as that observed in Cr(VI) K-edge spectra [50], which stems from 1s → 3d transitions allowed by tetrahedral $3d^2 4sp^3$ hybridisation (normally forbidden). The XANES region (Figure 3.6b, red) therefore describes multiple scattering interactions and is highly sensitive to the geometry and coordination number of valence determining ligands[2]. The EXAFS region (Figure 3.6b, green) describes the sum (Equation 3.10) of constructive (in-phase) and destructive (out-of-phase) interference between outgoing photoelectrons ejected from core orbitals, and the backscattered electrons from neighbouring atoms (Figure 3.6b, diagram) [51, 52]. This is related to the radial distribution function of the absorber, which if described as a propagating spherical wavefunction $\chi(k)$ of the photoelectron, may be understood by the EXAFS equation (Equation 3.11). $F_{eff}(k)$, $\varphi_i(k)$, and $\lambda(k)$ are the effective scattering amplitudes, phase shifts and the mean free path of the photoelectron, respectively; R_i, the half path length represents the absorber-scatterer separation distance, which is a sum of R_{0i}, the theoretical half path length from model, and ΔR_i. k is the excess kinetic energy of the photoelectron in wavenumbers, where E is energy in electronvolts (E_0 is the threshold energy).

$$\boldsymbol{\chi(k) = \sum_i \chi_i(k)} \qquad \text{Equation 3.10}$$

$$\boldsymbol{\chi_i(k) = \frac{(N_i S_0^2) F_{eff_i}(k)}{k R_i^2} \sin[2kR_i + \varphi_i(k)] e^{-2\sigma_i^2 k^2} e^{\frac{-2R_i}{\lambda(k)}}}$$

$$\boldsymbol{Where\ R_i = R_{0i} + \Delta R_i,}$$

$$\boldsymbol{and\ k^2 = \frac{4\pi m_e (E - E_0 + \Delta E_0)}{h},} \qquad \text{Equation 3.11}$$

$$\boldsymbol{where\ E - E_0 \approx 3.81 k^2}$$

For a single scattering path, the term $\mathbf{N_i S_0^2}$ is a k-independent term that describes the amplitude of the EXAFS signal of the i^{th} path, which is directly affected by $\mathbf{N_i}$. This is the path degeneracy, the coordination number for single paths, or number of

[2] Often described as surrounding scatterers due to the wave-like properties of radial photoelectron emissions to neighbouring atoms.

identical paths in multiple scattering. S_0^2 generally ranges 0.7 – 1.1 and accounts for the stabilisation effects caused by formation of the corehole. Whilst this is a material dependent term, it may be shared between absorbers with the same oxidation state and edge. $\mathbf{F_{effi}(k)}$ is the backscattering factor (c.a. atomic form-factor in XRD) [53], which accounts for the dependency between scattering and atomic number Z, whereby elements with higher electron counts scatter photoelectrons more strongly at higher wavenumbers [53, 54]. This term gives rise to the 'k-test' utilised in latter sections, which relies on heavier atoms such as U scattering more at higher k ($Å^{-1}$). The Fourier-Transform or R-space EXAFS spectrum at higher k-weighting (k, k^2, k^3) would give heavier scatterers a larger increase in amplitude for a given peak, relative to elements of lower atomic number Z [53, 55]. This is a powerful first approximation method in distinguishing the relative atomic weight of scattering atoms.

$\mathbf{R_i}$ is the radial contribution of atoms at distance R, and decreases in magnitude $\propto R^{-2}$. The $\mathbf{(2kR_i + \varphi_i(k))}$ term accounts for sinusoidal oscillations and the phase of the path in terms of the photoelectron path ($2R_i$) and the phase-shift $\varphi_i(k)$ caused by photoelectron interaction of absorber and scatterer; which in Fourier-Transform (FT) R-space ($Å^{-1}$) allows relation between peak positions with scatterer-absorber separation (phase shift is usually on the order of ~-0.5 Å from the real value). $\mathbf{\sigma^2}$ accounts for Debye-Waller oscillatory contributions of static (structural) or dynamic (thermal) disorder within the sample to the EXAFS signal [56].

3.5 XRD

Laboratory based diffractometers comprise of a cathode ray tube, which emits electrons that are accelerated through an electrical potential of 40 kV. These high energy electrons collide with a cooled copper plate, which emits K_α and K_β photoelectrons via $L_{1,2}$ ($2p_{3/2}$, $2p_{1/2}$) → K(1s) and $M_{2,3}$ (3p) → K(1s) transitions. The latter k_β is mostly removed via placement of a nickel foil, to ease data analysis. The interaction between an incident K_α X-ray of wavelength λ, and electron orbitals results in elastic scattering. Like that occurring for the photoelectrons in XAS, this secondary spherical wavefunction propagates outwards from affected atoms, interfering constructively and destructively (Figure 3.6b). Diffraction occurs from additive constructive interference between parallel planes of atoms with separation distance d (Figure 3.7a). When these conditions are met, the incident angle θ, X-ray wavelength and interplanar spacing d may be related via the Bragg law (Figure 3.7a), where n is any integer. This usually results in several maxima in diffracted X-ray intensity at specific 2θ (2theta) or d-spacing values, that are unique to distinct crystalline structures; allowing for fingerprinting of specific crystalline phases in a given sample. However, diffracted rays travel in an inverted cone (Debye diffraction cones) from

beyond the sample (Figure 3.7b), with each cone corresponding to a specific d-spacing. To maximise data collection, the detector arm is rotated eucentrically over the sample, resulting in a 2-dimensional diffraction pattern, where each reflection peak maxima coincides with a cone edge (Figure 3.7b).

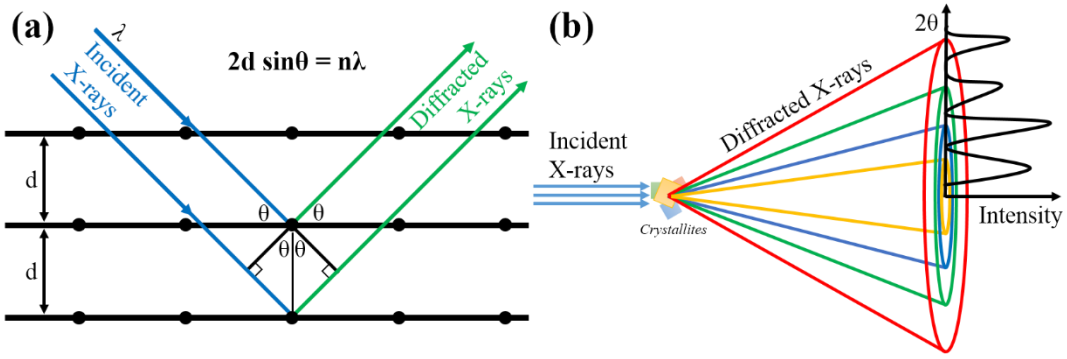

Figure 3.7 Conceptual diagram showing (a) diffraction of monochromatic X-rays by planes of atoms in a crystal, and (b) the intensity maxima of diffracted rays from Debye diffraction cones of various 2theta values, that correspond to unique HKL reflections in a crystalline structure.

Large databases such as the Crystallographic Open Database (COD), those held by the International Centre of Diffraction Data (ICDD) contain powder diffraction files (PDF) for known phases from the literature, which may be used to assign lattice planes (HKL) specific peaks, or determine unit cell parameters.

More specific information on sample analysis procedures are detailed in the following experimental sections, due the radioactive and chemotoxic nature of uranium compounds, a Bruker A100B109 airtight sample holder with cobalt knife edge (collimator) was usually used to contain powdered samples. Sample preparation involved gentle disaggregation followed by suspension in isopropyl alcohol, before deposition onto the silicon wafer. The sample is allowed to dry under fume-hood extraction, before sealing and analysis.

3.5.1 Crystallite size analysis

The Bragg equation relies on the sample being perfect and infinite, and on the incident beam being perfectly parallel and monochromatic. However, many materials comprise small crystallites that may contain defects, anti-phases etc., while XRD-instrumentation will also contain imperfections in calibration or materials that are unique to each instrument. The former stems from a lack of coherent interference from diffracted X-rays, which otherwise accumulate from larger numbers of crystal planes with spacing d in larger crystallites. Both sample and instrument contributions result in broadening of X-ray diffraction peaks, resulting in various Full Width Half Maximum (FWHM) values. This may be advantageously utilised in determining the

approximate coherent domain size of crystallites, though maximum crystallite size plateaus at up to ~500 nm. A typical analysis procedure is outlined.

Profile fitting of diffractograms was completed using an Si-standard to reveal Gaussian and Lorentzian broadening coefficients (A, B, C respectively) and saved as an instrument standard template file. All subsequent profile fitting analyses of crystalline samples then used this template to account for instrumental broadening when extracting phase Full Width Half Maximum (FWHM) values. A typical analysis is described as follows; the raw sample XRD-pattern is inserted into the template file created above and saved as a new file. Diffractograms were clipped to the 2theta range of 5 – 65 ° 2theta to remove poorly-resolved peaks from extreme 2theta values, then a polynomial (coefficients 1 – 3 and X^{-1}) background spline was fitted to the pattern (granularity 11, bending factor 3, input data smoothing on) with the minimum number of base points possible, whilst still following the baseline. A peak search was completed using significance parameters revealing the main peaks only (> 10), whilst artefact peaks not expected for the given phase were removed manually (peak list tab)[3]. In automatic profile fitting mode, default settings were allowed. A fit was deemed complete for samples when Goodness-of-Fit (GOF) factor was less than 5 (usually < ~4). The FWHM output values are checked for large outliers due excessive peak overlap and are excluded (blue) from further analysis.

The maximum average crystallite size (D) of crystalline domains are approximated via application of the Scherrer equation (Equation 3.12) [57] to the selected peaks, where k is the shape factor (usually assumed 0.94 as for equiaxed crystals); λ, X-ray wavelength (Å); β, the FWHM (radians); θ, the Bragg angle of the analyte peak [58].

$$\boldsymbol{D = \frac{k\lambda}{\beta_D cos\theta}, \quad where\ \beta_D{}^2 = \beta_{observed}{}^2 - \beta_{instrumental}{}^2} \qquad \text{Equation 3.12}$$

As the classical Scherrer method assumes that crystallite domains are unaffected by microstrain, the Williamson-Hall method [59, 60] was used to complement the former in determining strain and crystallite size values. The latter, an extension (Equation 3.13) of the Scherrer equation, assumes that overall XRD peak broadening (β_p) arises as a direct sum of both strain (crystal imperfections such as dislocations etc. β_S) and reduction in domain (grain) size (Scherrer contribution β_D)[4].

---

[3] i.e. If the sample is expected to be a mixed phase, then profile fitting and crystallite size determination is extracted for the main phase only. This becomes more prevalent towards over-stoichiometric typically with Ca/U >> 1.11.

[4] As size and strain contributions depend on $\cos\theta^{-1}$ and $\tan\theta^{-1}$ respectively, this allows separation of the two contribution to overall peak broadening

$$(\beta_S + \beta_D)cos\theta = \beta_p cos\theta = \frac{k\lambda}{D} + 4\varepsilon sin\theta, \ \ where\ \varepsilon \approx \frac{\beta_S}{tan\theta}$$

Equation 3.13

By plotting $\beta_p cos\theta$ as a function of $4sin\theta$ (Figure 3.8, inset), linear regression allows approximation of size and strain from Y-intercept and slope values respectively. As the strain was found to be lower than the uncertainty values, analysis was constrained assuming only broadening due to size (slope → 0 scenario).

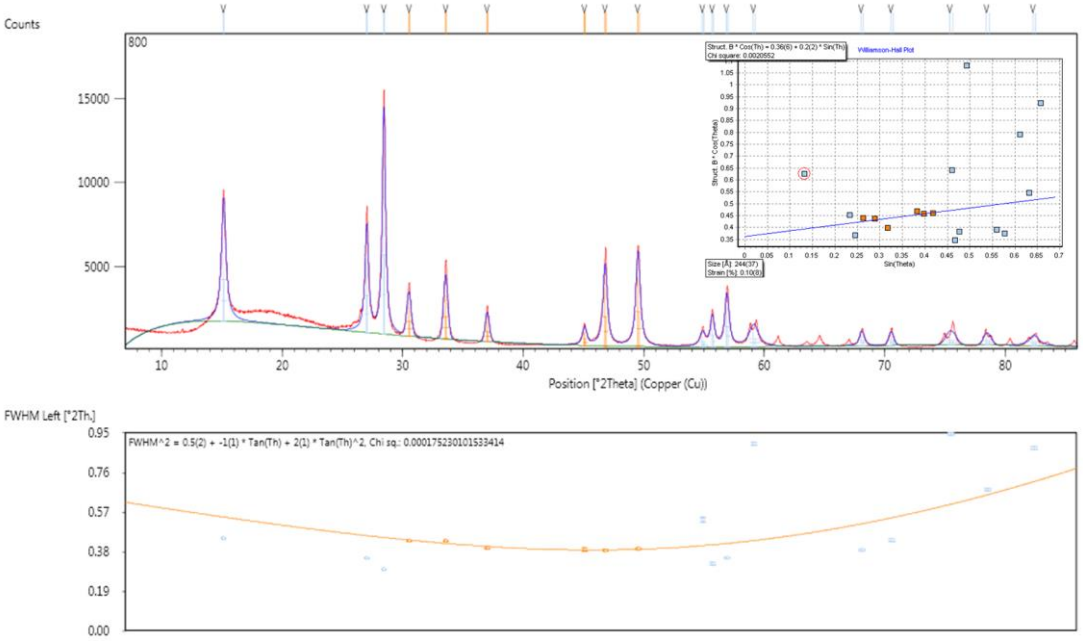

Figure 3.8 Typical profile fitting mode graphical output from PANanalytical Highscore Plus™ during crystallite size analysis of an XRD-pattern using the Williamson-Hall method.

3.6 Light scattering

Laser diffraction (LD) or static light-scattering relies upon the Fraunhofer theory [61] to measure particle size within a suspension. The theory states that when laser radiation interacts with particles, the intensity of diffracted light is directly proportional to particle size, whilst the (logarithmic) diffraction angle is inversely proportional (i.e. Larger particles provide smaller diffraction angles). By using a series of focusing lens, the laser beam passing through the sample is either diverted or focused onto beam-stop, whilst the detector is rotated eucentrically around the sample cuvette (cylindrical) to record counts or pulses of diffracted light at specific angles. By calibrating specific diffraction angles to known particle-size standards (Ludox™ silica spheres), the particle size analyte may be a quantified.

Dynamic light scattering (DLS) instead measures the velocity at which suspended particles travel due to Brownian motion. This is described by the Stokes-Einstein

equation (Equation 3.14), which shows the proportionality between hydrodynamic radius (d_H) and temperature (T), or inverse proportionality with solution viscosity, and the translational diffusion coefficient D, where K_B is the Boltzmann constant. This therefore ignores variations in particle morphology or shape, and more priority is given to particle factions with larger size when samples are polydisperse.

$$d_H = \frac{k_B T}{3\pi\eta D} \qquad \text{Equation 3.14}$$

The zeta potential or electrical potential at the slipping plane (Figure 3.3, upper) may be measured, due to an increase in migration velocity of a particle between an electrical potential as a function of the magnitude of the zeta potential. i.e. a colloid with higher zeta-potential will travel quicker towards an electrode of opposite charge [62].

3.7 References

1. Sauerbrey, G., *The Use of Quartz Crystal Oscillators for Weighing Thin Layers and for Microweighing Applications*. 1991.
2. Sauerbrey, G., *Verwendung Von Schwingquarzen Zur Wägung Dünner Schichten Und Zur Mikrowägung.* Zeitschrift für physik, 1959. **155**(2): p. 206-222.
3. Deakin, M.R. and Buttry, D.A., *Electrochemical Applications of the Quartz Crystal Microbalance.* Analytical Chemistry, 1989. **61**(20).
4. Rodahl, M., Höök, F., Krozer, A., Brzezinski, P., and Kasemo, B., *Quartz Crystal Microbalance Setup for Frequency and Q‐Factor Measurements in Gaseous and Liquid Environments.* Review of Scientific Instruments, 1995. **66**(7): p. 3924-3930.
5. Rodahl, M. and Kasemo, B., *On the Measurement of Thin Liquid Overlayers with the Quartz-Crystal Microbalance.* Sensors and Actuators A: Physical, 1996. **54**(1): p. 448-456.
6. Keiji Kanazawa, K. and Gordon, J.G., *The Oscillation Frequency of a Quartz Resonator in Contact with Liquid.* Analytica Chimica Acta, 1985. **175**: p. 99-105.
7. Johannsmann, D., *The Quartz Crystal Microbalance in Soft Matter Research.* Soft and Biological Matter, 2015: p. 191-204.
8. Choi, S. and Eastman, J., *Enhancing Thermal Conductivity of Fluids with Nanoparticles*. 1995, Argonne National Lab., IL (United States).
9. Shima, P. and Philip, J., *Tuning of Thermal Conductivity and Rheology of Nanofluids Using an External Stimulus.* The Journal of Physical Chemistry C, 2011. **115**(41): p. 20097-20104.
10. Gu, S., Zhang, Y., and Yan, B., *Solvent-Free Ionic Molybdenum Disulfide (Mos_2) Nanofluids with Self-Healing Lubricating Behaviors.* Materials Letters, 2013. **97**: p. 169-172.
11. Xuan, Y. and Li, Q., *Heat Transfer Enhancement of Nanofluids.* International Journal of Heat and Fluid Flow, 2000. **21**(1): p. 58-64.
12. Einstein, A., *Eine Neue Bestimmung Der Moleküldimensionen.* Annalen der Physik, 1906. **324**(2): p. 289-306.
13. Nguyen, C.T., Desgranges, F., Roy, G., Galanis, N., Maré, T., Boucher, S., and Angue Mintsa, H., *Temperature and Particle-Size Dependent Viscosity Data for Water-Based Nanofluids – Hysteresis Phenomenon.* International Journal of Heat and Fluid Flow, 2007. **28**(6): p. 1492-1506.
14. Timofeeva, E.V., Routbort, J.L., and Singh, D., *Particle Shape Effects on Thermophysical Properties of Alumina Nanofluids.* Journal of Applied Physics, 2009. **106**(1): p. 014304.
15. Brinkman, H.C., *The Viscosity of Concentrated Suspensions and Solutions.* The Journal of Chemical Physics, 1952. **20**(4): p. 571-571.
16. Vand, V., *Viscosity of Solutions and Suspensions. I. Theory.* The Journal of Physical Chemistry, 1948. **52**(2): p. 277-299.
17. Angell, C.A., *On the Importance of the Metastable Liquid State and Glass Transition Phenomenon to Transport and Structure Studies in Ionic Liquids. I. Transport Properties.* Journal of Physical Chemistry, 1966. **70**(9): p. 2793-2803.

18. Roy Choudhury, K. and Majumdar, D.K., *Viscocity of Tetraethylammonium Bromide and Tetrabutylammonium Bromide: High Concentration Range.* Electrochimica Acta, 1984. **29**(10): p. 1371-1373.
19. Alonso, U., Missana, T., Patelli, A., Ceccato, D., Albarran, N., Garcia-Gutierrez, M., Lopez-Torrubia, T., and Rigato, V., *Quantification of Au Nanoparticles Retention on a Heterogeneous Rock Surface.* Colloids and Surfaces A: Physicochemical and Engineering Aspects, 2009. **347**(1): p. 230-238.
20. Saha, N. and Das, B., *Viscosities of Some Symmetrical Tetraalkylammonium Salts in Acetonitrile at (288.15, 298.15, 308.15, and 318.15) K.* Journal of Chemical & Engineering Data, 2000. **45**(6): p. 1125-1128.
21. Brown, M.A., Goel, A., and Abbas, Z., *Effect of Electrolyte Concentration on the Stern Layer Thickness at a Charged Interface.* Angewandte Chemie International Edition, 2016. **55**(11): p. 3790-3794.
22. Rutland, M.W. and Pashley, R.M., *The Charging Properties of Monodisperse Colloidal Silica in Symmetrical Quaternary Ammonium Ion Solutions.* Journal of Colloid and Interface Science, 1989. **130**(2): p. 448-456.
23. de Keizer, A., van der Ent, E.M., and Koopal, L.K., *Surface and Volume Charge Densities of Monodisperse Porous Silicas.* Colloids and Surfaces A: Physicochemical and Engineering Aspects, 1998. **142**(2–3): p. 303-313.
24. Andrade, Â.L., Fabris, J.D., Ardisson, J.D., Valente, M.A., and Ferreira, J.M., *Effect of Tetramethylammonium Hydroxide on Nucleation, Surface Modification and Growth of Magnetic Nanoparticles.* Journal of Nanomaterials, 2012. **2012**: p. 15.
25. Ruan, X., Zhu, L., and Chen, B., *Adsorptive Characteristics of the Siloxane Surfaces of Reduced-Charge Bentonites Saturated with Tetramethylammonium Cation.* Environmental Science & Technology, 2008. **42**(21): p. 7911-7917.
26. Flynn, J.H. and Wall, L.A., *General Treatment of the Thermogravimetry of Polymers.* J Res Nat Bur Stand, 1966. **70**(6): p. 487-523.
27. Ozawa, T., *A New Method of Analyzing Thermogravimetric Data.* Bulletin of the chemical society of Japan, 1965. **38**(11): p. 1881-1886.
28. Kissinger, H.E., *Variation of Peak Temperature with Heating Rate in Differential Thermal Analysis.* Journal of research of the National Bureau of Standards, 1956. **57**(4): p. 217-221.
29. Kissinger, H.E., *Reaction Kinetics in Differential Thermal Analysis.* Analytical Chemistry, 1957. **29**(11): p. 1702-1706.
30. Akahira, T. and Sunose, T., *Method of Determining Activation Deterioration Constant of Electrical Insulating Materials.* Res Rep Chiba Inst Technol (Sci Technol), 1971. **16**: p. 22-31.
31. Starink, M., *The Determination of Activation Energy from Linear Heating Rate Experiments: A Comparison of the Accuracy of Isoconversion Methods.* Thermochimica Acta, 2003. **404**(1): p. 163-176.
32. Starink, M., *A New Method for the Derivation of Activation Energies from Experiments Performed at Constant Heating Rate.* Thermochimica Acta, 1996. **288**(1-2): p. 97-104.
33. Coats, A.W. and Redfern, J.P., *Kinetic Parameters from Thermogravimetric Data.* Nature, 1964. **201**(4914): p. 68-69.
34. Vyazovkin, S., Burnham, A.K., Criado, J.M., Pérez-Maqueda, L.A., Popescu, C., and Sbirrazzuoli, N., *Ictac Kinetics Committee Recommendations for Performing Kinetic Computations on Thermal Analysis Data.* Thermochimica Acta, 2011. **520**(1–2): p. 1-19.
35. Watt, I.M., *The Principles and Practice of Electron Microscopy*. 1997: Cambridge University Press.
36. Goodhew, P.J., Humphreys, J., and Beanland, R., *Electron Microscopy and Analysis*. 2000: CRC Press.
37. Goldstein, J., Newbury, D.E., Echlin, P., Joy, D.C., Romig Jr, A.D., Lyman, C.E., Fiori, C., and Lifshin, E., *Scanning Electron Microscopy and X-Ray Microanalysis: A Text for Biologists, Materials Scientists, and Geologists*. 2012: Springer Science & Business Media.
38. Postek, M.T., Howard, K.S., Johnson, A.H., and McMichael, K.L., *The Scanning Electron Microscope.* Handbook of Charged Particle Optics, 1997: p. 363-399.
39. Williams, D.B. and Carter, C.B., *The Transmission Electron Microscope*, in *Transmission Electron Microscopy*. 1996, Springer. p. 3-17.
40. Mendham, J., Denney, R.C., Barnes, J.D., and Thomas, M., *Vogel's Textbook of Quantitative Chemical Analysis*. 6th edition ed. 2000: Pearson Eductation Limited, Harlow.
41. Lajunen, L.H. and Perämäki, P., *Spectrochemical Analysis by Atomic Absorption and Emission*. 2004: Royal Society of Chemistry.

42. Günzler, H. and Heise, H., *Ir Spectroscopy: An Introduction. 2002*. Weinheim: Wiley-VCH. xiii.
43. Meinrath, G., *Uranium(Vi) Speciation by Spectroscopy.* Journal of Radioanalytical and Nuclear Chemistry, 1997. **224**(1-2): p. 119-126.
44. Denning, R., *Electronic Structure and Bonding in Actinyl Ions.* Complexes, clusters and crystal chemistry, 1992: p. 215-276.
45. Denning, R.G., *Electronic Structure and Bonding in Actinyl Ions and Their Analogs.* The Journal of Physical Chemistry A, 2007. **111**(20): p. 4125-4143.
46. Nockemann, P., Servaes, K., Van Deun, R., Van Hecke, K., Van Meervelt, L., Binnemans, K., and Görller-Walrand, C., *Speciation of Uranyl Complexes in Ionic Liquids by Optical Spectroscopy.* Inorganic Chemistry, 2007. **46**(26): p. 11335-11344.
47. Colletti, L.M., Copping, R., Garduno, K., Lujan, E.J.W., Mauser, A.K., Mechler-Hickson, A., May, I., Reilly, S.D., Rios, D., Rowley, J., and Schroeder, A.B., *The Application of Visible Absorption Spectroscopy to the Analysis of Uranium in Aqueous Solutions.* Talanta, 2017. **175**(Supplement C): p. 390-405.
48. Sayers, D.E., Stern, E.A., and Lytle, F.W., *New Technique for Investigating Noncrystalline Structures: Fourier Analysis of the Extended X-Ray—Absorption Fine Structure.* Physical Review Letters, 1971. **27**(18): p. 1204.
49. Lytle, F.W., *The Exafs Family Tree: A Personal History of the Development of Extended X-Ray Absorption Fine Structure.* Journal of Synchrotron Radiation, 1999. **6**(3): p. 123-134.
50. Buck, E.C., Brown, N.R., and Dietz, N.L., *Contaminant Uranium Phases and Leaching at the Fernald Site in Ohio.* Environmental science & technology, 1995. **30**(1): p. 81-88.
51. Landa, E.R. and Gray, J.R., *Us Geological Survey Research on the Environmental Fate of Uranium Mining and Milling Wastes.* Environmental Geology, 1995. **26**(1): p. 19-31.
52. Au, W.W., McConnell, M.A., Wilkinson, G.S., Ramanujam, V.M.S., and Alcock, N., *Population Monitoring: Experience with Residents Exposed to Uranium Mining/Milling Waste.* Mutation Research/Fundamental and Molecular Mechanisms of Mutagenesis, 1998. **405**(2): p. 237-245.
53. Dousma, J., Van den Hoven, T.J., and De Bruyn, P.L., *The Influence of Chloride Ions on the Formation of Iron(Iii) Oxyhydroxide.* Journal of Inorganic and Nuclear Chemistry, 1978. **40**(6): p. 1089-1093.
54. Amonette, J., Holdren Jr, G., Krupa, K., and Lindenmeier, C., *Assessing the Environmental Availability of Uranium in Soils and Sediments*. 1994, Nuclear Regulatory Commission, Washington, DC (United States). Div. of Waste Management; Pacific Northwest Lab., Richland, WA (United States).
55. Kelly, S., Hesterberg, D., and Ravel, B., *Analysis of Soils and Minerals Using X-Ray Absorption Spectroscopy*, in *Methods of Soil Analysis*. 2008. p. 387-463.
56. Morris, D.E., Allen, P.G., Berg, J.M., Chisholm-Brause, C.J., Conradson, S.D., Donohoe, R.J., Hess, N.J., Musgrave, J.A., and Tait, C.D., *Speciation of Uranium in Fernald Soils by Molecular Spectroscopic Methods: Characterization of Untreated Soils.* Environmental science & technology, 1996. **30**(7): p. 2322-2331.
57. Patterson, A., *The Scherrer Formula for X-Ray Particle Size Determination.* Physical review, 1939. **56**(10): p. 978.
58. Cullity, B.D. and Weymouth, J.W., *Elements of X-Ray Diffraction.* American Journal of Physics, 1957. **25**(6): p. 394-395.
59. Williamson, G. and Hall, W., *X-Ray Line Broadening from Filed Aluminium and Wolfram.* Acta metallurgica, 1953. **1**(1): p. 22-31.
60. Zak, A.K., Majid, W.A., Abrishami, M.E., and Yousefi, R., *X-Ray Analysis of Zno Nanoparticles by Williamson–Hall and Size–Strain Plot Methods.* Solid State Sciences, 2011. **13**(1): p. 251-256.
61. de Boer, G.B., de Weerd, C., Thoenes, D., and Goossens, H.W., *Laser Diffraction Spectrometry: Fraunhofer Diffraction Versus Mie Scattering.* Particle & Particle Systems Characterization, 1987. **4**(1‐4): p. 14-19.
62. Delgado, Á.V., González-Caballero, F., Hunter, R., Koopal, L., and Lyklema, J., *Measurement and Interpretation of Electrokinetic Phenomena.* Journal of colloid and interface science, 2007. **309**(2): p. 194-224.

4 Aqueous hydroxylation mediated synthesis of crystalline calcium uranate particles

This chapter has been adapted from a publication [1], and details a preliminary study that aims to answer objective (1) outlined previously (see section 1.2). It provides a simple, aqueous titration based synthesis for calcium polyuranate, with potential for integration with current uranic waste stabilisation, or dUF_6 deconversion processes [2]. Specifically, the precipitation and thermal phase development of calcium uranate particles formed via aqueous hydroxylation reactions are studied.

4.1 Introduction

Global legacy civil and military nuclear activities have accumulated ~1200 kt [3] of depleted uranium (dU at ~0.3% U-235). The low market cost of natural uranium and a lack in fast reactor technology until at least 2030 [4] reduces the economic case for using dU in civil power generation. Whilst down-blending of highly enriched uranium stocks (1.44 kt, ~90% U-235 [5]) with dU towards thermal fission fuel (~4% U-235 equivalent) is possible, this would consume only ~55 kt dU. The dU is therefore regarded as being a zero value asset [6] and may require long-term storage or disposal. In most nuclear states, some 80% of legacy dU is stored as uranium hexafluoride (UF_6) [3]; a hygroscopic crystalline solid that reacts violently with moisture to release highly chemo-toxic uranyl(VI) and hydrogen fluoride.

Currently, dU disposal is envisioned to be within deep cementitious geological disposal facilities (dGDF) [7]. The majority of dGDF post closure safety cases predict infiltration of groundwater, resulting in dissolution/re-precipitation of radionuclides present in the waste packages [8]. This precludes direct dGDF disposal as a viable option for UF_6, instead deconversion to U_3O_8 may be achieved through steam quench-calcination processes [9].

The majority of ILW will be encapsulated in Portland grouts and contained in stainless steel drums. When a dGDF is re-saturated with groundwater, Na^+, K^+ and Ca^{2+} ions will be released into porewater and near-field groundwater. Dissolution of K/Na hydroxide will initially alkalise groundwater towards pH 13.5, which is then buffered towards pH ~12.5 by Portlandite present in grouts. This hyperalkaline plume will be enriched with radionuclides such as Cs^+, Sr^{2+} and more so uranium as the largest radionuclide faction by mass. Although U(VI) exhibits low solubility under these pH 12.5 – 13.5 conditions, its ubiquity in the dGDF will increase U(VI) concentrations. U(VI) is present in almost all aqueous solutions as the uranyl(VI) ion (UO_2^{2+}) which forms uranyl(VI) hydroxide clusters in the presence of hydroxyl ions [10-12].

Subsequent inorganic polymerisation will result in nucleation of uranyl(VI) hydroxide precipitates that crystallise with aging towards uranyl(VI) oxide hydrates (Schoepite, meta-Schoepite [13]:

$$UO_{2(s)} \xrightarrow[Oxidation]{} UO_{2(s)}^{2+} \xrightarrow{Dissolution} UO_{2(aq)}^{2+} \xrightarrow{Hydration/hydroxylation} Metal\ uranates$$

Scheme 4.1

Crucial processes involved in the transition between U(VI)$O_{2(s)}$, metal uranates, and intermediate products.

Incorporation of background cations will cause phase alteration [14, 15] towards Ca^{2+}/Sr^{2+}-Becquerelite [16] or solubility-controlling uranates ($CaUO_4$, CaU_2O_7) [17, 18]. These geologically persistent U(VI)-phases could further sequester key radionuclides (e.g. Cs^+, Sr^{2+}, NpO_2^{2+}), affecting the long-term safety case of a dGDF [19-22].

Crystalline metal uranates may become suitable wasteforms for permanent disposal or interim storage of uranic wastes. However, demonstration of their synthesis pathways are generally limited in the literature to ceramic methods involving direct calcination. Due to poor mixing between uranium and alkali metal salt particles, repeated grinding and prolonged calcination periods at high temperature are usually required, increasing relative process energy intensity. This may be facilitated by preparation of a pre-calcination mixture of dehydrated metal- citrate [23] or oxalate [24] to promote molecular-mesoscale mixing reducing grinding-calcination process intensity. Despite this, the ease of tuning Ca/U stoichiometric purity in the end product has resulted in the successful laboratory scale synthesis of anhydrous calcium-uranium(VI) oxides with several calcium-uranium ratios with Ca/U= 0.25 [25], 0.5 [26], 0.337 [25], 1 [27], 2 [28], 3 [29]; in addition to those of many other alkali uranates [30-32].

Sol-gel or co-precipitation chemistry is an attractive solution based route to synthetic metal oxides [33, 34] that typically requires low temperature, room conditions and is low cost [35], making processing convenient whilst also allowing flexibility in end-product particle morphology via utilising frame-working agents [36]. Traditionally, metal alkoxides are used as solution phase precursors that readily undergo hydroxylation and condensation towards a solution of nanoscale particles, the sol. Further reaction results in a solid-solution gel network consisting of metal oxo bonds containing supernatant [37]. However alkoxides may be expensive or complex to prepare as well as being heat, moisture and photo- sensitive. With the exception of titanium and zirconium alkoxides, most transition metal and actinide alkoxides are unavailable commercially.

Alternatively, uranyl(VI) alkoxide precursors may be substituted by inorganic uranyl(VI) salts, which requires an additional hydroxylation agent to precipitate

uranyl(VI) oxide hydroxide particles. This route has been utilised during the synthesis of UO_2, U_3O_8 and UO_3 via direct or indirect [38] alkalisation of uranyl(VI) nitrate solution. The direct route involves addition of ammonium hydroxide addition to precipitate $(NH_4)_2U_2O_7$ [39], whereas the latter requires thermal decomposition of epoxide or urea solution to precipitate UO_3 and $(NH_4)_2U_2O_7$ respectively [40]. Regardless of the alkalisation method, precipitates are often amorphous, requiring calcination at 600^{o}C to crystallise the anhydrous uranium oxides [41, 42]. Sol-gel methods have only been used to explore pure uranium oxides, whilst tertiary U(VI) oxides have only been formally explored via the aforementioned solid state or molten salt reactions between pre-prepared uranium oxides and the corresponding metal salt [43].

4.1 Experimental

4.1.1 Materials and preparation

4.1.1.1 Stock solutions

All reagents were of AnalaR® grade and used as supplied without further purification.

Uranyl(VI) nitrate stock solution A 1.04 M uranyl(VI) nitrate solution was prepared by dissolving 1.51 g of uranyl(VI) nitrate hexahydrate ($UO_2(NO_3)_2.6H_2O$, BDH Laboratory supplies) in 2.89 ml of deaerated deionised water (18 MΩ) to form a clear bright yellow solution.

Calcium nitrate stock solution: 0.28 g of calcium nitrate tetrahydrate ($Ca(NO_3)_2.4H_2O$, BDH Laboratory supplies) was added to 1.145 ml of deionised water to give a 1.04 M solution.

Calcium hydroxide stock solution: 0.7 g of calcium oxide (CaO, Sigma Aldrich) was added to 1l of deaerated water (20 min N_2 sparged) in a stirred borosilicate Duran bottle. After solution becomes clear, a sealed cellulose semi-permeable tube containing 3 g/ml calcium hydroxide slurry was added to the solution and allowed to equilibrate to ~pH 12.5 over 14 days at 20 °C.

4.1.1.2 Synthesis reaction

Experimental procedure: In a typical synthesis, a 2.29 ml calcium enriched uranyl(VI) solution was prepared from mixing 1.145 ml of calcium and 1.145 ml of uranyl(VI) stock solutions to give 2.29 ml of preliminary reaction solution (pH 1.5) at 0.52 M : 0.52 M U(VI):Ca(II) concentrations respectively. To this initial solution, saturated calcium hydroxide solution was added slowly dropwise under vigorous stirring until pH 12 was reached. The reaction mixture was centrifuged at 14400 *g* for 3 minutes to collect and pelletize the bright orange precipitate. The remaining colourless clear

supernatant was removed with pipette. The precipitated particles were rinsed with DI water and pelletized. The rinsed solids were re-suspended in 40 ml of propan-2-ol and centrifuged to prevent further ripening/hydrolysis reactions via displacement of surface water with alcohol groups. This was repeated twice and the solids were concentrated into 5 ml of propan-2-ol for storage, allowing rapid drying prior to analysis using the methods described below.

4.1.2 Sample analyses

4.1.2.1 Quartz crystal microbalance (QCM)

A chrome-gold quartz crystal (d = 25.4 mm) (Stanford Research Systems, Sunnyvale, California) was rinsed using Millipore water followed by isopropanol then air dried. The crystal was mounted onto a 5 MHz Stanford Research Systems QCM200 probe and the sensor was left to reach a stable frequency and resistance reading in air, then repeated upon submersion in the stirring reaction solution. A shift of at least 0.75 Hz hr^{-1} and 0.34 Ohm hr^{-1} in air and 3 Hz hr^{-1} and 1.65 Ohm hr^{-1} in solution was considered stable. Calcium hydroxide solution was added to the reaction solution until pH 12 and the frequency and resistance data was recorded throughout the process.

4.1.2.2 Zeta potential measurements (ZP)

Precipitates were disaggregated using pestle and mortar then suspended in deionised water (18 MΩ). Remaining aggregates were allowed to settle and aliquots of the suspended fraction were added to prepared pH solutions buffered using 0.1 M HNO_3 and $(CH_3)_4NOH$ solutions to a final concentration of ~1000 ppm immediately prior to measurement. Triplicate samples were loaded into folded capillary zeta cells then analysed using a Malvern Instruments Zetasizer Nano. The refractive index was taken to be 1.63 (see Dynamic light scattering measurements below).

4.1.2.3 UV-vis spectroscopy (UV-vis)

Aliquots of reaction solution were removed at selected solution pH values followed by centrifugation to pelletize solids. The supernatant was removed and their single wavelength optical absorbance measured using a Jenway 6715 spectrophotometer to follow changing solution absorption throughout the reaction. 414 nm was found to be the maximum absorbance peak (A414) in a UV-vis spectrum of stock uranyl(VI) nitrate solution at ~pH 2.

The raw total spectrophotometric absorbance at 414 nm (A414) of the pelletised reaction aliquots was treated by subtracting the A414 of $UO_2(NO_3)_2$ solution of equivalent dilution to isolate ΔA414 due to variation of U(VI) speciation. This treated data was then fitted using a Gaussian function to guide the eye (Figure 4.4a black square, Gaussian fit in dashed black). Fresh solutions were prepared at 0.01 M initial

U(VI) concentration to pH 2 - 5 and their UV-vis spectra collected between wavelength range of 350 - 500 nm (Figure 4.4b).

4.1.2.4 Static light scattering (SLS)

Ex-situ SLS measurements were made using a 532 nm Nd:YAG laser and a Brookhaven digital correlator (BI-9000AT) controlled using the 9KDLSW data recording and analysis software package. The precursor Ca/U solution was filtered using a 0.22 µm syringe filter and the reaction vessel covered to reduce dust contamination. As the reaction proceeded, aliquots of reaction solution were extracted at 0.5 pH intervals from pH 2 until pH 5.5. A refractive index of R = 1.63 was derived for the particles via the Gladstone-Dale [44] relationship [45, 46] (see supporting information). Refractive energies used for the constituents UO_3, CaO and H_2O were included from literature [46] and the particle density was assumed the same as the closely related $CaU_2O_7.1.7H_2O$ (4.9g cm^{-3}) [47].

4.1.2.5 Thermal analysis (TGA-DSC)

Thermogravimetric and Differential Scanning Calorimetry analysis (TGA-DSC) was performed using a Mettler-Toledo TGA-DSC1 instrument on the solids to observe mass loss during calcination under a flow of N_2 gas at 50 cm^3 min^{-1}. In total, ten samples were analysed at different temperatures ranging between 50 °C and a maximum temperature, T_{max}, with T_{max} increasing in 100 °C increments between 100 – 1000 °C. These samples were placed in a 70 µl alumina crucible. The heating rate of the analyses was at 10 °C min^{-1} and the samples were held in isothermal plateau at the T_{max} for 300 minutes. All TGA-DSC data were blank subtracted and then derived with respect time to over a region of 20 data points to give the corresponding DTG trace (Figure 4.7).

4.1.2.6 X-Ray Diffractometry (XRD)

Calcined samples were pulverised and analysed on a Bruker D8 Diffractometer equipped with Cu Kα x-ray source and lynx eye detector. A hydrous sample (Figure 4.8a), 25 °C) was dried after 7 days of storage under IPA, then pulverised and analysed in the same manner as for the calcined samples. XRD patterns were compared to International Centre for Diffraction Data (ICDD) powder diffraction file database (PDF+4). The 25 – 600 °C XRD patterns were treated using a quadratic polynomial Savitzky-Golay filter [48] (10 point window) to improve data clarity in poorly crystalline samples that required no further analysis. Quantitative phase compositions were determined using the Rietveld method [49, 50] via the X'Pert Highscore Plus software using available crystal structural data for $CaUO_4$ and UO_2.

4.1.2.7 Electron microscopy

4.1.2.7.1 Scanning Electron Microscopy (SEM)

Solid samples were carbon coated and imaged using a FEI Quanta FEG 650 Environmental Scanning Electron Microscope (ESEM) equipped with an electron microprobe. EDS spectra were collected from a minimum of 3 regions per sample. The AZTEC software package was used during standardless quantification of Ca and U elemental concentrations.

4.1.2.7.2 Transmission Electron Microscopy (TEM)

Particle suspensions were dried onto amorphous carbon support copper grids prior to imaging using a FEI Tecnai TF20 FEGTEM. ImageJ [51] was used to measure particle size and lattice fringe spacing via Fast Fourier Transform patterns (FFT).

4.1.2.8 Inductively coupled plasma-optical emission spectroscopy (ICP-OES)

0.5 ml aliquots were removed from the reaction vessel and immediately passed through a 0.22 µm pore size filter and then centrifuged at 14400 *g* for 5 minutes. The supernatant was acidified overnight using Aristar HNO_3, diluted to 1 wt% acid concentration (~50 ppm U) and used for uranium ICP-OES analysis on a Thermo iCAP 7400 instrument. The solids from the TGA analyses were digested using a 100 µL aliquot of 70 % nitric acid, then diluted as for the solution samples. All samples were calibrated against calcium-uranium standards containing Yttrium as an internal standard.

4.2 Results

4.2.1 Thermodynamic modelling

The distribution of U(VI) species in aqueous solution was calculated using the software package PHREEQC [52, 53] loaded with the ANDRA ThermoChimie database [54] and updated thermodynamic data for uranium [55, 56]. Additional K_{sp} data was inserted into the working database to include an amorphous Schoepite phase [57]. Specific ion-interaction theory (SIT) was used for ionic strength corrections. Percentage speciation for Ca^{2+} and U(VI) and relevant crystalline phase saturation indices (SI) are presented (Figure 4.1). The latter being a logarithmic relationship between ion activity product (IAP) of dissolved species and solid phase solubility product (K_{sp}) to give phase saturation index (SI), where phase SI > 0 represents supersaturation; SI < 0 represents undersaturation and SI = 0 represents phase equilibrium between dissolution and precipitation.

Accordingly, the calculations show that the precursor solution is dominated by uncomplexed UO_2^{2+} and binuclear $[(UO_2)_2OH_3]^+$. UO_2^{2+} is consumed with increasing solution pH towards 2.5 and less rapidly from pH>3 until complete consumption by pH 5. Between pH 2 – 5, concentration maxima in U(VI) hydroxides occur at solution pH values of 3.5 $[(UO_2)_2OH^{3+}]$, 4.1 $[(UO_2)_2(OH)_2^{2+}]$, 4.3 $[(UO_2)_3(OH)_4^{2+}]$ and 4.8 $[(UO_2)_3(OH)_5^+]$ respectively and is reflected in a pH 3.75 maxima in total polymeric U(VI) hydroxides. There is also a rapid incremental increase in expected Ca^{2+} concentration between pH 3.5 (0.42 mol L^{-1}) and pH 5 (0.74 mol L^{-1}). Whereby the solution becomes supersaturated with respect to crystalline uranyl(VI) oxide hydrates (pH 3.5: $[UO_3.(0.9\text{-}2)H_2O]$; pH 3.9: [Becquerelite]; pH 4.1: $[UO_2(OH)_2]$). The continued increase in Ca^{2+} and OH^- concentration results in solution supersaturation in $CaUO_4$ and CaU_2O_7 whilst the $[(UO_2)_4(OH)_7^+]$ dominated region (pH 4.5 – 9) is rapidly exchanged for anionic $[(UO_2)_3(OH)_7^-]$ at pH 9.2. Excess OH^- in solution leads to depolymerisation of $[(UO_2)_3(OH)_7^-]$ to form monomeric hydroxides $[UO_2(OH)_3^-]$ and $[UO_2(OH)_4^{2-}]$.

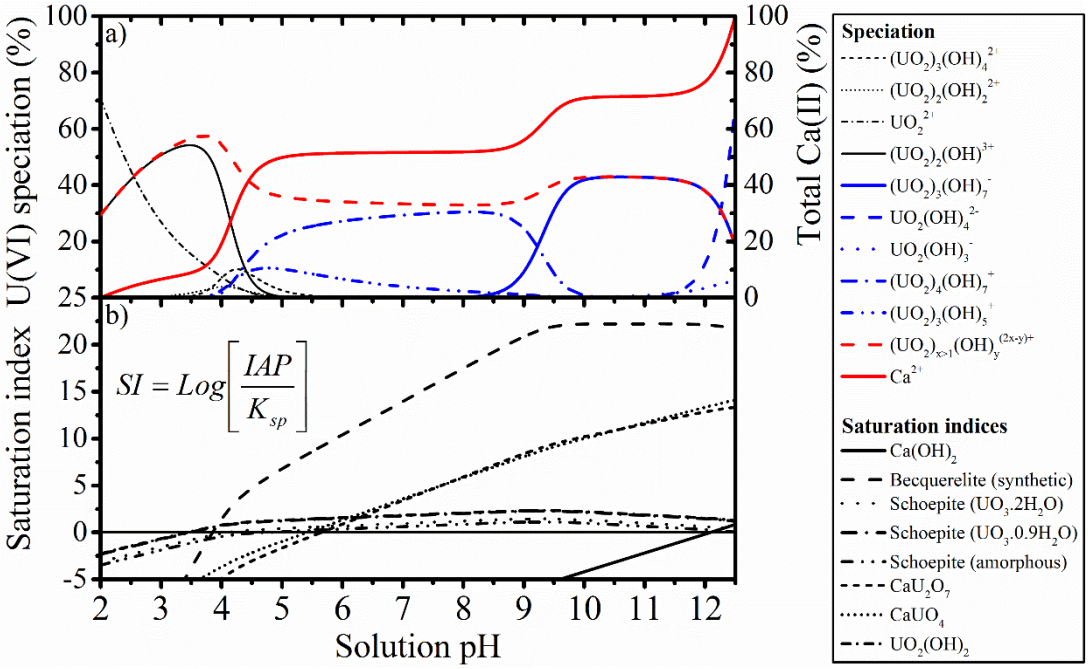

Figure 4.1 PHREEQC reaction model of a) major total U(VI) (left axis) and Ca(II) (right axis) speciation by percentage at 20 °C. b) Relevant saturation indices of solid phases (left axis) and total dissolved U(VI) content (right axis).

4.2.2 QCM measurements

During alkalisation of the initially bright yellow transparent precursor solution (Figure 4.2 circlet 1) by addition of clear transparent $Ca(OH)_2$ solution, a diminished change occurs in the frequency (ΔF) and resistance (ΔR) shifts up to pH 4.8. The almost linear decrease in ΔF is reflected by an opposing increase in ΔR in this region and a

progressive yellowing of the transparent solution. This 40 Hz (9 %) reduction in ΔF (Figure 4.2 solid line) corresponds to a comparatively minor +0.56 Ω (1.6%) increase in ΔR (proportional to vibrational dissipation [58]) and allows use of the Sauerbrey relationship [59, 60] to approximate an average mass of a rigidly adsorbed and evenly spread thin-film on the QCM crystal surface to ~3.5 µg. Using database values for the densities of Schoepite (ICSD 82477, $\rho = 4818.64$ kg m^{-3} and Metaschoepite (ICSD 23647, $\rho = 8017.66$ kg m^{-3}), an average film thickness of an adsorbed layer would range between 0.87 - 1.45 nm. Sharp increases in ΔF and ΔR gradients (dΔF, dΔR) coincide with the solution becoming visibly opaque (Figure 4.2* circlet 2) at pH 4.8. Subsequent reductions in dΔF / dΔR occur at pH 5.8 and pH 6.8 respectively to reach a plateau between pH 6.8 and pH 7.5, whilst the suspension darkens in colour. A final progressive increase in dΔF and dΔR up to pH 12 occurs with the formation of a clear colourless supernatant layer above the agitated particle bed.

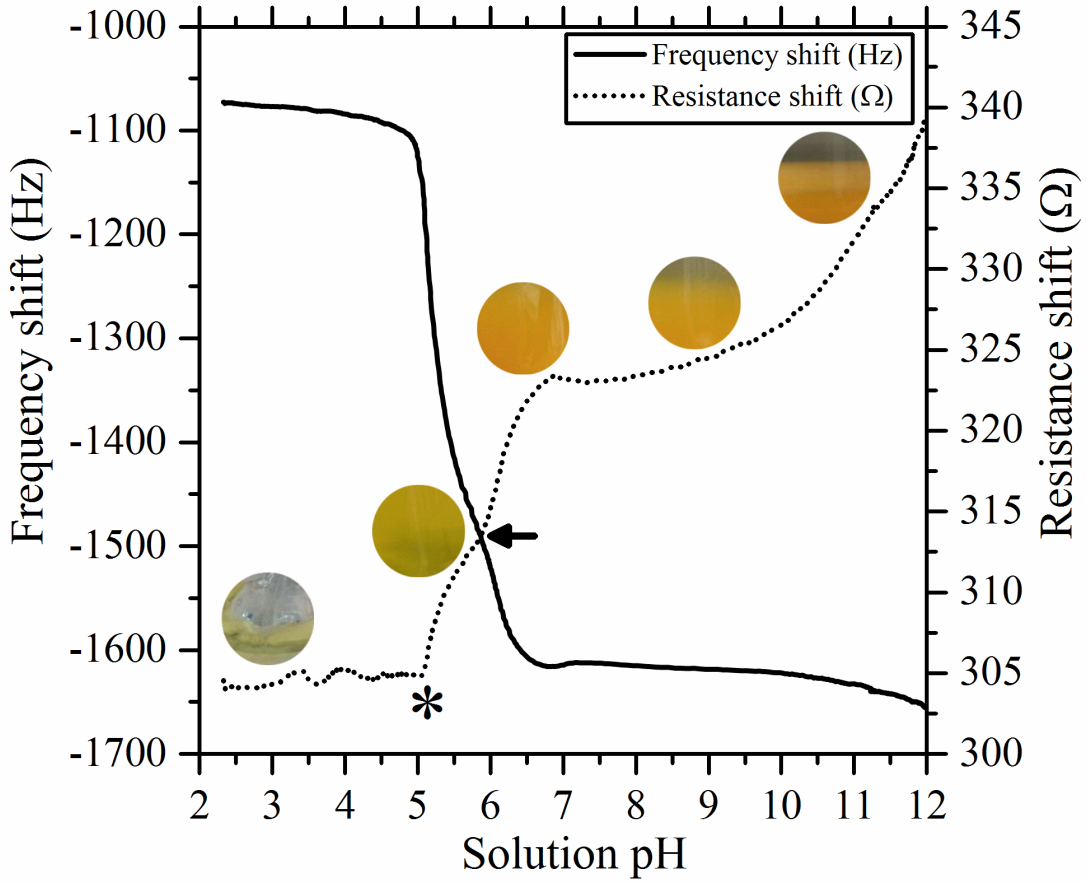

Figure 4.2 QCM frequency and resistance shift as a function of solution pH; with asterisk (*) representing the visible solution cloud point. Image circlets are ordered from left-right as 1 – 5; and show (1) initial uranyl(VI) nitrate solution followed by addition of calcium hydroxide titrant until (2) solution clouding point, (3) gelation, (4) – (5) collapse and settling.

4.2.3 ZP measurements

A point of zero charge (PZC) (Figure 4.3) was found for the precipitated particles at pH 4.1 regardless of electrolyte concentration in the aqueous matrix. However relative differences become immediately apparent in their rates of change by pH 4.8 (-16.2 and -8.0 mV respectively), resulting in a more negative pH 12 ZP for the pure water suspension (-35.7 mV) compared to the 0.01 M NaCl suspension (-22.0 mV). ZP trends for both suspensions coincide with similar hydrous divalent (Mg^{2+}, Mn^{2+}, Ni^{2+}) uranium oxides.

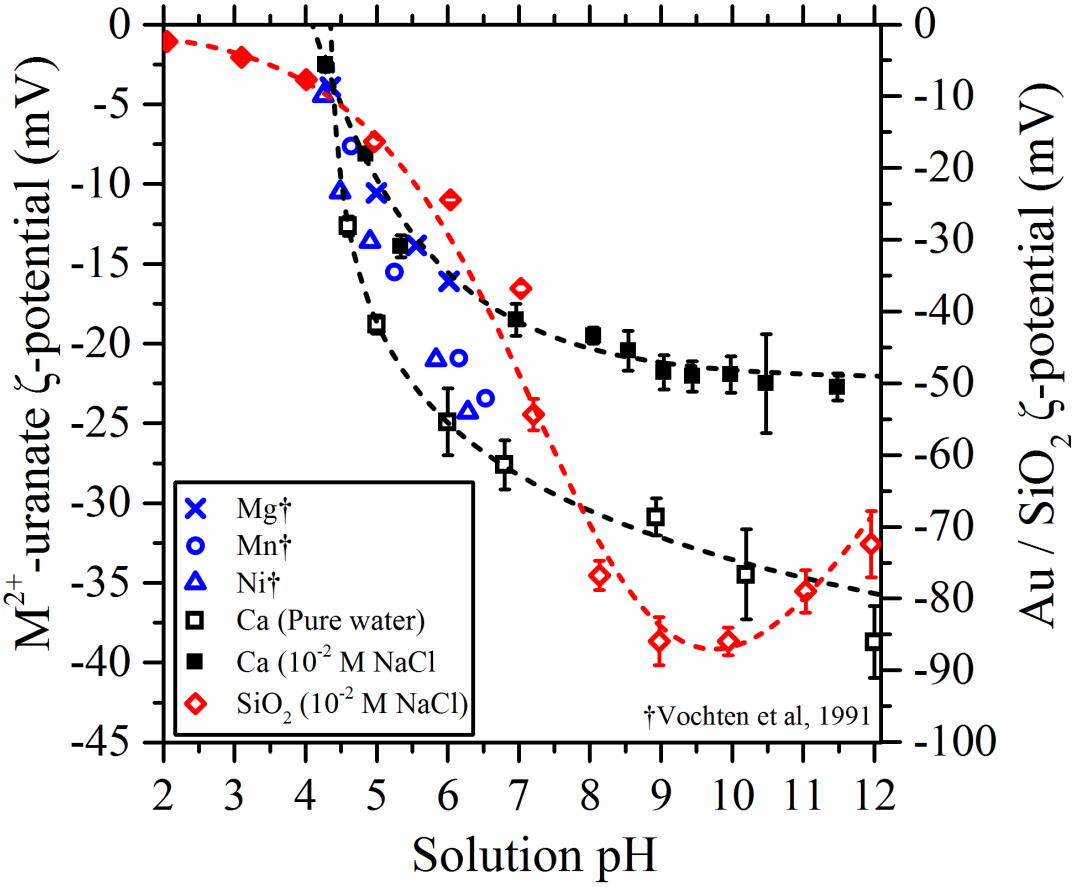

Figure 4.3 Particle zeta potential of hydrous Ca^{2+}-U(VI) oxide as a function of solution pH in DI water and 0.01 M NaCl; other divalent metal U(VI) oxides from Vochten et al. (blue) [61] and SiO_2 particles 0.01 M NaCl solution respectively are included for reference.

4.2.4 UV-vis absorbance

Solution aliquots develop in total absorbance between pH 3 – 5.7 before increasing rapidly at pH 5.7 towards a final plateau between pH 6 – 12. The centrifuged reaction aliquots (Figure 4.4a, black squares) exhibit a Gaussian shaped absorbance peak centred at pH 4.5 with a peak width of 3 pH values, no further changes in absorbance is apparent after pH6. The absorbance spectra of samples before the cloud point (pH 5.5) between pH 2 – 3.5 (Figure 4.4b) shows that A_{max} remains constant up to pH 3

(Figure 4.4b). They are characterised by three major A_{max} at (i) 403, (ii) 413.8, (iii) 426 nm with shoulders at 392 nm and 438 nm is consistent with previous spectroscopic data for the UO_2^{2+} ion [62]. The pH 3.5 spectrum is characterised by broadened peaks, though maintains the three A_{max} observed at lower pH values. Higher pH spectra (Figure 4.4b, pH 4 – 5) show consistently broadened characteristics whilst completely shifting the A_{max} peaks to 421.8 nm and 429 nm. U(VI) speciation data (Figure 4.1a, black lines) reveals a solution dominated by $[UO_2^{2+}]$ ions up to pH 3, followed by formation of $[(UO_2)_2(OH)_2]^{2+}$ up to its maximum at pH 4 and subsequently by the higher uranyl(VI) hydroxylation products $[(UO_2)_3(OH)^{5+}]$ and $[(UO_2)_4(OH)^{7+}]$ up to pH 5.

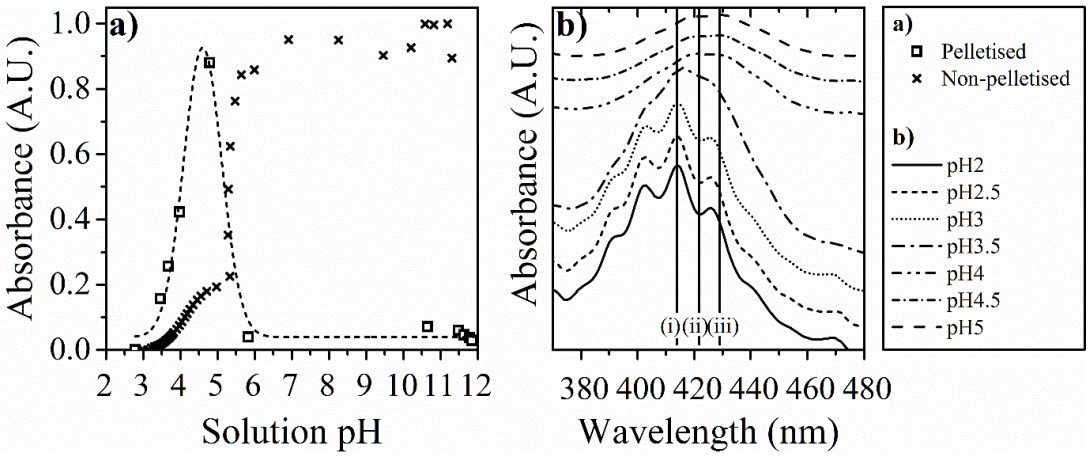

Figure 4.4 (a) Spectrophotometric absorbance at 414nm of pelletised (black square) and non-pelletised (black cross). (b) Stacked ex-situ UV-vis spectra of reaction aliquots with vertical solid lines showing the wavelengths of absorbance maxima for the U(VI) species (i) UO_2^{2+}, (ii) $[(UO_2)_2(OH)_2^{2+}]$ and (iii) $[(UO_2)_3(OH)_5^{+}]$.

4.2.5 ICP-OES analyses

Approximately 10 % of initial UO_2^{2+} and Ca^{2+} is removed (Figure 4.5) simultaneously from solution up to pH 5 whilst the Ca/U ratio of filtered solids reach unity. Between pH 5 – 7, almost complete removal of uranium is occurs whilst an additional ~48 % Ca^{2+} is gradually removed up to pH 12 to yield a final expected Ca/U ratio of ~0.6. The average calcium to uranium molar ratios of precipitates calcined between 25 – 1000°C (25 °C sample represents the untreated precipitate) were also analysed after dissolution in 1 % HNO_3 acid to give Ca/U = 0.68 ± 0.043 (Ca:U ~ 0.25:0.38) or a calculated stoichiometric formula of $Ca_2U_{2.92}O_{10.77}$.

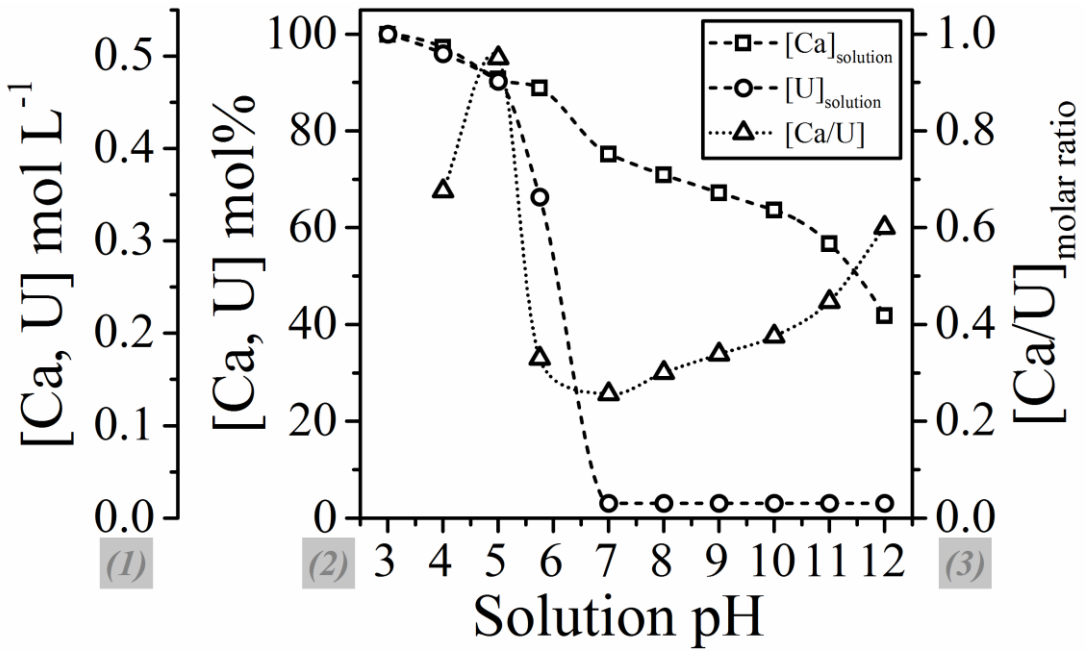

Figure 4.5 Change in concentration of U(VI) and Ca^{2+} remaining in solution as *(1)* mol L^{-1}; *(2)* mol%, and *(3)* molar Ca/U ratio of removed solids (triangles) with respect to solution pH.

4.2.6 SLS

Static light scattering performed on a range of 0.066 M / 0.01 M Ca^{2+}/UO_2^{2+} nitrate solutions buffered between pH 2 – 5.5 using HNO_3 and $(CH_3)_3NOH$, though only the pH 5 – 5.5 sample yielded scattered light count rates above background. Figure 4.6 shows that non-regularised (NNLS) and regularised (CONTIN) least squares fitting yielded a pH 5.5 particle size distribution (PSD) that is characterised by three major particle size populations that approximately corroborate between the two data fitting methods; [NNLs, CONTIN] hydrodynamic diameter = [144 – 193, 248 nm], [1750 – 3160, 1370 nm] and [5680 – 10240, 4260 – 10000 nm]. These correspond to d50s by volume as d_V50_{NNLS} = 5550 nm, d_V50_{CONTIN} = 5150 nm respectively.

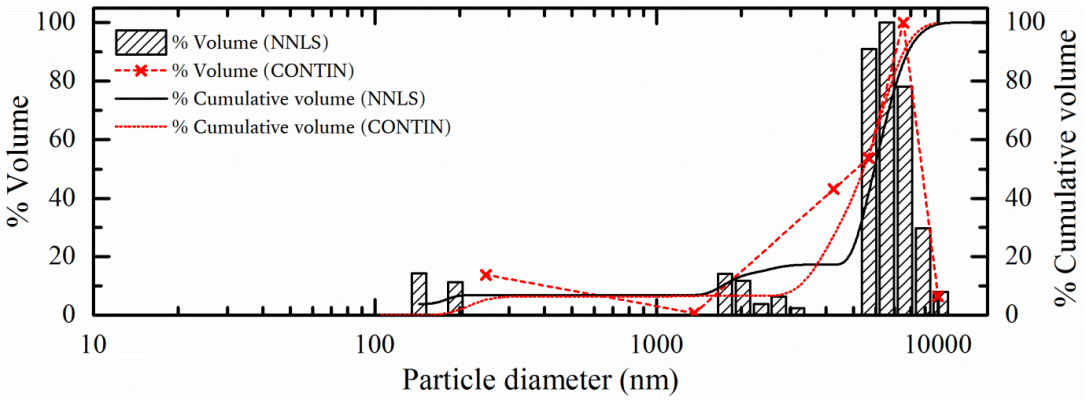

Figure 4.6 Distribution of hydrodynamic particle diameters in pH 5.5 solution as a function of %volume received from NNLS (shaded black bars) and CONTIN (red crosses) fitting methods.

4.2.7 TGA

Figure 4.7 shows ~10 % weight loss occurs when samples were heated from 50 °C to 1000 °C and the samples appeared to follow a 5 - region weight loss profile outlined below:

Region 1 - an initial steep ~5.80 % (6.63 mg) weight loss region between 50 – 175 °C with mild endothermic heat flux, which is reflected as a double minima in the DTG trace as two changes in weight loss regime within this region. Isothermal weight loss is highest in this range (Figure 4.7, inset).

Region 2 - a lesser ~3.94 % weight loss region between 175 – 700 °C which appears as a broad depression in the DTG trace, whilst isothermal weight loss stabilises. Particles deepen in colour to ochre from light orange.

Region 3 - samples became progressively darker in orange with increasing temperature until an ochre colouration is reached between 700 – 800 °C; where the ochre colouration is intermixed with dark green specks. Dynamic weight loss over this range is diminished, whilst isothermal weight loss begins to rise.

Region 4 - a ~1.55 % weight loss region between 800 – 950 °C this facile weight loss is reflected in a sharp depression in the DTG trace over the same temperature range and is accompanied by a change in colouration towards a green tinged black;

Region 5 - a secondary weight loss plateau beyond 950 °C accompanied by darkening of colour until a lustrous black solid of a brittle nature remained. A broad endotherm begins at 600 °C (*Regions 3)* until *Region 5* does not coincide with specific weight losses. Isothermal stability decreases linearly from the Region 2 minima up to region 5.

As carbon dioxide was excluded from precursor solutions and the reaction vessel, the gaseous decomposition product was assumed to be water. Mass loss was therefore used to calculate molar water loss and incorporated into the stoichiometric formulae as H_2O and OH groups for clarity (see Equation 4.1 – 5).

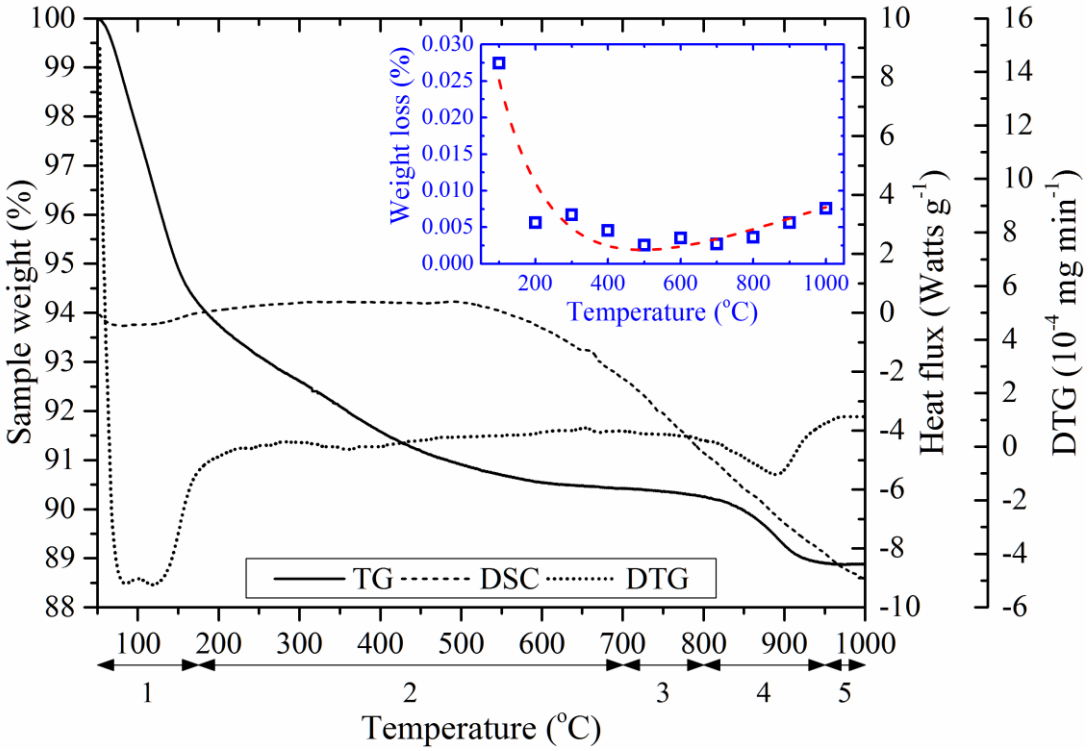

Figure 4.7 Dynamic heat treatment profile of samples in the temperature range 50 – 1000 °C, showing normalised thermogravimetric (TG), derivative TG (DTG) and differential scanning calorimetry (DSC) traces; with mass loss regions 1 – 5 labelled accordingly. The inset (blue) shows total isothermal weight loss over 300min with a fitted Log normal curve for guidance (red dashed).

4.2.8 XRD

Sample pXRD patterns (Figure 4.8a, 25 °C) below 700 °C show poor peak definition with broad intensity maxima resembling those of $Ca_{1.5}U_6(OH)7O_{16}.7H_2O$ [63]. Calcination of samples in a N_2 atmosphere up to 700 °C results in gradual increase in peak definition towards a $Ca_2U_3O_{11}$ phase. The samples calcined to 1000 °C match database peak maxima for $CaUO_4$ and UO_2. Phase quantification for the 900 °C sample was attempted using the Rietveld method [49, 50] with known structural data for UO_2 (PDF: 04-008-7779) and $CaUO_4$ (PDF: 04-007-9392). This yielded weight percentages for UO_2 and $CaUO_4$ of 34.4 wt% and 65.6 wt% respectively and a calculated bulk [Ca/U] stoichiometry of 0.601 ($Ca_2U_{2.3}O_{12}$). Parameters refined were specimen displacement, background, scale factor, unit cell parameters, peak shapes, W and U profile parameters. Goodness of Fit (GOF, χ^2) and R weighted profile (R_{wp}) values were monitored to improve the refinement. R and refined unit cell parameters are summarised in (Figure 4.8). As structural data is unavailable for $Ca_2U_3O_{11}$, structural refinement was not attempted on the 700 °C XRD pattern.

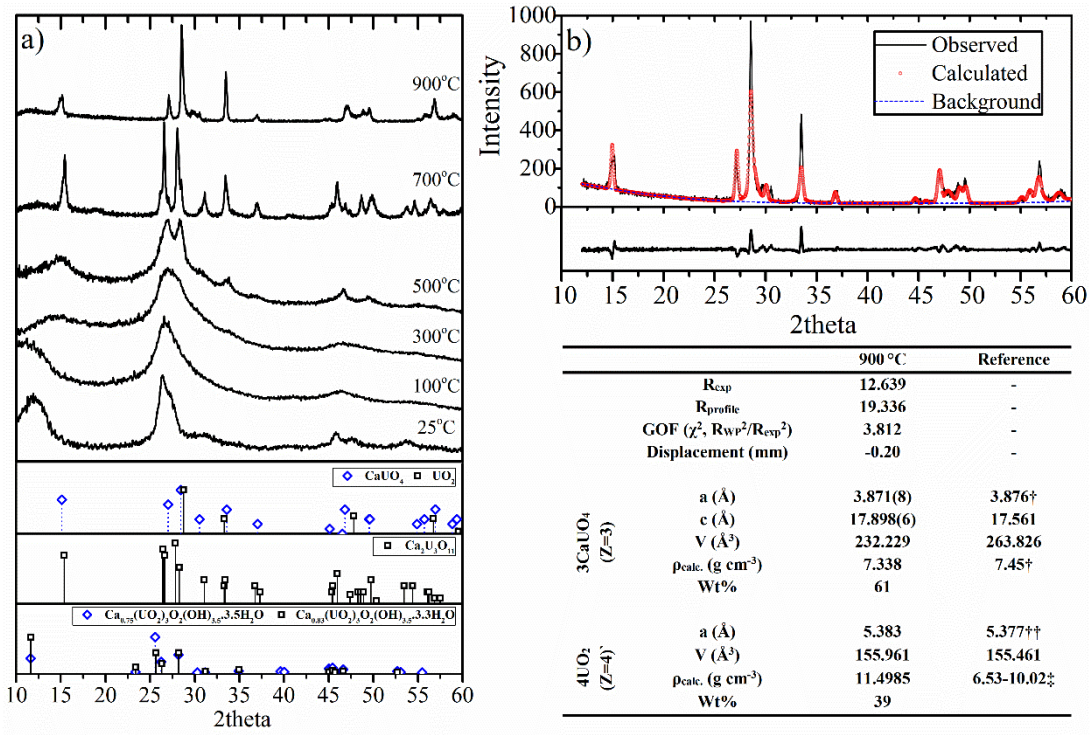

		900 °C	Reference
	R_{exp}	12.639	-
	$R_{profile}$	19.336	-
	GOF (χ^2, R_{WP}^2/R_{exp}^2)	3.812	-
	Displacement (mm)	-0.20	-
$3CaUO_4$ (Z=3)	a (Å)	3.871(8)	3.876†
	c (Å)	17.898(6)	17.561
	V (Å^3)	232.229	263.826
	$\rho_{calc.}$ (g cm^{-3})	7.338	7.45†
	Wt%	61	
$4UO_2$ (Z=4)	a (Å)	5.383	5.377††
	V (Å^3)	155.961	155.461
	$\rho_{calc.}$ (g cm^{-3})	11.4985	6.53-10.02‡
	Wt%	39	

Figure 4.8 (a) Selected powder XRD patterns of particles heat treated between 25 °C (precipitate) and 900 °C; and PDF-4+ database reference patterns for $Ca_{0.75}(UO_2)_3O_2(OH)_{3.5}.3.5H_2O$ [PDF00-047-0496], $Ca_{0.83}(UO_2)_3O_2(OH)_{3.5}.3.3H_2O$ [PDF 00-050-0039]; $Ca_2U_3O_{11}$ [PDF 00-045-0008]; $CaUO_4$ [PDF 04-007-5327] and UO_2 [PDF 04-017-6940]; (b) Calculated (red), observed (black), background (blue) and residual plots for 900 °C Rietveld XRD data with refinement R factors and unit-cell parameters for 900 °C and corresponding reference values for †$CaUO_4$ (PDF: 04-007-9392) [27] and ††, ‡UO_2 (PDF: 04-017-6940) [64, 65].

4.2.9 SEM and TEM

TEM micrographs are presented in Figure 4.9 of the solids extracted from the reaction solution at three pH values after initial onset of precipitation. The solids appear to be composed of a network of randomly distributed nanoparticle aggregates that warped during imaging for the pH 5.5 and to a lesser degree for the pH 8.5 - 11 aggregates. Size measurement of particles with coherent lattice fringes (Figure 4.9 circlets) revealed their diameters to be 14.06 ± 2.25 nm, 12.06 ± 2.14 nm and 9.17 ± 1.49 nm for pH 5.5, 8.5 and 11 samples respectively. The rectangular crystallites had average geometric anisotropy ratios (length/width) of 1.9 ± 0.2, 2.0 ± 0.4 and 2.1 ± 0.3 respectively. Inspection of the FFT interference patterns (Figure 4.9 square insets) derived from particle lattice fringes reveal spacings in order of decreasing intensity 3.1 - 3.3 Å, 2.6 - 2.7 Å and in the pH5.5 solids, also at 1.8 - 1.9 Å; corresponding approximately with the d - spacings for the (-111), (111) and (-311) diffraction peaks of crystalline $Ca_2U_3O_{11}$.

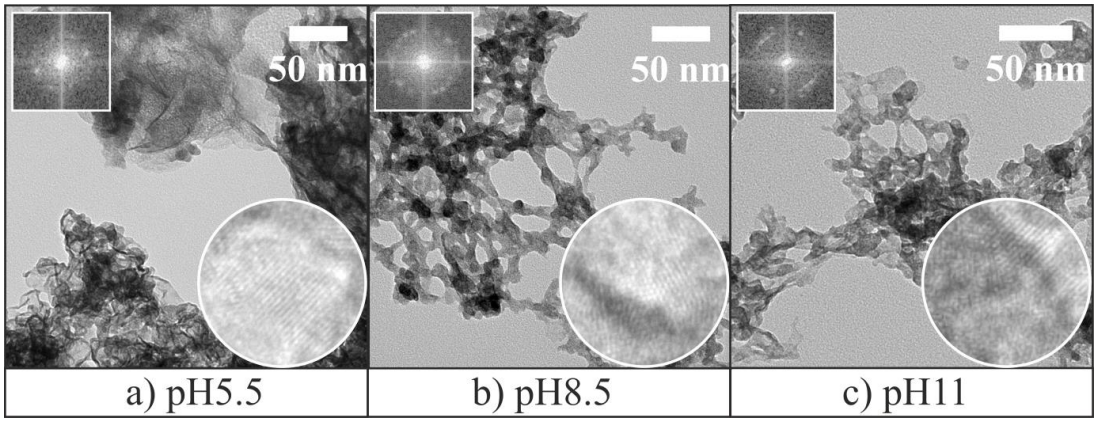

Figure 4.9 TEM micrographs of dried calcium uranate aggregates extracted from three pH solutions to show nanoscale particle morphology. Circlets are magnified single particle images (d = 10nm) and square insets are Fast Fourier Transform (FFT) patterns of respective circlets.

SEM photomicrographs of the 25 °C and 100 °C (Figure 4.10a, b) samples show irregular shaped and sized aggregates with average cluster diameters of ~146 nm and ~151 nm respectively. Between 700 - 900 °C, particle diameters decrease in 100 °C increments to ~140, ~124 and ~113 nm accompanied by an observable alteration from smooth spheroids at 700 °C towards spherical particle aggregates by 900 °C interspersed by an increasingly regular pore size distribution. By 1000 °C (Figure 4.10f), particle surfaces become smoother and consist of fused spherical particles of ~118 nm interspersed with larger pores. Standardless quantification from EDS data (Figure 4.10g) across all samples revealed calcium, uranium and oxygen atom percentages of 11.4 ± 1.2, 18.2 ± 1.9 and 70.3 ± 3.2 respectively and a Ca/U stoichiometry of 0.63 ± 0.02 ($Ca_{1.9}U_{3.01}O_{10.95}$).

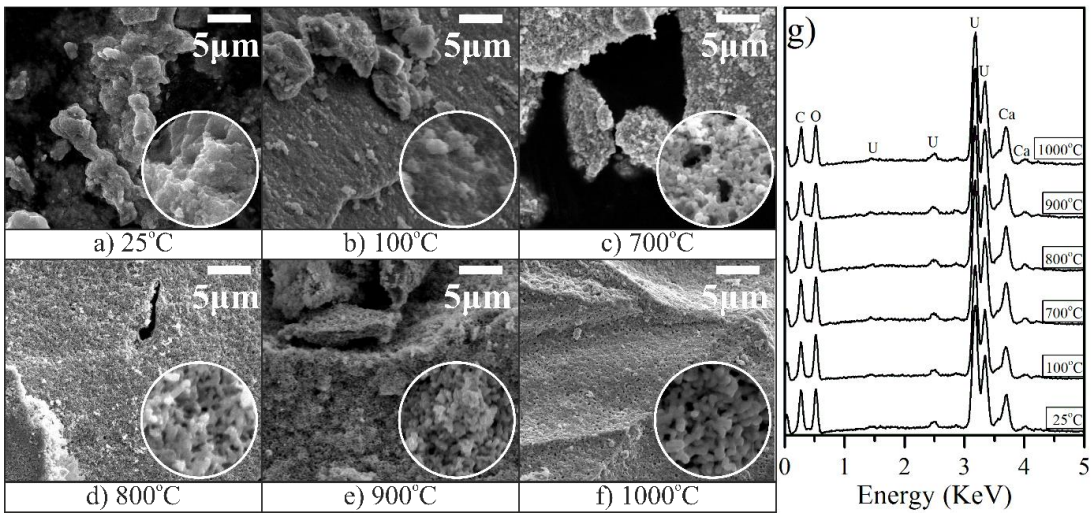

Figure 4.10 SEM micrographs of selected samples heat treated at temperatures between 25 °C and 1000 °C to show meso-scale particle surface morphology. Circlets highlight micro-scale morphology and are 2 µm diameter. a) Poorly-ordered Ca^{2+}-uranate; b) dehydrated precipitate at 100 °C; c) Ca^{2+}-uranate $Ca_2U_3O_{11}$; d) - f) Ca^{2+}-monouranate and U(IV)-oxide particles $CaUO_4$, UO_2; g) Corresponding EDS spectra of samples a) – f).

4.3 Discussion

4.3.1 Hydrous calcium uranate condenses from clusters of U(VI) hydroxide oligomers

The initial reaction solution is predicted to contain monomeric and partially hydrolysed U(VI) species as UO_2^{2+} or $[(UO_2)_2OH]^{3+}$ and dissociated calcium as Ca^{2+}. The former is responsible for the low initial pH of the precursor solution (~pH 2) as described by a proton release equilibria occurring during hydrolysis (Equation 4.1) where K_H is the hydrolysis equilibrium constant [66-68].

$$\boldsymbol{xUO_2^{2+} + yH_2O \overset{K_H}{\rightleftharpoons} (UO_2)_x(OH)_y^{(2x-y)+} + yH^+)} \qquad \textbf{Equation 4.1}$$

A progressive increase in hydroxide in solution during $Ca(OH)_{2aq}$ addition consumes protons to drive kinetic olation between uranyl(VI) ions towards oligomeric U(VI) species ($[(UO_2)_2(OH)_2]^{2+} \rightarrow [(UO_2)_3(OH)_4]^{2+} \rightarrow [(UO_2)_3(OH)_5]^{+}$). This is supported by a shift in the observed UV-vis spectra (Figure 4.4b) from a uranyl(VI) towards a U(VI) hydroxide (UOH) dominated system above pH 3 (Figure 4.4b). The redshift absorption maxima (lower energy) also indicates an increase in symmetry of U(VI)-centres [67] via changes in extent of vibronic coupling, or shifts in electronic transitions [62, 69]. Due to the 10 and 49 fold greater molar absorptivity coefficients of the polymeric uranyl(VI) hydroxides $[(UO_2)_2(OH)_2]^{2+}$ (101±2 mol^{-1} cm^{-1}) and $[(UO_2)_3(OH)_5]^{+}$ (474±7 mol^{-1} cm^{-1}) compared to UO_2^{2+} (9.7±0.2 mol^{-1} cm^{-1}) [62], the progressive increase in UOH concentration may be followed via spectrophotometric absorbance measurements (Figure 4.4 black).

The variation between the $A414_{pelletised}$ and $A414_{non\text{-}pelletised}$ samples indicate some removal of U(VI) solids from solution above pH 4.8 (Gaussian fit maxima) and almost complete removal by pH 5.5. However, the approximate minimum particle size that may be centrifugally removed from solution is ~44 - 62 nm (see appendix 1) whilst primary crystallites are ~14.06 nm (Figure 4.9a). Therefore, the increase in overall $A414_{pelletised}$ between pH 2 - 4.8 may be due to both non-aggregated nanoparticles and U(VI) hydroxides (Figure 4.4b).

The 0.87 - 1.45 nm film deposited onto the QCM crystal surface below the cloud point (Figure 4.2, pH 5) contains both U(VI) and Ca^{2+} according to ICP-OES (Figure 4.5); and could in part, be due to the $SiO_{2(s)}$-$UO_2^{2+}{}_{(aq)}$ inner – sphere complexation observed in aqueous U(VI)-silicate systems [70, 71] that appears unaffected by $[Ca^{2+}]$. Continuing pH elevation functionalises the deposited $SiO_{2(s)}$-$UO_2^{2+}{}_{(aq)}$ layer with higher [70] oligomeric U(VI) hydroxide clusters, trapping Ca^{2+} ions in a similar manner to the dynamically ordered liquid-like oxyanion polymers that form prior to calcium carbonate nucleation [72].

Both deposited and solution phase Ca^{2+}-U(VI) clusters subsequently undergo rapid crystallisation to primary crystals (Figure 4.9a) towards pH 5 driven by increasing supersaturation in oligomeric U(VI) hydroxides. Rapid isotropic aggregation [73] occurs simultaneously with nucleation due to the PZC lying at ~pH 4.3 (Figure 4.3 black squares) resulting in the apparent large discrete aggregates (d_V50 = 5.15 - 5.55 µm) detected at pH 5.5 (Figure 4.6). In accordance with the Ostwald step rule [74], a reduction in system Gibbs energy via the shortest reaction pathway favours the formation of less stable and poorly crystalline phases [75, 76]. The ICP-OES data (Figure 4.5) shows a Ca/U stoichiometry of ~1, implying that $CaUO_4$ crystallises (~pH 5) rather than the expected Becquerelite (Figure 4.1b).

The system transitions at pH 6 (Figure 4.2 arrow) from a suspension of discrete aggregates (Figure 4.6) to a Ca^{2+}-deficient ([Ca/U] ~ 0.26) gel at pH 6 via removal of 87 mol% solution U(VI) (Figure 4.5, black circle). This gel continues to uptake Ca^{2+} from solution as a function of pH (Figure 4.5) and Ca^{2+} solubility (Figure 4.1, SI: $Ca(OH)_2$) towards poorly-crystalline (Figure 4.8a, 25 °C) particles (d ~ 9 nm) with a final Ca/U ratio of ~0.67 (Figure 4.5, pH 12). This phenomena, common to hydrous U(VI) phases [76-78], is facilitated by a labile 1:2 [Ca^{2+}] : [$H_3O^+_{lattice}$] ion-exchange mechanism [61] and may be accommodated by minor crystallite lattice distortions (Figure 4.9).

4.3.2 Calcium uranate crystallises via concerted dehydroxylation-oxolation

The thermal decomposition resulting in particle mass losses (TG) up to 700 °C are due to dehydration processes [79, 80] (see supplementary information I, Figure 2). In TG region 1 (Figure 4.7 50 – 175 °C), ~3.5 moles of H_2O are volatilised per mole $Ca_2U_3O_{11}$ (Equation 4.2). The relatively low temperatures imply the presence of outer sphere complexation between molecular water and surface U(VI)-hydroxyl moieties. If hydrated uranates are intermediates between solvated U(VI) hydroxide clusters and crystalline U(VI) oxides [81], then this hydrogen-bound water is highly labile [82] and would require little structural or crystalline (Figure 4.8a 25 – 200 °C) rearrangement to accommodate the change. Indeed, there was little observed mesoscopic changes occurring in the particle morphology (Figure 4.10a, b).

$$\boldsymbol{Ca_2(UO_2)_3O_{3.75}(OH)_{2.5}.3.5H_2O \xrightarrow{\Delta(25-200\,^{\circ}C)} Ca_2(UO_2)_3O_{3.75}(OH)_{2.5} + 3.5H_2O} \qquad \textbf{Equation 4.2}$$

Conversely, dissociative water sorption occurs via inner sphere complexation to uranyl(VI) centres along the equatorial plane, requiring more energy to achieve the observed 1.25 mol dehydroxylation between 200 – 700 °C (Equation 4.3) during TG analysis (Figure 4.7).

$$Ca_2(UO_2)_3O_{3.75}(OH)_{2.5} \xrightarrow{\Delta(200-700\,^{\circ}C)} Ca_2(UO_2)_3O_5 + 1.25H_2O$$

Equation 4.3

This conversion increases sample crystallinity (Figure 4.8a, 700˚C) and therefore long-range structural order considerably, implying a concerted dehydroxylation – oxolation reaction between adjacent (UO_2)-OH groups. This phase development is accompanied by extensive particle shrinkage and solid-state ripening processes to form the spherical particles and apparent porosity observed at 700˚C (Figure 4.10d). Despite the hydrous Ca^{2+}-uranate particles (Figure 4.9c) being most consistent with the formula $Ca_{0.75\text{-}0.83}(UO_2)_3O_2(OH)_{3.5}.(3.3\text{-}3.5)H_2O$ (Figure 4.8a), stoichiometric analysis ([Ca/U] ~ 0.64), FTIR analysis (supplementary information I, Figure 2) and the early weight loss measurements (Figure 4.7) discussed above indicate a structure with a lower overall water content and therefore a composition closer to $Ca_2(UO_2)_3O_{3.75}(OH)_{2.5}.3.5H_2O$.

The colour change to black in TG region 4 suggests a U(VI)→U(IV) reduction accompanied by microscale structural changes (Figure 4.10d – f). This transition may be accommodated by conversion of $Ca_2U_3O_{11}$ to biphasic $CaUO_4$ and UO_2 particles (Figure 4.8a, 900 °C) via dissociation of 0.5 mol oxygen (Equation 4.4) implying that a higher Ca^{2+}-loading towards [Ca/U] = 1 would increase thermal stability.

$$Ca_2(UO_2)_3O_5 \xrightarrow{\Delta(700-1000\,^{\circ}C)} 2Ca(U^{VI}O_2)O_2 + U^{IV}O_2 + \frac{1}{2}O_2$$

Equation 4.4

Whilst the presence of green specks at 800 °C could indicate partial reduction to $Ca_2U_3O_{10}$ [83], the relative thermal stability of $Ca_2U_3O_{11}$ (Figure 4.7, inset) in addition to requiring a reductive atmosphere precludes this pathway from being likely.

4.4 Summary and implications

The alkalisation of aqueous U(VI) - Ca(II) solutions results in hydroxylation of uranyl(VI) species towards oligomeric U(VI) clusters. The majority of U(VI) (~87 mol%) was removed from solution between pH 5 – 7 via nucleation into poorly-ordered nanoparticles of 14 nm. These Ca^{2+}-deficient aggregates continued to uptake Ca^{2+} until a final Ca/U ratio of 0.67 was reached. This hydrous calcium uranate ($Ca_2(UO_2)_3O_{3.75}(OH)_{2.5}.3.5H_2O$) underwent a two-stage dehydration-dehydroxylation between 100 – 700 °C under a redox-neutral atmosphere to form crystalline $Ca_2U_3O_{11}$; which subsequently decomposed into a biphasic $CaUO_4/UO_2$ mixture at 800 °C. The simple and rapid process studied here may be integrated with existing processes [2] to remove U(VI) from aqueous waste streams, whilst creating a crystalline low

solubility uranate phase that may be used for long-term storage or permanent disposal of waste uranium.

4.5 References

1. Ding, W., Botha, J.A., Hanson, B.C., and Burke, I.T., *Aqueous Hydroxylation Mediated Synthesis of Crystalline Calcium Uranate Particles.* Journal of Alloys and Compounds, 2016. **688, Part B**: p. 260-269.
2. Baxter, W., *Plutonium Finishing and Product Packaging at Thorp*. 1989.
3. OECD, *Management of Depleted Uranium: A Joint Report by the Oecd Nuclear Energy Agency and the International Atomic Energy Agency*. 2001, Organisation for Economic Co-operation and Development: France.
4. OECD, *Technology Roadmap Update for Generation Iv Nuclear Energy Systems*. 2014, OECD.
5. IPFM, *Global Fissile Material Report 2011: Nuclear Weapon and Fissile Material Stockpiles and Production*. 2011, International Panel on Fissile Materials.
6. NDA, *Strategy: Effective from April 2011*. 2011: UK.
7. Environment, G.B.D.f., Affairs, R., Environment, D.f., Food, Staff, R.A., Business, G.B.D.f., Enterprise, and Reform, R., *Managing Radioactive Waste Safely: A Framework for Implementing Geological Disposal*. Vol. 7386. 2008: The Stationery Office.
8. Baker, R.J., *Uranium Minerals and Their Relevance to Long Term Storage of Nuclear Fuels.* Coordination Chemistry Reviews, 2014. **266–267**(0): p. 123-136.
9. Roach, A.M., *Consideration of Safeguards Requirements During the Design of the Urenco Tails Management Facility*. 2010, International Atomic Energy Agency.
10. Denecke, M.A., *Actinide Speciation Using X-Ray Absorption Fine Structure Spectroscopy.* Coordination Chemistry Reviews, 2006. **250**(7-8): p. 730-754.
11. Mace, N., Wieland, E., Dahn, R., Tits, J., and Scheinost, A.C., *Exafs Investigation on U(Vi) Immobilization in Hardened Cement Paste: Influence of Experimental Conditions on Speciation.* Radiochimica Acta, 2013. **101**(6): p. 379-389.
12. Clark, D.L., Conradson, S.D., Donohoe, R.J., Keogh, D.W., Morris, D.E., Palmer, P.D., Rogers, R.D., and Tait, C.D., *Chemical Speciation of the Uranyl Ion under Highly Alkaline Conditions. Synthesis, Structures, and Oxo Ligand Exchange Dynamics.* Inorganic Chemistry, 1999. **38**(7): p. 1456-1466.
13. Moroni, L.P. and Glasser, F.P., *Reactions between Cement Components and U(Vi) Oxide.* Waste Management, 1995. **15**(3): p. 243-254.
14. Burns, P.C., Ewing, R.C., and Miller, M.L., *Incorporation Mechanisms of Actinide Elements into the Structures of U6+ Phases Formed During the Oxidation of Spent Nuclear Fuel.* Journal of Nuclear Materials, 1997. **245**(1): p. 1-9.
15. Pearcy, E.C., Prikryl, J.D., Murphy, W.M., and Leslie, B.W., *Alteration of Uraninite from the Nopal I Deposit, Pena Blanca District, Chihuahua, Mexico, Compared to Degradation of Spent Nuclear Fuel in the Proposed U.S. High-Level Nuclear Waste Repository at Yucca Mountain, Nevada.* Applied Geochemistry, 1994. **9**(6): p. 713-732.
16. Burns, P.C. and Li, Y., *The Structures of Becquerelite and Sr-Exchanged Becquerelite.* American Mineralogist, 2002. **87**(4): p. 550-557.
17. Finch, R.J. and Ewing, R.C., *Clarkeite: New Chemical and Structural Data.* American Mineralogist, 1997. **82**(5-6): p. 607-619.
18. Bots, P., Morris, K., Hibberd, R., Law, G.T.W., Mosselmans, J.F.W., Brown, A.P., Doutch, J., Smith, A.J., and Shaw, S., *Formation of Stable Uranium(Vi) Colloidal Nanoparticles in Conditions Relevant to Radioactive Waste Disposal.* Langmuir, 2014. **30**(48): p. 14396-14405.
19. Burns, P.C., Deely, K.M., and Skanthakumar, S., *Neptunium Incorporation into Uranyl Compounds That Form as Alteration Products of Spent Nuclear Fuel: Implications for Geologic Repository Performance.* Radiochimica Acta/International journal for chemical aspects of nuclear science and technology, 2004. **92**(3/2004): p. 151-160.
20. Klingensmith, A.L., Deely, K.M., Kinman, W.S., Kelly, V., and Burns, P.C., *Neptunium Incorporation in Sodium-Substituted Metaschoepite.* American Mineralogist, 2007. **92**(4): p. 662-669.

21. Douglas, M., Clark, S.B., Friese, J.I., Arey, B.W., Buck, E.C., and Hanson, B.D., *Neptunium(V) Partitioning to Uranium(Vi) Oxide and Peroxide Solids.* Environmental Science & Technology, 2005. **39**(11): p. 4117-4124.
22. Cahill, C. and Burns, P., *The Structure of Agrinierite: A Sr-Containing Uranyl Oxide Hydrate Mineral.* American Mineralogist, 2000. **85**(9): p. 1294-1297.
23. Pradhan, M., Sarkar, S., Sinha, A.K., Basu, M., and Pal, T., *Morphology Controlled Uranium Oxide Hydroxide Hydrate for Catalysis, Luminescence and Sers Studies.* CrystEngComm, 2011. **13**(8): p. 2878-2889.
24. Hingant, N., Clavier, N., Dacheux, N., Hubert, S., Barré, N., Podor, R., and Aranda, L., *Preparation of Morphology Controlled $Th_{1-x}u_xo_2$ Sintered Pellets from Low-Temperature Precursors.* Powder Technology, 2011. **208**(2): p. 454-460.
25. Cordfunke, E.H.P. and Loopstra, B.O., *Preparation and Properties of the Uranates of Calcium and Strontium.* Journal of Inorganic and Nuclear Chemistry, 1967. **29**(1): p. 51-57.
26. Hoekstra, H.R. and Katz, J.J., *Studies on the Alkaline Earth Diuranates.* Journal of the American Chemical Society, 1952. **74**(7): p. 1683-1690.
27. Zachariasen, W.H., *Crystal Chemical Studies of the 5f- Series of Elements. 4. The Crystal Structure of $Ca(Uo_2)O_2$ and $Sr(Uo_2)O_2$.* Acta Crystallographica, 1948. **1**(1-6): p. 281-285.
28. Loopstra, B.O. and Rietveld, H.M., *The Structure of Some Alkaline-Earth Metal Uranates.* Acta Crystallographica Section B, 1969. **25**(4): p. 787-791.
29. Rietveld, H., *The Crystal Structure of Some Alkaline Earth Metal Uranates of the Type M_3uo_6.* Acta Crystallographica, 1966. **20**(4): p. 508-513.
30. Volkovich, V.A., Griffiths, T.R., Fray, D.J., and Fields, M., *Vibrational Spectra of Alkali Metal (Li, Na and K) Uranates and Consequent Assignment of Uranate Ion Site Symmetry.* Vibrational Spectroscopy, 1998. **17**(1): p. 83-91.
31. A. Volkovich, V., R. Griffiths, T., J. Fray, D., and C. Thied, R., *Solubilities and Solubilisation Enthalpies of Alkali Metal Uranates(Vi) in Carbonate Melts.* Physical Chemistry Chemical Physics, 1999. **1**(14): p. 3297-3302.
32. Volkovich, V., Griffiths, T.R., Fray, D.J., Fields, M., and Wilson, P.D., *Oxidation of Uo2 in Molten Alkali-Metal Carbonate Mixtures: Formation of Uranates and Diuranates.* Journal of the Chemical Society-Faraday Transactions, 1996. **92**(24): p. 5059-5065.
33. Antonelli, D.M. and Ying, J.Y., *Synthesis of Hexagonally Packed Mesoporous Tio_2 by a Modified Sol–Gel Method.* Angewandte Chemie International Edition in English, 1995. **34**(18): p. 2014-2017.
34. Lu, Y., Yin, Y., Mayers, B.T., and Xia, Y., *Modifying the Surface Properties of Superparamagnetic Iron Oxide Nanoparticles through a Sol-Gel Approach.* Nano letters, 2002. **2**(3): p. 183-186.
35. Jolivet, J.-P., Henry, M., and Livage, J., *Metal Oxide Chemistry and Synthesis: From Solution to Solid State*. 2000: Wiley-Blackwell.
36. Gupta, A.K. and Gupta, M., *Synthesis and Surface Engineering of Iron Oxide Nanoparticles for Biomedical Applications.* Biomaterials, 2005. **26**(18): p. 3995-4021.
37. Laurent, S., Forge, D., Port, M., Roch, A., Robic, C., Vander Elst, L., and Muller, R.N., *Magnetic Iron Oxide Nanoparticles: Synthesis, Stabilization, Vectorization, Physicochemical Characterizations, and Biological Applications.* Chemical Reviews, 2008. **108**(6): p. 2064-2110.
38. Seneda, J., Figueiredo, F., Abrao, A., Carvalho, F., and Frajndlich, E., *Recovery of Uranium from the Filtrate of 'Ammonium Diuranate'prepared from Uranium Hexafluoride.* Journal of alloys and compounds, 2001. **323**: p. 838-841.
39. Janov, J., Alfredson, P.G., and Vilkaitis, V.K., *The Influence of Precipitation Conditions on the Properties of Ammonium Diuranate and Uranium Dioxide Powders.* Journal of Nuclear Materials, 1972. **44**(2): p. 161-174.
40. Reibold, R.A., Poco, J.F., Baumann, T.F., Simpson, R.L., and Satcher Jr, J.H., *Synthesis and Characterization of a Low-Density Urania (Uo_3) Aerogel.* Journal of Non-Crystalline Solids, 2003. **319**(3): p. 241-246.
41. Le Page, A.H. and Fane, A.G., *The Kinetics of Hydrogen Reduction of Uo_3 and U_3o_8 Derived from Ammonium Diuranate.* Journal of Inorganic and Nuclear Chemistry, 1974. **36**(1): p. 87-92.
42. Ball, M.C., Birkett, C.R.G., Brown, D.S., and Jaycock, M.J., *The Thermal Decomposition of Ammonium Diuranate.* Journal of Inorganic and Nuclear Chemistry, 1974. **36**(7): p. 1527-1529.

43. Griffiths, T.R. and Volkovich, V.A., *A Review of the High Temperature Oxidation of Uranium Oxides in Molten Salts and in the Solid State to Form Alkali Metal Uranates, and Their Composition and Properties.* Journal of Nuclear Materials, 1999. **274**(3): p. 229-251.
44. Gladstone, J.H. and Dale, T., *Researches on the Refraction, Dispersion, and Sensitiveness of Liquids.* Philosophical Transactions of the Royal Society of London, 1863. **153**: p. 317-343.
45. Larsen, E.S., *The Microscopic Determination of the Nonopaque Minerals*. 1921: US Government Printing Office.
46. Mandarino, J., *The Gladstone-Dale Relationship. Part I: Derivation of New Constants.* Canadian Mineralogist, 1976. **14**(4): p. 498-502.
47. Rogova, V., Belova, L., Kiziyarov, G., and Kuznetsova, N., *Bauranoite and Metacalciouranoite, New Minerals of the Hydrous Uranium Oxides Group.* International Geology Review, 1974. **16**(2): p. 214-219.
48. Savitzky, A. and Golay, M.J.E., *Smoothing and Differentiation of Data by Simplified Least Squares Procedures.* Analytical Chemistry, 1964. **36**(8): p. 1627-1639.
49. Hill, R. and Howard, C., *Quantitative Phase Analysis from Neutron Powder Diffraction Data Using the Rietveld Method.* Journal of Applied Crystallography, 1987. **20**(6): p. 467-474.
50. Young, R.A., *The Rietveld Method*. Vol. 5. 1993: International union of crystallography.
51. Abràmoff, M.D., Magalhães, P.J., and Ram, S.J., *Image Processing with Imagej*. Biophotonics international, 2004. **11**(7): p. 36-42.
52. Parkhurst, D.L. and Appelo, C., *User's Guide to Phreeqc (Version 2): A Computer Program for Speciation, Batch-Reaction, One-Dimensional Transport, and Inverse Geochemical Calculations.* 1999.
53. Parkhurst, D.L. and Appelo, C., *Description of Input and Examples for Phreeqc Version 3: A Computer Program for Speciation, Batch-Reaction, One-Dimensional Transport, and Inverse Geochemical Calculations*. 2013, US Geological Survey.
54. Giffaut, E., Grivé, M., Blanc, P., Vieillard, P., Colàs, E., Gailhanou, H., Gaboreau, S., Marty, N., Madé, B., and Duro, L., *Andra Thermodynamic Database for Performance Assessment: Thermochimie.* Applied Geochemistry, 2014. **49**: p. 225-236.
55. Grenthe, I., Fuger, J., Konings, R.J., Lemire, R.J., Muller, A.B., Nguyen-Trung, C., and Wanner, H., *Chemical Thermodynamics of Uranium*. 1992, Amsterdam, Netherlands: Elsevier.
56. Guillaumont, R., Fanghänel, T., Neck, V., Fuger, J., Palmer, D.A., Grenthe, I., and Rand, M.H., *Update on the Chemical Thermodynamics of Uranium, Neptunium, Plutonium, Americium and Technetium*. 2003, Amsterdam, the Netherlands: Elsevier.
57. Bruno, J. and Sandino, A. *The Solubility of Amorphous and Crystalline Schoepite in Neutral to Alkaline Aqueous Solutions*. in *MRS Proceedings*. 1988. Cambridge Univ Press.
58. Rodahl, M., Höök, F., Krozer, A., Brzezinski, P., and Kasemo, B., *Quartz Crystal Microbalance Setup for Frequency and Q‐Factor Measurements in Gaseous and Liquid Environments.* Review of Scientific Instruments, 1995. **66**(7): p. 3924-3930.
59. Sauerbrey, G., *Verwendung Von Schwingquarzen Zur Wägung Dünner Schichten Und Zur Mikrowägung.* Zeitschrift für physik, 1959. **155**(2): p. 206-222.
60. Sauerbrey, G., *The Use of Quartz Crystal Oscillators for Weighing Thin Layers and for Microweighing Applications*. 1991.
61. Vochten, R., Van Haverbeke, L., and Sobry, R., *Transformation of Schoepite into Uranyl Oxide Hydrates of the Bivalent Cations Mg^{2+}, Mn^{2+} and Ni^{2+}*. Journal of Materials Chemistry, 1991. **1**(4): p. 637-642.
62. Meinrath, G., *Uranium(Vi) Speciation by Spectroscopy.* Journal of Radioanalytical and Nuclear Chemistry, 1997. **224**(1-2): p. 119-126.
63. Skakle, J., Moroni, L., and Glasser, F., *X-Ray Diffraction Data for Two New Calcium Uranium (Vi) Hydrates.* Powder Diffraction, 1997. **12**(02): p. 81-86.
64. Zhang, F., Pointeau, V., Shuller, L., Reaman, D., Lang, M., Liu, Z., Hu, J., Panero, W., Becker, U., and Poinssot, C., *Structural Transitions and Electron Transfer in Coffinite, $Usio_4$, at High Pressure.* American Mineralogist, 2009. **94**(7): p. 916-920.
65. Burdick, M. and Parker, H., *Effect of Particle Size on Bulk Density and Strength Properties of Uranium Dioxide Specimens.* Journal of the American Ceramic Society, 1956. **39**(5): p. 181-187.
66. Quilès, F. and Burneau, A., *Infrared and Raman Spectra of Uranyl(Vi) Oxo-Hydroxo Complexes in Acid Aqueous Solutions: A Chemometric Study.* Vibrational Spectroscopy, 2000. **23**(2): p. 231-241.

67. Quilès, F., Nguyen-Trung, C., Carteret, C., and Humbert, B., *Hydrolysis of Uranyl(Vi) in Acidic and Basic Aqueous Solutions Using a Noncomplexing Organic Base: A Multivariate Spectroscopic and Statistical Study.* Inorganic Chemistry, 2011. **50**(7): p. 2811-2823.
68. Palmer, D. and Nguyen-Trung, C., *Aqueous Uranyl Complexes. 3. Potentiometric Measurements of the Hydrolysis of Uranyl(Vi) Ion at 25°C.* Journal of Solution Chemistry, 1995. **24**(12): p. 1281-1291.
69. Colletti, L.M., Copping, R., Garduno, K., Lujan, E.J.W., Mauser, A.K., Mechler-Hickson, A., May, I., Reilly, S.D., Rios, D., Rowley, J., and Schroeder, A.B., *The Application of Visible Absorption Spectroscopy to the Analysis of Uranium in Aqueous Solutions.* Talanta, 2017. **175**(Supplement C): p. 390-405.
70. Froideval, A., Del Nero, M., Barillon, R., Hommet, J., and Mignot, G., *Ph Dependence of Uranyl Retention in a Quartz/Solution System: An Xps Study.* Journal of Colloid and Interface Science, 2003. **266**(2): p. 221-235.
71. Sylwester, E.R., Hudson, E.A., and Allen, P.G., *The Structure of Uranium (Vi) Sorption Complexes on Silica, Alumina, and Montmorillonite.* Geochimica et Cosmochimica Acta, 2000. **64**(14): p. 2431-2438.
72. Demichelis, R., Raiteri, P., Gale, J.D., Quigley, D., and Gebauer, D., *Stable Prenucleation Mineral Clusters Are Liquid-Like Ionic Polymers.* Nat Commun, 2011. **2**: p. 590.
73. Soler-Illia, G.J.D.A.A., Jobbágy, M., Candal, R.J., Regazzoni, A.E., and Blesa, M.A., *Synthesis of Metal Oxide Particles from Aqueous Media: The Homogeneous Alkalinization Method.* Journal of Dispersion Science and Technology, 1998. **19**(2-7): p. 207-228.
74. Van Santen, R., *The Ostwald Step Rule.* The Journal of Physical Chemistry, 1984. **88**(24): p. 5768-5769.
75. Jang, J.-H., Dempsey, B.A., and Burgos, W.D., *Solubility of Schoepite: Comparison and Selection of Complexation Constants for U(Vi).* Water Research, 2006. **40**(14): p. 2738-2746.
76. Díaz Arocas, P. and Grambow, B., *Solid-Liquid Phase Equilibria of U(Vi) in Nacl Solutions.* Geochimica et Cosmochimica Acta, 1998. **62**(2): p. 245-263.
77. Vochten, R. and Vanhaverbeke, L., *Transformation of Schoepite into the Uranyl Oxide Hydrates - Becquerelite, Billietite and Wolsendorfite.* Mineralogy and Petrology, 1990. **43**(1): p. 65-72.
78. Vochten, R., Degrave, E., and Lauwers, H., *Transformation of Synthetic U3o8 into Different Uranium Oxide Hydrates.* Mineralogy and Petrology, 1990. **41**(2-4): p. 247-255.
79. Chernorukov, N.G., Nipruk, O.V., and Kostrova, E.L., *Synthesis and Study of Sodium Uranate $Na_2u_2o_7·6h_2o$ and of Products of Its Dehydration and Thermal Decomposition.* Radiochemistry, 2016. **58**(2): p. 124-127.
80. Cejka, J., *Infrared Spectroscopy and Thermal Analysis of the Uranyl Minerals.* Reviews in Mineralogy and Geochemistry, 1999. **38**(1): p. 521-622.
81. Baran, V. and Tympl, M., *Uranates as a Form of Uranyl Hydrolytic Complexes.* Journal of Inorganic and Nuclear Chemistry, 1966. **28**(1): p. 89-98.
82. Harju, M., Mäntylä, T., Vähä-Heikkilä, K., and Lehto, V.-P., *Water Adsorption on Plasma Sprayed Transition Metal Oxides.* Applied Surface Science, 2005. **249**(1–4): p. 115-126.
83. Sali, S.K., Sampath, S., and Venugopal, V., *Thermal Studies on Alkaline Earth Uranates.* Journal of Nuclear Materials, 2000. **277**(1): p. 106-112.

5 The influence of stoichiometry on the precipitation mechanisms of Ca^{2+}-U(VI)-oxyhydrate particles

Expanding on preliminary synthesis of Ca^{2+}-U(VI)-oxyhydrate particles (chapter 4) [1], the mechanistic and kinetic influences of solution conditions on U(VI)-precipitation are explored in this chapter; focusing in particular, on how the macroscopic energetics of precipitation are affected by the presence of dissolved calcium and tetramethylammonium ions. To the knowledge of the author, past studies involving the quartz crystal microbalance (QCM) on inorganic precipitation in aqueous environments are scarce. The few that do exist rely on Sauerbrey-like assumptions [2-6], where nucleation and growth are assumed surface-specific, in addition to utilising precipitation reactions that are well-defined. Therefore, this section also aims to provide an alternative insight on the in-situ capabilities of the quartz crystal microbalance (QCM), in characterising reaction kinetics and mechanisms from both qualitative and semi-quantitative standpoints.

5.1 Introduction

Numerous crystalline uranyl(VI) oxide hydrate phases (e.g. Becquerelite, Compreignacite, etc. [7]) have been identified as source-terms in controlling surface and below-ground exposure of geo- and bio-sphere to uranium via migration or uptake. Given the chemo- and radio-toxicity of uranium [8], exploring the influence of environmental conditions on source-term formation or alteration is critical in understanding implications on industry, environment [9-11] and human health [12]. Many past studies have focused on long-term equilibrium studies [7]. Whereas, reaction conditions throughout near- to far-field scales of time and distance could lend itself to far-from-equilibrium processes spanning nano-, micro-, meso- and macro-scale. Early-stage equilibration of U(VI)-containing materials in aqueous solution could undergo complexation, condensation and nucleation of colloids, particularly at partitioning interfaces between high and low alkalinity regions given the stability regions of the U(VI)-OH ligand [13, 14]. Studies in formation of actinide colloids has received particular interest given their mobility in aqueous environments [15-21] (e.g. groundwater, mine leachates), and novel chemical (catalysis, organometallic chemistry) or structural properties [22-24]. Precipitation studies on aqueous precipitation of uranyl(VI) hydroxides or uranates have been limited exclusively to ammonium ($(NH_4)_2U_2O_7$) [25-27] or sodium diuranate [28, 29], and less commonly Schoepite or Metaschoepite [24, 30]. Throughout the majority of literature, reactions were used as a means of studying the physical [31], chemical [27, 32-35], and

structural [25, 36, 37] properties of precipitated particles. However, the kinetics and reaction mechanisms of colloid or particle formation are almost entirely unexplored in contemporary literature.

5.2 Experimental

5.2.1 Reaction set-up and rig design

Two reaction regimes were employed to study the precipitation processes during titration and batch reactions. Both reactions were carried out within the same reactor set-up (Figure 5.1). The reactor is composed of a jacketed 2-layer borosilicate glass (7) vessel (I.D. 50 mm) connected to a heated water bath (5, Grant Instruments GD100) to control reaction temperature; and is mounted upon a stirrer hotplate (7, below) (Stuart Scientific SB162-3) with polystyrene foam insulation layer to reduce temperature losses to surroundings whilst allowing the reaction to be agitated by stir-bar (10) (Sigma Aldrich, PTFE circular disk stir bar , double ridge. D. ~1/3 * reactor I.D.). A nitrogen (N_2) line (4) with glass flow rate ~25 ml min^{-1} is connected to the vessel (7) and bypasses to the base reservoirs (1) containing tetraethylammonium hydroxide (TEAH) solution. This prevents influx of carbon dioxide during longer flow through reactions given the tendency of both U(VI) and TEAH to form stable carbonate complexes.

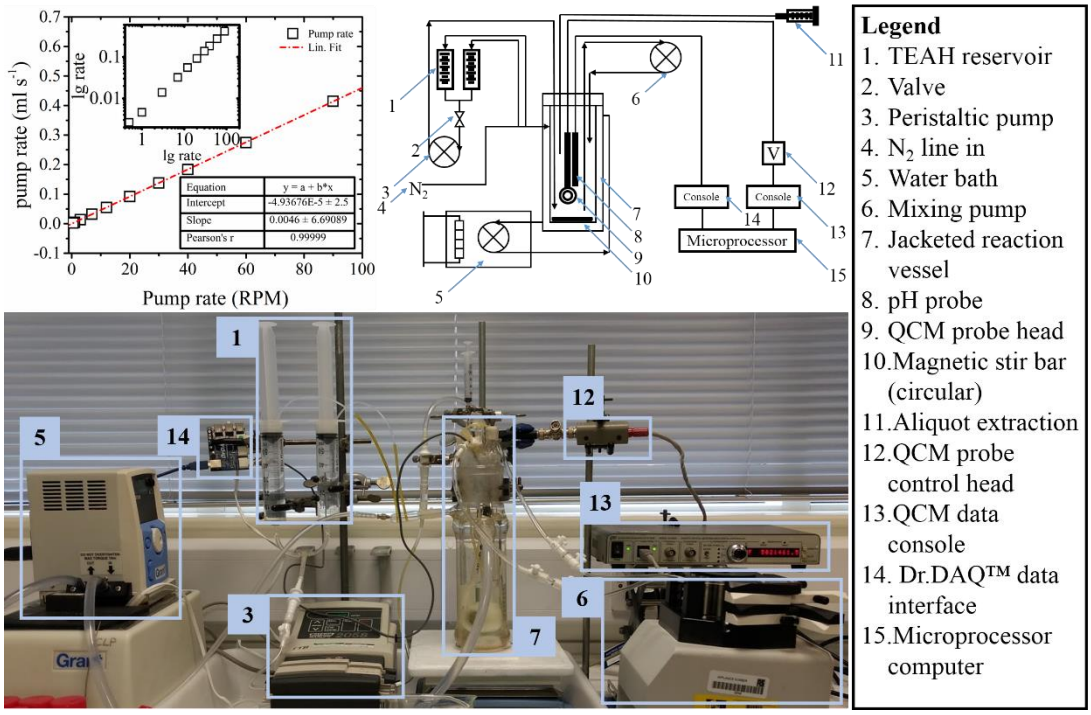

Figure 5.1 Upper-left: Peristaltic pump rate calibration plot (3). Upper-right: scheme of reaction rig with legend of parts. Lower: Photo of typical reaction set-up with numbered labels corresponding to the legend.

The TEAH base solution is fed into the vessel via high precision (Figure 5.1) peristaltic pump (3) and outputs next to the stir-bar, whilst a secondary pump (6) is used to recirculate the reaction solution from reactor bottom to top to improve homogeneity. Within the reactor is the QCM crystal resonator probe (9), glass calomel pH (8) and thermal probe (not shown on the diagram). The QCM outputs in sequence to the voltage head mount (12), QCM data console (13) and the raw frequency and resistance data is subsequently logged by supplied computer software. The pH and thermal probe both output to a Dr. DAQ™ (Pico Technology) data logger (14) and to the PicoLog software on a computer (15). A syringe (11) and line-in is fixed and sealed for removing reaction aliquots for ex-situ analyses in the titration reactions, or for spiking reactants in the batch reactions.

5.2.1.1 Titration reactions

Pseudo-steady-state precipitation was characterised using semi-batch continuously stirred tank reactions (CSTR). From Ca^{2+}, U(VI) stock solutions prepared using the same methodology described earlier (Chapter 4), precursor reaction solutions were prepared with uranium concentration fixed at $4.5*10^{-3}$ mol l^{-1}, whilst the calcium concentration was altered for each reaction depending on the target initial Ca/U ratio (Table 5.1).

Table 5.1 Initial precursor solution conditions for Ca, U(VI) and TMA^+ concentration. Counterions present are NO_3^- and Cl^-.

Ca/U	[Ca(II)]	[U(IV)]	[TMA^+]
	Concentration $*10^{-3}$ mol l^{-1}		
0.124	0.558	4.5	150
0.5	2.25	4.5	145
1	4.5	4.5	139
8	36	4.5	0

The expected ionic strengths were calculated in PHREEQC using the SIT database [38], whilst tetramethylammonium chloride (TMACl) electrolyte was added to reduce the variation in ionic strength between different Ca/U ratios without affecting Ca^{2+}-U(VI)-phase formation. The expected ionic strengths used in the experiments fall within the expected range for lower to moderately brackish groundwaters (See Figure B1-Figure B3). A strong organic base, tetramethylammonium hydroxide (TMAH, 0.0754 mol l^{-1}) was used instead of saturated $Ca(OH)_2$ solution to remove the saturation limitations (< ~0.04 mol l^{-1} solubility), thereby reducing dilution effects. Tetraalkyammonium ions (R_4N^+) being non-complexing due to their steric bulk are therefore expected not to participate directly in the reactions studied, reducing contamination of the precipitate by cations from the alkalising agent.

In a typical reaction, 100 ml of the precursor Ca(II)-U(VI)-TMA^+ precursor solution was introduced into the stirring reactor vessel (Figure 5.1, (7)) and equilibrated

thermally (T_{target} ± 0.5 °C) under N_2 headspace. This is continued until pH and QCM signals stabilise (see 5.2.2.1 for further details) over a time period equivalent to that required for a complete reaction (i.e. a 60-minute reaction would require a stable signal over 60 minutes). Once stabilised, TMAH inflow is initiated at a fixed rate of 0.00261 ml s^{-1}. Throughout the reaction, 1 ml aliquots of the reaction mixture were periodically removed from the solution for ICP-MS analysis (See section 5.2.2.2 for further details).

5.2.1.2 Batch reactions

Reaction kinetics were explored during batch reactions using similar operating procedure as outlined in 5.2.1.1 with some alterations. In these experiments, the reactor vessel was instead filled and equilibrated with TMAH base solution (100 ml, 0.0067 mol l^{-1}, ~pH 12) containing the same equivalent TMACl concentrations as used in the titration reactions. Once QCM (see 5.2.2.1), pH and temperature (see Chapter 4, methodology) readings had stabilised, the reaction was then spiked with a 1 ml aliquot of Ca(II)-U(VI) stock solution at the same equivalent concentrations and stoichiometry as used in the titration reactions. Due to the rapid nature of the reactions, between 3 and 9 repetitions were completed for each Ca/U ratio and temperature to increase reliability of the data.

5.2.2 Solution analyses

5.2.2.1 pH measurements

Continuous in-situ pH and temperature measurements were used to compliment the QCM data. Thermal drift and losses between the set water bath temperature and measured values within the reaction vessel has been measured during each reactions and calibrated for ($T_{reaction}$= 0.97T_{bath} + 0.3; R = 0.999) prior to incorporation into the processed data. pH calibrations are completed every 24 hours and prior to each new reaction temperature change. pH readings at varying temperatures are calibrated using pH 4, 7, 10 and 12.46 buffer solutions with the calibration data recorded within the PicoLog software via a linear equation. Datasets with $R^2 < 0.95$ are rejected (higher is better).

5.2.2.2 Inductively coupled plasma-optical emission spectroscopy (ICP-OES)

During titration reactions, 0.5 ml aliquots of reaction solution were removed from the reaction vessel periodically via the attached syringe (Figure 5.1, above 7). Starting from the pH of precipitation onset (solution clouding) in a progressively extended time format (i.e. t ~ 0, 15, 30, 60, 120… n s) as the reaction slows, until pH 11. Once removed, each aliquot was immediately pass through a 0.22 µm pore size syringe filter and centrifuged at 14400 g for 5 minutes. The supernatant was acidified overnight using Aristar® HNO_3, diluted to 1 wt% acid concentration (~50 ppm U) and used for

uranium ICP-OES analysis on a Thermo iCAP 7400 instrument. All samples were calibrated against calcium-uranium standards containing yttrium or chromium as internal standards.

5.2.2.3 Quartz crystal microbalance (QCM)

A 5 MHz Stanford Research Systems QCM200 probe was used to follow in-situ changes in fluid or suspension properties during the reaction. The same apparatus and pre-usage cleaning procedures were used as detailed in the previous chapter for QCM measurements. In brief, for titration reactions a shift of <3 Hz hr^{-1} and <2 Ohm hr^{-1} in solution was considered stable, with a stabilisation check carried out prior to each measurement for a period of time equal or longer than the overall reaction. The resistive compensation is adjusted periodically throughout the stabilisation processes to reduce noise within the resistance output data.

The same crystal was used throughout all reactions wherever possible to reduce base resonance frequency variation throughout the data, though reaction conditions vary between pH and temperature extremes, promoting accelerated corrosion and dissolution of the quartz and gold surface.

Due to coupling between crystal shear mode oscillation and the temperature dependency of fluid viscosity or density (i.e. attenuation of the oscillating crystal is coupled to the changing viscosity of the sorbed fluid layer), temperature has a profound effect on the absolute frequency values measured between reaction trials. Baseline raw F values varied on the order of 10^2 between 20 and 50 °C reactions. Although this could be mostly circumvented by using frequency shift ($\Delta F = F_{initial} - F_{current}$) values, it was found that baseline noise and stability became prohibitive (ΔF > 10 Hz hr^{-1}) above ~60 °C for the time periods required when submersed in water.

5.2.3 PHREEQC modelling

5.2.3.1 Titration reactions (CSTR)

Using the PHREEQC mass transport functions, a simple closed continuously stirred tank reactor (CSTR) (Figure 5.2) was used to model experimental data from the titration reactions (Figure 5.4) (see section 5.6, Appendices). Stagnant layers were removed (distance set as 0) and a single cell was used to represent the reaction vessel with ideal mixing. The model consists of initial solutions 0, 1 and 2. Solution 0 is the inlet base solution equilibrated with TMAH; solution 1 represents the mixing cell; solution 2 contains the precursor solution containing Ca^{2+}, UO_2^{2+} and TMACl concentrations equivalent to those used in the experiments (Figure 5.2). Irreversible kinetic reactions were allowed to occur between Ca^{2+}, UO_2^{2+} and OH^-; the elemental stoichiometry for Becquerelite was used under the assumption that precipitation is congruent and ideal. As the precipitates are poorly-defined, their chemical properties

are unknown. Instead, available hydrous Ca^{2+}-uranates, Ca^{2+}-uranyl(VI) oxyhydrate, $CaUO_4$ and Portlandite ($Ca(OH)_2$) phases from the SIT database were included.

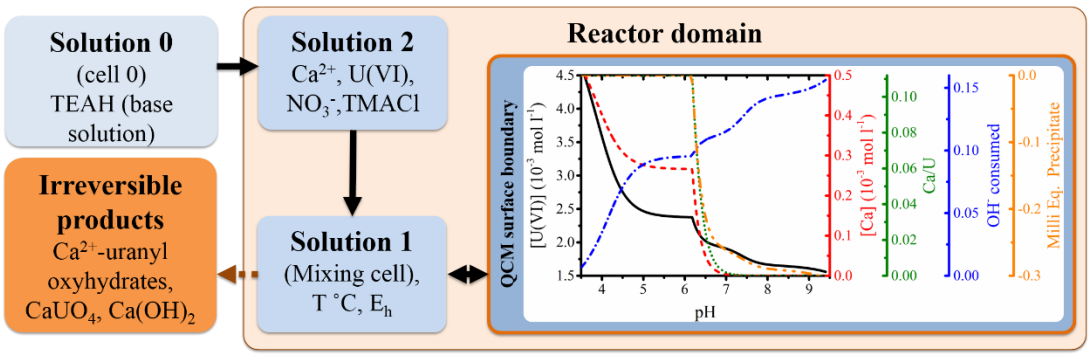

Figure 5.2 Conceptual representation of kinetic CSTR model (left) used to predict QCM response during steady-state hydroxide consumption and precipitation associated with each reaction environment. The plot (right) represents a typical output from the code used.

5.2.3.2 Batch reaction (ion transport)

Batch reactions were modelled around a 1-dimensional transport array (Figure 5.3) with a distance that is (~2 μm) - greater than the maximum QCM detection depth (~250 nm). The transport column is laid out as an array of 10 cells containing solutions equilibrated to a given TEAH-concentration and temperature. Where the spike aliquot containing Ca^{2+} and UO_2^{2+} is introduced at cell 0 and allowed to diffuse into cell (n+1) consecutively until cell 10, which represents the QCM surface.

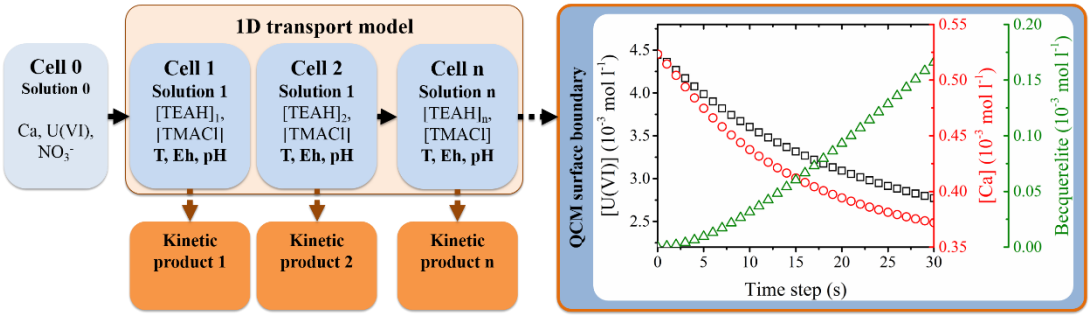

Figure 5.3 Conceptual representation of kinetic mass transport model (left) used to predict QCM response during transient precipitation and diffusion coefficients associated with each reaction environment. The plot (right) represents a typical output from the code used.

Within each cell, irreversible precipitation is allowed to occur, removing Ca^{2+} and U(VI) from the flow based on Becquerelite stoichiometry via reaction between oligomeric U(VI) species of highest polymerisation at pH 6. The kinetics were encoded based on a 1st-order Arrhenian rate equation using E_a and ln A values calculated from preliminary ΔF data (Table 5.6). A simulation was carried out for each reaction temperature and Ca/U stoichiometry used. Ca^{2+}, U(VI) and precipitate concentrations at cell 10 were exported after each simulation and plotted with ΔF

against reaction time (Figure 5.17). The diffusion constants controlling bulk mass transfer of aqueous species were iterated until maximum overall linearity in ΔF versus $[U]_{cell\ 10}$ plots were found in the range 20 – 50 °C for each fixed Ca/U.

5.3 Results

As demonstrated in earlier experimental (see Chapter 4) and theoretical derivations (Chapter 3), frequency (ΔF) and resistance (ΔR) shifts detected by the QCM is related to physical and chemical processes occurring at the crystal-solution interface. The magnitude of ΔF is closely related to the density and viscosity of the fluid layer in contact with the crystal. Therefore, in reactions that affect these properties directly or indirectly, ΔF may be used to approximate the reaction progression in-situ. The precipitation reactions described here expand on preliminary work (chapter 4); utilising a semi-batch CSTR containing Ca^{2+} and U(VI) precursor solution that is progressively alkalised by a hydroxide donor. Foregoing saturated $Ca(OH)_2$ solution, the strong organic base (TEAH) used here allows better control of solution conditions (Ca^{2+} concentration, OH^- concentration, solution volume) throughout the reactions.

5.3.1 Titration reactions

5.3.1.1 pH

During titration of an acidic solution (pH 3 – 4) containing dissolved Ca^{2+} and U(VI) via steady addition of base (TEAH solution), the measured solution pH increases non-monotonically (Figure 5.4). At 20 °C, the titration exhibits two plateau regions at ~5.5 and 12 ml of base added, whereby the pH increases at a substantially lower rate. Whilst this trend is common to reactions across all temperatures (Figure 5.4a) and precursor Ca/U stoichiometry (Figure 5.4b) used, the relative plateau positions are shifted for the former and diminished in magnitude for the latter.

As the base influx rate is known, the total added hydroxide concentration is also known. This allows calculation of the total consumed hydroxide (OH^-_c) by reaction processes (Equation 5.1), whereby the concentration of free hydroxide in solution at time t, is derived from pH (Equation 5.1, red term). By dividing the total consumed OH by the precursor U(VI)-concentration, the overall extent of hydrolysis (h) of uranyl(VI)-ions may be deduced (Figure 5.4, 2nd x-axis).

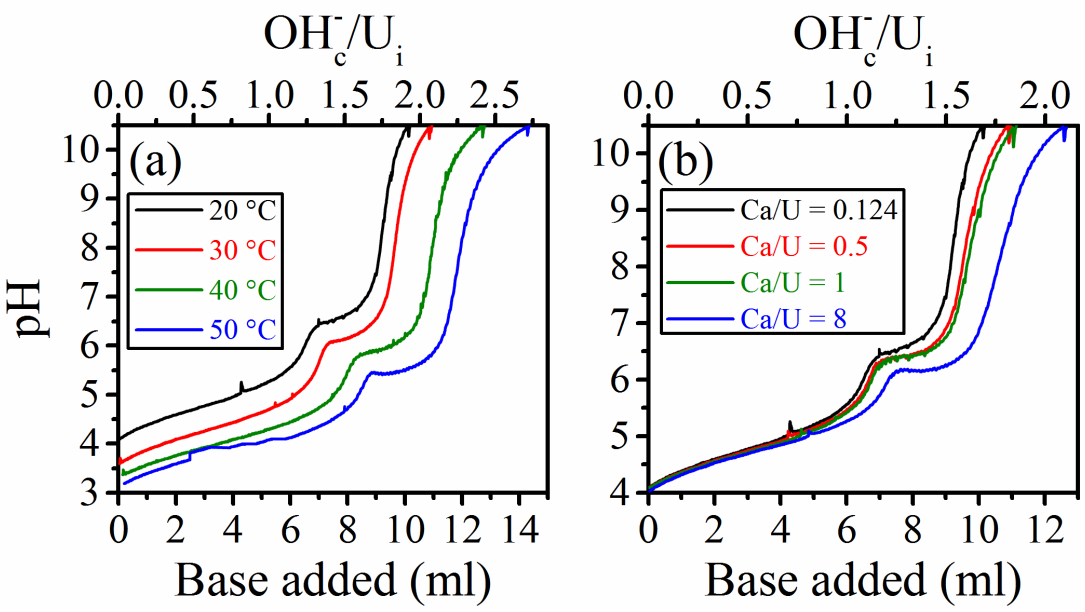

Figure 5.4 Solution pH as a function of base added for reactions at (a) fixed Ca/U-stoichiometry and reaction temperatures 20, 30, 40 and 50 °C; and at (b) fixed temperature (20 °C) for precursor Ca/U of 0.124, 0.5, 1 and 8. The second X-axis represents the calculated bulk extent of hydrolysis of U(VI) as OH/U. See Figure B5 for complete data set.

The two plateaus observed in pH titration data (Figure 5.4) coincide with peaks in di- and mono-positive U-species respectively (Figure 5.7, Figure 5.8c, d), confirming the progressive hydroxylation and condensation of uranyl(VI) ions with increasing base concentration (chapter 4) [39]. At the second plateau, rates of base influx and hydroxide-consumption are approximately equivalent, coinciding with the majority of U(VI)-removal as precipitation occurs (see Figure 5.6). Therefore the average solution OH/U (h) (Figure 5.4, Figure 5.22b) corresponds to that of chemical species present (Figure 5.5).

$$h = \frac{OH_c^-}{[U]_i} = \frac{\left(\frac{R_p t[TMAH]}{V_R}\right) - \left(\frac{K_w 10^{-14}}{10^{-pH_t}}\right)}{[U]_i}$$

Where OH^-_c is the amount of hydroxide consumed at time t, $[U]_i$ is the precursor U(VI) concentration (0.0045 mol l^{-1}); R_p, the influx rate in l s^{-1}; t, time elapsed from reaction start; [TEAH], the concentration of base; V_R, reaction volume at time t; K_w, the ionic product for water calculated from the semi-empirical relationship log $K_w = -4046.16\ T^{-1} + 3.537 - 0.01323T$ [40]; pH_t, solution pH at time t. The term in blue represents the total hydroxide concentration to the reaction and the term in red represents solution hydroxide concentration at time t.

Equation 5.1

These acid-base reactions occurring between U-species and hydroxide ions (Equation 5.3) may be represented by the Henderson-Hasselbalch relationship (Equation 5.2) [41]. Assuming only same-charge species may coexist in solution (i.e. $[(UO_2)_3(OH)_5]^+$) (Figure 5.7, Figure 5.8, Equation 5.3), then second plateau midpoint therefore corresponds to the midpoint of the neutralisation reaction. Therefore, when

the molar ratio of the weak acid $[(UO_2)_x(OH)_y]^{(2x-y)+}$ and its conjugate base $[(UO_2)_x(OH)_{y+1}]^{(2x-y+1)+}$ reaches unity, the second term in this relationship reduces to zero (Equation 5.2 blue), allowing approximation of the pK_a of the nucleating solid from its precipitation-onset pH. An increase in log Ca^{2+}-concentration correlates with an increase in average basicity of condensing U-species and the structural unit formed (Figure 5.22b) [42, 43].

$$\boldsymbol{pH_{midpoint} \approx pK_a + log\left(\frac{\left[(UO_2)_x(OH)_y^{(2x-y)+}\right]}{\left[(UO_2)_x(OH)_{y+1}^{(2x-(y+1))+}\right]}\right)} \qquad \text{Equation 5.2}$$

Precipitation [44] occurs upon further alkalisation from the pK_a (Figure 5.5). Re-dissolution of condensed bodies above a critical size (Equation 5.3, k_b) is likely much slower than precipitation (condensation) (Equation 5.3, k_f) due to nascent particles lying at solubility minima ($k_f >> k_b$, where $K_a = k_f k_c/k_b$) [45, 46].

$$\begin{pmatrix} h = 1.67, (UO_2)_3(OH)_5^+ \\ h = 1.75, (UO_2)_4(OH)_7^+ \end{pmatrix} + \boldsymbol{OH^-} \overset{\boldsymbol{k_f}}{\underset{\boldsymbol{k_b}}{\rightleftharpoons}} \left[(\boldsymbol{UO_2})_x(\boldsymbol{OH})_{y+1}^{(2x-(y+1))+}\right]^* \xrightarrow{\boldsymbol{k_c}} [(\boldsymbol{UO_2})_x(\boldsymbol{OH})_{y+1}^{(2x-(y+1))+}]_{\boldsymbol{n}} \qquad \text{Equation 5.3}$$

Furthermore, if the smallest possible condensed solid is a single unit of the neutral intermediate (Equation 5.3, $[(UO_2)_x(OH)_{y+1}^{(2x-(y+1))+}]$), then the apparent pK_a values (Figure 5.22a) are also equivalent to the pH of zero charge (PZC) for the solid phase.

5.3.1.2 QCM

The majority of shifts in frequency (ΔF) (Figure 5.5a, b) and resistance (ΔR) (Figure B6) occur above the onset pH of precipitation (Figure 5.4) and almost exclusively within the plateau region where pH remains approximately constant in the range 5.5 < pH < 7 (Figure 5.4). These distinctly sigmoidal trends are similar in shape, though ΔF is significantly larger in magnitude compared to ΔR. With increasing reaction temperature (Figure 5.5a) or precursor Ca/U (Figure 5.5b), the total ΔF_{RXN} ($F_{end} - F_{initial}$) and ΔR_{RXN} increases. ΔR is plotted against ΔF to ensure a consistent interaction mechanism between precipitated solids and the QCM-crystal (Figure 5.5c, d), revealing an approximately linear trend. During alkalisation of the precursor Ca^{2+}, U(VI) solution, ΔF trends are pseudo-sigmoidal, where reaction induction (pH < ~ 6) occurs before decreasing sharply and plateauing once again by ~pH 7. In the precipitation region, ΔF values trend almost vertically with pH ($\delta\Delta F/\delta pH \rightarrow \infty$), with the step-size becoming more prominent with higher temperature and precursor Ca/U. Vertical regions display some non-linearity, where pH reduces slightly (ΔF < ~-200 Hz) before recovering (ΔF > ~-500 Hz). A secondary ΔF decrease due to Ca^{2+}-sorption processes (chapter 4, ~pH 9 – 10) also increase in magnitude with higher temperature, though to a lesser degree (see Figure B6).

Although a decrease in ΔF corresponds to an increase in mass or viscoelastic loading on the resonating QCM-crystal, values were converted to relative particle fraction (ϕ) as a more intuitive scale (Figure 5.5e, f). This indicates that as nucleation occurs, a nanofluid forms containing a particle volume fraction that is dependent on the extent of reaction. This conversion is developed in the methodology section and is based on the proportionality between solution viscosity and particle volume fraction [47, 48] (see chapter 3 for further details).

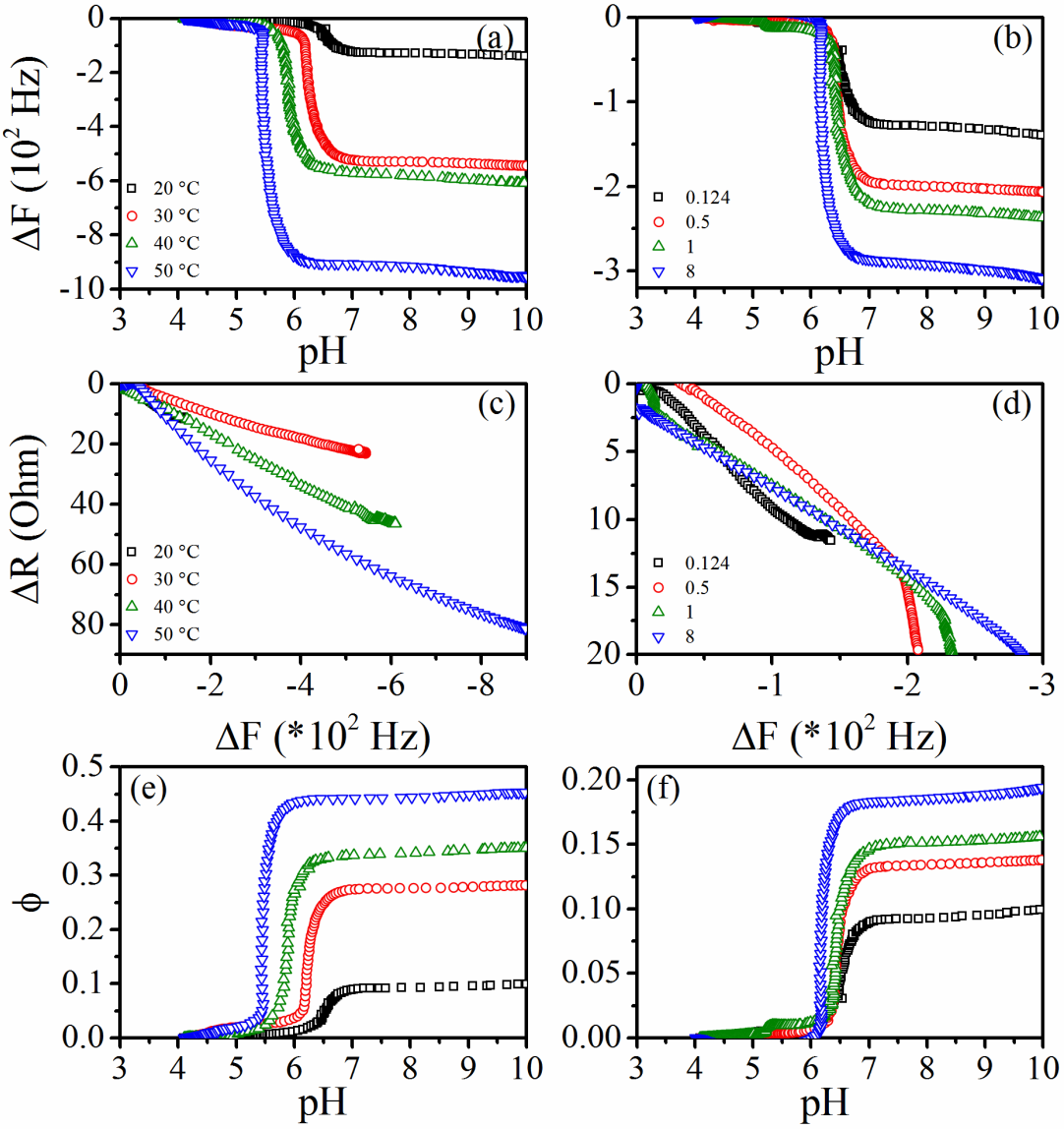

Figure 5.5 ΔF trends are represented as a function solution pH for (a) a fixed Ca/U at reaction temperatures of 20, 30, 40 and 50 °C; and (b) for a fixed temperature at Ca/U of 0.124, 0.5, 1 and 8. ΔR versus ΔF plots are represented by (c) and (d) respectively. Corresponding calculated particle volume fraction (ϕ) as a function of solution pH is presented in (e) and (f) for variation of temperature and Ca/U respectively. See complete dataset in Figure B6.

5.3.1.3 ICP-OES

Within the second pH-plateau (Figure 5.4) and onwards from the onset of precipitation (Figure 5.5), both U(VI) (Figure 5.6a, b) and Ca^{2+} (Figure 5.6c,d) were removed rapidly from solution under all reaction conditions (T, Ca/U, see Figure B9).

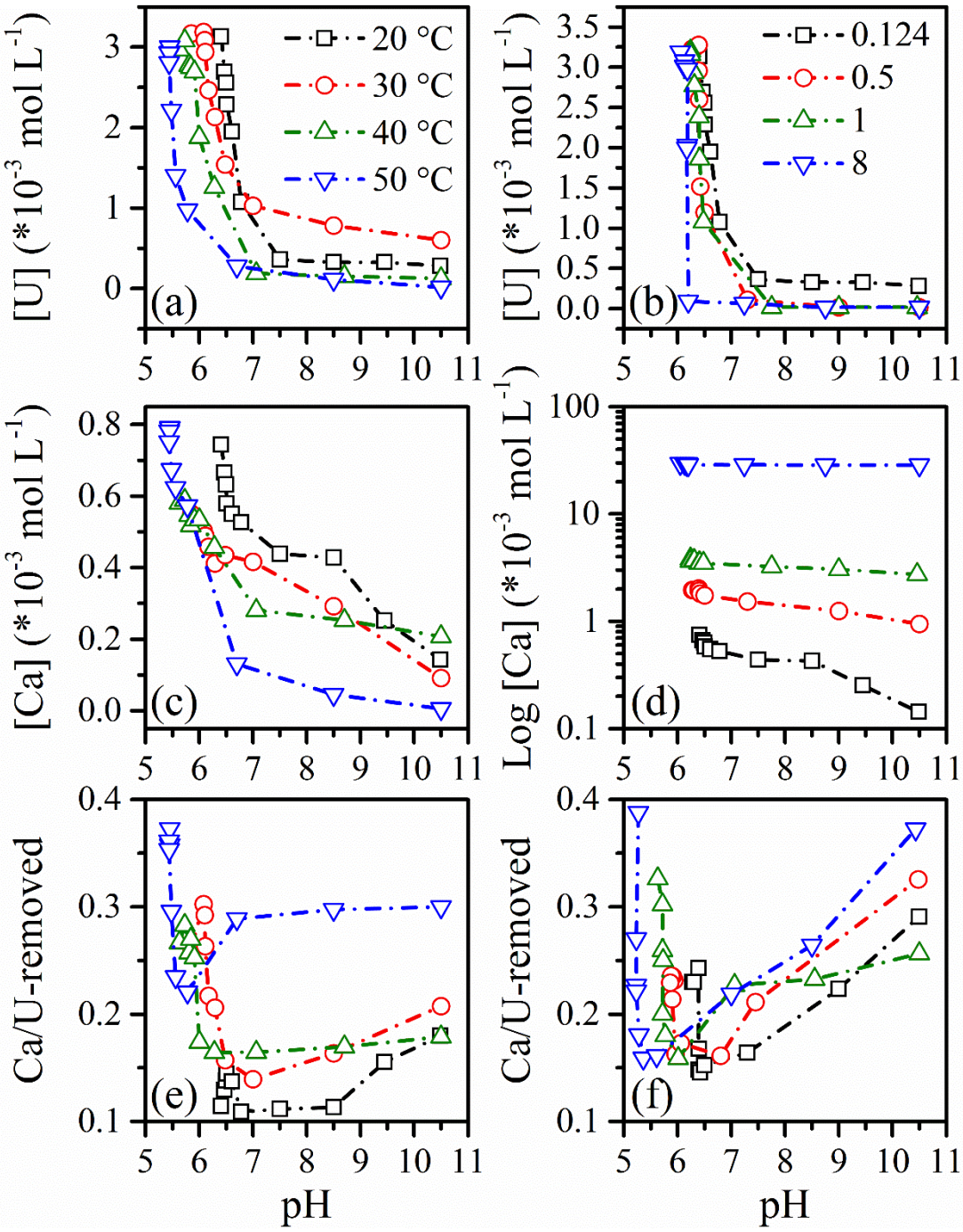

Figure 5.6 Measured solution U(VI)-concentration (a, b); Ca^{2+}-concentration (c, d); Ca/U stoichiometry of filtered solids (e, f), Ca^{2+}-concentration presented in log scale for clarity; as functions of pH at fixed precursor Ca/U (0.124) and varying temperatures (20, 30, 40 and 50 °C) (a, c, e); or at fixed temperature (20 °C) and varying Ca/U (0.124, 0.5, 1 and 8) (b, d, f).

The majority of U(VI)-removal coincides with a rapid increase in particle fraction (Figure 5.5). Whilst some dependency between total U(VI)-removal and total ϕ-increase within the precipitation region is present, the broad spread in U(VI)-concentration data prevents any meaningful calibration between the two trends in this study. Total U(VI)-removal increases by ~8 and ~11 mol% in the temperature range 20 – 50 °C and in the Ca/U range 0.124 – 8 respective (Table B2). The reduction in pH of secondary pH-plateaus (Figure 5.4) or of precipitation onset (Figure 5.5) with higher temperature and Ca/U is also reflected here, whereby rapid U(VI)- and Ca^{2+}-removal is shifted to lower pH. As observed in earlier studies for precipitation at higher initial U(VI)-concentration (Ca/U ~ 0.67) [1], whilst U(VI)-removal is complete by circumneutral pH, Ca^{2+}-removal continues towards alkaline pH. This incongruent precipitation and its dependency on temperature or initial Ca/U is then reflected by an inflection in the Ca/U-stoichiometry of filtered solids at circumneutral pH (Figure 5.6e, f); where a rapid decrease in filtered Ca/U is followed subsequently by a slower increase after ~ pH 7.

5.3.1.4 PHREEQC modelling

To explore the mechanistic nature of Ca^{2+}- and U(VI)-precipitation, a simple 1-cell CSTR code (see a) was used to model the alkalisation (titration) of an acidic solution equilibrated with Ca^{2+}- and U(VI)-ions by inflowing TEAH solution. The model allows for the precipitation of Ca^{2+}-U(VI)-oxide and oxyhydrate phases once the relevant saturation index (> 0) is surpassed (see 5.2.3.1 and a for further details). In a typical modelled reaction, the equilibrated precursor solution is rich in free uranyl(VI) (UO_2^{2+}) species (Figure 5.7, black dash-dot). As hydroxide (as TEAH) is introduced to the solution, uranyl(VI) species undergo hydrolysis via complexation and condensation reactions to form U-hydroxide complexes of higher h-ratio (Figure 5.7, OH/U-stoichiometry).

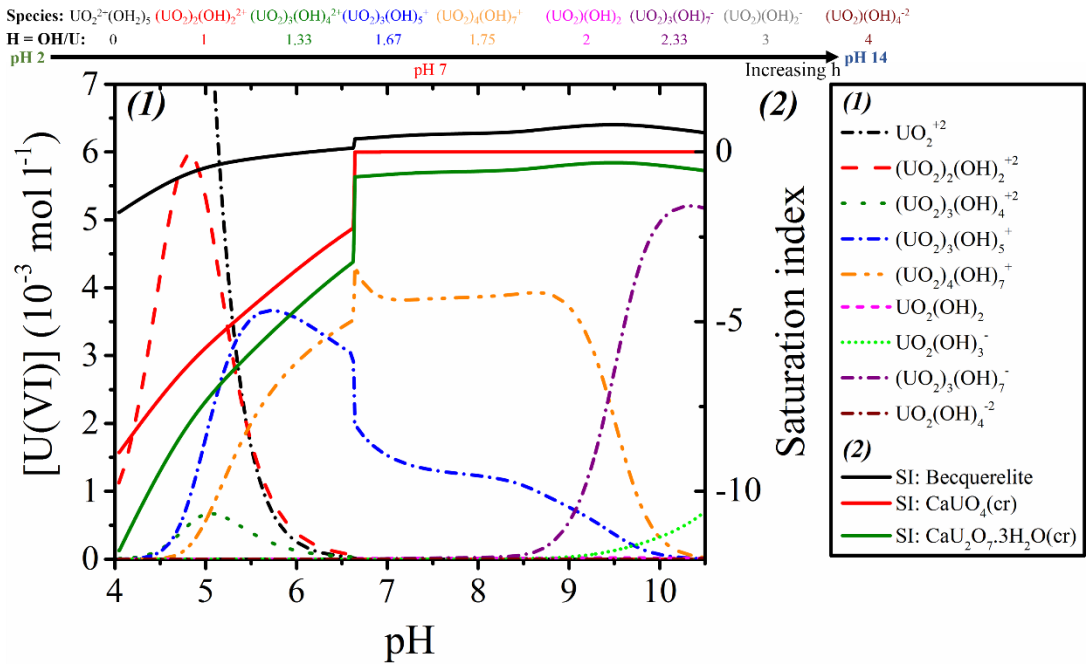

Figure 5.7 Predicted *(1)* U(VI) speciation (dashed lines) and *(2)* saturation indices (solid lines) of Ca^{2+}-U(VI)-oxide or hydroxide phases allowed to precipitate in the model.

Towards neutral pH (~ 7), the formation of tri- ($[(UO_2)_3(OH)_5]^+$, Figure 5.7 blue dash-dot, Scheme 5.1a circlet 2) and tetra- ($[(UO_2)_4(OH)_7]^+$ Figure 5.7 orange dash-dot-dot) nuclear U(VI)-hydroxides becomes more stabilised. With increasing alkalinity (pH → 10.5) and extent of hydrolysis (h = OH/U), the solution becomes more dominated by the anionic polynuclear complexes $[(UO_2)_3(OH)_7]^-$ (purple dash-dot), $[UO_2(OH)_3]^-$ (green dot) and $[UO_2(OH)_4]^{2-}$ (brown dash-dot). The rapid removal of $[(UO_2)_3(OH)_5]^+$ (and $[(UO_2)_4(OH)_7]^+$) coincides with the downwards shift in pH of precipitation onset (Figure 5.8c, d) for both increasing temperature and precursor Ca/U. Nevertheless, the increase in h ($OH_{consumed}/U_{precursor}$) measured from titration reactions (Figure 5.22b) corroborate with higher expected concentrations of polymerised U(VI)-hydroxide oligomer (Figure 5.8d, $[(UO_2)_3(OH)_5]^+$) as functions of precursor Ca/U. Notably, the rapid consumption of cationic polymeric U(VI)-hydroxides occur in parallel with the saturation index of Becquerelite becoming positive (Figure 5.7, black line).

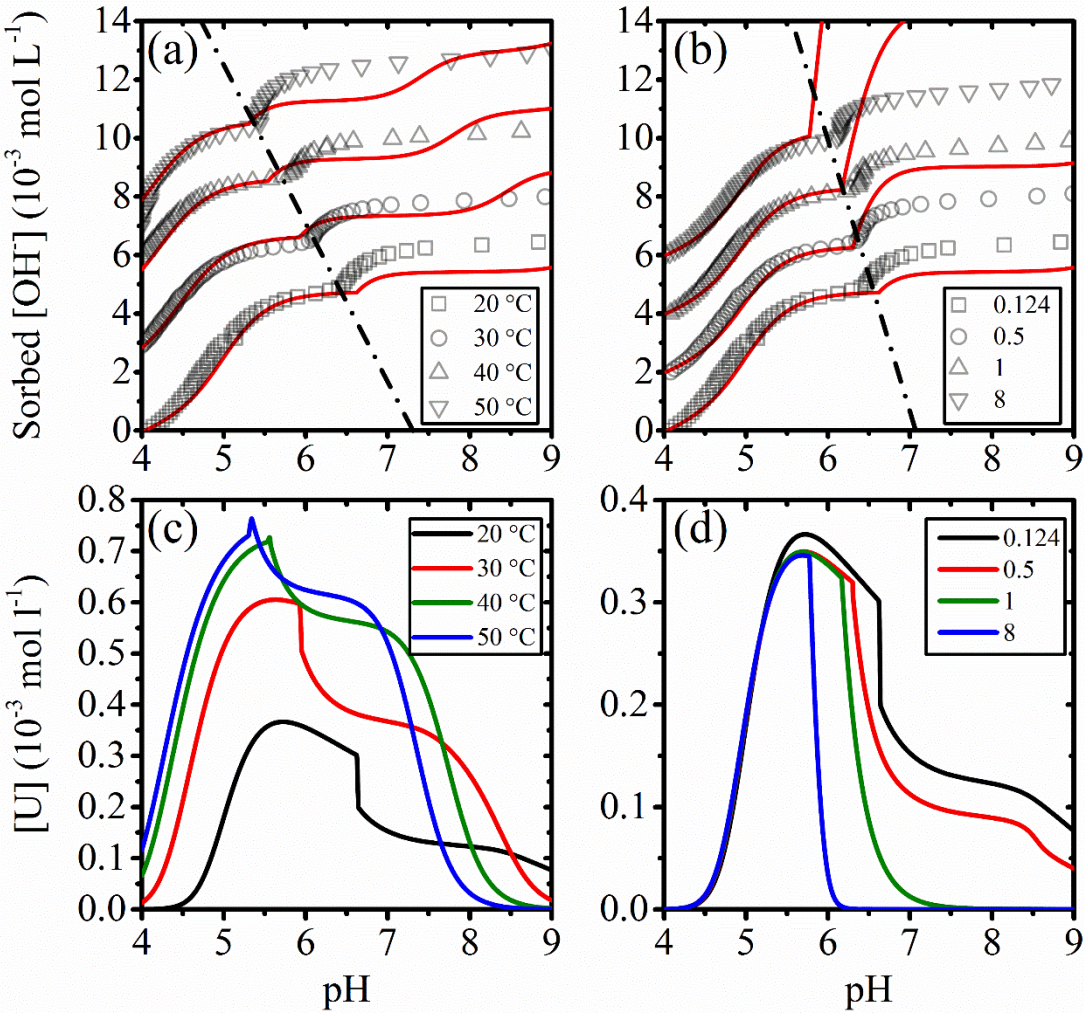

Figure 5.8 Calculated (symbols) and corresponding model predicted (red lines) consumption of hydroxide as a function of solution pH at (a) fixed Ca/U (0.124) and varying temperature (20 – 50°C); and (b) at fixed temperature (20 °C) and varying Ca/U. Corresponding predicted concentrations of $[(UO_2)_3(OH)_5]^+$ are presented in (c) and (d) respectively. 5See Figure B11 for full dataset.

According to the model, the precipitation of Becquerelite occurs via removal of Ca^{2+} and U(VI) from solution. Given that the stability constants used for Becquerelite are for well crystallized samples, its precipitation is expected to occur slowly up to the saturation limits for $CaUO_4$ and $CaU_2O_7.3H_2O$. Indeed, precipitation is not expected to become significant until circumneutral pH (Figure 5.5). The measured U(VI)-removal (Figure 5.9, symbols) is reflected relatively well by the modelled trend during early-stage precipitation in 20 – 50 °C reactions (Ca/U = 0.124). However, as dissolved U(VI) becomes depleted (→ 90 %), the modelled trend deviates from measured values. This deviation from empirical data appears more evident in terms of total % of U-removed at low Ca/U (Figure 5.9b, black), and in terms of onset pH towards high Ca/U (Figure 5.9b, blue).

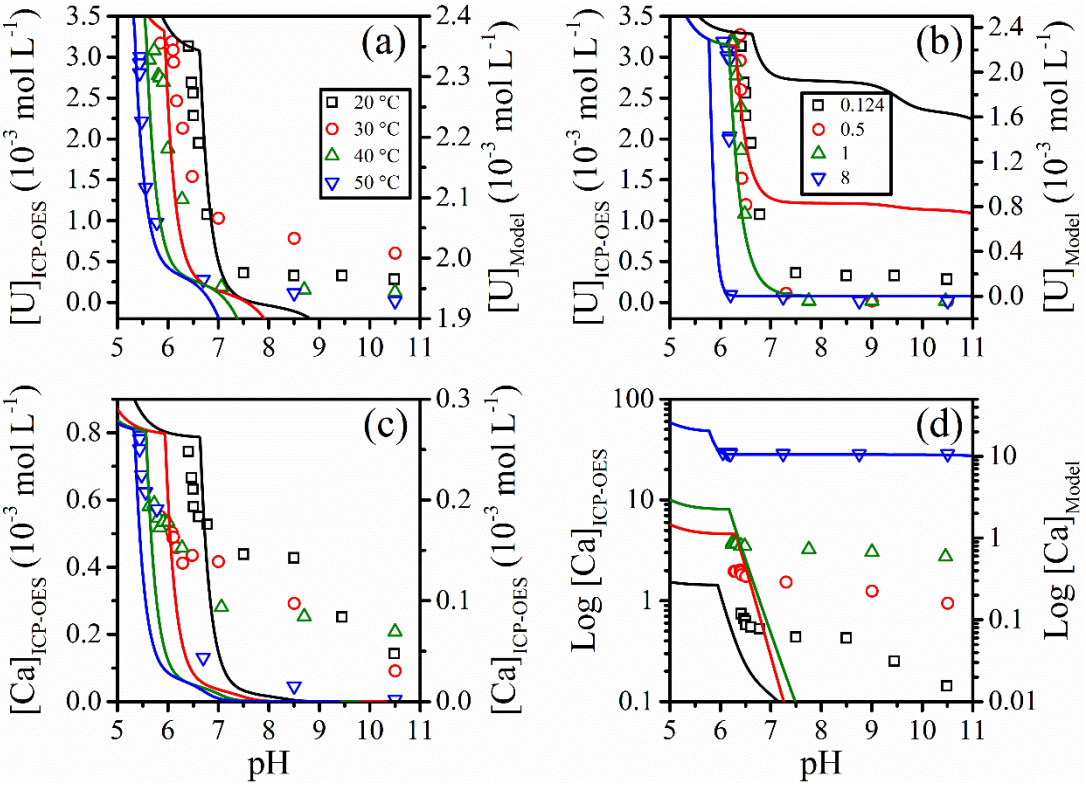

Figure 5.9 Measured (symbols) and modelled (solid lines) (a) U(VI)-removal and (c) Ca^{2+}-removal at fixed precursor Ca/U (0.124); (b) U(VI)-removal and (d) Ca^{2+}-removal at fixed temperature (20 °C) and varying Ca/U (0.124 - 8). See Figure B13 and Figure B14 for the full data set.

The modelled removal of Ca^{2+} from solution reaches ~90 % towards pH 7 and occurs congruently with U-precipitation. This trend appears consistent throughout the temperatures used (20 – 50 °C) and precursor Ca/Us (Figure 5.9c, d), unlike the measured concentrations, which instead exhibit a lagged response with increasing pH.

5.3.1.5 Johnson-Mehl-Avrami-Kolmogorov (JMAK) kinetic analysis

ΔF relates directly to particle volume fraction (ϕ) and therefore to the extent of precipitation (reaction extent). Using the same assumptions defined earlier (constant bulk density), the sigmoidal trends (accelerating, then decelerating) in particle volume fraction (Figure 5.5, ϕ) were further analysed using the Johnson-Mehl [49]-Avrami [50-52]-Kolmogorov [53] (JMAK) model (Equation 5.4).

$$\boldsymbol{\alpha = 1 - exp(-kt^n)} \qquad \text{Equation 5.4}$$

Where t is relative reaction time (s); k, is the transformation rate constant (s^{-1}) (Table 5.2); n, is the JMAK exponent. The magnitude of n relates to the nucleation rate, reaction mechanism and nuclei geometry (dimensionality) by which the transformation occurs. Traditionally, a single n value is found for each linear region. However, by using the instantaneous n (Equation 5.5, n_t), the dimensionality of the

precipitation may be quantified as a function of increasing particle volume fraction ϕ (Figure 5.10).

$$\frac{\partial \ln[-\ln(1-\phi)]}{\partial \ln(t)} = n_t \qquad \text{Equation 5.5}$$

Accordingly, n_t values in Ca^{2+}-deficient reactions (Figure 5.10a, Ca/U = 0.124) peak at ~4 at the onset of precipitation ($\phi \rightarrow 0$), then decays exponentially through n_t of 3 and 1 before subsequently, falling to 0 by reaction end. This corresponds to a reduction from transformations that are 3-, 2-, 1- and 0-dimensional.

Table 5.2 Rate constants derived using ΔF, particle volume fraction (ϕ) and JMAK fitting analyses.

T °C	ΔF rate constants (k)				ϕ rate constants (*10^{-3} k)				JMAK rate constants (s^{-1})			
	$k_{0.124}$	$k_{0.5}$	k_1	k_8	$k_{0.124}$	$k_{0.5}$	k_1	k_8	$k_{0.124}$	$k_{0.5}$	k_1	k_8
20	0.27	0.46	0.61	0.54	0.20	0.323	0.433	0.44	0.025	0.026	0.034	0.043
30	1.05	0.55	0.88	0.70	0.66	0.35	0.62	0.49	0.079	0.045	0.037	0.049
40	1.39	0.89	1.01	0.87	1.02	0.65	0.71	0.66	0.112	0.054	0.056	0.057
50	1.91	1.19	1.64	0.96	1.38	0.93	0.96	0.78	0.148	0.105	0.08	0.059

This decay in the dimensionality of precipitation is temperature dependent, whereby at lower temperatures, the dimensionality reaches zero at a lower final particle volume fraction (Figure 5.10a, black squares).

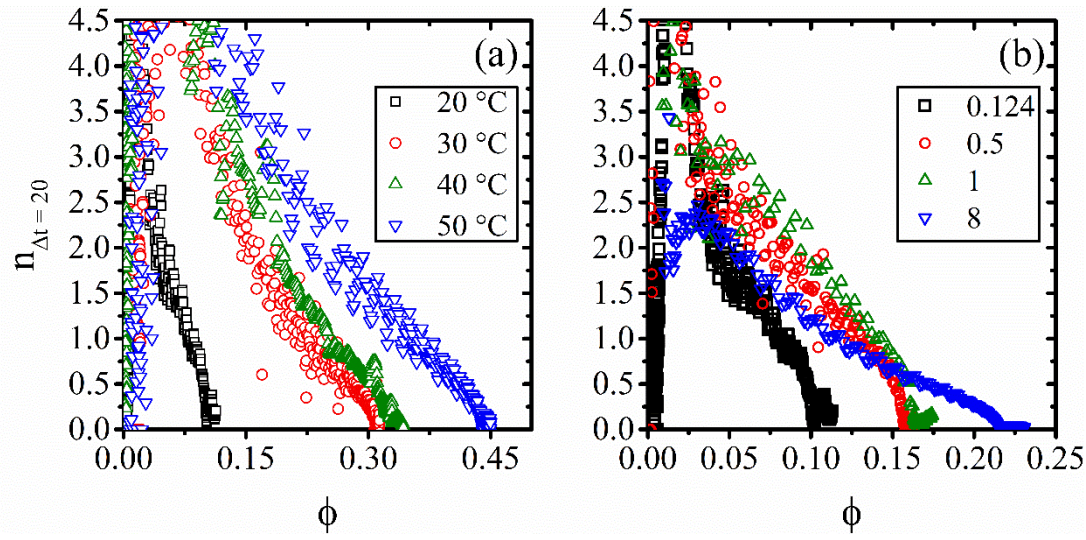

Figure 5.10 Change in instantaneous dimensionality (n) factors as a function of increasing particle volume fraction (ϕ) for (a) a fixed Ca/U (0.124) and varying temperatures (20 – 50 °C); and (b) fixed temperature (20 °C) and varying Ca/U (0.124 – 8). See Figure B16 for full data set.

At constant temperature (20 °C, see Figure B16 for full range), n_t begins at progressively lower values with increasing Ca/U-stoichiometry of the precursor solution. This indicates that the precipitation transitions through spheroidal (n_t ~4) (Figure 5.10b, black), platelet (n_t ~3) Figure 5.10b, and phase-boundary controlled (n_t ~2) transformations at deficient, moderate and excessive Ca^{2+}-concentrations

respectively. For comparison, linear regression analysis was also directly applied to ΔF and particle volume fraction (ϕ) data within the same time regions as used for JMAK-fitting. The trends were modelled best using apparent 0th order kinetics (see Figure B17), results in three sets of k-constants from each data set (Table 5.2).

5.3.1.6 Apparent activation energy of precipitation

Despite reactions being performed at constant precursor U(VI)-concentration base addition rate, the apparent rate constants at varying Ca/U-stoichiometry are distinctly temperature dependant (Table 5.2). Therefore, the apparent activation energy associated with precipitation was calculated using the Arrhenius equation (Equation 5.6), where k is the process constant; A, the pre-exponential factor (frequency factor for 1st order chemical reactions); E_a, the activation energy; R, the molar gas constant; T, absolute temperature (K).

$$\boldsymbol{lnk_{Ca/U} = lnA_{Ca/U} - \frac{E_a}{RT_{20-50\,°C}}} \qquad \text{Equation 5.6}$$

Apparent E_a valid between 20 – 50 °C were calculated from plot gradients (Figure 5.11) at each precursor Ca/U stoichiometry. From the plots using each data set, there appears to be some crossover at different stoichiometry. In particular, at Ca/U = 0.124, some linearity is lost below 30 °C (Figure 5.11, dashed and solid black lines), where $k_{20\,°C}$ is significantly lower than expected to give a convex ln(k)-T^{-1} trend.

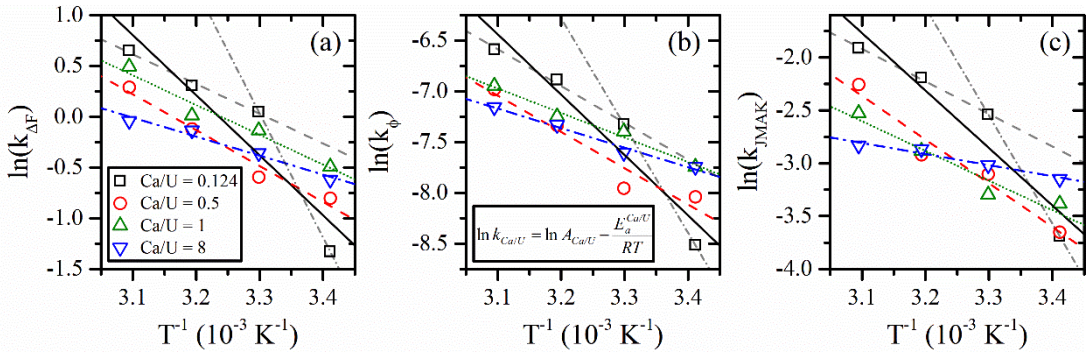

Figure 5.11 Arrhenius plots using (a) ΔF $k_{ΔF}$, (b) ϕ $k_ϕ$ and (c) JMAK k_{JMAK} rate constants across all reaction temperatures and Ca/U precursor stoichiometry. Coloured lines are linear regression lines for each data set, where faded lines represent linear regions within convex data (Ca/U = 0.124).

With increasing precursor Ca^{2+}-concentration, activation energies associated with changes in ΔF and ϕ decreases exponentially with Ca/U (Figure 5.12a), or linearly with log Ca^{2+}-concentration (Figure 5.12b). Under Ca^{2+}-excessive conditions, activation barriers are consistent with a diffusion limited regime < ~21 kJ mol^{-1} [54], where particles form via spontaneous condensation from precursors. However, towards Ca^{2+}-deficient conditions (Ca/U < 1), precipitation becomes surface-limited, reaching values of the order 40 – 80 kJ mol^{-1} [54] (Figure 5.12, Ca/U = 0.124 1,

$45.2_{JMAK} - 49.5\,_{\phi}$ kJ mol^{-1}), indicating that inner-sphere complexation could become rate-limiting (rapid association, slower permanent bond formation).

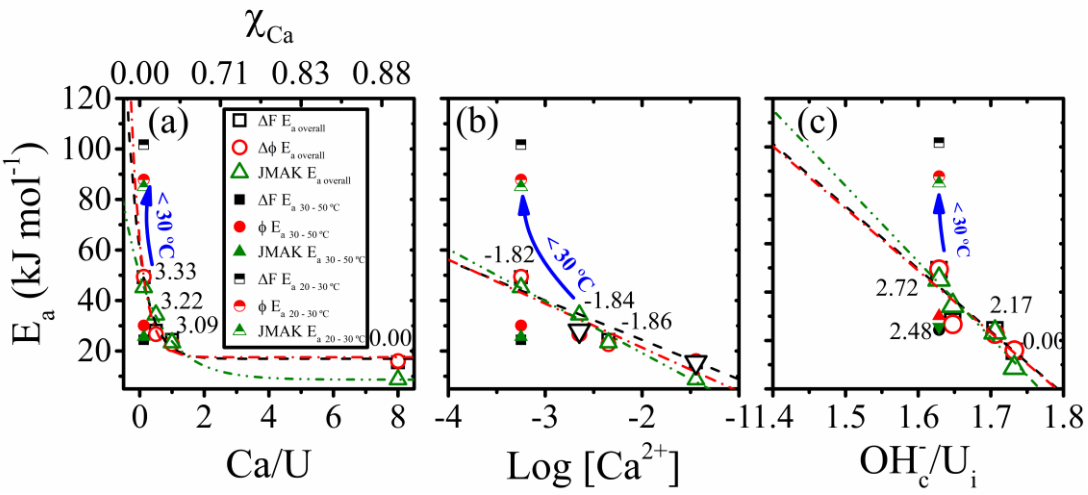

Figure 5.12 Apparent activation energies derived from ΔF, Δϕ and JMAK Arrhenius plots as a function of initial (a) solution Ca/U and Ca^{2+} mole fraction; (b) log Ca^{2+} concentration; (c) average consumed OH^- / initial U(VI) at the onset pH of precipitation. Labels are TMA content as (a) TMA/U ratio, (b) log TMA^+ concentration and (c) TMA/OH_c ratio. See

Extrapolating the OH_c/U_i trend (Figure 5.12c) provides a predicted $E_{\Delta F}$ and E_{ϕ} value of 113.3 kJ mol^{-1} or E_{JMAK} of 126.3 kJ mol^{-1} for precipitation at a OH_c/U_i stoichiometry of 1.3 (Log [Ca^{2+}] = -1).

Table 5.3 Apparent activation energies derived from ΔF, predicted ϕ and JMAK data as a function of precursor solution Ca/U stoichiometry. Values in parentheses are secondary fits for non-convex ln(k) – T regions 20 °C ≤ T ≤ 30 °C and 30 °C ≤ T ≤ 50 °C respectively.

Ca/U stoichiometry	0.124	0.5	1	8
ΔF E_a (kJ mol^{-1})	49.2 (101.7, 24.4)	29.4	24.3	15.5
Ln A	19.2 (40.4, 9.71)	11.2	9.5	5.8
R^2	0.96 (N/A, 0.99)	0.97	0.99	0.99
ϕ E_a (kJ mol^{-1})	49.5 (87.9, 30.1)	29.7	20.1	16.0
Ln A	11.9 (27.5, 4.65)	4.0	0.51	-1.19
R^2	0.92 (N/A , 0.99)	0.93	0.98	0.98
JMAK E_a (kJ mol^{-1})	45.2 (85.0, 25.6)	34.3	23.3	8.7
Ln A	15.08 (31.2, 7.62)	10.44	6.09	0.44
R^2	0.95 (N/A , 0.99)	0.98	0.97	0.98

A 2-region Arrhenius fit (Figure 5.11, faded black dash dot) reveals an activation barrier of 85 – 102 kJ mol^{-1} (Figure 5.12a, b, half-shaded symbols) at low Ca/U (0.124)

and temperatures (20 – 30 °C), significantly larger than the expected 20 – 50 °C average (Figure 5.12a, b)[1].

If Ca/U = 0.124 data were considered between 20 – 30 °C, E_a values would rise to 218 – 253.6 kJ mol^{-1} when a linear trend is assumed (R^2 = 0.65 – 0.81, higher is better) or 85 – 101.7 kJ mol^{-1} when assuming a sigmoidal growth trend (R^2 = 0.91 – 0.98). Comparing with 30 – 50 °C reactions, E_a values instead reach 47.6 – 74.8 kJ mol^{-1} (R^2 = 0.69 – 0.95) and 26.4 – 31.4 kJ mol^{-1} (R^2 = 0.92 – 0.97) for linear and logarithmic trends respectively.

5.3.2 Batch reactions

5.3.2.1 pH

Upon injecting the stirring base solution with an aliquot of Ca(II)-U(VI) solution (volume < 1 ml), the solution pH (Figure 5.13a, b) reduces rapidly from ~pH 12 towards ~pH 5.5 ~5, before recovering immediately to a higher pH ~5.5 - 6, then decaying slowly. This indicates that the initial stabilisation region involves a rapid sorption and partial desorption of free hydroxide ions, before a slower exponential hydroxide-sorption occurs towards reaction end. In reactions completed across all injection Ca/U, solution opacity was observed to increase after the pH-recovery (Figure 5.13a, asterisk), indicating that precipitation initiates after an initial stabilisation process. When the Ca/U-stoichiometry of the injected aliquot is fixed, the pH-minima was lowered and the recovered pH (second pH maxima, asterisk) was increased by higher temperatures (Figure 5.13c, 20 – 50 °C). This upshift recovered pH does not appear to be dependent on injection Ca/U at 20 °C (Figure 5.13d, 0.124 - 8), though does appear to be more prominent at higher temperatures (Figure B20). In contrast to observations from the titration reactions, the OH_c/U_i at precipitation onset remains almost constant at ~2.22, revealing only minor variations (Figure B22c, f); and indicating that subsequent hydroxide release after initial consumption varies little.

[1] Precipitation is diminished at zero Ca^{2+}-concentration (slight opacity by pH 11). Presumably without the stabilising effects of Ca, a higher h is required (Figure 5.22c, dashed lines) whilst steric repulsions from non-complexing TMA^+ cations dominates.

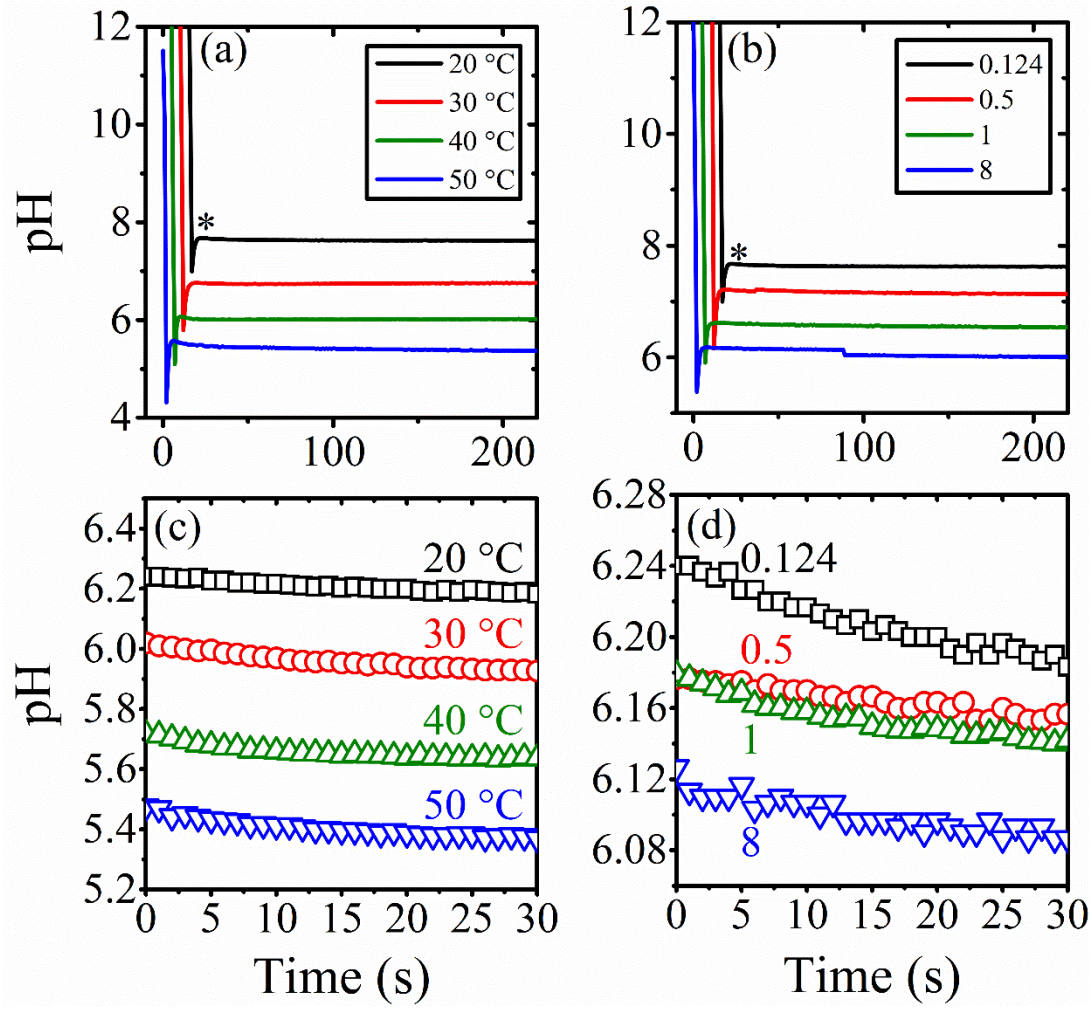

Figure 5.13 Measured pH-trends after rapid injection of Ca, U-aliquot into base solution at (a) constant Ca/U (0.124) and varying temperature (20 – 50 °C); and (b) constant temperature (20 °C) and varying Ca/U-stoichiometry (0.124 - 8). Both sets of trends were offset (x, y of 10, 0.5) for clarity. Raw data trends are presented in Appendices (Figure B20). Magnified (non-offset) graphs are presented in c, d respectively, from the asterisk onwards.

5.3.2.2 QCM

Upon injecting (see section 5.2.1.2) Ca^{2+} and U(VI) into the reacting solution, ΔF increases sharply to a maxima within the first ~5 seconds, the magnitude of which decreases with lower Ca/U-stoichiometry in the aliquot (Figure 5.14a, asterisk). However, this becomes less prominent above 30 °C, where exponential decay begins almost immediately (Figure 5.14b, red line). Due to the rapid and unpredictable nature of this initial region, data used for further processing and analyses were truncated to the exponential decay region only.

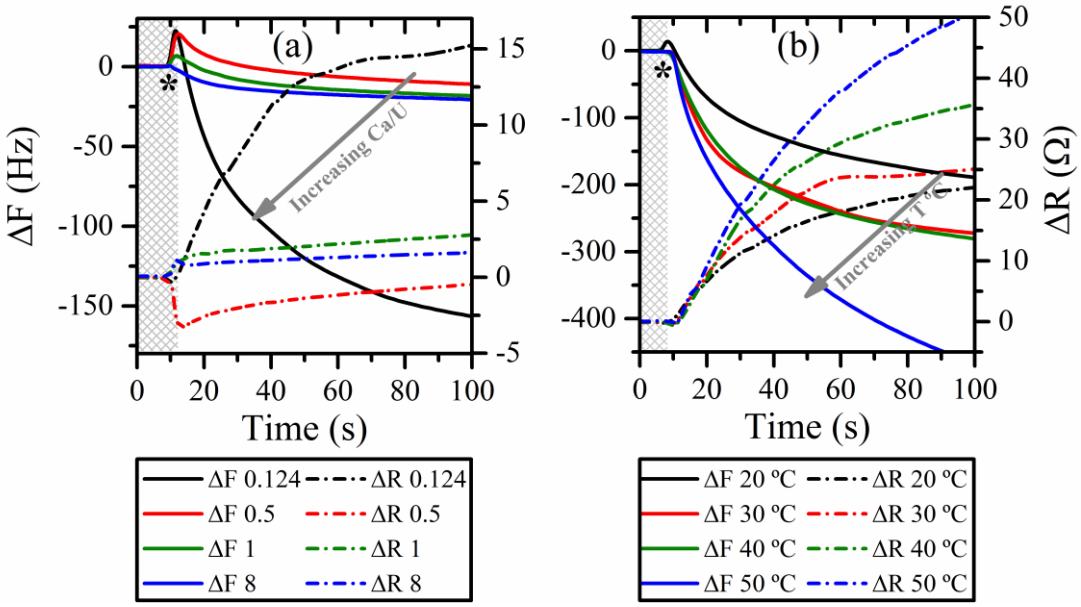

Figure 5.14 A selection of initial reaction regions for ΔF (solid lines) and ΔR (dashed lines) data as a function of reaction time at increasing (a) Ca/U stoichiometry and (b) isothermal temperature.

After the stabilisation region (Figure 5.14, shaded), ΔF decreases pseudo-exponentially from original values as reflected by the increasing magnitude of ΔF (Figure 5.15a – d) and therefore particle fraction (ϕ) (Figure 5.15 (e) – (f)) with time. The final ΔF and ϕ values at 200 seconds relative to t = 0 s correlate positively with increasing temperature (Figure 5.15a, e) at constant Ca/U. The same is true for decreasing injection Ca/U (Figure 5.15b, f) at a constant temperature. Most ΔF versus ΔR plots exhibit some non-linearity with increasing temperature and Ca/U (Figure 5.15c, d respectively), indicating some transition in the interaction mechanism between substrate and QCM-crystal as t → 200 s.

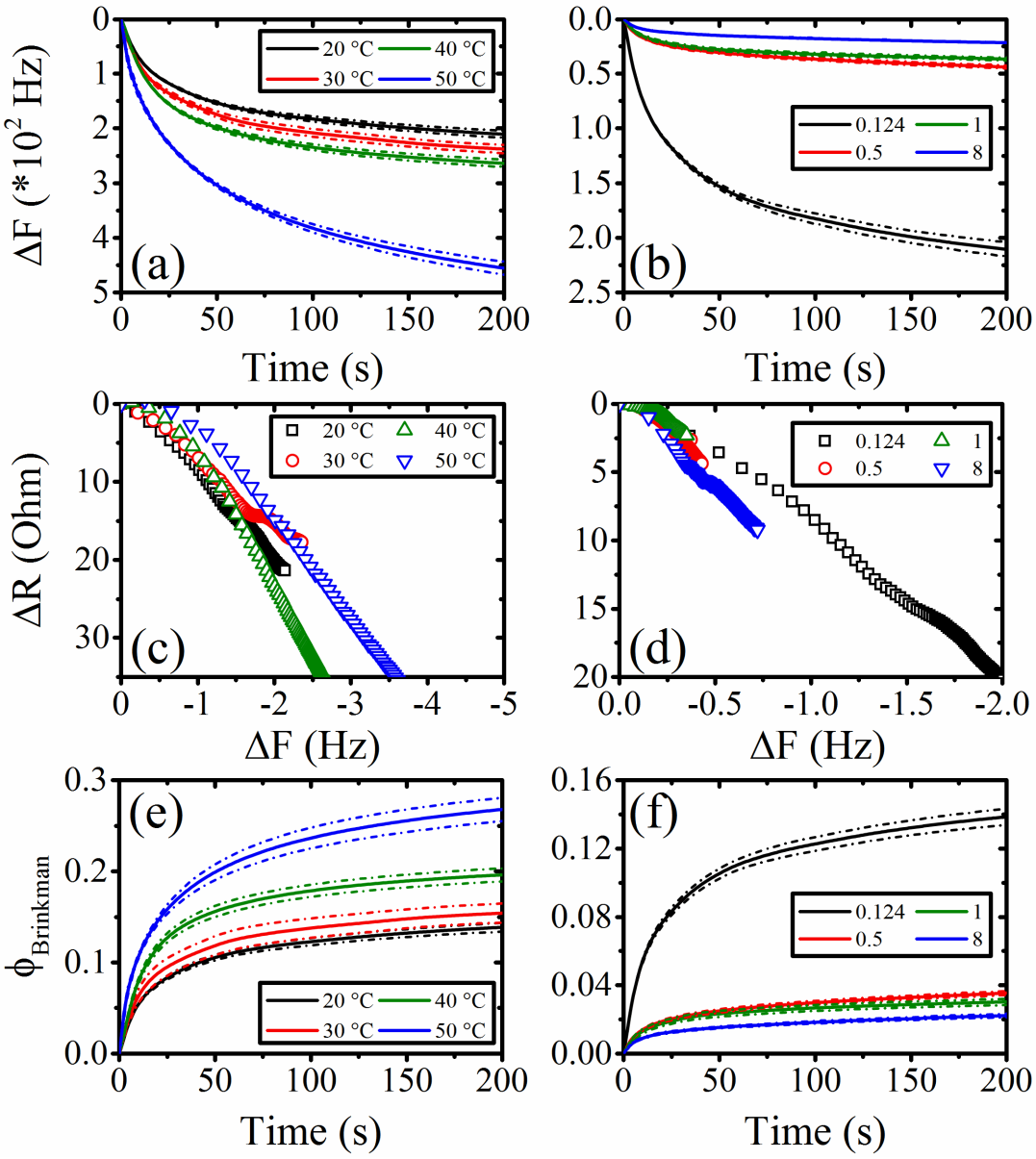

Figure 5.15 ΔF trends are presented as a function solution pH for (a) a fixed Ca/U (0.124) at reaction temperatures of 20, 30, 40 and 50 °C; and (b) for a fixed temperature at varying Ca/U (0.124 – 8). ΔR versus ΔF plots are presented by (c) and (d) respectively. Corresponding particle volume fraction (ϕ) as a function of solution pH is presented in (e) and (f) for variation of temperature and Ca/U respectively. See complete datasets Figure B23, Figure B24).

5.3.2.3 PHREEQC modelling

To determine whether the QCM-response could be explained by U-transport-mediated precipitation during the initial aliquot injection (i.e. due to changing or direct sorption), a simple mass-transport functions in PHREEQC was used to model the precipitation reaction, allowing for kinetic precipitation of Becquerelite (see 5.2.3.2 for further details). According to the modelled data, a series of U(VI)-hydroxide complexes are expected to become stabilised in the substrate adjacent to the QCM-

crystal surface (cell 10) throughout the reaction (Figure 5.13). Initially, the monomeric anionic U(VI)-hydroxides $[UO_2(OH)_3]^-$ (Figure 5.13a, magenta) and $UO_2(OH)_4^{-2}$ (Figure 5.13a, brown) with high h ratios (OH/U = 3, 4 respectively) are expected to dominate solution chemistry. However, as more Ca^{2+} and UO_2^{2+}-ions are transported towards the surface, a reduction in average h-ratio of U(VI)-hydroxides occurs. This reduction in substrate pH stabilises the same cationic U-species as indicated by modelling of titration reactions (Figure 5.7), $[(UO_2)_3(OH)_5]^+$ (green) and $[(UO_2)_4(OH)_7]^+$ (blue).

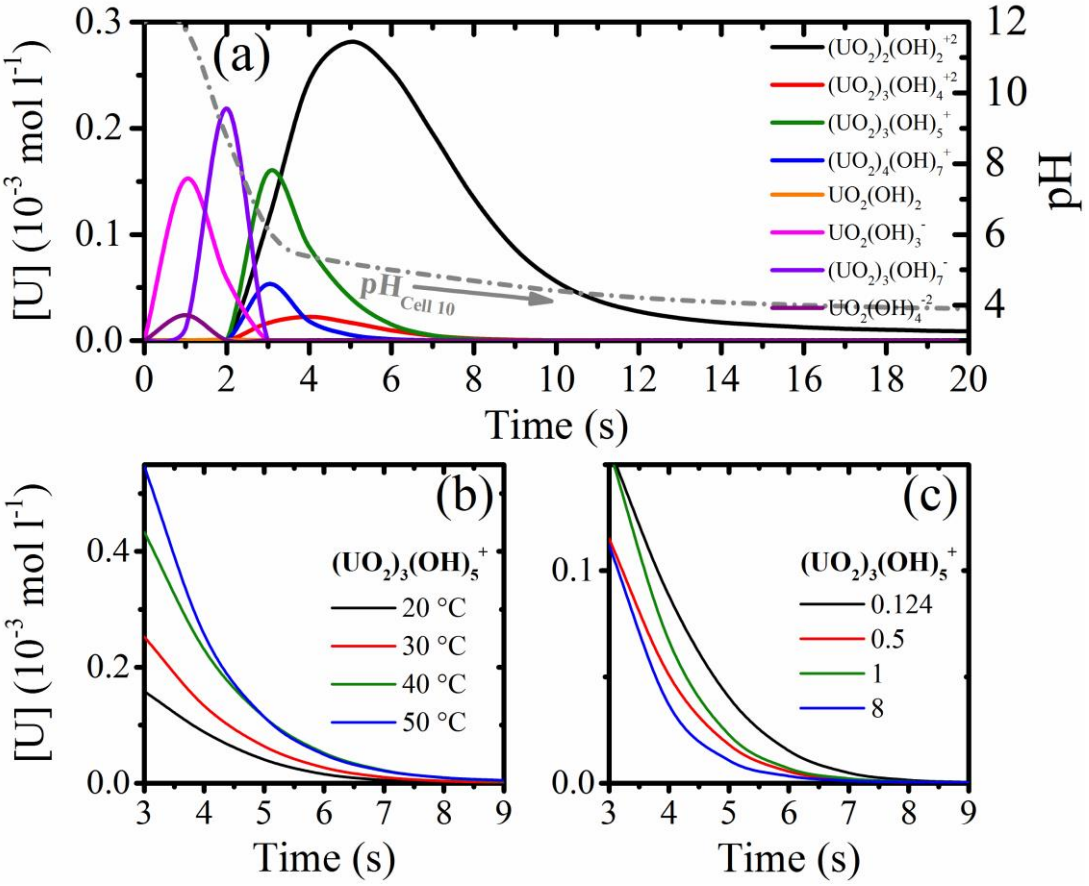

Figure 5.16 (a) A typical plot presenting the modelled transitions between differing U(VI)-hydroxide species with progressing time. The trends for consumption of $[(UO_2)_3(OH)_5]^+$ (solid) at (b) constant Ca/U-stoichiometry (0.124) and varying temperature (20 – 50 °C); and at (c) constant temperature (20 °C) and varying Ca/U-stoichiometry (0.124 - 8).

As the model over-predicts OH-sorption, uranyl(VI) ions continue to de-hydrolyse towards $[(UO_2)_3(OH)_4]^{2+}$ (red) and $[(UO_2)_2(OH)_3]^{2+}$ (black). As the solution pH at which $[(UO_2)_3(OH)_5]^+$ is stabilised corroborates with a positive saturation index for Becquerelite (Figure 5.7), it becomes unlikely that U-species of lower h ($[(UO_2)_3(OH)_4]^{2+}$, $[(UO_2)_2(OH)_3]^{2+}$) would form before total-U(VI) is removed via precipitation processes. Indeed, the observed increase in solution opacity coincides with stability maxima for $[(UO_2)_3(OH)_5]^+$ (green), at time ~3 seconds. The modelled

concentrations of $[(UO_2)_3(OH)_5]^+$ exhibits a positive temperature dependence at constant injection Ca/U (Figure 5.16b), and a negative dependence on injection Ca/U at constant temperature (Figure 5.16c).

The modelled U(VI)-removal (Figure 5.17) due to congruent precipitation of Becquerelite from $[(UO_2)_3(OH)_5]^+$ (Figure 5.16a, green line) appears to follow measured ΔF-trends between 20 and 50 °C at constant injection Ca/U (Figure 5.17a, Figure B27). Whilst predicted trends in the T-range 20 – 50 °C reflected empirical data at each Ca/U, when a comparison is made between different Ca/U (at constant temperature), the predicted U-precipitation deviate significantly from empirical ΔF (Figure 5.17b).

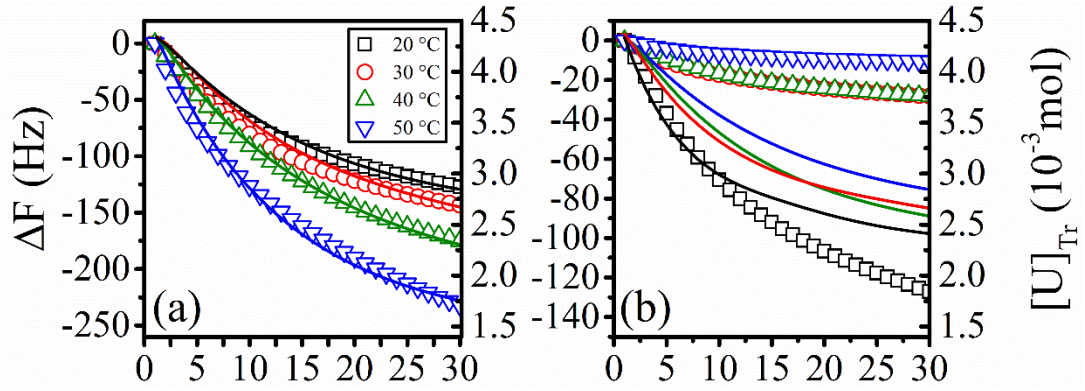

Figure 5.17 Modelled (solid) U(VI)-removal trends plotted overlapped with empirical ΔF (symbols) at (a) constant injection Ca/U (0.124) and varying temperature (20 – 50 °C); and (b) constant temperature (20 °C) and varying injection Ca/U (0.124 - 8). See Figure B27 for full data set.

5.3.2.4 Kinetic analyses

5.3.2.4.1 Early-stage kinetics

By quantifying the rate of hydroxide consumption (Figure 5.13), or rate of change in ΔF (Figure 5.15a, b) and particle volume fraction (ϕ) (Figure 5.15e, f), the dependence of precipitation kinetics on reaction temperature and injection Ca/U-stoichiometry may be determined. To this end, elementary 0^{th}, 1^{st} and 2^{nd} order rate equations were used to model the trends (Ca/U = 0.124 – 8, T = 20 – 50 °C), resulting in total, 16 apparent k-constants for each data set. The data across all reaction conditions were modelled best by an integral 1^{st} order rate equation (Equation 5.7) of the form y = mx + c (see Figure B28, Figure B29), where A represents $[OH^-]$, ΔF or ϕ.

$$\ln[A] = -kt + \ln[A_0] \qquad \text{Equation 5.7}$$

However, much like the mass-transport model, the deviation from empirical data after ~ 30 seconds (R2 < 0.95) becomes prohibitive, with regions of linearity becoming shorter as a function of increasing temperature (~ 10 s). Therefore, the apparent rate constants may only describe processes occurring at the onset of precipitation (Figure

5.14, asterisk); and indicates the presence of a mechanism more complex than apparent using an elementary rate equation (Equation 5.7).

Table 5.4 Apparent kinetic parameters from 1st order linear fits

T °C	$k_{[Ca/U] = 0.124}$	$k_{[Ca/U] = 0.5}$	$k_{[Ca/U] = 1}$	$k_{[Ca/U] = 8}$
hydroxide-consumption rate constants k_{OH} (10^{-3} s^{-1})				
20	5.84 ± 1.63	1.85 ± 1.41	5.02 ± 2.35	1.83 ± 1.31
30	9.45 ± 1.12	2.26 ± 0.04	4.17 ± 0.01	4.67 ± 1.03
40	14.97 ± 1.86	6.23 ± 1.39	15.39 ± 0.36	6.69 ± 0.05
50	17.76 ± 6.19	6.91 ± 0.69	20.72 5.42	15.55 ± 3.15
ΔF rate constants $k_{\Delta F}$ (s^{-1})				
20	35.11 ± 1.0	36.95 ± 1.1	32.17 ± 0.02	24.53 ± 1.4
30	38.9 ± 1.8	42.63 ± 4.3	37.8 ± 0.8	37.47 ± 3.4
40	40.7 ± 0.1	52.79 ± 5.2	49.8 ± 0.8	66.35 ± 3.8
50	47.35 ± 4.8	71.23 ± 1.5	77.35 ± 1.1	96.83 ± 1.8
Particle fraction (ϕ) rate constants k_{ϕ} (s^{-1})				
20	0.326 ± 0.0003	0.12 ± 0.01	0.125 ± 0.001	0.064 ± 0.02
30	0.326 ± 0.008	0.13 ± 0.02	0.169 ± 0.006	0.17 ± 0.004
40	0.36 ± 0.01	0.148 ± 0.005	0.27 ± 0.03	0.18 ± 0.01
50	0.42 ± 0.02	0.196 ± 0.002	0.409 ± 0.009	0.261 ± 0.05

5.3.2.4.2 Double exponential kinetics

As neither ΔF nor ϕ trends could be explained using elementary n^{th} order kinetics above t ~30 s. A double-exponential decay model (Equation 5.8) was used to fit the entire data range for particle volume fraction ϕ. Where ϕ_t is ϕ at time t; ϕ_f, final ϕ value at t = 200 s; $A_{1, 2}$, pre-exponential factors 1 and 2; $k_{1, 2}$, rate constants 1 and 2; t, reaction time in seconds.

$$\boldsymbol{\phi_t = \phi_f + A_1 e^{-k_1 t} + A_2 e^{-k_2 t}} \qquad \text{Equation 5.8}$$

Fitting was performed in the OriginLab® OriginPro 2016 software package using the native exponential decay 2 model. The in-built Levenberg-Marquardt least-squares minimisation algorithm was used to iterate the non-linear curve fit until minima was reached, allowing for a tolerance of $1*10^{-9}$ and maximum iterative step count of 400. An initial iteration cycle was completed with all parameters floated, then repeated stepwise each time with a new parameter fixed. Once completed, all parameters were released and a final cycle was completed. If parameters do not change (< ~5%), then the values are accepted; otherwise a refit is performed. This model represents the data significantly better compared to elementary rate equations (see Figure B28, Figure B29), with R^2 values of ~0.999 across all Ca/U-stoichiometry and temperatures (Figure 5.18a-d).

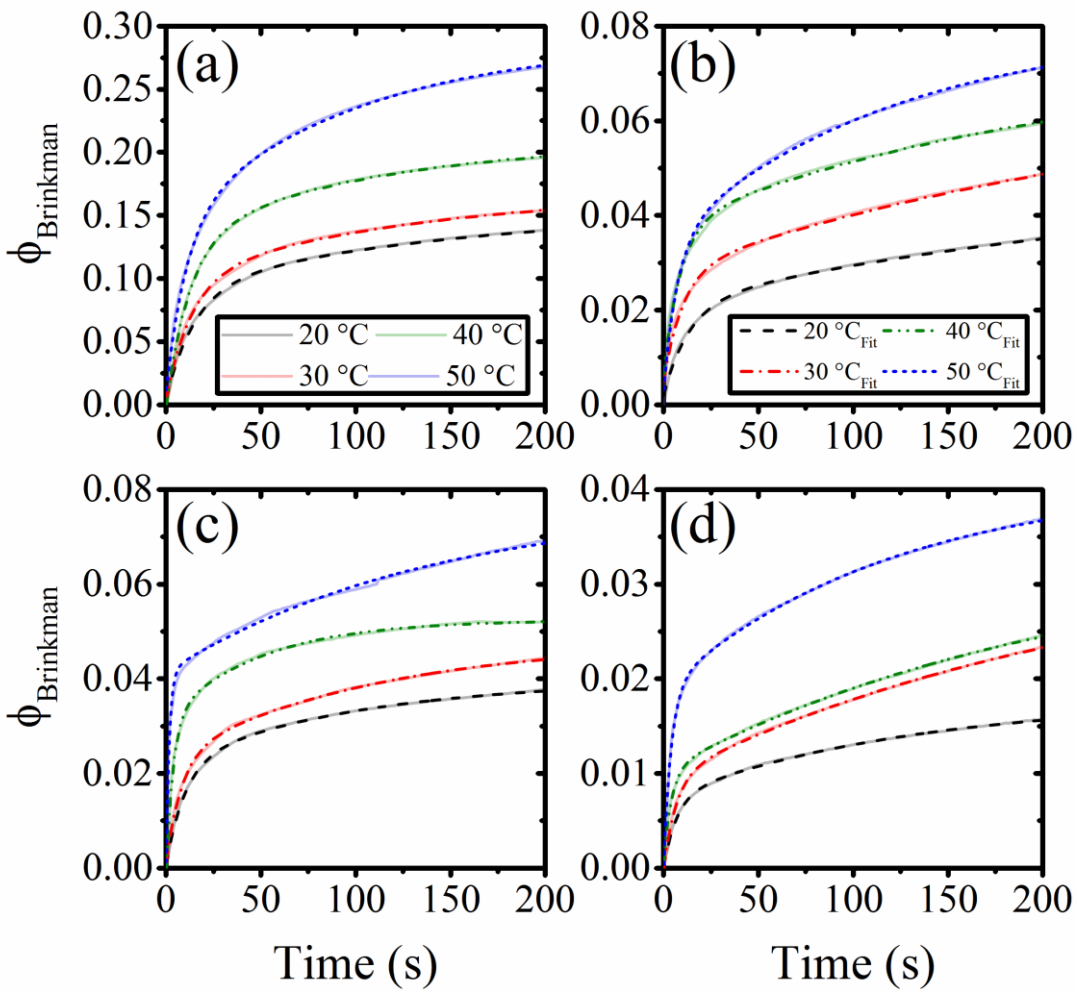

Figure 5.18 Transient ϕ growth (faded coloured solid lines) derived from measured ΔF data overlapped with double exponential function decay fits (coloured dashed lines) (Equation 5.8) at reaction temperatures 20 – 50 °C (ΔT = 10 °C) for precursor stoichiometry of (a) 0.124, (b) 0.5, (c) 1 and (d) 8. (See supplementary information II for data deviation ranges).

This rate equation (Equation 5.8) indicates the presence of two overlapping kinetic processes that are represented by rate constants k_1 and k_2, whereby the former more rapid process (Table 5.5, k_1 values larger) dominates upon first injection Ca^{2+} and UO_2^{2+}-ions ($t \rightarrow 0$ s), and the slower latter process prevails with progressing time ($t \rightarrow$ 200 s). Both k_1 and k_2 constants exhibit a positive temperature dependence, with the former (Table 5.5, upper) ranging ~6.7 – 9.9*10^{-2} at 20 °C to ~0.068 – 0.41 at 50 °C for Ca/U = 0.124 – 8; and the latter ~6.9 – 2.7*10^{-3} at 20 °C to ~1.0 – 5.9*10^{-3} at 50 °C for Ca/U = 0.124 – 8 respectively. Notably however, when the injection stoichiometry (Ca/U) is increased, the temperature dependency of k_1 is enhanced whilst that of k_2 becomes inhibited.

Table 5.5 Apparent transient precipitation reaction k_1 and k_2 constants from non-linear least squares minimisation. Error values are standard deviation from the mean of 3 – 9 data sets.

T °C	Transient (Tr., QCM) double-exponential k_1 (10^{-3} s^{-1})			
	$k_{Ca/U=0.124}$	$k_{Ca/U=0.5}$	$k_{Ca/U=1}$	$k_{Ca/U=8}$
20	67.33 ± 0.39	79.81 ± 0.03	74.86 ± 0.29	68.12 ± 2.48
30	71.75 ± 0.78	85.86 ± 0.53	129.19 ± 0.53	131.36 ± 0.58
40	80.05 ± 0.09	111.16 ± 0.72	196.13 ± 0.43	251.58 ± 0.19
50	82.46 ± 0.14	137.38 ± 0.22	283.2 ± 0.16	412.91 ± 0.72
T °C	Transient (Tr., QCM) double-exponential k_2 (10^{-3} s^{-1})			
20	6.91 ± 0.25	4.33 ± 0.01	4.76 ± 0.15	2.69 ± 0.37
30	7.80 ± 0.12	4.71 ± 0.007	7.33 ± 1.15	3.54 ± 0.11
40	9.56 ± 0.07	5.62 ± 0.14	7.94 ± 1.09	4.06 ± 0.16
50	10.13 ± 0.35	6.97 ± 0.56	8.16 ± 0.64	5.89 ± 0.64

5.3.2.4.3 Apparent activation energy of precipitation

To determine the apparent activation energies associated with the consumption of hydroxide and changes in ΔF or particle volume fraction ϕ, the Arrhenius equation (Equation 5.6) was applied to respective empirical rate constants (Table 5.5) via plotting the natural logarithm of k as functions of T^{-1} (Figure 5.19).

As temperature dependence was also present in the iterated ion-diffusion coefficients used in the PHREEQC mass transport models, apparent activation barriers to diffusion were also derived for comparison. Some crossover is present for ΔF and ϕ data at different Ca/U stoichiometry within this temperature range. At 30 °C, the $k_{\Delta F}$ trends in particular reveals an almost isosbestic rate across all Ca/U.

All macroscopic activation barriers (Figure 5.20, Table 5.6) associated with early-stage precipitation ($t \rightarrow 0$) exhibit a positive logarithmic dependency on the Ca/U-stoichiometry, Ca^{2+}-mole fraction (Figure 5.20a, Ca/U, χ_{Ca}) and Ca^{2+}-concentration (Figure 5.20b) in the injected aliquot. However, there appears to be substantial variation between barrier heights throughout the range. Energy values tending towards minimum Ca^{2+}-content are expected to be 23.2, 5.2, 3.7 and 9.95 kJ mol^{-1} for OH^--consumption, ΔF-change, ϕ-increase and ion-diffusion respectively (Figure 5.20a, solid lines)[2].

Contradicting the trends observed in titration reactions (Figure 5.12), activation barriers become larger as a function of precursor Ca^{2+}-concentration; increasing from ~8 kJ mol^{-1} (ΔF, ϕ) and 19 – 30 kJ mol^{-1} (D, OH) under Ca^{2+}-deficient (Ca/U → 0.124); towards ~40 kJ mol^{-1} (ΔF, ϕ, D) and ~53 kJ mol^{-1} (OH) under Ca^{2+}-excessive conditions (Ca/U → 8). This barrier height dependency on increasing Ca^{2+}-concentration may also be considered inverse to respective TMA^+-concentrations

[2] Values are determined from the intersection of fitted logarithmic trends (solid lines) with the y-axis (x=0).

(Figure 5.20 data labels). As the pH at which precipitation begins (Figure 5.13, asterisk at pH maxima) is related to the total hydroxide ions sorbed by complexation to Ca^{2+} and UO_2^{2+}-ions in the stabilisation region (Figure 5.14, shaded area), activation barriers exhibit a positive trend with lower average pH after stabilisation (Figure 5.13c, pH at beginning of exponential decay). By extrapolating linear trends (Figure 5.20c, solid lines), the apparent activation energy of solid formation (ΔF, ϕ) reduces to zero at pH 6.4, whereas that associated with ion-transport and hydroxide-sorption occurs at a higher pH (7.1 – 7.4).

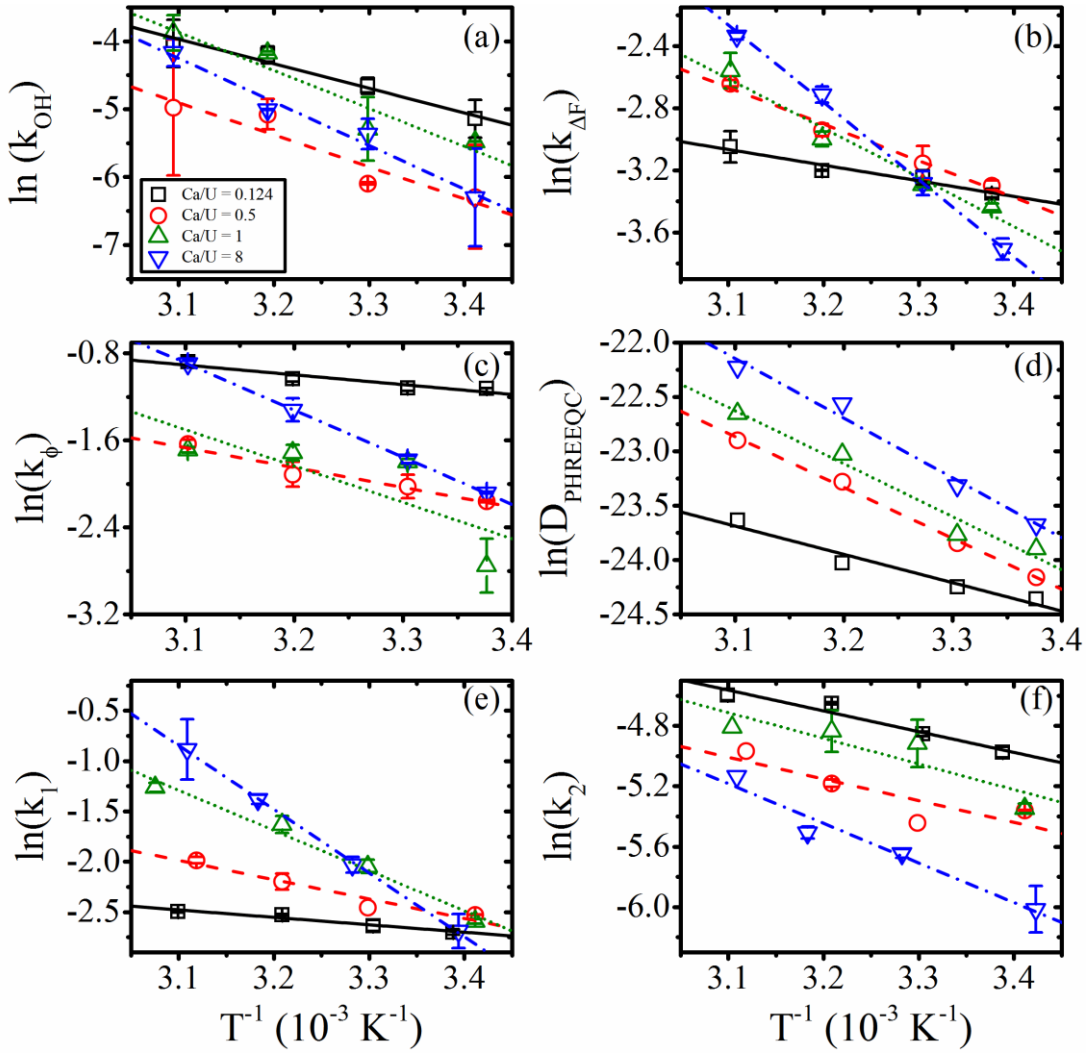

Figure 5.19 Arrhenius plots used in derivation of activation energies using (a) OH-consumption; (b) ΔF change; (c) particle volume fraction (ϕ) change; (d) iterated ion-diffusion coefficients; (e, f) double exponential fast (k_1) and slow (k_2) step rate constants; valid for the temperature range 20 – 50 °C and Ca/U of 0.124 – 8. Coloured lines are linear regression lines for each data set.

The activation energies associated with the fast and slow (E_a^1, E_a^2) kinetic processes exhibit similar trends to those found for early-stage kinetics with increasing Ca/U-stoichiometry and Ca^{2+}-concentration (Figure 5.21a, b), as well as decreasing values

of pH-maxima (Figure 5.21c). Comparatively, the slow process (E_a^2) appears to be more energetically demanding under Ca^{2+}-deficient conditions (Figure 5.21a, b, Ca/U = 0.124). However, as it is less enhanced by increasing Ca/U, the rapid process (E_a^1) dominates at Ca/U of 0.5 and above.

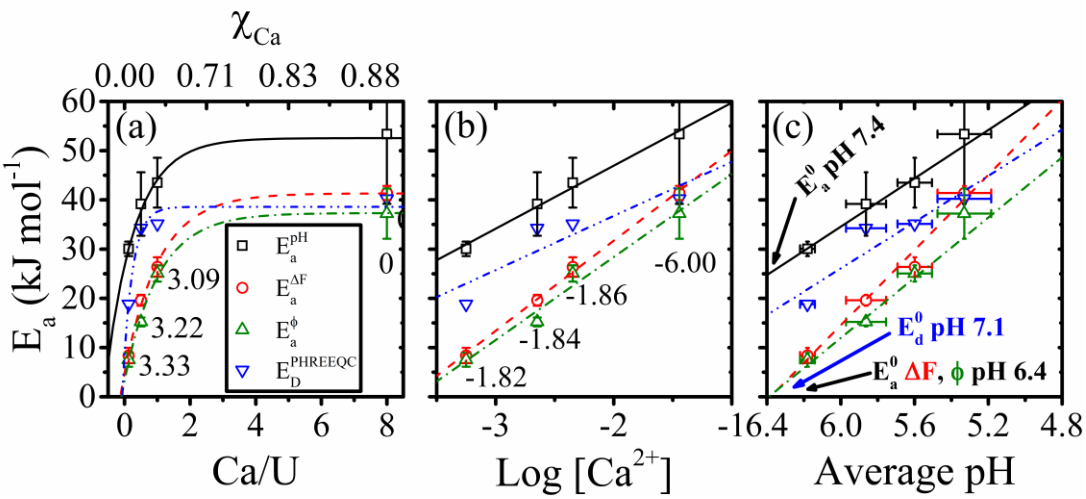

Figure 5.20 Apparent activation energies derived from ΔF, ϕ and PHREEQC mass transport modelling data as functions of initial (a) solution Ca/U-stoichiometry (lower) and Ca^{2+} mole fraction (upper); (b) log Ca^{2+} concentration; (c) second pH-maxima after the stabilisation region. Labelled values are precursor TMA^+ content as (a) TMA/U ratio, (b) log TMA^+-concentration and (c) average pH at precipitation onset. Y-error bars represent standard deviation of the mean of 3 – 9 trends, x-error bars in (c) represent variance of pH-maxima between 20 – 50 °C.

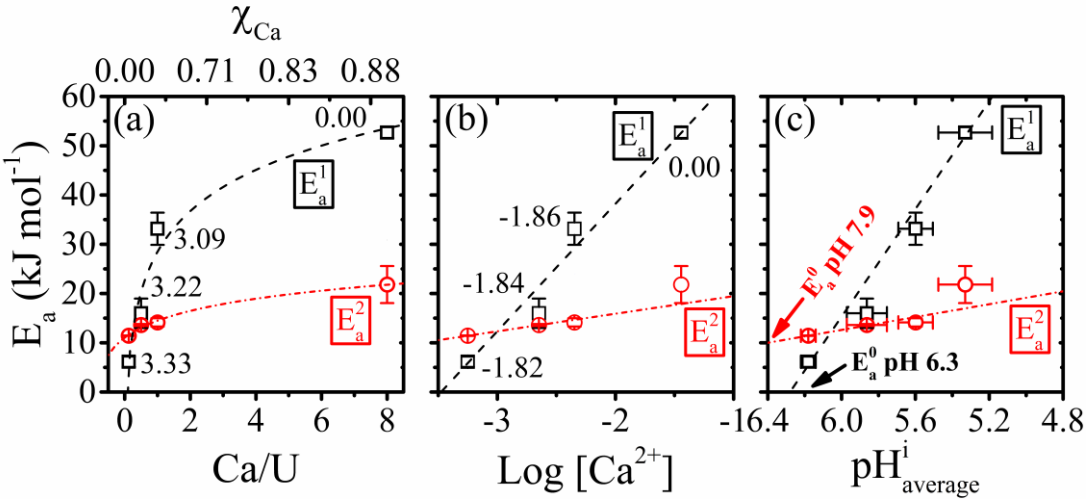

Figure 5.21 Derived activation energies E_a^1 (black) and E_a^2 (red) from k_1 and k_2 rate constants as a function of (a) spiked aliquot Ca/U stoichiometry and χ_{Ca}, (b) log Ca^{2+} concentration and (c) average initial pH of analyses, x-error bars represent pH variation between 20 and 50 °C.

This incongruent stoichiometry-dependence of the two kinetic processes results in a shift in the pH of zero activation (E_a^0), where the slow step (pH 7.9) appears similar

to that observed for hydroxide-sorption (Figure 5.20c, black, pH 7.4) and the fast step (pH 6.3) is closer to solid formation (Figure 5.20c, green, red, pH 6.4).

Table 5.6 Apparent activation energies derived from $lnk_{Tr.pH}$-T^{-1} Arrhenius plots Apparent activation energies derived from ΔF, ϕ and PHREEQC predicted mass transport data as a function of precursor solution Ca/U stoichiometry. Error values are standard deviation of the mean of 3 – 9 data sets.

Ca/U-stoichiometry	0.124	0.5	1	8
OH (pH) E_a (kJ mol^{-1})	30.06 ± 1.48	39.17 ± 6.44	43.49 ± 5.06	53.37 ± 14.18
Ln A	7.24 ± 0.79	9.69 ± 3.02	13.52 ± 1.25	15.65 ± 5.26
R^2	0.97	0.89	0.91	0.98
ΔF E_a (kJ mol^{-1})	8.4 ± 1.6	19.6 ± 1.1	26.4 ± 1.9	41.4 ± 1.4
Ln A	0.06	4.64	7.22	1.44
R^2	0.95	0.99	0.97	0.99
ϕ E_a (kJ mol^{-1})	7.5 ± 1.4	15.2 ± 0.9	25.05 ± 1.65	37.2 ± 5.1
Ln A	1.89 ± 0.56	3.9 ± 0.3	7.98 ± 0.71	12.6 ± 1.9
R^2	0.89	0.96	0.87	0.80
PHREEQC E_d (kJ mol^{-1})	18.8	34.2	35.1	40.2
D_0 (m^2 s^{-1})	$5.40*10^{-12}$	$3.73*10^{-9}$	$6.73*10^{-9}$	$7.10*10^{-8}$
R^2	0.95	0.99	0.95	0.97
D. Exp. E_a^1 (kJ mol^{-1})	6.1 ± 1.1	15.9 ± 2.9	33.1 ± 3.3	52.7 ± 1.1
Ln A_1	-0.187 ± 0.006	3.974 ± 0.005	11.068 ± 0.002	18.79 ± 0.01
R^2	0.94	0.93	0.97	0.98
D. Exp. E_a^2 (kJ mol^{-1})	11.4 ± 0.04	13.6 ± 0.2	14.1 ± 0.8	21.8 ± 3.8
Ln A_2	$-0.307 \pm 5*10^{-5}$	0.0027 ± 0.0008	0.557 ± 0.002	2.95 ± 0.01
R^2	0.94	0.93	0.98	0.99

5.4 Discussion

5.4.1 Titration reactions

The acid-base reactions (Figure 5.4) leading to the formation of uranyl(VI) oxyhydrate colloids appear to be influenced by reaction conditions such as temperature (20 – 50 °C) and the presence of electrolytes at fixed U(VI)-concentration. The associated kinetic barriers (Figure 5.12) and geometry (Figure 5.10) of precipitation exhibit dependency on the stoichiometry of background electrolytes, suggesting that the presence of TMA^+, Ca^{2+} and respective counter-ions (Cl^-, NO_3^-) could have a profound effect on reaction mechanisms that facilitate nucleation and growth. In addition to the data presented above, a series of precipitates were aged in solution at 30 °C for up to 70 days. During this time, some re-dissolution occurred (see Figure B18), whilst little growth (Figure B19, no broadening in 100% XRD peak) or phase change was apparent (Figure B19, no shift in XRD, FTIR peak positions). This indicates that primary precipitates probably have rather low interfacial energy, lying closely in stability to the pre-nucleation species rather than crystalline endmembers (see section 2.3.3.2). Furthermore, nucleation, growth, and aggregation processes could be coincident in controlling overall precipitation (see

section 2.3.3.1) [55]. Thusly, several factors that may contribute to uranyl(VI) oxyhydrate precipitation are discussed.

Mechanistic considerations: If cationic U(VI)-hydroxides in pre-nucleation clusters [1, 15] are stabilised by equatorial aqua-ligands [56], then condensation could occur via nucleophilic substitution (SN_1) [57] given the lability of aqua-ligands and stericity of oligomeric U(VI)-hydroxides [3] [39]. However, several studies indicate that associative, or associative interchange (SN_2) mechanisms are more likely during ligand exchange between hydroxo- and aqua- U(VI)-complexes with saturated coordination [58-62]. As hydroxo-functional groups (5.7 – 2.3e^-) are better electron-donors compared to aqua-ligands (1.9e^-), they likely act as nucleophile (Chernyaev-Schelokov series [63-65]). Regardless, the removal of electrostatic repulsion contributions (see section 2.3.4.2) between U-species could be required prior to coalescence, which may proceed via association of free hydroxide (e.g. $[(UO_2)_3(OH)_5]^+$) [57, 66]. The equatorial coordination of trimeric U-hydroxide complexes are stabilised by one or two aqua-ligands per U-centre until coordination saturation, where the U-hydroxo complex is more accurately represented as $[(UO_2)_3O(OH)_3(H_2O)_6]^+$ [67]. This indicates that condensation between cationic U(VI)-hydroxides (Figure 5.7, Figure 5.8, $[(UO_2)_3(OH)_5]^+$) probably occur via olation (H_2O-displacement) rather than oxolation as would be expected for anions that are coordination saturated with single-ligand types (e.g. $[UO_2(OH)_4]^{2-}$). Uranyl(VI)-hydroxides oligomerise[4] via this process (SN_2 associative-interchange) as a function of increasing pH [57] until its solution saturation-limit is reached, or the uranyl(VI)-equatorial-coordination substitution is completed (n = 6); if either condition is satisfied, coalescence of polymeric intermediates becomes favoured thermodynamically [57, 68]. However, studies on the formation of dinuclear and trinuclear uranyl(VI) hydroxide complexes under similar conditions (temperature and ionic strength) revealed hydrolysis enthalpies on the order of ~50 and ~120 kJ mol^{-1} respectively [69]. As precipitation likely occurs from the trimeric U-hydroxide species, its hydrolysis reaction becomes an unlikely candidate in limiting the rate of precipitation given that derived kinetic barriers (Figure 5.12) were considerably smaller regardless of Ca/U-ratio.

---

[3] An associative SN_2 by free hydroxide would require initial over-saturation of the U(VI)-coordination sphere in terms of number (steric) and electron-density before removal of an aqua ligand.

[4] For a given enthalpy of polymerisation ($\Delta G=\Delta H-T\Delta S$), entropy is negative (monomers → oligomer). Therefore $\Delta H-T\Delta S$ becomes more positive as a function of increasing T, whereby ΔG becomes more positive; destabilising larger polymers c.f. reduction in the extent of hydrolysis (polymerisation) h in Figure 5.22b.

Common-ion influence: The coalescence of uranyl(VI)-hydroxide polyhedra occurs when sheet valence reaches sufficiently neutral values (0.11 – 0.20 v.u.), stacking along the c-axis to form Schoepite[5] under low-Ca^{2+} conditions, or Becquerelite (0.14 – 0.23 v.u.) (Figure 5.22a) under the pH and Ca^{2+}-concentrations used [70, 71]. However, models assuming congruent precipitation of calcium and uranium reflected empirical data poorly (Figure 5.9), and the stoichiometry of filtered solids (Fig, Ca/U ~0.124 – 2.1) diverged significantly from that of Becquerelite (~0.17), as well as other known crystalline (0.25) [72] or amorphous Ca^{2+}-U(VI)-oxyhydrates [73, 74]. This suggests that towards higher precursor-Ca/U, a common-ion influence could increase the U(VI)-removal efficiency (Figure 5.6b), where excess-Ca^{2+} (Ca/U > 0.17) is removed as a uranyl(VI) oxyhydrate and Portlandite co-precipitate rather than a congruous hydrous uranate as suggested previously [1, 75]. This is supported by good consistency between empirical (Figure 5.22, m ~-0.41) and literature (Equation B1, m = -0.5) values for pK_a versus log [Ca^{2+}] plot gradients imposed by the law of mass action for uranyl(VI)-hydroxide phases [43]. In accordance with Le Chatelier's Principle, this favouring of the forward reaction stabilises the formation of end-member U-oxo-hydroxide complexes (Figure 5.8d, $[(UO_2)_3(OH)_5]^+$), consequently reducing the onset pH of precipitation (Figure 5.5, Figure 5.22a) despite higher extents of hydrolysis (h) (Figure 5.5, Figure 5.8, Figure 5.22b).

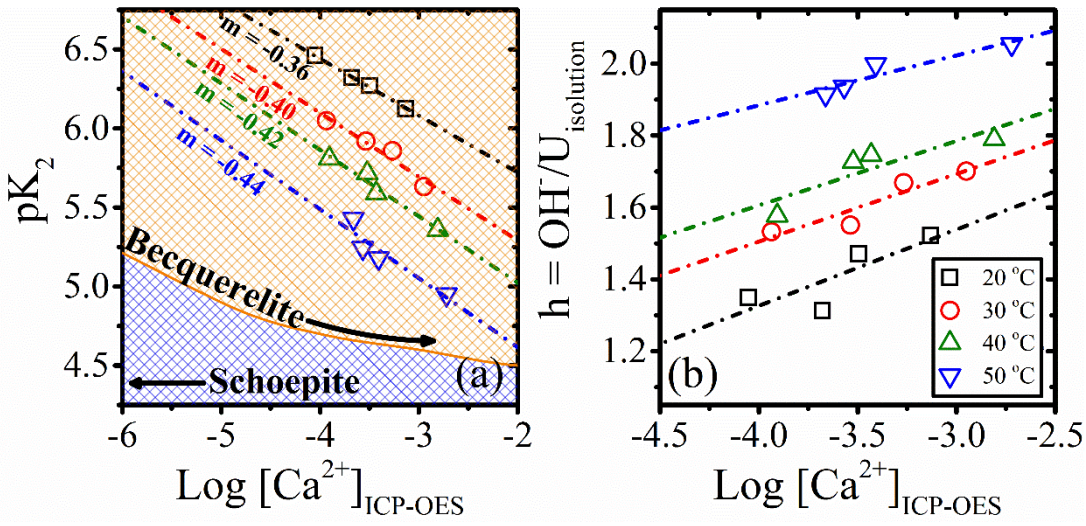

Figure 5.22 (a) pH (pK_2); and (b) consumed OH^- versus initial U(VI) (OH/U) ratio at onset of precipitation; as functions of measured log Ca^{2+} concentration.

The epitaxial association[6] or precipitation of Ca^{2+} onto basal-planes (c-axis [001]) of pre-nucleation species, or nascent nuclei, could favour growth along the equatorial b-

[5] Stacking is stabilised by μ_2-mode (bridging) hydrogen-bonding $^{U}_{U}> O - H - O - H - O <^{U}_{U}$

[6] $\mu_2 Ca - O <^{U}_{U}$ mode association

axis [76]. Given the expected stability fields (Figure 5.22a), this promotes formation of platelet-like (Figure 5.10b) particles that become more akin to Becquerelite in structure[7].

Intra-, and intermolecular influences on precipitation: If the coalescence of UO-polyhedral layers is favoured thermodynamically, and if the formation of prenucleation complexes is precluded, then the kinetic coalescence of pre-nucleation complexes could become pertinent in controlling nucleation and growth. From classical nucleation theory, an increase in effective ionic strength (higher Ca^{2+}, NO_3^-) would reduce interfacial energy (γ) via cation adsorption at the nuclei-solution interface [57, 79], favouring nucleation. The precursor ions OH^- [80, 81], Ca^{2+} [82], UO_2^{2+} [83] with high charge-density are classified as kosmotropes [84] due to their positive influence on the structural-order of water within immediate solvation shells. Combination of kosmotropic cations with chaotropic counterions (NO_3^-) or background species (TMA^+) results in oppositely-hydrated ion-pairs (kosmotrope-chaotrope), which increases kosmotrope-chaotrope ion separation distance to further enhance cation-hydration [84]. This reduces the mobility of bound water relative to bulk water [85], and promotes competitive ion-solvent interactions in multi-electrolyte systems. Hence, with increasing precursor Ca/U or Ca/TMA ratio, the relative mobility of water within solvation shells of prenucleation U(VI)-complexes is expected to increase [1]. It is further enhanced if kosmotropicity is additionally reduced by [U ←:OH] charge-donation in polynuclear U(VI)-hydroxides [86]. This alleviates kinetic desolvation barriers (lower residence water times [87-89]), which in turn reduces interfacial tension [90] and critical nuclei radii according to classical nucleation theory [91, 92]. The decrease in apparent pK_a (increase in K_a) with respect to formation of the neutral adduct from charged prenucleation U(VI)-complexes indicates favouring of the forward reaction, and is in line with the derived macroscopic kinetic barriers associated with precipitation (Figure 5.12b), which suggests that diffusion-controlled nucleation-coalescence dominates with increasing Ca/U (nucleation becomes favoured[8]), whilst surface-controlled nucleation-growth prevails at low precursor-Ca/U. According to DLVO theory (see section 2.3.4.2), the electrical double layer is likely compressed (smaller Debye length), resulting in

---

[7] After Hiemstra [77] and Schindler [78] (Equation B2a, b), formation of an equatorial bridging oxo-ligand between neighbouring U(VI) (Equation B2c) in dehydrated Schoepite should have an intrinsic pK_a of 7.72 [78] (literature value of ~7 [78]), significantly larger than that of Becquerelite (pK_a = 5.35).

[8] i.e. High Ca^{2+}-concentration decreases interfacial energy, favouring classical nucleation, whilst Ca^{2+}-hydration reduces solvent H-bonding, improving uranyl(VI) hydroxide complex hydration, disfavouring both nucleation and growth. Overall, nucleation is favoured, and growth disfavoured.

smaller inter-crystallite separation distances in the former (high Ca). This reduces the average degrees of freedom of crystallites undergoing reorientation, limiting oriented growth towards the coalescence stage (Figure 2.6, stage IV). This is supported by XRD, and TEM data in following sections (see section 6) which reveal a significant reduction in crystallite domain-size of precipitates with Ca/U above ~0.124. Moreover, their poorly-ordered nature indicates that crystallite orientation effects (see Figure 2.6) are probably insignificant, manifesting within JMAK geometric parameters (n) that exhibit isotactic (3D) growth towards low Ca/U, or aggregation (2D) towards high Ca/U. Notably, the occurrence of classical instead of oriented growth at the lowest Ca/U ratio, cannot be precluded.

As the coordination environment of pre-nucleation species $[(UO_2)_3(OH)_5(H_2O)_6]^+$ [93, 94] (Figure 5.7) is preserved during nucleation into the uranyl(VI) oxyhydrate sheet structure (Figure 5.22a) [78, 95], each complete olation could require a 2-step substitution (S_N2) to form the edge-sharing product. However, the electrophilicity of U-centres would be lowered after the first substitution, due to greater HO:→U charge-transfer compared to H_2O:→U [96]. Whilst this enhances the lability of aqua-ligands (dissociation step) in the intra-molecular second step, the nucleophilicity (basicity) of the U-OH functional group would be inhibited. From non-electrostatic considerations, sorption of tetraalkylammonium cations (NR_4^+) to bridging oxide moieties can occur regardless of surface charge [97-99], where NR_4-association[9] to hydrophobic μ_2-(M-O-M) functional-groups is favoured due to a reduction in the exposed surface area.

An increase in bulk NR_4^+-concentration is reflected in the electrical double layer, which could inhibit growth and enhance nucleation. Remarkably however, recent studies reveal that NMe_4^+ (TMA^+) deviates from this behaviour due to the hydrophilicity-enhancing effects of methyl groups via electronic induction [100]. Whilst this indicates that TMA^+ could have a similar mechanistic influence as Ca^{2+}, it is a lesser peptising agent due to its lower charge-density. Instead, Ca^{2+}-association to OH-functional groups would have a larger reduction on the basicity of the nucleophile, further inhibiting the second step. However, kinetic barriers associated with growth become less surface-limited with increasing Ca/U (Figure 5.12), which could preclude TMA^+- or Ca^{2+}-peptisation as key inhibitors. Conversely, the substantial increase in nitrate counter-ion concentration (2:1 NO_3:Ca) could increase $[(UO_2)_3(OH)_5^+$-$NO_3^-]$ complexation, which via a reduction in average separation

---

[9] Alkyl-groups on TMA^+-cations are highly hydrophobic. TMA^+-concentration in the electrical double layer (edl) may be approximated using the Boltzmann Distribution: $\frac{c_{edl}}{c_{bulk}} = \exp(\frac{-ze\varphi}{K_b T})$, where c_{edl}, c_{bulk} are TMA^+ concentrations in the double layer and bulk solution respectively; z, is the ionic charge; e, elementary charge; φ, the edl potential; K_b, the Boltzmann constant; T, absolute temperature.

distance, enhances inter-molecular oligomerisation (Figure 5.12c), and therefore nucleation (Figure 5.12, lower E_a) [101-103][10]. If nitrate- and TMA^+/Ca^{2+}-association are both contributing factors, then the increase in observed Ca^{2+}-removal at acidic pH (Figure 5.6) could be enhanced by sorption to peptised-NO_3^-, whilst a reduction in double layer steric hindrance (lower-TMA^+) would favour diffusion-limited growth.

5.4.2 Batch reactions

An instantaneous increase in Ca^{2+}-, UO_2^{2+}-concentration causes OH^--sorption from solution within the injected plume (Figure 5.13, pH minima, inset). Rapid neutralisation and homogenisation of Ca^{2+} and UO_2^{2+} discharges hydronium ions, protonating negatively charged Si- and Au-O^- functional groups on the QCM crystal surface (chapter 4, Figure 3 [1]). This reduces electrostatic charge, releasing TMA^+-cations from the stern- (specifically sorbed Au-O-TMA^+ [97]) and diffuse-layers, and is characterised by a reduction in interaction strength[11] (Figure 5.14, asterisk) [105] or effective energy-loss (Figure 5.14, ΔR dashed lines) between QCM-crystal and fluid-substrate [106]. The hydrolysis appears to be competitive between Ca^{2+}- and U(VI)-monomers given the increasing ΔF-peak magnitude with higher Ca/U (Figure 5.13b, inset) i.e. more OH-sorption. From the secondary pH-maxima (Figure 5.13c, d) onwards, kinetic modelling (Figure 5.3) indicates that ion-transport between the plume and QCM-crystal surface could elicit the early-stage ΔF-response. When Becquerelite is allowed to precipitate after the diffusion front (low pH side), the iteration of ion diffusion coefficients (Table B6, $2.64 – 22*10^{-10}$ $m^2\ s^{-1}$) deviated substantially from literature values ($D_{U(VI)} = 7.6*10^{-10}$, $D_{Ca} = 7.9*10^{-10}$ $m^2\ s^{-1}$ [107]). As uranate-precipitation behind the diffusion front (high pH side) was unaccounted for in the model, any competitive Ca^{2+}- and U(VI)-complexation would become enhanced by higher Ca/U, effective ionic strength and temperature. This would hinder formation of endmember U(VI)-hydroxides (e.g. $[(UO_2)_3(OH)_5]^+$), Becquerelite-precipitation; and in turn, inflating diffusion coefficients required to meet measured ΔF values with increasing solution Ca^{2+}-concentration and temperature (Table B6). However, this also increases apparent early-stage diffusion barriers (Figure 5.20, green) towards a boundary-limited regime (~ 40 kJ mol^{-1}), indicating that whilst Ca^{2+}-

[10] Association of anionic ligands is hypothesised to reduce the separation distance between metal centres of condensing hydroxide complexes, which could have extensive influence on subsequent nucleation via coalescence of precursor complexes.

[11] F is a measurement of crystal and substrate properties, a positive increase in ΔF suggests a reduction in rate of energy transfer to substrate (i.e. more energy loss); and usually suggests a more intimate contact between two discrete surfaces [104]. Resistance may be analogised as the efficiency of the energy transfer. With more viscoelastic collisions between surfaces, the resistance would also increase in opposition to the frequency, as more energy is lost to the working medium than to the elastic body. See Figure 3.3.

, U(VI)-transport appear contributory to early-stage (t → 0 s) ΔF-response, it is unlikely to be the sole mechanism.

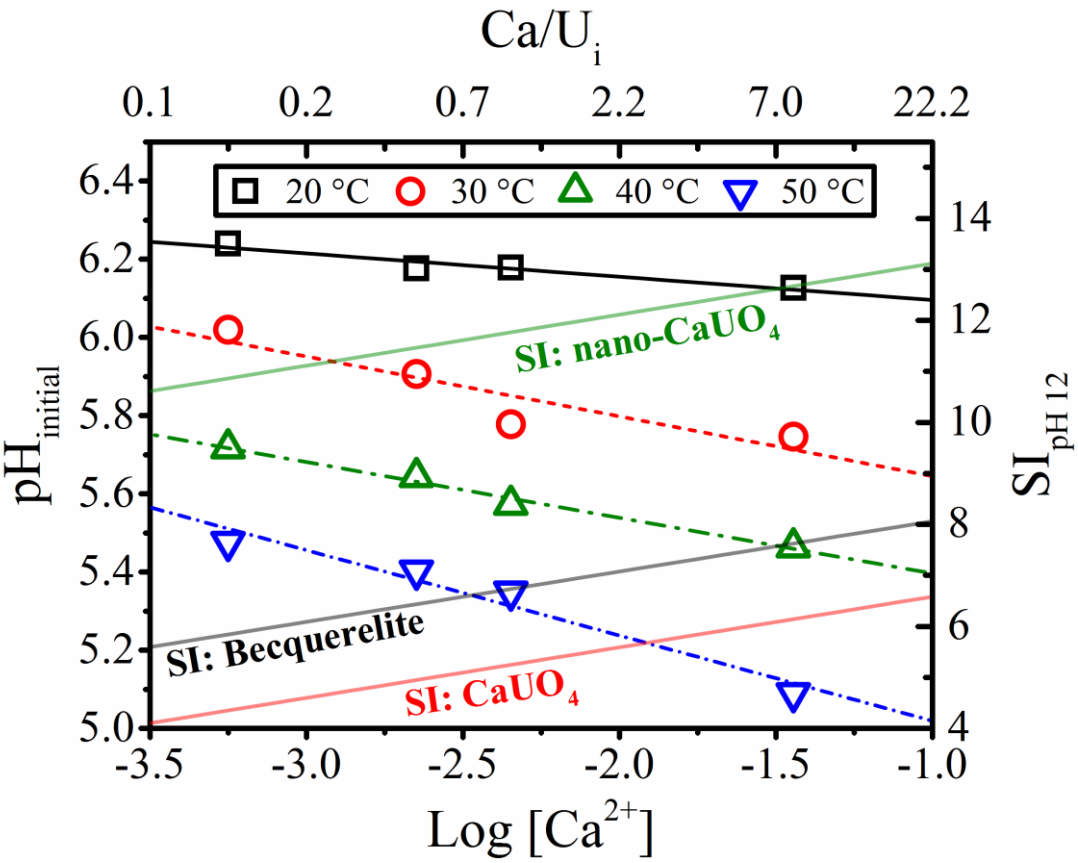

Figure 5.23 Values of secondary pH-maxima (Figure 5.13a, b) as a function of Ca/U-stoichiometry of injected aliquot (left) and; corresponding saturation indices of poorly-ordered Ca^{2+}-Clarkeite (nano-$CaUO_4$) [15], crystalline $CaUO_4$ and Becquerelite at pH 12 (right), as functions of log Ca^{2+}-concentration.

At t = 0 s (pH 12), highly basic uranate-phases (Figure 5.23, right y-axis)[12] could nucleate at the heterogeneous plume-solution interface from correspondingly anionic U(VI)-species [108] ($[UO_2OH_4]^{2-}$, h = 4, etc.) [15]; becoming more favoured with increasing Ca^{2+}-concentration [43] and higher local ionic strength, allowing condensation of larger or more numerous [109] nuclei according to the Gibbs-Thompson equation (Equation 5.9) [92].

$$r_c = \frac{2\Omega\sigma}{k_B T ln\left(\frac{IAP}{K_{sp}}\right)}$$

Equation 5.9

Where r_c is critical nuclei radius limit; Ω, the crystal volume per unit formula; k_B, Boltzmann constant; IAP, ion activity product of the phase; K_{sp}, solubility of the phase.

[12] See also: Section 4, Figure 4.1.

However, as homogenisation progresses (t > 0 s), the disparity in basicity between solution and nuclei becomes larger. Transiently formed uranates, now disfavoured under an increasingly acidic environment (Figure 5.13, ~pH 4.5 ~5.5) re-dissociate (Figure 5.21c, higher pH-increase with lower Ca/U, more OH^--release) into U(VI)-complexes of significantly lower OH/U (h) (Figure 5.16e, h = 1.67, 1.33 $[(UO_2)_3(OH)_5]^+$, $[(UO_2)_3(OH)_4]^{2+}$). Assuming secondary nucleation of less basic phases (Becquerelite-like) occurs in the following region from these dissolution-products, then a direct SN_1-condensation mechanism from anionic species could be precluded (Figure 5.14, OH^--releases first). If larger uranate particles were to form in the preceding step with increasing Ca^{2+}-concentration [92][13], this could inhibit subsequent re-dissolution rates given the reduction in total available surface area (A) or energy (σ), of larger nuclei (Equation 5.10) [110-112].

$$\log\left[K_{sp}^{small}\right] = \log\left[K_{sp}^{large}\right] + A\frac{2\sigma}{3RT}$$

Where K_{sp}^{small} is the solubility of smaller nuclei; K_{sp}^{large}, solubility of larger nuclei; A, the specific surface area; R, molar gas constant; T, absolute temperature. Equation 5.10

Therefore, with increasing injection-Ca/U, dissolution and condensation steps overlap more extensively, altering the apparent activation barriers for early-stage precipitation from that of diffusion-control via direct condensation of free U-oligomers (Figure 5.20, Figure 5.21, 8.4 – 6.1 kJ mol^{-1}), towards a surface-controlled mechanism limited by U-dissociation (Figure 5.20, Figure 5.21, 37.2 – 52.7 kJ mol^{-1}).

The considerable increase in activation barriers (Figure 5.21, black dash) coupled with a 7-fold reduction in final reaction extent going from Ca/U 0.124 to 8 (Figure 5.18a-d, ϕ values at t = 200 s), suggests that dissolution may become less complete before available surface-sites are completely shielded by zero-charge Becquerelite-like layers (PZC ~ pK_a). As this reduces total solution U-availability, the effective background Ca/U-stoichiometry becomes larger (as [U] → 0, Ca/U → ∞), further enhancing epitaxial Becquerelite precipitation. This reduces the net charge of uranate-Becquerelite core-shell colloids (PZC → $pK_{Becquerelite}$), encouraging particle aggregation at the QCM-surface to increase overall interaction strength ($\propto \Delta F^{-1}$). Therefore, when the rate of aggregation at a given temperature is enhanced by the rate of Becquerelite formation, the apparent reaction rates (Table 5.4, Table 5.5) increase with higher-Ca/U, despite larger apparent activation barriers (Figure 5.20, Figure 5.21) and a lower expected U-availability. In addition to early-stage dissolution-

[13] Larger Ionic Activity Product (IAP) term in the Gibbs-Thompson equation allows for a lower critical nuclei radii-limit (r_c) before the uranate-phase becomes stable. i.e. Higher $Ca^{2+} \propto \ln IAP \propto r^{*-1}$; allowing for larger uranate crystallites to form in the same time period.

precipitation-aggregation, a slower (Figure 5.21, k_2) process was apparent (Figure 5.21) with a similar mechanism of interaction with the QCM. Presumably, the inadequate representation of the reaction above t ~10 s by elementary rate expressions (Figure B28, Figure B29) is due to increasing overlap between the two processes (fast k_1 and slow k_2) at t → 200 s. Nevertheless, general activation barrier heights corresponding pH of zero-activation are similar, suggesting the same mechanism between the two data sets (Figure 5.20, $E_a^{\Delta F}$, E_a^{ϕ} and Figure 5.21, E_a^1).

The slower process (k_2) could relate to particle ripening effects [113, 114], given the diffusion-limited activation barriers found for all Ca^{2+}-concentrations (Figure 5.21 < ~20 kJ mol^{-1}). An increase in particle size through particle-particle crosslinking (intermolecular olation) in aggregated particle clusters would enhance QCM-resonator to substrate energy transfer (more rigid particles), increasing final ΔF-values (Figure 5.18, increasing Ca/U). Indeed, the slower process appears dominant (Figure 5.21, $E_a^2 > E_a^1$ at Ca/U = 0.124) when there is least overlap between dissolution-precipitation mechanisms, where a better uranate to Becquerelite conversion is expected to occur initially, allowing for more extensive aggregation of neutral particles. Ripening (Figure 5.21c, E_a^2) and early-stage hydroxide-sorption (Figure 5.20c, E_a^{OH}) could have the same mechanistic influences, given their comparable pH of zero-activation values (7.9, 7.4). If the former involves U-migration from small to large neighbouring particles, then an higher hydroxide availability (pH) could enhance ripening by promoting complexation-dissociation of U-oligomers [76, 115].

5.5 Summary and implications

The kinetics of U(VI)-colloid formation in the presence of calcium, nitrate and tetramethylammonium [116, 117] ions were quantified under moderate conditions[14]. The influence of precursor stoichiometry (Ca/U) on kinetic barriers to precipitation was explored using titration and batch reactions. In the former, precipitation mechanisms are controlled by concerted nucleation, growth and aggregation/coalescence processes. Diffusion-controlled nucleation and aggregation becomes favoured with increasing solution Ca/U (Scheme 5.1a, black trend), whereas surface-limited growth via classical or non-classical (oriented attachment) mechanisms dominate at low Ca/U (Scheme 5.1a, blue trend).

[14] Oxic waters, 20 < T °C < 50, ~0.11< γ < ~0.04 mol Kg^{-1}.

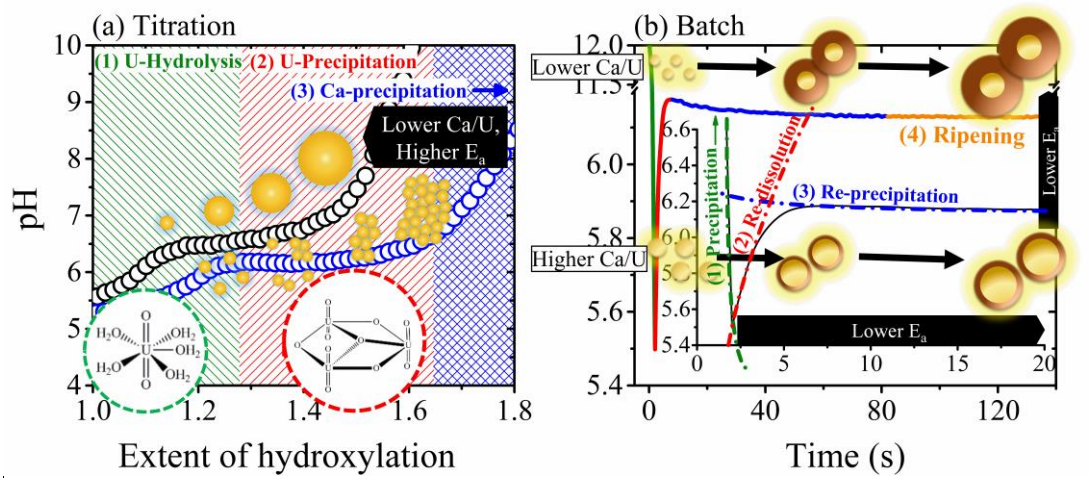

Scheme 5.1 Conceptual diagrams for titration and batch reactions that summarise study findings.

In batch experiments, the injection of Ca^{2+} and UO_2^{2+} ions into a pH 12 solution favoured nucleation of uranate-like phases via rapid sorption of hydroxide [15, 93, 118, 119], reducing solution pH (Scheme 5.1b, green-trend). Subsequent dissolution of nascent nuclei (Scheme 5.1b, red-trend) releases cationic U-hydroxide species are expected to re-precipitate as Becquerelite (Scheme 5.1b, blue trend). This was represented in ΔF-trends, revealing two kinetic mechanisms attributable to nucleation and growth. The two processes became more overlapped as a function of increasing Ca/U-stoichiometry in the injected aliquot. In contradiction to the former regime, the activation barriers associated with precipitation increased in magnitude towards higher Ca^{2+}-concentration. However, whilst growth remained diffusion-limited, nucleation became boundary-limited under Ca^{2+}-excessive conditions. As larger uranate nuclei were favoured by higher injected-Ca/U, this was attributed to a reduction in total U-availability as a result of inhibited dissolution rates (reduction in surface area).

The studies outlined here reveal that formation mechanisms and kinetic barriers associated with uranyl(VI) oxyhydrate precipitation, as well as their particle morphology and meso-structure, are profoundly affected by the presence of background electrolytes such as calcium, nitrate and quaternary alkyl-ammonium ions; on top of previously defined factors such as temperature [35], U(VI)-concentration [27] or homogeneity [26]. This adds a significant level of complexity to industrial and environmental colloidal uranium chemistry, emphasising the need for further investigation.

5.6 Further recommendations

The quartz crystal microbalance has been highlighted as a method applicable to in-situ characterisation of the kinetics of precipitation of poorly-ordered U(VI) particles. However, significant simplifications and assumptions were made to allow semi-quantitative analysis of the data obtained. In particular, that the nucleation and growth particles are homogenous and that the sorbed substrate, the nanofluid, increases its viscosity due to increasing particle fraction ϕ. This provides a theoretical alternative to that of previous studies which assume that nucleation and growth occurs via specific sorption of a homogenous and rigid layer on the QCM-crystal (with ideal energy transfer), allowing for Sauerbrey-like conditions. A new study [120] has since made significant theoretical improvements on in-situ dynamic QCM for inorganic precipitation reactions, whereby the precipitating phase is rigid and crystallographically well-defined. It develops the theoretical framework provided by Johannsmann and Pomorska [104, 105] by combining the viscoelastic changes caused by fluid trapping during heterogeneous nucleation, as well as the effects of primary crystallites on the energy transfer (frequency loading) with the resonating QCM-crystal. By correlating a population density function to the QCM-crystal impedance, and using nuclei population numbers from parallel microscopy analysis, a direct correlation was made between the effective ΔF and the nuclei population. However, it appears in its current form inapplicable to the studies here, where both solid phase and reaction mechanisms are poorly-defined.

To improve on this study, several in-situ laboratory and synchrotron techniques could complement current understanding of mechanisms occurring at the crystal-substrate interface. In particular, small- and wide-angle scattering (SAX/WAX) could provide excellent supporting information on the nucleation mechanisms in terms of the nuclei size and shape, whilst in-situ X-ray absorption spectroscopy (XAS, fast-XAFS, XANES) would provide valuable structural data on evolving or reacting precursor species as well as nuclei identities without some of the light-opacity issues associated with optical techniques. In particular, classical and oriented growth mechanisms during precipitation could be discriminated by aging oxyhydrate crystallite suspensions. Specifically, the titration reaction is stopped at the onset pH of precipitation at a fixed Ca/U-stoichiometry, at various temperatures, then allowed to age at constant pH. The subsequent QCM response is then related to growth via classical or oriented growth. If activation barriers are quantified for reactions containing TMA^+ ions, a positive trend should coincide with larger XRD-Scherrer diameters [121] as a function of increasing TMA^+-concentration [122].

5.7 References

1. Ding, W., Botha, J.A., Hanson, B.C., and Burke, I.T., *Aqueous Hydroxylation Mediated Synthesis of Crystalline Calcium Uranate Particles.* Journal of Alloys and Compounds, 2016. **688, Part B**: p. 260-269.
2. Abdel-Aal, N., Satoh, K., and Sawada, K., *Study of the Adhesion Mechanism of Caco3 Using a Combined Bulk Chemistry/Qcm Technique.* Journal of Crystal Growth, 2002. **245**(1–2): p. 87-100.
3. Zarga, Y., Ben Boubaker, H., Ghaffour, N., and Elfil, H., *Study of Calcium Carbonate and Sulfate Co-Precipitation.* Chemical Engineering Science, 2013. **96**: p. 33-41.
4. Abdel-Aal, N. and Sawada, K., *Inhibition of Adhesion and Precipitation of Caco3 by Aminopolyphosphonate.* Journal of Crystal Growth, 2003. **256**(1–2): p. 188-200.
5. Chen, T., Neville, A., and Yuan, M., *Influence of on Formation—Bulk Precipitation and Surface Deposition.* Chemical Engineering Science, 2006. **61**(16): p. 5318-5327.
6. Zhang, Q., Lai, W.S., Yang, G.W., and Liu, B.X., *Solid-State Interfacial Reaction and Asymmetric Growth of Amorphous Interlayers in Ni/Nb Multilayers. Molecular-Dynamics Simulation Together with Experiments.* European Physical Journal B, 2000. **16**(2): p. 223-231.
7. Gorman-Lewis, D., Burns, P.C., and Fein, J.B., *Review of Uranyl Mineral Solubility Measurements.* The Journal of Chemical Thermodynamics, 2008. **40**(3): p. 335-352.
8. Group, C.T., *Individual Monitoring for Intakes of Radionuclides by Workers: Design and Interpretation*. 1988, No longer published by Elsevier.
9. Bertsch, P.M., Hunter, D.B., Sutton, S.R., Bajt, S., and Rivers, M.L., *In Situ Chemical Speciation of Uranium in Soils and Sediments by Micro X-Ray Absorption Spectroscopy.* Environmental science & technology, 1994. **28**(5): p. 980-984.
10. Buck, E.C., Brown, N.R., and Dietz, N.L., *Contaminant Uranium Phases and Leaching at the Fernald Site in Ohio.* Environmental science & technology, 1995. **30**(1): p. 81-88.
11. Morris, D.E., Allen, P.G., Berg, J.M., Chisholm-Brause, C.J., Conradson, S.D., Donohoe, R.J., Hess, N.J., Musgrave, J.A., and Tait, C.D., *Speciation of Uranium in Fernald Soils by Molecular Spectroscopic Methods: Characterization of Untreated Soils.* Environmental science & technology, 1996. **30**(7): p. 2322-2331.
12. Amonette, J., Holdren Jr, G., Krupa, K., and Lindenmeier, C., *Assessing the Environmental Availability of Uranium in Soils and Sediments*. 1994, Nuclear Regulatory Commission, Washington, DC (United States). Div. of Waste Management; Pacific Northwest Lab., Richland, WA (United States).
13. Clark, D.L., Conradson, S.D., Donohoe, R.J., Keogh, D.W., Morris, D.E., Palmer, P.D., Rogers, R.D., and Tait, C.D., *Chemical Speciation of the Uranyl Ion under Highly Alkaline Conditions. Synthesis, Structures, and Oxo Ligand Exchange Dynamics.* Inorganic Chemistry, 1999. **38**(7): p. 1456-1466.
14. Wahlgren, U., Moll, H., Grenthe, I., Schimmelpfennig, B., Maron, L., Vallet, V., and Gropen, O., *Structure of Uranium (Vi) in Strong Alkaline Solutions. A Combined Theoretical and Experimental Investigation.* The Journal of Physical Chemistry A, 1999. **103**(41): p. 8257-8264.
15. Bots, P., Morris, K., Hibberd, R., Law, G.T.W., Mosselmans, J.F.W., Brown, A.P., Doutch, J., Smith, A.J., and Shaw, S., *Formation of Stable Uranium(Vi) Colloidal Nanoparticles in Conditions Relevant to Radioactive Waste Disposal*. Langmuir, 2014. **30**(48): p. 14396-14405.
16. Froideval, A., Del Nero, M., Barillon, R., Hommet, J., and Mignot, G., *Ph Dependence of Uranyl Retention in a Quartz/Solution System: An Xps Study.* Journal of Colloid and Interface Science, 2003. **266**(2): p. 221-235.
17. Harfouche, M., Wieland, E., Dähn, R., Fujita, T., Tits, J., Kunz, D., and Tsukamoto, M., *Exafs Study of U(Vi) Uptake by Calcium Silicate Hydrates.* Journal of colloid and interface science, 2006. **303**(1): p. 195-204.
18. Priyadarshini, N., Sampath, M., Kumar, S., Mudali, U.K., and Natarajan, R., *A Combined Spectroscopic and Light Scattering Study of Hydrolysis of Uranium(Vi) Leading to Colloid Formation in Aqueous Solutions.* Journal of Radioanalytical and Nuclear Chemistry, 2013. **298**(3): p. 1923-1931.
19. Priyadarshini, N., Sampath, M., Kumar, S., Mudali, U.K., and Natarajan, R., *Probing Uranium (Iv) Hydrolyzed Colloids and Polymers by Light Scattering.* Journal of Nuclear Chemistry, 2014. **2014**.

20. Swanton, S.W. and Vines, S., *Equilibrium Leach Tests: Colloid Generation and the Association of Radionuclides with Colloids under Simulated Repository Conditions.* Colloids and Surfaces A: Physicochemical and Engineering Aspects, 2003. **217**(1–3): p. 71-79.
21. Walther, C. and Denecke, M.A., *Actinide Colloids and Particles of Environmental Concern.* Chemical Reviews, 2013. **113**(2): p. 995-1015.
22. Hudry, D., Apostolidis, C., Walter, O., Gouder, T., Courtois, E., Kubel, C., and Meyer, D., *Controlled Synthesis of Thorium and Uranium Oxide Nanocrystals.* Chemistry-a European Journal, 2013. **19**(17): p. 5297-5305.
23. Hudry, D., Apostolidis, C., Walter, O., Gouder, T., Courtois, E., Kübel, C., and Meyer, D., *Non-Aqueous Synthesis of Isotropic and Anisotropic Actinide Oxide Nanocrystals.* Chemistry – A European Journal, 2012. **18**(27): p. 8283-8287.
24. Reibold, R.A., Poco, J.F., Baumann, T.F., Simpson, R.L., and Satcher Jr, J.H., *Synthesis and Characterization of a Low-Density Urania (Uo_3) Aerogel.* Journal of Non-Crystalline Solids, 2003. **319**(3): p. 241-246.
25. Janov, J., Alfredson, P.G., and Vilkaitis, V.K., *The Influence of Precipitation Conditions on the Properties of Ammonium Diuranate and Uranium Dioxide Powders.* Journal of Nuclear Materials, 1972. **44**(2): p. 161-174.
26. Manna, S., Basak, C., Thakkar, U.R., Thakur, S., Roy, S.B., and Joshi, J.B., *Study on Effect of Process Parameters and Mixing on Morphology of Ammonium Diuranate.* Journal of Radioanalytical and Nuclear Chemistry, 2016. **310**(1): p. 287-299.
27. Murty, B.N., Balakrishna, P., Yadav, R., and Ganguly, C., *Influence of Temperature of Precipitation on Agglomeration and Other Powder Characteristics of Ammonium Diuranate.* Powder technology, 2001. **115**(2): p. 167-183.
28. Kim, K.-W., Kim, Y.-H., Lee, S.-Y., Lee, J.-W., Joe, K.-S., Lee, E.-H., Kim, J.-S., Song, K., and Song, K.-C., *Precipitation Characteristics of Uranyl Ions at Different Phs Depending on the Presence of Carbonate Ions and Hydrogen Peroxide.* Environmental Science & Technology, 2009. **43**(7): p. 2355-2361.
29. Manna, S., Thakkar, U.R., Satpati, S.K., Roy, S.B., Joshi, J.B., and Chakravartty, J.K., *Study of Crystal Growth and Effect of Temperature and Mixing on Properties of Sodium Diuranate.* Progress in Nuclear Energy, 2016. **91**: p. 132-139.
30. Riba, O., Walker, C., and Ragnarsdottir, K.V., *Kinetic Studies of Synthetic Metaschoepite under Acidic Conditions in Batch and Flow Experiments.* Environmental Science & Technology, 2005. **39**(20): p. 7915-7920.
31. Ainscough, J. and Oldfield, B., *Effect of Ammonium Diuranate Precipitation Conditions on the Characteristics and Sintering Behaviour of Uranium Dioxide.* Journal of Chemical Technology and Biotechnology, 1962. **12**(9): p. 418-424.
32. Ball, M.C., Birkett, C.R.G., Brown, D.S., and Jaycock, M.J., *The Thermal Decomposition of Ammonium Diuranate.* Journal of Inorganic and Nuclear Chemistry, 1974. **36**(7): p. 1527-1529.
33. Eloirdi, R., Ho Mer Lin, D., Mayer, K., Caciuffo, R., and Fanghänel, T., *Investigation of Ammonium Diuranate Calcination with High-Temperature X-Ray Diffraction.* Journal of Materials Science, 2014. **49**(24): p. 8436-8443.
34. Le Page, A.H. and Fane, A.G., *The Kinetics of Hydrogen Reduction of Uo_3 and U_3o_8 Derived from Ammonium Diuranate.* Journal of Inorganic and Nuclear Chemistry, 1974. **36**(1): p. 87-92.
35. Manna, S., Karthik, P., Mukherjee, A., Banerjee, J., Roy, S.B., and Joshi, J.B., *Study of Calcinations of Ammonium Diuranate at Different Temperatures.* Journal of Nuclear Materials, 2012. **426**(1–3): p. 229-232.
36. Stuart, W.I. and Whateley, T.L., *Composition and Structure of Ammonium Uranates.* Journal of Inorganic and Nuclear Chemistry, 1969. **31**(6): p. 1639-1647.
37. Deane, A., *The Infra-Red Spectra and Structures of Some Hydrated Uranium Trioxides and Ammonium Diuranates.* Journal of Inorganic and Nuclear Chemistry, 1961. **21**(3-4): p. 238-252.
38. Ciavatta, L., *The Specific Interaction Theory in Evaluating Ionic Equilibria.* 1980.
39. Steppert, M., Walther, C., Fuss, M., and Büchner, S., *On the Polymerization of Hexavalent Uranium. An Electrospray Mass Spectrometry Study.* Rapid Communications in Mass Spectrometry, 2012. **26**(6): p. 583-591.
40. MacDonald, D.D., Butler, P., and Owen, D., *High Temperature Aqueous Electrolyte Concentration Cells and the Ionization of Liquid Water to 200 °C.* Canadian Journal of Chemistry, 1973. **51**(15): p. 2590-2595.

41. Po, H.N. and Senozan, N., *The Henderson-Hasselbalch Equation: Its History and Limitations.* J. Chem. Educ, 2001. **78**(11): p. 1499.
42. Schindler, M. and Hawthorne, F.C., *A Bond-Valence Approach to the Structure, Chemistry and Paragenesis of Hydroxy-Hydrated Oxysalt Minerals. Ii. Crystal Structure and Chemical Composition of Borate Minerals.* The Canadian Mineralogist, 2001. **39**(5): p. 1243-1256.
43. Schindler, M. and Hawthorne, F.C., *A Bond-Valence Approach to the Uranyl-Oxide Hydroxy-Hydrate Minerals: Chemical Composition and Occurrence.* The Canadian Mineralogist, 2004. **42**(6): p. 1601-1627.
44. Agmon, N., Bakker, H.J., Campen, R.K., Henchman, R.H., Pohl, P., Roke, S., Thämer, M., and Hassanali, A., *Protons and Hydroxide Ions in Aqueous Systems.* Chemical Reviews, 2016. **116**(13): p. 7642-7672.
45. Yoon, R.H., Salman, T., and Donnay, G., *Predicting Points of Zero Charge of Oxides and Hydroxides.* Journal of Colloid and Interface Science, 1979. **70**(3): p. 483-493.
46. Parks, G.A. and Bruyn, P.L.d., *The Zero Point of Charge of Oxides I.* The Journal of Physical Chemistry, 1962. **66**(6): p. 967-973.
47. Einstein, A., *Eine Neue Bestimmung Der Moleküldimensionen.* Annalen der Physik, 1906. **324**(2): p. 289-306.
48. Brinkman, H.C., *The Viscosity of Concentrated Suspensions and Solutions.* The Journal of Chemical Physics, 1952. **20**(4): p. 571-571.
49. Johnson, W.A. and Mehl, R.F., *Reaction Kinetics in Processes of Nucleation and Growth.* Trans. Aime, 1939. **135**(8): p. 396-415.
50. Avrami, M., *Kinetics of Phase Change. I General Theory.* The Journal of Chemical Physics, 1939. **7**(12): p. 1103-1112.
51. Avrami, M., *Kinetics of Phase Change. Ii Transformation ‐ Time Relations for Random Distribution of Nuclei.* The Journal of Chemical Physics, 1940. **8**(2): p. 212-224.
52. Avrami, M., *Granulation, Phase Change, and Microstructure Kinetics of Phase Change. Iii.* The Journal of Chemical Physics, 1941. **9**(2): p. 177-184.
53. Kolmogorov, A., *Selected Works. Vol. Ii.* 1992.
54. Lasaga, A.C., *Chemical Kinetics of Water-Rock Interactions.* Journal of Geophysical Research: Solid Earth, 1984. **89**(B6): p. 4009-4025.
55. Jolivet, J.-P., Tronc, É., and Chanéac, C., *Synthesis of Iron Oxide-Based Magnetic Nanomaterials and Composites.* Comptes Rendus Chimie, 2002. **5**(10): p. 659-664.
56. Krivovichev, S., Burns, P., and Tananaev, I., *Structural Chemistry of Inorganic Actinide Compounds*. 2006: Elsevier.
57. Jolivet, J.-P., Henry, M., and Livage, J., *Metal Oxide Chemistry and Synthesis: From Solution to Solid State*. 2000: Wiley-Blackwell.
58. Tsushima, S., *Hydration and Water-Exchange Mechanism of the Uo_2^{2+} Ion Revisited: The Validity of the "N + 1" Model.* The Journal of Physical Chemistry A, 2007. **111**(18): p. 3613-3617.
59. Vallet, V., Wahlgren, U., and Grenthe, I., *Probing the Nature of Chemical Bonding in Uranyl(Vi) Complexes with Quantum Chemical Methods.* The Journal of Physical Chemistry A, 2012. **116**(50): p. 12373-12380.
60. Farkas, I., Bányai, I., Szabó, Z., Wahlgren, U., and Grenthe, I., *Rates and Mechanisms of Water Exchange of $Uo_2^{2+(Aq)}$ and $Uo_2(Oxalate)F(H_2o)_2^-$: A Variable-Temperature ^{17}o and ^{19}f Nmr Study.* Inorganic chemistry, 2000. **39**(4): p. 799-805.
61. Bühl, M. and Kabrede, H., *Mechanism of Water Exchange in Aqueous Uranyl(Vi) Ion. A Density Functional Molecular Dynamics Study.* Inorganic Chemistry, 2006. **45**(10): p. 3834-3836.
62. Kerisit, S. and Liu, C., *Structure, Kinetics, and Thermodynamics of the Aqueous Uranyl (Vi) Cation.* The Journal of Physical Chemistry A, 2013. **117**(30): p. 6421-6432.
63. Shchelokov, R., *Khimiya Platinovykh I Tyazhelykh Metallov (the Chemistry of Platinum and Heavy Metals)*. 1975, Moscow: Nauka.
64. Vdovenko, V., Mashirov, L., and Suglobov, D., *Bond Orders in Uranyl Compounds.* Dokl. Akad. Nauk SSSR, 167: 1299-1302 (Apr. 21, 1966). 1966.
65. Suglobov, D. and Mashirov, L., *Chemical Bond in Actinide Oxocation Compounds.* Radiokhimiya, 1975. **17**(5): p. 699-705.
66. Livage, J., Henry, M., and Sanchez, C., *Sol-Gel Chemistry of Transition Metal Oxides.* Progress in solid state chemistry, 1988. **18**(4): p. 259-341.
67. Quilès, F. and Burneau, A., *Infrared and Raman Spectra of Uranyl(Vi) Oxo-Hydroxo Complexes in Acid Aqueous Solutions: A Chemometric Study.* Vibrational Spectroscopy, 2000. **23**(2): p. 231-241.

68. Henry, M., Jolivet, J., and Livage, J., *Aqueous Chemistry of Metal Cations: Hydrolysis, Condensation and Complexation.* Chemistry, Spectroscopy and Applications of Sol-Gel Glasses, 1992: p. 153-206.
69. Zanonato, P., Di Bernardo, P., Bismondo, A., Liu, G., Chen, X., and Rao, L., *Hydrolysis of Uranium(Vi) at Variable Temperatures (10−85 °C).* Journal of the American Chemical Society, 2004. **126**(17): p. 5515-5522.
70. Weller, M.T., Light, M.E., and Gelbrich, T., *Structure of Uranium(Vi) Oxide Dihydrate, $Uo_3.2h_2o$; Synthetic Meta-Schoepite $(Uo_2)_4o(Oh)6.5h_2o$.* Acta Crystallographica Section B, 2000. **56**(4): p. 577-583.
71. Alam, T.M., Liao, Z., Nyman, M., and Yates, J., *Insight into Hydrogen Bonding of Uranyl Hydroxide Layers and Capsules by Use of 1h Magic-Angle Spinning Nmr Spectroscopy.* The Journal of Physical Chemistry C, 2016. **120**(19): p. 10675-10685.
72. Glatz, R.E., Li, Y., Hughes, K.-A., Cahill, C.L., and Burns, P.C., *Synthesis and Structure of a New Ca Uranyl Oxide Hydrate, $Ca[(Uo_2)_4o_3(Oh)_4](H_2o)_2$, and Its Relationship to Becquerelite.* The Canadian Mineralogist, 2002. **40**(1): p. 217-224.
73. Rogova, V., Belova, L., Kiziyarov, G., and Kuznetsova, N., *Calciouranoite, a New Hydroxide of Uranium.* International Geology Review, 1974. **16**(11): p. 1255-1256.
74. Rogova, V., Belova, L., Kiziyarov, G., and Kuznetsova, N., *Bauranoite and Metacalciouranoite, New Minerals of the Hydrous Uranium Oxides Group*. International Geology Review, 1974. **16**(2): p. 214-219.
75. Moroni, L.P. and Glasser, F.P., *Reactions between Cement Components and U(Vi) Oxide.* Waste Management, 1995. **15**(3): p. 243-254.
76. Schindler, M., Hawthorne, F.C., Burns, P.C., and Maurice, P.A., *Dissolution of Uranyl-Oxide-Hydroxy-Hydrate Minerals. Ii. Becquerelite.* The Canadian Mineralogist, 2006. **44**(5): p. 1207-1225.
77. Hiemstra, T., Venema, P., and Van Riemsdijk, W.H., *Intrinsic Proton Affinity of Reactive Surface Groups of Metal (Hydr) Oxides: The Bond Valence Principle.* Journal of colloid and interface science, 1996. **184**(2): p. 680-692.
78. Schindler, M., Mutter, A., Hawthorne, F.C., and Putnis, A., *Prediction of Crystal Morphology of Complex Uranyl-Sheet Minerals. I. Theory.* The Canadian Mineralogist, 2004. **42**(6): p. 1629-1649.
79. Nielsen, A.E., *Kinetics of Precipitation*. Vol. 350. 1964: Pergamon Press Oxford.
80. Tuckerman, M., Laasonen, K., Sprik, M., and Parrinello, M., *Ab Initio Molecular Dynamics Simulation of the Solvation and Transport of Hydronium and Hydroxyl Ions in Water.* The Journal of Chemical Physics, 1995. **103**(1): p. 150-161.
81. Ruiz-Agudo, C., Putnis, C.V., Ruiz-Agudo, E., and Putnis, A., *The Influence of Ph on Barite Nucleation and Growth.* Chemical Geology, 2015. **391**: p. 7-18.
82. Peschke, M., Blades, A.T., and Kebarle, P., *Hydration Energies and Entropies for Mg^{2+}, Ca^{2+}, Sr^{2+}, and Ba^{2+} from Gas-Phase Ion−Water Molecule Equilibria Determinations.* The Journal of Physical Chemistry A, 1998. **102**(48): p. 9978-9985.
83. Chopra, M. and Choudhury, N., *Effect of Uranyl Ion Concentration on Structure and Dynamics of Aqueous Uranyl Solution: A Molecular Dynamics Simulation Study.* The Journal of Physical Chemistry B, 2014. **118**(49): p. 14373-14381.
84. Hribar, B., Southall, N.T., Vlachy, V., and Dill, K.A., *How Ions Affect the Structure of Water*. Journal of the American Chemical Society, 2002. **124**(41): p. 12302-12311.
85. Samoĭlov, O.I.A.k., *Structure of Aqueous Electrolyte Solutions and the Hydration of Ions*. 1965: Consultants Bureau.
86. Chien, W., Anbalagan, V., Zandler, M., Van Stipdonk, M., Hanna, D., Gresham, G., and Groenewold, G., *Intrinsic Hydration of Monopositive Uranyl Hydroxide, Nitrate, and Acetate Cations.* Journal of the American Society for Mass Spectrometry, 2004. **15**(6): p. 777-783.
87. Kowacz, M., Prieto, M., and Putnis, A., *Kinetics of Crystal Nucleation in Ionic Solutions: Electrostatics and Hydration Forces.* Geochimica et Cosmochimica Acta, 2010. **74**(2): p. 469-481.
88. Kowacz, M. and Putnis, A., *The Effect of Specific Background Electrolytes on Water Structure and Solute Hydration: Consequences for Crystal Dissolution and Growth.* Geochimica et Cosmochimica Acta, 2008. **72**(18): p. 4476-4487.
89. Ruiz-Agudo, E., Kowacz, M., Putnis, C., and Putnis, A., *The Role of Background Electrolytes on the Kinetics and Mechanism of Calcite Dissolution.* Geochimica et cosmochimica acta, 2010. **74**(4): p. 1256-1267.

90. Kowacz, M., Putnis, C., and Putnis, A., *The Effect of Cation: Anion Ratio in Solution on the Mechanism of Barite Growth at Constant Supersaturation: Role of the Desolvation Process on the Growth Kinetics.* Geochimica et Cosmochimica Acta, 2007. **71**(21): p. 5168-5179.
91. Thomson, W., *Ix. On the Equilibrium of Vapour at a Curved Surface of Liquid*. Philosophical Magazine, 1871. **42**(282): p. 448-452.
92. De Yoreo, J.J. and Vekilov, P.G., *Principles of Crystal Nucleation and Growth.* Reviews in mineralogy and geochemistry, 2003. **54**(1): p. 57-93.
93. Baran, V., *Relation between Precipitated and High-Temperature Sodium Uranates.* Journal of Radioanalytical and Nuclear Chemistry-Letters, 1988. **128**(2): p. 155-163.
94. Baran, V. and Tympl, M., *Uranates as a Form of Uranyl Hydrolytic Complexes.* Journal of Inorganic and Nuclear Chemistry, 1966. **28**(1): p. 89-98.
95. Moll, H., Reich, T., and Szabo, Z., *The Hydrolysis of Dioxouranium (Vi) Investigated Using Exafs and 17o-Nmr.* Radiochimica acta, 2000. **88**(7): p. 411-416.
96. Hemmingsen, L., Amara, P., Ansoborlo, E., and Field, M.J., *Importance of Charge Transfer and Polarization Effects for the Modeling of Uranyl−Cation Complexes.* The Journal of Physical Chemistry A, 2000. **104**(17): p. 4095-4101.
97. Rutland, M.W. and Pashley, R.M., *The Charging Properties of Monodisperse Colloidal Silica in Symmetrical Quaternary Ammonium Ion Solutions.* Journal of Colloid and Interface Science, 1989. **130**(2): p. 448-456.
98. de Keizer, A., van der Ent, E.M., and Koopal, L.K., *Surface and Volume Charge Densities of Monodisperse Porous Silicas.* Colloids and Surfaces A: Physicochemical and Engineering Aspects, 1998. **142**(2–3): p. 303-313.
99. Van der Donck, J., Vaessen, G., and Stein, H., *Adsorption of Short-Chain Tetraalkylammonium Bromide on Silica.* Langmuir, 1993. **9**(12): p. 3553-3557.
100. Koga, Y., Westh, P., Nishikawa, K., and Subramanian, S., *Is a Methyl Group Always Hydrophobic? Hydrophilicity of Trimethylamine-N-Oxide, Tetramethyl Urea and Tetramethylammonium Ion.* The Journal of Physical Chemistry B, 2011. **115**(12): p. 2995-3002.
101. Dousma, J. and De Bruyn, P.L., *Hydrolysis-Precipitation Studies of Iron Solutions. I. Model for Hydrolysis and Precipitation from Fe(Iii) Nitrate Solutions.* Journal of Colloid and Interface Science, 1976. **56**(3): p. 527-539.
102. Dousma, J., Van den Hoven, T.J., and De Bruyn, P.L., *The Influence of Chloride Ions on the Formation of Iron(Iii) Oxyhydroxide.* Journal of Inorganic and Nuclear Chemistry, 1978. **40**(6): p. 1089-1093.
103. Scheck, J., Lemke, T., and Gebauer, D., *The Role of Chloride Ions During the Formation of Akaganéite Revisited.* Minerals, 2015. **5**(4): p. 778-787.
104. Johannsmann, D., *The Quartz Crystal Microbalance in Soft Matter Research.* Soft and Biological Matter, 2015: p. 191-204.
105. Pomorska, A., Shchukin, D., Hammond, R., Cooper, M.A., Grundmeier, G., and Johannsmann, D., *Positive Frequency Shifts Observed Upon Adsorbing Micron-Sized Solid Objects to a Quartz Crystal Microbalance from the Liquid Phase.* Analytical Chemistry, 2010. **82**(6): p. 2237-2242.
106. Keiji Kanazawa, K. and Gordon, J.G., *The Oscillation Frequency of a Quartz Resonator in Contact with Liquid.* Analytica Chimica Acta, 1985. **175**: p. 99-105.
107. Liu, C., Shang, J., and Zachara, J.M., *Multispecies Diffusion Models: A Study of Uranyl Species Diffusion.* Water Resources Research, 2011. **47**(12).
108. Quilès, F., Nguyen-Trung, C., Carteret, C., and Humbert, B., *Hydrolysis of Uranyl(Vi) in Acidic and Basic Aqueous Solutions Using a Noncomplexing Organic Base: A Multivariate Spectroscopic and Statistical Study.* Inorganic Chemistry, 2011. **50**(7): p. 2811-2823.
109. Laaksonen, A., Talanquer, V., and Oxtoby, D.W., *Nucleation: Measurements, Theory, and Atmospheric Applications.* Annual Review of Physical Chemistry, 1995. **46**(1): p. 489-524.
110. Giammar, D.E. and Hering, J.G., *Influence of Dissolved Sodium and Cesium on Uranyl Oxide Hydrate Solubility.* Environmental Science & Technology, 2004. **38**(1): p. 171-179.
111. Lifshitz, I.M. and Slyozov, V.V., *The Kinetics of Precipitation from Supersaturated Solid Solutions.* Journal of physics and chemistry of solids, 1961. **19**(1-2): p. 35-50.
112. Wagner, C., *Theorie Der Alterung Von Niederschlägen Durch Umlösen (Ostwald ‐ Reifung).* Berichte der Bunsengesellschaft für physikalische Chemie, 1961. **65**(7 ‐ 8): p. 581-591.
113. Hu, Z., Escamilla Ramírez, D.J., Heredia Cervera, B.E., Oskam, G., and Searson, P.C., *Synthesis of Zno Nanoparticles in 2-Propanol by Reaction with Water*. The Journal of Physical Chemistry B, 2005. **109**(22): p. 11209-11214.

114. Oskam, G., Hu, Z., Penn, R.L., Pesika, N., and Searson, P.C., *Coarsening of Metal Oxide Nanoparticles.* Physical Review E, 2002. **66**(1): p. 011403.
115. Schindler, M., Hawthorne, F.C., Mandaliev, P., Burns, P.C., and Maurice, P., *An Integrated Study of Uranyl Mineral Dissolution Processes: Etch Pit Formation, Effects of Cations in Solution, and Secondary Precipitation.* Radiochimica Acta International journal for chemical aspects of nuclear science and technology, 2011. **99**(2): p. 79-94.
116. Morss, L.R., Edelstein, N.M., Fuger, J., and Katz, J.J., *The Chemistry of the Actinide and Transactinide Elements (Volumes 1-5): Vol. 1*. Vol. 1. 2007: Springer.
117. Horwitz, E., Sauro, L., and Bloomquist, C., *The Extraction Chromatography of Californium and Einsteinium with a High Molecular Weight Quaternary Ammonium Nitrate.* Journal of Inorganic and Nuclear Chemistry, 1967. **29**(8): p. 2033-2040.
118. Chernorukov, N.G., Nipruk, O.V., and Kostrova, E.L., *Synthesis and Study of Sodium Uranate $Na_2u_2o_7·6h_2o$ and of Products of Its Dehydration and Thermal Decomposition.* Radiochemistry, 2016. **58**(2): p. 124-127.
119. Baran, V., Sourkova, L., and Spalova, J., *Water-Free Precipitation Uranate with Maximum Sodium Content, Na/U = 1.0.* Journal of Radioanalytical and Nuclear Chemistry, 1985. **95**(5): p. 331-338.
120. Lapidot, T., Sedransk Campbell, K.L., and Heng, J.Y.Y., *Model for Interpreting Surface Crystallization Using Quartz Crystal Microbalance: Theory and Experiments.* Analytical Chemistry, 2016. **88**(9): p. 4886-4893.
121. Huang, F., Zhang, H., and Banfield, J.F., *The Role of Oriented Attachment Crystal Growth in Hydrothermal Coarsening of Nanocrystalline Zns.* The Journal of Physical Chemistry B, 2003. **107**(38): p. 10470-10475.
122. Zhang, J., Lin, Z., Lan, Y., Ren, G., Chen, D., Huang, F., and Hong, M., *A Multistep Oriented Attachment Kinetics: Coarsening of Zns Nanoparticle in Concentrated Naoh.* Journal of the American Chemical Society, 2006. **128**(39): p. 12981-12987.

6 Solid-state crystallisation mechanisms of crystalline and amorphous Ca^{2+}-U(VI)-oxyhydrates

This chapter draws the previous two chapters (Chapters 4, 5) together, by characterising the influence of elemental variations in stoichiometry and intercalation of organic frame-working agents, on dehydration and crystallisation of poorly-ordered uranyl(VI) oxyhydrates. In particular, structural relationships with stoichiometry is revealed for precipitates and crystalline endmembers, whilst mechanistic effects on structural transformation is explored.

6.1 Introduction

Numerous uranyl(VI) oxyhydrates, hydrous uranates, as well as anhydrous uranates have been defined in the literature (see section 2.4), whereas poorly-crystalline or amorphous uranate [1-3] and di- or poly-uranates [4-10] are rarely studied. Thermodynamic data for calcium diuranate ($CaU_2O_7.3H_2O$) exists [6] in spite of its poorly-defined structure and origin [1, 2, 11-13], which indicates contention regarding the validity of single phase calcium diuranate, compared to a solid solution between nano-Clarkeite and uranyl(VI) hydroxide. In addition, naturally occurring Ca^{2+}-uranates (Clarkeite-like phases) are rare [14], and usually contain sodium as the dominant secondary cation, with structures most akin to $CaUO_4$, or the oxygen deficient anhydrous sodium di- and poly-uranates ($Na_2U_2O_7$ [15], $Na_6U_7O_{24}$ [16]) [1, 2]. Although isomorphous Ca^{2+}/Na^{+} substitution is possible via an increase in U-O coordination [1, 17-19]. A transition in uranium oxide coordination sphere from that resembling uranyl(VI) oxyhydrate to uranate-like, is expected either as a result of higher hydrolysis ratios (higher OH/U ratio) during precipitation, or due to aging via oxolation-mediated dehydration [11, 20-22]. Extensive work on molten salt precipitation [23-27], has revealed a large variety of stable anhydrous phases that span alkali, alkaline-earth, rare-earth, and transition-metal uranates, and exhibit a far wider stoichiometric flexibility in congruous metal-uranium stoichiometry.

Herein lies several overlapping relationships between structural order, stoichiometry, and extent of hydration. Accordingly, crystalline uranates lie at the intersection between low-water content and high or low metal-uranium stoichiometry, whereas crystalline uranyl(VI) oxyhydrates lie at the intersection between high water content and low metal-uranium stoichiometry. However, with increasing metal-uranium stoichiometry, known phases tend towards lower crystallinity; a factor that coincides with extent of dehydration during amorphous/hydrous to crystalline transformation, is time. This suggests that kinetic mechanisms influencing dehydration, and in

relation, structural changes, may be key to understanding the overlap between precursor uranyl(VI)-hydroxides, and crystalline metal uranates. However, such concerted studies have yet to be undertaken within contemporary literature. In addition, the effects of elemental stoichiometry on subsequent dehydration, and crystallisation are largely untouched. Thusly, this chapter aims to characterise the mechanisms that influence the dehydration of uranyl(VI) oxide hydrate phases, and the influence of bulk stoichiometry (Ca/U) on the crystallinity of starting products, and structural changes that occur during endmember phase formation.

6.2 Experimental

6.2.1 Materials and preparation

Calcium uranyl(VI) hydroxide particles synthesised using titration reactions (Chapter 5) were selected based upon bulk Ca/U-stoichiometry (measured using ICP-OES, see below) ranging from low (0.124) to high (7.2). Further aging (hydration, ripening) processes were quenched after rinsing using propan-2-ol via the methodology described previously (Chapter 4, section 4.2.1.2). Quenched samples were dis-aggregated using a spatula and via ultrasonic bath under a dry N_2-headspace within sealed containment (Nalgene™ centrifuge tubes) for 2 hours at 20 °C.

6.2.2 Sample analyses

6.2.2.1 Inductively Coupled Plasma – Optical Emission Spectrometry (ICP-OES)

Solid precipitates removed from steady-state reactions at selected pH values for 20 °C and 70 °C reactions were digested in 100 µL aliquot of 70 % nitric acid (Aristar) and diluted to 1 wt% acid concentration (~50 ppm U). Diluted samples were used for Ca^{2+} and U(VI) ICP-OES analysis on a Thermo iCAP 7400 instrument, using Ca^{2+} and UO_2^{2+} standards containing yttrium as internal standard. A summary of titration-end pH, and reaction temperature on the resultant bulk Ca/U-stoichiometry, is available in the supplementary information section.

6.2.2.2 Fourier-transform infra-red spectroscopy (FTIR)

Solid samples with the same Ca/U-stoichiometry as used for XRD analysis was also analysed using a portable A2 Technology Microlab Portable mid-IR spectrometer in ATR-mode (Diamond attenuated total reflection cell, DATR) after a 2 hour equilibration period. The diamond cell was cleaned using deionised water followed by propan-2-ol and Kimwipe™ to dry. Samples were scanned between 650 and 4000 cm^{-1} ($\Delta\lambda^{-1}$ = 1 cm^{-1}) and averaged (1024 spectra) in triplicate, with the use of a new powder sample between each repetition.

6.2.2.3 Thermal analysis (TGA-DSC-MS)

Disaggregated powder samples (10 ± 1 mg) with bulk Ca/U-stoichiometry of 0.124, 0.361, 0.521, 0.671, 1.11 (ICP-OES) were loaded into palladium crucibles (30 μL) in duplicate and heated to the temperatures 200, 300, 400 and 800 °C under pure dry air (70:30 N_2:O_2) at a flow rate of 50 cm^3 min^{-1} in a TGA-DSC (Mettler Toledo™). Heating rates for all samples was carried out at 10 °min^{-1}. Specifically, the samples heated to 800 °C were repeated in triplicate at three additional heating rates (9, 11, 12 °min^{-1}). The output gas-flow was connected to a quadrupole mass spectrometer (MKS™ Instruments) to analyse gas-phase decomposition products from the calcination processes for heating rate of 10 °min^{-1} and at a spectrum scan-rate of ~0.2 s^{-1}. All samples were held at isothermal plateau for 60 minutes before cooling at the same rate as used for respective heating profiles. The apparent activation energies associated with decomposition or dehydration steps were calculated using the Flynn-Wall-Ozawa (FWO) [28, 29], Kissinger-Akahira-Sunose (KAS) [30-32] and Starink [33, 34] integral methods (see section 3.2).

6.2.2.4 Electron microscopy

Samples were suspended in propan-2-ol and deposited onto amorphous holey carbon support copper grids prior to TEM-imaging using a FEI Tecnai TF20 FEGTEM. ImageJ [35] was used to measure particle size, and the Crystallographic Tool Box (CrysTBox) package [36] was used for processing radial intensity patterns from selected area electron diffraction patterns (SAEDs). Samples used in TEM-analyses were subsequently imaged using a Hitachi SU8230 cold field emission SEM equipped with Aztec Energy EDS (80 mm X-Max SDD detector). The AZTEC software package was used during standardless quantification of Ca and U elemental concentrations.

6.2.2.5 X-ray Diffractometry (XRD)

Disaggregated samples of bulk Ca/U-stoichiometry 0.124, 0.361, 0.521, 0.59, 0.671, 0.83, 1.11, 1.59, 1.78, 5.18, 7.21 were analysed on a Bruker D8 diffractometer equipped with Cu Kα x-ray source (40 kV, 40 mA) and lynx eye detector. Diffractograms were collected for the 2theta range of 2 – 85 °2theta (Δ°2theta = 0.01). Scans were completed over 9 hours for crystalline samples (800 °C) of Ca/U = 0.124, 0.36, 0.521, 0.671, 1.11; whilst poorly-crystalline samples were completed over 4.5 hours. XRD patterns were compared to International Centre for Diffraction Data (ICDD) powder diffraction file database (PDF+4) within the PANanalytical Highscore™ plus software. Rietveld fitting was attempted using PDF+4 structural files for α-U_3O_8, $CaUO_4$ and α-Ca_3UO_6, and profile fitting was performed using CaU_2O_7 and $Ca_2U_3O_{11}$ using PDF+4 XRD-reflections. Goodness of fit parameters

were inversed and normalised for ease of comparison. A crystalline Si-standard was scanned to reveal instrumental broadening coefficients (Gaussian and Lorentzian) with each sample; and crystallite sizes of calcined samples (800 °C) were approximated by applying the Scherrer equation to 100% XRD-reflections and via Williamson-Hall plots, the methodology is described in further detail elsewhere (see section 3).

6.2.2.6 X-ray Absorption Spectroscopy (XAS)

Precipitated particles and heat treated intermediates (20, 200, 300, 400, 800 °C) with Ca/U-stoichiometry of 0.124, 0.52 and 1.11 were analysed using synchrotron X-ray absorption spectroscopy (XAS). For Ca/U of 0.36 and 0.67, only the precipitate (20 °C) and crystallised samples (800 °C) were analysed. Na-uranate (NaU_2O_7) and hydrous uranyl(VI) oxide ($UO_3.xH_2O$) were used as U(VI)-standards. Disaggregated samples were homogenised with polyvinylpyrollidone (PVP) powder, then compressed into 1 cm diameter circular solid pellets of 2 mm thickness. Pellets were double-contained in Kapton™ and 1.5 ml Nalgene™ cryotubes. The amount of sample required per pellet was calculated using Absorbix [37], assuming ideal single phase stoichiometry (Ca, U, O) and a target $\Delta\mu X$ of unity for the uranium L_{III}-edge (17166 eV). Transmission XAS (XANES, XAFS) data were collected at the B18 beamline of the Diamond Light Source in transmission mode. Between 3 – 5 scans per sample were completed singularly over a range of 16966 – 18850 eV (K-range of 0 – 21 $Å^{-1}$), with step-size of 1 eV ($1.8*10^{-3}$ ° min^{-1} dwell time). Measurements were carried out at -196 °C within a liquid nitrogen (LN_2) cryostat to reduce thermal contributions to Debye-Waller factors during XAFS modelling. Sample spectra were averaged to improve noise-signal ratio, and aligned with respect to the crystalline sample (800 °C) within each Ca/U-series for ease of modelling. Linear combination fitting (LCF) was performed on the X-ray absorption near edge spectra (XANES) in the Athena v1.2.11d interface (Demeter 0.9.24). Extended X-ray absorption fine structure (EXAFS) data were analysed in Artemis, where the structural parameters scatterer coordination number (CN), mean shift in interatomic distance (ΔR), and Debye-Waller factor (σ^2), were optimised. The passive electron reduction factor (S_0^2) and the photoelectron energy shift(s) (ΔE_0) were initially fixed at 0.8, and 0 respectively. These values were relaxed once after fitting of the uranyl(VI) U=O scattering path (known CN) and the relaxed values fixed for all future refinements. Many of the fits were improved by using a separate ΔE_0 value for U-O and U-U/Ca paths; whereby the latter ΔE_0-value was also fixed at the beginning and relaxed after the first U-shell. A shell-by-shell fitting approach was first completed using theoretical stoichiometry (coordination numbers) for aggregated U-O, U-Ca, and U-U single-scattering (SS) paths (degeneracy margin = 0.1, beta = 3), whilst including

multiple-scattering (MS) paths arising from the first U-O coordination sphere. A new shell was accepted if the fit quality was improved via reduction in the χ^2 and R^2 goodness of fit parameters of at least 5% (lower values are better). Periodically, S_0^2 and ΔE_0 were floated to check for significant drift, and would otherwise remain at their original values. Wherever possible, constraints between SS and MS paths were used to reduce the number of floated parameters via algebraic relationships. Upon reaching fitting limits, ~4.5 – 5 Å for poorly-ordered, and up to ~7 Å for well-crystallised samples, the shell-by-shell refinement was repeated for coordination numbers (CN). All parameters were floated upon completion, and the tabulated fitting parameters and quality of fit presented (Table C4 – Table C8) are extracted thusly.

6.3 Results

Calcium uranyl(VI) oxyhydrate particles were precipitated via titration of precursor calcium and uranyl(VI) nitrate solutions using tetramethylammonium hydroxide (see sections 4, 5 and reference [11], for further details). Reaction temperatures, precursor Ca/U stoichiometry, and titration pH endpoints were varied. Precipitates analysed using ICP-OES revealed that variation in bulk Ca/U-stoichiometry are highly dependent on temperature, as well as precursor-Ca/U (Figure 6.1a).

Across all three extraction pH values considered, particle-Ca/U at 20 °C exhibit decreasing and increasing sensitivity to precursor-Ca/U, with an inflexion point lying at $Ca/U_{solution}$ ~20. However, the sensitivity ($Ca/U_{solution}$ >20) at 70 °C increases significantly, resulting in a bulk particle Ca/U of 7.2 when solution-Ca/U reaches 50. This indicates an increasing non-congruency in the precipitation reaction as precursor Ca/U is elevated, that is enhanced by temperature.

There is significant contribution of water in the FTIR-spectra for all samples (Figure 6.1b), which manifest as broad OH $\nu_{1,3}$ and sharp OH ν_2 peaks lying at 3657.1-3755.9 and 1594.7 cm^{-1} respectively. The relative positions of peak minima (Figure 6.1c, red) and integral peak areas (Figure 6.1c, black) for both OH-bands change as a function of stoichiometry, indicating changes in molecular O-H or hydrogen bond strengths [38, 39]. With increasing Ca/U, $\nu_{1,3}$ shifts inversely with ν_2, towards larger values. Whilst this stoichiometric relationship appears linear, its sensitivity increases significantly when sample-Ca/U exceeds the 1.11-1.5 Ca/U region (Figure 6.1, shaded area); and is mirrored by their integral peaks areas (Figure 6.1a, black symbols).

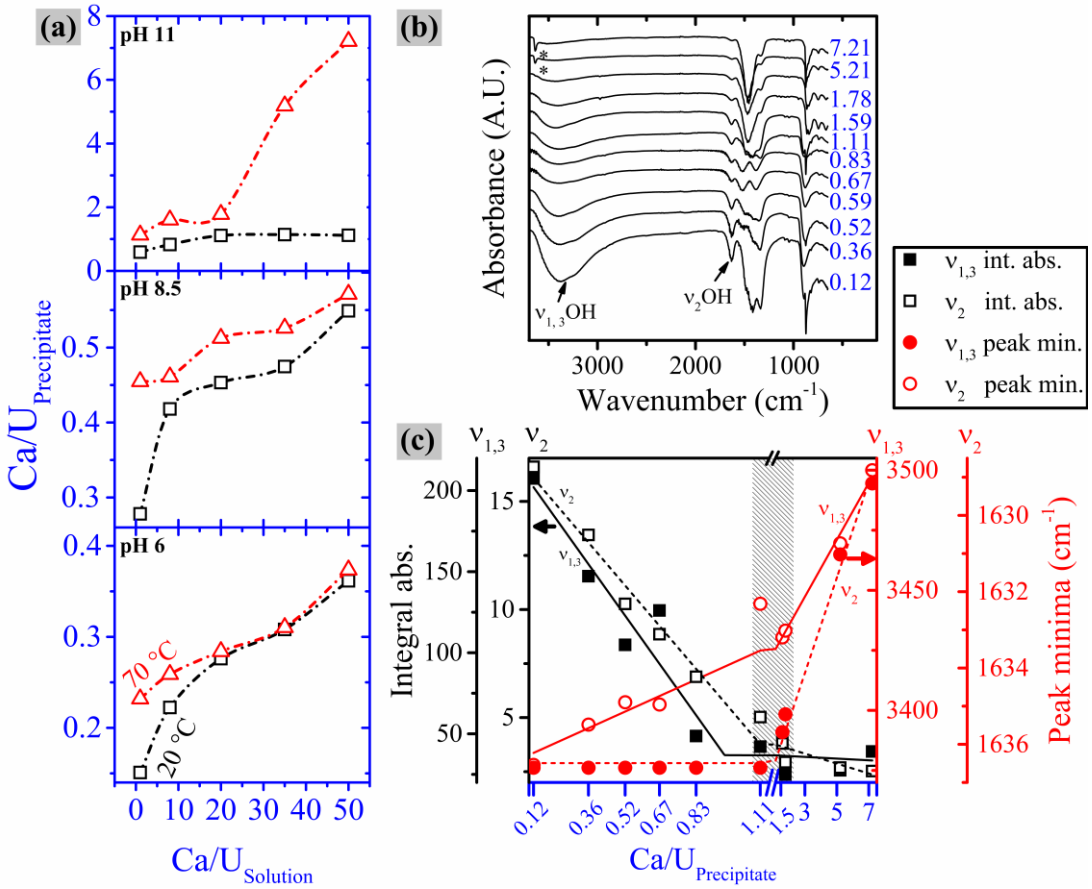

Figure 6.1 (a) Bulk Ca/U-stoichiometry of calcium uranyl(VI) oxyhydrate precipitates from ICP-OES. (b) Raw FTIR-spectra of precipitated calcium uranyl(VI) oxyhydrates with various bulk Ca/U-stoichiometry, with labelled $\nu_{1,3}$ and ν_2 OH-stretching bands; (c) relative integrated peak areas (left axis) and peak minima positions (right axis) of $\nu_{1,3}$ and ν_2 stretching bands as a function of bulk Ca/U-stoichiometry. Asterisks correspond to portlandite OH-bands.

6.3.1 TGA-DSC-MS

TGA-DSC (Figure 6.2a) was performed on precipitated Ca^{2+}-U(VI)-hydroxide particles to characterise decomposition processes occurring during thermal treatment, whilst mass-spectrometry was used to follow gas-phase decomposition products. By calcining precipitates at 9, 10, 11 and 12 ° min^{-1}, the activation energies (Figure 6.3) associated with each decomposition step were also calculated using FWO [1, 2], KAS [3-5] and Starink [6, 7] methods (Figure 6.2). The precipitates across all Ca/U-stoichiometry undergo between 3 – 4 mass-loss steps that decrease in magnitude, with each step coinciding with the detection of gas-phase by-products by the mass-spectrometer. Remarkably, the temperature, total mass-loss (Figure 6.2c), reaction enthalpy (Figure 6.2d), and activation energies (Figure 6.3), associated with each stage of decomposition is reduced as a function of increasing bulk Ca/U-stoichiometry in precipitates.

In step 1 (T <150 °C), Ca^{2+}-U(VI)-oxyhydrates undergo endothermic dehydration (Figure 6.2a, b) to liberate 6 – 11 wt% of water (Ca/U 0.124 – 1.11) mostly via a 3-dimensional diffusion controlled mechanism (Table 6.1). As the bulk particle Ca/U increases from 0.124 to 1.11, the reaction enthalpies decrease from 94 to 22 kJ mol^{-1} (Figure 6.2d, black), which corresponds to a reduction in activation energy from ~72 to 26 kJ mol^{-1} (Figure 6.3a-e, black). As the dehydration reaction progresses (Figure 6.3, α), the barriers to dehydration ΔE ($0.2 \leq \alpha \leq 0.8$) increase by ~35 kJ mol^{-1} at Ca/U 0.124, whilst ΔE = 0 for Ca/U 1.11.

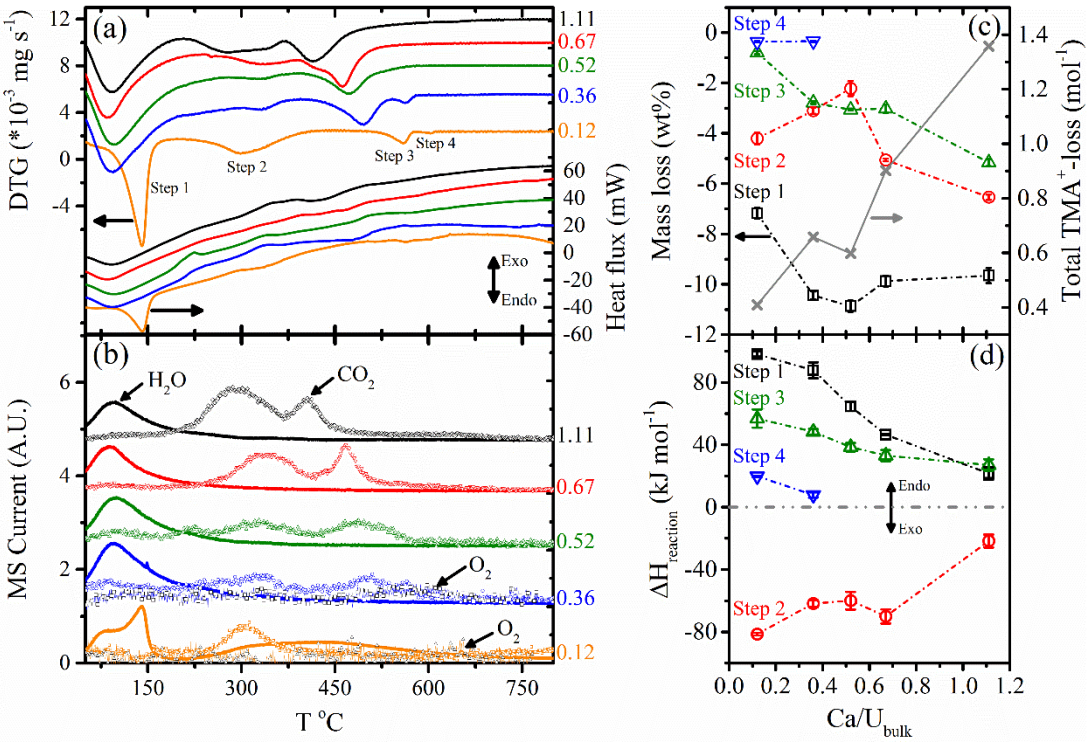

Figure 6.2 (a) TG (left) and derivative-TG (right) heat-flux through sample; (b) mass fragments 18, 32 and 44 g mol-1 detected in gas outflow; (d) stepwise mass-loss values (left) and total TMA^+ liberated per formula unit; as functions of temperature. (e) Stepwise reaction enthalpies for decomposition steps 1-4; as functions of bulk Ca/U-stoichiometry.

A smaller mass-loss (~2 – 6 wt%) at 300 – 350 °C releases CO_2 and water (Figure 6.2b), via mechanisms that are consistent with both chemical (2nd order) and diffusion control (Table 6.1). The reaction enthalpies decrease in magnitude from -81 to -22 kJ mol^{-1} (Ca/U 0.124 – 1.11) and are the only exothermic processes throughout (Figure 6.2d, red). This is reflected by a reduction in initial activation barriers (α = 0.2) from 57 to 55 kJ mol^{-1} (Figure 6.3, red), that decrease in magnitude for Ca/U 0.124 to 1.11, whilst 0.67 Ca/U is higher at 118 kJ mol^{-1}.

A secondary liberation of CO_2 (1 – 5 wt%) and some water at ~500 °C (step 3) follows for Ca/U 0.36 – 1.11, whilst for Ca/U 0.124, continuing dehydration occurs (Figure 6.2b). Step 3 is endothermic, absorbing 57 – 27 kJ mol^{-1} (Ca/U 0.124 – 1.11) of heat

to reach completion (Figure 6.2d, green), which is consistent with the physisorption enthalpies for H_2O (-59 kJ mol^{-1}), and CH_4 (~-21 kJ mol^{-1}) or CO_2 (-25 kJ mol^{-1}) [40]. The reaction appears more complex as several reaction mechanisms were relevant (R^2 = 0.99, higher is better). Whereby, towards higher Ca/U (0.52 → 1.11), 1st order reaction is dominant, whilst diffusion control features in 0.36 and 0.12 Ca/U Figure 6.3, Table 6.1, step 3).

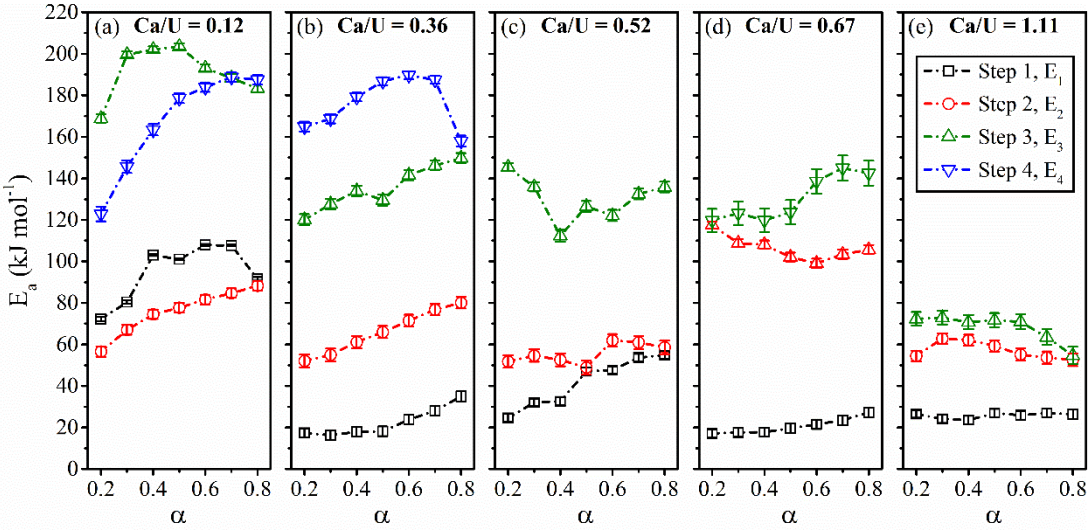

Figure 6.3 Activation energies (E_a) derived from FWO, KAS and Starink methods are averaged and presented as a function of increasing reaction extent (α) during decomposition steps 1 – 4, for solids with bulk Ca/U-stoichiometry of 0.124 – 1.11 in graphs (a) – (e) respectively.

Dissociation of O_2 (Figure 6.2b, line-scatter) occurs at temperatures 600 °C for bulk Ca/U of 0.124 and 0.36. These endothermic ~0.47 and 0.34 wt% mass-losses (Figure 6.2c, d) coincide with darkening of sample colouration to dark-orange and black with green-tinge for 0.36 and 0.124 respectively. The reaction enthalpies are relatively low at 19.8 (0.124) and 7.8 kJ mol^{-1} (0.36), and activation barriers are similar to those observed for step 3, ranging 120 – 188 and 165 – 188 kJ mol^{-1} respectively (Figure 6.3a, b, blue). Despite the similar range in activation, 0.36 and 0.12 Ca/U lose O_2 via 2D, and 3D-nucleation (Avrami-Erofeev) respectively (Figure 6.1, step 4).

Table 6.1 Coats-Redfern (CR) [41] reaction mechanisms.

Step	Ca/U-stoichiometry				
	0.12	**0.36**	**0.52**	**0.67**	**1.11**
1	Contracting sphere	3D diffusion control		3D diffusion control	
2	Contracting sphere	2nd order reaction 1D diffusion control	2D diffusion control	3D diffusion control	
3	1D diffusion control	Contracting cylinder 2D diffusion control		1st order reaction	
4	Avrami-Erofeev 3D nucleation	Avrami-Erofeev 2D nucleation		-	

Activation energies are significantly larger, and range ~169 – 72 kJ mol^{-1} for Ca/U 0.124 – 1.11 (Figure 6.3a-e, green). Both steps 2 and 3 exhibit some change in

activation barrier as the reaction progresses for all Ca/U. At the lowest Ca/U (0.12), most steps feature increasing or inverse parabolic trends, whilst towards higher Ca/U (1.11), activation barriers exhibit some decrease with reaction progression.

6.3.2 XRD

After decomposition steps 1, 2 and 3 (Figure 6.2), the solids were quenched and ex-situ XRD was performed to characterise phase transformations occurring for each Ca/U-stoichiometry (Figure 6.4).

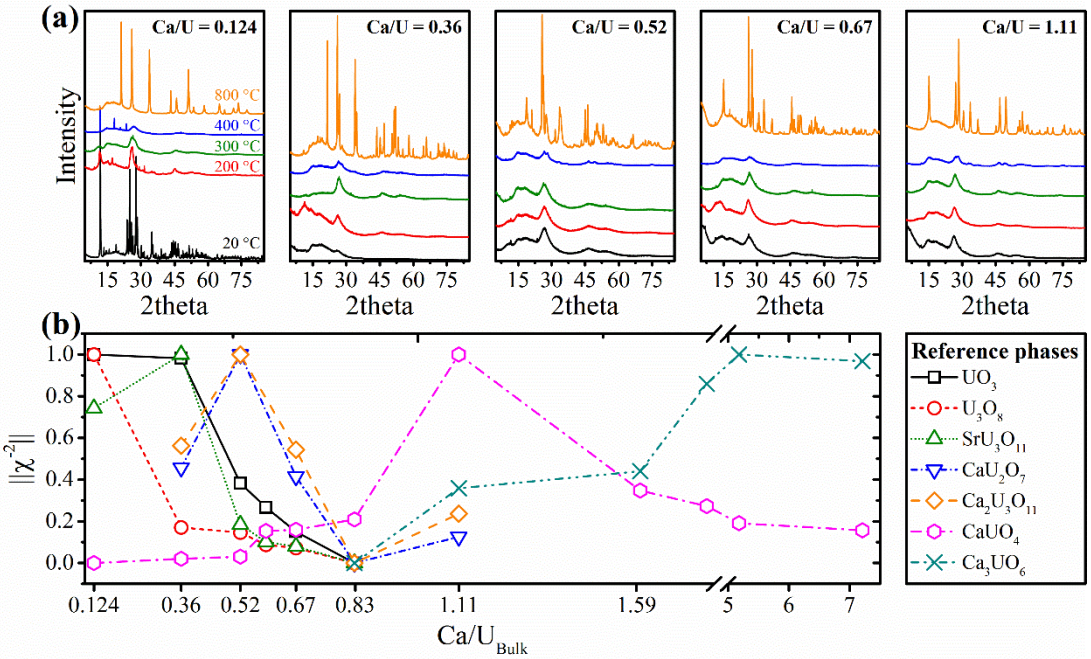

Figure 6.4 (a) Stacked ex-situ X-ray diffractograms for precipitates calcined between 200 and 800 °C with bulk solids with Ca/U-stoichiometry 0.12 – 1.11. (b) Inverse goodness of fit parameters (χ^{-2}) from single phase profile fitting as a function of bulk Ca/U-stoichiometry.

The XRD-patterns of precipitates (Figure 6.4a, black) appear poorly-crystalline (weak, broad reflections) with the exception of 0.124, where intensity maxima resemble those of Becquerelite, and higher Ca^{2+}-U(VI)-hydroxides such as $Ca_{0.75}(UO_2)_3O_2(OH)_{3.5}.3.5H_2O$ and $Ca_{0.83}(UO_2)_3O_2(OH)_{3.5}.3.3H_2O$ [9-11]; in agreement with previous observations for Ca/U of ~0.67 [11]. Notably, the Ca/U 0.124 particles are highly crystalline, and reflections are consistent with the naturally occurring U(VI)-phase Becquerelite (ICDD PDF+4 [42]). Although relative peak positions remain constant with each decomposition, reflections appear weaker (reducing peak intensity) and undergo significant broadening, with the least crystalline samples appearing after the liberation of CO_2 (Figure 6.2b) at ~400 °C. Whilst this is true for Ca/U 0.36 – 1.11, some minor peak maxima appear in 0.124 by 400 °C. This position of these maxima resemble that of β-UO_3 [43-45], a decomposition product of ammonium diuranate [$(NH_4)_2U_2O_7$], comprising interlinked layers of distorted $UO_{6,7}$-polyhedra with voids that run vertically along the c-axis.

All samples crystallise by 800 °C to match the phases (Figure 6.4b) α-U_3O_8/α-UO_3, CaU_2O_7, $Ca_2U_3O_{11}$, and $CaUO_4$ for Ca/U of 0.124, 0.52, 0.67, and 1.11 respectively (Figure 6.4a). The 0.36 sample could not be matched to any known Ca^{2+}-uranate phase, though a strontium polyuranate $Sr_3U_{11}O_{36}$ was found to match the pattern well, indicating an isomorphous crystal structure. Single-phase profile analysis was performed on samples across all available Ca/U stoichiometry to qualitatively assess the closeness between database structural files and experimental data.

The maxima in GOF-parameters of crystalline samples (Figure 6.4b) coincide with Ca/U-stoichiometry of 0 (α-U_3O_8), 0.5 (CaU_2O_7), 0.67 ($Ca_2U_3O_{11}$), 1 ($CaUO_4$) and 3 (Ca_3UO_6). The XRD pattern for α-U_3O_8 was also consistent with that of α-UO_3 and are hypothesised to be isomorphic to each other, with the inclusion of O_2-anion defects in the former [46], though given the black with green tinge colouration of the sample, U_3O_8 was assumed most probable. The majority of phases appeared to have some impurity content, though given the small peak sizes, this is expected to be minor. Notably, Ca_3UO_6 becomes more dominant in samples with Ca/U >1, where its XRD-reflection height grows as a function of increasing Ca^{2+}-content.

6.3.3 SEM, TEM

The precipitates with bulk Ca/U above 0.124 comprise of irregularly shaped primary particles (Figure 6.5) that resemble rounded rhombohedra, where primary particles range in size between 30 and 100 nm in diameter. However, for 0.124, particles resemble flattened hexagonal platelets of ~0.5 – 1.5 nm in diameter and ~0.5nm in thickness (Figure 6.5a, Figure 6.6a). The intermediates exhibit size-reduction from 200 to 400 °C. Whilst the morphology of Ca/U 0.12 and 0.52 particles (Figure 6.5b, e) change little, those of 1.11 (Figure 6.5h) become more interspersed by flattened platelet-like particles ranging 250 – 500 nm in diameter. By 800 °C, particles segregate into two size populations for Ca/U 0.124 (Figure 6.5c, Figure 6.6c), contiguous layered sheets of 0.5 – 2 μm in diameter, and a smaller group of rhombohedroids ranging 30 – 50 nm. Crystalline particles with Ca/U above 0.124 are almost exclusively rhombohedral and are composed of parallel stacked sheets (Figure 6.5f, inset) measuring between 5 – 10 nm in thickness. This layering effect appears less prominent for Ca/U 1.11, which comprises of flattened rhombohedra with smooth edges.

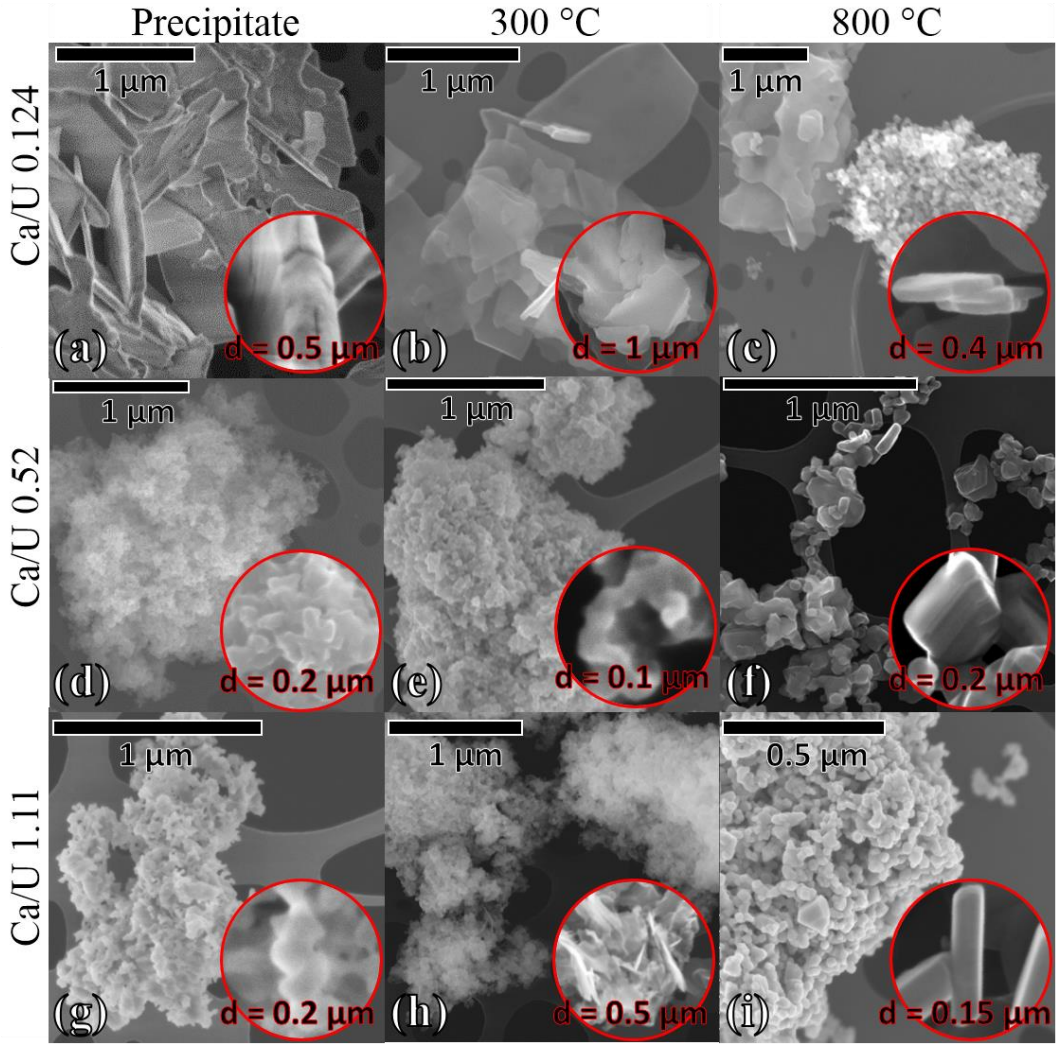

Figure 6.5 Scanning electron micrographs of selected samples. Columns left to right are precipitate, 300 °C product and 800 °C products respectively. Rows from top to bottom are samples with Ca/U-stoichiometry of 0.124, 0.52, and 1.11 respectively. Circlet insets are labelled with frame-diameter for scale. Complete images set available in supplementary information III – Figure C8.

All precipitates and intermediates below 800 °C exhibited beam-damage during TEM-analysis. This induced crystallization and particle shrinkage in intermediates below 300 °C (see Figure C10), presumably via dehydration. Due to this, the presence of ~5 – 10 nm crystallites appear in all precipitate micrographs (Figure 6.6a-g, red-dash) that were not observed initially. Whilst this also occurred for 400 °C intermediates, crystallites of similar size were already present, indicating that calcination and electron beam-induced damage have similar effects on sample crystallinity (Figure 6.6b-h, 200 – 400 °C, red dash). Nevertheless, lattice spacings of crystallite particles in all samples were measured using ImageJ (Figure 6.8c), which reveal spacings that range between ~3 – 3.32 Å across all Ca/U. In particular, samples with 0.12 (orange)

and 1.11 (black) Ca/U undergo a ~ 0.08 Å collapse, whilst 0.52 (green) Ca/U reaches a minimum (3.09 Å) at 200 °C, before all samples recover from 400 °C onwards.

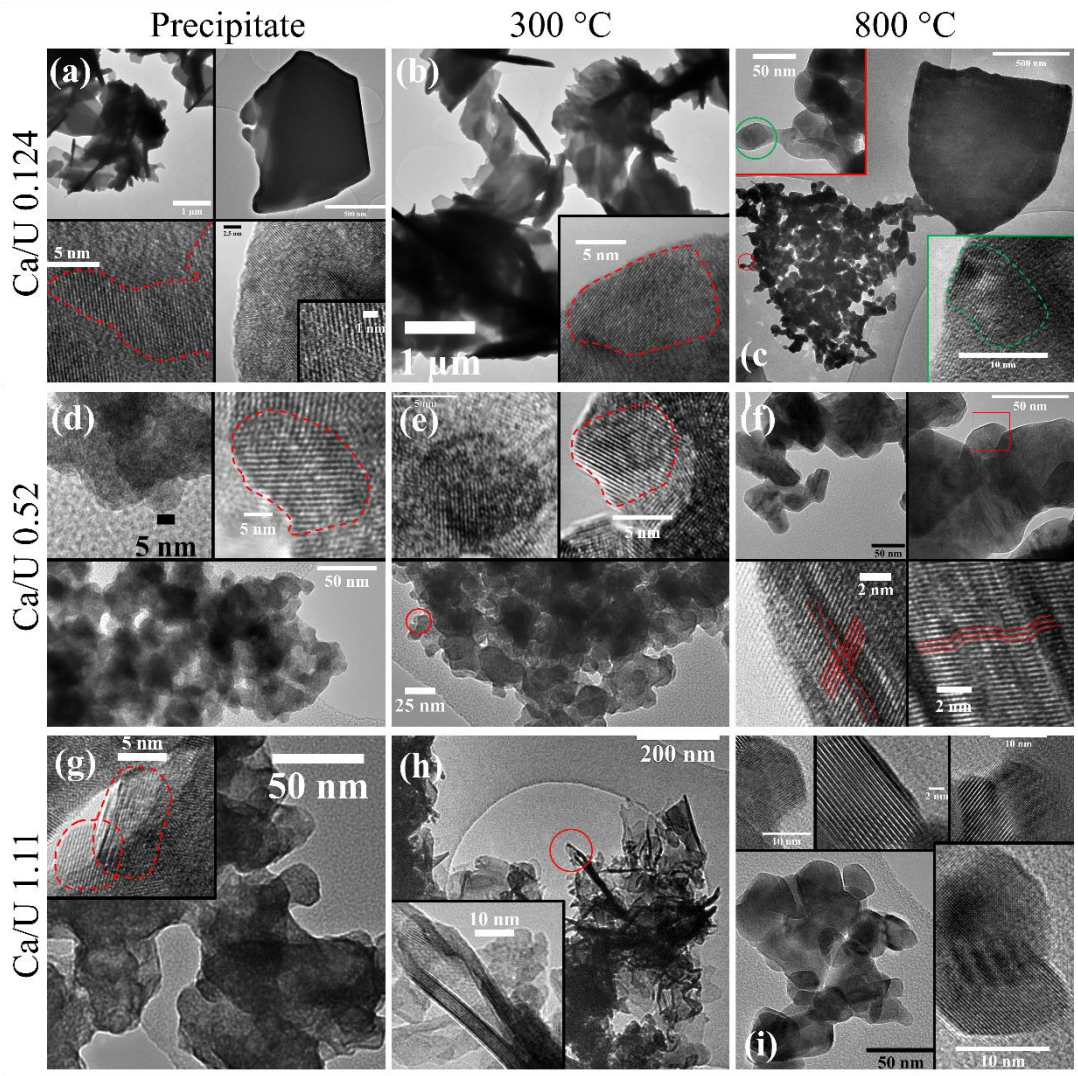

Figure 6.6 Transmission electron micrographs summarising observed changes in particle morphology with increasing Ca/U-stoichiometry (top to bottom), and increasing calcination temperature (left to right). Where available, images include particle clusters, single particles, and observed crystallite domains (dotted lines). Full image set available in Figure C9.

By collecting selected area electron diffraction (SAED) patterns on particles prior to imaging, the native sample crystallinity may be analysed (Figure 6.7). The crystallinity of precipitated 0.124 (Figure 6.7a, 1) is consistent with that expected from its bulk XRD-pattern, and its radial intensity profile is characterised by 4 main peaks lying at 2.84, 2.97, 4.41, 4.99, and 5.84 nm^{-1}, with a predicted zone axis parallel to the c-direction i.e. UVW [001], indicating preferential hydroxylation along the equatorial uranyl(VI) plane during precipitation. At 200 °C, the 2.84 and 2.97 nm^{-1} peaks merge, whilst the shoulder feature at ~3.42 nm^{-1} becomes resolved. Two particle morphologies in the form of sheets and small particle clusters appear, and have the

same profiles (Figure 6.7a, 2a, 2b). These peaks become further resolved with continuing decomposition (Figure 6.7a, 3). By 400 °C, some crystalline particles were found (Figure 6.7a, 4) with peaks at ~3, ~4 and ~5.1 nm^{-1}, which upon analysis of the SAED pattern produced d-space values of 0.17, 0.25, 0.27, and 0.29 nm, consistent with the β-UO_3 HKL-planes [040]/[221], [340], and [421] respectively [45].

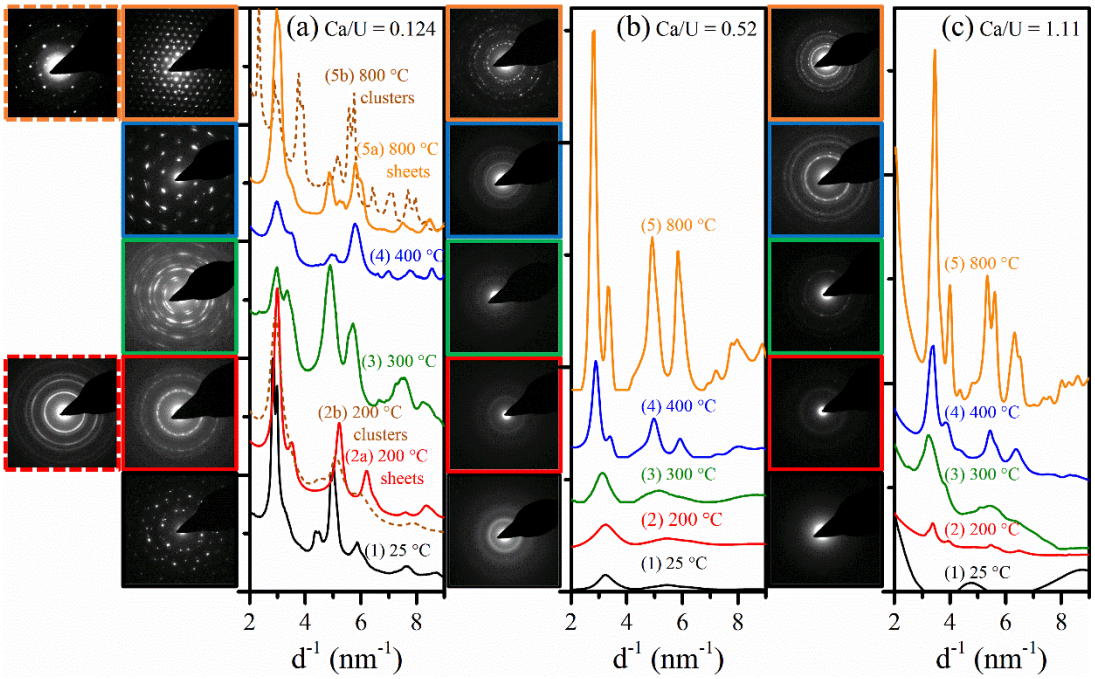

Figure 6.7 Stacked azimuthally averaged radial intensity (arbitrary units) profiles from corresponding selected area electron diffraction (SAED) patterns in reciprocal space (d^{-1}), of particles calcined between 200 and 800 °C, with selected Ca/U-stoichiometry (0.124, 0.52, 1.11). Radial intensity patterns are the average of 3 – 5 particle clusters and are colour coded to reference.

The large contiguous sheets in crystallised 0.124 (Figure 6.6c) measure ~420 nm in diameter (Figure 6.8b), and are composed of α-U_3O_8 with considerably smaller crystallite (lower-bound) domains measuring ~50 nm in the bulk (Figure 6.8a). A minor faction of smaller ~50 nm particles were also present (Figure 6.6c, red circled), containing a mixture of α-U_3O_8 (Figure 6.7a, 5a) and $CaUO_4$ (Figure 6.7a, 5b), with crystallite domains measuring ~10 nm (Figure 6.6c). However, elemental EDS quantification (standardless) of small (0.21 ±0.01) and large (0.19 ±0.06) reveal less variation than expected from phase stoichiometry. Analysis of SAED patterns from large sheets (Figure 6.7a, solid orange box) in CrysTbox [36] indicates that basal crystal faces are parallel to the equatorial plane of α-U_3O_8 (UVW [-100]). The reduction in SAED resolution towards higher Ca/U (Figure 6.6b1, c1) reflects the poorly-ordered nature expected from XRD-analysis (Figure 6.4). However, whilst peak resolution reduces in XRD-patterns with increasing temperature, single particle SAED radial intensity profiles exhibit the opposite trend. Where a progressive

development in peak intensity occurs towards 800 °C with almost no shifts in relative peak positions, where the 400 °C intermediate closely resembles the endmember phases in 0.52 and 1.11 (Figure 6.7b, c). Minimum crystallite sizes generally reduce with increasing Ca/U in 800 °C samples (Figure 6.8a).

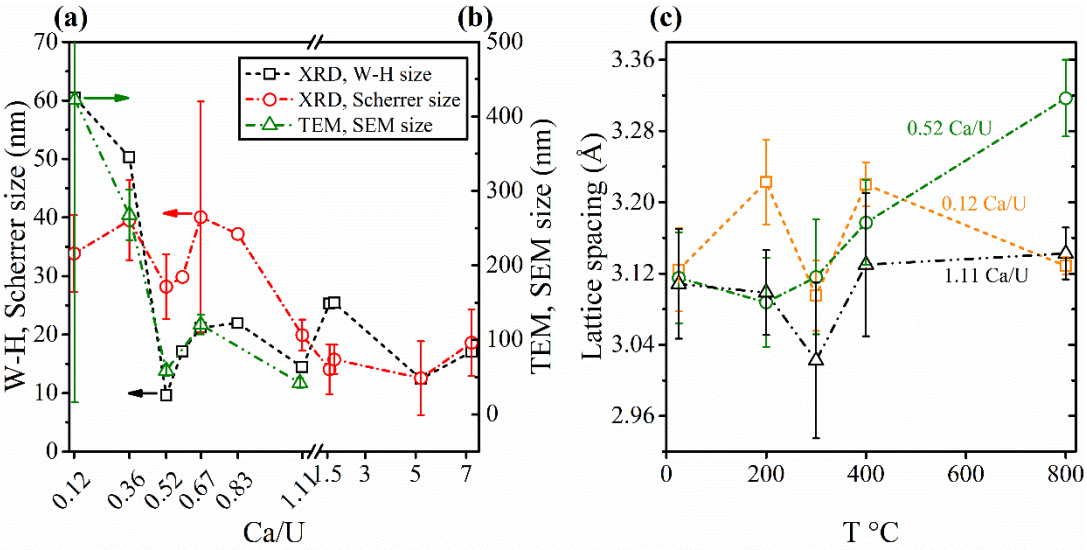

Figure 6.8 Comparison between (a) lower bound crystallite diameters (Scherrer and Williamson-Hall size) from XRD data (Figure C4b), with (b) directly measured particle sizes from TEM-images, for crystallised samples (800 °C) at varying Ca/U-stoichiometry. (c) Ex-situ lattice spacings from TEM-images for 0.12, 0.52, and 1.11 Ca/U, as a function of increasing temperature.

There is a size-minima at 0.52 Ca/U (~10 – 25 nm), before increasing to ~30 nm by 0.67 Ca/U, then decreasing to ~17 nm by 1.11 Ca/U. These size trends are reflected in average values measured from TEM and SEM images, though given the ~10-fold difference, observed particles (Figure 6.8) likely comprise of several crystallites. This is supported by a shift in SAED patterns towards those indicative of polycrystalline samples (Figure 6.7a-c).

Some isolated single crystals were found for 0.36 (Figure C11a) and 0.67 (Figure C11b), and upon processing of associated SAED patterns, peaks at ~4.2, 3.4, 2.7, and 1.5 Å for the former, and ~5.72, 3.4, 3.24, 2.73, 2, 1.86 Å for the latter were revealed in radial intensity profiles. Comparison of d-spacings with bulk powder XRD patterns (Figure C4b) confirmed the presence of a phase that could be isomorphous to $Sr_3U_{11}O_{36}$ [47] for 0.36, whilst the latter is directly consistent with $Ca_2U_3O_{11}$ [11, 48-50].

The spacings of lattice-fringes lying parallel to rhombohedra edge-sites in 0.36 crystals (800 °C) measured ~6.3 Å, whilst those running perpendicular to edge-sites in 0.52 (Figure 6.6f, red lines) and 0.67 measured ~3.4 and ~3.1 Å respectively. Regions of high contrast lie along edge-sites of particles with 0.124< Ca/U <1.11

(Figure 6.6f, red lines), where lattice-fringes appear discontinuous across layered regions. Direct measurement of edge-site lattice fringes in crystalline 1.11 samples gave a mixture of spacings 5.9, 3.3-3.1, 2.7, 1.8-1.6 Å, that coincide with d-spacings of the respective HKL planes [111], [001], [112], [012], and [123] in $CaUO_4$, indicating that crystals are isotropic compared to samples of lower Ca/U.

6.3.4 FTIR

In addition to precipitates, FTIR-spectra was collected on crystallisation intermediates and endmember products for solids with Ca/U between 0.12 – 1.11 (Figure 6.9a-c). With increasing temperature, the OH-bond asymmetric/symmetric $\nu_{1,3}$ (~2500-3500 cm^{-1}), and bending ν_2 (~1617 cm^{-1}) modes decrease in peak area and height, until almost complete removal by 800 °C. The νOH peak lying at 3504 cm^{-1} in the precipitated 0.124 spectrum (Figure 6.8a, 25 °C) is consistent with that of natural Becquerelite [51], whilst the higher peak-resolution corroborates with a higher structural order compared to other samples (Figure 6.4a, 25 °C).

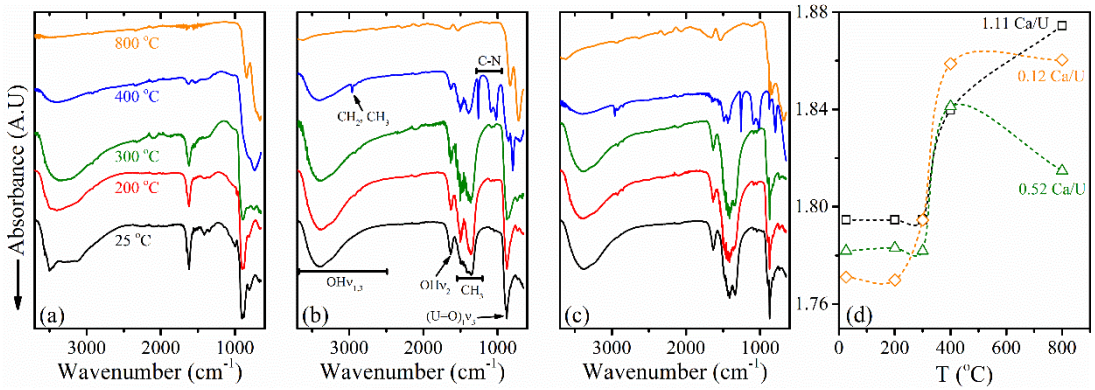

Figure 6.9 Room temperature FTIR spectra of precipitates, intermediates and crystalline products between 4000 – 600 cm^{-1} for (a) 0.124, (b) 0.52, and (c) 1.11. (d) Approximated uranyl(VI) U=O bond lengths from the Badger relationship.

The primary asymmetric ν_3U=O vibration at 800 – 1000 cm^{-1} [52-54] is common to all spectra, confirming the presence of the uranyl(VI) species in all samples, though positional variations indicate distortion of equilibrium $U=O_{yl}$ bond lengths. The $\nu_3U=O_{yl}$ peak position for the precipitated 0.124 spectrum (Figure 6.8a, 25 °C) is slightly smaller than that observed by Čejka et al [51], and more akin to the doublet (~902 cm^{-1}) by Amayri et al [55]. A broad doublet lies between ~1118 and ~1550 cm^{-1} in all spectra below 300 °C, and appears more prominently in samples with Ca/U above 0.36. In combination with the observed CO_2 release (Figure 6.2b), this was attributed to methyl C-H vibrations of TMA^+ ($N(CH_3)_4^+$) present in samples [56, 57], which by 400 °C, resolves into several aliphatic C-N vibrations lying between ~1000 – 1550 cm^{-1} [58]. The removal of OH-absorption bands (Figure 6.9) confirm the expected continuous water removal (Figure 6.2b) throughout the intermediates.

The Badger relationship [52-54, 59] was used to approximate uranyl(VI) bond lengths from peak positions associated with the U-O_{yl} ν_3 asymmetric stretch (Figure 6.9, ~800 – 1000 cm^{-1}). U-O_{yl} bond lengths (Figure 6.9d) increase with increasing temperature, ranging 1.77 – 1.86; 1.78 – 1.81; and 1.79 – 1.87 Å; for sample series with Ca/U stoichiometry of 0.124, 0.52, and 1.11 respectively (Table C1).

6.3.5 XAS

6.3.5.1 XANES

The background-subtracted and normalised U L_{III}-edge XANES spectra of all samples (Figure 6.10) feature a strong white-line (A) peak characteristic of high oxidation state U-compounds due to $2p_{3/2} \rightarrow 5f$ and split 6d (t_{2g} d_{xy}, d_{xz}, d_{yz}, e_g d_x^2-$_y^2$, d_z^2) transitions [60-63]. A shoulder (B) and peak (C) on the high energy side is common to precipitates across all Ca/U stoichiometry (Figure 6.10a), which are commonly attributed to multiple scattering contributions from the linear uranyl(VI) (UO_2^{2+}) unit and equatorial ligands respectively [60, 61]. The shoulder position appears stoichiometry-sensitive, where sample spectra with higher and lower Ca/U resemble the hydrous reference materials $Na_2U_2O_7$ (magenta dash-dot) and UO_3 (green dash-dot) respectively. Feature (B) also becomes less prominent with increasing temperature (Figure 6.10d-f) or less $UO_3.xH_2O$-like [60]. By 800 °C, feature (B) reappears somewhat for moderate Ca/U samples 0.36, 0.52 and 0.67, whilst a broad asymmetric white line characterises the endmembers 0.12 and 1.11 (Figure 6.10b). The 1st-derivative of 800 °C XANES spectra (Figure 6.10c) reveal a linear decrease in 1st maxima-position with a reduction in Ca/U from 1.11 – 0.36 by ~0.26 eV (Figure 6.10c, inset). The 1.11-0.124 ΔE value is ~0.85 eV, which is consistent with a shift from pure U(VI) to the mixed U(VI), U(V) environment in α-U_3O_8 [64-67].

Arctan and Gaussian functions were used to model the edge step (Figure C13, Figure C14), and features (A-C). The inverse energy differences A-B, and A-C were extracted from subtraction of Gaussian peak maxima for peaks A, B and C, then used to predict general trends in nearest-neighbour axial (B) and equatorial (C) resonant scattering contributions [68]. Accordingly, samples 0.12 – 1.11 exhibit little change in nearest neighbour MS-contributions up to 200 °C, except a minor reduction for 0.124. However, a sigmoidal increase in ΔE occurs for shoulder B (Figure C15a), which is inversely reflected for feature C (Figure C15b), to give an approximately linear relationship between axial and equatorial MS-contributions to the XANES spectra (Figure C15c).

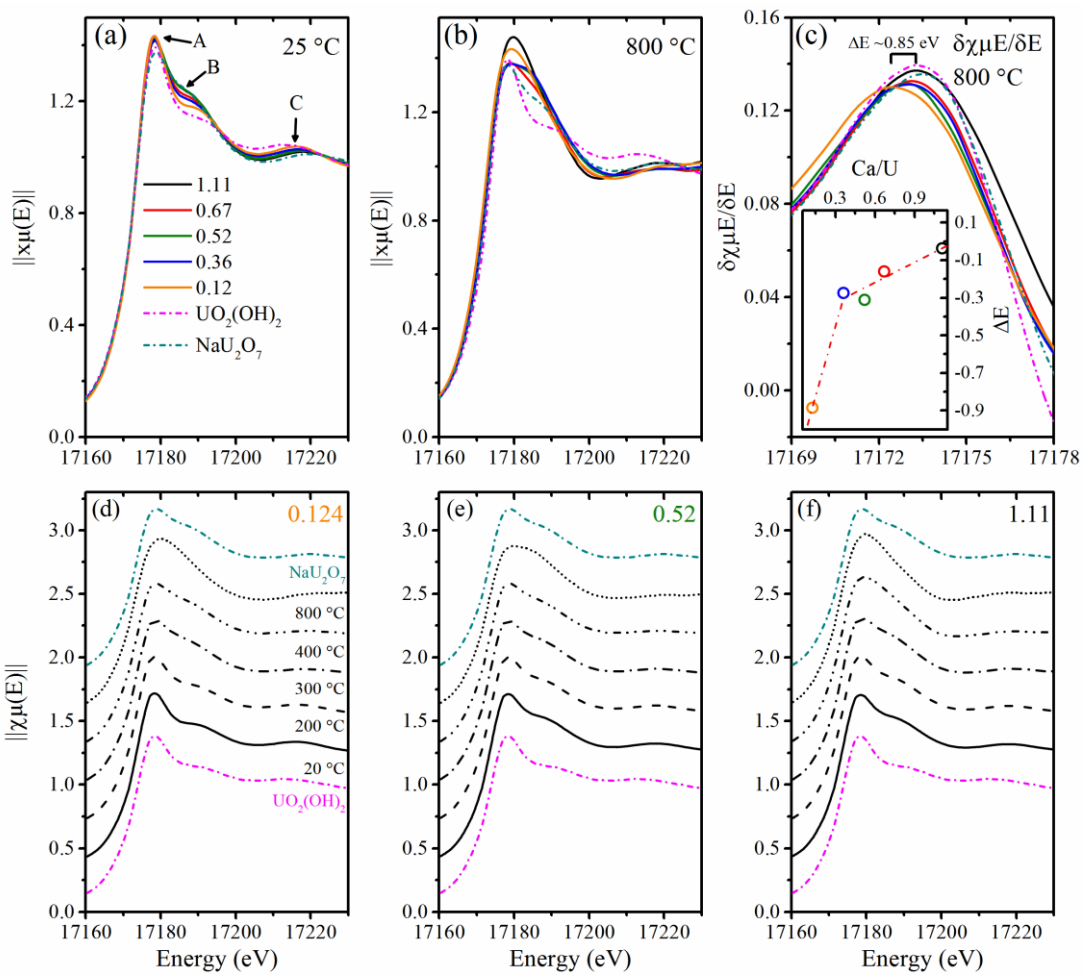

Figure 6.10 Normalised U L_{III}-edge XANES spectra for (a) precipitates; and (b) 800 °C samples; with bulk Ca/U-stoichiometry 0.124 – 1.11. Corresponding first derivative peak of 800 °C XANES are presented in (c) with ΔE positions plotted in the inset plot. The calcination series for samples with bulk Ca/U-stoichiometry of (a) 0.124; (b) 0.52; and (c) 1.11. Reference samples $Na_2U_2O_7$ and $UO_3.xH_2O$ are plotted in dashed lines.

Linear combination fitting (LCF) was performed on precipitates, intermediates and crystallised sample XANES with bulk Ca/U of 0.124, 0.52, and 1.11 (Figure 6.11a-c), using the endmember samples 0.12-25 °C (Becquerelite), 1.11-800 °C ($CaUO_4$); and references $Na_2U_2O_7.xH_2O$, $UO_3.xH_2O$. Fitting results are presented as apparent fit weighting (left axis) and χ^2 of fit (right axis). Accordingly, multiple-scattering (MS) contributions of precipitates become more Becquerelite-like (black squares) at lower bulk Ca/U (Figure 6.11c), and more akin to a hydrous uranate-like phase towards higher Ca/U (Figure 6.11a), with Ca/U 0.52 samples (Figure 6.11b) lying at the approximate equivalence point.

With increasing temperature, multiple-scattering contributions become more uranate-like, causing an abrupt switch-over in the 200 – 300 °C intermediates. However, as χ^2-values increase in all samples except 1.11 (Figure 6.11a), the immediate coordination environments are unique to that of $Na_2U_2O_7.xH_2O$ and $CaUO_4$.

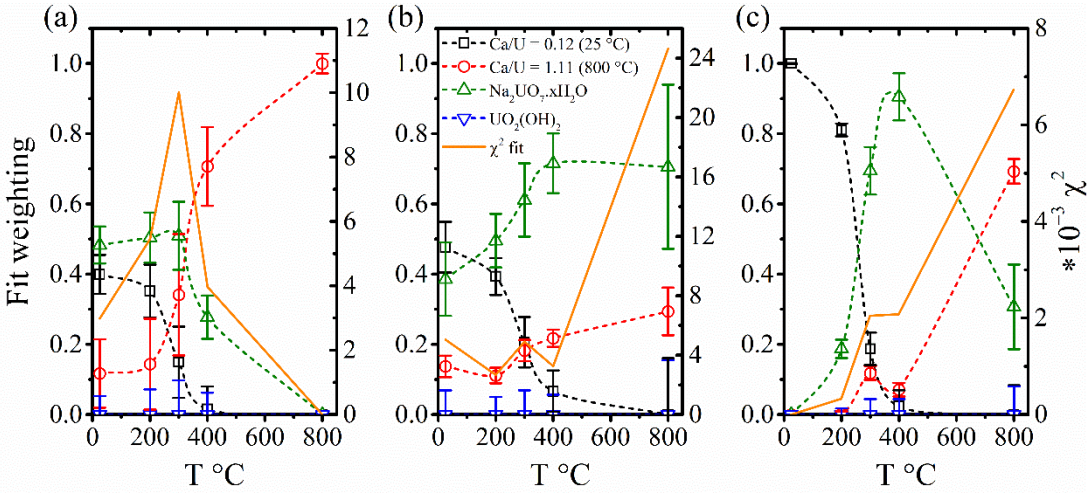

Figure 6.11 Linear combination fitting (LCF) summaries for calcination products in the Ca/U-stoichiometry (a) 1.11, (b) 0.52, and (c) 0.12, using diagonally endmember phases 1.11-800 °C, 0.124-25 °C; and reference sample spectra for $Na_2U_2O_7.xH_2O$, $UO_3.xH_2O$. Scatter-line trends are fit weighting values for each reference, whilst orange solid-lines are χ^2 values for the fit.

6.3.5.2 EXAFS

K-tests [57, 69] were performed to determine relative changes in coordination shell orders in poorly-ordered and crystalline phase spectra (see section a for further details).

6.3.5.2.1 Ca^{2+}-U(VI)-oxyhydrate precipitates

The EXAFS of precipitates (25 °C) with bulk Ca/U ranging 0.124 – 1.11 (fig, solid lines), were modelled using the uranyl(VI) oxyhydrates Schoepite [70] (red dashed line), Ca^{2+}-Becquerelite [42] (blue dotted line), K-Compreignacite [71] (green dashed-dot line), and $Ca[UO_2)_4O_3(OH)_4](H_2O)_2$ [72] (orange dash-dot). Partial occupancy in structural files were initialised as full, then altered during refinement of coordination number (CN), whilst half of potassium positions in K-Compreignacite were replaced with calcium and the rest removed prior to path generation in Artemis. Refinement parameters are presented in the appendices (Table C4 – Table C8).

All spectra were modelled using split U-O, U-U coordination shells. The 0.124 (25 °C) precipitate (Figure 6.12a, b, Ca/U 0.12) was best modelled (lowest R^2, χ^2, lower is better) by Becquerelite ($Ca[UO_2)_6O_4(OH)_6]\cdot 8(H_2O)$) with a theoretical Ca/U of 0.167, and is consistent with expectations from powder XRD patterns (Figure 6.4a, 25 °C) and FTIR spectra (Figure 6.9a, 25 °C). Conversely, a hydrous Ca^{2+}-U(VI)-hydroxide phase ($Ca[UO_2)_4O_3(OH)_4](H_2O)_2$) with higher structural Ca^{2+}-incorporation (Ca/U = 0.25) [72] provided lower χ_v^2 and R^2 values for spectra of precipitates with higher bulk-Ca^{2+} (Figure 6.12a, b, Ca/U 0.36 – 1.11).

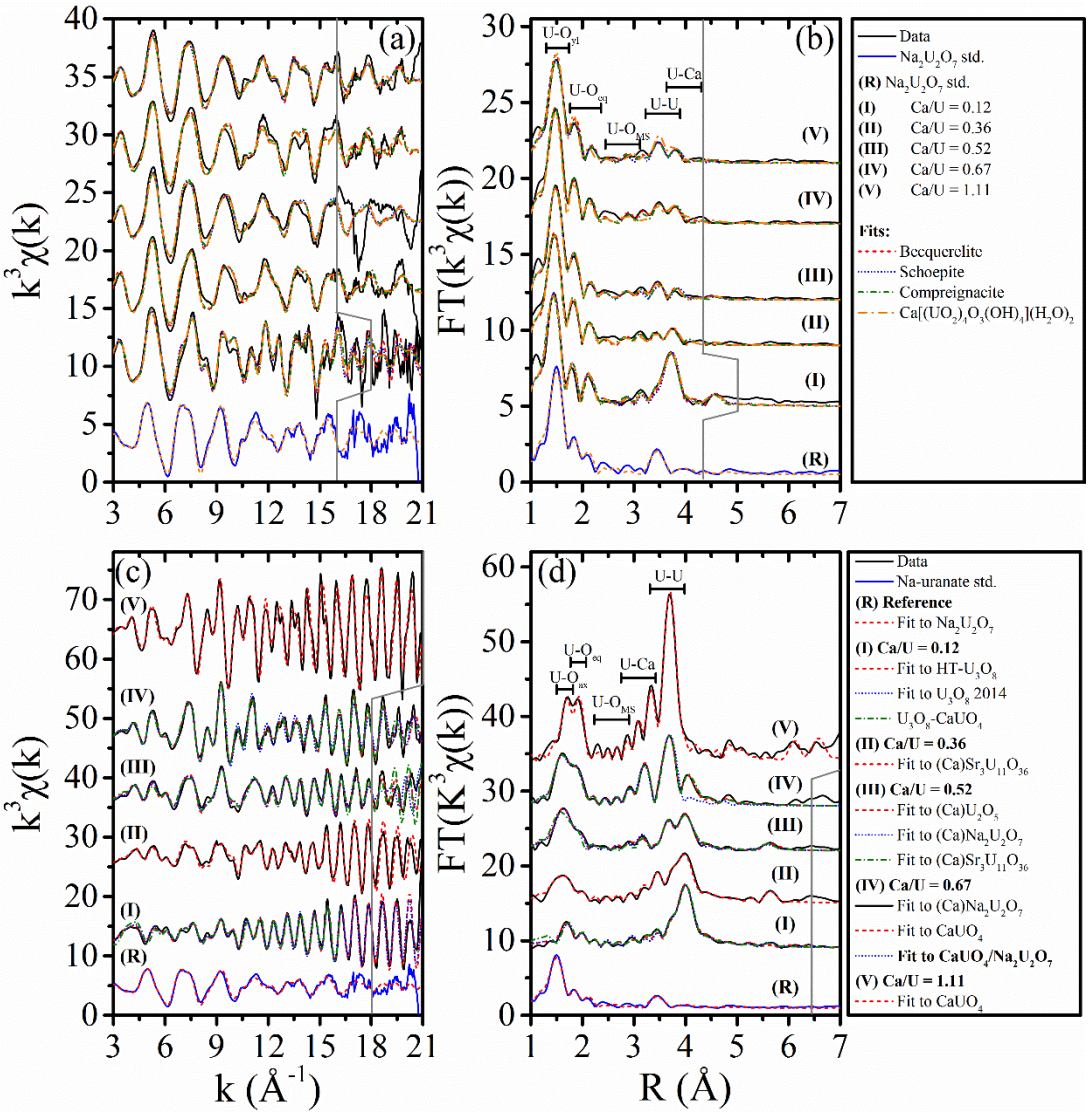

Figure 6.12 Normalised U L_{III}-edge k-space and R-space EXAFS for (a, b) precipitates; and (c, d) crystalline (800 °C) samples with bulk Ca/U-stoichiometry of (I) 0.124, (II) 0.36, (III) 0.52, (IV) 0.67, and (V) 1.11. (R) is reference material $Na_2U_2O_7.xH_2O$. Solid lines are background subtracted data, dashed coloured lines are refined fits for relevant structural models. Grey solid line represents fitting limits used for each spectrum.

6.3.5.2.2 Intermediate phases

The k^3 (Figure 6.13a-c) and R-space (Figure 6.13d-f) EXAFS of crystallisation intermediates for 0.12, 0.52, and 1.11 Ca/U (200 – 400 °C) were modelled using the same structures as tested in their corresponding precipitates, though remarkably, the best fits were obtained in all Ca/U and temperatures using the $Ca[UO_2)_4O_3(OH)_4].2H_2O$ structure [72] (Figure 6.13a-c, d-f). The contributions from U-U and U-Ca scatterers (~3 – 4 Å) appear to decrease up to 400 °C for 0.12 and 0.52 Ca/U (Figure 6.13d, e), whereas the 1.11 Ca/U R-space EXAFS at 400 °C (Figure 6.13f) already begins to resemble that of its crystalline endmember, though refinement using $CaUO_4$ produced lesser (χ_v^2 ~422, R^2 ~0.030, lower is better) fits compared to

$Ca[UO_2)_4O_3(OH)_4].2H_2O$ (χ_v^2 ~317, R^2 ~0.019). Models were marginally improved with the addition of U-U and U-Ca scattering paths (>5 %), which were therefore retained in final fits.

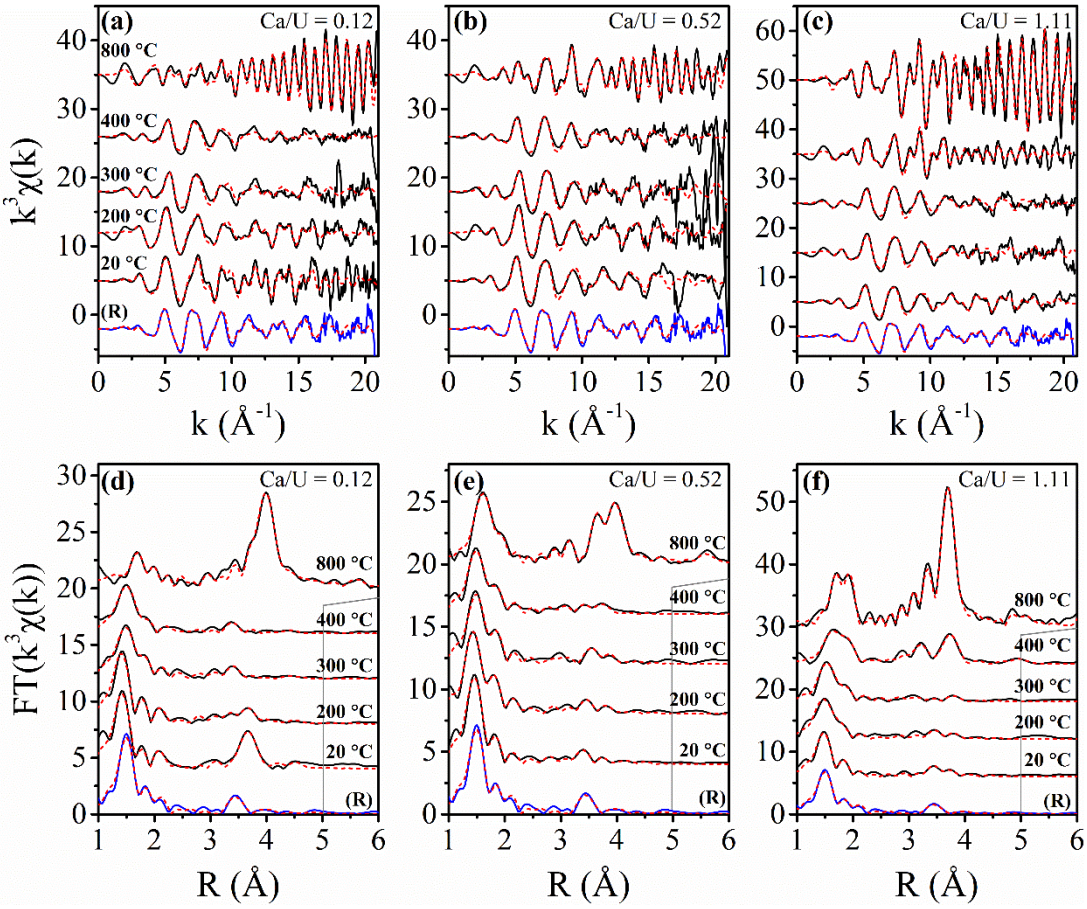

Figure 6.13 Normalised U L_{III}-edge k-space EXAFS of reference material ($Na_2U_2O_7.xH_2O$), precipitate (20 °C), crystallisation intermediates 200, 300, 400 °C, and crystallised (800 °C) samples with Ca/U-stoichiometry of (a) 0.124; (b) 0.52; and (c) 1.11. Corresponding R-space spectra are presented in graphs (d) – (f). Solid lines are background subtracted data, and dashed lines are best fit models. Grey lines represent the fitting window for each spectrum.

6.3.5.2.3 U-oxide and uranate endmembers

The 800 °C spectra (Figure 6.12c, d) were modelled independently using various crystalline phases. At 0.124 Ca/U, two synthetic α-$U^{V,\ VI}{}_3O_8$ structures [73, 74] provided significantly better fits compared to the structurally similar [75] α-$U^{VI}O_3$ [76-78] and δ-$U^{V}{}_2O_5$ [79, 80]. The fit was improved somewhat ($\Delta\chi_v^2$ ~70) with the inclusion of a Ca-shell at ~3.16 Å, which refined towards R_{eff} ~3.22 Å and a lower CN of ~0.4 Ca/U. The 0.36 Ca/U spectrum was modelled well using a Ca^{2+}-replaced $Sr_3U_{11}O_{36}$ [47] structure (χ_v^2 ~160, R^2 ~0.013) (Figure 6.12d-II) as expected from XRD (Figure 6.1b, Figure 6.4b-800 °C). Similarly, the 1.11 Ca/U spectra (Figure 6.12d-V) was modelled well (χ_v^2 ~212, R^2 ~0.016) using the $CaUO_4$ structure

revealed in XRD analysis (Figure 6.1b, Figure 6.4e-800 °C), resulting in a split U-O shell containing 8 oxygens (~1.9, 2.3 Å), followed by a ~5.5*U-U coordination shell at R = 3.87 Å.

Structural data for Ca^{2+}-diuranate (CaU_2O_7) is unavailable and its structure is poorly-understood, preventing direct fitting of the 0.52 Ca/U phase. As the stoichiometry of the 0.52 Ca/U phase lies approximately halfway between 1.11 Ca/U ($CaUO_4$) and 0.124 Ca/U (α-U_3O_8), the likeness of its coordination environment to uranate or U-oxide environments were tested using known phases. A reasonable fit (χ_v^2 ~395.16, R^2 ~0.0195) was found when using a δ-U_2O_5 structure with directly bound U-oxide layers, including a U-Ca SS-path inserted at 3.54 Å (N = 3) to reflect that of $CaUO_4$. However, upon repetition with $Ca_3U_{11}O_{36}$, 0.52 Ca/U phase was reflected poorly (χ_v^2 ~1665, R^2 ~0.09) in spite of the structural similarity between the two coordination environments. Using the Ba-diuranate (BaU_2O_7) [81, 82] as a structural model yielded an improved fit (χ_v^2 ~602, R^2 ~0.022) for the first U-O coordination sphere, though deteriorated significantly upon reaching the U-U coordination shell at ~3.5 – 3.8 Å. Finally, using the structure of alpha Na-diuranate ($Na_2U_2O_7$) [83], an improved fit was found with R_{max} = 6.5 Å (χ_v^2 ~249, R^2 ~0.017) (Figure 6.12d-III, blue dots).

Modelling of crystalline 0.67 Ca/U (Figure 6.12d-IV) was first attempted using $CaUO_4$ given the closeness in spectral features to 1.11 Ca/U (Figure 6.12d-V). However, fitting was only possible as far as R_{max} ~3.9 Å, whilst the U-U sub-shell centred at ~4.1 (k-test) was unaccounted for (Figure 6.12d-IV, blue-dotted line). Instead, the Ca^{2+}-replaced Na^+-diuranate used for 0.52 Ca/U modelled the spectra well (χ_v^2 ~212, R^2 ~0.011). This resulted in a Ca-shell at 3.63 Å (CN = 4), and a 3-layer shell containing 2, 3, and 1 U-scatterers at ~3.77, 3.9, and 4.2 Å respectively.

6.3.5.2.4 U-O and U-Ca coordination

The axial U-O_{yl} bond lengths within Ca^{2+}-U(VI)-oxyhydrate precipitates increase from ~1.81 – 1.84 Å with higher bulk Ca/U (Figure 6.14a), whilst average U-O_{eq} bonds lie closer, ranging ~2.34 – 2.35 Å (Figure 6.14b); both of which corroborate with predictions from FTIR-spectroscopy (Figure 6.9d) and XANES (Figure C15) data. This compression of the first U-O coordination sphere in the axial direction (Figure 6.15a) appears dependent on both Ca/U and OH/U stoichiometry given the reduction in precipitation-pH (Figure C1), resulting in a shift from a Schoepite-like (Figure 6.15a, blue line) to a uranate-like coordination environment (Figure 6.15a, black line). The axial U-O_{ax} decreases marginally after the first dehydration at ~200 °C (Figure 6.2b, step 1), and whilst this appears true for U-O_{eq} in 0.52 Ca/U (Figure 6.14b, green), opposing expansion and compression is observed for 0.12 and 1.11 Ca/U respectively (Figure 6.14b, orange, black). During the two-step CO_2-removal (Figure 6.2b) up to 400 °C, axial U-O_{ax} bonds expand by ~0.04-0.07 Å, with 1.11

Ca/U exhibiting the largest increase. The exothermic decomposition step (Figure 6.2d, step 2) is also accompanied by an inflection in U-O_{eq} distances at 300 °C (Figure 6.14b).

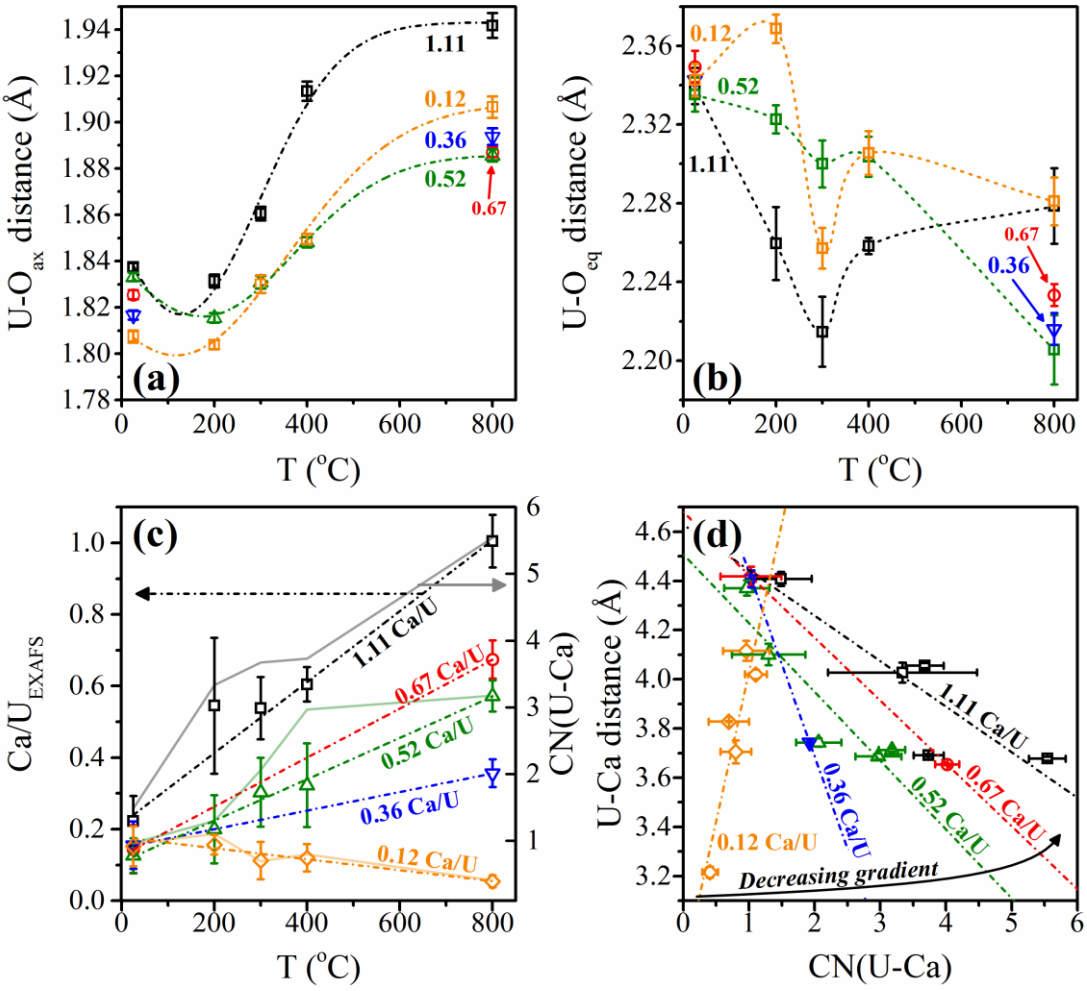

Figure 6.14 Extracted trends from modelled EXAFS spectra showing (a) change in axial U-O distance; (b) CN-normalised average equatorial U-O distance; as functions of temperature; (c) Ca/U_{EXAFS} (symbols) and U-Ca coordination number (solid lines) as a function of increasing temperature; and (d) The dependence of U-Ca separation R(U-Ca) on the coordination number for different crystallisation series.

During crystallisation between 400 – 800 °C, U-O_{ax} distances continue to elongate, whilst U-O_{eq} compresses slightly, with the midpoint Ca/U (0.52) exhibiting the largest decrease. These changes manifest throughout the stoichiometric ensemble as an overall axial compression in the first uranyl(VI)-oxide coordination sphere, that coincides with dehydroxylation and decarbonation processes. Endmembers with minimal (0.12) and maximal (1.11) initial Ca^{2+}-content exhibit a recovery in equatorial U-O distance in their crystallized states. These changes are also coincident with changes in the approximate CN of the 1st UO-shell, which peaks at 300 °C for 1.11 and 0.52, whilst 0.12 peaks at 400 °C (see supplementary information III, Figure C17 and Table C4 – Table C8 for further details).

The average CN of U-Ca scatterers lying within ~5 Å of U-absorbers is significantly lower in the precipitates than that of the bulk (Figure 6.14c, 25 °C), and varies between 0.22 – 0.12 Ca/U, or 1 - 1.5 Ca-scatters. Samples with bulk Ca/U between 0.36 – 1.11 exhibit almost linear increases in Ca^{2+}-content as a function of increasing temperature (Figure 6.14c), to reach Ca/U ratios (~1, 0.67, 0.57, 0.36) similar to that expected from bulk values by 800 °C. Some deviations from this trend occur between 25 – 200 °C that coincide with larger expected errors (Figure 6.14c, 200 °C). Whilst the growth in Ca^{2+}-content appears true for 0.12 Ca/U up to 200 °C (~0.15 – 0.16 Ca/U_{EXAFS}), this reverses towards higher temperature (Figure 6.14c, orange), where Ca/U_{EXAFS} decreases from ~0.16 (NCa ~1) to ~0.06 (NCa ~0.4) within ~6.5 Å. As the average number of Ca^{2+}-scatterers increase, average U-Ca separation distance reduces linearly from ~4.4 – 3.2 Å; for 1.11 – 0.12 Ca/U respectively (Figure 6.14d). The decrease in gradient (Figure 6.14d, arrow) represents a reduction in the sensitivity of separation distance on bulk Ca/U, and is inverse for 0.12 Ca/U (Figure 6.14d, orange).

6.4 Discussion

6.4.1 Ca^{2+}-U(VI) oxyhydrate precipitates

A change in in bulk precipitate Ca/U from 0.12 to 1.11 increases molecular stretching (symmetric, asymmetric, $\nu_{1,3}$) and decreases intermolecular bending (ν_2) frequencies of water (Figure 6.1a). This constitutes a simultaneous increase in OH-bond covalency and weakening of hydrogen bonding within samples [38, 39], indicating a shift in the state of water from hydrate towards hydroxide. This may be related to the extent of hydrolysis achieved during precipitation (Figure 6.13, Figure C1), as well as continued Ca^{2+}-H_3O^+ exchange driven by increasing alkalinity (pH 11) [11, 84, 85]. Under Ca^{2+}-deficient conditions and low OH^--availability, rapid crystallisation of Becquerelite occurs; presumably via oriented attachment given the rapid kinetics [86-90] compared literature observations [42, 51, 55, 91] (see chapter 5). Increasing pH and Ca^{2+}-availability promotes incomplete structural rearrangement via hydroxylation and occlusion of calcium hydroxide nanoclusters within primary amorphous precipitates, resulting in some localised structures suspended in a matrix of amorphous material (secondary amorphous state) [92-94], that become more uranate-like (Figure 6.15a, pH 6→11) [95]. Above ~1.5 Ca/U, segregation of crystalline Portlandite (Figure C4a) causes the distinctive covalent OH-peak at 3641 cm^{-1} (Figure C2a, asterisk) [96], revealing an apparent congruency limit for poorly-ordered Ca^{2+}-U(VI)-oxyhydrates.

6.4.2 Dehydration mechanisms

A shift in the mechanism of step 1 towards surface dehydration could cause the reduction in reaction endothermicity (Figure 6.2d, green), and lower activation barriers (Figure 6.15b, black squares) towards values considerably lower than that expected from dehydroxylation [97, 98]. Given the increase in TMA^+-removal (Figure 6.2c, grey) and exothermicity of step 2 (Figure 6.2d-red, stronger sorption), this could be caused by higher concentrations of structurally incorporated TMA^+-ions, rather than via a direct Ca^{2+}-influence, positions which would otherwise be occupied by hydrate. Indeed, an isomorphic TMA^+-Ca^{2+} substitution is conceivable given their similar ionic radii (i.r.TMA^+ ~3.22 Å [99, 100], i.r.$Ca^{2+}(H_2O)_8$ ~4.3 Å [42]) and permeability [101]. This is compatible with an increase in surface-volume ratios (Figure 6.5, Figure 6.6, smaller particles) or occluded-water despite extensive alcohol-rinsing of precipitates; as well as more prominent alkyl or amide bands in the FTIR spectra with higher Ca/U (Figure 6.9).

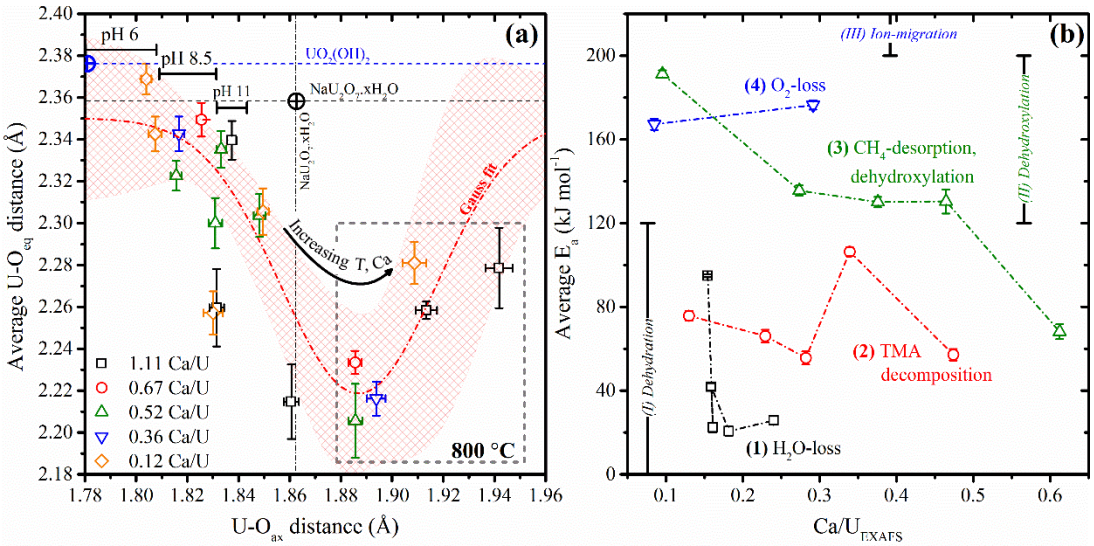

Figure 6.15 Summary of EXAFS-fitting and TGA-DSC data showing (a) Axial versus average equatorial U-O distances, and (b) Average activation energies as a function of the amount of structurally incorporated Ca^{2+} (Ca/U_{EXAFS}) prior to the corresponding reaction, respectively.

Precursor Ca/U and TMA/U-stoichiometry were altered inversely during synthesis, indicating that structural incorporation of TMA^+ and Ca^{2+} could be mutually exclusive. However, the increase in Ca-scatterers (ΔCa~0.15 to 0.2) at U-Ca distances ~4.4 Å (Figure 6.14c), is highly suggestive of Ca^{2+}-occupancy within the interlayer. Consequently, interlayer-Ca^{2+} could act as a Lewis catalyst to reduce activation barriers associated with both dehydration and dehydroxylation (Figure 6.15b, steps 1 and 3), via the disruption of H-bonding in bridging hydrate or hydroxyl groups (Figure 6.1a) [102]. Though, as the U-O polyhedra become more uranate-like (Figure 6.12), the latter is expected to dominate interlayer reactions towards 1.11 Ca/U [1, 2, 103].

Contrary to other intermediate stages, thermal activation of the first TMA^+-removal exhibits a lesser reduction (Figure 6.3a-e, red line) towards higher Ca/U (Figure 6.2, step 2). This is contradictory to the reduction in crystallinity or crystalline-domain size (Figure 6.4, Figure 6.6, Figure 6.7, 20 °C), which given the diffusion-limited mechanism (Figure 6.1, reaction step 2), should promote interstitial TMA^+-expulsion from the shorter uranyl(VI)-hydroxide layers. This would suggest that excess-TMA^+ in 0.36 – 1.11 Ca/U precipitates could be present as epitaxial-sorbates or inter-particle occlusions, supported by a volume-limited (3D) (Table 6.1) CH_4/CO_2-release[1] (Figure 6.2b, c).

Conversely, the interlayer-TMA^+ could undergo a 2^{nd}-order (Figure 6.1– step 2) elimination reaction (200 – 300 °C) to leave U-O-CH_3 moieties [56, 94, 104, 105], which is supported by approximately chemisorptive activation barriers (Figure 6.3b, green) [40]. This diffusion influenced process (Table 6.1) causes a collapse in lattice spacing (Figure 6.8b, 300 °C), whilst mostly preserving the crystallite size (Figure 6.4 - no peak FWHM change, Figure 6.6). The thermal activation increases as a function of reaction progression α (Figure 6.3), suggesting the mechanism could be topotactic given the reduction in escape pathways with degradation of frame-working TMA^+ [106]. If there is concurrent interlayer Ca^{2+}/TMA^+-occupancy, then subsequent desorption (Figure 6.2d) and lateral-effusion of decomposition (CH_4, $N(CH_4)_3$) products could become hindered by comparatively less mobile Ca^{2+}-ions. However, this is somewhat inconsistent with the decrease in magnitudes of activation barriers (Figure 6.15b-3) and reaction enthalpy (Figure 6.2d) towards higher-Ca/U, which indicates that a higher interlayer Ca^{2+}-content could catalyse CH_4/CO_2-desorption.

The reduction in sensitivity of (U-Ca)-separation distance to Ca^{2+}-occupancy within the interlayer (Figure 6.14b) could cause the U-O polyhedra distortion (Figure 6.15a) via increased $U\text{-}O_{yl} \rightarrow Ca^{2+}$ electrostatic interactions, weakening $U\text{-}O_{yl}$ bonds. This would be stabilised by $\sigma \rightarrow 6d$ electron donation from increasing equatorial O-ligands (Figure C17) [107] and further enhanced by an inductive charge transfer from methyl moieties $CH_3 \rightarrow O_{eq} \rightarrow U$. This binary influence on interlayer separation could consequently enhance outward-diffusion of gaseous products in particles with higher interlayer-Ca^{2+} (Figure 6.15b-3), whilst progressing TMA^+-degradation hinders CH_4/CO_2-removal.

[1] Whilst reaction enthalpies are consistent with both CO_2 and CH_4, whilst outflow mass-spectrometry detects CO_2, the oxic atmosphere likely causes $CH_4 \rightarrow CO_2$ oxidation upon release from the interlayer.

6.4.3 Crystallisation mechanisms

The local (Table C4 - Table C8, larger O, Ca, and U-shell fitted σ^2-values), long-range disorder (Figure 6.4), and average Ca-scatterers within ~4.5 Å increase in intermediates phases (Figure 6.14c, 200 → 400 °C). Reaction enthalpy magnitudes for step 1 and 2 (Figure 6.2d) are similar, whilst activation barriers increase (Figure 6.15b-step 2) for most samples though remain lower than that of similar phases ($(NH_4)_2U_2O_7$, ~109 kJ mol^{-1} [108]) [109]. An increase in the number of nanocrystallites (Figure 6.6) and bright-spots in SAED-patterns (Figure 6.7) towards 400 °C indicates some (re)crystallisation between steps 2 and 3 to form either complex phase mixtures, or a poorly-ordered precursor. Though given the similar 2theta (Figure 6.4) and nm^{-1} (Figure 6.7) peak positions between intermediates and endmembers, the latter is more probable.

The EXAFS modelled Ca/U of Becquerelite upon reaching 200 °C (Figure 6.14a-orange, ~0.16 Ca/U) exceeds the bulk precipitate Ca/U (Figure C1, 0.12), suggesting that some of the apparent Ca^{2+}-increase in other samples could also be due to differences in hydrate content or spectra resolution. This is unsurprising, as the low activation barriers (Figure 6.15b, step 1), are probably insufficient to support solid-state migration [109]. With further heating, Becquerelite (0.124 Ca/U) underwent partial amorphisation and recrystallization (Figure 6.7a) into β-UO_3 [43], which could allow some Ca^{2+} to remain intercalated. As the 2-stage formation of α-U_3O_8[2] between 400 – 800 °C occurs via geometric contraction-diffusion controlled H_2O/O_2-loss (Figure 6.2b) [45, 110], β-UO_3 must contain some remnant hydroxide. However, kinetic barriers to dehydroxylation (Figure 6.15b, ~191 kJ mol^{-1}) are significantly larger compared to corresponding reaction enthalpies (Figure 6.2d, ~57 kJ mol^{-1}), as well as those expected from similar phases (Schoepite ~49 kJ mol^{-1} [111]). Instead values are more typical of solid-state ion-diffusion [109], indicating that dehydroxylation of a β-UO_3-like[3] $Ca_{0.12}.UO_3.xH_2O$-phase is strongly hindered by the presence of structurally incorporated calcium. Dehydroxylation of $Ca_{0.12}.UO_3.xH_2O$ likely occurs via an oxolation mechanism [11, 21, 114] to form anhydrous-UO_3 [115, 116], eliminating water, whilst the reduction to α-U_3O_8 occurs via O_2-hole formation (anion vacancy) [117]. Self-reduction of UO_3 is probably hindered by elevated partial pressure of O_2 (oxic atmosphere during calcination) [118] in addition to a similar

[2] If β-UO_3 is formed at the end of step 3 in 0.124, then a loss of 0.32 mol.O per mol.UO_3 (0.13 mol.O_2 mol.UO_3^{-1}) during step 4 (620 °C), would reduce UO_3 to $UO_{2.74\pm0.08}$. The black colouration of the sample, the downshift in the XANES white-line position, and EXAFS modelling to α-U_3O_8 confirms its formation, rather than the isomorphic α-UO_3.

[3] B-UO_3 may undergo transformation to γ-UO_3 prior to forming α-U_3O_8 [112], a structural isomer with more pronounced interstices [113].

interaction with Ca, whilst particle size (Figure 6.6) appears mostly independent [119]. The U-Ca distance of the $Ca_x.\alpha\text{-}U_3O_8$ product (Figure 6.14b-orange, ~3.2 Å) is significantly shorter than in all samples, including the range expected for uranates or uranyl(VI) oxyhydrates (~3.6 – 4.5 Å) [120-122]. Therefore whilst the former phase may be present as a uranate or mixed phase, some Ca^{2+} must undergo cation-migration into 9-coordinate vacancies [123]. Although previous attempts in synthesising Mg-$Ca_{0.06}.\alpha\text{-}U_3O_8$ bronze were unsuccessful, lower temperatures than that used here were used, whilst precursors were crystalline ($CaUO_4$ and UO_2, UO_3) [124], which could require higher thermal activation; Mg^{2+}-insertion has been demonstrated in latter studies [125, 126]. The lower insertion ratios observed here are substantiated by considerable activation barriers (Figure 6.3a, step 4), which probably control a concerted O_2-hole formation during $\beta\text{-}UO_3 \leftrightarrow \alpha\text{-}U_3O_8$ interconversion, incidentally preserving crystallite size (Figure C9) [46].

The similar reduction barriers for 0.36 Ca/U (Figure 6.15b-step 4, ~176 kJ mol^{-1}) and UO-sheet structure of $(Ca)Sr_3U_{11}O_{36}$ implies the same Ca^{2+}-inhibited migration mechanism, though a direct $[UO_{6\text{-}7}] \rightarrow [Ca(Sr)O_{6\text{-}7}]$ polyhedra replacement [47] occurs via nucleation with reduced geometry (Figure 6.1, 2D). Furthermore, resemblance between step 3 activation energies (Figure 6.15b, green) and apparent mechanisms of reaction (Table 6.1) for 0.36 – 0.67 Ca/U intermediates, imply extension to their crystallisation pathways. This is somewhat supported by nanolayering in endmembers (Figure 6.5, Figure 6.6, Figure 6.8a) and release of CO_2 rather than H_2O in steps 2 and 3. If crystallisation is controlled by Ca^{2+}-diffusion, then an increase in bulk Ca/U (0.36→0.67) would conceivably enhance nuclei growth rates due to higher localised Ca^{2+}-availability (Figure 6.8a-larger crystallites) [127]. Though the significantly larger crystallite domains (Figure 6.8a) and reduction-mediated transition (Figure 6.2b) of 0.36 Ca/U suggests a crystallisation mechanism more related to $\alpha\text{-}U_3O_8$ than uranates of higher Ca/U. Indeed $Sr_3U_{11}O_{36}$ was an unsuitable model during modelling of 0.52 Ca/U in EXAFS analysis compared to a phase with separated UO-layers. Though notably, the $Na_2U_2O_7$ UO-sheet structure is somewhat associated with that of $\alpha\text{-}U_3O_8$ [83, 128], indicating that improved EXAFS-fits may have arisen due to the higher flexibility in UO-bond lengths. The high-contrast regions running parallel to basal planes in endmembers (Figure 6.5, Figure 6.6, see also Figure C8, Figure C9) are indicative of stacking faults, or formation of incongruous layers. Though the latter could be precluded, as EDS line-profiling revealed little evidence of non-stoichiometry relative to the basal plane. Therefore 0.36, 0.52, and 0.67 Ca/U particles could undergo similar transformations unique to that of U_3O_8 (0.12 Ca/U) or $CaUO_4$ (1.11 Ca/U). Crystallite size at 400 °C did not exhibit significant deviation from ~5 nm (Figure 6.5, Figure 6.6), whereas those at 800 °C increase as a function of Ca^{2+}-content between 0.52 – 0.83 (Figure 6.8a), and lie closer to platelet thickness than

basal diameters (Figure 6.6). Therefore, equatorial growth is probably favoured, and as activation barriers are reduced slightly (Figure 6.15b) towards higher Ca^{2+}-content, vertical stacking could be limited by Ca^{2+}-diffusion (Table 6.1) to contact-sites. Conversely, prominent stacking faults are entirely lacking in particles (Figure 6.5i) at the upper-limits of both precursor (Figure 6.1a, ~1.11 – 1.5 Ca/U) and structurally incorporated (Figure 6.14a) Ca^{2+}-content. In addition, step 3 activation energies (Figure 6.15b-green, ~140 kJ mol^{-1}), crystallite size (Figure 6.8a, ~15 nm) and standard deviation across several XRD-reflections are significantly smaller, which indicates a shift towards isotropic crystallisation.

Therefore, when hydroxide and calcium availability is low (Ca/U → 0.124), precipitation of crystalline Becquerelite is favoured, and solid-state transformations are dominated by amorphisation-crystallisation-reduction processes. However, as the extent of hydrolysis (higher pH), temperature, and long-range order reduces above the 0.36 Ca/U limit, solid-state transformations become more akin to 2-stage nucleation, where crystallisation into endmember phases is preceded by formation of secondary from primary amorphous precursors. It may be that primary and secondary amorphous states are overlapped, where the former lies closer to the oligomeric uranyl(VI) hydroxide complexes in the precursor solution, and the latter tends towards uranate-like endmembers. An increase in extent of hydrolysis (Figure 6.15a, higher pH) or concentration of Ca^{2+}-rich occlusions favours transition to the latter (uranate-like coordination with poor long-range order), which consequently favours crystallisation into endmember uranates via secondary nucleation and growth [92-94].

6.5 Summary and conclusions

A series of Ca^{2+}-U(VI)-oxyhydrates were synthesised in the presence of tetramethylammonium and calcium ions. The Ca/U-stoichiometry of precipitates were highly dependent on pH, precursor-Ca/U, and temperature. Precipitates with bulk-Ca/U of 0.124 crystallised as Becquerelite, whilst solids between 0.36 and 1.11 Ca/U were amorphous. Above this apparent limit of congruency, Portlandite formed as a discrete phase in addition to Ca^{2+}-U(VI)-oxyhydrate. Through TGA-DSC and in-situ mass-spectrometry, the amount of trapped frame-working TMA^{+} in particles increased with higher bulk Ca/U. A combination of spectroscopic and diffraction techniques (FTIR, XAS, XRD, TEM/SEM) revealed that Ca^{2+}-U(VI)-oxyhydrates precipitate as secondary amorphous phases towards the latter (0.52 – 1.11 Ca/U), and undergo 2-stage nucleation and growth via dehydration, decarbonation, and desorption-dehydroxylation, whereas solid-state transformations of 0.12 – 0.36 Ca/U precursors are characterised more by amorphisation-crystallisation and reduction (O_2-loss).

Activation energies associated with dehydration and dehydroxylation processes were lowered with progressing TMA^+-removal, and is facilitated by inwards Ca^{2+}-migration between layers of stacking U-O-OH polyhedra, whereby higher interlayer Ca^{2+}-occupancy prior to each transformation catalyses further reaction. The U-O coordination environment of crystallised endmembers become more uranate-like as a function of structurally incorporated calcium.

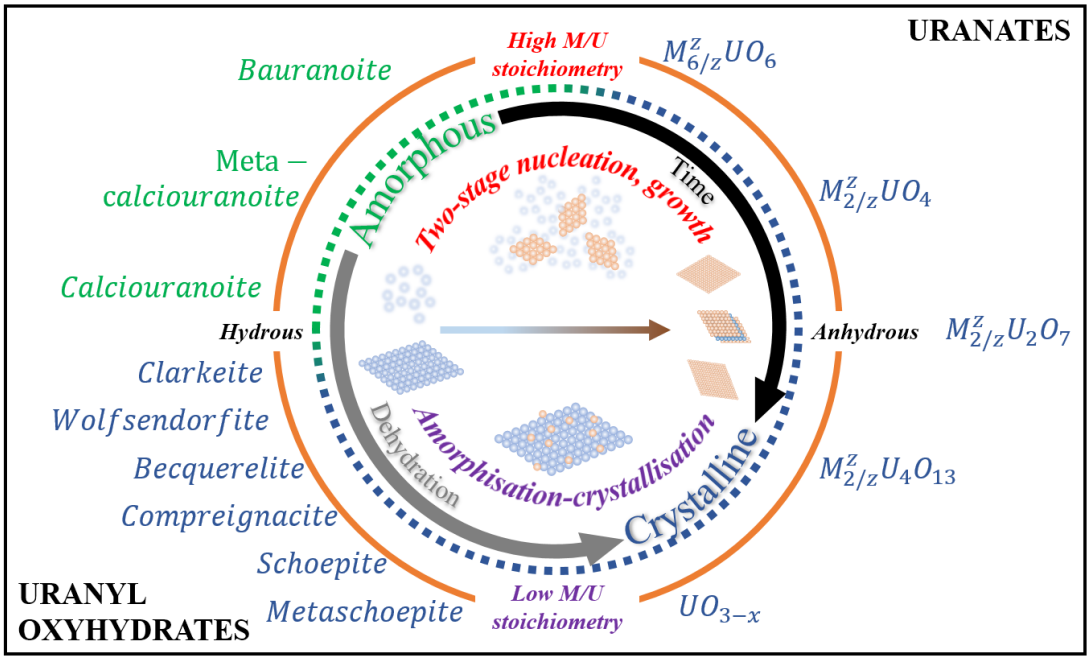

Figure 6.16 Summary figure of relationship between naturally occurring and anthropogenic uranyl(VI) oxyhydrates and metal uranates, with the expected transformation mechanisms influencing their conversion.

A new phase $Ca_3U_{11}O_{36}$ has been synthesised with Ca/U-stoichiometry of 0.36, and is isostructural to $Sr_3U_{11}O_{36}$. $Ca_3U_{11}O_{36}$ has a unique structure in that trimeric chains of UO-polyhedra are directly replaced by Ca^{2+}-O polyhedra, resulting in a tertiary Ca^{2+}-U(VI)-O phase that is closer to α-U_3O_8 in structure than the uranates of higher Ca^{2+}-content, due to U-O-U bonding in the vertical axis. Below the 0.36 Ca/U limit, Becquerelite undergoes amorphisation and recrystallisation into β-UO_3, and reduction to α-U_3O_8. During which, an insertion compound $Ca_{0.06}.U_3O_8$ forms during dehydroxylation to preserve the α-U_3O_8 crystal structure, whilst the remainder is removed during dehydroxylation to significantly hinder crystallisation. Discrete uranyl(VI) units are lost in both 0.12 and 0.36 Ca/U endmembers to form interlinked UO-polyhedra. Above the 0.36 Ca/U limit, structures more typical of metal uranates form, comprising discrete layers of UO-polyhedra stabilised by interlayer calcium ions.

6.6 Further recommendations

Non-classical crystallisation mechanisms are poorly understood, and are exacerbated by the lack in empirical data on non-zeolites. In particular, studies on crystallisation and solid-state chemistry of actinide materials are exceedingly rare. Whilst this alleviating study has revealed the profound influence of stoichiometry on the crystallisation mechanisms of amorphous uranyl(VI) oxyhydrates, significant improvements may be garnered via in-situ U L_{III} and Ca K-edge synchrotron-XAS and diffraction experiments to cover the entire temperature range during solid-state transformations. In addition, comparison with cations of different ionic radii or Lewis acidity (i.e. Na^{+}, Sr^{2+}, Al^{3+}) could provide a deeper understanding of occlusion-induced nucleation within primary or secondary amorphous states.

6.7 References

1. Finch, R.J. and Ewing, R.C., *Clarkeite: New Chemical and Structural Data.* American Mineralogist, 1997. **82**(5-6): p. 607-619.
2. Gruner, J., *The Chemical Formula of Clarkeite.* American Mineralogist, 1954. **39**(9-10): p. 836-838.
3. Brownsword, M., Buchan, A., Ewart, F., McCrohon, R., Ormerod, G., Smith-Briggs, J., and Thomason, H. *The Solubility and Sorption of Uranium (Vi) in a Cementitious Repository*. in *MRS Proceedings*. 1989. Cambridge Univ Press.
4. Altmaier, M., Neck, V., Mueller, R., and Fanghaenel, T., *Solubility of U(Vi) and Formation of $Cau_2o_7.3h_2o(Cr)$ in Alkaline $Cacl_2$ Solutions.* 2005.
5. Díaz Arocas, P. and Grambow, B., *Solid-Liquid Phase Equilibria of U(Vi) in Nacl Solutions.* Geochimica et Cosmochimica Acta, 1998. **62**(2): p. 245-263.
6. Guillaumont, R., Fanghänel, T., Neck, V., Fuger, J., Palmer, D.A., Grenthe, I., and Rand, M.H., *Update on the Chemical Thermodynamics of Uranium, Neptunium, Plutonium, Americium and Technetium*. 2003, Amsterdam, the Netherlands: Elsevier.
7. Valsami-Jones, E. and Ragnarsdottir, K.V., *Solubility of Uranium Oxide and Calcium Uranate in Water, and $Ca(Oh)_2$-Bearing Solutions.* Radiochimica Acta, 1997. **79**(4): p. 249-257.
8. Wellman, D.M., Mattigod, S.V., Arey, B.W., Wood, M.I., and Forrester, S.W., *Experimental Limitations Regarding the Formation and Characterization of Uranium-Mineral Phases in Concrete Waste Forms.* Cement and Concrete Research, 2007. **37**(2): p. 151-160.
9. Moroni, L.P. and Glasser, F.P., *Reactions between Cement Components and U(Vi) Oxide.* Waste Management, 1995. **15**(3): p. 243-254.
10. Skakle, J., Moroni, L., and Glasser, F., *X-Ray Diffraction Data for Two New Calcium Uranium (Vi) Hydrates.* Powder Diffraction, 1997. **12**(02): p. 81-86.
11. Ding, W., Botha, J.A., Hanson, B.C., and Burke, I.T., *Aqueous Hydroxylation Mediated Synthesis of Crystalline Calcium Uranate Particles.* Journal of Alloys and Compounds, 2016. **688, Part B**: p. 260-269.
12. Rogova, V., Belova, L., Kiziyarov, G., and Kuznetsova, N., *Calciouranoite, a New Hydroxide of Uranium.* International Geology Review, 1974. **16**(11): p. 1255-1256.
13. Rogova, V., Belova, L., Kiziyarov, G., and Kuznetsova, N., *Bauranoite and Metacalciouranoite, New Minerals of the Hydrous Uranium Oxides Group.* International Geology Review, 1974. **16**(2): p. 214-219.
14. Khoury, H.N., Sokol, E.V., and Clark, I.D., *Calcium Uranium Oxide Minerals from Central Jordan: Assemblages, Chemistry, and Alteration Products.* The Canadian Mineralogist, 2015. **53**(1): p. 61-82.
15. Cordfunke, E.H.P. and Loopstra, B.O., *Sodium Uranates: Preparation and Thermochemical Properties.* Journal of Inorganic and Nuclear Chemistry, 1971. **33**(8): p. 2427-2436.
16. Toussaint, C.J. and Avogadro, A., *Concerning Uranate Formation in Alkali Nitrate Melts.* Journal of Inorganic and Nuclear Chemistry, 1974. **36**(4): p. 781-784.

17. Cejka, J., *To the Chemistry of Andersonite and Thermal Decomposition of Dioxo-Tricarbonatouranates.* Collection of Czechoslovak Chemical Communications, 1969. **34**(6): p. 1635-1656.
18. Cejka, J., *Infrared Spectroscopy and Thermal Analysis of the Uranyl Minerals.* Reviews in Mineralogy and Geochemistry, 1999. **38**(1): p. 521-622.
19. Čejka, J. and Urbanec, Z., *Thermal and Infrared Spectrum Analyses of Natural and Synthetic Andersonites.* Journal of thermal analysis, 1988. **33**(2): p. 389-394.
20. Chakraborty, A.K., *Dehydroxylation Mechanism*, in *Phase Transformation of Kaolinite Clay*. 2014, Springer India: New Delhi. p. 313-322.
21. Van Groos, A.K. and Guggenheim, S., *Dehydroxylation of Ca-and Mg-Exchanged Montmorillonite.* American Mineralogist, 1989. **74**(5-6): p. 627-636.
22. Baran, V. and Tympl, M., *Uranates as a Form of Uranyl Hydrolytic Complexes.* Journal of Inorganic and Nuclear Chemistry, 1966. **28**(1): p. 89-98.
23. A. Volkovich, V., R. Griffiths, T., J. Fray, D., and C. Thied, R., *Solubilities and Solubilisation Enthalpies of Alkali Metal Uranates(Vi) in Carbonate Melts.* Physical Chemistry Chemical Physics, 1999. **1**(14): p. 3297-3302.
24. Carnall, W.T., Neufeldt, S.J., and Walker, A., *Reactions in Molten Salt Solutions .I. Uranate and Neptunate Formation in Molten Lithium Nitrate-Sodium Nitrate.* Inorganic Chemistry, 1965. **4**(12): p. 1808-&.
25. Griffiths, T.R. and Volkovich, V.A., *A Review of the High Temperature Oxidation of Uranium Oxides in Molten Salts and in the Solid State to Form Alkali Metal Uranates, and Their Composition and Properties.* Journal of Nuclear Materials, 1999. **274**(3): p. 229-251.
26. Hester, R.E. and Krishnan, K., *Vibrational Spectra of Molten Salts .2. Infrared Spectra of Some Divalent Metal Nitrates in Alkali-Metal Nitrate Solutions.* Journal of Chemical Physics, 1967. **47**(5): p. 1747-&.
27. Volkovich, V., Griffiths, T.R., Fray, D.J., Fields, M., and Wilson, P.D., *Oxidation of Uo2 in Molten Alkali-Metal Carbonate Mixtures: Formation of Uranates and Diuranates.* Journal of the Chemical Society-Faraday Transactions, 1996. **92**(24): p. 5059-5065.
28. Flynn, J.H. and Wall, L.A., *General Treatment of the Thermogravimetry of Polymers.* J Res Nat Bur Stand, 1966. **70**(6): p. 487-523.
29. Ozawa, T., *A New Method of Analyzing Thermogravimetric Data.* Bulletin of the chemical society of Japan, 1965. **38**(11): p. 1881-1886.
30. Kissinger, H.E., *Variation of Peak Temperature with Heating Rate in Differential Thermal Analysis.* Journal of research of the National Bureau of Standards, 1956. **57**(4): p. 217-221.
31. Kissinger, H.E., *Reaction Kinetics in Differential Thermal Analysis.* Analytical Chemistry, 1957. **29**(11): p. 1702-1706.
32. Akahira, T. and Sunose, T., *Method of Determining Activation Deterioration Constant of Electrical Insulating Materials.* Res Rep Chiba Inst Technol (Sci Technol), 1971. **16**: p. 22-31.
33. Starink, M., *The Determination of Activation Energy from Linear Heating Rate Experiments: A Comparison of the Accuracy of Isoconversion Methods.* Thermochimica Acta, 2003. **404**(1): p. 163-176.
34. Starink, M., *A New Method for the Derivation of Activation Energies from Experiments Performed at Constant Heating Rate.* Thermochimica Acta, 1996. **288**(1-2): p. 97-104.
35. Abràmoff, M.D., Magalhães, P.J., and Ram, S.J., *Image Processing with Imagej.* Biophotonics international, 2004. **11**(7): p. 36-42.
36. Livage, J., Henry, M., and Sanchez, C., *Sol-Gel Chemistry of Transition Metal Oxides.* Progress in solid state chemistry, 1988. **18**(4): p. 259-341.
37. Alain, M., Jacques, M., Diane, M.-B., and Karine, P. *Max: Multiplatform Applications for Xafs.* in *Journal of Physics: conference series*. 2009. Iop Publishing.
38. Betz, U., Scipione, G., Bonetti, E., and Hahn, H., *Low-Temperature Deformation Behavior of Nanocrystalline 5 Mol% Yttria Stabilized Zirconia under Tensile Stresses.* Nanostruct. Mater., 1997. **8**: p. 845.
39. Dogan, F., Roosen, A., and Hausner, H., *Influence of Hydroxide-Precursor Processing on the Densification of Yttrium Oxide Powders.* Adv. Ceram., 1987. **21**: p. 681.
40. Hayward, D.O. and Trapnell, B.M.W., *Chemisorption*. 1964: Butterworths London.
41. Coats, A.W. and Redfern, J., *Kinetic Parameters from Thermogravimetric Data.* Nature, 1964. **201**(4914): p. 68-69.
42. Burns, P.C. and Li, Y., *The Structures of Becquerelite and Sr-Exchanged Becquerelite.* American Mineralogist, 2002. **87**(4): p. 550-557.
43. Debets, P., *The Structure of B-Uo_3.* Acta Crystallographica, 1966. **21**(4): p. 589-593.

44. Chandrasekaran, B., Rao, R.J., Sreeram, K., Nair, B.U., and Ramasami, T., *Chrome Tanning: State-of-Art on the Material Composition and Characterization.* Journal of scientific & industrial research, 1999. **58**(1): p. 1-10.
45. Eloirdi, R., Ho Mer Lin, D., Mayer, K., Caciuffo, R., and Fanghänel, T., *Investigation of Ammonium Diuranate Calcination with High-Temperature X-Ray Diffraction.* Journal of Materials Science, 2014. **49**(24): p. 8436-8443.
46. Hoekstra, H.R. and Siegel, S., *The Uranium-Oxygen System: U_3O_8 · UO_3.* Journal of Inorganic and Nuclear Chemistry, 1961. **18**(0): p. 154-165.
47. Cordfunke, E.H.P., Van Vlaanderen, P., Onink, M., and Ijdo, D.J.W., *$Sr_3U_{11}O_{36}$: Crystal Structure and Thermal Stability.* Journal of Solid State Chemistry, 1991. **94**(1): p. 12-18.
48. Brisi, C. and Montorsi Appendino, M., *Studies on Calcium Uranates.* Ann. Chim. (Rome), 1969. **59**(400).
49. Sali, S.K., Sampath, S., and Venugopal, V., *Thermal Studies on Alkaline Earth Uranates.* Journal of Nuclear Materials, 2000. **277**(1): p. 106-112.
50. Scheck, J., Lemke, T., and Gebauer, D., *The Role of Chloride Ions During the Formation of Akaganéite Revisited.* Minerals, 2015. **5**(4): p. 778-787.
51. Cejka, J., Sejkora, J., Skala, R., Cejka, J., Novotna, M., and Ederova, J., *Contribution to the Crystal Chemistry of Synthetic Becquerelite, Billietite and Protasite.* Neues Jahrbuch Fur Mineralogie Abhandlungen, 1998. **174**: p. 159-180.
52. Hoekstra, H.R., *Infra-Red Spectra of Some Alkali Metal Uranates.* Journal of Inorganic and Nuclear Chemistry, 1965. **27**(4): p. 801-808.
53. Dousma, J. and De Bruyn, P.L., *Hydrolysis-Precipitation Studies of Iron Solutions. I. Model for Hydrolysis and Precipitation from Fe(Iii) Nitrate Solutions.* Journal of Colloid and Interface Science, 1976. **56**(3): p. 527-539.
54. Allen, G.C. and Griffiths, A.J., *Vibrational Spectroscopy of Alkaline-Earth Metal Uranate Compounds.* Journal of the Chemical Society, Dalton Transactions, 1979(2): p. 315-319.
55. Amayri, S., Arnold, T., Foerstendorf, H., Geipel, G., and Bernhard, G., *Spectroscopic Characterization of Synthetic Becquerelite, $Ca[(UO_2)_6O_4(OH)_6]\cdot 8H_2O$, and Swartzite, $CaMg[UO_2(CO_3)_3]\cdot 12H_2O$.* The Canadian Mineralogist, 2004. **42**(4): p. 953-962.
56. Bourgeat-Lami, E., Di Renzo, F., Fajula, F., Mutin, P.H., and Des Courieres, T., *Mechanism of the Thermal Decomposition of Tetraethylammonium in Zeolite. Beta.* The Journal of Physical Chemistry, 1992. **96**(9): p. 3807-3811.
57. Dousma, J., Van den Hoven, T.J., and De Bruyn, P.L., *The Influence of Chloride Ions on the Formation of Iron(Iii) Oxyhydroxide.* Journal of Inorganic and Nuclear Chemistry, 1978. **40**(6): p. 1089-1093.
58. Group, C.T., *Individual Monitoring for Intakes of Radionuclides by Workers: Design and Interpretation*. 1988, No longer published by Elsevier.
59. Bertsch, P.M., Hunter, D.B., Sutton, S.R., Bajt, S., and Rivers, M.L., *In Situ Chemical Speciation of Uranium in Soils and Sediments by Micro X-Ray Absorption Spectroscopy.* Environmental science & technology, 1994. **28**(5): p. 980-984.
60. Allen, P., Shuh, D., Bucher, J., Edelstein, N., Palmer, C., Silva, R., Nguyen, S., Marquez, L., and Hudson, E., *Determinations of Uranium Structures by Exafs: Schoepite and Other U(Vi) Oxide Precipitates.* Radiochimca Acta, 1996. **75**(1): p. 47-54.
61. Hudson, E., Rehr, J., and Bucher, J., *Multiple-Scattering Calculations of the Uranium L3-Edge X-Ray-Absorption near-Edge Structure.* Physical Review B, 1995. **52**(19): p. 13815.
62. Fillaux, C., Auwer, C., Guillaumont, D., Simoni, E., Barre, N., Shuh, D., and Tyliszczak, T. *Studies of Structural and Electronic Properties of Uranium Compounds, by Xanes Spectroscopy*. in *MATERIALS RESEARCH SOCIETY SYMPOSIUM PROCEEDINGS*. 2006. Warrendale, Pa.; Materials Research Society; 1999.
63. Bès, R., Rivenet, M., Solari, P.-L., Kvashnina, K.O., Scheinost, A.C., and Martin, P.M., *Use of Herfd–Xanes at the U L3- and M4-Edges to Determine the Uranium Valence State on $[Ni(H_2O)_4]_3[U(Oh,H_2O)(UO_2)_8O_{12}(Oh)]$.* Inorganic Chemistry, 2016. **55**(9): p. 4260-4270.
64. Hamilton, E.I., *Depleted Uranium (Du): A Holistic Consideration of Du and Related Matters.* Science of The Total Environment, 2001. **281**(1–3): p. 5-21.
65. Shinonaga, T., Steier, P., Lagos, M., and Ohkura, T., *Airborne Plutonium and Non-Natural Uranium from the Fukushima Dnpp Found at 120 Km Distance a Few Days after Reactor Hydrogen Explosions.* Environmental science & technology, 2014. **48**(7): p. 3808-3814.
66. Joseph, D., Nayak, C., Babu, P.V., Jha, S., and Bhattacharyya, D., *Chemical Shift of U L3 Edges in Different Uranium Compounds Obtained by X-Ray Absorption Spectroscopy with Synchrotron Radiation.* Bulletin of Materials Science, 2014. **37**(3): p. 643-647.

67. Kvashnina, K., Kvashnin, Y., and Butorin, S., *Role of Resonant Inelastic X-Ray Scattering in High-Resolution Core-Level Spectroscopy of Actinide Materials.* Journal of Electron Spectroscopy and Related Phenomena, 2014. **194**: p. 27-36.
68. Chamberlain, A.C., *Emissions from Sellafield and Activities in Soil.* Science of The Total Environment, 1996. **177**(1): p. 259-280.
69. Amonette, J., Holdren Jr, G., Krupa, K., and Lindenmeier, C., *Assessing the Environmental Availability of Uranium in Soils and Sediments*. 1994, Nuclear Regulatory Commission, Washington, DC (United States). Div. of Waste Management; Pacific Northwest Lab., Richland, WA (United States).
70. Finch, R.J., Cooper, M.A., Hawthorne, F.C., and Ewing, R.C., *The Crystal Structure of Schoepite,[(Uo2)8o2(Oh)12](H2o)12.* Canadian Mineralogist, 1996. **34**: p. 1071-1088.
71. Burns, P.C., *The Structure of Compreignacite, K2[(Uo2)3o2(Oh)3]2(H2o)7.* The Canadian Mineralogist, 1998. **36**(4): p. 1061-1067.
72. Glatz, R.E., Li, Y., Hughes, K.-A., Cahill, C.L., and Burns, P.C., *Synthesis and Structure of a New Ca Uranyl Oxide Hydrate, Ca[(Uo2)4o3(Oh)4](H2o)2, and Its Relationship to Becquerelite.* The Canadian Mineralogist, 2002. **40**(1): p. 217-224.
73. Herak, R., *The Crystal Structure of the High Temperature Modification of U3o8.* Acta Crystallographica Section B: Structural Crystallography and Crystal Chemistry, 1969. **25**(12): p. 2505-2508.
74. Zhang, F.X., Lang, M., Wang, J.W., Li, W.X., Sun, K., Prakapenka, V., and Ewing, R.C., *High-Pressure U3o8 with the Fluorite-Type Structure.* Journal of Solid State Chemistry, 2014. **213**: p. 110-115.
75. Berggren, G. and Brown, A., *Influence of Oxide Additions on the Reduction of Uo3 and U3o8 as Measured by Dta and Tg*, in *Thermal Analysis*. 1969.
76. Duff, M.C., Mason, C.F., and Hunter, D.B., *Comparison of Acid and Base Leach for the Removal of Uranium from Contaminated Soil and Catch-Box Media.* Canadian journal of soil science, 1998. **78**(4): p. 675-683.
77. Small, J., Lennon, C., Kwong, S., and Scott, R. *Development and Validation of a Model of Uranium Release to Groundwater from Legacy Disposals at the Uk Low Level Waste Repository*. in *MRS Proceedings*. 2008. Cambridge Univ Press.
78. Manna, S., Basak, C., Thakkar, U.R., Thakur, S., Roy, S.B., and Joshi, J.B., *Study on Effect of Process Parameters and Mixing on Morphology of Ammonium Diuranate.* Journal of Radioanalytical and Nuclear Chemistry, 2016. **310**(1): p. 287-299.
79. Berggren, G. and Brown, A., *The Influence of Oxide Additions on the Reduction of Uo3 and U3o8 as Measured by Dta and Tg*, in *Thermal Analysis*, P.D. Garn, Editor. 1969, Academic Press. p. 881-891.
80. Fokema, M.D., Chiu, E., and Ying, J.Y., *Synthesis and Characterization of Nanocrystalline Yttrium Oxide Prepared with Tetraalkylammonium Hydroxides.* Langmuir, 2000. **16**(7): p. 3154-3159.
81. Allpress, J.G., *The Crystal Structure of Barium Diuranate, Bau2o7.* Journal of Inorganic and Nuclear Chemistry, 1965. **27**(7): p. 1521-1527.
82. Allpress, J.G., *Barium Polyuranates.* Journal of Inorganic and Nuclear Chemistry, 1964. **26**(11): p. 1847-1851.
83. Ijdo, D.J.W., Akerboom, S., and Bontenbal, A., *Crystal Structure of A- and B-Na2u2o7: From Rietveld Refinement Using Powder Neutron Diffraction Data.* Journal of Solid State Chemistry, 2015. **221**: p. 1-4.
84. Jolivet, J.-P., Henry, M., and Livage, J., *Metal Oxide Chemistry and Synthesis: From Solution to Solid State*. 2000: Wiley-Blackwell.
85. Vochten, R., Van Haverbeke, L., and Sobry, R., *Transformation of Schoepite into Uranyl Oxide Hydrates of the Bivalent Cations Mg^{2+}, Mn^{2+} and Ni^{2+}.* Journal of Materials Chemistry, 1991. **1**(4): p. 637-642.
86. Huang, F., Zhang, H., and Banfield, J.F., *The Role of Oriented Attachment Crystal Growth in Hydrothermal Coarsening of Nanocrystalline Zns.* The Journal of Physical Chemistry B, 2003. **107**(38): p. 10470-10475.
87. Niederberger, M. and Cölfen, H., *Oriented Attachment and Mesocrystals: Non-Classical Crystallization Mechanisms Based on Nanoparticle Assembly.* Physical chemistry chemical physics, 2006. **8**(28): p. 3271-3287.
88. Penn, R.L. and Soltis, J.A., *Characterizing Crystal Growth by Oriented Aggregation.* CrystEngComm, 2014. **16**(8): p. 1409-1418.

89. Xue, X., Penn, R.L., Leite, E.R., Huang, F., and Lin, Z., *Crystal Growth by Oriented Attachment: Kinetic Models and Control Factors.* CrystEngComm, 2014. **16**(8): p. 1419-1429.
90. Yuwono, V.M., Burrows, N.D., Soltis, J.A., and Penn, R.L., *Oriented Aggregation: Formation and Transformation of Mesocrystal Intermediates Revealed.* Journal of the American Chemical Society, 2010. **132**(7): p. 2163-2165.
91. Vochten, R. and Vanhaverbeke, L., *Transformation of Schoepite into the Uranyl Oxide Hydrates - Becquerelite, Billietite and Wolsendorfite.* Mineralogy and Petrology, 1990. **43**(1): p. 65-72.
92. Cundy, C.S. and Cox, P.A., *The Hydrothermal Synthesis of Zeolites: Precursors, Intermediates and Reaction Mechanism.* Microporous and Mesoporous Materials, 2005. **82**(1–2): p. 1-78.
93. Gabelica, Z., Nagy, J., Debras, G., and Derouane, E., *Characterization of X-Ray Amorphous Zsm-5 Zeolites by Thermal Analysis and High Resolution Solid State Multinuclear Nmr Spectroscopy.* Acta Chimica Hungarica, 1985. **119**(2-3): p. 275-284.
94. Geus, E., Jansen, J., and Van Bekkum, H., *Calcination of Large Mfi-Type Single Crystals: Part 1. Evidence for the Occurrence of Consecutive Growth Forms and Possible Diffusion Barriers Arising Thereof.* Zeolites, 1994. **14**(2): p. 82-88.
95. Allen, P., Shuh, D., Bucher, J., Edelstein, N., Palmer, C., and Marquez, L. *Exafs Spectroscopic Studies of Uranium(Vi) Oxide Precipitates*. in *MRS Proceedings*. 1996. Cambridge Univ Press.
96. Fokema, M.D. and Ying, J.Y., *Mechanistic Study of the Selective Catalytic Reduction of Nitric Oxide with Methane over Yttrium Oxide.* Journal of Catalysis, 2000.
97. Goldburt, E.T., Kulkarni, B., Bhargava, R.N., Taylor, J., and Libera, M., *Size Dependent Efficiency in Tb Doped Y2o3 Nanocrystalline Phosphor.* J. Lumin., 1997. **72**: p. 190.
98. Troczynski, T.B. and Nicholson, P.S., *Effect of Additives on the Pressureless Sintering of Aluminum Nitride between 1500 and 1800 C.* J. Am. Ceram. Soc., 1989. **72**: p. 1488.
99. Kim, W.J., Park, J.Y., Oh, S.J., Kim, Y.S., Hong, G.W., and Kuk, I.H., *Characteristics and Sintering Behavior of Yttria Powders Synthesized by the Combustion Process.* J. Mater. Sci. Lett., 1999. **18**: p. 411.
100. Skandan, G., Hahn, H., and Parker, J.C., *Nanostructured Y_2o_3: Synthesis and Relation to Microstructure and Properties.* Scr. Metall. Mater., 1991. **25**: p. 2389.
101. McCleskey, E. and Almers, W., *The Ca Channel in Skeletal Muscle Is a Large Pore.* Proceedings of the National Academy of Sciences, 1985. **82**(20): p. 7149-7153.
102. Alam, T.M., Liao, Z., Nyman, M., and Yates, J., *Insight into Hydrogen Bonding of Uranyl Hydroxide Layers and Capsules by Use of 1h Magic-Angle Spinning Nmr Spectroscopy.* The Journal of Physical Chemistry C, 2016. **120**(19): p. 10675-10685.
103. King, R.B., *Some Aspects of Structure and Bonding in Binary and Ternary Uranium(Vi) Oxides.* Chemistry of Materials, 2002. **14**(9): p. 3628-3635.
104. Perez-Pariente, J., Martens, J.A., and Jacobs, P.A., *Factors Affecting the Synthesis Efficiency of Zeolite Beta from Aluminosilicate Gels Containing Alkali and Tetraethylammonium Ions.* Zeolites, 1988. **8**(1): p. 46-53.
105. Musker, W.K., *A Reinvestigation of the Pyrolysis of Tetramethylammonium Hydroxide.* Journal of the American Chemical Society, 1964. **86**(5): p. 960-961.
106. Galwey, A.K., *Structure and Order in Thermal Dehydrations of Crystalline Solids.* Thermochimica acta, 2000. **355**(1): p. 181-238.
107. Sonnenberg, J.L., Hay, P.J., Martin, R.L., and Bursten, B.E., *Theoretical Investigations of Uranyl− Ligand Bonding: Four-and Five-Coordinate Uranyl Cyanide, Isocyanide, Carbonyl, and Hydroxide Complexes.* Inorganic chemistry, 2005. **44**(7): p. 2255-2262.
108. Ball, M.C., Birkett, C.R.G., Brown, D.S., and Jaycock, M.J., *The Thermal Decomposition of Ammonium Diuranate.* Journal of Inorganic and Nuclear Chemistry, 1974. **36**(7): p. 1527-1529.
109. Lasaga, A.C., *Chemical Kinetics of Water-Rock Interactions.* Journal of Geophysical Research: Solid Earth, 1984. **89**(B6): p. 4009-4025.
110. Nipruk, O., Knyazev, A., Chernorukov, G., and Pykhova, Y.P., *Synthesis and Study of Hydrated Uranium(Vi) Oxides, $Uo_3{\cdot}Nh_2o$.* Radiochemistry, 2011. **53**(2): p. 146-150.
111. Vochten, R., De Gravel, E., and Lauwers, H., *Transformation of Synthetic U3o8 into Different Uranium Oxide Hydrates.* Mineralogy and Petrology, 1990. **41**(2): p. 247-255.
112. El-Fekey, S.A., Rofail, N.H., and Khilla, M.A., *The Thermal Decomposition of Ammonium Uranates Precipitated from Sulphate and Nitrate Media by Urea.* Thermochimica Acta, 1983. **67**(2): p. 137-146.

113. Engmann, R.d. and De Wolff, P., *The Crystal Structure of Γ-UO_3.* Acta Crystallographica, 1963. **16**(10): p. 993-996.
114. Russell, J. and Farmer, V., *Infra-Red Spectroscopic Study of the Dehydration of Montmorillonite and Saponite.* Clay Minerals Bulletin, 1964. **5**(32): p. 443-464.
115. Greaves, C.t. and Fender, B., *The Structure of A-UO_3 by Neutron and Electron Diffraction.* Acta Crystallographica Section B: Structural Crystallography and Crystal Chemistry, 1972. **28**(12): p. 3609-3614.
116. Loopstra, B.O. and Cordfunke, E.H.P., *On the Structure of A-UO_3.* Recueil des Travaux Chimiques des Pays-Bas, 1966. **85**(2): p. 135-142.
117. Elfekey, S.A., Elhakim, M.N.A., Rofail, N.H., and Khilla, M.A., *Solid-Phase Decomposition of Ammonium Uranate.* Thermochimica Acta, 1982. **54**(3): p. 327-336.
118. Price, G.H., *Self-Reduction in Ammonium Uranates.* Journal of Inorganic and Nuclear Chemistry, 1971. **33**(12): p. 4085-4092.
119. Le Page, A.H. and Fane, A.G., *The Kinetics of Hydrogen Reduction of UO_3 and U_3O_8 Derived from Ammonium Diuranate.* Journal of Inorganic and Nuclear Chemistry, 1974. **36**(1): p. 87-92.
120. Kelly, S., Hesterberg, D., and Ravel, B., *Analysis of Soils and Minerals Using X-Ray Absorption Spectroscopy*, in *Methods of Soil Analysis*. 2008. p. 387-463.
121. Burns, P.C., Miller, M.L., and Ewing, R.C., *U6+ Minerals and Inorganic Phases: A Comparison and Hierarchy of Crystal Structures.* Canadian Mineralogist, 1996. **34**: p. 845-880.
122. Krivovichev, S., Burns, P., and Tananaev, I., *Structural Chemistry of Inorganic Actinide Compounds*. 2006: Elsevier.
123. Richard, G., *Computer-Simulation Study of Alkali-Metal Insertion into A-U_3O_8.* Journal of Materials Chemistry, 1991. **1**(3): p. 415-421.
124. Greaves, C., Cheetham, A.K., and Fender, B.E.F., *Sodium Uranium Bronze and Related Phases.* Inorganic Chemistry, 1973. **12**(12): p. 3003-3007.
125. Dueber, R.E., Fleetwood, J.M., and Dickens, P.G., *The Insertion of Magnesium into A-U_3O_8.* Solid State Ionics, 1992. **50**(3): p. 329-337.
126. Patat, S., Dueber, R.E., and Dickens, P.G., *Thermochemical and Electrochemical Study of Magnesium Insertion into A-UO_3.* Solid State Ionics, 1993. **59**(1): p. 151-155.
127. Çelikbilek, M., Ersundu, A.E., and Aydın, S., *Crystallization Kinetics of Amorphous Materials.* Advances in crystallization processes, 2012.
128. Manna, S., Thakkar, U.R., Satpati, S.K., Roy, S.B., Joshi, J.B., and Chakravartty, J.K., *Study of Crystal Growth and Effect of Temperature and Mixing on Properties of Sodium Diuranate.* Progress in Nuclear Energy, 2016. **91**: p. 132-139.

7 Conclusions and further recommendations

Knowledge of solution and solid-state chemistry of uranium compounds has increased considerably since the inception of radiochemistry over a century ago. However, understanding of actinide chemistry has paled compared to that of the transition metal compounds. The overarching aims of this project were to explore the solution and solid-state chemistry of uranium, with particular focus on transitional processes across the interface, and in doing so, to synthesise discrete uranate phases with varying stoichiometry for both industrial and academic applications. These aspects have been addressed via simple sol-gel reactions involving steady alkalisation of aqueous U(VI) and Ca^{2+} precursors.

Uranyl(VI) ions undergo hydrolysis in aqueous solution as a function of increasing pH, forming oligomeric U(VI)-hydroxide complexes. Continuing alkalisation results in nucleation and agglomeration of calcium deficient uranyl(VI) oxyhydrate particles in the range pH 5 – 7, which continuously uptake calcium driven by increasing pH. The relative calcium content of precipitates is adjustable by changing precursor Ca/U-stoichiometry, reaction temperature, and endpoint pH; whereby bulk solids Ca/U is enhanced by an increase in any, or all three variables.

In particular, the influence of precursor Ca/U on precipitation kinetics was explored through novel application of a Quartz Crystal Microbalance. During steady titration reactions, activation barriers associated with precipitation decreased as a function of increasing calcium availability in solution. This was attributed to several potential mechanistic influences ranging inter- or intramolecular, ion-solvation, hydrogen bonding, as well as colloidal (DLVO) contributions. As such, precipitation is expected to become dominated by nucleation-aggregation with increasing precursor-Ca/U, whereas nucleation and non-classical oriented-growth becomes more probable from Ca^{2+}-deficient precursors (Figure 7.1). Opposing trends in activation barriers were observed for batch reactions involving rapid injection of Ca^{2+} and U(VI) into an alkaline solution. By combining thermodynamic (PHREEQC) and double-exponential kinetic modelling of empirical data, this was postulated as the favouring of transient uranate-nucleation by high Ca^{2+}-availability; which hinders re-dissolution and secondary nucleation or growth of oxyhydrate phases.

A remarkable consequence of increasing Ca/U-stoichiometry in precipitates, is a significant reduction in crystallinity or long-range order (*'XRD-amorphous'*), whilst preserving localised structural order according to spectroscopic analyses (synchrotron-XAS, FTIR). This was related to primary and secondary amorphous U(VI)-oxyhydrate phases resembling zeolite precursors, where the long-range order

is disrupted by increasing the extent of hydrolysis during titration (higher pH), and consequently, the concentration of Ca^{2+}-rich occlusions (Figure 7.1). This was coincident with an increase in OH-bond covalency and weakening in hydrogen bonding interactions, caused by progressively crystalline calcium hydroxide occlusions. This manifests as the formation of a discrete Portlandite beyond the bulk congruency limit of Ca/U ~1.5.

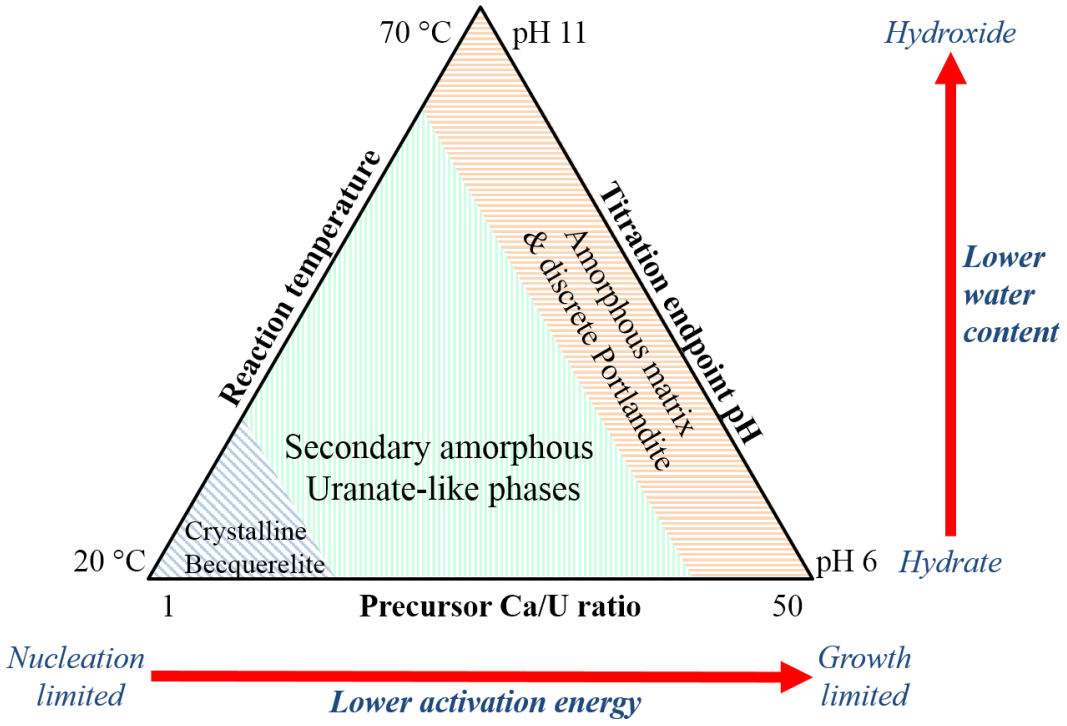

Figure 7.1 Phase diagram summarising precipitate crystallinity and extent of dehydration as a function of precursor Ca/U-ratio, titration endpoint pH, and reaction temperature.

When a sample of poorly-crystalline Ca^{2+}-U(VI)-oxyhydrate with Ca/U of 0.67 was calcined up to 1000 °C under a redox neutral atmosphere, a series of decomposition processes occurred via concerted dehydration-dehydroxylation-oxolation to crystallise calcium polyuranate ($Ca_2U_3O_{11}$). Further heating resulted in partial reduction and phase segregation into a $CaUO_4$-UO_2 solid-solution. Repeating this under an oxic atmosphere for samples with 0.124 – 7.21 Ca/U up to 800 °C formed several additional calcium uranate as well as uranium oxide phases; $Ca_3U_{11}O_{36}$, CaU_2O_7, $CaUO_4$, β-UO_3, α-U_3O_8. A binary temperature-stoichiometry phase diagram (Figure 7.2) summarises the synthesised precipitates, intermediates and crystalline endmembers, with literature data on calcium uranates and uranium oxides.

Kinetic barriers increased in the order dehydration, dehydroxylation/decarbonation, desorption, and reduction in the case of 0.124 – 0.36 Ca/U. Precipitates with higher calcium content incurred smaller kinetic barriers, and is reflected in respective

thermodynamic barriers of dehydration and desorption, whilst crystallite sizes of endmembers also reduced significantly.

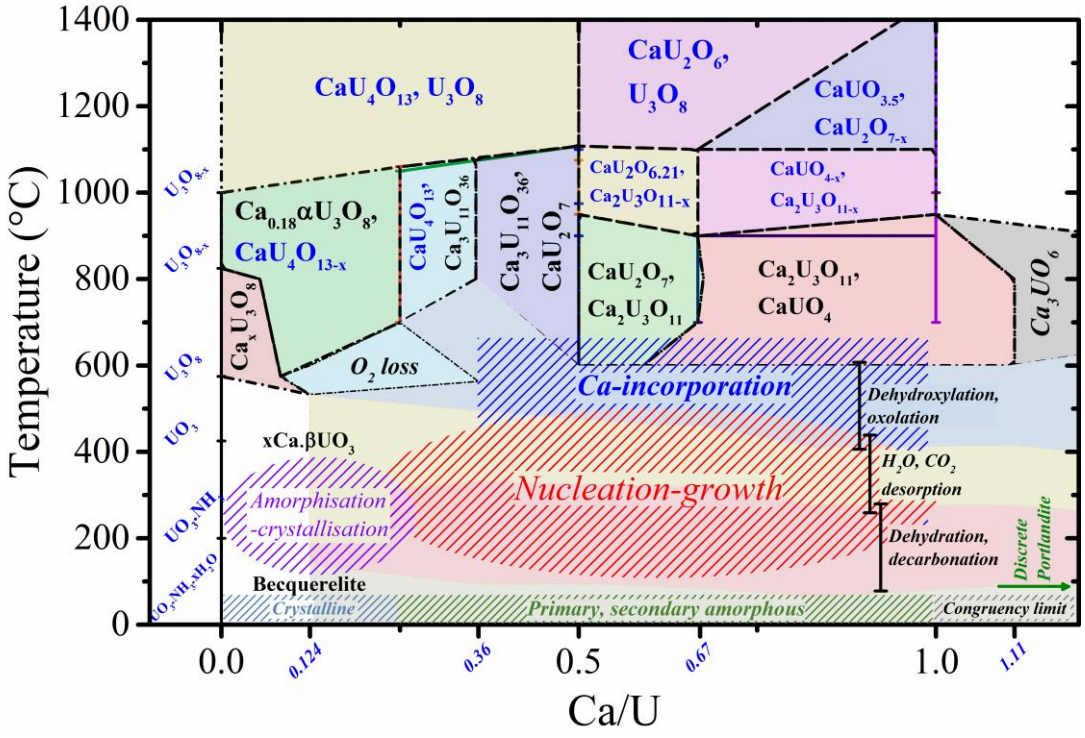

Figure 7.2 Temperature-stoichiometry (Ca/U) phase diagram summarising anhydrous calcium uranates extracted from the literature (phases in blue font), and contributions made from this project (phases in black font). Line-shade regions represent the mechanisms predominant in solid-state transformations.

Progressive transition from amorphous to endmember phases occurred via a concerted axial compression of the UO-coordination environment, with the inwards migration of interlayer calcium ions. Conversely, at the lower stoichiometric limit (0.124 Ca/U), crystalline Becquerelite underwent amorphisation-crystallisation into β-UO_3 followed by reduction to $Ca_{0.18}$.α-U_3O_8. The latter is a novel intercalation compound, that has yet to be reported in the literature. The amorphisation and partial ex-migration of calcium from Becquerelite appears vital. Another previously undiscovered compound lying at the interface between uranium oxide and calcium uranate was synthesised, with a Ca/U-stoichiometry of 0.36, $Ca_3U_{11}O_{36}$ lies closer in structure to α-U_3O_8 due to O-U-O bonding between vertically stacked layers of uranate polyhedra. Trimeric calcium oxo-polyhedra lie in unique positions that directly displace UO-polyhedra within the sheet structure. Finally, it was deduced that with increasing concentration of occluded calcium, crystallisation was predominantly controlled by nucleation and growth from amorphous precursors, whereas below the 0.36 Ca/U limit, phases tend towards amorphisation-crystallisation with no significant change in crystallite size.

The profound influence of stoichiometry on U-coordination and crystallisation during the transition [prenucleation U-complexes] → [oxyhydrate precipitates] → [anhydrous final crystalline phases] is likely not only relevant for understanding physical transformations within the Ca-U-O system, but has likely more general relevance for understanding the formation of natural and synthetic materials such as bone, shell, teeth, or mineral phases.

7.1 Further recommendations

Further recommendations have been provided in greater detail in chapters 5 and 6 (see sections 5.6, 6.6). Briefly;

- In-situ small- and wide-angle scattering (SAX/WAX) experiments to validate QCM data on precipitation of uranyl(VI) oxyhydrate particles (Chapter 5).
- In-situ X-ray absorption spectroscopy (XAS, fast-XAFS and XANES) to validate mechanistic and thermodynamic models leading to nucleation.
- Static aging experiments using uranyl(VI) oxyhydrate suspensions. i.e. Fixed Ca/U-stoichiometry, and various temperatures, then allowed to age at constant pH. Subsequent QCM response is then related to growth via classical or oriented growth. If activation barriers are quantified for reactions containing TMA^+ ions, a positive trend should coincide with larger XRD-Scherrer diameters [1] as a function of increasing TMA^+-concentration [2].
- In-situ U L_{III} and Ca K-edge synchrotron-XAS and diffraction experiments on solid-state transformations of primary or secondary amorphous uranyl(VI) oxyhydrates. Comparison with cations of different ionic radii or Lewis acidity, focusing on occlusion-induced nucleation mechanisms.

8 Publications, Conferences, and Scholarships

8.1 Publications directly associated with thesis

Ding, W., Botha, J. A., Hanson, B. C., & Burke, I. T. (2016). Aqueous hydroxylation mediated synthesis of crystalline calcium uranate particles. *Journal of Alloys and Compounds, 688*, 260-269.

Ding, W., Botha, J. A., Hanson, B. C., & Burke, I. T. (2016). Synthesis of Calcium Monouranate Particles via an Aqueous Route. *MRS Advances, 1*(62), 4123-4129.

8.2 Other publications

Ding, W., Stewart, D. I., Humphreys, P. N., Rout, S. P., & Burke, I. T. (2016). Role of an organic carbon-rich soil and Fe (III) reduction in reducing the toxicity and environmental mobility of chromium (VI) at a COPR disposal site. *Science of the Total Environment, 541*, 1191-1199.

Fuller, S. J., Burke, I. T., McMillan, D. G., Ding, W., & Stewart, D. I. (2015). Population changes in a community of alkaliphilic iron-reducing bacteria due to changes in the electron acceptor: implications for bioremediation at alkaline Cr (VI)-contaminated sites. *Water, Air, & Soil Pollution, 226*(6), 180.

Botha, J. A., Hunter, T. N., Ding, W., Biggs, S., Mackay, G. A., Cowley, R., ... & Harbottle, D. (2016). A Novel Technology for Complex Rheological Measurements. In *Annual Waste Management Conference (WM2016): Education & Opportunity in Waste Management*. WM Symposia.

8.3 Conferences

Crossroads of Particle Science and Technology: Joint conference of the 5th UK-China and 13th UK Particle Technology Forum, 2015. Leeds, UK. Poster presentation.

Scientific Basis for Nuclear Waste Management XXXIX, 2015. Montpelier, France. Oral presentation.

2016 Waste Management Symposia. Phoenix, Arizona. Poster presentation.

Actinide XAS (AnXAS) 2017. Oxford, UK. Poster presentation.

8.4 Scholarships

Leeds for Life Foundation, Travel Abroad Grant, 2016

Royal Society of Chemistry, Travel Grant, 2016

Roy G. Post Foundation Scholarship recipient, Waste Management Symposia, 2016

Supplementary information I

1. Gladstone-Dale relationship

The Gladstone-Dale relationship between the refractive energy K; refractive index n; density ρ of a mineral and its respective constituents. Where k_1, k_2 and w_1, w_2 represent the constituent refractive energies and weight ratios respectively.

$$K = \frac{(n-1)}{\rho} = k_1 w_1 + k_2 w_2 + \cdots k_n w_n \ (2)$$

2. Particle settling under centrifugation

Particle settling in centrifugal field is acted upon by two opposing forces, a centrifugal force and a drag force. Under laminar flow conditions (small particle sizes):

Inertial centrifugal force acting on a spherical particle:

$$F_{IC} = m\omega^2 R = \frac{4}{3}\pi r^3 \rho_{particle} \omega^2 R$$

Buoyancy force acting on particle, where α is angular acceleration:

$$F_B = \frac{4}{3}\pi r^3 \rho_{fluid} \alpha = \frac{4}{3}\pi r^3 \rho_{fluid} \omega^2 R$$

Viscous drag force acting on particle:

$$F_D = 6\pi r \mu V$$

Relative centrifugal force:

$$RCF = \frac{\omega^2 R}{g}$$

Force balance acting on a spherical particle at terminal velocity falling through a viscous fluid:

$$F_{IC} = F_B + F_D$$

$$\frac{4}{3}\pi r^3 \rho_{particle} \omega^2 R - \frac{4}{3}\pi r^3 \rho_{fluid} \omega^2 R = 6\pi r \mu V$$

$$\frac{2}{9}\frac{r^2 \Delta\rho \omega^2 R}{\mu} = V_s$$

$$\boxed{\frac{2}{9}\frac{r^2 \Delta\rho \omega^2 R}{\mu} = t_s}$$

Where:

$$\rho_{particle} = particle\ density$$

$$\rho_{fluid} = fluid\ density$$

$$\omega = angular\ velocity$$

$$\alpha = angular\ acceleration = \omega^2 R$$

$$R = radius\ of\ centrifugation$$

$$r = spherical\ particle\ radius$$

$$V_s = terminal\ particle\ velocity$$

$$t_s = terminal\ particle\ settling\ time$$

For a centrifugation time of 3minutes (180s), supernatant travel distance of 2cm; a graph may be constructed (Figure A1) to approximate terminal particle settling time:

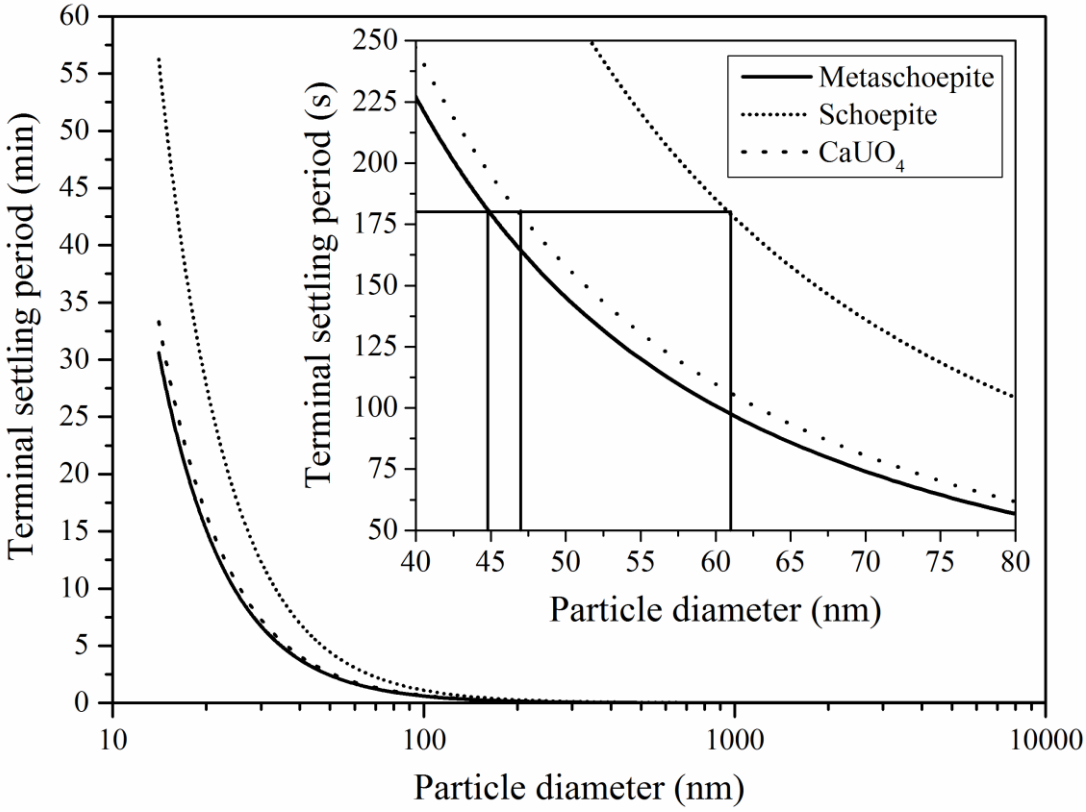

Figure A1 Graph of predicted nanometric spherical particles settling times. (Water at 25°C μ= 0.89 mN s m^{-2} [3]); ρ_p is particle density (Schoepite: ICSD 82477, ρ=4818.64 kg m^{-3}, Metaschoepite: ICSD 23647, ρ=8017.66 kg m^{-3}, $CaUO_4$: ICSD 31631, ρ=7450 kg m^{-3}); ρ_f is fluid density (Water at 25°C, ρ= 997.1kg m^{-3} [3]); R is 0.06m.

3. Fourier Transform Infra-Red spectroscopy (FTIR)

Powdered samples (~20 mg) were analysed using an A2 Microlab Portable mid-IR spectrometer with a Diamond Internal reflection cell (DATR). 10 measurements were completed for each sample and merged.

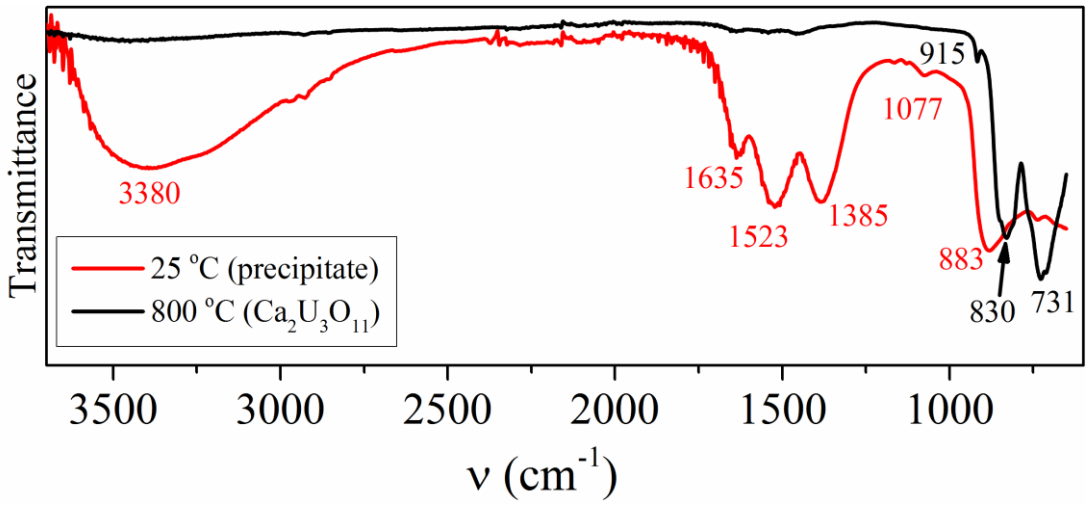

Literature data				This study		
$Na_2U_2O_7.6H_2O$ [4]	Becquerelite [5]	CaU_2O_7 [6]	$Ba_2U_3O_{11}$ [6]	25 °C	800 °C	Assignment
3379-3578	3504			2500-3700		ν H_2O, OH
1645	1625			1635		δ H_2O
				1385-1523		ν_3 IPA, NO_3^-
	1250			1077		δ UOH in-plane
	997					
936	927					
882	840			883		ν_3 UO_2^{2+}
	812					
		835	830		830	U=O
		730	750		731	U-O

Figure A2 FTIR spectra of poorly crystalline hydrous Ca^{2+}-uranate (25 °C) formed at pH 12 and crystalline Ca^{2+}-uranate ($Ca_2U_3O_{11}$) after dehydration at 800 °C with summarised tentative band assignments based on literature data for analogous compounds.

Table A1 Summary of derived molar Ca/U stoichiometry and formulae from analyses

Method	Molar [Ca/U] ratio	Stoichiometric formula
SEM-EDS	0.63 ± 0.02	$Ca_2U_{3.18}O_{11.5}$
pXRD-Rietveld	0.60 ± 0.03	$Ca_2U_{3.32}O_{12}$
ICP-OES	0.68 ± 0.04	$Ca_2U_{2.92}O_{10.77}$
TG	-	(I) $Ca_2(UO_2)_3O_{3.75}(OH)_{2.5}.3.5H_2O$ (II) $Ca_2(UO_2)_3O_{3.75}(OH)_{2.5}$ (III) $Ca_2U_3O_{11}$ (IV) $CaUO_4$, UO_2
Average	0.64 ± 0.03	$Ca_2U_{3.1}O_{11.4}$

Supplementary information II

1. Literature groundwater conditions

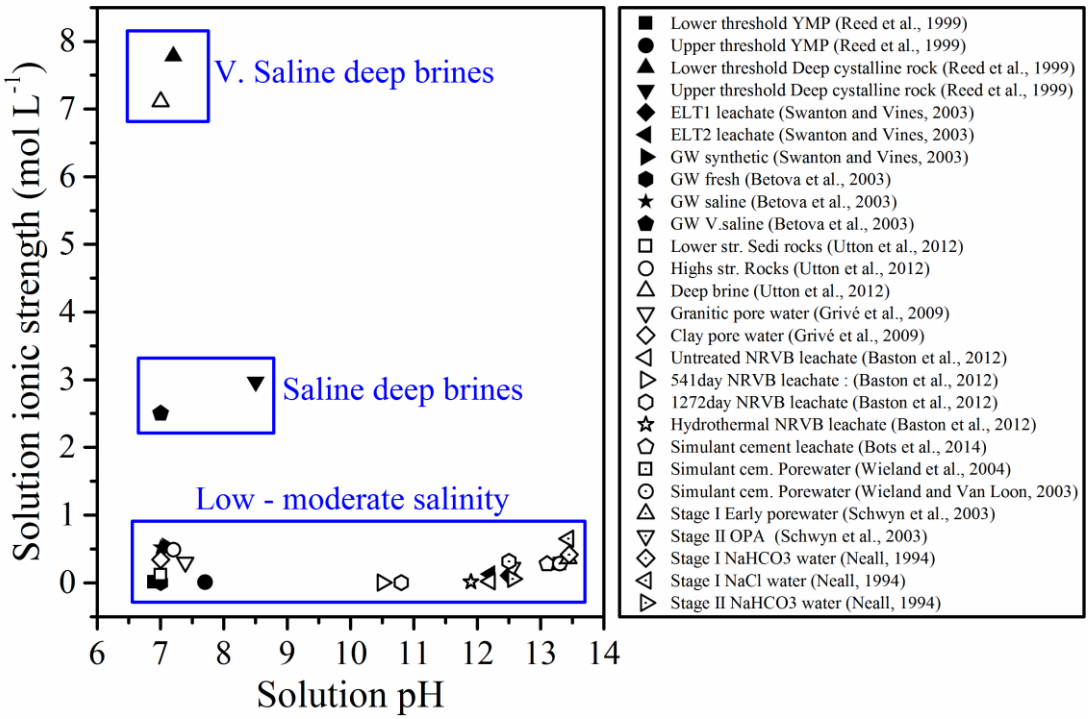

Figure B1 Calculated ionic strength (0 – 8 mol kg^{-1}) as a function of pH using experimental conditions used for performance testing conditions from literature [7-17]. (SIT database).

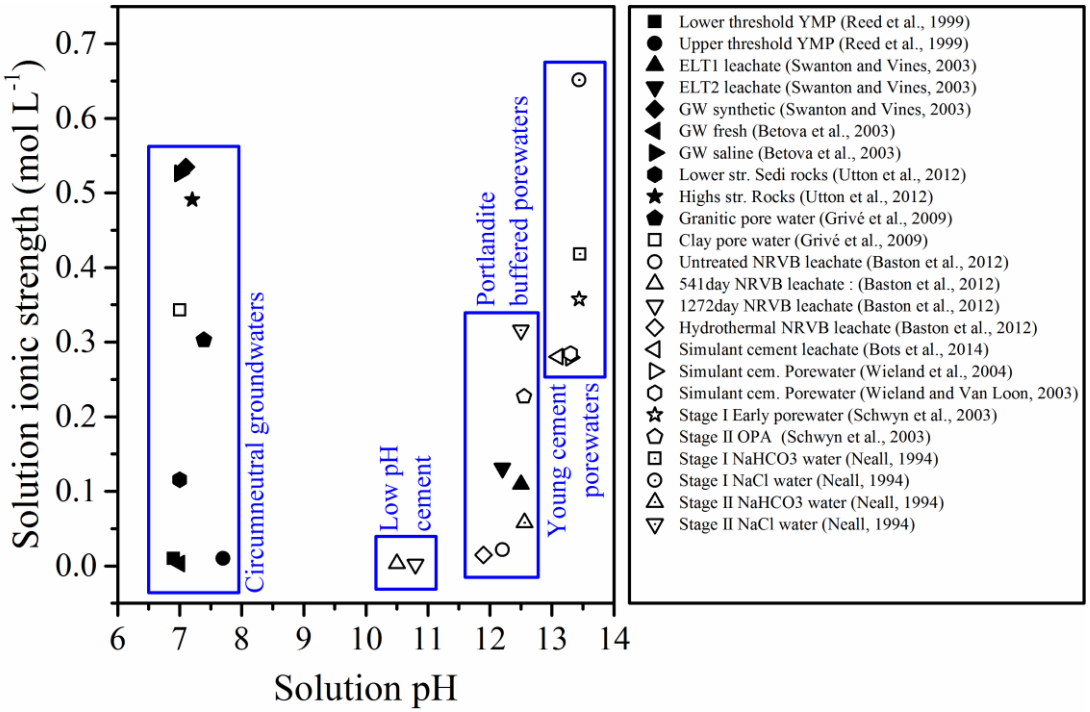

Figure B2 Calculated ionic strength (0 – 0.7 mol kg^{-1}) as a function of pH using experimental conditions used for performance testing conditions from literature [7-17]. (SIT database)

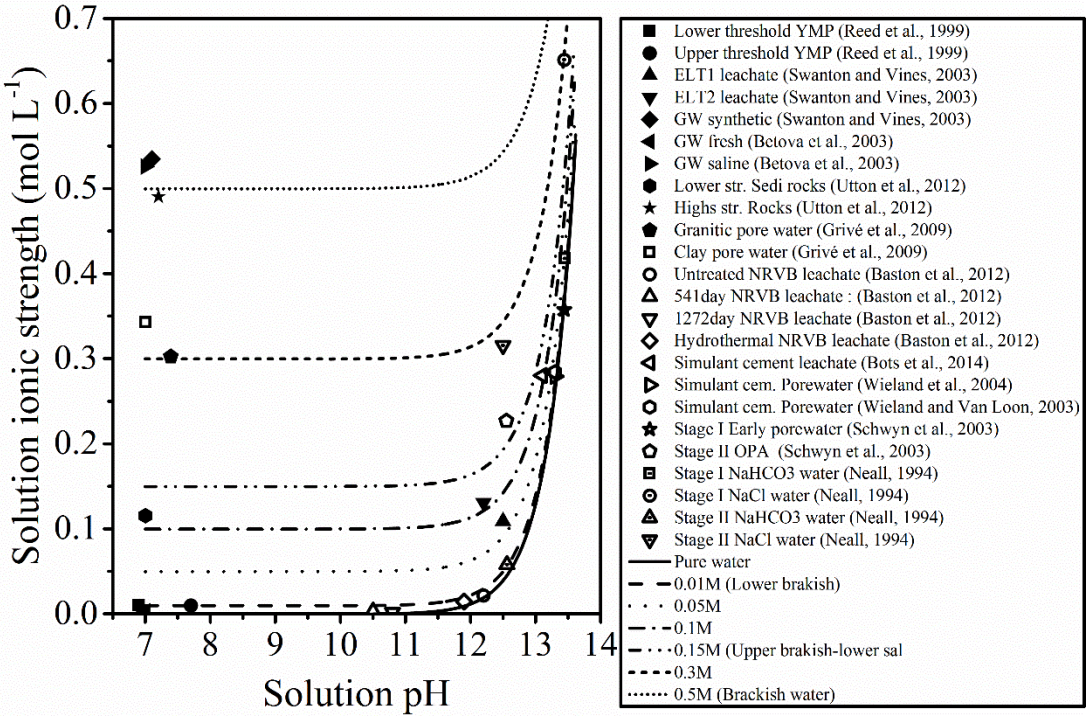

Figure B3 Calculated ionic strength (0 – 0.7 mol kg^{-1}) as a function of pH using experimental conditions used for performance testing conditions from literature [7-17]. Continuous trends (lines) for ionic strength regions of groundwater are overlaid for reference. (SIT database)

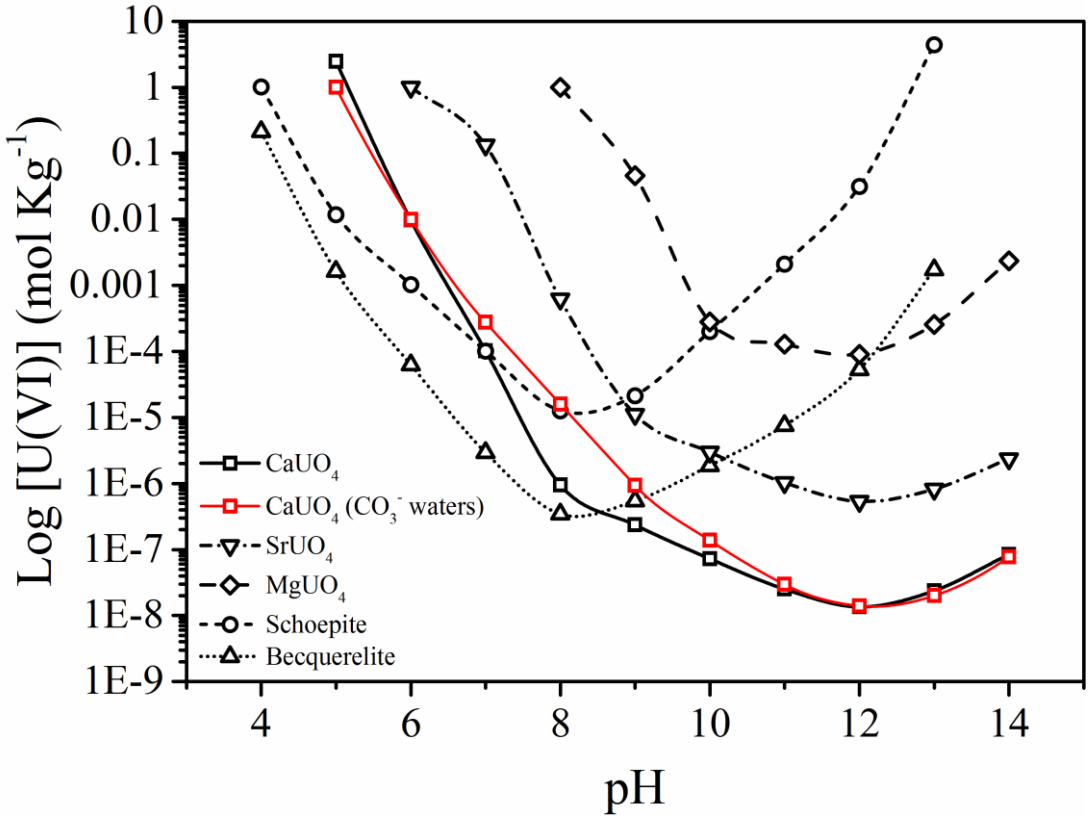

Figure B4 Calculated U(VI)-concentrations at equilibrium for some solubility limiting U-phases of interest as a function of pH. Sr^{2+}- and Mg^{2+}-uranates are plotted for reference. (SIT database).

2. Titration reaction

a. pH

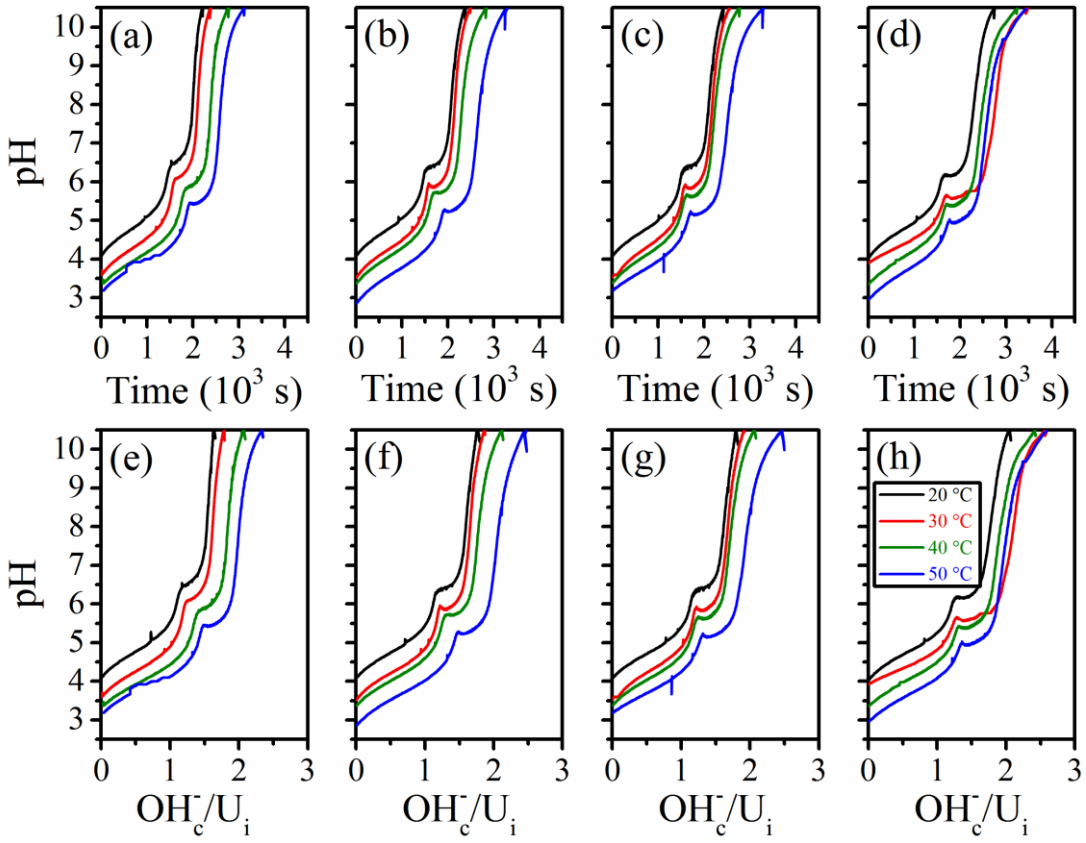

Figure B5 (a) – (d) Change in solution pH with increasing time (10^3 s); (e) – (h) changing ratios of consumed hydroxide and initial U(VI) as a function of solution pH for precursor Ca/U values 0.124, 0.5, 1, 8 respectively. Each plot shows reaction data across all temperatures.

$$pH = \frac{1}{2} logK - \frac{1}{2} \log[M^{2+}] \qquad \textbf{Equation B1}$$

Table B1 pK_2 values and gradients from pK_2 versus log [Ca^{2+}] plots

T	Ca/U = 0.124	Ca/U = 0.5	Ca/U = 1	Ca/U = 8	m = ΔpK_2/log [Ca]
20	6.46	6.05	5.81	5.43	-0.36
30	6.32	5.92	5.72	5.24	-0.40
40	6.27	5.86	5.59	5.18	-0.42
50	6.13	5.63	5.36	4.95	-0.44

a) $pK_i = -A(\sum s_j + v) = -19.8 * (1.73 - 2)$

b) $\sum s_j = [ms_H + n(1 - s_H)] = 3 * 0.51 + 1 * (1 - 0.8)$

c) $U - O - U_2 + H^+ \underset{k_b}{\overset{k_c k_f}{\rightleftharpoons}} U - (OH) - U_2$ **Equation B2**

Where A is 19.8; v, the valence of surface oxygen (-2); $\sum s_j$, bond valence sum at the surface oxygen defined by Equation 5.9b (1.73 for Becquerelite, 1.61 for Schoepite); s_M, the metal-oxygen bond valance (0.51 vu [18]); (1-s_H), the hydrogen bond valence of solvation sphere to surface anions (MO→H) (0.2 vu); m (3) and n (1), number of strong and weak O-H bonds respectively.

b. QCM

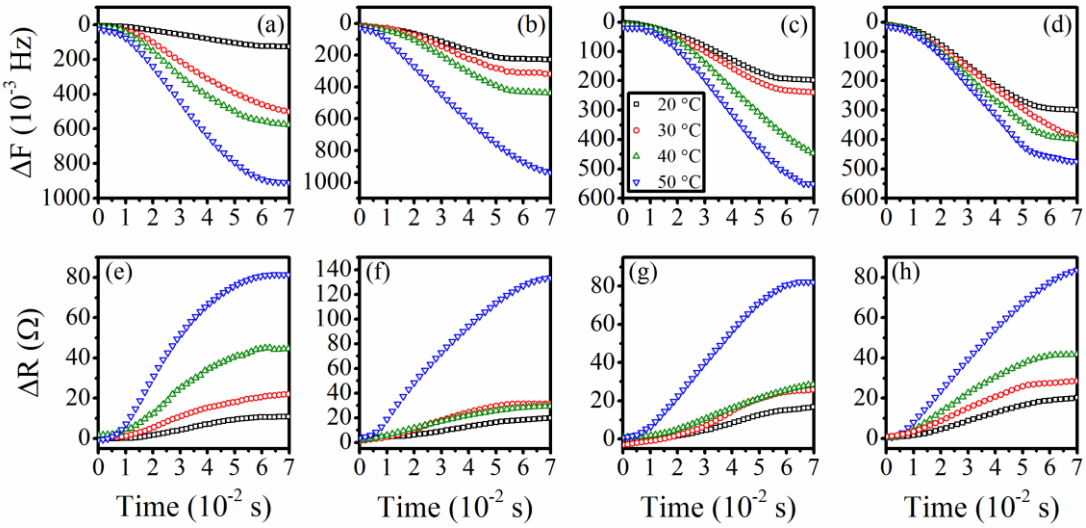

Figure B6 (a) – (d) QCM frequency (ΔF) and (e) – (h) resistance shift (ΔR) as a function of relative time in 10^2 seconds.

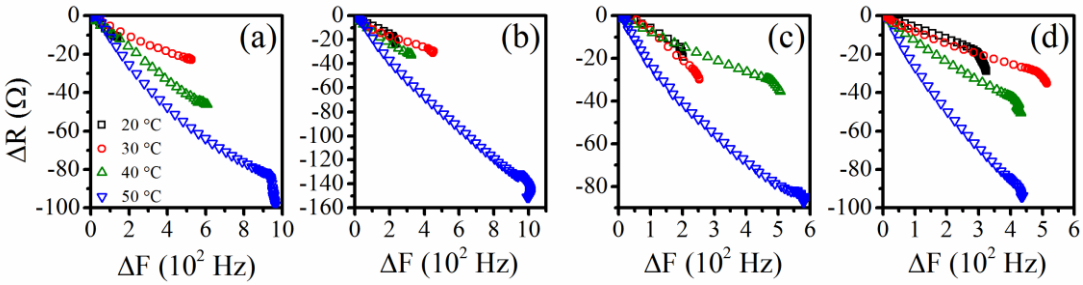

Figure B7 ΔR versus ΔF trends for 20 – 30 °C reactions at initial solution Ca/U of (a) 0.124, (b) 0.5, (c) 1 and (d) 8.

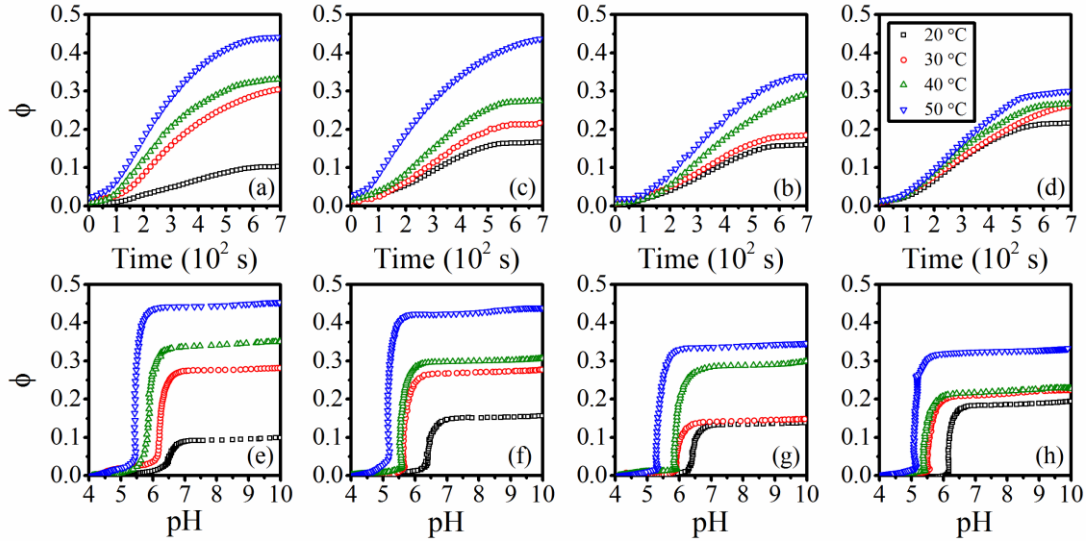

Figure B8 Expected solids volume fraction as a function of (a) – (d) reaction time (seconds) and (e) – (h) solution pH for precursor Ca/U ratios 0.124 – 8 respectively.

c. ICP-OES

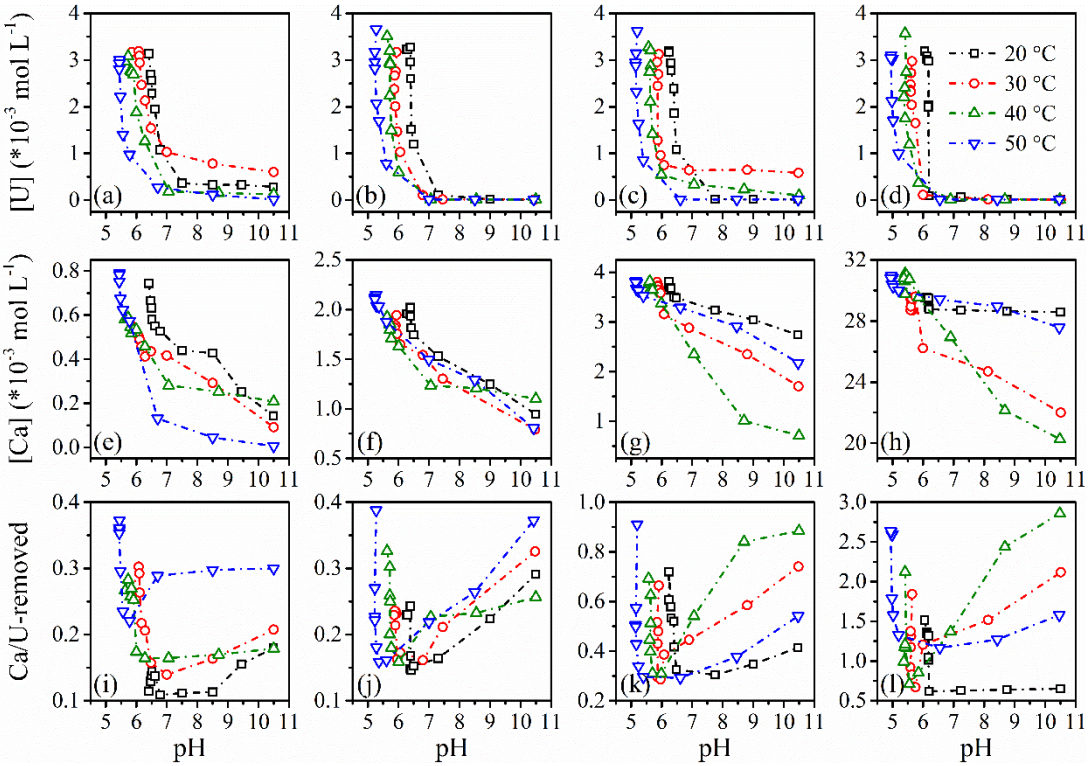

Figure B9 Measured solution U(VI)-concentration (a-d); Ca^{2+}-concentration (e-h); Ca/U stoichiometry of removed solids; as functions of pH at reaction temperatures 20, 30, 40 and 50 °C. Panels from left to right represent precursor Ca/U-stoichiometry of 0.124, 0.5, 1 and 8 respectively.

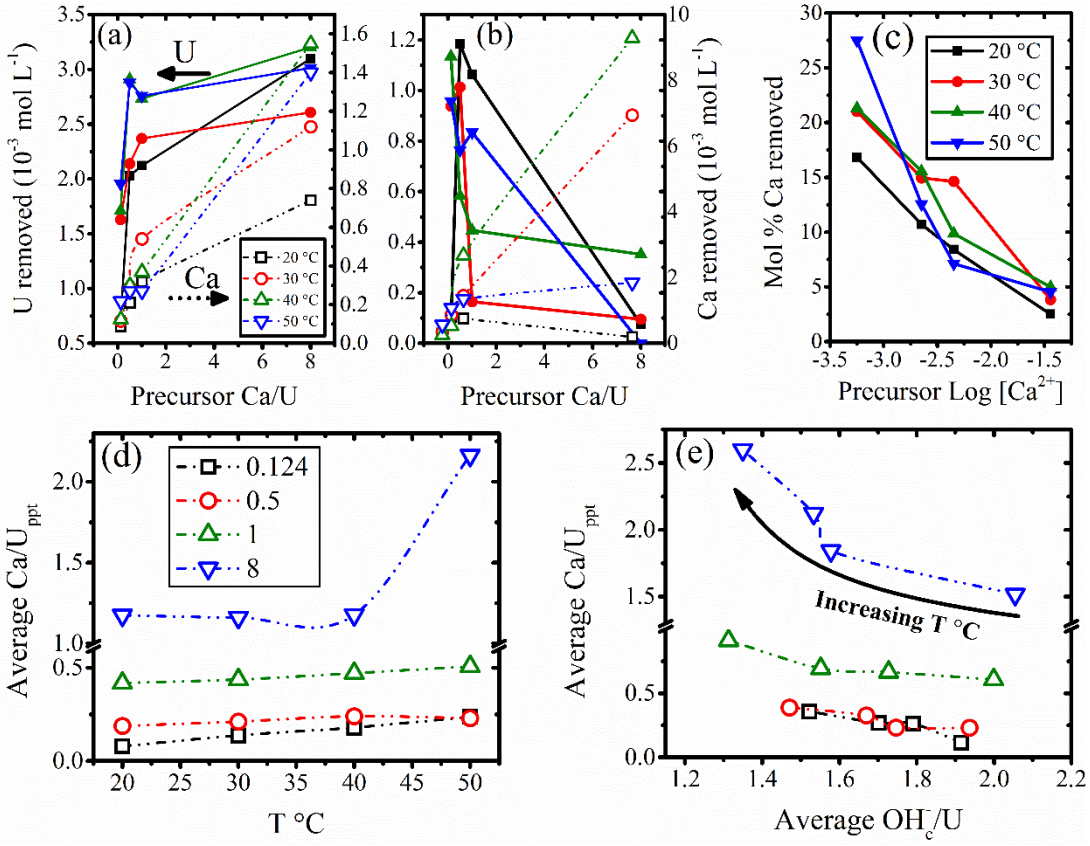

Figure B10 Total removed (filtered) U(VI) and Ca^{2+} during (a) precipitation and (b) within the alkaline region, as a function of precursor Ca/U stoichiometry. Average Ca/U (measured, ICP-OES) stoichiometry from removed Ca^{2+} and U(VI) at precipitation onset as a function of (c) reaction temperature and (d) $OH^-_c/U(VI)_i$.

Table B2

	U_1	U_2	ΔU	ΔU	ϕ_1	ϕ_2	$\Delta\phi_1$
	$*10^{-3}$ mol L^{-1}	$*10^{-3}$ mol L^{-1}	$*10^{-3}$ mol L^{-1}	(mol%)			
Ca/U = 0.124							
20	3.13	0.33	2.81	0.90	0.44	0.00	0.44
30	3.17	0.78	2.39	0.75	0.34	0.02	0.32
40	2.97	0.15	2.81	0.95	0.28	0.01	0.27
50	2.93	0.11	2.82	0.96	0.09	0.02	0.07
Ca/U = 0.5							
20	3.23	0.11	3.12	0.97	0.42	0.00	0.42
30	3.17	0.10	3.06	0.97	0.30	0.01	0.29
40	3.51	0.02	3.49	1.00	0.27	0.01	0.26
50	3.66	0.02	3.64	1.00	0.15	0.03	0.12
Ca/U = 1							
20	3.20	0.02	3.19	0.99	0.34	0.00	0.33
30	3.12	0.64	2.48	0.79	0.29	0.01	0.28
40	3.28	0.34	2.94	0.90	0.14	0.01	0.13
50	3.61	0.02	3.60	1.00	0.13	0.01	0.12

Ca/U = 8							
20	3.19	0.06	3.12	0.98	0.32	0.00	0.32
30	2.97	0.11	2.86	0.96	0.22	0.00	0.21
40	3.57	0.02	3.55	1.00	0.21	0.01	0.20
50	3.03	0.02	3.01	0.99	0.18	0.02	0.17

d. PHREEQC data output

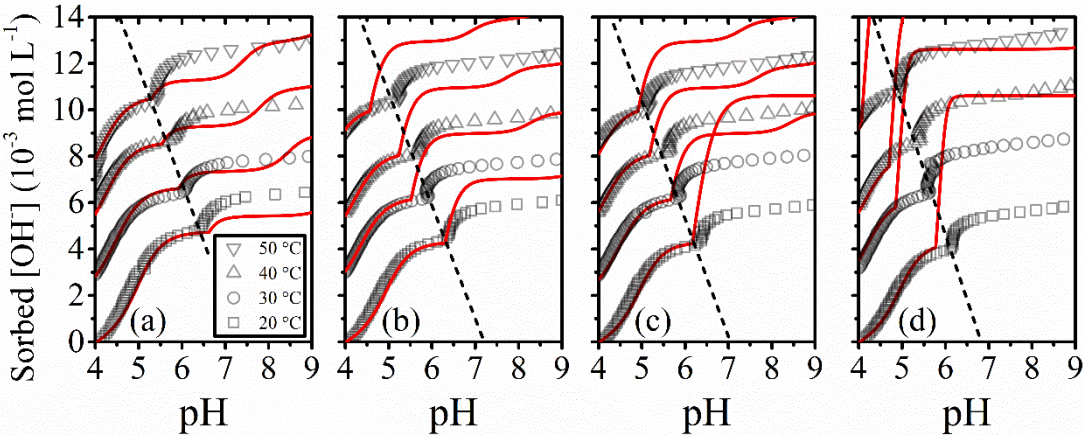

Figure B11 From (a) to (d) [Ca/U] ratios 0.124, 0.5, 1 and 8 respectively. Trends were offset for clarity.

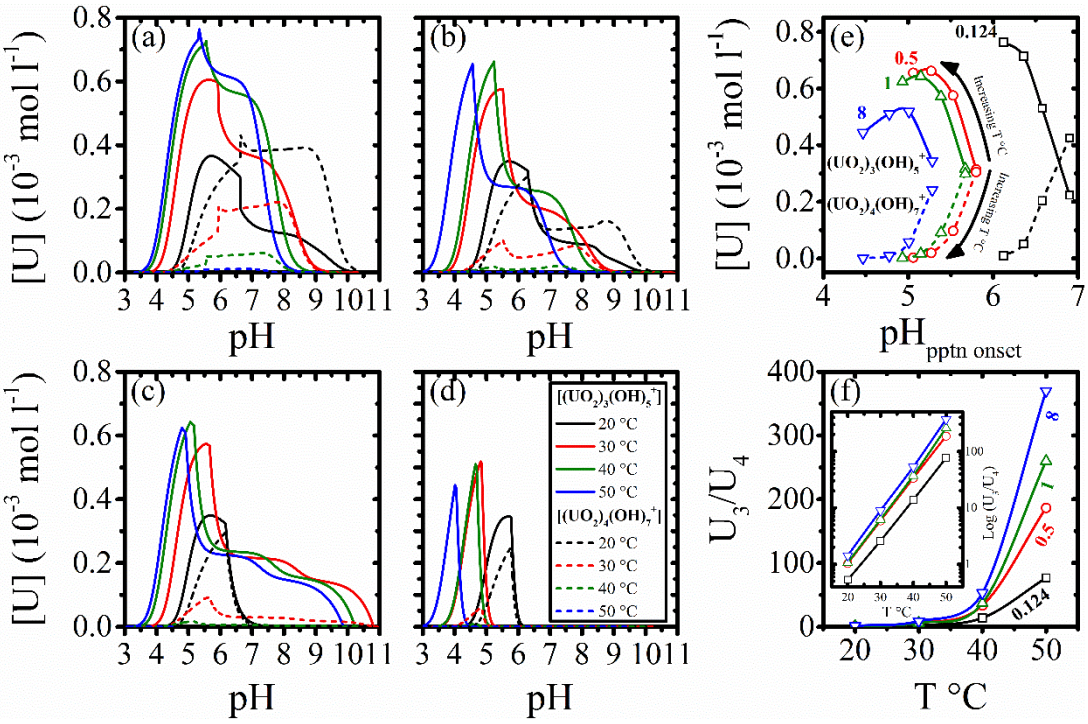

Figure B12 (a) – (d) Modelled $[(UO_2)_3(OH)_5]^+$ (solid coloured lines) and $[(UO_2)_4(OH)_7]^+$ (dashed coloured lines) concentrations as a function of solution pH at varying temperatures. (e) Predicted concentrations of tri- and tetrameric uranyl(VI) hydroxide complexes at pH of precipitation onset. (f) Trimeric/tetrameric stoichiometry as a function of temperature (inset: log tri/tetrameric stoichiometry).

Table B3 Thermodynamic calculations for $[CaOH]^+/Ca^{2+}$ stoichiometry with increasing TMA^+ concentration.

Ca/U	$[TMA^+]$	$[CaOH]^+/Ca^{2+}$ ($*10^{-8}$)			
		20 °C	30 °C	40 °C	50 °C
0.124	0.15	5.56	15.38	39.81	96.93
0.5	0.145	5.47	15.17	39.29	95.71
1	0.139	5.37	14.89	38.59	94.10
8	0	4.47	12.54	32.85	80.93

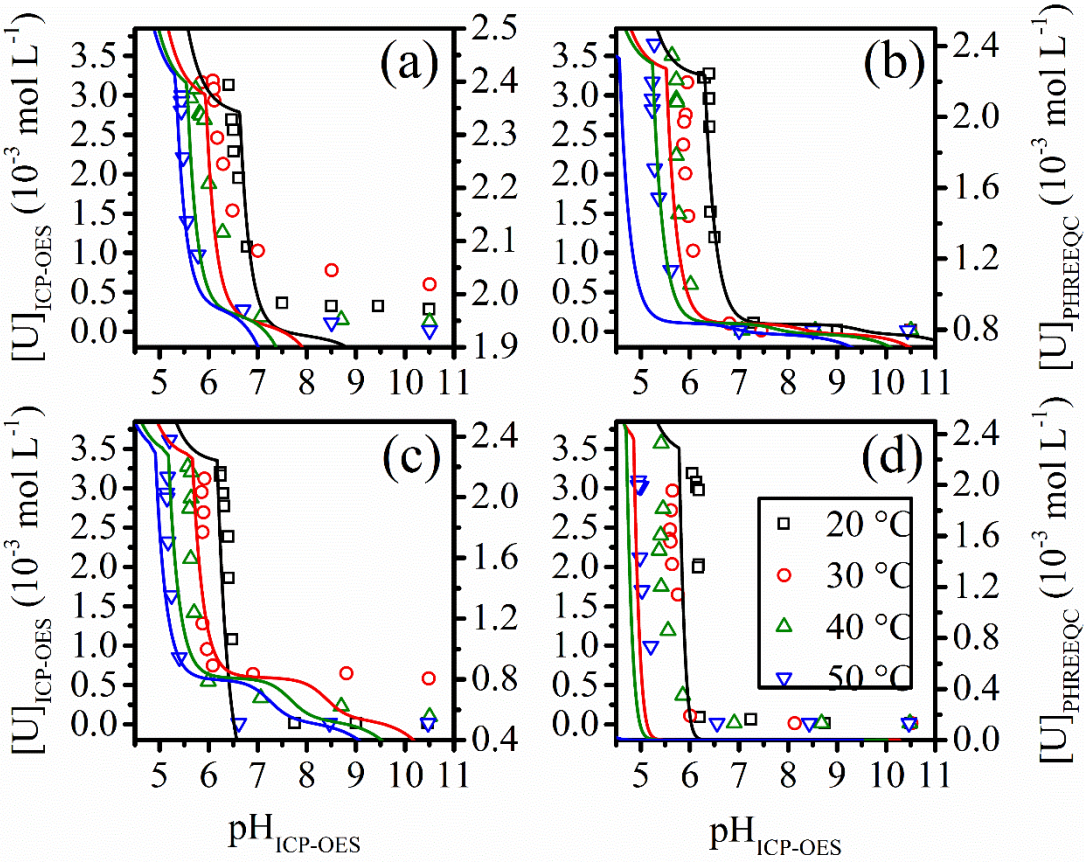

Figure B13 Ex-situ U(VI) concentrations from extract aliquots as a function of pH (symbols) at 20 – 50 °C (ΔT = 10 °C) at precursor Ca/U stoichiometry of (a) 0.124, (b) 0.5, (c) 1 and (d) 8. PHREEQC predicted U(VI) concentration from the CSTR model are matched for pH and concentration (solid lines)

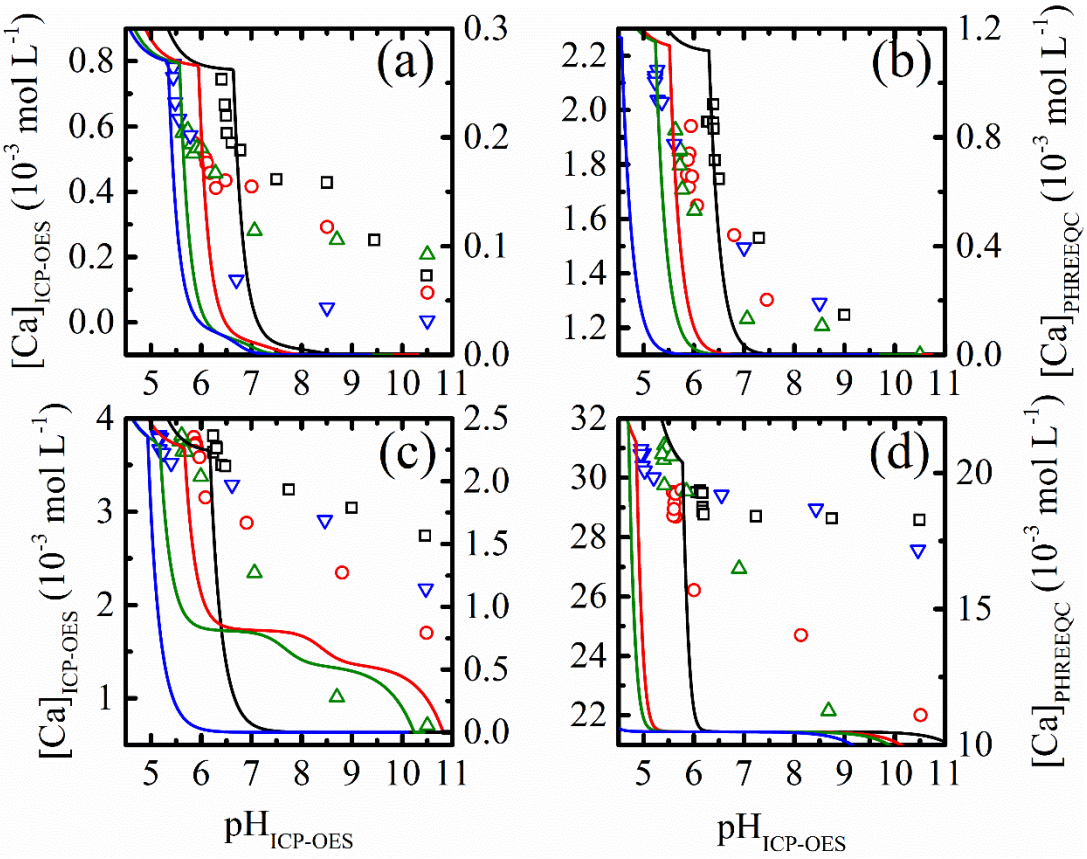

Figure B14 Ex-situ Ca^{2+} concentrations from extract aliquots as a function of pH (symbols) at 20 – 50 °C (ΔT = 10 °C) at precursor Ca/U stoichiometry of (a) 0.124, (b) 0.5, (c) 1 and (d) 8. PHREEQC predicted Ca^{2+} concentration from the CSTR model are matched for pH and concentration (solid lines)

e. Kinetic analyses

i. JMAK analyses

From linearization of Equation 5.4, Equation B3 is used in JMAK fitting of ϕ-data.

$$\ln(-\ln(1-\phi)) = n\ln(t) + \ln(k) \qquad \textbf{Equation B3}$$

Upon linearizing Equation 5.4 to give Equation B3, double ln-plots (ln(-ln(1-ϕ) versus $\ln(t_{relative})$) were used to extract n (gradient) and k (y-intercept) (Figure B15) parameters from the data (see Figure B15e – h). The precipitation onset times found from pH measurements (Figure 5.4, Figure 5.22) were used as t = 0 s for each respective reaction. The sigmoidal ϕ-trends (Figure B15a – d) were derived to determine time periods of maximum rate of change $([\delta\phi/\delta t]_{max}$, $([\delta^2\phi/\delta^2 t]_0)$ for each trend (see Kissinger method [19]). The ln[-ln(1-ϕ)]) values (Figure B15a – d) within these rate maxima (Δt ± 10 s) were linearly regressed (Figure B15e – h, dash-dot lines) to reaction initiation at $\ln(t_0)$ to give k-constants for each reaction, where $\ln(t_0)$ = 6.75, 6.5, 6.4, 5.7 for Ca/U ratios of 0.124, 0.5, 1, 8 respectively.

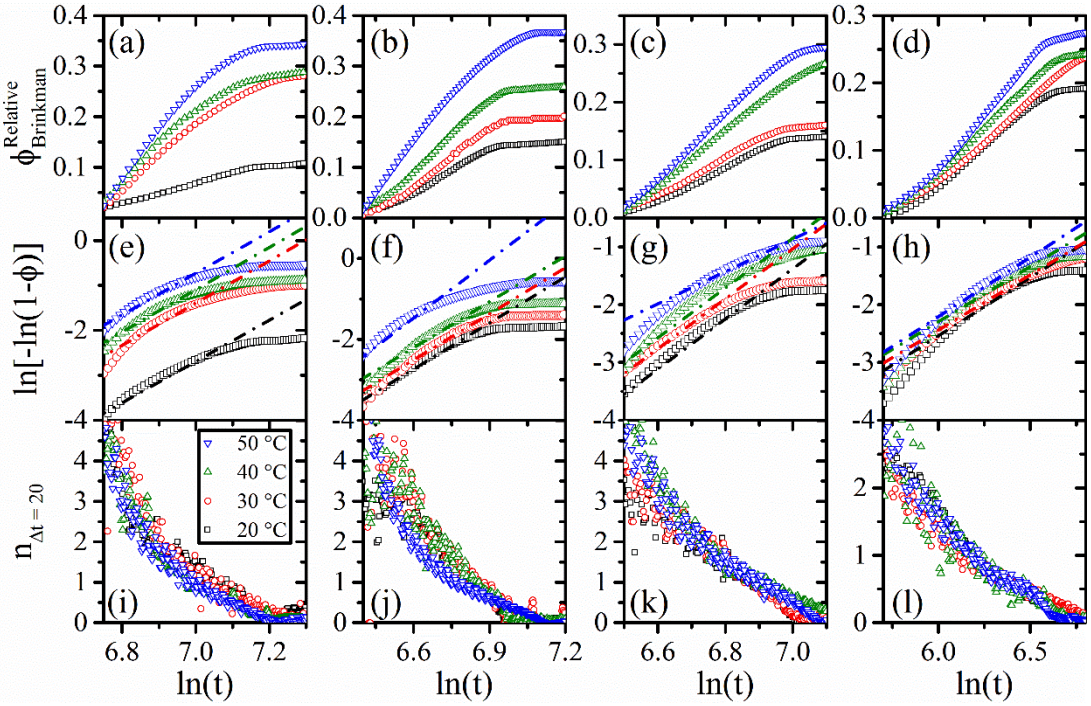

Figure B15 (a-d) Volume conversion fraction; (e – h) JMAK ln-ln plots; (I – l) Instantaneous n factors ($n_{\Delta t = 20}$) as functions of relative ln(t). Left to right columns are Ca/U values 0.124, 0.5, 1 and 8 respectively.

Table B4 Kinetic parameters derived from JMAK analysis of particle volume fraction ϕ.

T °C	JMAK k-constants (s^{-1})			
	$k_{0.124}$	$k_{0.5}$	k_1	k_8
20	0.025	0.026	0.034	0.043
30	0.079	0.045	0.037	0.049
40	0.112	0.054	0.056	0.057
50	0.148	0.105	0.08	0.059

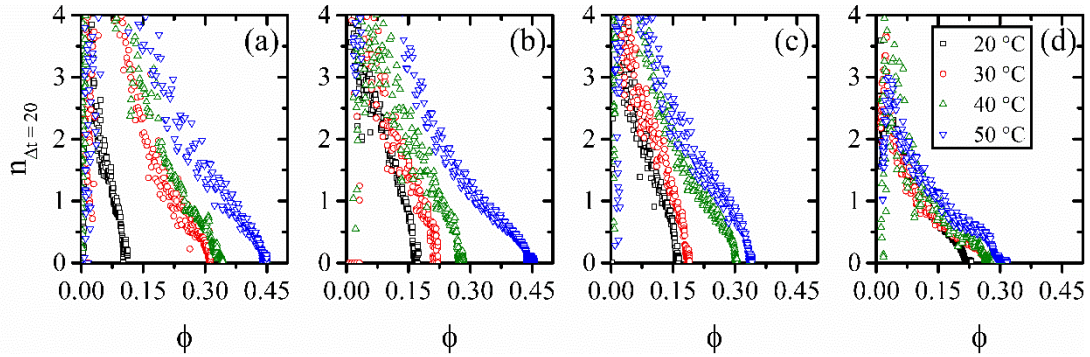

Figure B16 Instantaneous n factors ($n_{\Delta t = 20}$) for precursor Ca/U ratios of (a) 0.124, (b) 0.5 (c) 1 (d) 8 at 20 – 50 °C (ΔT = 10 °).

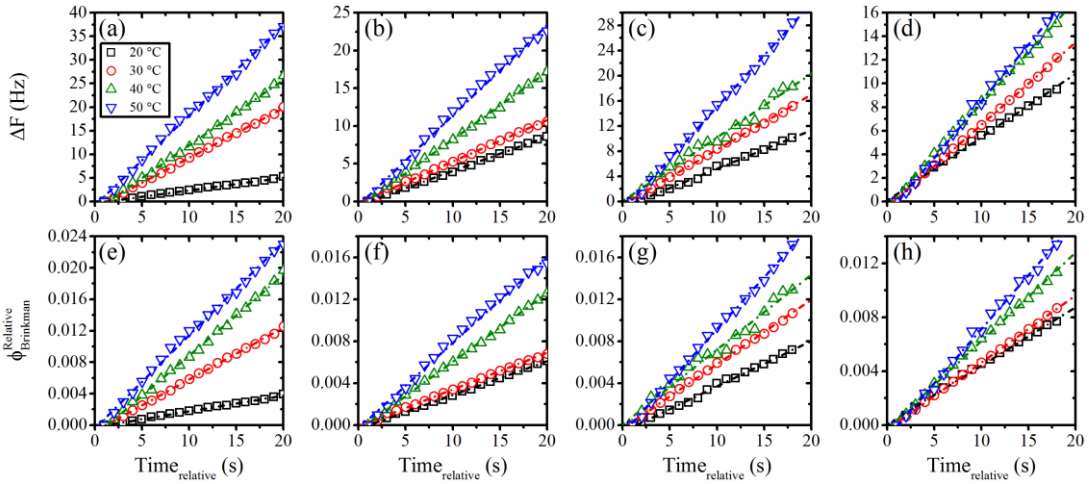

Figure B17 Relative ΔF and ϕ as functions of time at δF/δt minima.

Table B5 Apparent precipitation rate constants from ΔF and ϕ data

T °C	ΔF reaction constants (k)				ϕ reaction constants (*10^{-3} k)			
	$k_{0.124}$	$k_{0.5}$	k_1	k_8	$k_{0.124}$	$k_{0.5}$	k_1	k_8
20	0.27	0.46	0.61	0.54	0.20	0.323	0.433	0.44
30	1.05	0.55	0.88	0.70	0.66	0.35	0.62	0.49
40	1.39	0.89	1.01	0.87	1.02	0.65	0.71	0.66
50	1.91	1.19	1.64	0.96	1.38	0.93	0.96	0.78

Ln $k_{Ca/U}$ versus T^{-1} graphs using apparent rate constants from ΔF, ϕ and JMAK data were used (Figure 5.11a-c) in accordance with the linearized Arrhenius equation (Equation 5.6) to determine Arrhenius parameters

f. Aging effects

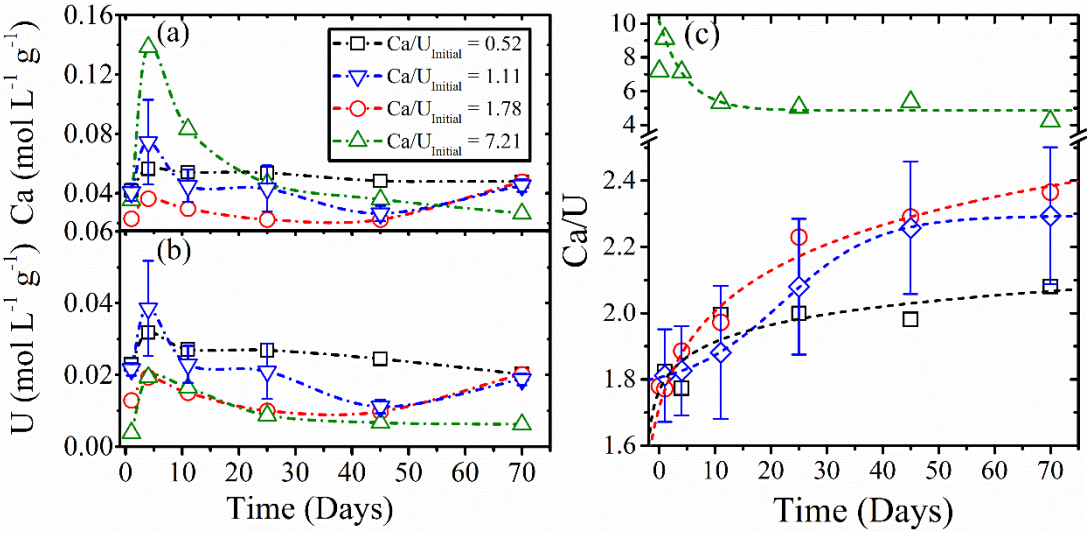

Figure B18 ICP-OES data showing change in (a) Ca, (b) U, and (c) Ca/U stoichiometry of 0.52, 1.11, 1.78, and 7.21 Ca/U particles as a function of aging time.

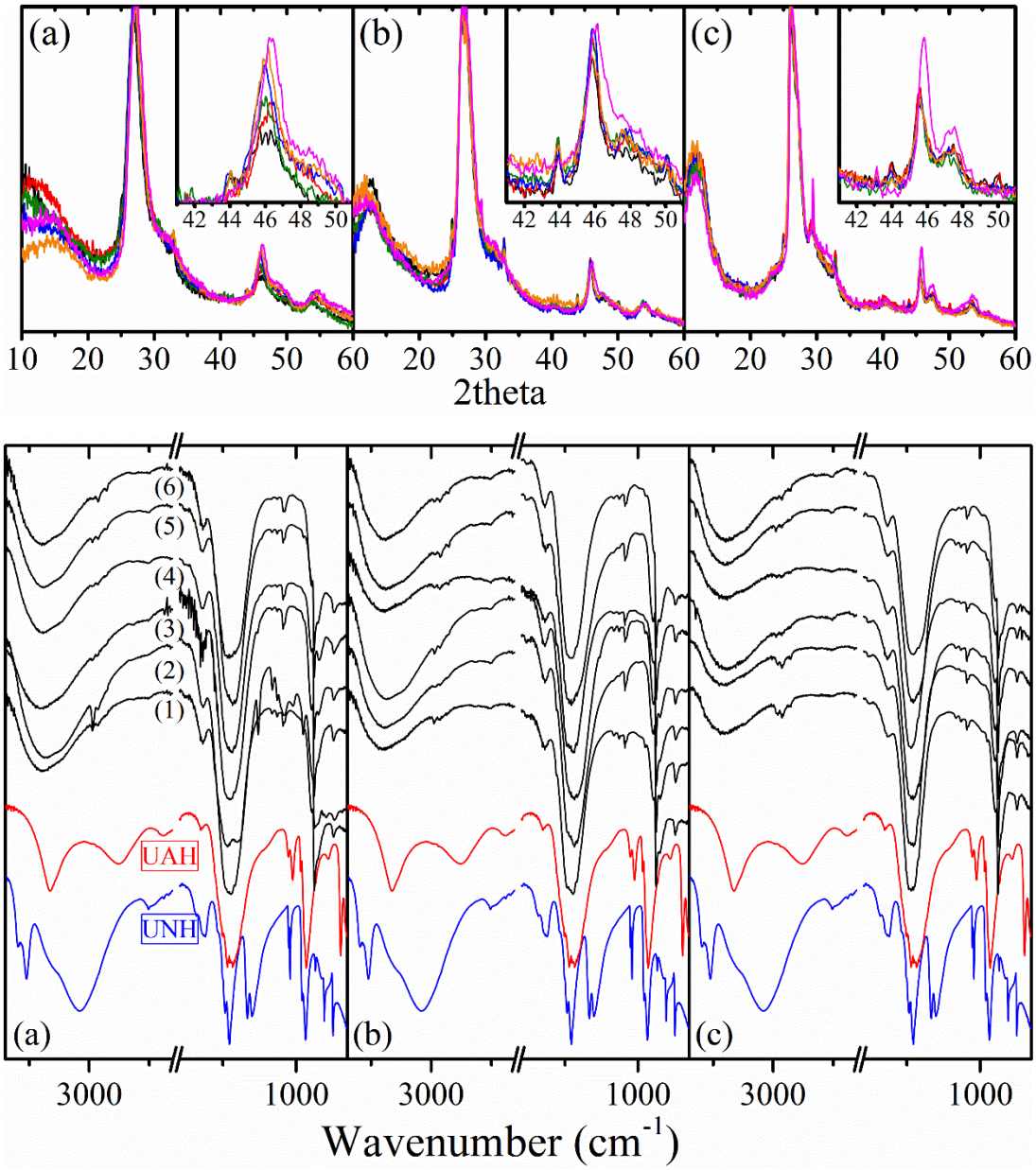

Figure B19 XRD (top), and FTIR (bottom) data for (a) – (c) 0.52, 1.11 and 1.78 Ca/U respectively. (1) – (6) samples measured at 1, 4, 11, 25, 45, 70 days respectively. (UAH) uranyl(VI) acetate hydrate and (UNH) uranyl(VI) nitrate hydrate standards.

3. Batch reactions

a. pH

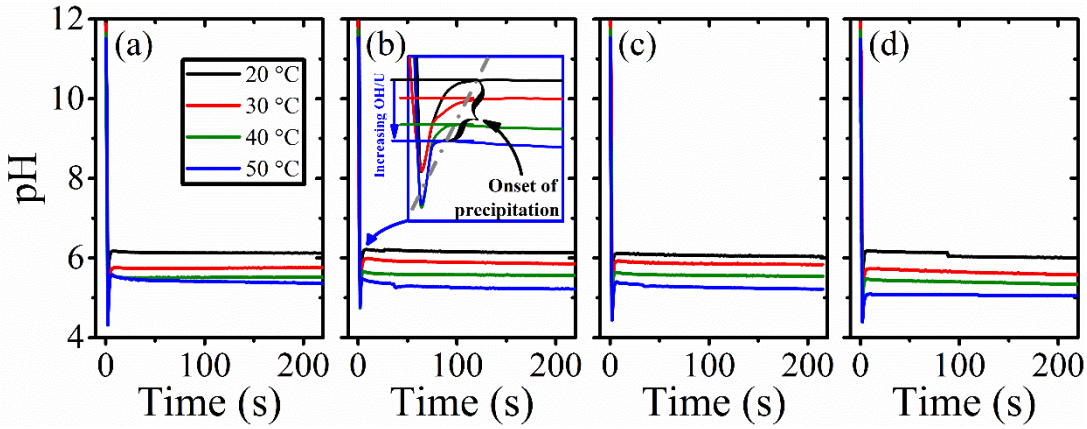

Figure B20 Raw in-situ pH trends for 20 – 50 °C (ΔT °C = 10 °C) reactions as a function of time for Ca/U stoichiometry of (a) 0.124, (b) 0.5, (c) 1 and (d) 8.

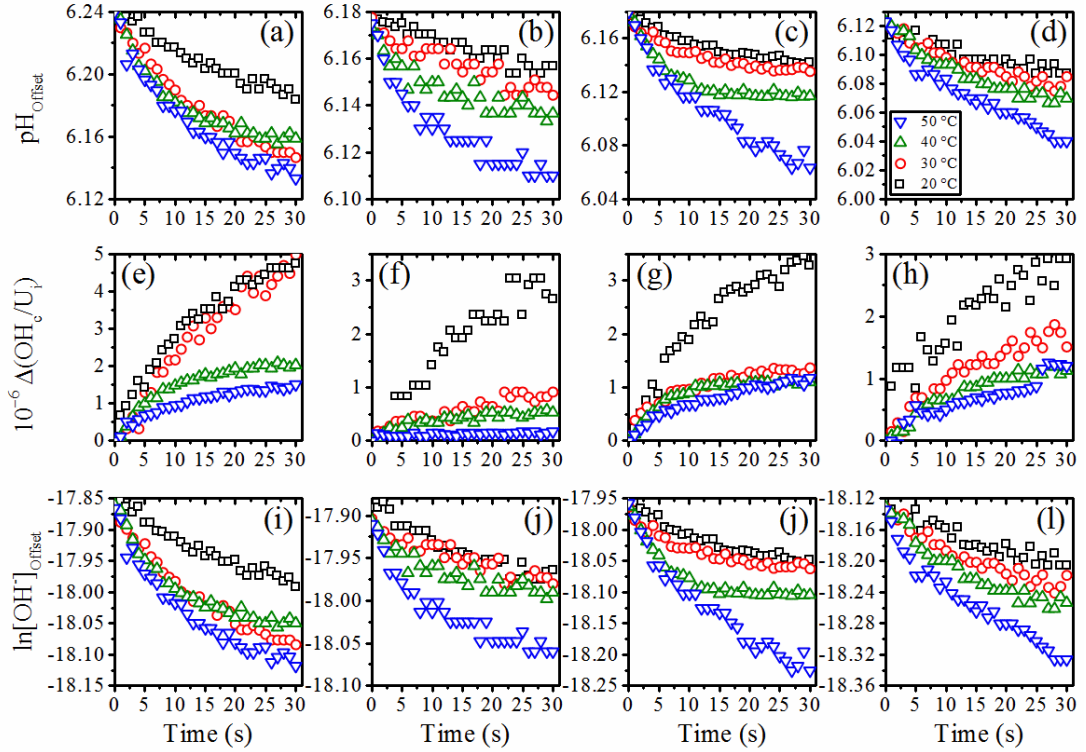

Figure B21 (a) – (d) relative pH change; (e) – (h) relative change in OH_c/U_i ratio; (i) – (l) relative ln hydroxide concentration change for Ca/U_i 0.124, 0.5, 1, 8 as a function of time respectively.

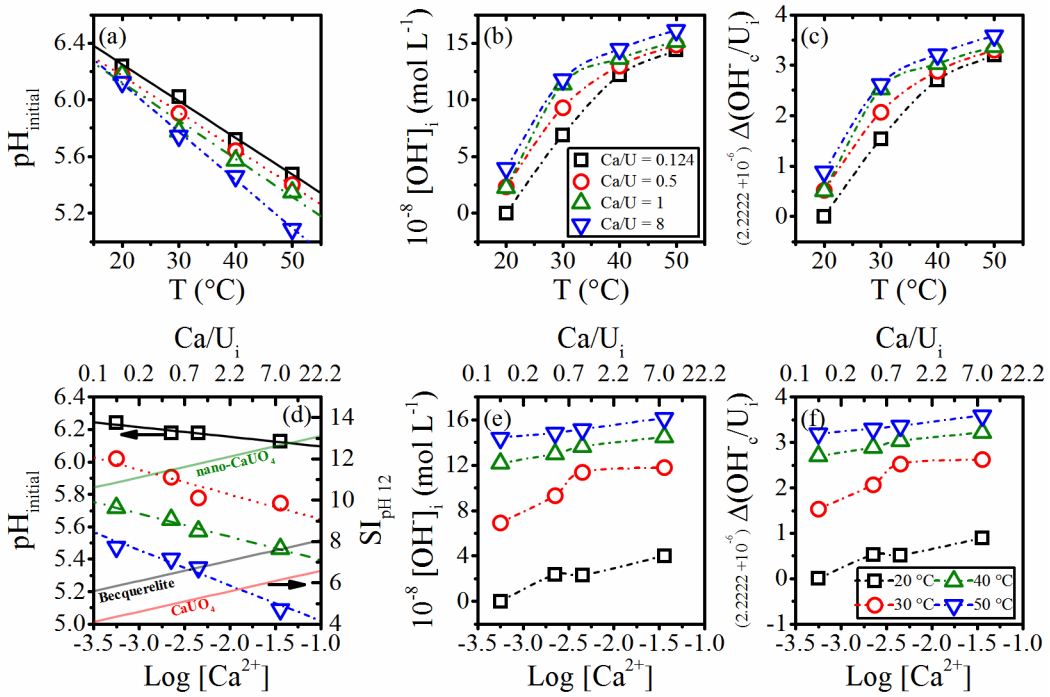

Figure B22 (a) pH value after reaction stabilisation; (b) relative change in OH^- concentration; (c) relative change in $OH^-_{consumed}/U_i$ ratio as a function of increasing temperature. (d) – (f) The same plots as a function of precursor (spiked aliquot) Ca/U stoichiometry (x-axis$_{upper}$) and log Ca^{2+}-concentration (x-axis$_{lower}$). Calculated SI values for Becquerelite (black), crystalline $CaUO_4$ (red) and nano-$CaUO_4$ (green) (Ca^{2+}-clarkeite K_{sp} from [13]) at pH 12 (t = 0) are plotted in graph (d) 2nd x-axis for reference.

b. QCM

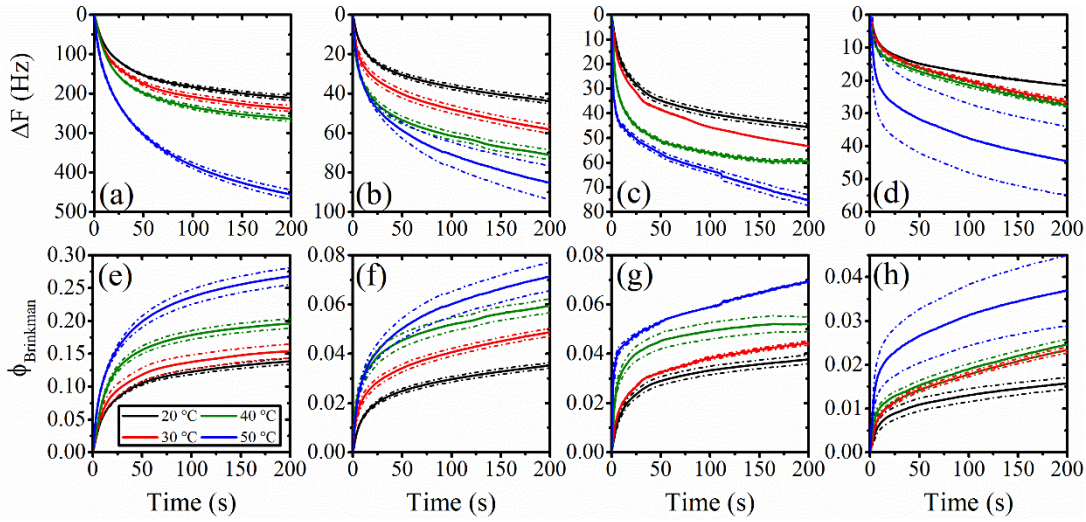

Figure B23 Measured ΔF and calculated ϕ trends for reaction temperatures ranging 20 – 50 °C at precursor stoichmioetry of 0.124, 0.5, 1 and 8 for (a) – (d) and (e) – (h) respectively. Dash-dot lines represent standard deviation from the average of 3 – 9 raw trends.

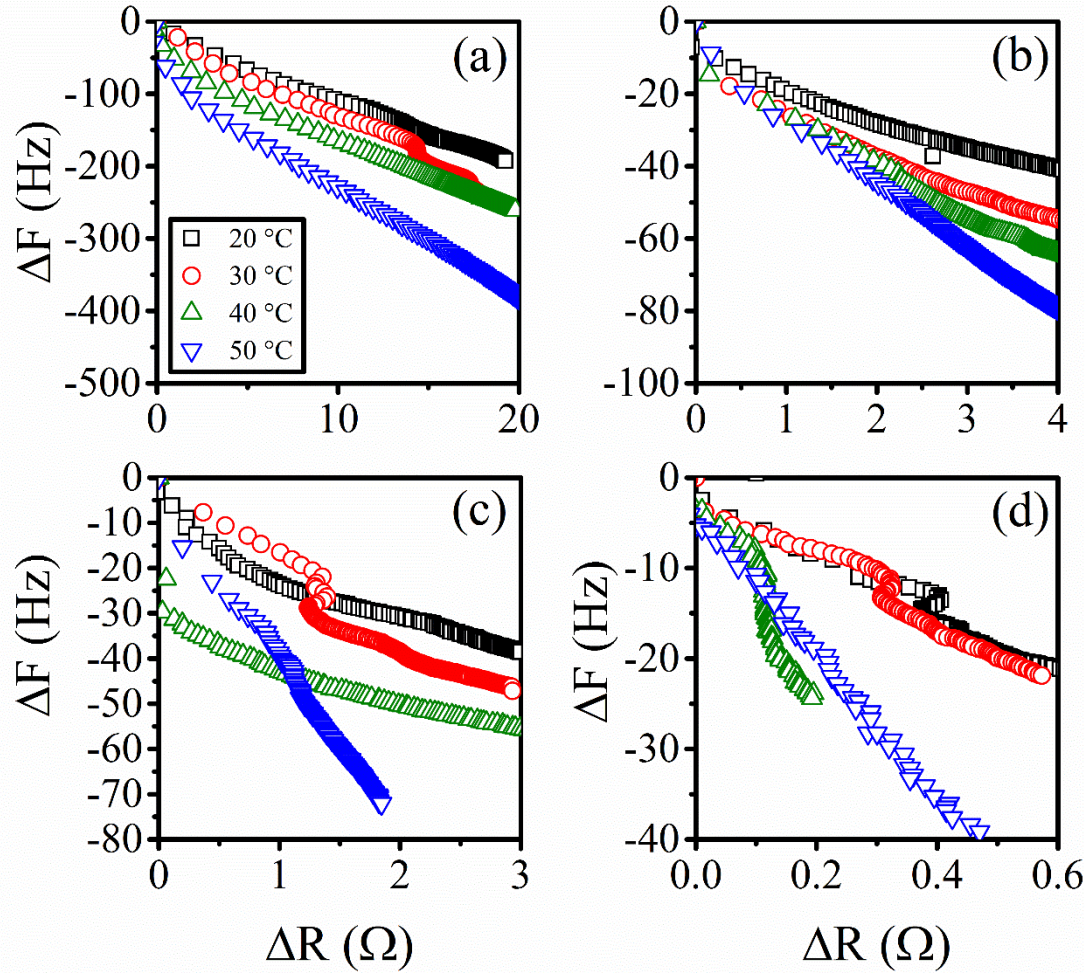

Figure B24 Plots of measured ΔR versus ΔF for reaction temperatures ranging 20 – 50 °C at precursor Ca/U stoichiometry of 0.124, 0.5, 1 and 8 for (a) – (d) respectively.

c. PHREEQC data output

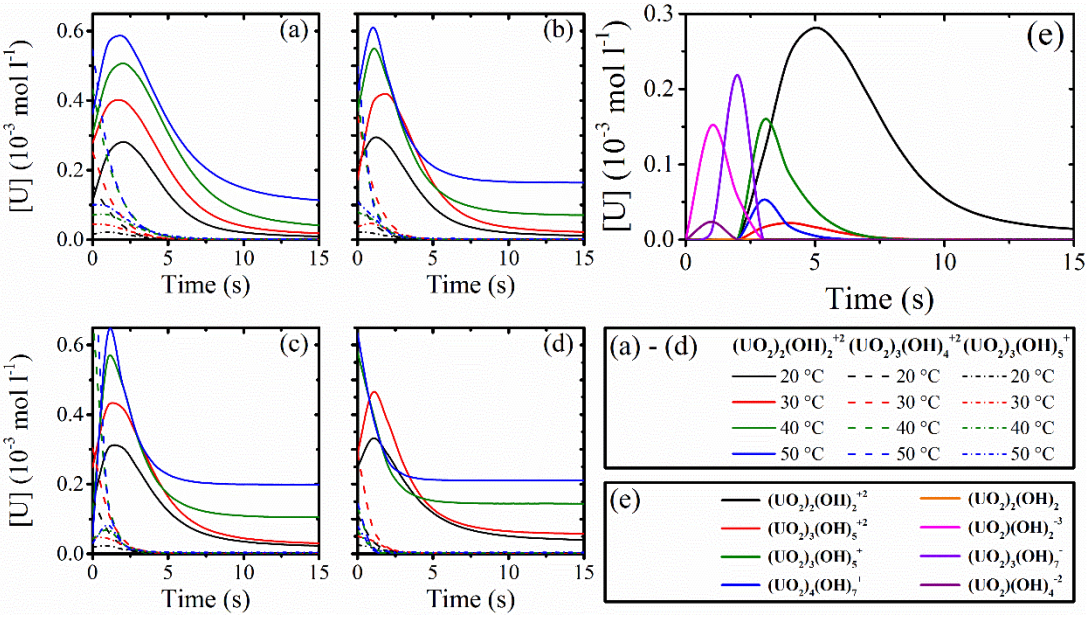

Figure B25 Modelled U-hydroxide speciation transported to the QCM surface as a function of relative reaction time between 20 and 50 °C (ΔT = 10) for Ca/U stoichiometry of (a) 0.124, (b) 0.5, (c) 1 and (d) 8. A typical full speciation versus time plot is displayed for reference (Ca/U = 0.124, 20 °C).

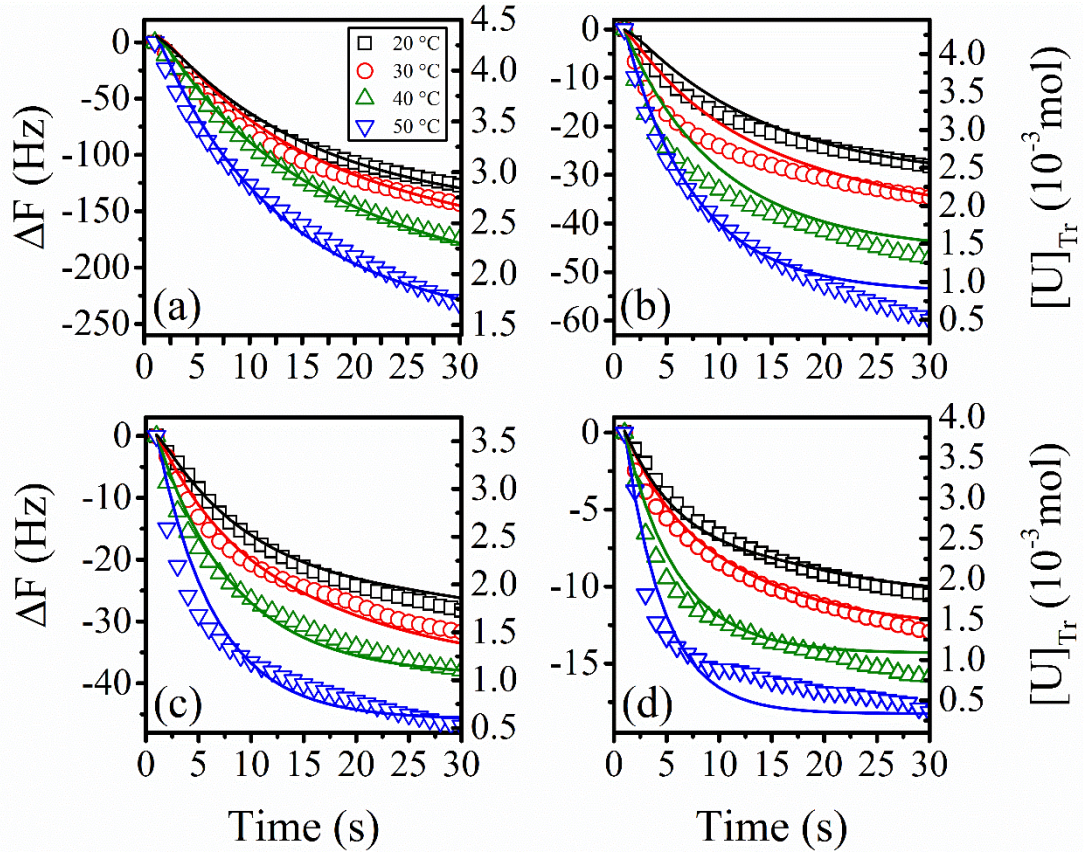

Figure B26 Initial exponential decay region showing measured ΔF and PHREEQC modelled U(VI) consumed between cell 0 and the QCM crystal surface.

Table B6 Apparent U(VI) diffusion rate constants from PHREEQC modelled U(VI) transport data.

T °C	Apparent diffusion constants (10^{-10} m^2 s^{-1})			
	$D_{Ca/U = 0.124}$	$D_{Ca/U = 0.5}$	$D_{Ca/U = 1}$	$D_{Ca/U = 8}$
20	2.64	3.23	4.18	5.23
30	2.95	4.41	4.77	7.50
40	3.68	7.77	10.00	15.97
50	5.45	11.36	14.55	22.27

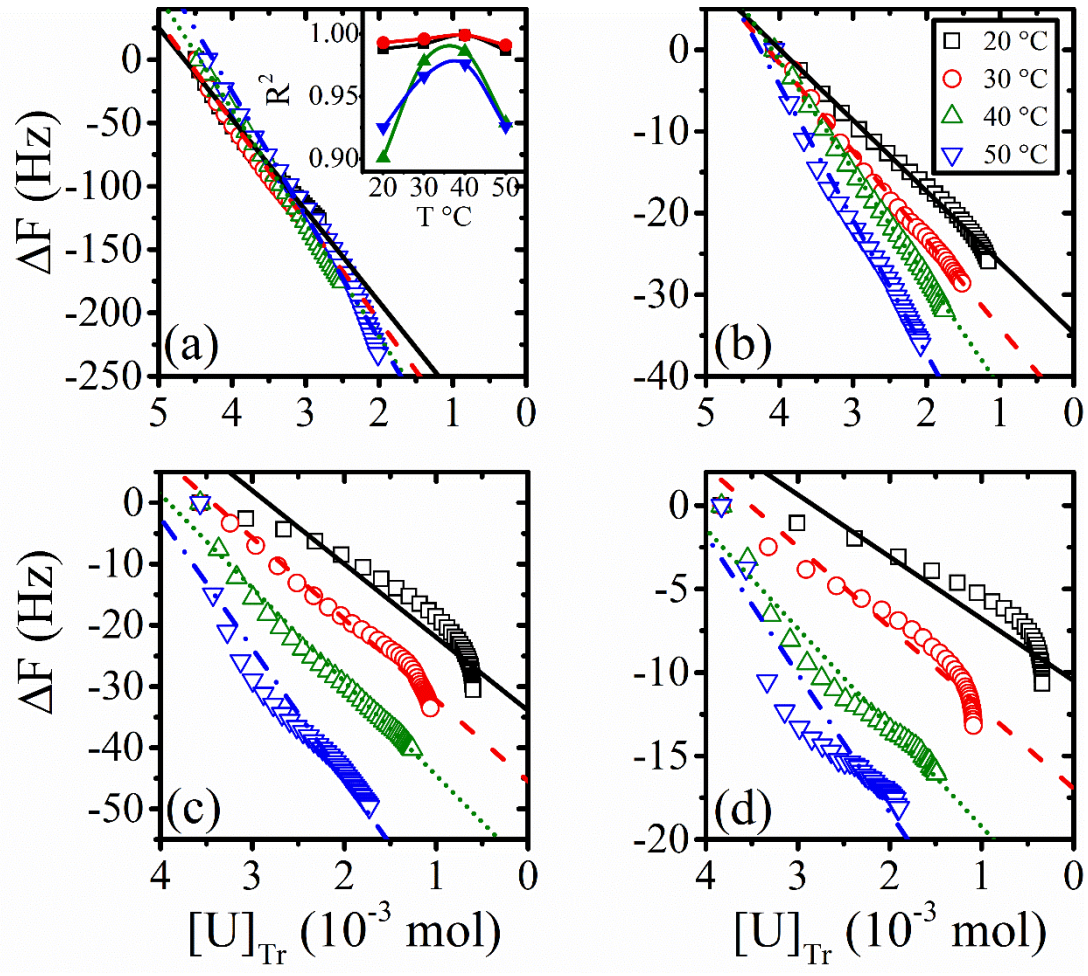

Figure B27 Empirical ΔF versus modelled U(VI) concentration in 20 – 50 °C reactions at precursor Ca/U stoichiometry of (a) 0.124, (b) 0.5, (c) 1 and (d) 8. Coloured lines are linear regression lines with R^2 values (higher is better) plotted in (a), inset.

d. Kinetic analyses

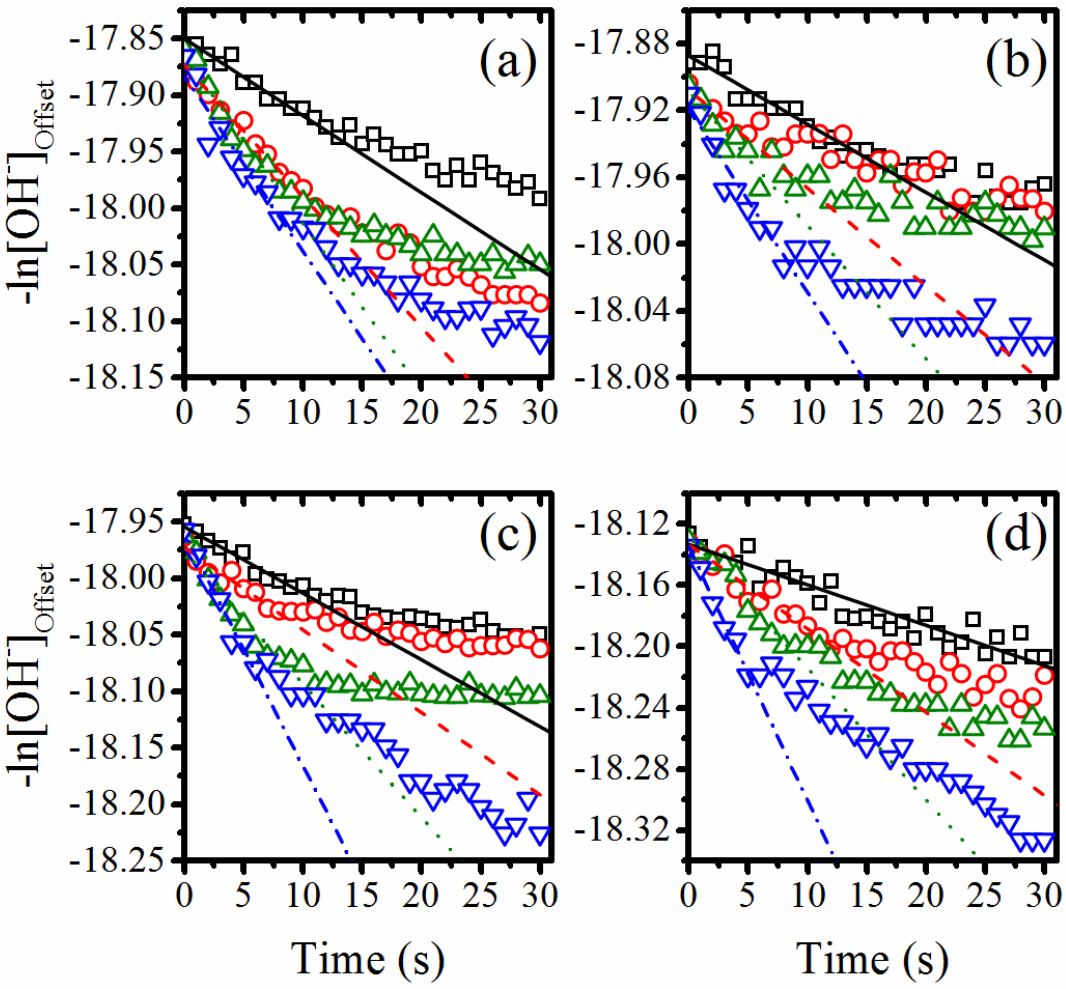

Figure B28 -ln[OH^-] versus time plots and linear regression lines for initial reaction regions (post stabilisation) for 20 – 50 °C reactions at precursor Ca/U stoichiometry of (a) 0.124, (b) 0.5, (c) 1 and (d) 8 respectively.

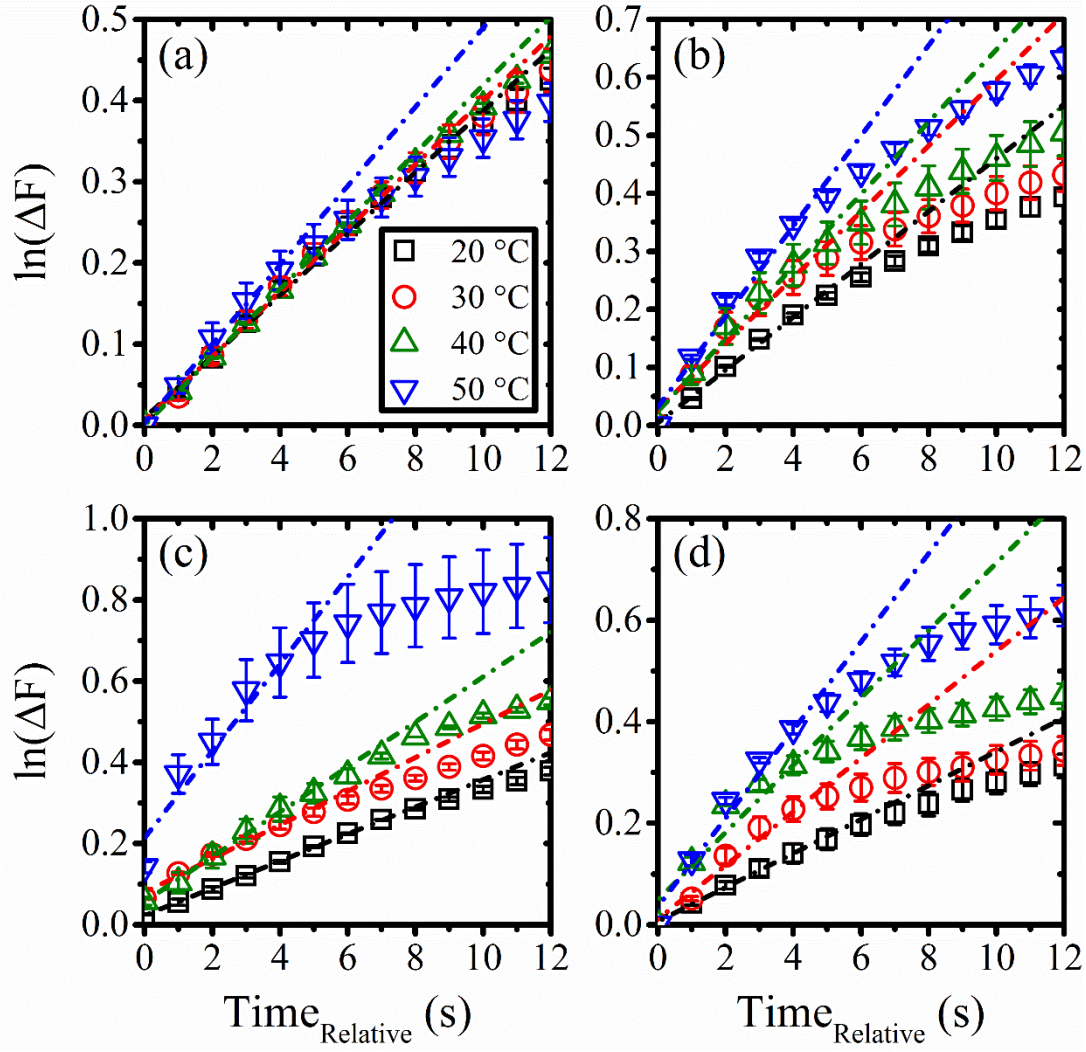

Figure B29 ln(ΔF) versus time plots and linear regression lines for initial reaction regions (post stabilisation) for 20 – 50 °C reactions at precursor Ca/U stoichiometry of (a) 0.124, (b) 0.5, (c) 1 and (d) 8 respectively.

In all trends, ln(k)-T^{-1} dependence is positive, whilst some crossover is present for ΔF and ϕ data at different Ca/U stoichiometry. At 30 °C, the $k_{\Delta F}$ trends in particular shows an almost isosbestic rate across all Ca/U. Given the T-dependence of iterated diffusion coefficients, the apparent activation energies associated with diffusion of U(VI)-species (diffusion barriers) were derived alongside those for ΔF and ϕ data using Arrhenius plots. As found for the steady-state data (Figure 5.12), E_a for ΔF and ϕ follow each other closely. However, batch reaction E_a exhibit an inverse dependency on precursor Ca/U and stoichiometry in comparison.

e. Activation barriers

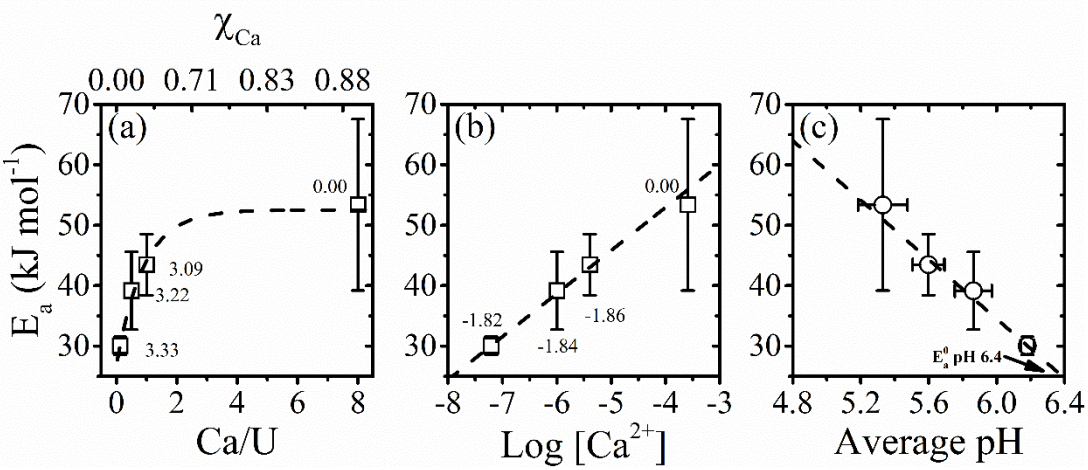

Figure B30 Derived apparent activation energies from ln $k_{Tr.pH}$ – T^{-1} plots as a function of initial Ca^{2+} content in solution. E_a are plotted as function of (a) initial Ca/U, (b) initial log Ca^{2+} concentration and (c) the average pH between 20 – 50 °C. Error bars represent the standard deviations of 3-9 trends.

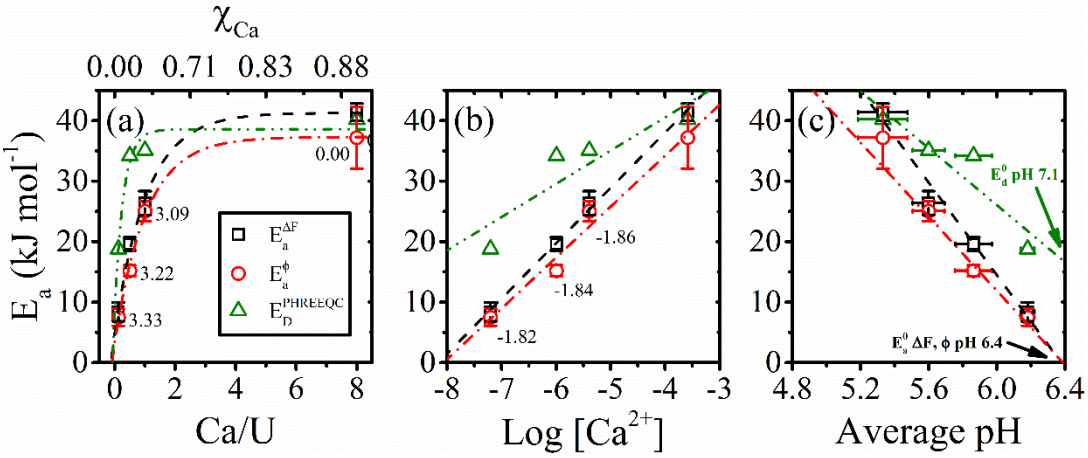

Figure B31 Apparent activation energies derived from ΔF, ϕ and PHREEQC mass transport modelling data as functions of initial (a) solution Ca/U-stoichiometry (lower) and Ca^{2+} mole fraction (upper); (b) log Ca^{2+} concentration; (c) second pH-maxima after the stabilisation region. Labelled values are precursor TMA^+ content as (a) TMA/U ratio, (b) log TMA^+-concentration and (c) average pH at precipitation onset. Y-error bars represent standard deviation of the mean of 3 – 9 trends, x-error bars represent variance of pH between 20 – 50 °C.

4. PHREEQC codes

a. CSTR reactor model

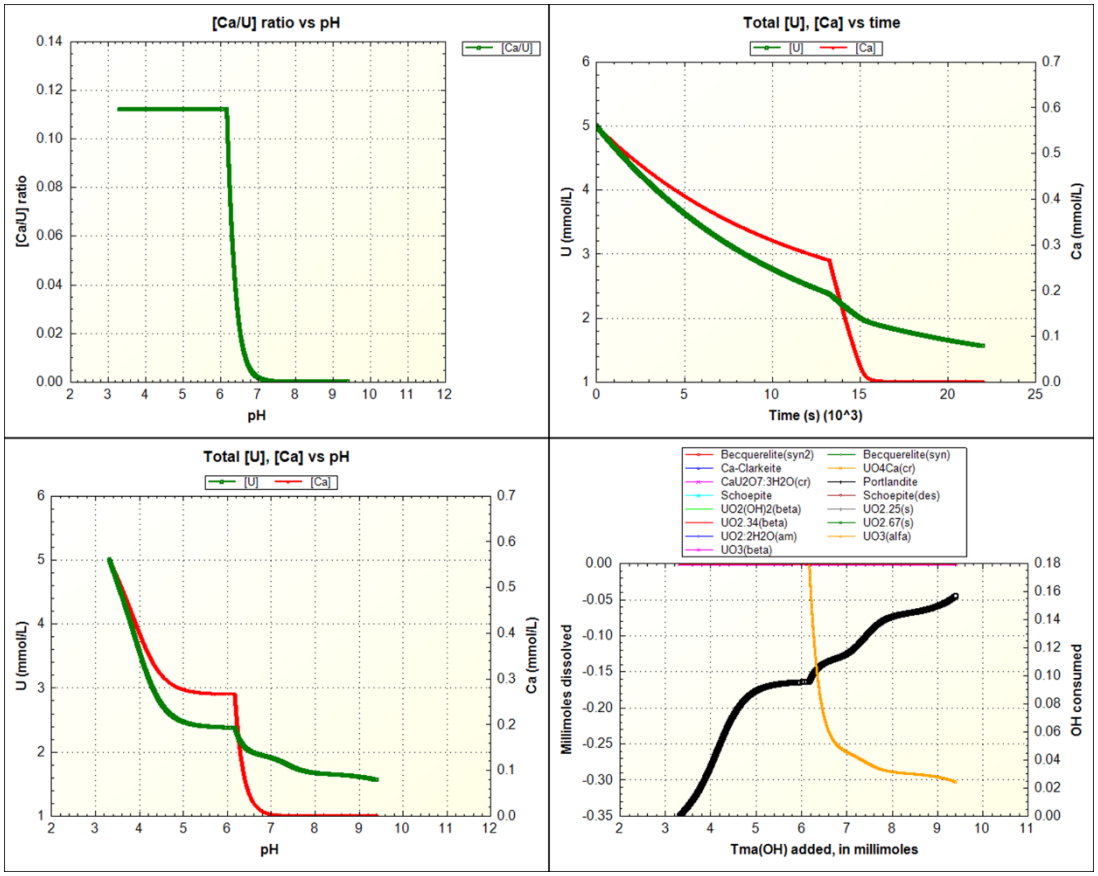

SELECTED_OUTPUT
-file PPT multi kin U2O7+UO4+edted-analyt 50.xls
-selected_out true
-user_punch true
-high_precision false
-distance false
-sim false
-state false
-solution false
-time true
-step false
-pH true
-pe false
-alkalinity true
-ionic_strength true
-totals Ca U Tma
-molalities Tma+ Ca(OH)+ UO2+2 (UO2)2(OH)2+2
(UO2)3(OH)4+2 (UO2)3(OH)5+ (UO2)4(OH)7+ UO2(OH)2 UO2(OH)3- (UO2)3(OH)7-
UO2(OH)4-2

-saturation Becquerelite(nat) Becquerelite(syn) schoepite UO4Ca(cr) CaU2O7:3H2O(cr) portlandite

SOLUTION 0 # inlet solution 10 mM Ca(OH)2
units mol/L
temp 50

EQUILIBRIUM_PHASES 1

```
Tma(OH) 0 0.00754
SAVE SOLUTION 0
END

SOLUTION 1   # Also define solution 1 since PHREEQC wants at least 1 cell in the column
temp 50

SOLUTION 3   # the tank solution
units mol/L
temp 50

EQUILIBRIUM_PHASES 2
UO2(NO3)2 0 0.005
Ca(NO3)2(s) 0 0.00056
Tma(Cl) 0 0.15

SAVE SOLUTION 3
END

MIX 3; 3 0.9995394269907; 0 4.605730092742870E-04;         # tR = V / (dV/dt) = 0.1 L / (0.05 L / 1
hour) = 2 hours.

RATES

Portlandite
-start
1 si_caoh = si("Portlandite")
20 if (m <= 0  and si_caoh < 0) then goto 200
#30 SA = 4.5 * m/m0
100 rate = 2.1 * (4.76e-6 - act("Ca+2") * act("OH-")^2) #SA
110 moles = rate * time
200 SAVE moles
-end

CaU2O7:3H2O(cr)
  -start
10 si_cau2o7 = si("CaU2O7:3H2O(cr)")
20 if (m <= 0 and si_bc < 0) then goto 200

30 kf = 50 #forwards precipitation reaction constant, dm mol?1 m?2 s?1, guess this until fits data
40 Ksp = 2.51189E+23 #equilibrium constant

#50 Hdisk = 1 #particle assumed to be disk shape, height #parameter, nm, guess from TEM images
#60 Rdisk = 10 #particle assumed to be disk shape, radius #parameter, nm, guess from TEM images
#70 Vdisk = Pi * Rdisk * Rdisk * Hdisk #volume of disk
#80 Sdisk = (2 * Pi * Rdisk * Hdisk) + (2 * Pi * Rdisk * Rdisk) #surface area of disk
#90 rhobec = 5.5 #density of becquerelite, g/cm3, literature #values
#100 Vrho = Vdisk * rhobec
#110 SA = Sdisk / Vrho #apparent surface area m2/g.

120 rate = kf * SA * ((act("Ca+2")^1 * act("U(+6)")^2 * act("OH-")^6) - Ksp)
130 moles = rate * time
140 if (moles > m) then moles = m
150 if (moles >= 0) then goto 200
160 temp = tot("U")
170 mc  = tot("OH-")
180 if mc < temp then temp = mc
190 if -moles > temp then moles = -temp
200 save moles
-end
```

```
UO4Ca(cr)
  -start
10 si_uo4ca = si("UO4Ca(cr)")
20 if (m <= 0 and si_bc < 0) then goto 200
30 kf = 50 #forwards precipitation reaction constant, dm mol?1 m?2 s?1, guess this until fits data
40 Ksp = 8.51138*10^15 #equilibrium constant of Ca-clarkeite, literature value

50 Hdisk = 1 #particle assumed to be disk shape, height parameter, nm, guess from TEM images
60 Rdisk = 10 #particle assumed to be disk shape, radius parameter, nm, guess from TEM images
70 Vdisk = Pi * Rdisk * Rdisk * Hdisk #volume of disk
80 Sdisk = (2 * Pi * Rdisk * Hdisk) + (2 * Pi * Rdisk * Rdisk) #surface area of disk
90 rhobec = 7.45 #density of becquerelite, g/cm3, literature values
100 Vrho = Vdisk * rhobec
110 SA = Sdisk / Vrho #apparent surface area m2/g.

120 rate = kf * SA * ((act("Ca+2")^1 * act("U(+6)")^1 * act("OH-")^4) - Ksp)
130 moles = rate * time
140 if (moles > m) then moles = m
150 if (moles >= 0) then goto 200
160 temp = tot("U")
170 mc  = tot("OH-")
180 if mc < temp then temp = mc
190 if -moles > temp then moles = -temp
200 save moles
-end

KINETICS 1
UO4Ca(cr)
-m0 0

Portlandite
-m0 0

CaU2O7:3H2O(cr)
-m0 0

INCREMENTAL_REACTIONS True

EQUILIBRIUM_PHASES 3
        CaU2O7:3H2O(cr) 0 0
        Portlandite 0 0
        UO4Ca(cr) 0 0
END

TRANSPORT
-cells 1
-boundary_conditions constant closed
-flow_direction diffusion_only
-stagnant 1  6.8e-6   0.3   0.1      # 1 stagnant layer, but more are possible, for modeling bad mixing in
the tank;
#number of stagnant layers, exchange factor (s-1), porosity in each mobile cell, porosity in each
immobile cell.
-lengths 0.05
-dispersivities 0.1
-correct_disp true
-diffusion_coefficient 1.0e-9

-time_step 10 # each time_step, the MIX is performed, 0.00261% mixed per minute, 1/60 hours.
-shifts 2200          # number of time_steps, total reaction time was about 1 hour. 1/0.016667hr
-punch_cells 3         # only graph the tank solution
-punch_frequency 1      # sample every step
```

```
USER_GRAPH 1 Total [U], [Ca] vs pH
-headings [U] [Ca]
-axis_titles "pH", "U (mmol/L)", "Ca (mmol/L)"
-chart_title "Total [U], [Ca] vs pH"
-axis_scale x_axis 2 12 1
-axis_scale y_axis auto
-initial_solutions true
-start
10 PLOT_XY -LA("H+"), TOT("U")*1000, color = Green,symbol = Square, symbol_size = 2, y-axis
= 1, line_width = 2
20 PLOT_XY -LA("H+"), TOT("Ca")*1000, color = Red, symbol = Diamond, symbol_size = 2, y-
axis = 2, line_width = 2
-end

USER_GRAPH 2 [Ca/U] ratio vs pH
-headings [Ca/U]
-axis_titles "pH", "[Ca/U] ratio"
-chart_title "[Ca/U] ratio vs pH"
-axis_scale x_axis 2 12 1
-axis_scale y_axis auto
-initial_solutions true
-start
10 PLOT_XY -LA("H+"), TOT("Ca")/TOT("U"), color = Green,symbol = Square, symbol_size = 2,
y-axis = 1, line_width = 2
-end


USER_GRAPH 3 Total [U], [Ca] vs time
-headings                              [U] [Ca]
-axis_titles "Time (s)", "U (mmol/L)", "Ca (mmol/L)"
-chart_title "Total [U], [Ca] vs time"
-axis_scale x_axis auto
-axis_scale y_axis auto
-initial_solutions true
-start
10 PLOT_XY total_time,TOT("U")*1000, color = Green, symbol = Square, symbol_size = 2, y-axis
= 1, line_width = 2
20 PLOT_XY total_time,TOT("Ca")*1000, color = Red, symbol = Diamond, symbol_size = 2, y-axis
= 2, line_width = 2
-end

USER_GRAPH 20degC
-headings Becquerelite(syn2)        Becquerelite(syn) Ca-Clarkeite      UO4Ca(cr)
          CaU2O7:3H2O(cr)           Portlandite       Schoepite         Schoepite(des)
          UO2(OH)2(beta) UO2.25(s)        UO2.34(beta)     UO2.67(s)        UO2:2H2O(am)
          UO3(alfa)         UO3(beta)
-axis_titles "Tma(OH) added, in millimoles" "Millimoles dissolved" "OH consumed"

10 x = - LA ("H+")
20        PLOT_XY        x,1.00E+03*(-EQUI("Becquerelite(syn2)")), symbol_size = 2
30        PLOT_XY        x,1.00E+03*(-EQUI("Becquerelite(syn)")) , symbol_size = 2
40        PLOT_XY        x,1.00E+03*(-EQUI("Ca-Clarkeite")), symbol_size = 2
50        PLOT_XY        x,1.00E+03*(-EQUI("UO4Ca(cr)")), symbol_size = 2
60        PLOT_XY        x,1.00E+03*(-EQUI("CaU2O7:3H2O(cr)")), symbol_size = 2
70        PLOT_XY        x,1.00E+03*(-EQUI("Portlandite")), symbol_size = 2
80        PLOT_XY        x,1.00E+03*(-EQUI("Schoepite")), symbol_size = 2
90        PLOT_XY        x,1.00E+03*(-EQUI("Schoepite(des)")), symbol_size = 2
100       PLOT_XY        x,1.00E+03*(-EQUI("UO2(OH)2(beta)")), symbol_size = 2
110       PLOT_XY        x,1.00E+03*(-EQUI("UO2.25(s)")), symbol_size = 2
```

```
120     PLOT_XY         x,1.00E+03*(-EQUI("UO2.34(beta)")), symbol_size = 2
130     PLOT_XY         x,1.00E+03*(-EQUI("UO2.67(s)")), symbol_size = 2
140     PLOT_XY         x,1.00E+03*(-EQUI("UO2:2H2O(am)")), symbol_size = 2
150     PLOT_XY         x,1.00E+03*(-EQUI("UO3(alfa)")), symbol_size = 2
160     PLOT_XY         x,1.00E+03*(-EQUI("UO3(beta)")), symbol_size = 2
#170    PLOT_XY         x, TOT("Tma")-ALK , y-axis = 2, line_width = 2, symbol = Circle, \
#       symbol_size = 2, color = Magenta
170     PLOT_XY         x, (((0.15/TOT("Tma"))-1)/10)-ALK , y-axis = 2, line_width = 2, symbol
= Circle, \
        symbol_size = 5, color = black

END
```

b. Kinetic mass transport model

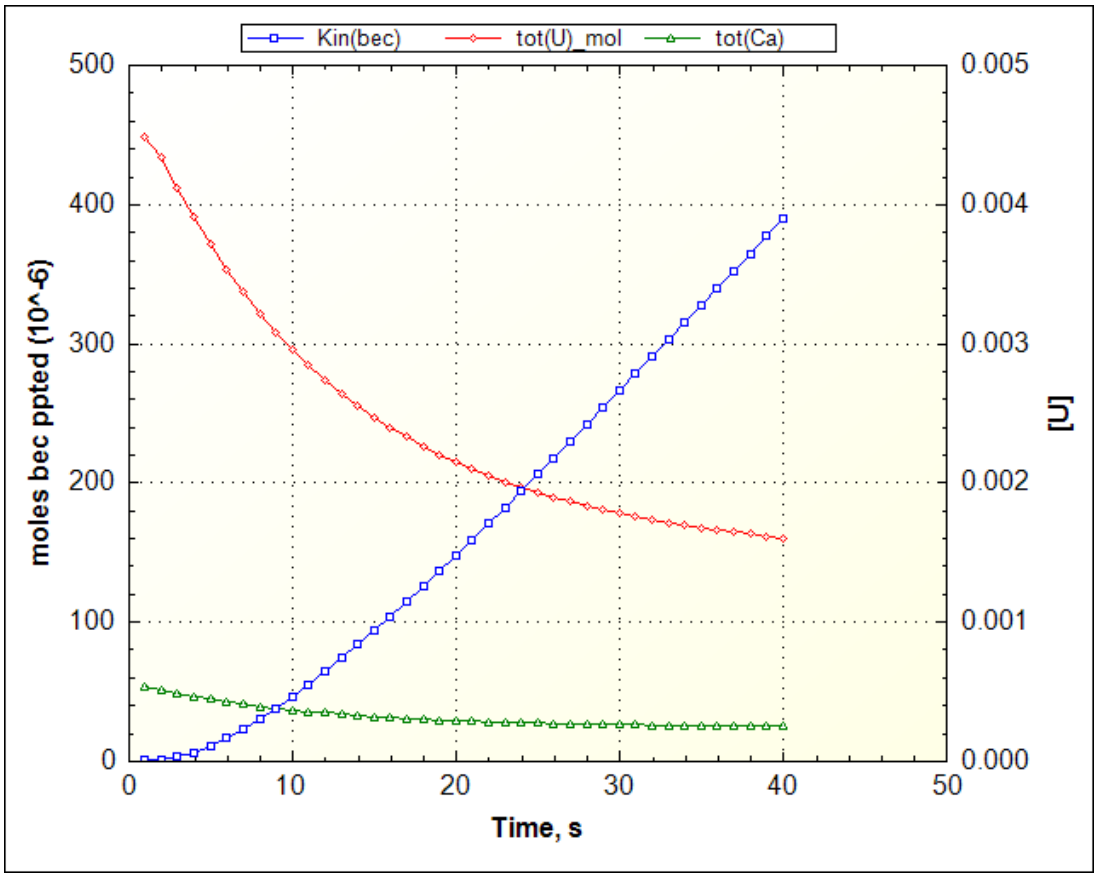


```
PRINT
        -reset false
        -echo_input true
                        -status false

SOLUTION 0 #inlet solution
units mol/L
temp 50 ########################################################################## change this
U(+6)   0.0045
Ca      0.00053
N(+5)   0.01 charge
pH      3.48
#EQUILIBRIUM_PHASES 1
#UO2(NO3)2 0 0.0045
#Ca(NO3)2(s) 0 0.00225
#SAVE SOLUTION 0

SOLUTION 1-10 Background solution
units mol/L
```

```
temp 50 ########################################################################## change this
pH      11.5
EQUILIBRIUM_PHASES 20
Becquerelite(nat) 0 0
#COPY solution 0 100 # for use later on, and in
#COPY solution 1 101 # 20 cells model
END

RATES
Becquerelite
-start
10          Ur = (act("(UO2)3(OH)5+")^0.55) * (act("(UO2)4(OH)7+")^0.45)^6
20          Cal = act("Ca+2")
30          proto = tot("H+")^-14
40          K1 = parm(1)*((TK/293.15)^parm(3))*EXP((-parm(2)/(8.314*TK)))

#40         K1 = parm(1)*((TK/273.15)^parm(3))*EXP((-parm(2)/(8.314*TK)))     #parm(1) is A,
parm(2) is Ea, parm(3) is beta fudge factor
#40         K1 = parm(1)*EXP(-(parm(2)/(8.314*TK))^parm(3))#parm(1) is A, parm(2) is Ea, parm(3)
is beta fudge factor
#60         rate = 0.5 * K1 * ((-(((Ur)^6 + (cal)))))
#60         rate = 0.5 * K1 * ((-(((Ur)^6 + (cal) + (proto)^-14))))

#60    rate = 2 * K1 * (-(((Ur) + (cal) + proto)) / (SI("becquerelite(nat)")))
60    rate = -2 * K1 * ((((Ur) + (cal) + proto)))
70    moles = rate*TIME
80          if (moles > M) then moles = M
200   SAVE moles
-end

KINETICS 1-10 kinetic reactions for all cells
becquerelite
-formula      Ca(UO2)6O4(OH)6(H2O)8  1
-m0    0 #0.00005
-parms    1.06 8380 0 #pre-exp factor, energy (j/mol), extended arrh factor (0 usually)
#-tol    1e-0015
#-steps          20 in 20 steps
#-step_divide   1
#-cvode true
#-runge_kutta 6
#-bad_step_max 500
#-cvode_order 5 #5
#-cvode_steps 100

#INCREMENTAL_REACTIONS true
#COPY kinetics 1 101
        END
SELECTED_OUTPUT
       -file   ex15_50_0.5.sel ######################################### change this
USER_PUNCH
       -headings        s   Ca U Bec pH
       -start
10 punch TOTAL_TIME
20 punch (0.00053-tot("Ca"))
30 punch (0.0045-tot("U"))
40 punch KIN("becquerelite")
50 punch -la("H+")

USER_GRAPH 1
       -headings Kin(bec) tot(U)_mol tot(Ca)
 -initial_solutions false
```

```
        -chart_title ""
        -axis_titles "Time, s"  "moles bec ppted" \
            "[U]"
        -axis_scale x_axis 0 auto
        -axis_scale y_axis 0 auto
        -plot_concentration_vs t
        -start
10 x = TOTAL_TIME
#20 PLOT_XY x, mol("becquerelite"), y-axis = 1, symbol_size = 4, color = blue
20 PLOT_XY x, KIN("becquerelite"), y-axis = 1, symbol_size = 4, color = blue
30 plot_xy total_time,  (0.0045-tot("U")), y-axis =2, symbol_size = 4, color = Red
40 plot_xy total_time,  (0.00053-tot("Ca")), y-axis =2, symbol_size = 4, color = green
        -end

USER_GRAPH 2
        -headings pH
 -initial_solutions false
        -chart_title ""
        -axis_titles "Time, s"  "pH"
        -axis_scale x_axis 0 auto
        -axis_scale y_axis 0 auto
-start
10 x = TOTAL_TIME
20 PLOT_XY x, -la("H+"), y-axis = 1, symbol_size = 4, color = black
-end

TRANSPORT
        -cells              10
        -lengths             10*0.0022
        -shifts             40 #100
        -time_step           1 #0.1
              #-stagnant                                1 7e-6 0.3 0.1
        -flow_direction       diffusion_only
        -boundary_conditions  constant closed
        -dispersivities       10*0.05
              #-thermal_diffusion         3.0   0.5e-6
        -correct_disp         true
        -diffusion_coefficient 0.71E-05 #cm2/s ################################### change this
        -punch_cells          7 #which cell do you want to punch?
        -punch_frequency      1 #how often?
        -print_cells          7 #which cell do you want to print?
        -print_frequency      1 #how often?
    #COPY solution 100 0 # initial column solution becomes influent
END
```

5. UV-vis spectroscopy

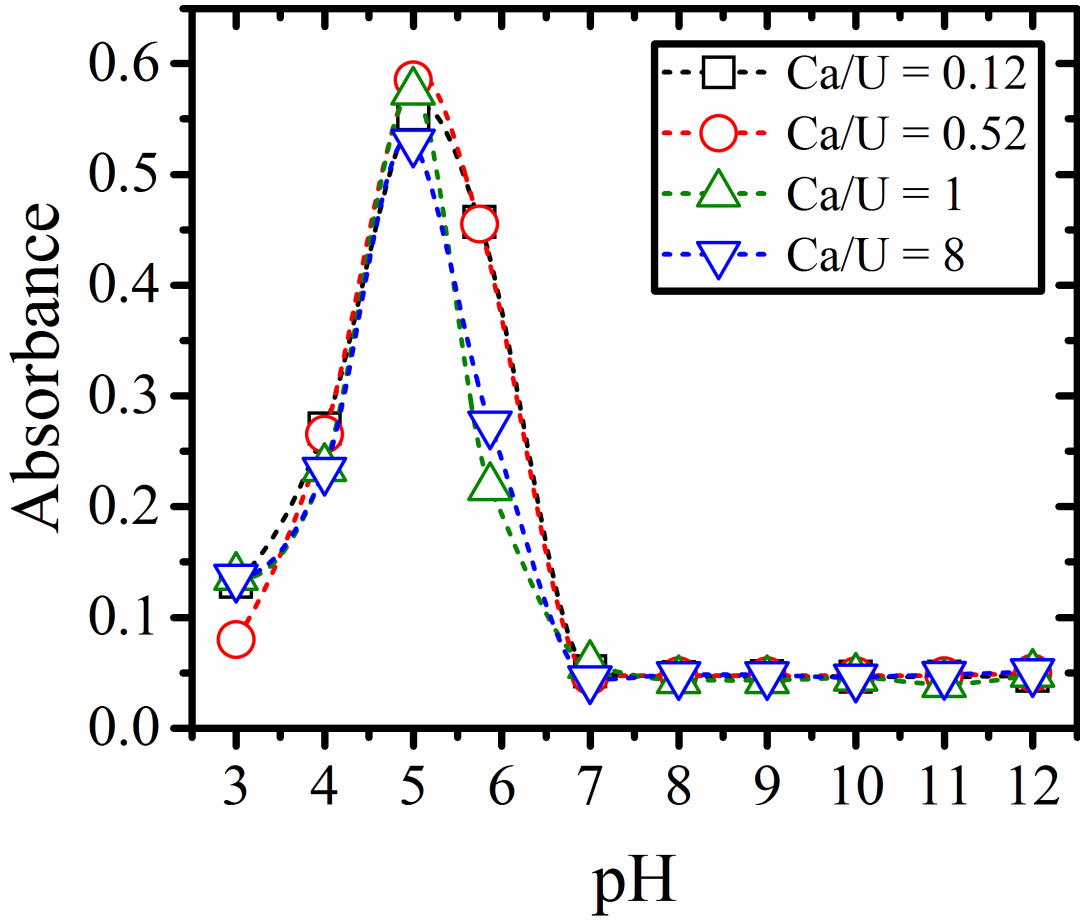

Figure B32 UV-vis spectra of absorbance as a function of solution pH. Samples are ex-situ aliquots taken from 20 °C reactions at Ca/U ratios of 0.124, 0.5, 1 and 8.

Supplementary information III

1. ICP-OES

Across all three extraction pH considered, the particle-Ca/U at 20 °C exhibit decreasing and increasing sensitivity to precursor-Ca/U, with an inflexion point lying at a solution-Ca/U of ~20. However, the sensitivity ($Ca/U_{solution}$ >20) at 70 °C, becomes significantly larger in magnitude, resulting in a bulk particle-Ca/U of 7.2 when solution-Ca/U reaches 50. This indicates an increasing non-congruency in the precipitation reaction as precursor Ca/U is elevated, which is enhanced by higher temperatures. This effect becomes particularly evident when the data is represented in log-log form (Figure C1d-f), where two distinct linear regions arise, which intersect at the inflexion observed in linear plots (Figure C1a-c).

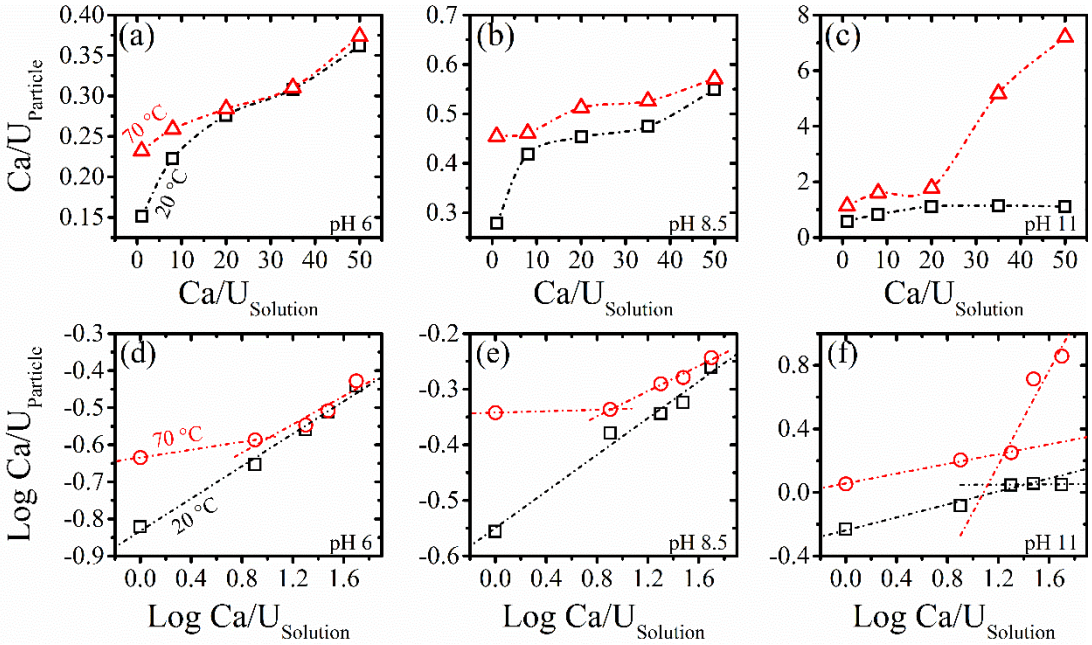

Figure C1 Ca/U (top row) and log Ca/U (bottom row) stoichiometry for acid-digested Ca^{2+}-U(VI)-oxyhydrate particles filtered at (a, d) pH 6, (b, e) pH 8.5 and (c, f) pH 11; as functions of precursor solution Ca/U for 2 reaction temperatures, 20 (black) and 70 °C (red).

2. FTIR

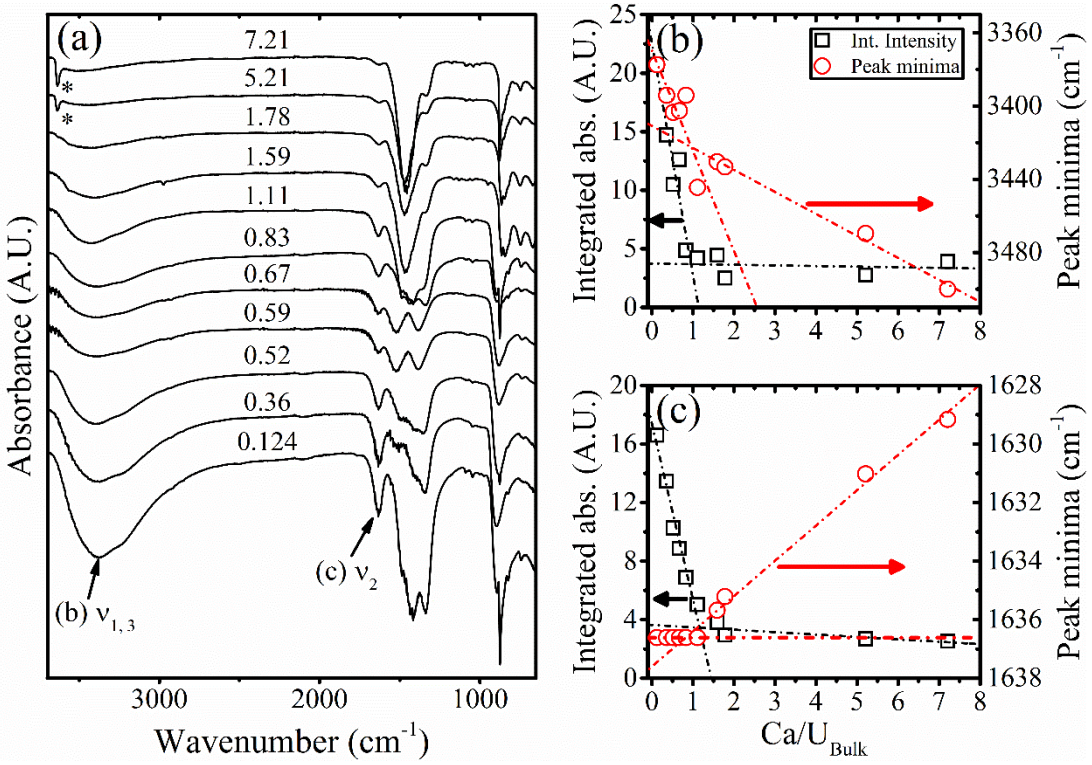

Figure C2 (a) Stacked FTIR spectra in order of increasing bulk Ca/U-stoichiometry (bottom to top) ranging 0.124 – 7.21. The integral peak area (2000-3700 cm^{-1}) (left) and minima (right) values are presented for the $\upsilon_{1,3}$ and υ_2 absorbance bands in (b) and (c) respectively. Asterisks at 3640 cm^{-1} represent $Ca(OH)_2$ OH-bands.

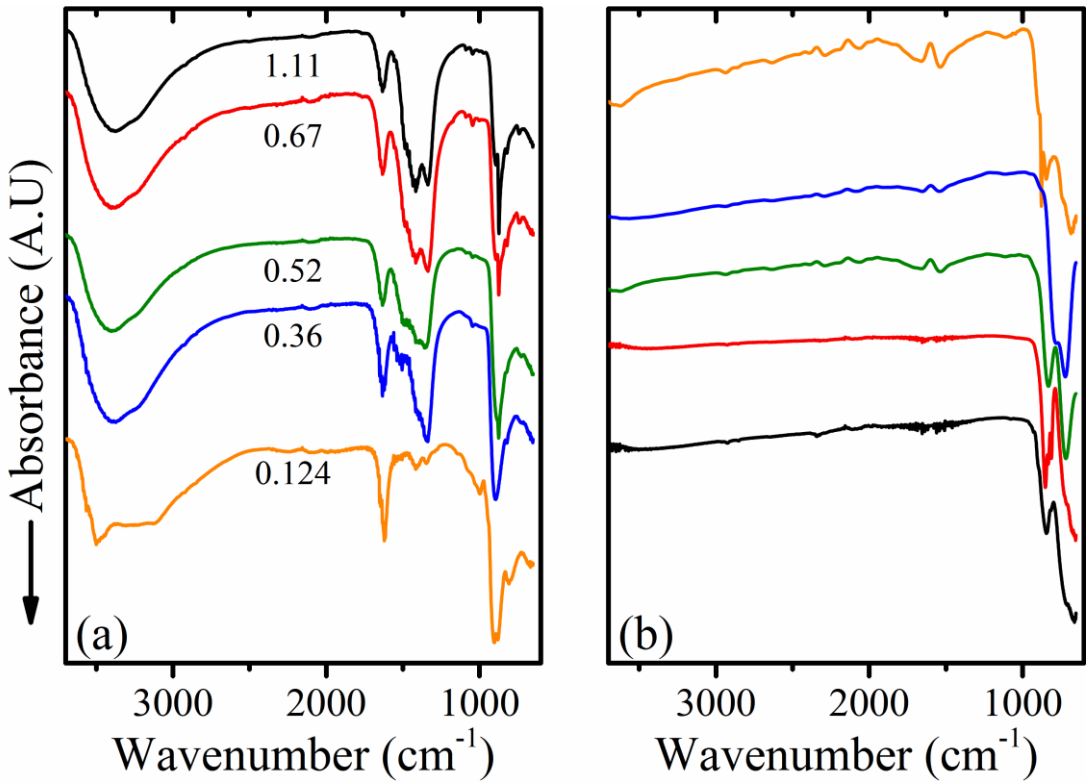

Figure C3 FTIR spectra of Ca/U 0.124 – 1.11 as (a) precipitates; and (b) 800 °C.

Table C1 Badger relationship predicted U-O_{yl} bond lengths for precipitate, intermediate and crystalline samples with bulk Ca/U stoichiometry ranging 0.124 – 1.11.

T °C	Predicted U-O_{yl} bond lengths, Å				
	0.124	**0.36**	**0.52**	**0.67**	**1.11**
precipitate	1.77	1.79	1.78	1.83	1.79
200	1.77		1.78		1.79
300	1.79		1.78		1.79
400	1.86		1.84		1.84
800	1.86	1.82	1.81	1.81	1.87

3. XRD

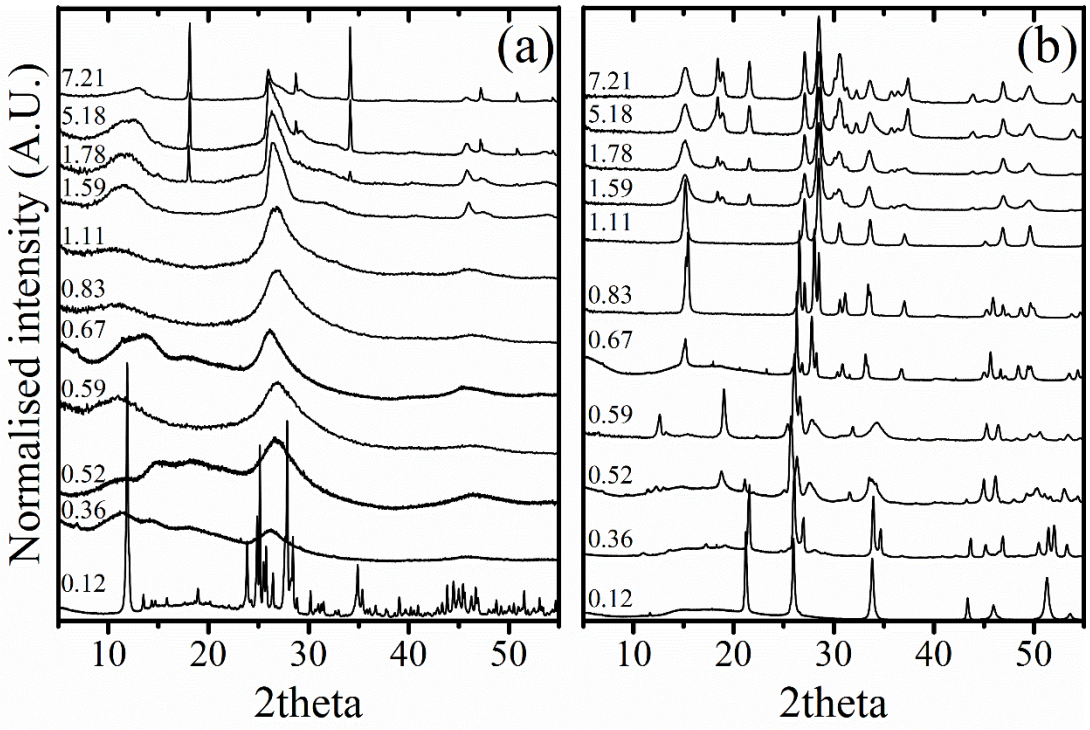

Figure C4 Stacked X-ray diffractograms for (a) precipitated and propan-2-ol washed Ca^{2+}-U(VI)-oxyhydrate; and (b) precipitates calcined at 800 °C for 30 minutes under oxic conditions; with bulk Ca/U-stoichiometry ranging 0.124 – 7.21, as measured via ICP-OES.

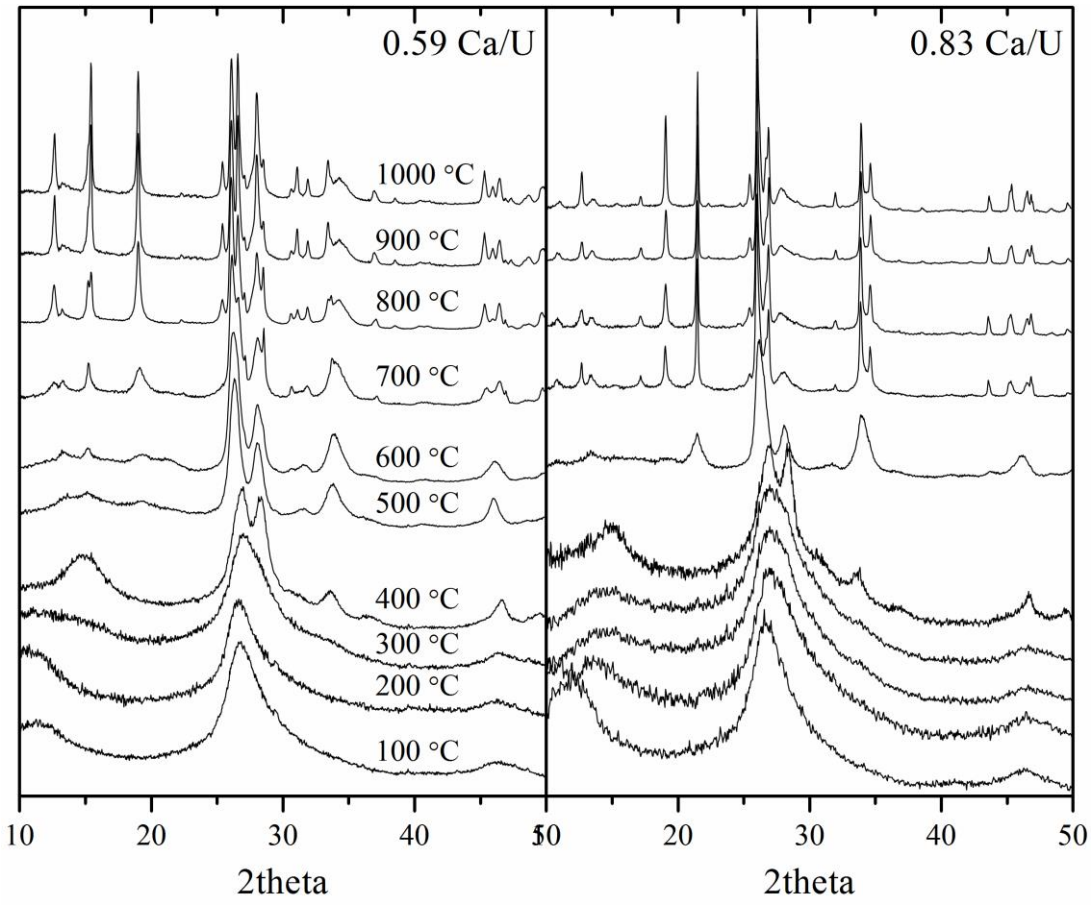

Figure C5 Full calcination series for 0.59 and 0.83 Ca/U samples showing little apparent phase change between poorly-ordered (500 °C) and crystalline endmembers (1000 °C).

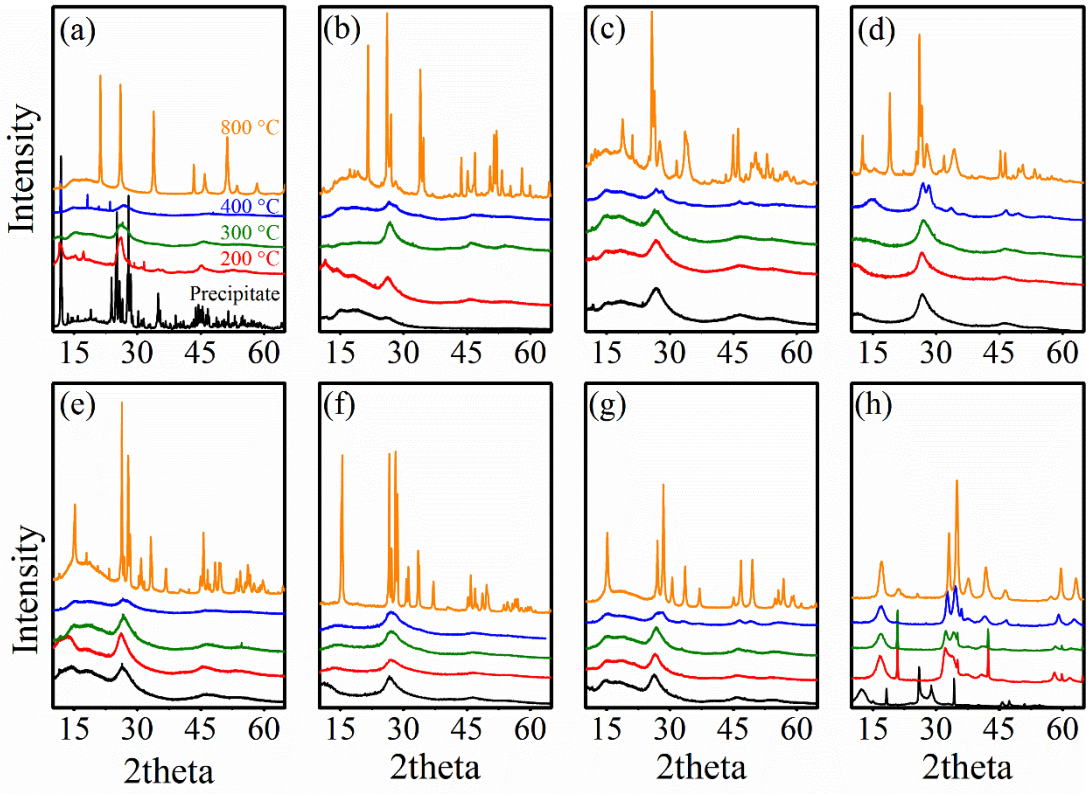

Figure C6 Ex-situ X-ray diffractograms for precipitates calcined between 200 and 800 °C with bulk solids with Ca/U-stoichiometry 0.12, 0.36, 0.52, 0.60, 0.67, 0.83, 1.11, 7.21 in graphs (a) – (h) respectively.

4. ZP

Disaggregated calcined samples of Ca/U-stoichiometry of 0.124, 0.361, 0.521, 0.671 and 1.11 were suspended in deionised water (18 MΩ) containing 0.01 mol L^{-1} NaCl electrolyte at ~1000 ppm. Triplicate samples were loaded into folded capillary zeta cells then analysed using a Malvern Instruments Zetasizer Nano. The refractive index was taken to be 1.63 (see 4.2.2.2). Measurements between repeats were found to be more stable after some equilibration; results are therefore from samples allowed to equilibrate for 6 hrs prior to measurement. Full ZP trends are presented in Figure C7 and summarised in Figure 6.1c.

The average ξ-potential of crystalline samples comprised of predominantly single phases (Ca/U 0.124, 0.36, 0.52, 0.67, and 1.11) were measured over the pH-range 3 – 10 (see Figure C7). Towards higher Ca^{2+}-content in crystallized solids, the apparent isoelectronic points (Figure 6.1c, $\xi\text{-IEP}_{fit}$) also increased in a sigmoidal trend from ~pH 2.3 at Ca/U 0.124 to ~pH 5.1 by Ca/U 1.11.

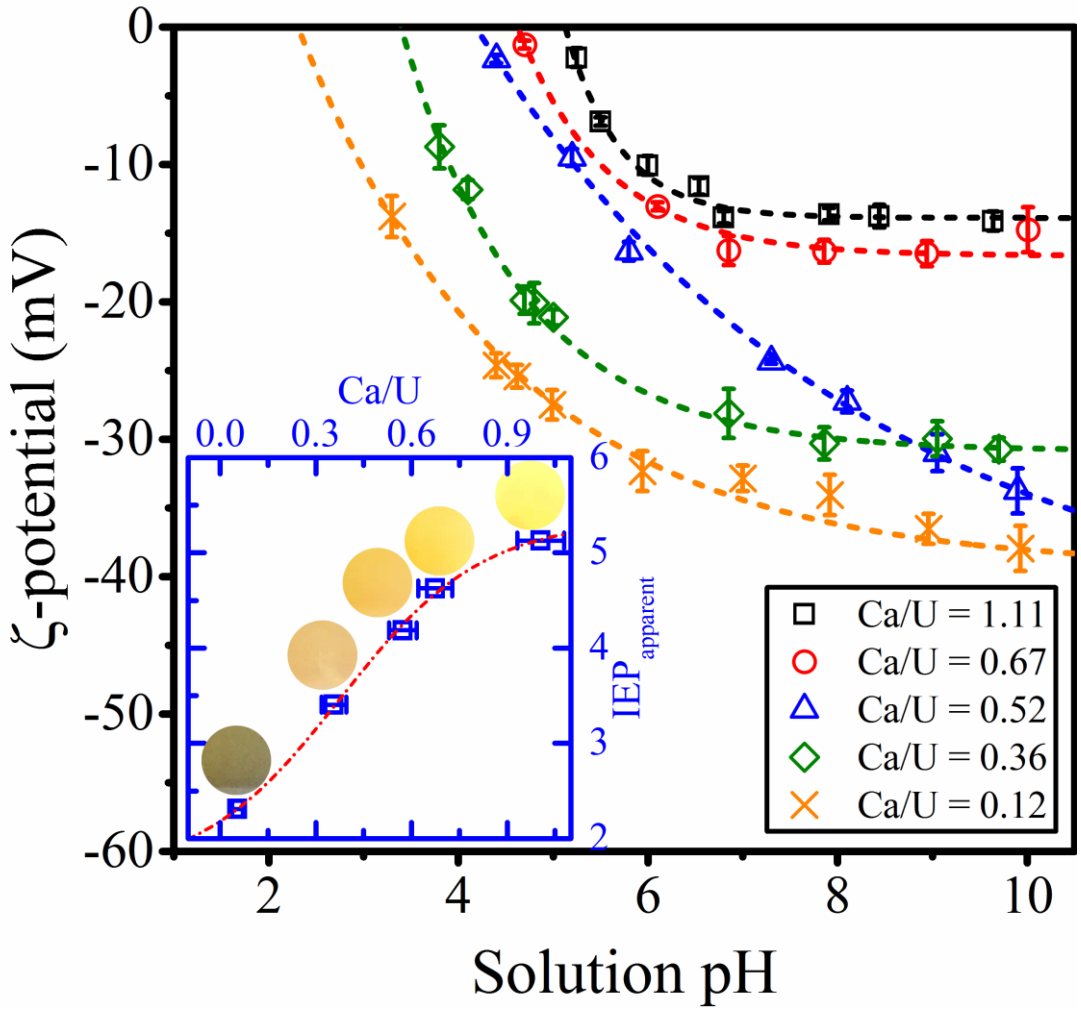

Figure C7 Full ξ-potential (ZP) trends for crystallised solids at Ca/U-stoichiometry between 0.124 – 1.11, measured between pH 3 – 10 (0.01 mol L^{-1} KNO_3 solution). Trends were fit with an exponential decay function and extrapolated to ξ-potential of zero. The apparent isoelectronic points ($IEP_{apparent}$) are presented as a function of bulk-Ca/U in the inset graph (blue).

5. SEM, TEM

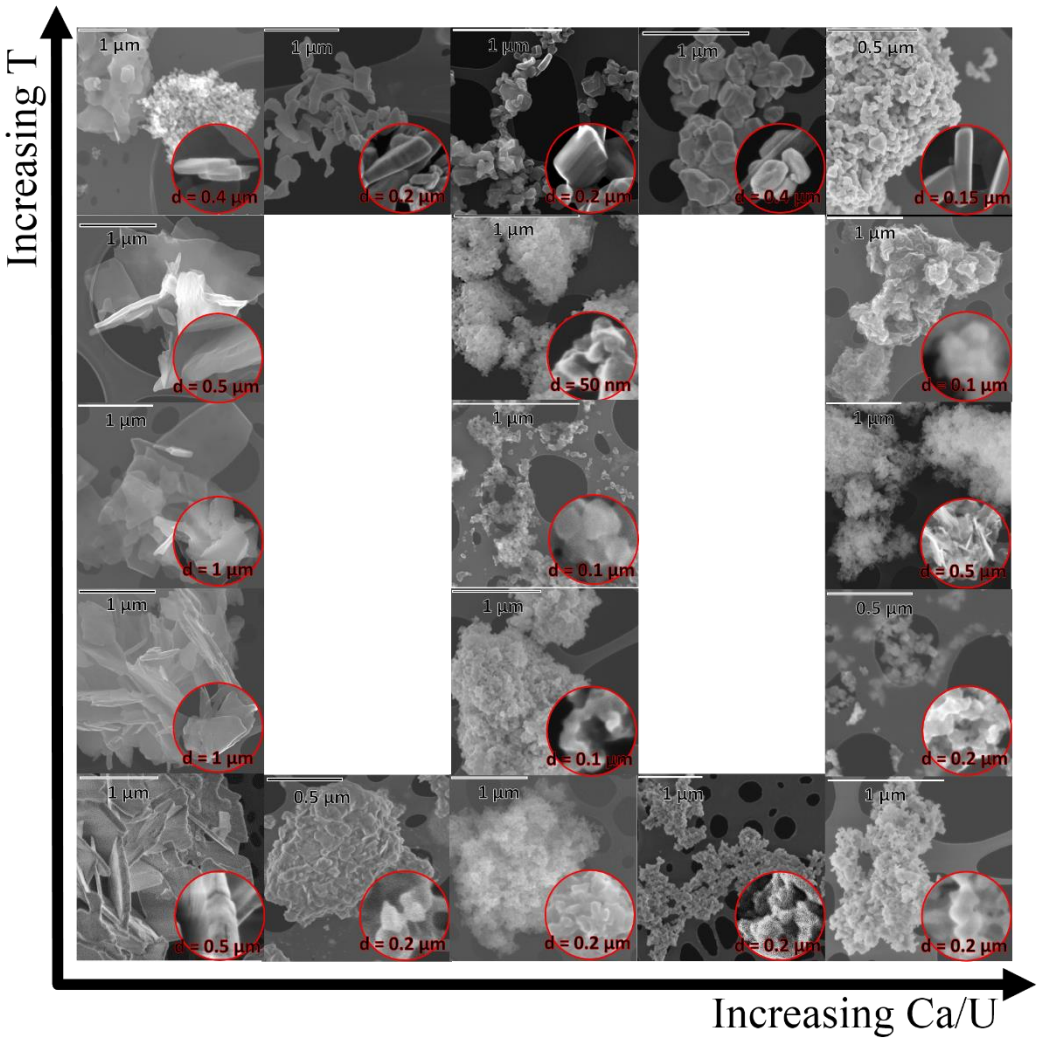

Figure C8 SEM images, columns left to right are Ca/U of 0.124, 0.36, 0.52, 0.67, 1.11 respectively. Rows bottom to top are precipitate, 200, 300, 400, 800 °C respectively.

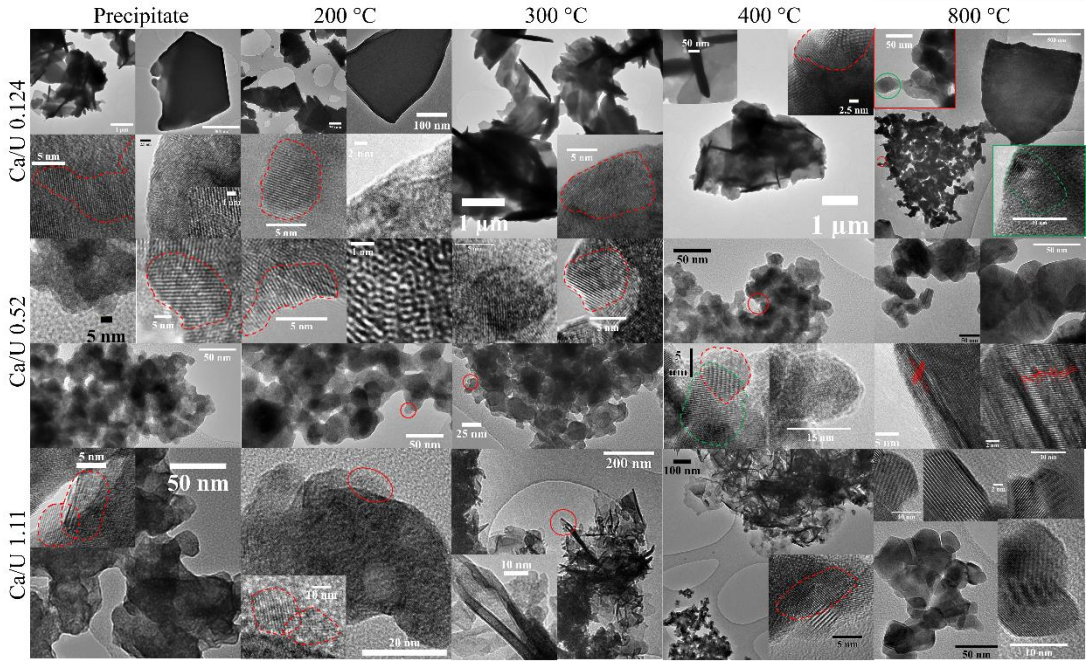

Figure C9 Full TEM images, columns left to right are precipitate, 200, 300, 400, 800 °C respectively. Rows bottom to top are Ca/U of 0.124, 0.52, and 1.11 respectively.

Table C2 Standardless EDS quantification of small and large particles in crystallised samples with Ca/U of 0.124.

Small particles								
	1		**2**		**3**		**Average at%**	**Std. Dev**
	wt%	At%	wt%	At%	wt%	At%		
Ca	1.81	1.36	1.39	0.92	1.72	1.26		
U	48.99	6.19	41.63	4.64	47.76	5.9		
O	49.2	92.46	56.98	94.45	50.52	92.84		
Ca/U		*0.22*		*0.19*		*0.21*	*0.21*	*0.01*
Large sheets								
	1		**2**		**3**			
Ca	2.12	1.51	0.96	0.7	2.16	2.76		
U	45.9	5.52	47.42	5.79	72.29	15.54		
O	51.98	92.97	51.62	93.53	25.55	81.7		
Ca/U		*0.27*		*0.12*		*0.18*	*0.19*	*0.06*

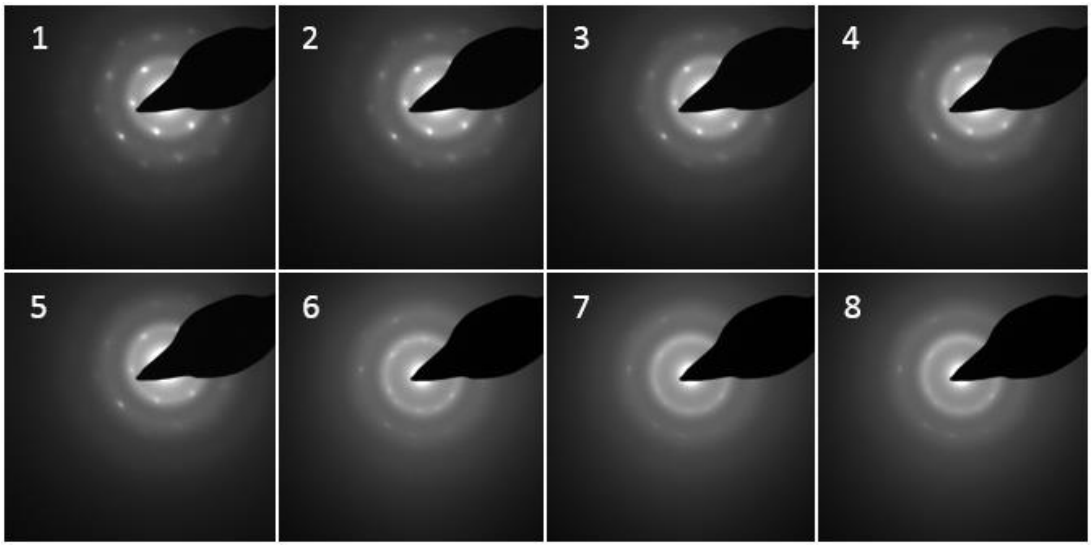

Figure C10 Typical SAED-pattern showing increasing sample damage of a Becquerelite crystal with increasing time (images 1 – 8). Temporal spacing between images are ~10s. Samples with higher Ca/U exhibit the opposite trend, and more rapidly. Note the longer transition time in SAED-mode in comparison to the higher electron flux occurring during imaging.

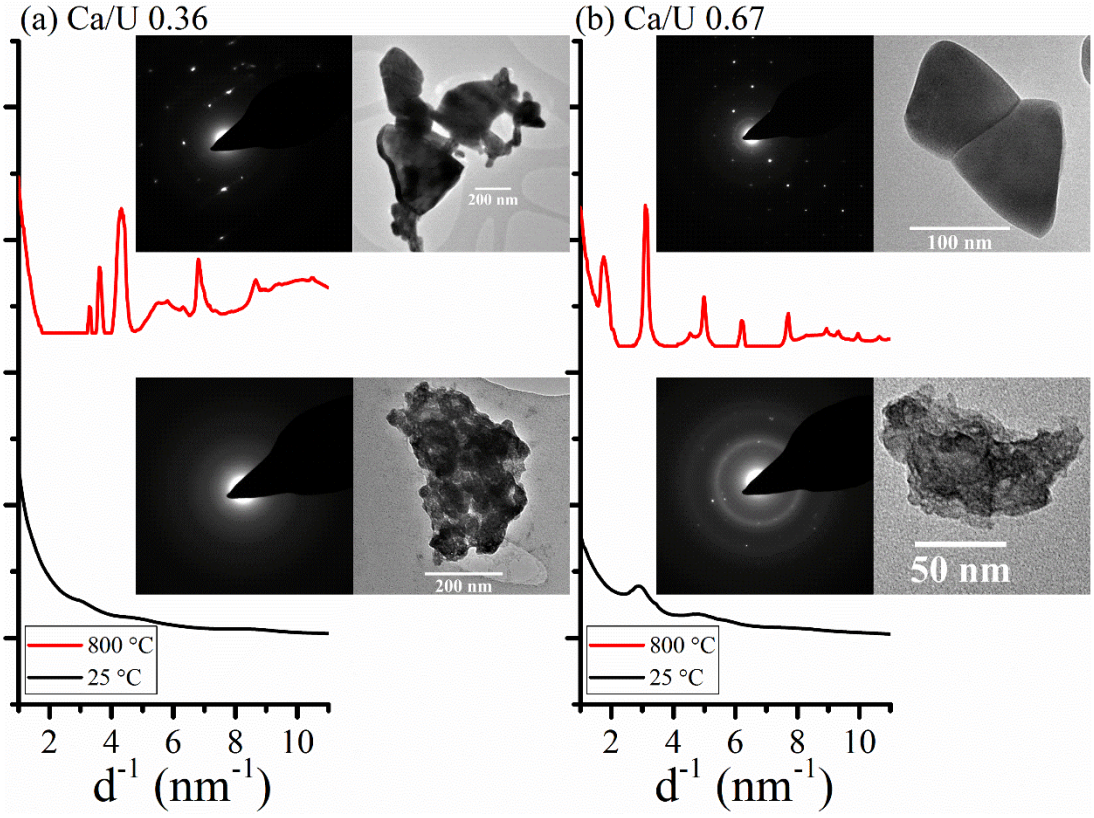

Figure C11 Radial intensity profiles for particles with Ca/U stoichiometry of (a) 0.36; and (b) 0.67; before (25 °C) and after crystallisation (800 °C)

6. TGA-DSC-MS

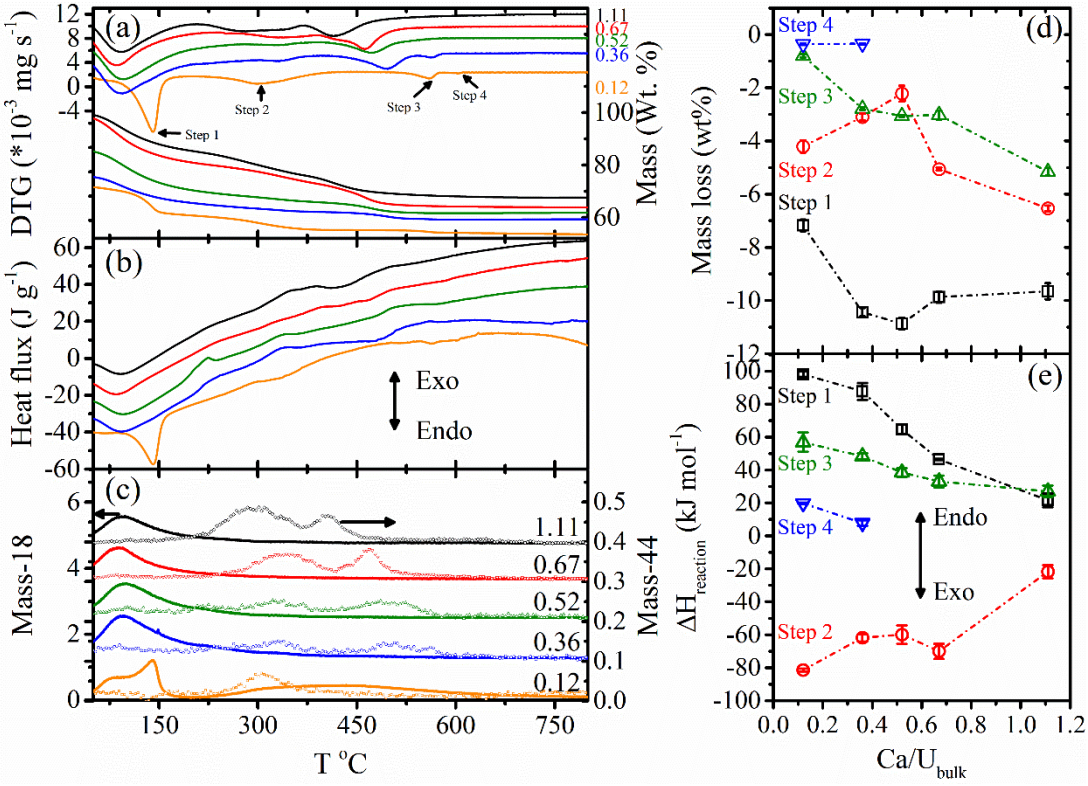

Figure C12 (a) TG (left) and derivative-TG (right) sample mass trends; (b) heat-flux through sample; (c) mass fragments 18, 32 and 44 g mol^{-1}; (d) stepwise mass-loss values; as functions of temperature. (e) Stepwise reaction enthalpies for decomposition steps 1-4 are calculated per mole of dominant gas product detected by mass spectrometry (c); as functions of bulk Ca/U-stoichiometry.

Table C3 Calculated weight loss for each decomposition step at Ca/U stoichiometry of 0.124, 0.36, 0.52, 0.67, 1.11. Values represent the average of 4 heating rates (8, 10, 12, 14 ° min^{-1}). Molar reaction enthalpies were calculated per mole of gaseous product produced. The TGA mass loss and dominant gaseous product from mass spectrometry were used. Reactant stoichiometry were assumed to be the phases used in EXAFS-models. i.e. The 1.11 Ca/U precipitate would be represented by $Ca[UO_2)_4O_3(OH)_4](H_2O)_2$, whereas 0.124 Ca/U would be based on Becquerelite stoichiometry.

Ca/U	Step 1	Step 2	Step 3	Step 4
Peak minima temperatures (°C)				
0.124	139.8	297.3	533	605.1
0.36	94.4	332.2	495.6	563.4
0.52	94.3	329.9	473.9	
0.67	85.1	329.9	460.2	
1.11	92.1	277.5	415.2	
TGA stepwise mass-loss (mg)				
0.124	-0.72 ±0.1	-0.47 ±0.08	-0.08 ±0.01	-0.05 ±0.02
0.36	-1.97 ±0.5	-0.58 ±0.1	-0.5 ±0.1	-0.06 ±0.02

0.52	-1.54 ±0.2	-0.32 ±0.1	-0.43 ±0.07	
0.67	-2.01 ±0.3	-1.03 ±0.2	-0.61 ±0.07	
1.11	-0.84 ±0.1	-0.57 ±0.08	-0.45 ±0.06	
TGA stepwise mass-loss (Wt.%)				
0.124	-7.18 ±0.2	-4.21 ±0.2	-0.80 ±0.06	-0.47 ±0.01
0.36	-10.44 ±0.2	-3.10 ±0.1	-2.78 ±0.05	-0.34 ±0.02
0.52	-10.87 ±0.2	-2.22 ±0.3	-3.06 ±0.04	
0.67	-9.87 ±0.2	-5.06 ±0.05	-3.02 ±0.1	
1.11	-9.65 ±0.3	-6.54 ±0.1	-5.16 ±0.1	
DSC $\Delta H_{reaction}$ (kJ $mol_{gaseous\ product}^{-1}$)				
0.124	32.68 ±2	-77.58 ±5	296.3 ±5	98 ±1.5
0.36	28.55 ±1	-53.48 ±6	153.97 ±2	49 ±12
0.52	24.84 ±6	-28.87 ±4	53.74 ±4	
0.67	28.83 ±2	-31.75 ±5	39.02 ±4	
1.11	23.27 ±4	-17.69 ±4	70.20 ±3	
DSC $\Delta H_{reaction}$ (kJ $mol_{reactant}^{-1}$)				
0.124	98.18 ±2	-81.41 ±1	56.85 ±6	19.83 ±0.4
0.36	87.82 ±5	-61.82 ±2	48.37 ±2	7.82 ±2
0.52	64.58 ±3	-59.99 ±6	38.52 ±3	
0.67	46.46 ±0.3	-70.07 ±5	33.07 ±4	
1.11	21.60 ±4	-21.69 ±4	27.02 ±4	

7. XANES

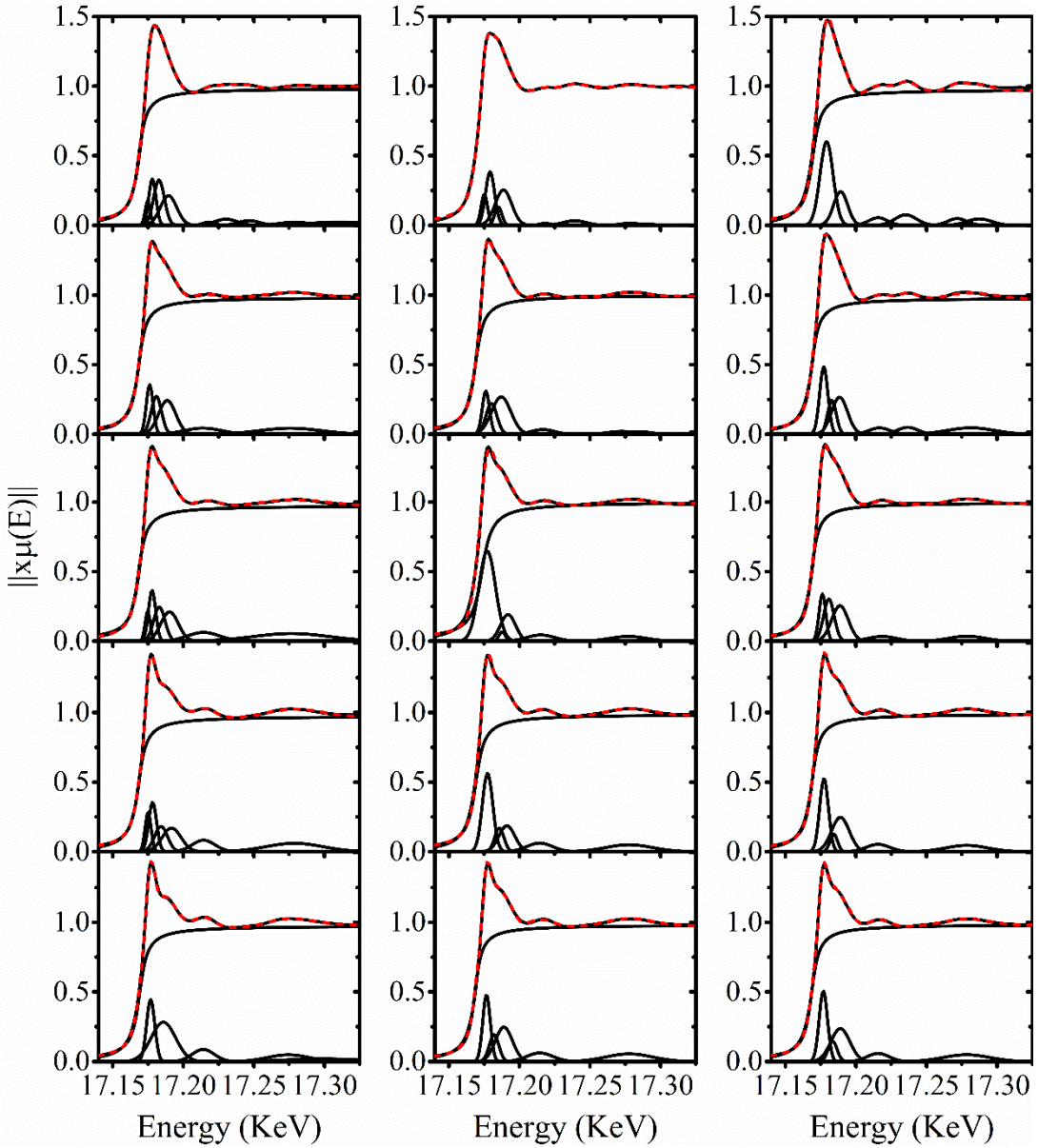

Figure C13 Fitted peaks from Arctan and Gaussian contributions in solid black below experimental data. Dashed red line is the fitted data. Columns left to right are Ca/U 0.124, 0.52, and 1.11 respectively. Rows from bottom to top are in order of increasing calcination temperature precipitate, 200, 300, 400, and 800 °C.

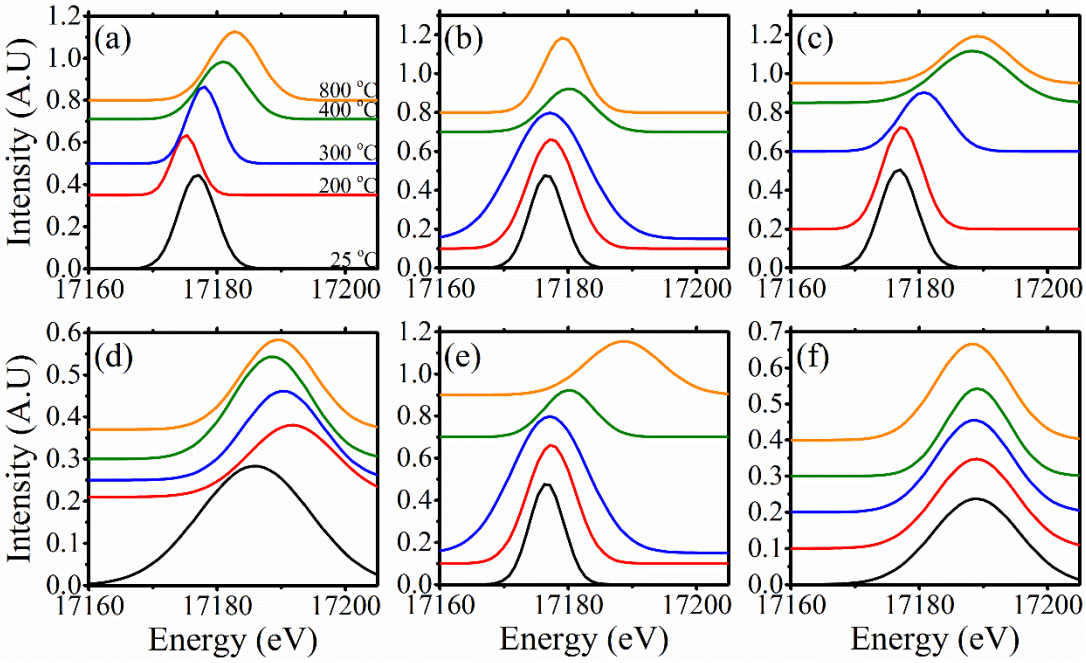

Figure C14 (a-c) Isolated Gaussian peaks from Figure C13 for the shoulder (feature B) contribution in sample spectra 0.124, 0.52, 1.11 respectively; (d-f) Gaussian peaks for feature (C), representing equatorial multiple scattering contributions.

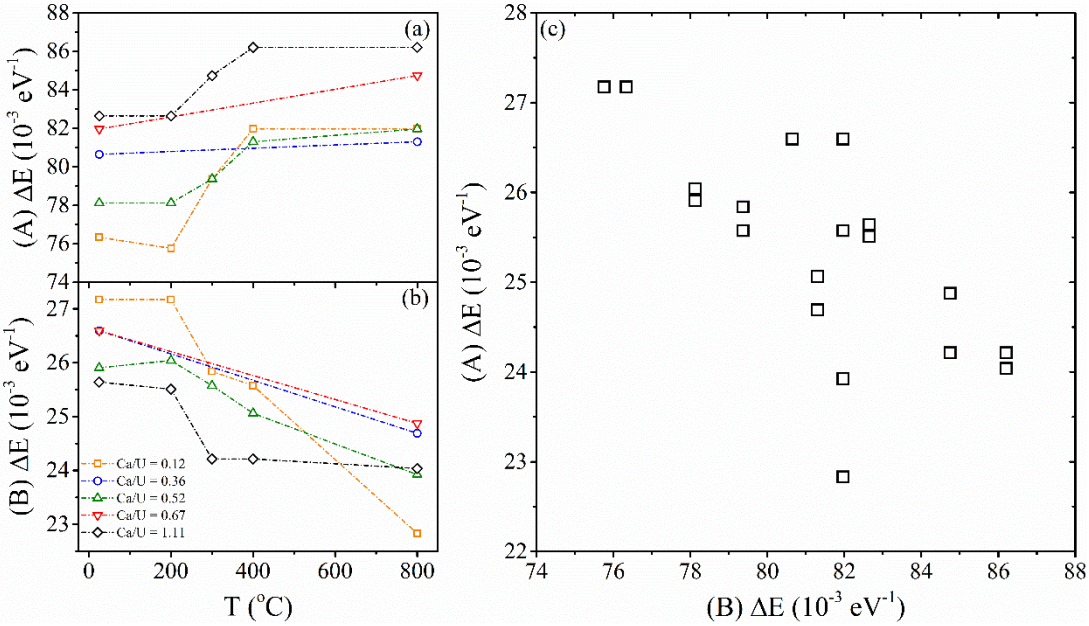

Figure C15 Relative energy values of (a) shoulder feature B (E_A-E_B); and (b) peak feature C; as functions of increasing temperature. (c) Plot of ΔE^{-1} values of features A and B.

8. EXAFS

a. K-test

The contribution to the EXAFS signal by scattering bodies is sensitive to atomic number (Z) due to the backscattering sensitivity factor $F_{eff}(k_i)$ term in the EXAFS equation, where a heavier element (U) scatters more than a lighter one (Ca). Therefore, the k-test [20, 21] (Figure C16) was performed on relatively crystallised sample spectra (400 – 800 °C) in both k (Figure C16b) and R-space (Figure C16a) to approximate the identities of scattering elements[1]. Briefly, the spectra in k-weights between 1 – 3 were aligned and normalised relative to the first scattering contribution at ~1.8 Å (~3.9 $Å^{-1}$), usually belonging to the first U-O coordination sphere in uranyl(VI) compounds. The scattering contributions at ~3.3 Å exhibit a larger k-dependency compared to the first CN-shell, whilst that at ~3.8 Å is significantly larger. The CN-shell order U-O, U-Ca, and U-U (Figure 6.12b), was true for the majority of crystalline samples, whilst the Ca and U shells were switched in hydrous or poorly-ordered intermediates (Figure 6.12d).

[1] Clear apparent U-U peaks (~3.5-4.5 Å). Only the 400 and 800 ^{o}C samples with Ca/U ratio between 0.12-1.11 (graph a), top to bottom respectively) had strong enough U-U and U-Ca contributions to compare.

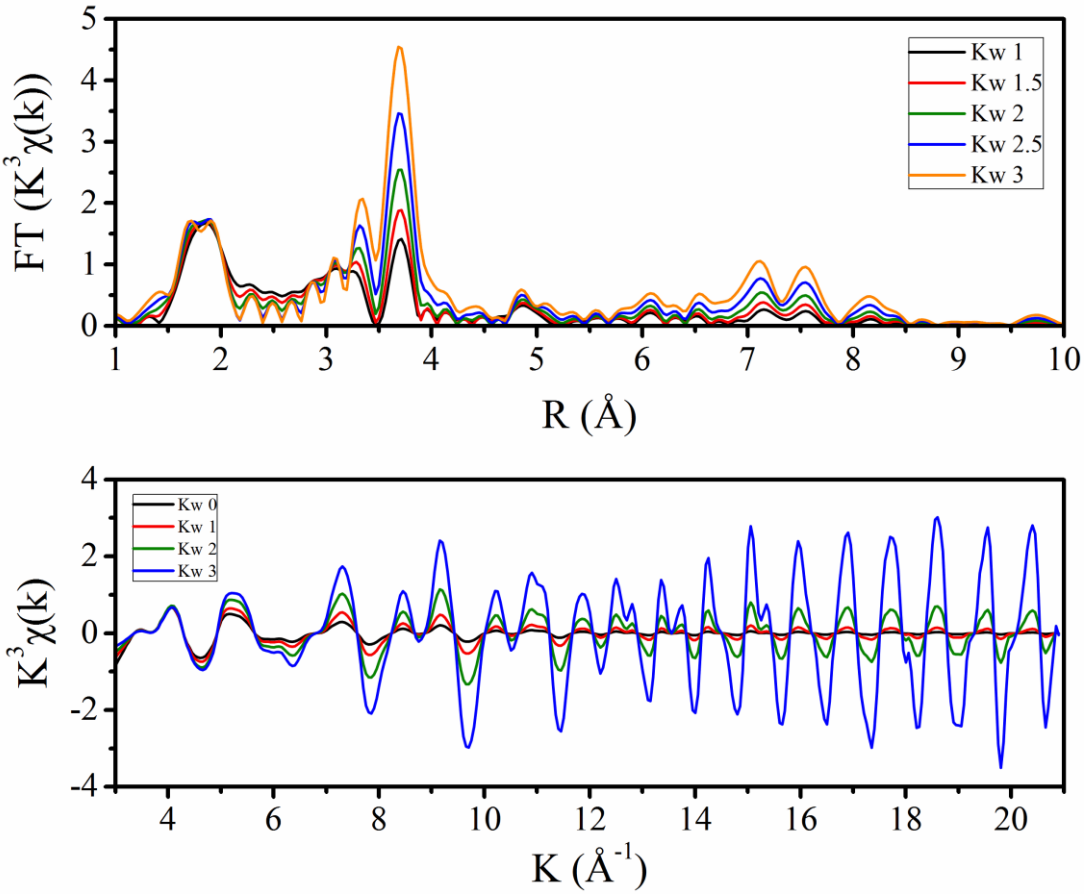

Figure C16 Typical K-test comparison, where spectral intensity is normalised at the first scattering contribution (~1.8 Å), and subsequent peaks in R and K-space are compared for relative increases in scattering contribution. i.e. Larger spread signifies heavier scatterers.

b. Fitting outputs

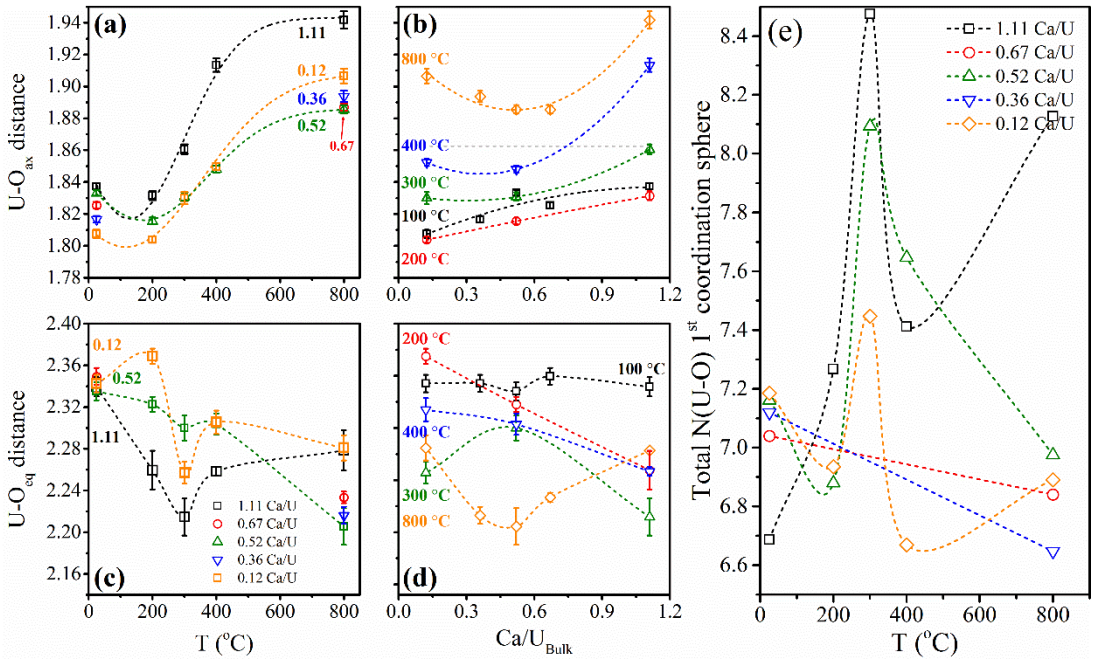

Figure C17

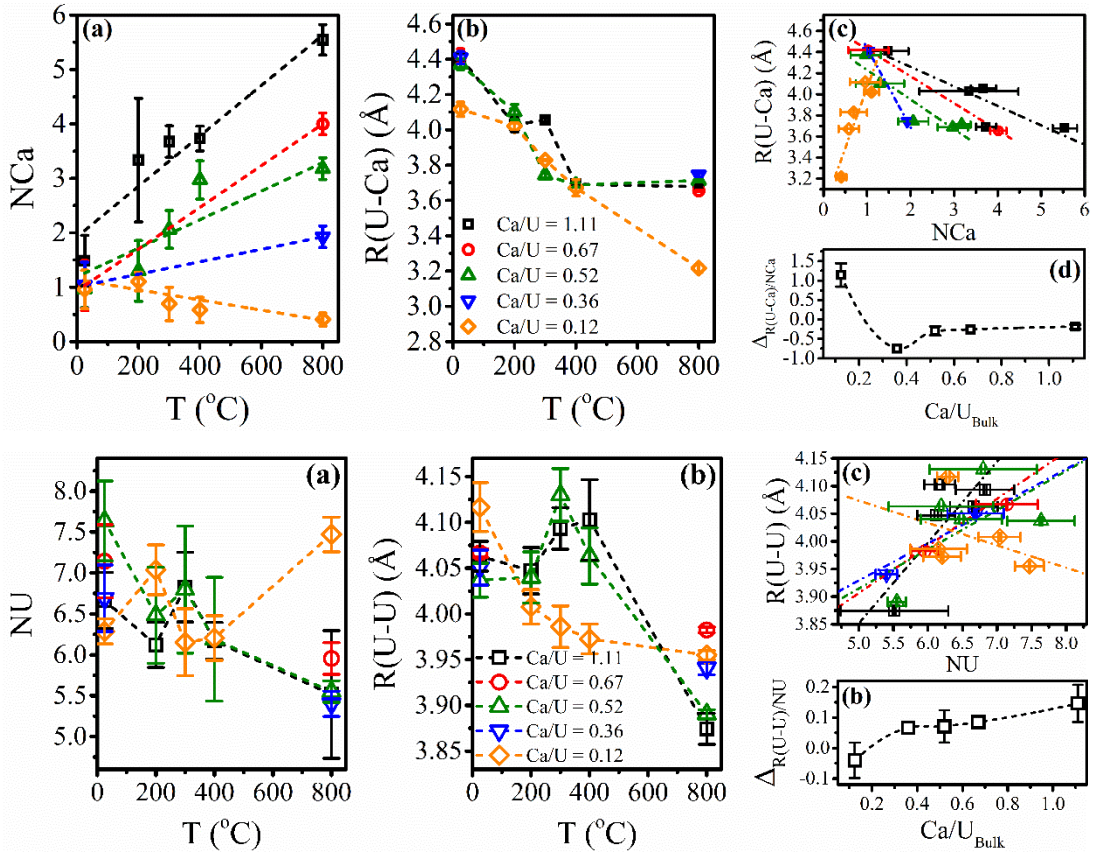

Figure C18 Additional plots exhibiting path degeneracy and U-Ca (upper) or U-U (lower) path lengths. Panels c, d, compare pathlength and its sensitivity to the U-Ca degeneracy or Ca/U ratio respectively. i.e. The U-Ca pathlength is most perturbed between 0.36 – 0.124 bulk Ca/U, whereas the U-U pathlength becomes more perturbed as a function of increasing Ca/U

Table C4 EXAFS modelling output parameters for 1.11 Ca/U samples

Ca/U 1.11											
Path		**N**	**$S0^2$**	**σ^2**	**ΔR**	**R_{eff}**	**R**	**Enot**	**err**	**χ^2**	**R**
25											
O7.1		2(*)	1.70	0.0024(2)	0.02(2)	1.82	1.84	2.44	0.17	234.306	0.010
O14.1		2.01(5)	1.71	0.004(7)	-0.03(6)	2.28	2.25	2.44	0.17		
O15.1		2.7(**)	2.27	0.012(2)	-0.06(6)	2.46	2.41	2.44	0.17		
U4.1		2.2(1)	1.86	0.0057(6)	-0.05(7)	3.74	3.69	-0.44	0.39		
O7.1	O9.1	2(*)	**0.85**	0.0024(0)	0.02	3.68	3.69	2.44	0.17		
O7.1	O9.1	2(*)	**0.85**	0.0024(0)	0.02)	3.68	3.69	2.44	0.17		
O9.1	O9.1	1(*)	**0.85**	0.0096(0)	0.06	3.71	3.78	2.44	0.17		
U2.1		1.6(2)	1.39	0.0054(8)	0.01(1)	3.84	3.85	-0.44	0.39		
Ca1.2		1.5(5)	1.26	0.009(4)	0.18(3)	4.23	4.41	-0.44	0.39		
U2.3		2.9(***)	2.42	0.016(5)	0.07(3)	4.58	4.65	-0.44	0.39		
200											
O7.1		2(*)	1.80	0.0033(3)	0.01(3)	1.82	1.83	3.55	0.20	80.893	0.019
O2.1		2.05(5)	1.85	0.002(1)	-0.017(7)	2.21	2.20	3.55	0.20		
O13.1		2.1(7)	1.89	0.003(2)	-0.053(7)	2.37	2.32	3.55	0.20		
O13.1		1.12(**)	1.00	0.003(3)	-0.03(2)	2.49	2.46	3.55	0.20		
O10.1	O8.1	2(*)	**0.90**	0.0033(0)	0.01	3.62	3.63	3.55	0.20		
O10.1	O8.1	2(*)	**0.90**	0.0033(0)	0.01	3.62	3.63	3.55	0.20		
U4.1		0.9(1)	0.85	0.0036(8)	-0.07(1)	3.74	3.66	3.72	0.57		
U1.1		2.9(***)	2.63	0.01(2)	-0.01(2)	3.84	3.83	3.72	0.57		
Ca1.2		3(1)	3.00	0.025(7)	-0.2(4)	4.23	4.03	-5.39	1.82		
U1.3		2.3(4)	2.03	0.017(8)	0.06(5)	4.58	4.64	3.72	0.57		
300											
O11.1		2(*)	1.60	0.0026(3)	0.022(3)	1.84	1.86	2.44	0.16	159.530	0.012
O5.1		1.48(4)	1.19	0.003(2)	-0.02(1)	2.17	2.15	2.44	0.16		
O2.1		2.77(6)	2.21	0.002(1)	-0.006(7)	2.26	2.26	2.44	0.16		
O12.1		2.23(**)	1.78	0.006(2)	-0.009(9)	2.40	2.39	2.44	0.16		
O10.1	O8.1	2(*)	**0.80**	0.0026(0)	0.022	3.62	3.64	2.44	0.16		
O10.1	O8.1	2(*)	**0.80**	0.0026(0)	0.022	3.62	3.64	2.44	0.16		
U4.1		2.6(2)	2.11	0.007(2)	0.02(1)	3.74	3.76	2.44	0.16		
U1.1		1.6(2)	1.25	0.004(1)	0.032(9)	3.84	3.87	0.26	0.29		
Ca1.2		3.7(3)	2.94	0.008(2)	-0.11(1)	4.16	4.06	-4.04	0.41		
U1.3		2.6(9)	2.11	0.019(8)	0.07(5)	4.58	4.65	2.44	0.16		
400											
O11.1		2(4)	1.80	0.0043(5)	0.075(4)	1.84	1.91	1.88	0.28	211.808	0.017
O2.1		5.4(*)	4.87	0.0068(4)	-0.003(3)	2.26	2.26	1.88	0.28		
Ca1.1		3.7(2)	3.36	0.0058(7)	-0.175(6)	3.87	3.69	6.21	0.41		

O10.1	O8.1	2(0)	**0.90**	0.0043(0)	0.075(0)	3.62	3.69	1.88	0.28		
O10.1	O8.1	2(0)	**0.90**	0.0043(0)	0.075(0)	3.62	3.69	1.88	0.28		
U4.1		2.6(***)	2.37	0.007(2)	0.04(1)	3.74	3.78	-1.48	0.39		
U1.1		1.9(1)	1.71	0.0023(4)	0.029(6)	3.84	3.87	-1.48	0.39		
U1.3		1.6(3)	1.47	0.02(2)	0.08(9)	4.58	4.66	-1.48	0.39		
800											
O1.1		2(0)	1.60	0.0025(5)	-0.022(5)	1.96	1.94	4.21	0.17	212.179	0.016
O2.1		6.1(1)	4.90	0.0033(3)	-0.019(2)	2.30	2.28	4.21	0.17		
O1.1	O2.1	12.3(0)	9.80	0.0041(0)	-0.031(1)	3.46	3.43	4.21	0.17		
Ca1.1		5.5(3)	4.44	0.0036(4)	-0.008(4)	3.69	3.68	4.21	0.17		
O1.1	O2.1	12.3(0)	9.80	0.0041(0)	-0.031(1)	3.80	3.77	4.21	0.17		
U1.1		5.5(2)	4.41	0.002(1)	-0.004(1)	3.88	3.87	4.21	0.17		
O1.2		15(1)	11.73	0.006(1)	0.03(1)	4.35	4.37	4.21	0.17		
Ca1.2		4(2)	3.30	0.0019(8)	-0.02(1)	5.35	5.33	4.21	0.17		
U1.2		5(1)	4.10	0.0041(7)	0(1)	6.27	6.27	4.21	0.17		
U1.3		4(8)	3.25	0.002(1)	0.05(2)	6.72	6.77	4.21	0.17		

Table C5 EXAFS modelling output parameters for 0.67 Ca/U samples

Ca/U 0.67											
Path		**N**	**$S0^2$**	**σ^2**	**ΔR**	**R_{eff}**	**R**	**Enot**	**err**	**χ^2**	**R**
25											
O7.1		2(0)	1.80	0.0024(2)	0.004(2)	1.82	1.83	2.04	0.18	196.805	0.012
O14.1		3.27(8)	2.95	0.0072(6)	-0.001(4)	2.28	2.28	2.04	0.18		
O15.1		1.77(9)	1.59	0.005(1)	0.014(7)	2.46	2.48	2.04	0.18		
O10.1	O8.1	2(0)	**0.90**	0.0024(0)	0.0038(0)	3.62	3.62	2.04	0.18		
O10.1	O8.1	2(0)	**0.90**	0.0024(0)	0.0038(0)	3.62	3.62	2.04	0.18		
O8.1	O8.1	1(0)	**0.90**	0.0096(0)	0.0152(0)	3.67	3.69	2.04	0.18		
U4.1		2.1(2)	1.90	0.006(7)	0.026(9)	3.67	3.70	0.70	0.38		
U2.1		2.1(2)	1.89	0.0059(9)	0.02(1)	3.84	3.86	0.70	0.38		
Ca1.2		1(5)	0.93	0.008(4)	0.25(4)	4.16	4.42	-1.11	1.89		
U2.3		2.9(9)	2.64	0.017(7)	0.06(4)	4.58	4.64	0.70	0.38		
800											
O1.1		2(9)	$N\sigma^2$	0.0015(2)	-0.013(2)	1.90	1.89				
O2.1		2.85(8)	$N\sigma^2$	0.0014(5)	0.132(4	2.05	2.18				
O2.1		1.85(2)	$N\sigma^2$	0.0015(7)	0.030(7)	2.23	2.26				
Ca2.1		4.5(2)	$N\sigma^2$	0.0033(3)	0.022(3)	3.63	3.66				
U2.1		3.0(1)	$N\sigma^2$	0.0020(2)	0.066(4)	3.77	3.84		0.1		
U1.1		2.9(3)	$N\sigma^2$	0.006(1)	-0.04(1)	3.93	3.89				
U2.4		1.0(1)	$N\sigma^2$	0.0014(3)	0.029(5)	4.20	4.23				
U1.2	O4.2	4	0.7	0.00618	-0.035	5.09	5.05				
O3.2	O1.4	4	0.7	0.0037	0.075	5.16	5.24				
U1.4	O5.2	4	0.7	0.00137	0.028	5.25	5.28	4.6			

Ca2.3		5(1)	$N\sigma^2$	0.007(1)	-0.10(1)	5.43	5.32				

Table C6 EXAFS modelling output parameters for 0.52 Ca/U samples

Ca/U 0.52											
Path		**N**	**$S0^2$**	**σ^2**	**ΔR**	**R_{eff}**	**R**	**Enot**	**err**	**χ^2**	**R**
25											
O7.1		2(0)	0.90	0.0026(2)	0.012(2)	1.82	1.83	0.59	0.18	382.425	0.009
O14.1		3.32(0.8)	2.99	0.0067(6)	-0.012(4)	2.28	2.27	0.59	0.18		
O15.1		1.84(1)	1.65	0.007(1)	-0.009(8)	2.46	2.45	0.59	0.18		
O10.1	O8.1	2(0)	**0.90**	0.0026(0)	0.012(0)	3.62	3.63	0.59	0.18		
O10.1	O8.1	2(0)	**0.90**	0.0026(0)	0.012(0)	3.62	3.63	0.59	0.18		
U4.1		1.2(1)	1.07	0.005(8)	-0.01(8)	3.67	3.66	-0.88	0.37		
O8.1	O8.1	1(0)	**0.90**	0.0102(0)	0.046(0)	3.67	3.72	0.59	0.18		
U2.1		3.3(3)	2.98	0.011(2)	-0.04(1)	3.84	3.80	-0.88	0.37		
Ca1.2		1(3)	0.87	0.006(3)	0.21(3)	4.16	4.37	-4.04	1.73		
U2.3		3.1(1)	2.83	0.019(6)	0.06(4)	4.58	4.65	-0.88	0.37		
200											
O7.1		2(0)	1.60	0.0025(3)	-0.006(2)	1.82	1.82	3.52	0.15	146.811	0.009
O2.1		2.5(1)	1.99	0.0026(5)	-0.019(4)	2.26	2.24	3.52	0.15		
O15.1		2.4(1)	1.92	0.007(1)	-0.058(6)	2.46	2.41	3.52	0.15		
O10.1	O8.1	2(0)	**0.80**	0.00247(0)	-0.006(0)	3.62	3.61	3.52	0.15		
O10.1	O8.1	2(0)	**0.80**	0.00247(0)	-0.006(0)	3.62	3.61	3.52	0.15		
O8.1	O8.1	1(0)	**0.80**	0.00988(0)	-0.024(0)	3.67	3.65	3.52	0.15		
U4.1		0.8(2)	0.67	0.003(1)	-0.01(1)	3.67	3.66	3.52	0.15		
U2.1		2.9(3)	2.33	0.009(3)	-0.02(2)	3.84	3.82	3.52	0.15		
Ca1.2		1.3(6)	1.04	0.01(8)	-0.13(4)	4.23	4.10	3.52	0.15		
U2.3		3(1)	2.19	0.02(1)	0.05(5)	4.58	4.63	3.52	0.15		
300											
O11.1		2(0)	1.40	0.0028(3)	-0.008(3)	1.84	1.83	-0.22	0.21	42.915	0.017
O2.1		4.95(1.2)	3.47	0.0077(5)	-0.002(3)	2.26	2.26	-0.22	0.21		
O15.1		1.14(1.2)	0.80	0.003(1)	0.01(1)	2.46	2.48	-0.22	0.21		
O10.1	O8.1	2(0)	**0.70**	0.00277(0)	-0.008(0)	3.62	3.61	-0.22	0.21		
O10.1	O8.1	6(0)	**0.70**	0.00277(0)	-0.008(0)	3.62	3.61	-0.22	0.21		
O8.1	O8.1	2(0)	**0.70**	0.01108(0)	-0.031(0)	3.67	3.64	-0.22	0.21		
U3.1		2.12(3.5)	1.49	0.01(2)	0.06(2)	3.67	3.73	2.22	0.81		
Ca1.1		2.06(3.5)	1.44	0.011(3)	-0.08(2)	3.83	3.74	2.22	0.81		
U2.1		0.89(1.9)	0.62	0.004(1)	0.08(1)	3.84	3.92	2.22	0.81		
U2.3		4(2)	2.65	0.02(1)	0.16(6)	4.58	4.74	2.22	0.81		
400											
O11.1		2(0)	1.40	0.0031(3)	0.009(2)	1.84	1.85	-0.36	0.19	73.737	0.012
O2.1		4.56(0)	3.19	0.0066(4)	0.003(2)	2.26	2.27	-0.36	0.19		
O12.1		1.09(0.5)	0.76	0.003(1)	0.064(1)	2.40	2.46	-0.36	0.19		
O10.1	O8.1	2(0)	**0.70**	0.00311(1)	0.009(0)	3.62	3.63	-0.36	0.19		
O10.1	O8.1	2(0)	**0.70**	0.00311(1)	0.009(0)	3.62	3.63	-0.36	0.19		
Ca1.1		3(4)	2.08	0.015(2)	-0.21(1)	3.87	3.66	-1.86	0.31		
U4.1		2.4(0)	1.68	0.011(2)	-0.057(1)	3.74	3.68	-1.86	0.31		
U1.1		1.4(2)	1.01	0.005(9)	0.023(1)	3.84	3.86	-1.86	0.31		

U1.3		2(10)	1.65	0.02(1)	0.066(7)	4.58	4.65	-1.86	0.31		
800 (Ca)$Na_2U_2O_7$											
O1.1		2(0)	1.40	0.0022(3)	-0.014(3)	1.90	1.89	3.03	0.34		
O7.1		1.81(0.7)	1.27	0.0012(6)	0.076(5)	2.09	2.16	3.03	0.34		
O3.1		1.98(0.8)	1.39	0.001(6)	-0.003(0)	2.27	2.26	3.03	0.34		
O		1.2(4)	0.83	0.024(7)	0.06(4)	2.51	2.58	3.03	0.34		
U22		1.9(2)	1.33	0.004(9)	-0.245(7)	3.94	3.69	-6.52	0.33		
Ca1.1		3.2(2)	2.22	0.0064(8)	-0.036(6)	3.75	3.71	4.75	0.41	248.760	0.017
U11		1.9(1)	1.32	0.0025(5)	0.012(0)	3.77	3.79	-6.52	0.33		
U33		1.8(1)	1.24	0.0014(2)	0.039(0)	4.16	4.20	-6.52	0.33		
O3.2	O1.4	2(0)	**0.70**	0.0015(0)	-0.005(0)	5.16	5.16	3.03	0.34		
U1.1	O1.5	2(1)	**0.70**	0.0045(0)	0.005(0)	5.59	5.60	-6.52	0.33		
Ca1.4		2.2(6)	1.55	0.001(1)	0.26(2)	5.67	5.93	4.75	0.41		
800 (Ca)U_2O_5											
O6.1		2	0.778	0.0026(3)	-0.053(3)	1.93	1.88				
O8.1		2	0.778	0.0019(8)	0.000(5)	2.14	2.14				
O2.1		2	0.778	0.0013(7)	0.001(5)	2.24	2.24				
O13.1		1	0.778	0.009(4)	-0.04(2)	2.64	2.60				
O12.1	O5.1	2	0.778			3.53	3.54				
U1.1		1	0.778	0.0015(2)	0.09(2)	3.54	3.62				
Ca1.1		3	0.778	0.0058(1)	0.085(7)	3.54	3.63				
U2.1		3	0.778	0.0051(5)	-0.034(6)	3.81	3.77	0.15	0.02	395.161	0.020
O8.1	O14.1	2	0.778			3.98	3.94				
O8.1	O12.1	2	0.778			4.02	3.95				
U4.2		2	0.778	0.0014(2)	-0.010(5)	4.20	4.19				
O8.1	U4.2	2	0.778			4.24	4.23				
U1.7		3	0.778	0.006(2)	-0.05(2)	5.83	5.78				
U2.6		1	0.778	0.003(3)	0.02(4)	5.96	5.98				

Table C7 EXAFS modelling output parameters for 0.36 Ca/U samples

Ca/U 0.36											
Path		**N**	**$S0^2$**	**σ^2**	**ΔR**	**R_{eff}**	**R**	**Enot**	**err**	**χ^2**	**R**
25											
O7.1		2(0)	1.80	0.0027(2)	-0.005(2)	1.82	1.82	3.00	0.19		
O14.1		3.4(1)	3.02	0.0074(6)	-0.005(4)	2.28	2.28	3.00	0.19		
O15.1		1.8(1)	1.59	0.005(1)	0.006(7)	2.46	2.47	3.00	0.19		
O10.1	O8.1	2(0)	**0.90**	0.00268(0)	-0.005(0)	3.62	3.61	3.00	0.19		
O10.1	O8.1	2(0)	**0.90**	0.00268(0)	-0.005(0)	3.62	3.61	3.00	0.19		
O8.1	O8.1	1(0)	**0.90**	0.01072(0)	-0.02(0)	3.67	3.65	3.00	0.19	335.101	0.011
U4.1		2.1(3)	1.92	0.008(1)	0.016(1)	3.67	3.69	1.96	0.40		
U2.1		2.1(2)	1.89	0.006(8)	0.007(9)	3.84	3.85	1.96	0.40		
Ca1.2		1.0(4)	0.94	0.006(4)	0.244(3)	4.16	4.41	0.92	1.81		
U2.3		2.5(7)	2.22	0.013(5)	0.036(4)	4.58	4.62	1.96	0.40		
800											

		2	1.60	0.0036(3)	-0.01(4)	1.90	1.89	6.75	0.18		
		0.82(7)	0.65	0.003(2)	-0.16(1)	2.27	2.11	6.75	0.18		
		2.95(6)	2.36	0.005(1)	0.075(6)	2.16	2.24	6.75	0.18		
		0.9(3)	0.70	0.03(1)	0.11(6)	2.35	2.46	6.75	0.18		
		1.28(8)	1.02	0.0024(2)	-0.081(4)	3.77	3.69	6.75	0.18		
		1.9(2)	1.54	0.017(2)	-0.05(1)	3.80	3.74	6.75	0.18		
		1.3(1)	1.03	0.0024(2)	-0.047(0)	3.88	3.83	6.75	0.18		
		1.71(9)	1.37	0.0022(5)	0.082(8)	3.97	4.05	6.75	0.18	159.508	0.013
U4.1		4(0)	**0.80**	0.0024(0)	-0.047(0)	4.19	4.14	6.75	0.18		
U4.1	O4.1	2(0)	**0.80**	0.0036(0)	-0.01(0)	4.19	4.18	6.75	0.18		
		1.4(4)	1.14	0.009(2)	0.02(1)	4.17	4.19	6.75	0.18		
U5.2		2(0)	**0.80**	0.009(0)	0.017(0)	4.40	4.42	6.75	0.18		
U5.2	O14.1	1(0)	**0.80**	0.009(0)	0.017(0)	4.41	4.42	6.75	0.18		
		5(1)	3.66	0.012(3)	-0.04(3)	5.51	5.47	6.75	0.18		
		3.6(6)	2.90	0.0051(7)	0.061(9)	5.75	5.81	6.75	0.18		

Table C8 EXAFS modelling output parameters for 0.12(4) Ca/U samples

Ca/U 0.12												
Path			**N**	**S0^2**	**σ^2**	**ΔR**	**R$_{eff}$**	**R**	**Enot**	**err**	**χ^2**	**R**
25												
O1.1			2(0)	1.80	0.0029(3)	0.004(3)	1.80	1.81	1.00	0.21		
O14.1			2.6(1)	2.34	0.0056(8)	0.005(5)	2.24	2.24	1.00	0.21		
O21.1			2.59(0)	2.33	0.006(1)	0.021(7)	2.42	2.44	1.00	0.21		
O2.1	O1.1		2(0)	**0.90**	0.0116(0)	0.015(0)	3.57	3.59	1.00	0.21		
O1.1	O1.1		1(0)	**0.90**	0.0116(0)	0.015(0)	3.61	3.62	1.00	0.21	110.61	0.02
U5.2			1.2(1)	1.06	0.002(3)	-0.03(3)	3.86	3.82	0.51	0.34		
U5.1			1.7(2)	1.49	0.003(3)	-0.02(2)	3.92	3.89	0.51	0.34		
Ca1.1			1(4)	0.86	0.006(5)	0.02(4)	4.10	4.12	0.51	0.34		
U2.2			3.5(0)	3.11	0.011(3)	-0.01(2)	4.64	4.63	0.51	0.34		
200												
O7.1			2(0)	1.80	0.0034(2)	-0.018(2)	1.82	1.80	0.59	0.15		
O2.1			1.99(7)	1.79	0.0047(7)	-0.005(5)	2.26	2.26	0.59	0.15		
O15.1			2.9(1)	2.65	0.008(1)	-0.019(5)	2.46	2.44	0.59	0.15		
O10.1	O8.1		2(0)	**0.90**	0.0034(0)	-0.018(0)	3.62	3.60	0.59	0.15		
O8.1	O8.1		2(0)	**0.90**	0.0134(0)	-0.071(0)	3.67	3.60	0.59	0.15		
O10.1	O8.1		2(0)	**0.90**	0.0034(0)	-0.018(0)	3.62	3.60	0.59	0.15	263.11	0.01
U4.1			1.1(1)	0.99	0.0041(8)	-0.047(7)	3.67	3.62	-3.97	0.27		
U2.1			4.7(3)	4.25	0.009(1)	-0.07(1)	3.84	3.77	-3.97	0.27		
Ca1.1			1.1(2)	0.99	0.002(1)	0.15(2)	3.87	4.02	-3.97	0.27		
O6.1	Ca1.2		2(0)	**0.90**	0.0042(0)	0.14(0)	4.24	4.38	-3.97	0.27		
U1.3			1.2(5)	1.10	0.009(5)	0.05(4)	4.58	4.63	-3.97	0.27		
300												
O11.1			2(0)	1.80	0.0055(4)	-0.009(4)	1.84	1.83	1.75	0.18		
O1.1			1.11(6)	1.00	0.003(1)	-0.107(8)	2.21	2.10	1.75	0.18		
O5.1			2.06(5)	1.86	0.002(1)	-0.043(5)	2.27	2.23	1.75	0.18	135.61	0.02
O12.1			2.27(*)	2.04	0.005(1)	-0.037(6)	2.40	2.36	1.75	0.18		

U3.1			1.9(3)	1.69	0.008(3)	-0.032(2)	3.62	3.59	1.40	0.74		
O10.1	O8.1		5(0)	**0.90**	0.0055(0)	-0.009(0)	3.62	3.61	1.75	0.18		
O10.1	O8.1		5(0)	**0.90**	0.0055(0)	-0.009(0)	3.62	3.61	1.75	0.18		
O8.1	O8.1		1(0)	**0.90**	0.0218(0)	-0.034(0)	3.67	3.64	1.75	0.18		
U4.1			2(3)	1.83	0.013(5)	0.02(2)	3.74	3.75	1.40	0.74		
Ca1.1			0.7(3)	0.62	0.008(5)	0(4)	3.83	3.83	1.42	3.00		
U2.3			2.2(7)	2.02	0.014(1)	0.03(3)	4.58	4.61	1.40	0.74		
400												
U3.1			0.3(1)	0.250	0.0032(1)	-0.07(2)	3.6707	3.60553	-0.007	0.19		
Ca1.1			0.8(3)	0.628	0.0139(7)	-0.12(4)	3.8269	3.70581	-0.007	0.19		
U1.3			1.0(4)	0.829	0.0083(3)	0.01(3)	4.5815	4.59232	-0.007	0.19		
O9.1			1.77(3)	1.416	0.0044(3)	-0.007(3)	1.8564	1.84957	3.954	0.31		
O5.1			1.83(1)	1.466	0.0064(1)	-0.04(1)	2.268	2.23113	3.954	0.19	287.82	0.017
O10.1	O8.1			0.8			3.618	3.61117	3.954	0.19		
O10.1	O8.1			0.8			3.6182	3.61137	3.954	0.31		
O15.1			3.1(3)	2.454	0.0150(3)	-0.083(9)	2.4629	2.37997	3.954	0.31		
U2.1			5.0(2)	4.012	0.0205(2)	-0.0034(9)	3.7185	3.71512	-0.007	0.31		
800												
O2.1			2.1(1)	1.668	0.0054(7)	-0.173(6)	2.08	1.91	0.9	0.2		
O3.1			2.01(7)	1.605	0.0020(5)	-0.042(4)	2.15	2.11	0.9	0.2		
O4.1			2.1(1)	1.642	0.0020(5)	-0.028(5)	2.27	2.24	0.9	0.2		
O3.2			0.7(2)	0.598	0.005(3)	0.11(2)	2.74	2.85	0.9	0.2		
Ca1.1			0.4(1)	0.342	0.005(3)	0.06(2)	3.17	3.23	1.3	0.2		
O2.1	O4.1		12	0.8	0.00409(1)	-0.0569(1)	3.70	3.64	0.9	0.2		
U2.1			3.3(3)	2.626	0.011(1)	-0.038(1)	3.76	3.73	1.3	0.2	186.78	0.02
O2.1	O1.1		8	0.8	0.00409(1)	-0.0569(1)	3.95	3.89	0.9	0.2		
U1.1			4.3(1)	3.428	0.00186(9)	0.016(9)	4.17	4.19	1.3	0.2		
O2.1	U1.1		4	0.8	0.00373(1)	0.0320(1)	4.16	4.19	0.9	0.2		
O2.1	U1.1	O2.1	2	0.8	0.00373(1)	0.0320(1)	4.16	4.20	0.9	0.2		
U2.5			4(2)	3.27	0.016(7)	-0.13(5)	5.70	5.57	1.3	0.2		
U2.6			1.2(6)	0.932	0.004(2)	-0.10(3)	5.90	5.80	1.3	0.2		
800 - No Ca												
O2.1			2.76	2.21	0.0079(8)	-0.171(7)	2.08	1.91	0.69	0.22		
O3.1			1.99	1.59	0.0019(5)	-0.046(5)	2.15	2.11	0.69	0.22		
O4.1			2.49	1.99	0.0028(6)	-0.028(5)	2.27	2.24	0.69	0.22		
O3.2			0.95	0.76	0.015(9)	0.192 (5)	2.74	2.93	0.69	0.22		
O2.1	O4.1		12.00	**0.80**	0.0057(0)	-0.055 (0)	3.70	3.65	0.69	0.22		
U2.1			3.14	2.51	0.011(1)	-0.036 (9)	3.76	3.73	0.69	0.22		
O2.1	O1.1		8.00	**0.80**	0.0057(0)	-0.055 (0)	3.95	3.89	0.69	0.22	258.22	0.02
U1.1			4.40	3.52	0.0019(1)	0.016(1)	4.17	4.19	1.07	0.25		
O2.1	U1.1		4.00	**0.80**	0.0038(0)	0.0324(0)	4.16	4.19	0.69	0.22		
O2.1	U1.1	O2.1	2.00	**0.80**	0.0038(0)	0.032 (0)	4.16	4.20	0.69	0.22		
U2.5			4.13	3.30	0.016(7)	-0.132 (5)	5.70	5.57	1.07	0.25		
U2.6			1.14	0.91	0.004(2)	-0.100 (3)	5.90	5.80	1.07	0.25		

9. XPS of $CaUO_4$

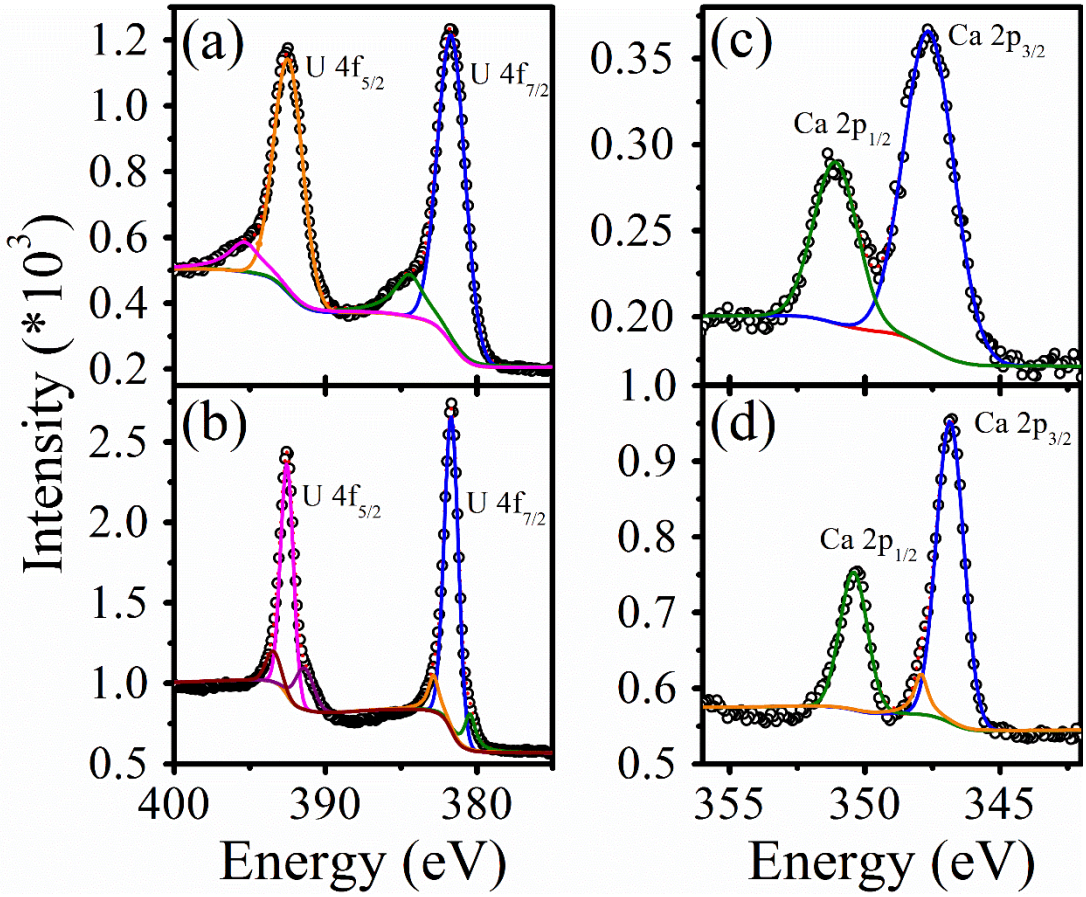

Figure C19 (a) precipitate U4f XPS, (b) 800degC sintered U4f XPS, (c) precipitate Ca2p XPS, (d) 800degC sintered Ca2p XPS

Table C9

	Binding energies (eV)		Literature coordination numbers	
	Precipitate	**Sintered**	**Bond**	**CN**
Ca $2p_{1/2}$	351.08	350.38	CN(Ca-O) $Ca(OH)_2$	6
Ca $2p_{3/2}$	347.68 (78)	346.88	CN(Ca-O) $CaUO_4$	8
ΔE	3.4	3.5	CN(Ca-Oxo) Becquerelite	3
			CN(Ca-OH_2) Becquerelite	4
U $4f_{5/2}$ (eV)	392.58	392.58		
U$4f_{7/2}$	381.68	381.68	CN(U-O) Becquerelite	7
ΔE (eV)	10.9	10.9	CN(U-O) $CaUO_4$	8

The BE value for U$4f_{7/2}$ for the sintered $CaUO_4$ reference is slightly higher than the expected 380.7 [22] -381.1 [23], signifying either some minor U(IV) character, possible due to the presence of oxygen vacancies or disorder in the crystal structure. Indeed many of the samples used in legacy XPS studies on the uranates are generated using the ceramic method involving several days of heat treatment under pure oxygen atmospheres; increasing the likelihood of the containing higher crystallite size distributions compared to the samples used here.

Whilst an increase in $U4f_{7/2}$ binding energy was expected upon crystallisation from the hydrous precipitate to the crystalline $CaUO_4$, this was not observed. Indeed the centroids of the fitted peaks were the same.

There was an evident reduction in the Ca2p binding energy upon crystallisation, signifying an increase in electron density towards the Ca^{2+} ion. So whilst there is an increase in the expected coordination number surrounding the calcium (from 6 in a $Ca(OH)_2$ environment or the hydrate-stabilised 3 Ca-oxo bonds in Becquerelite to the 8 Ca-O- bonds in $CaUO_4$), the average electron donor ability of the surrounding ligands has increased upon crystallising. Particle size may also be a contributing factor, but the literature appears to be mixed here. In some studies, increasing crystallite size reduces BE, in others the opposite, but normalising for increasing or decreasing oxygen content is rarely done. Making it difficult to account for this. Going from U(VI) hydroxyl hydrates to U(VI)-$O^{2-,}$ the difference in Lewis acidity of the equatorial ligands affects the binding energy of the U 4f electrons. i.e. if a more electrophilic ligand is present on the U(VI) centre, there is a decrease in covalency of the U-O bond. Electron density is moved towards the ligand, increasing the binding energy of the U4f photoelectrons. The maximum peak positions of the U $4f_{7/2}$ show little change between non-sintered and sintered samples. Therefore the main uranium bonding environment has changed little. However the satellite peak at 385eV is gone. Using the Chernyaev-Schelokov row for solution complexes, $O_2^{2-} \geq CO_3^{2-} \geq OH^- \geq F^- \geq \ldots\ldots \geq H_2O$, this is related to the electron donor ability of the ligand. Hydroxide donates 4.1 electrons compared to 6.7 for O^{2-} when shared between two U centres (p49, book). Therefore, the broad hump at 384.8, 395.6eV for U7/2 and U5/2 respectively may be due to uranyl(VI) hydroxides species. i.e. electron density for U-OH^- moieties lies closer to the OH^- as it is a poorer electron donor. Therefore the U 4f7/2 or 5/2 electron binding energy is increased.

Supplementary references

1. Huang, F., Zhang, H., and Banfield, J.F., *The Role of Oriented Attachment Crystal Growth in Hydrothermal Coarsening of Nanocrystalline Zns.* The Journal of Physical Chemistry B, 2003. **107**(38): p. 10470-10475.
2. Zhang, J., Lin, Z., Lan, Y., Ren, G., Chen, D., Huang, F., and Hong, M., *A Multistep Oriented Attachment Kinetics: Coarsening of Zns Nanoparticle in Concentrated Naoh.* Journal of the American Chemical Society, 2006. **128**(39): p. 12981-12987.
3. Kestin, J., Sokolov, M., and Wakeham, W.A., *Viscosity of Liquid Water in the Range− 8 C to 150 C.* Journal of Physical and Chemical Reference Data, 1978. **7**(3): p. 941-948.
4. Chernorukov, N.G., Nipruk, O.V., and Kostrova, E.L., *Synthesis and Study of Sodium Uranate $Na_2u_2o_7·6h_2o$ and of Products of Its Dehydration and Thermal Decomposition.* Radiochemistry, 2016. **58**(2): p. 124-127.
5. Cejka, J., *Infrared Spectroscopy and Thermal Analysis of the Uranyl Minerals.* Reviews in Mineralogy and Geochemistry, 1999. **38**(1): p. 521-622.
6. Allen, G.C. and Griffiths, A.J., *Vibrational Spectroscopy of Alkaline-Earth Metal Uranate Compounds.* Journal of the Chemical Society, Dalton Transactions, 1979(2): p. 315-319.
7. Reed, D.T., Clark, S.B., and Rao, L., *Actinide Speciation in High Ionic Strength Media: Experimental and Modeling Approaches to Predicting Actinide Speciation and Migration in the Subsurface*. 1999: Springer Science & Business Media.
8. Swanton, S.W. and Vines, S., *Equilibrium Leach Tests: Colloid Generation and the Association of Radionuclides with Colloids under Simulated Repository Conditions.* Colloids and Surfaces A: Physicochemical and Engineering Aspects, 2003. **217**(1–3): p. 71-79.
9. Betova, I., Beverskog, B., Bojinov, M., Kinnunen, P., Mäkelä, K., Pettersson, S.-O., and Saario, T., *Corrosion of Copper in Simulated Nuclear Waste Repository Conditions.* Electrochemical and Solid-State Letters, 2003. **6**(4): p. B19-B22.
10. Utton, C.A., Swanton, S.W., Schofield, J., Hand, R.J., Clacher, A., and Hyatt, N.C., *Chemical Durability of Vitrified Wasteforms: Effects of Ph and Solution Composition.* Mineralogical Magazine, 2012. **76**(8): p. 2919-2930.
11. Grivé, M., Duro, L., Domènech, C., and Salas, J., *Model of the Redox Conditions in the near Field of a Cementitious Geological Disposal Facility (Gdf)*, NDA, Editor. 2009, Amphos21. p. 1-144.
12. Baston, G.M.N., Cowper, M.M., and Marshall, T.A., *Sorption Properties of Aged Cements.* Mineralogical Magazine, 2012. **76**(8): p. 3411-3423.
13. Bots, P., Morris, K., Hibberd, R., Law, G.T.W., Mosselmans, J.F.W., Brown, A.P., Doutch, J., Smith, A.J., and Shaw, S., *Formation of Stable Uranium(Vi) Colloidal Nanoparticles in Conditions Relevant to Radioactive Waste Disposal.* Langmuir, 2014. **30**(48): p. 14396-14405.
14. Wieland, E. and Van Loon, L.R., *Cementitious near-Field Sorption Data Base for Performance Assessment of an Ilw Repository in Opalinus Clay*. 2003, Paul Scherrer Institut, CH-5232 Villigen PSI (Switzerland).
15. Wieland, E., Tits, J., and Bradbury, M.H., *The Potential Effect of Cementitious Colloids on Radionuclide Mobilisation in a Repository for Radioactive Waste.* Applied Geochemistry, 2004. **19**(1): p. 119-135.
16. Schwyn, B., Wersin, P., Berner, U., Wieland, E., and Neall, F., *Near-Field Chemistry of an Ilw Repository in Opalinus Clay.* Unpubl. Nagra Internal Rep. Nagra, Wettingen, Switzerland, 2003.
17. Neall, F., *Modelling of the near-Field Chemistry of the Sma Repository at the Wellenberg Site: Application of the Extended Cement Degradation Model*. 1994: NAGRA.
18. Burns, P.C. and Li, Y., *The Structures of Becquerelite and Sr-Exchanged Becquerelite.* American Mineralogist, 2002. **87**(4): p. 550-557.
19. Kissinger, H.E., *Reaction Kinetics in Differential Thermal Analysis.* Analytical Chemistry, 1957. **29**(11): p. 1702-1706.
20. Dousma, J., Van den Hoven, T.J., and De Bruyn, P.L., *The Influence of Chloride Ions on the Formation of Iron(Iii) Oxyhydroxide.* Journal of Inorganic and Nuclear Chemistry, 1978. **40**(6): p. 1089-1093.
21. Amonette, J., Holdren Jr, G., Krupa, K., and Lindenmeier, C., *Assessing the Environmental Availability of Uranium in Soils and Sediments*. 1994, Nuclear Regulatory Commission, Washington, DC (United States). Div. of Waste Management; Pacific Northwest Lab., Richland, WA (United States).

22. Chadwick, D., *Uranium 4f Binding Energies Studied by X-Ray Photoelectron Spectroscopy.* Chemical Physics Letters, 1973. **21**(2): p. 291-294.
23. Allen, G., Griffiths, A., and Lee, B., *X-Ray Photoelectron Spectroscopy of Alkaline Earth Metal Uranate Complexes.* Transition Metal Chemistry, 1978. **3**(1): p. 229-233.